

NASA Contractor Report 3098

NASA-CR-3098

19790024992

Rotary Balance Data for a Typical  
Single-Engine General Aviation  
Design for an Angle-of-Attack  
Range of  $8^{\circ}$  to  $90^{\circ}$   
II - Low-Wing Model B

William Bihrlé, Jr., and Randy S. Hultberg

CONTRACT NAS1-14849  
SEPTEMBER 1979

LIBRARY COPY

OCT 30 1979

LANGLEY RESEARCH CENTER  
LIBRARY, NASA  
HAMPTON, VIRGINIA

**NASA**







3 1176 01455 3508

## NASA Contractor Report 3098

# Rotary Balance Data for a Typical Single-Engine General Aviation Design for an Angle-of-Attack Range of $8^\circ$ to $90^\circ$

## II - Low-Wing Model B

William Bihrlle, Jr., and Randy S. Hultberg  
*Bihrlle Applied Research, Inc.*  
*Jericho, New York*

Prepared for  
Langley Research Center  
under Contract NAS1-14849



National Aeronautics  
and Space Administration

Scientific and Technical  
Information Branch

1979



## SUMMARY

Aerodynamic characteristics obtained in a rotational flow environment utilizing a rotary balance located in the Langley spin tunnel are presented in plotted form for a 1/6.5-scale, single-engine, low-wing, general aviation airplane model. The configurations tested included the basic airplane, various wing leading-edge devices, tail designs, and rudder control settings as well as airplane components. Data are presented without analysis for an angle-of-attack range of  $8^{\circ}$  to  $90^{\circ}$  and clockwise and counter-clockwise rotations covering an  $\frac{\Omega b}{2V}$  range from 0 to 0.85.

## INTRODUCTION

The NASA Langley Research Center has initiated a broad general aviation stall/spin research program which includes spin-tunnel and free-flight radio control model tests, as well as full-scale flight tests for a number of configurations typical of light, general aviation airplanes. To support this effort, rotary balance wind tunnel force tests covering these same configurations will be conducted to establish a data base for analysis of model and full-scale flight results, and to develop design charts for desirable stall/spin characteristics.

A 1/6.5-scale, single-engine, general aviation airplane model, referred to as model B, having a low-wing location was tested in a rotational flow environment utilizing a rotary balance located in the Langley spin tunnel. This report presents the data obtained for the basic configuration, various wing leading-edge devices, tail designs and rudder control settings as well as airplane components. Data for model B having a high-wing location are presented in reference 1.

## SYMBOLS

The units for physical quantities used herein are presented in the International System of Units (SI) and U.S. Customary Units. The measurements were made in the U.S. Customary Units; equivalent dimensions were determined by using the conversion factors given in reference 2.

$b$	wing span, m (ft)
$\bar{c}$	mean aerodynamic chord, cm (in.)
$C_L$	lift-force coefficient, $\frac{\text{Lift force}}{qS}$
$C_N$	normal-force coefficient, $\frac{\text{Normal force}}{qS}$
$C_A$	axial-force coefficient, $\frac{\text{Axial force}}{qS}$
$C_Y$	side-force coefficient, $\frac{\text{Side force}}{qS}$
$C_l$	rolling moment coefficient, $\frac{\text{Rolling moment}}{qSb}$
$C_m$	pitching-moment coefficient, $\frac{\text{Pitching moment}}{qS\bar{c}}$
$C_n$	yawing-moment coefficient, $\frac{\text{Yawing moment}}{qSb}$
$q$	free-stream dynamic pressure, N/m <sup>2</sup> (lb/ft <sup>2</sup> )
$S$	wing area, m <sup>2</sup> (ft <sup>2</sup> )
$V$	free-stream velocity, m/sec (ft/sec)
$\alpha$	angle of attack, deg
$\beta$	angle of sideslip, deg
$\Omega$	angular velocity about spin axis, rad/sec
$\frac{\Omega b}{2V}$	spin coefficient, positive for clockwise spin
$\delta_a$	aileron deflection, positive when right aileron is down $(\delta_{a_{\text{right}}} - \delta_{a_{\text{left}}})/2$ , deg
$\delta_e$	elevator deflection, positive when trailing edge is down, deg

$\delta_r$  rudder deflection, positive when trailing edge is to left, deg

Abbreviations:

cg center of gravity

LE leading edge

SR spin radius

TE trailing edge

TEST EQUIPMENT

A rotary balance measures the forces and moments acting on an airplane while subjected to rotational flow conditions; the background for this apparatus is discussed in reference 3. A photograph and sketch of the rotary balance apparatus installed in the Langley spin tunnel are shown in figures 1 and 2, respectively. The rotating portion of the balance system, mounted on a horizontal supporting boom which is hinged at the wall, is moved from the wall to the center of the tunnel by cables. The rotary arm of the balance system, which rotates about a vertical axis, is attached to the outer end of the horizontal supporting boom and is driven by a drive shaft through couplings and gears.

A test model is mounted on a strain gauge balance which is affixed to the bottom of the rotary balance apparatus. Controls located outside the tunnel are used to activate motors on the rig which position the model to the desired attitude. The angle-of-attack range of the rig is 8 to 90 degrees and the sideslip angle range is  $\pm 15$  degrees. The spin radius and the lateral displacement motors allow the operator to position the moment center of

the balance on the spin axis or at a specific distance from the spin axis. This is done for each combination of angle of attack and sideslip angle. The general practice is to mount the moment center of the balance at the cg location about which the aerodynamic moments are desired. Electrical current from the balance, and to the motors on the rig, is conducted through slip-rings located at the rig head. Examples of how the rig is positioned for different angle of attack and sideslip angles are shown in figures 2a and 2b, respectively.

The model can be rotated up to 90 rpm in either direction. By using different rotational speeds and a specific airflow in the tunnel, the motions of a steady spinning airplane can be simulated. The aerodynamic forces and moments can then be measured for values of  $\frac{\Omega b}{2V}$ , including the case of  $\frac{\Omega b}{2V} = 0$ , where static aerodynamic forces and moments can be obtained.

A NASA six-component strain gauge balance is mounted inside the model and measures the normal, lateral and longitudinal forces and the yawing, rolling and pitching moments acting about the model body axis. The interactions that exist between the six components are available from balance calibration tests and are accounted for after the balance voltages are converted to forces and moments.

The data acquisition, reduction and presentation system for the rotary balance set-up is composed of a 12-channel scanner/voltmeter, a mini-computer and a plotter. With this equipment,

on-line digital print-out and/or graphical plots of data are possible.

#### TEST PROCEDURES

Rotary aerodynamic data are obtained in two steps. The first step is to record the inertial forces and moments (tares) acting on the model at different attitudes and rotational speeds. To accomplish this, a covered bird-cage like structure is mounted to the upper rig which encloses the model without touching it. In this manner, the air immediately surrounding the model is rotated with it. As the rig is rotated at the desired attitude and rate, the inertial forces and moments generated by the model are measured and stored on magnetic tape for later use.

The second step in the data-gathering process is to measure aerodynamic and inertial forces at different attitudes and rotational speeds for a selected tunnel velocity with, of course, the cage structure removed. The tares are subtracted from these values, and the remaining aerodynamic forces and moments are then converted to coefficient form and stored on magnetic tape.

#### MODEL

A 1/6.5-scale fiberglass/aluminum model of a configuration considered to be a typical low-wing, single-engine, light general aviation airplane was tested in the present study. A three-view drawing of this model is shown in figure 3, dimensional characteristics of the model are presented in Table I, and a photograph of the model installed on the rotary balance located in the Langley spin tunnel is presented in figure 1.

The model was fabricated such that various airplane components were removable for component build-up tests and for testing alternate wing leading edges and tail configurations. In addition, allowance was made for attaching various fuselage modifications.

The four tail configurations tested involved different locations of the horizontal tail as shown in figure 4. The fuselage shape and wing leading-edge modifications tested are shown in figures 5 and 6, respectively.

The model control surfaces could be set at any position prior to the test. The maximum deflections for the control surfaces were:

Elevator, deg	28 up, 23 down
Rudder, deg	25 right, 25 left
Aileron, deg	20 up, 15 down

#### TEST CONDITIONS

The tests were conducted in the spin tunnel at a tunnel velocity of 7.62m/sec (25 ft/sec) which corresponds to a Reynolds number of 119,378 based on the model mean aerodynamic chord. Unless noted otherwise in Table II, all the configurations were tested through an angle of attack range of 8 to 90° at a zero sideslip angle with the spin axis passing through the full-scale airplane cg location of  $.25\bar{c}$  for angles of attack above 30°. For angles of attack below 35°, the spin axis was set 99 cm (39 in.) forward of the cg. Consequently, data was obtained for both a 0 and 99 cm (39 in.) spin radius at angles of attack of 30 and 35°. At each spin attitude, measurements



were obtained for nominal  $\frac{\Omega b}{2V}$  values of .1, .2, .3, .4, .45, .55, .65, .75 and .85 in both clockwise and counter-clockwise directions, as well as for  $\frac{\Omega b}{2V} = 0$  (static value).

#### DATA PRESENTATION

Table II identifies the configurations tested and the corresponding appendix figure numbers which present the aerodynamic data. The aerodynamic coefficients vs.  $\frac{\Omega b}{2V}$  are presented for each configuration in six sequentially numbered figures in the following order:  $C_n$ ,  $C_\ell$ ,  $C_m$ ,  $C_N$ ,  $C_Y$  and  $C_A$ . Each figure, in turn, consists of four pages which present the subject aerodynamic coefficient vs.  $\frac{\Omega b}{2V}$  for the following angles of attack and spin radii, unless noted otherwise in Table II.

- a)  $\alpha = 8, 10, 12, 14, 16$  deg      SR= 99 cm (39 in.)
- b)  $\alpha = 18, 20, 25, 30, 35$  deg      SR= 99 cm (39 in.)
- c)  $\alpha = 30, 35, 40, 45, 50$  deg      SR= 0
- d)  $\alpha = 55, 60, 70, 80, 90$  deg      SR= 0

All the moment data are presented for a cg position of 0.25c.

Lift coefficient as a function of angle of attack for zero rotation rate is presented at the end of the Appendix for several configurations cited in Table II.

## REFERENCES

1. Bihrlé, William, Jr.; Hultberg, Randy S.: Rotary Balance Data for a Typical Single-Engine General Aviation Design for an Angle-of-Attack Range of  $8^{\circ}$  to  $90^{\circ}$ . I- High-Wing Model B. NASA CR 3097, 1979.
2. Mechtly, E.A.: The International System of Units - Physical Constants and Conversion Factors. NASA SP-7012, 1973.
3. Bihrlé, William, Jr.; Hultberg, Randy S.; and Mulcay, William: Rotary Balance Data for a Typical Single-Engine Low-Wing General Aviation Design for an Angle-of-Attack Range of  $30^{\circ}$  to  $90^{\circ}$ . NASA CR 2972, 1978.

TABLE I.- DIMENSIONAL CHARACTERISTICS OF THE BASIC MODEL

Overall length, m (ft) . . . . . 1.24 (4.05)

Wing:

Span, m (ft) . . . . . 1.68 (5.51)

Area, m<sup>2</sup> (ft<sup>2</sup>). . . . . .38 (4.12)

Root chord, cm (in.). . . . . 25.02 (9.85)

Tip chord, cm (in.) . . . . . 17.39 (6.85)

Mean aerodynamic chord, cm (in.). . . . . 22.81 (8.98)

Leading edge of  $\bar{c}$ , distance rearward of leading

edge of root chord, cm (in.). . . . . .53 (.21)

Aspect ratio . . . . . 7.37

Dihedral at 0.25  $\bar{c}$  along top surface, deg . . . . 1.7

Incidence:

Root, deg . . . . . 1.5

Tip, deg . . . . . -1.5

Airfoil section . . . . . NACA 2412

Horizontal tail:

Span, m (ft). . . . . 0.53 (1.74)

Incidence, deg . . . . . -3.5

Airfoil section:

Root . . . . . NACA 0009

Tip . . . . . NACA 0006

Vertical tail:

Airfoil section:

Root . . . . . NACA 0009

Tip . . . . . NACA 0006

TABLE II.- CONFIGURATIONS TESTED AND FIGURE INDEX  
(Unless noted otherwise, all configurations tested through  $\alpha = 8$  to  $90^\circ$  at  $\beta = 0^\circ$ .)

FIGURE NO.	CONFIGURATION	$\delta_e$ deg	$\delta_a$ deg	$\delta_r$ deg	REMARKS
<sup>a</sup> A1-A6	Basic	0	0	0	$\alpha = 8-50^\circ$ only
A7-A12	↓	↓	↓	-25	
A13-A18	↓	-28	↓	-18	
A19-A24	#1 Horizontal tail	0	↓	0	
A25-A30	↓	↓	↓	-25	
A31-A36	#2 Horizontal tail	↓	↓	0	
A37-A42	↓	↓	↓	-25	
A43-A48	T tail	↓	↓	0	
A49-A54	↓	↓	↓	-25	
A55-A60	Sharp-edged fuselage bottom aft of wing TE	↓	↓	0	
A61-A66	Sharp-edged fuselage bottom aft of engine cowling	↓	↓	↓	
A67-A72	Wing off	↓	↓	↓	
<sup>a</sup> A73-A78	Full-span LE wing droop having moderate nose radius	↓	↓	↓	
<sup>a</sup> A79-A84	Outboard LE wing droop	↓	↓	↓	

<sup>a</sup>  $C_L$  vs.  $\alpha$  presented in figure A85.

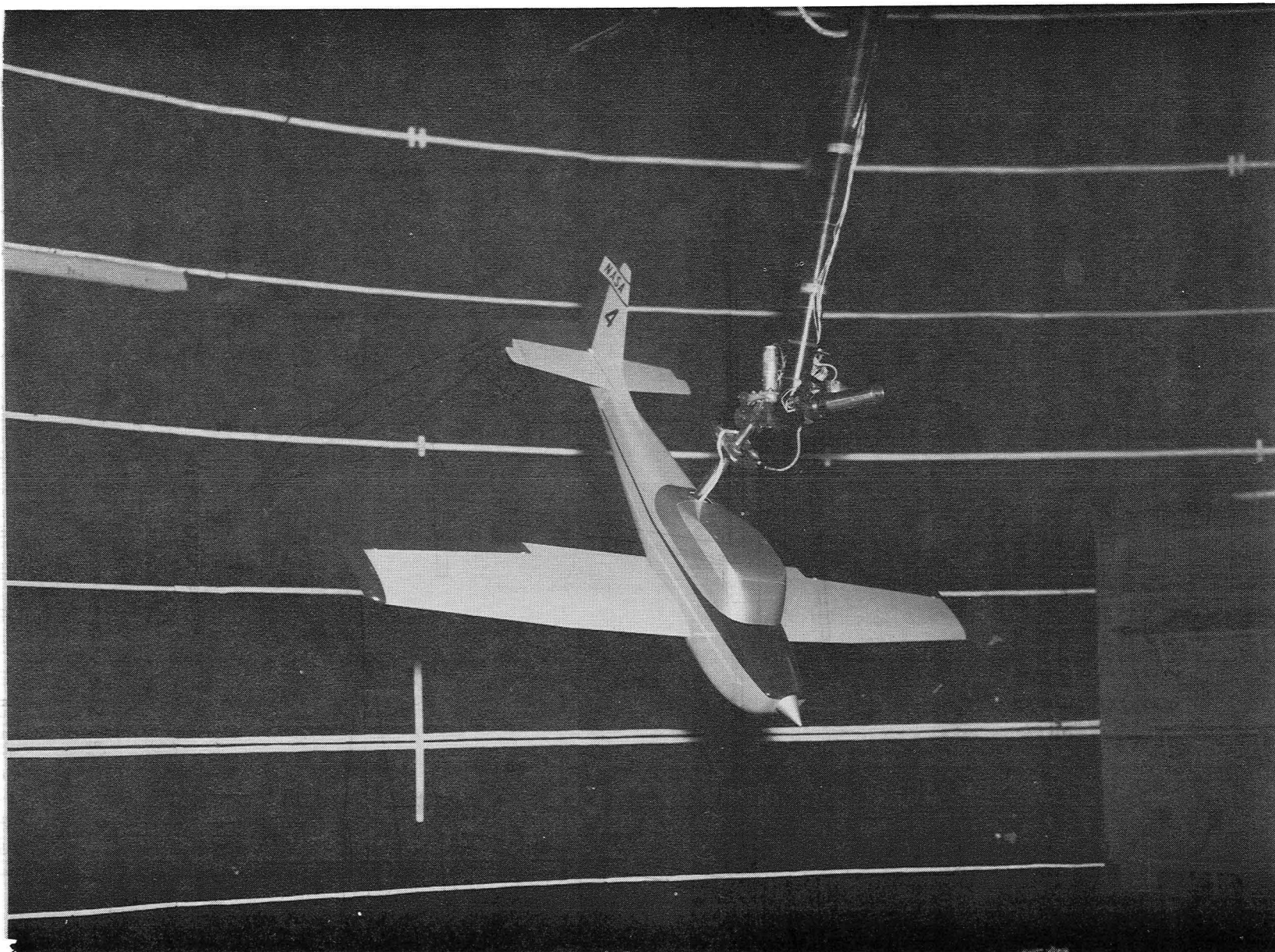
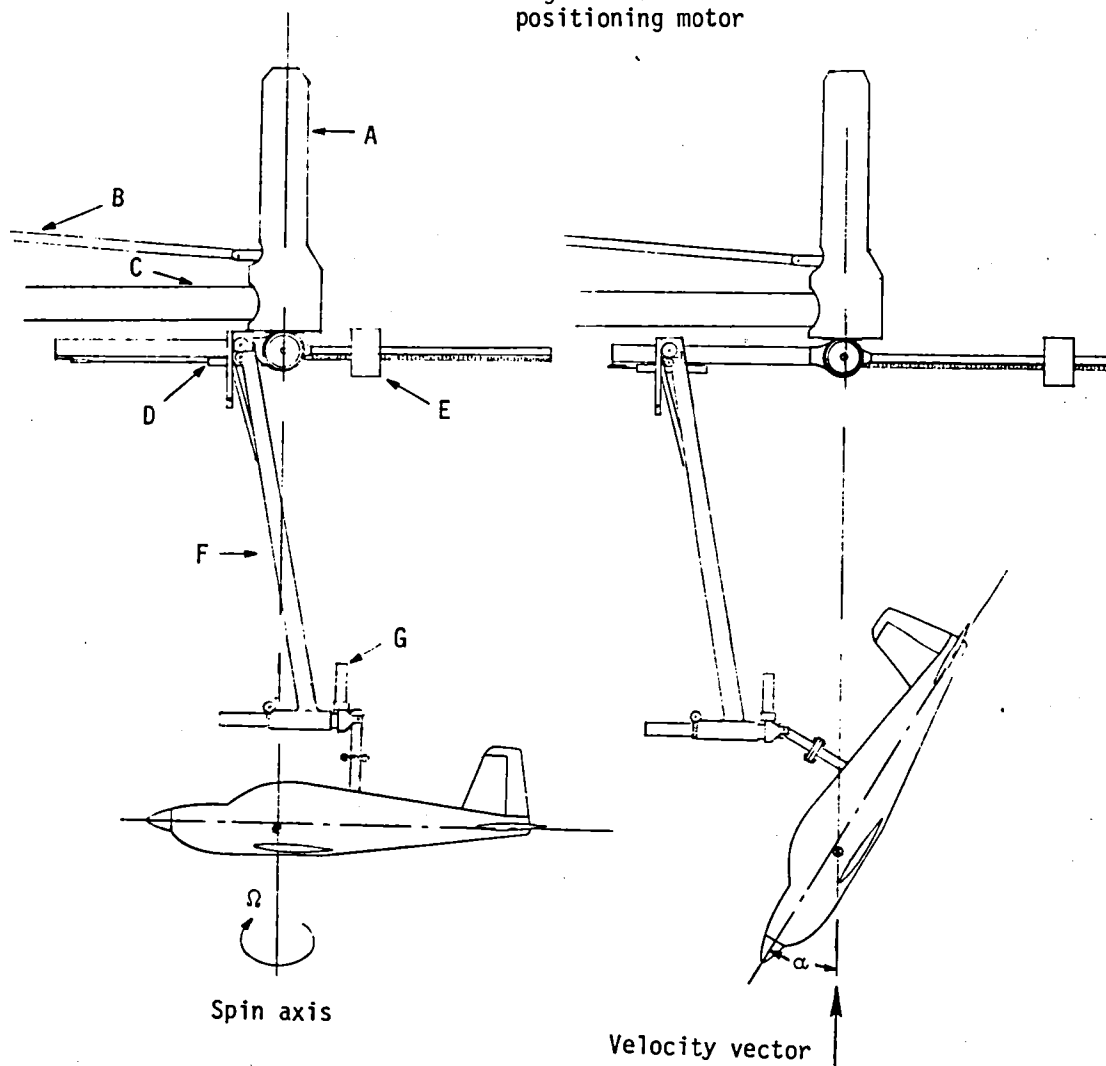


Figure 1.- Photograph of 1/6.5-scale model installed on rotary balance apparatus.

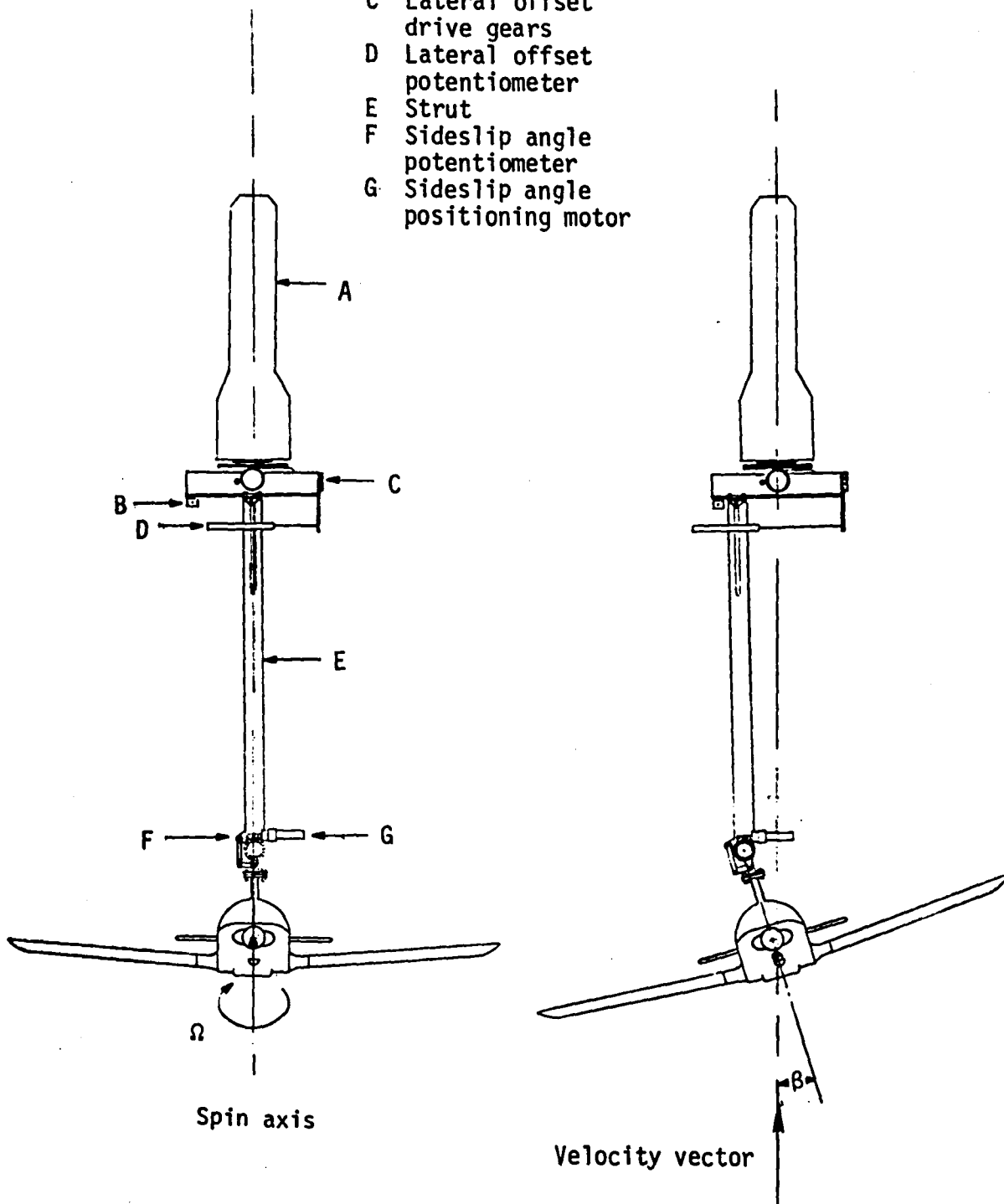
- A Slip ring housing
- B Drive shaft
- C Support boom
- D Spin radius offset potentiometer
- E Counterweight
- F Strut
- G Angle of attack positioning motor



(a) Side view of model.

Figure 2.- Sketch of rotary balance apparatus.

- A Slip ring housing
- B Spin radius offset potentiometer
- C Lateral offset drive gears
- D Lateral offset potentiometer
- E Strut
- F Sideslip angle potentiometer
- G Sideslip angle positioning motor



(b) Front view of model.

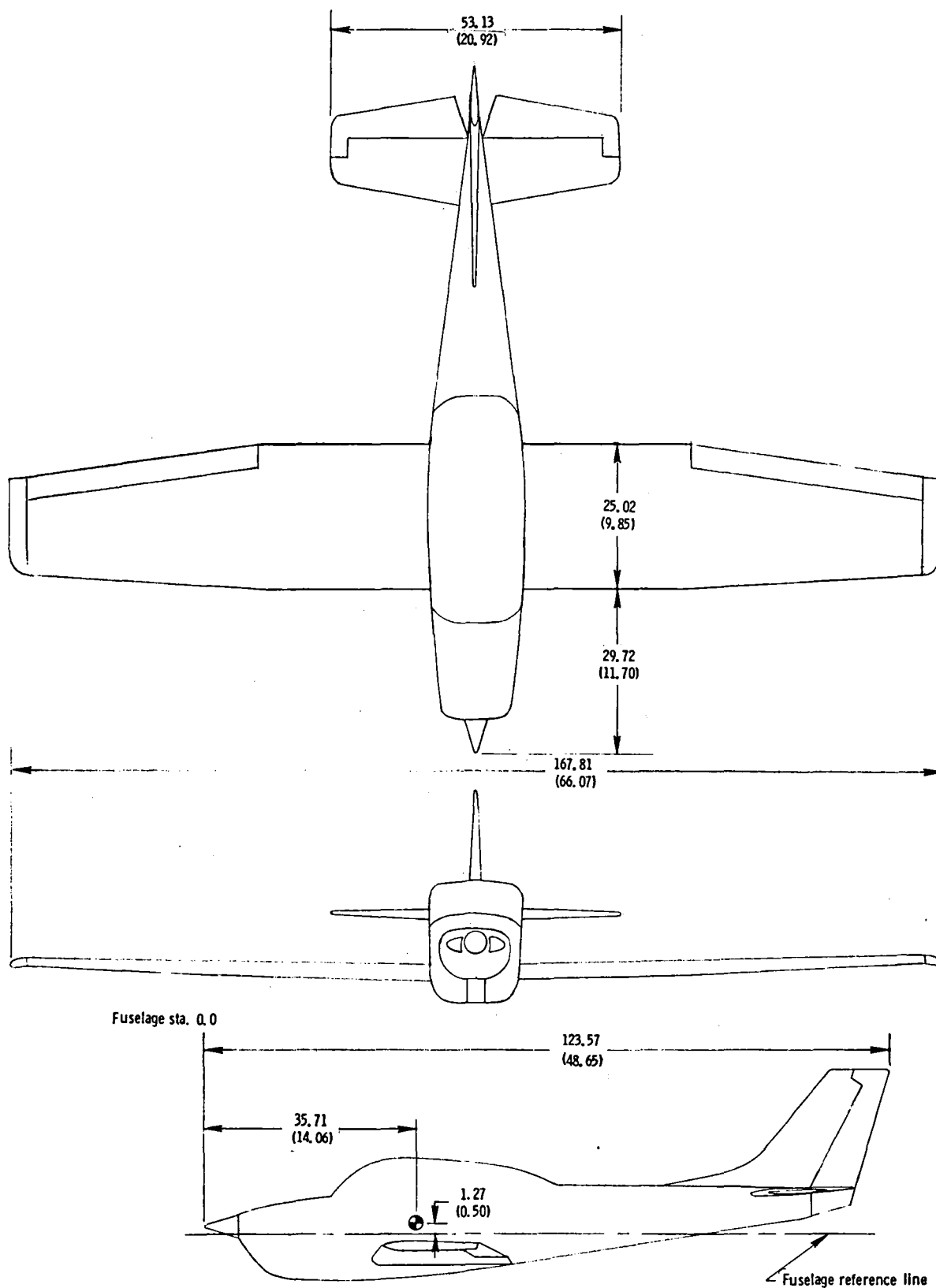
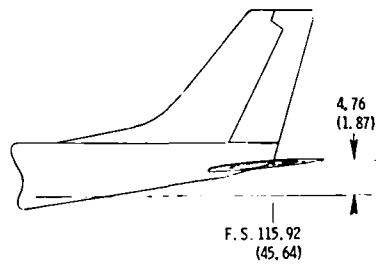
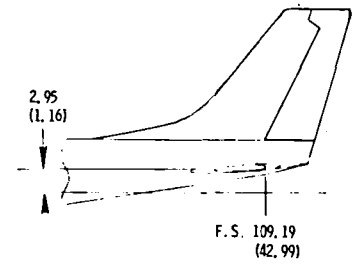


Figure 3. - Three-view drawing of basic 1/6.5-scale low-wing general aviation model B. Center-of-gravity positioned at 0.25  $\bar{c}$ . Dimensions are given in centimeters(inches), model scale.

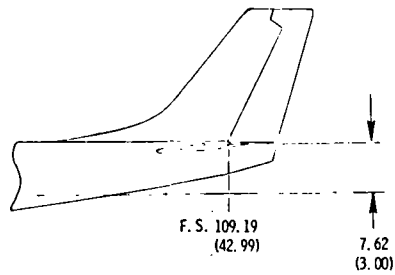




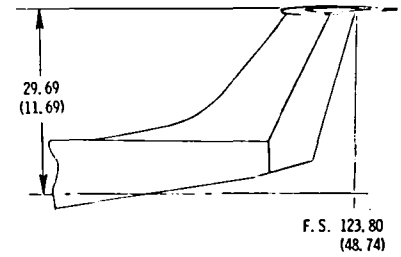
(a) Tail 1



(b) Tail 2



(c) Basic tail



(d) T-tail

Figure 4. -Tail configurations tested on model. Dimensions are given in centimeters (inches), model scale.

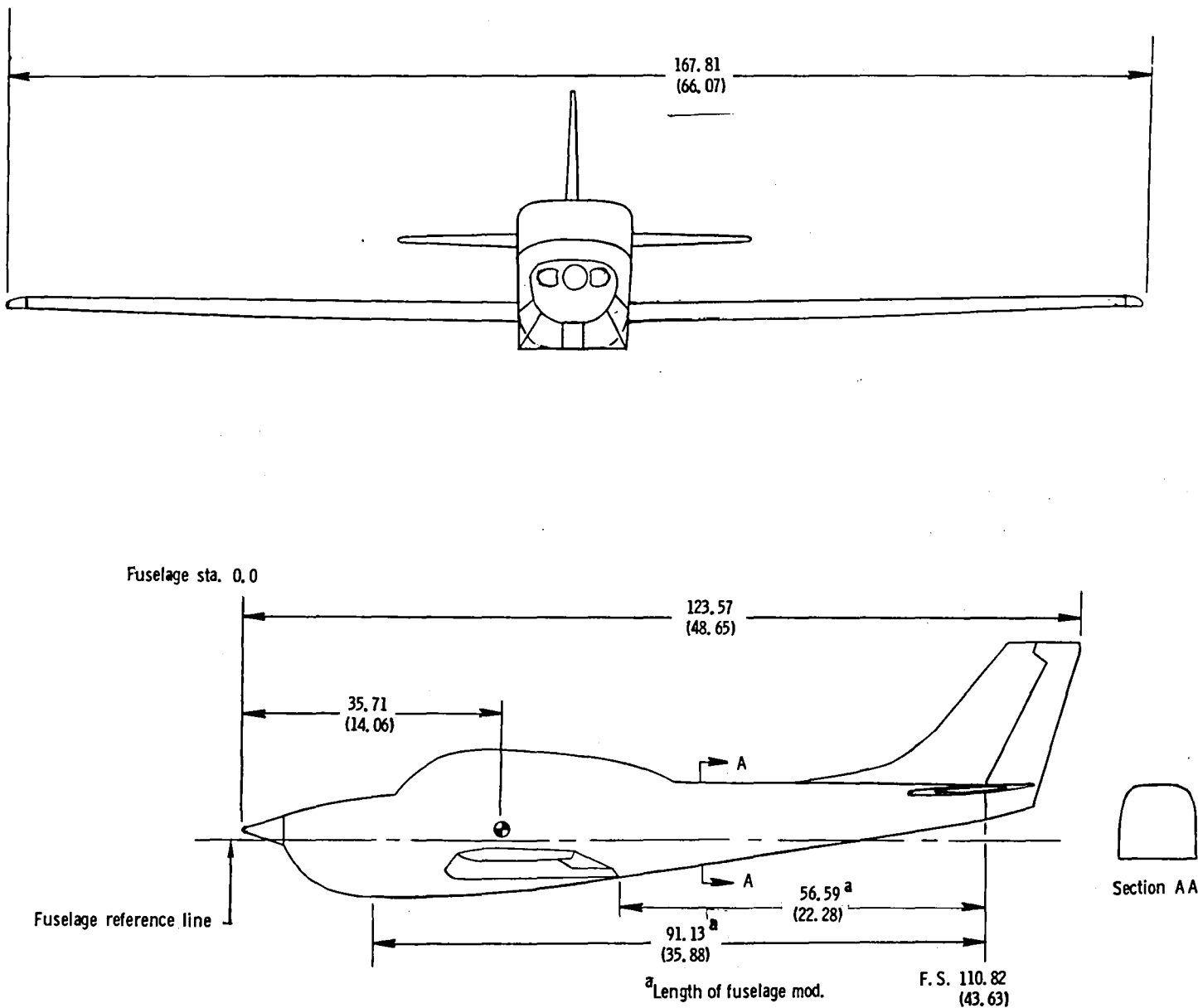
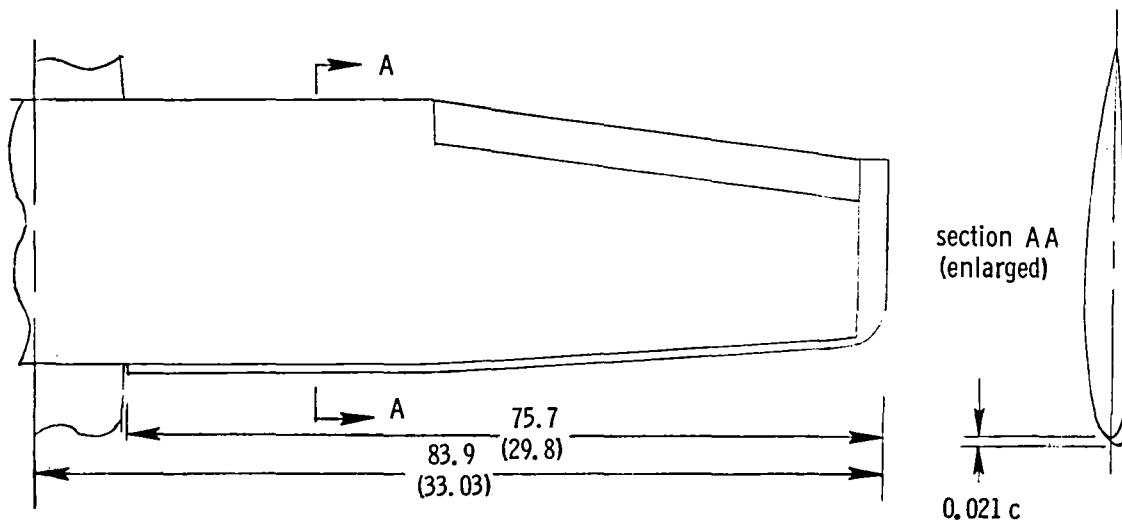
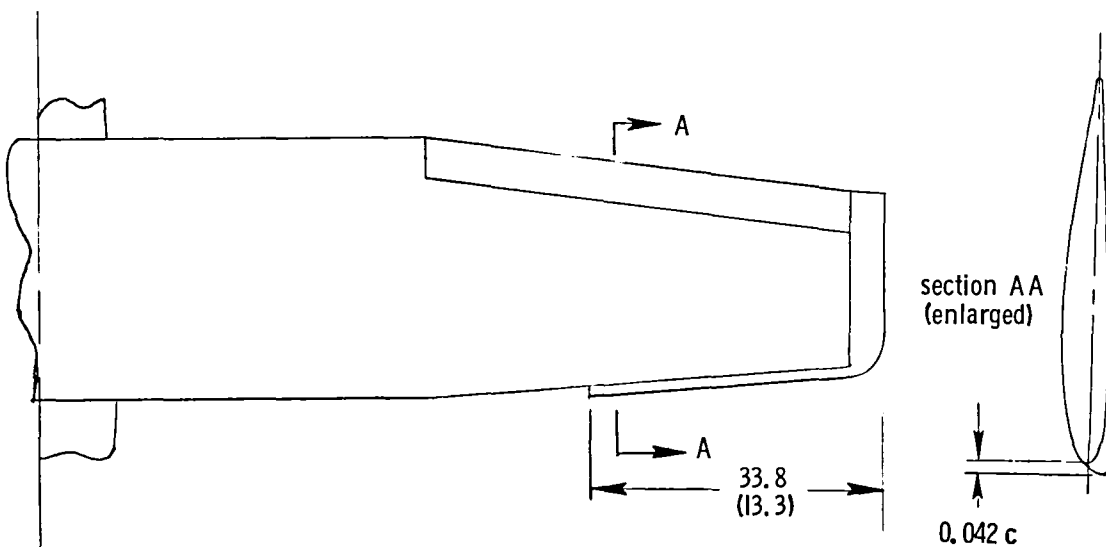


Figure 5. - Fuselage shape modifications tested on model. Dimensions are given in centimeters (inches), model scale.



(a) Full-span LE modification with moderate nose radius.

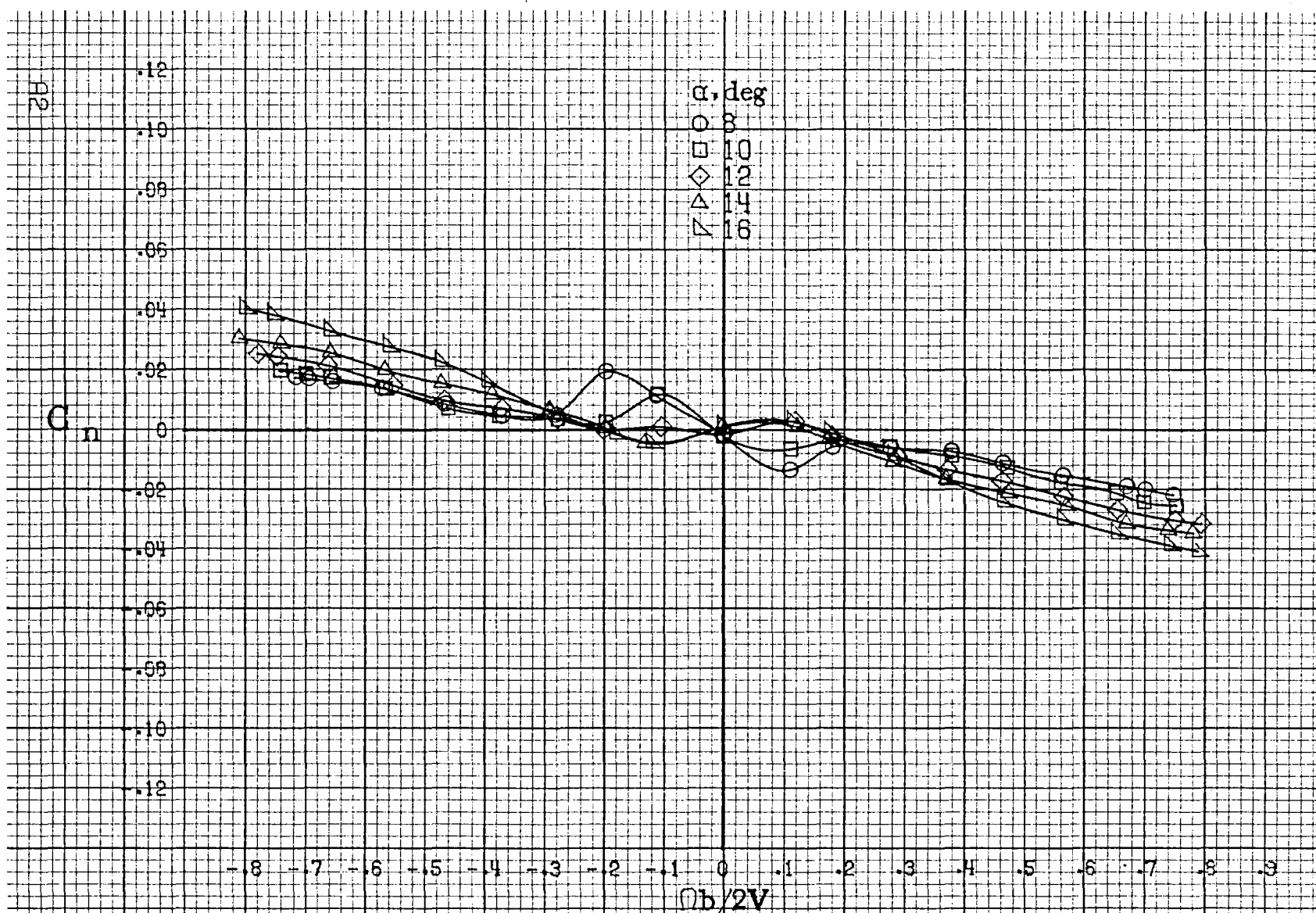


(b) Outboard LE wing droop.

Figure 6. - Wing leading-edge modifications tested on model. Dimensions are given in centimeters (inches), model scale.

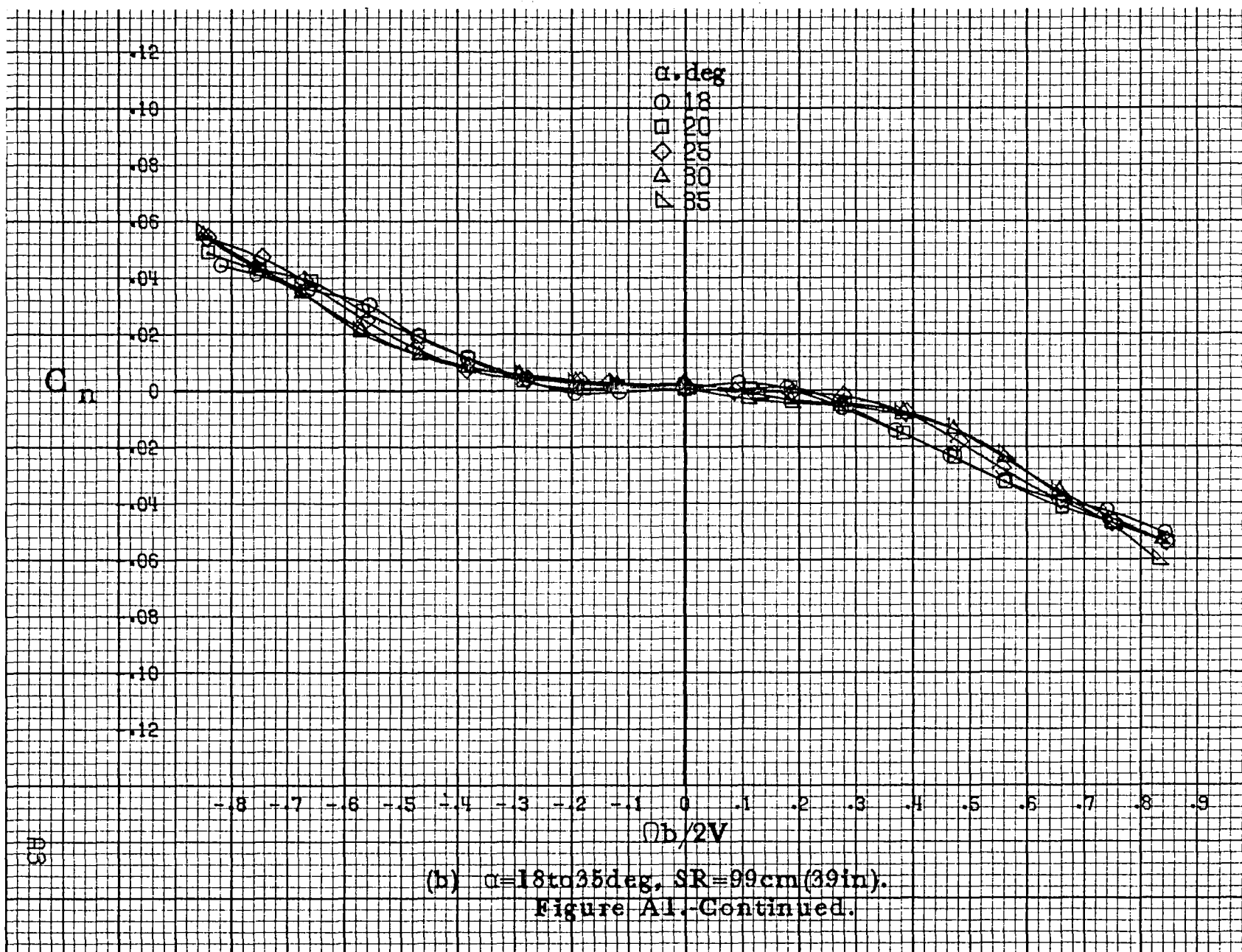


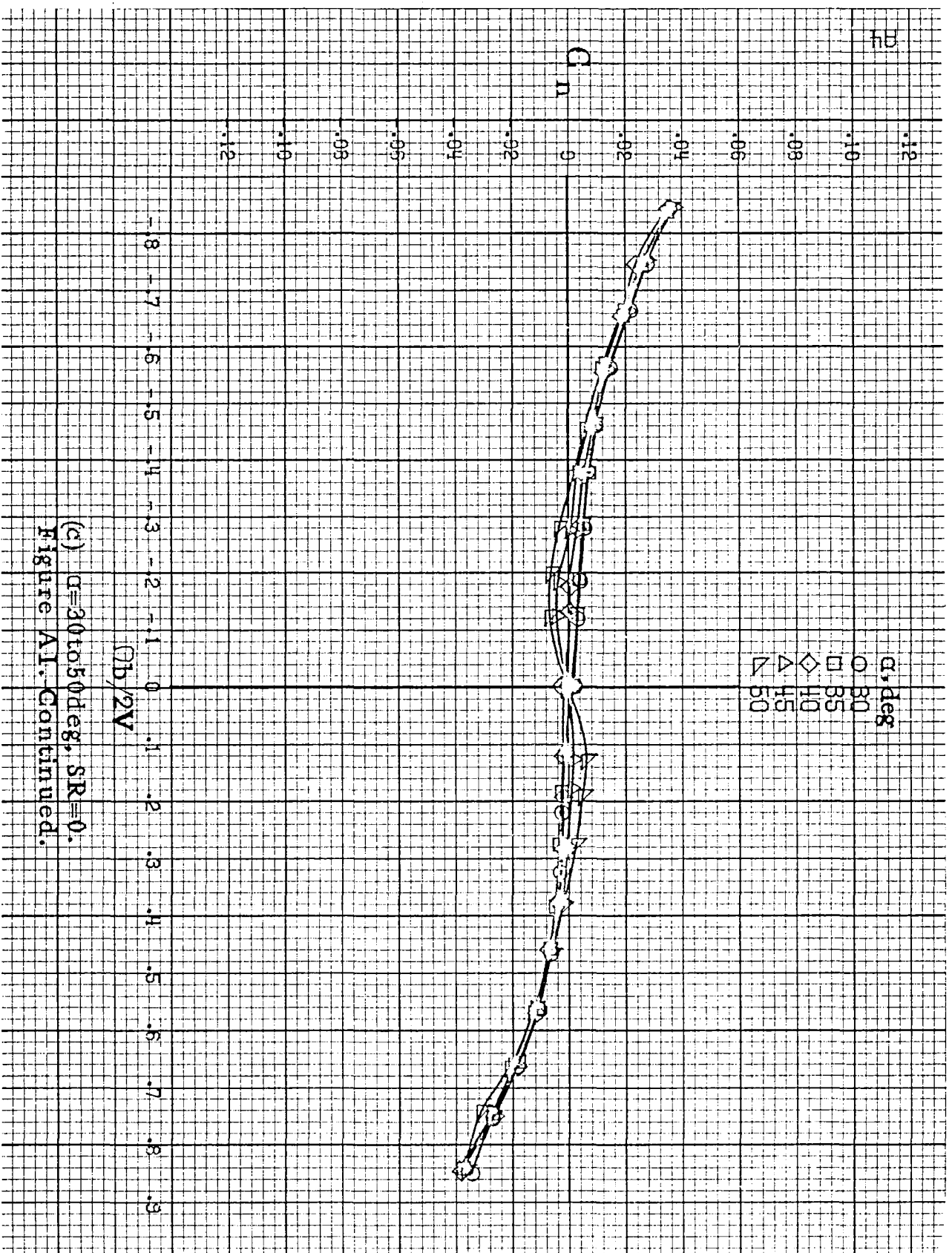
## APPENDIX



(a)  $\alpha=8$  to  $16^\circ$ ,  $SR=99\text{cm}$  (39in).

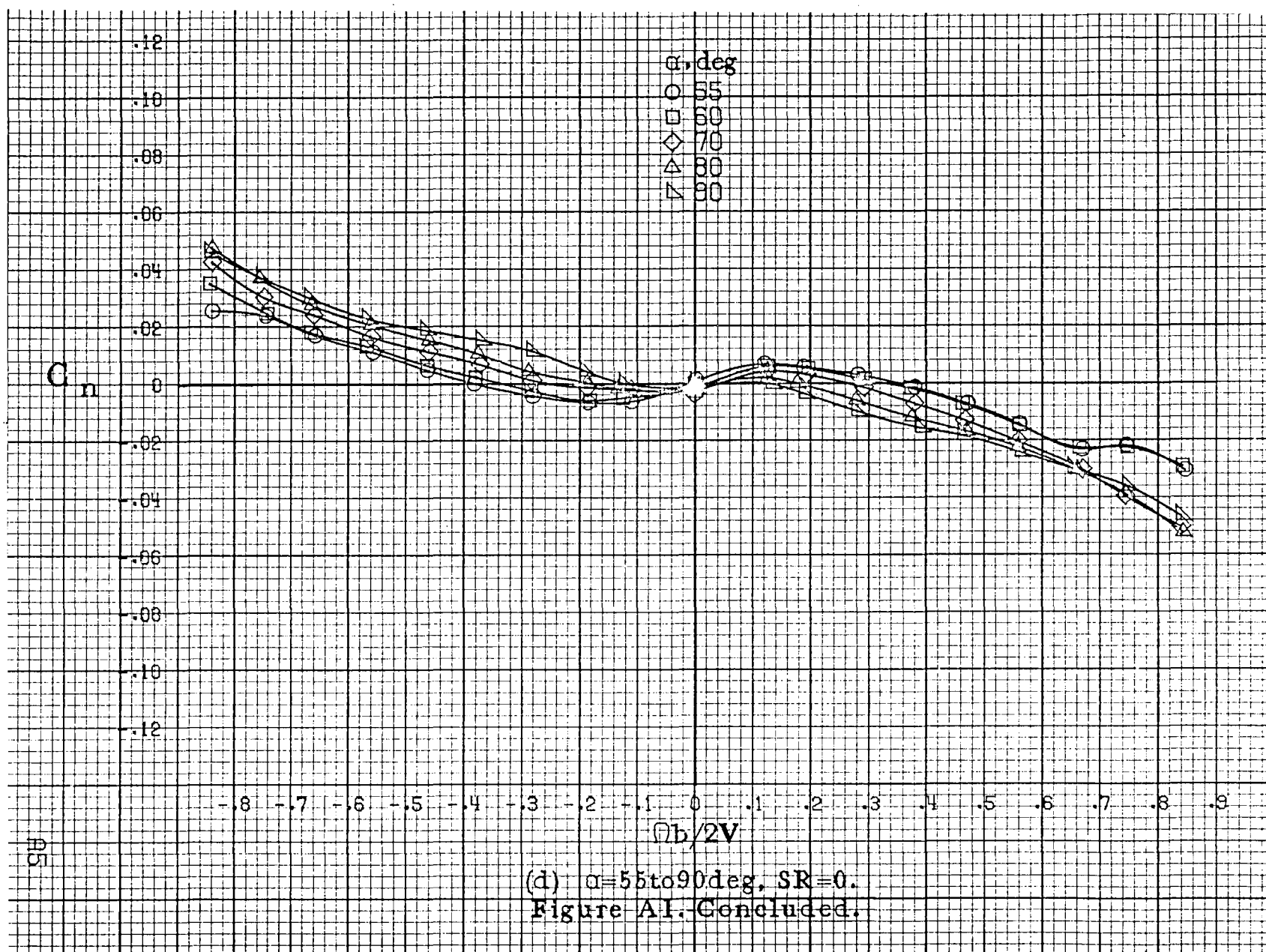
Figure A1.-Effect of rotation rate and angle of attack on yawing moment coefficient for basic configuration.  $\delta_e=0^\circ$ ,  $\delta_a=0^\circ$ ,  $\delta_r=0^\circ$ ,  $\beta=0^\circ$ .

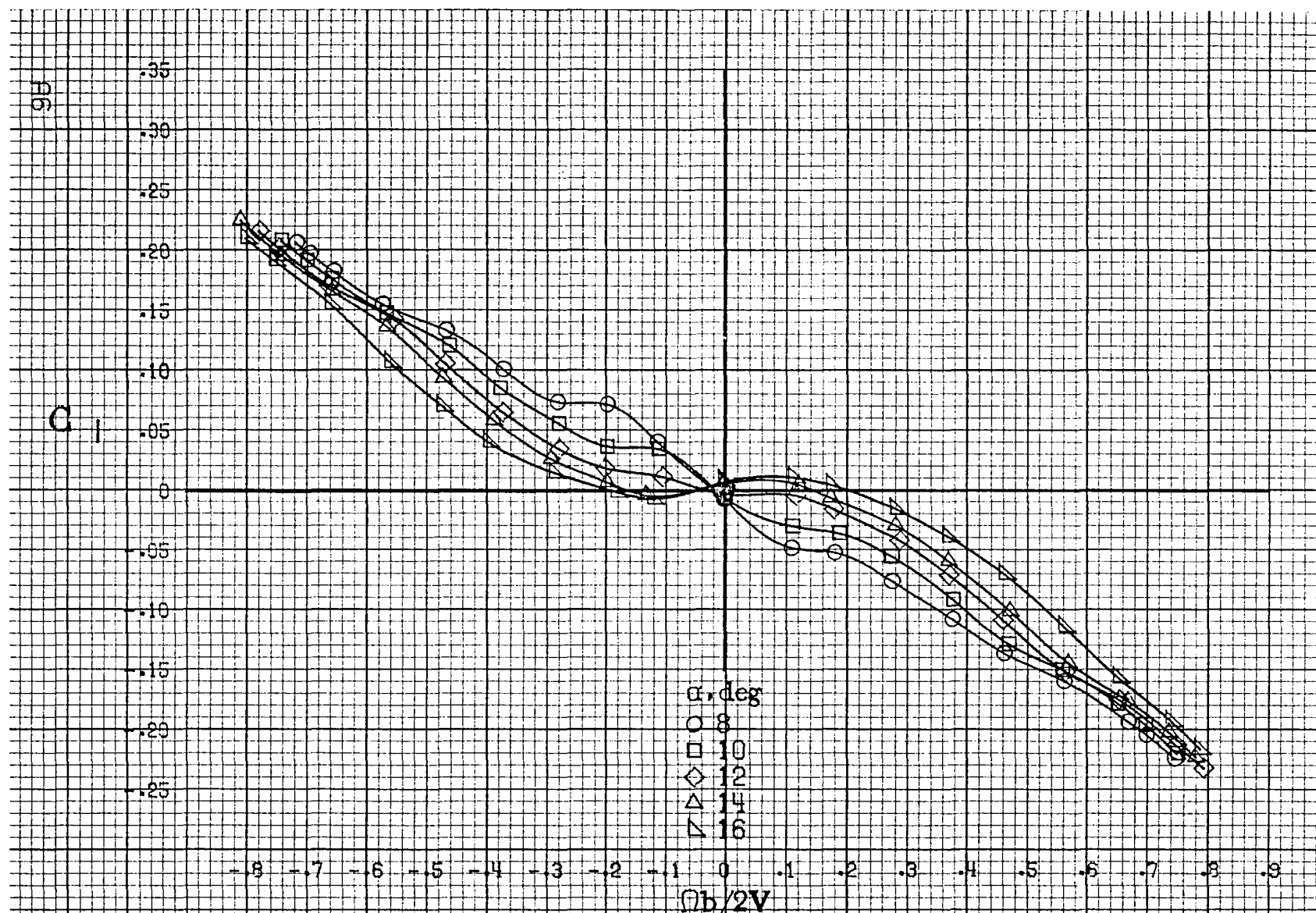




(c)  $\alpha=30$  to  $50^\circ$ ,  $SR=0$ .  
Figure A1. Continued.

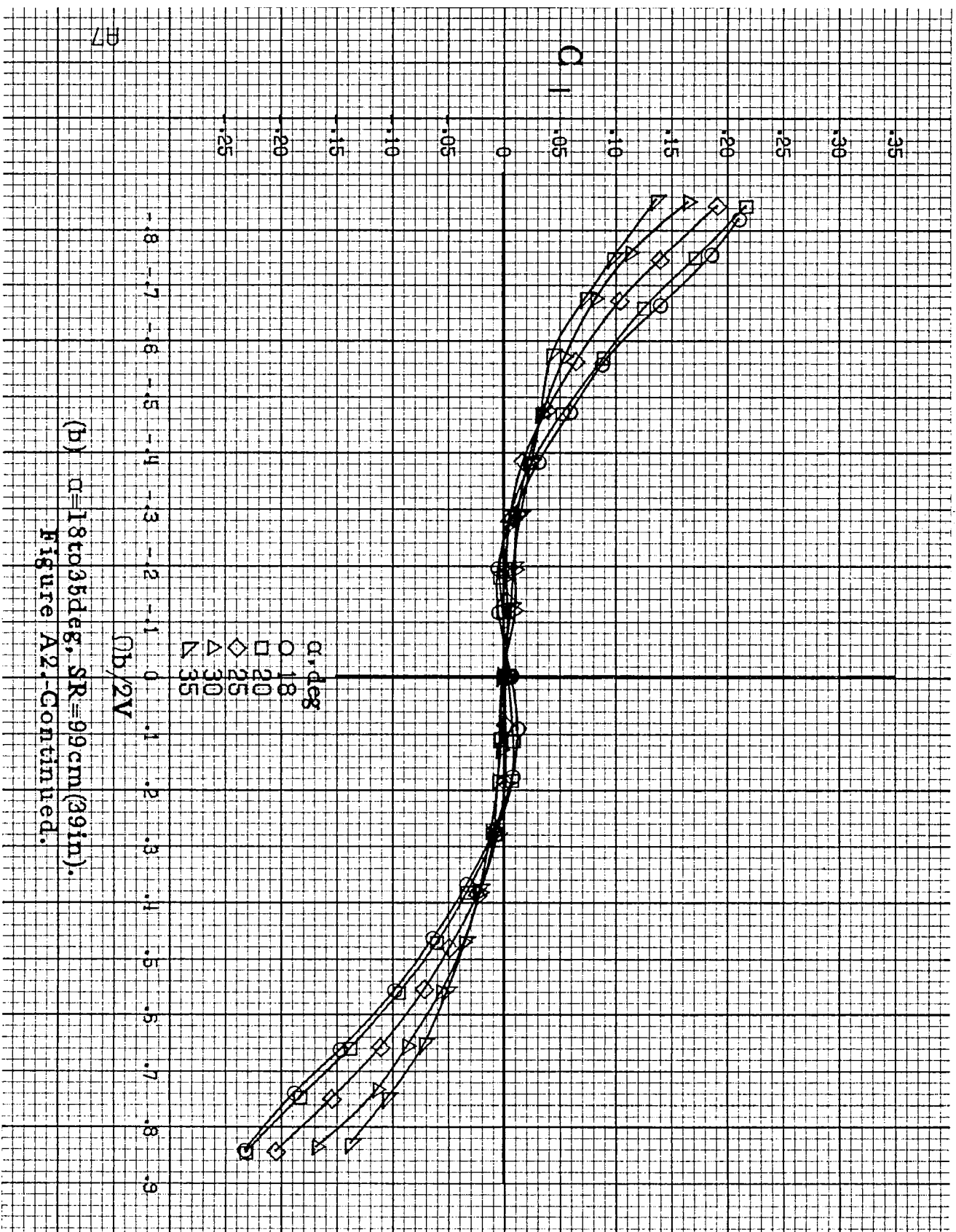




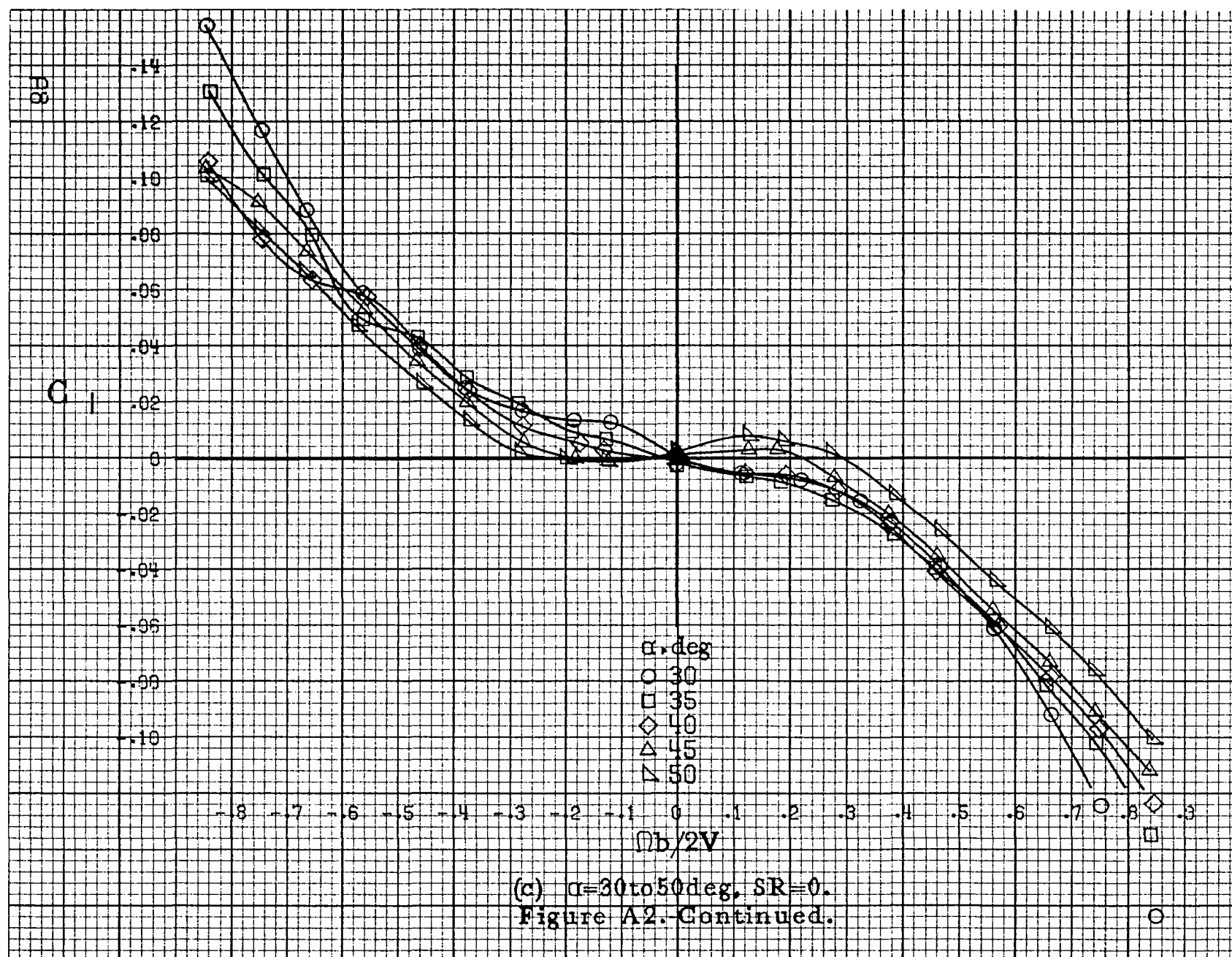


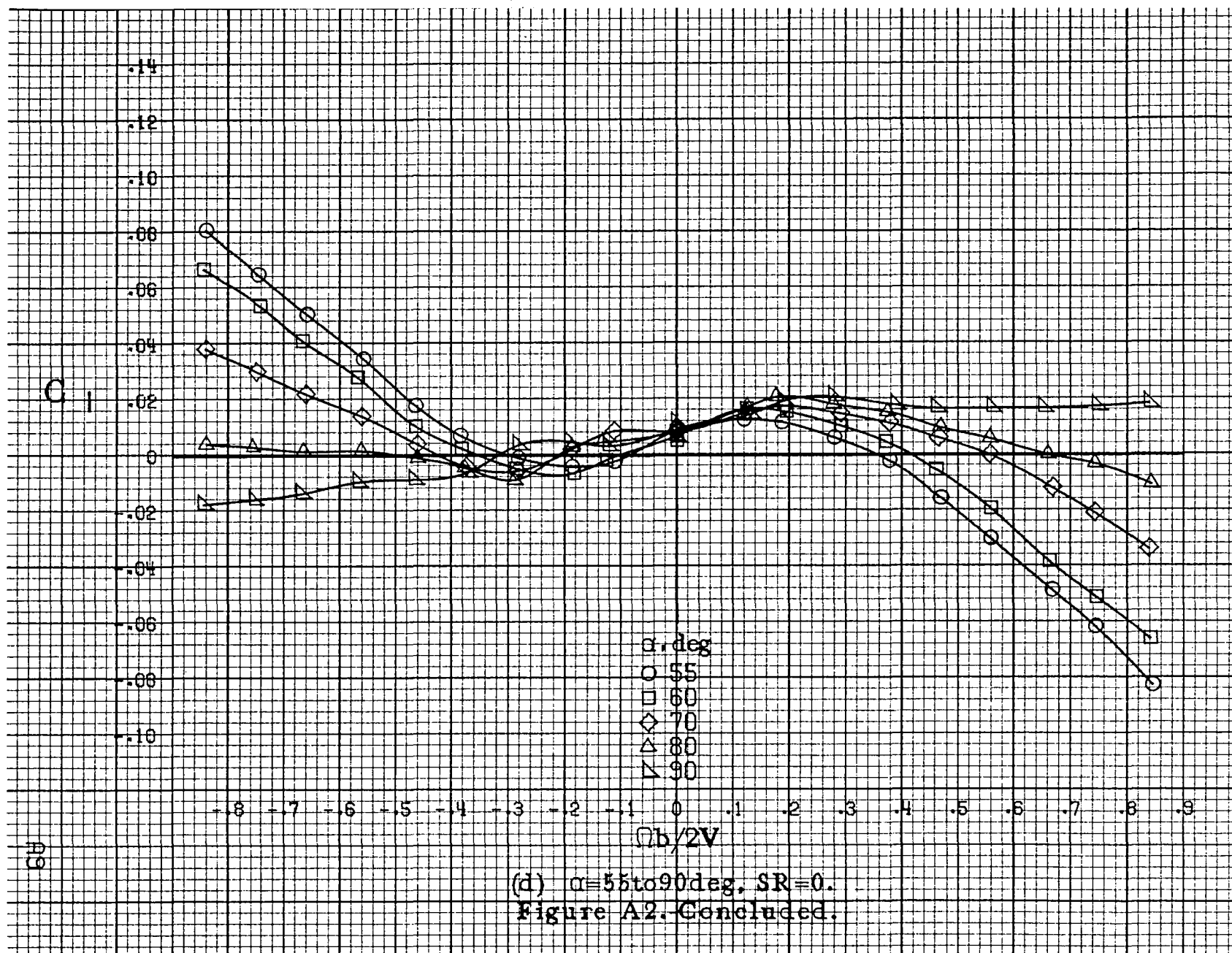
(a)  $\alpha=8$  to  $16^\circ$ ,  $SR=99\text{cm}(39\text{in})$ .

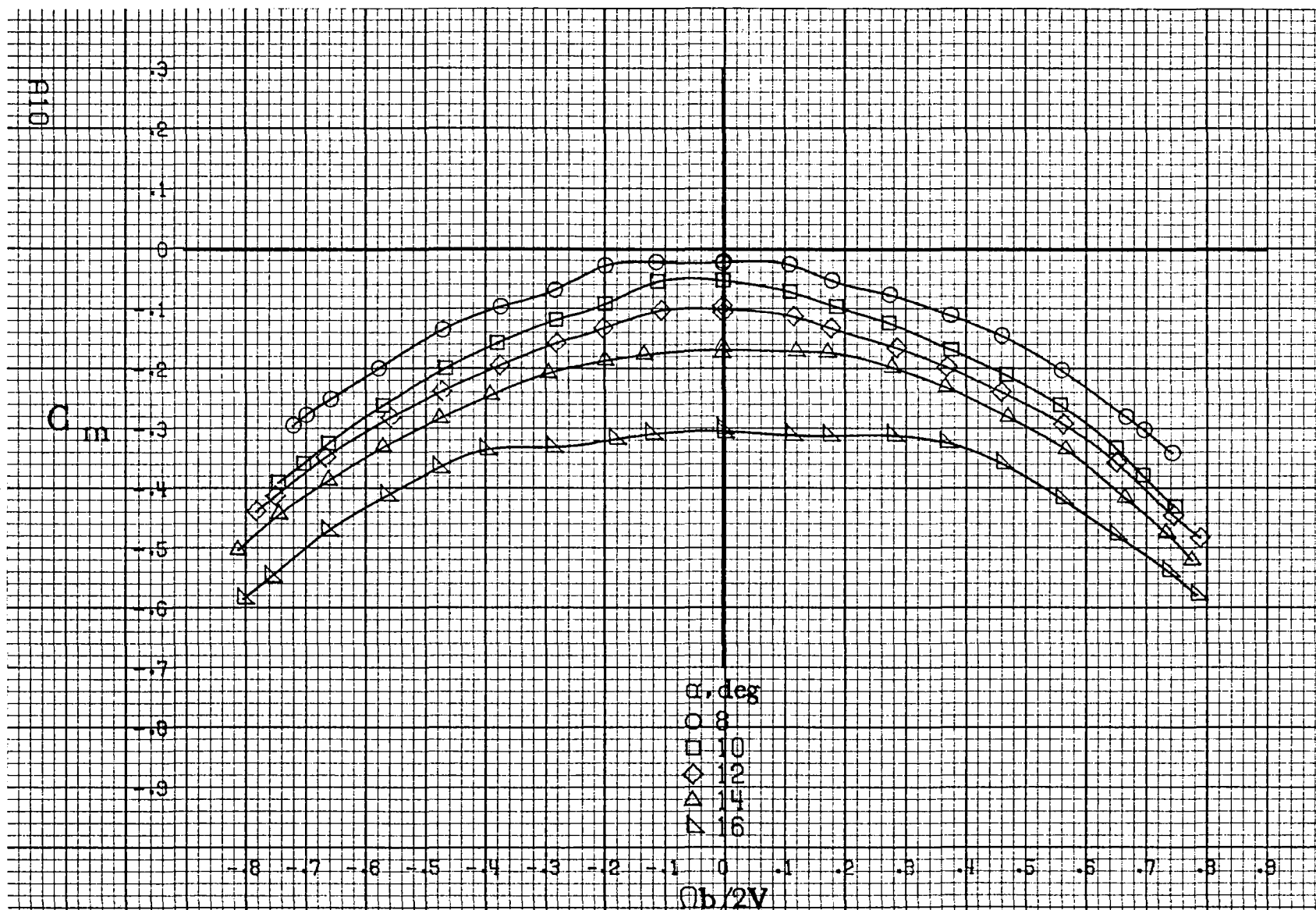
Figure A2.-Effect of rotation rate and angle of attack on rolling-moment coefficient for basic configuration.  $\delta_e=0^\circ$ ,  $\delta_a=0^\circ$ ,  $\delta_r=0^\circ$ ,  $\beta=0^\circ$ .



(b)  $\alpha = 18$  to  $35$  deg,  $SR = 99$  cm (39 in).  
Figure A2. Continued.

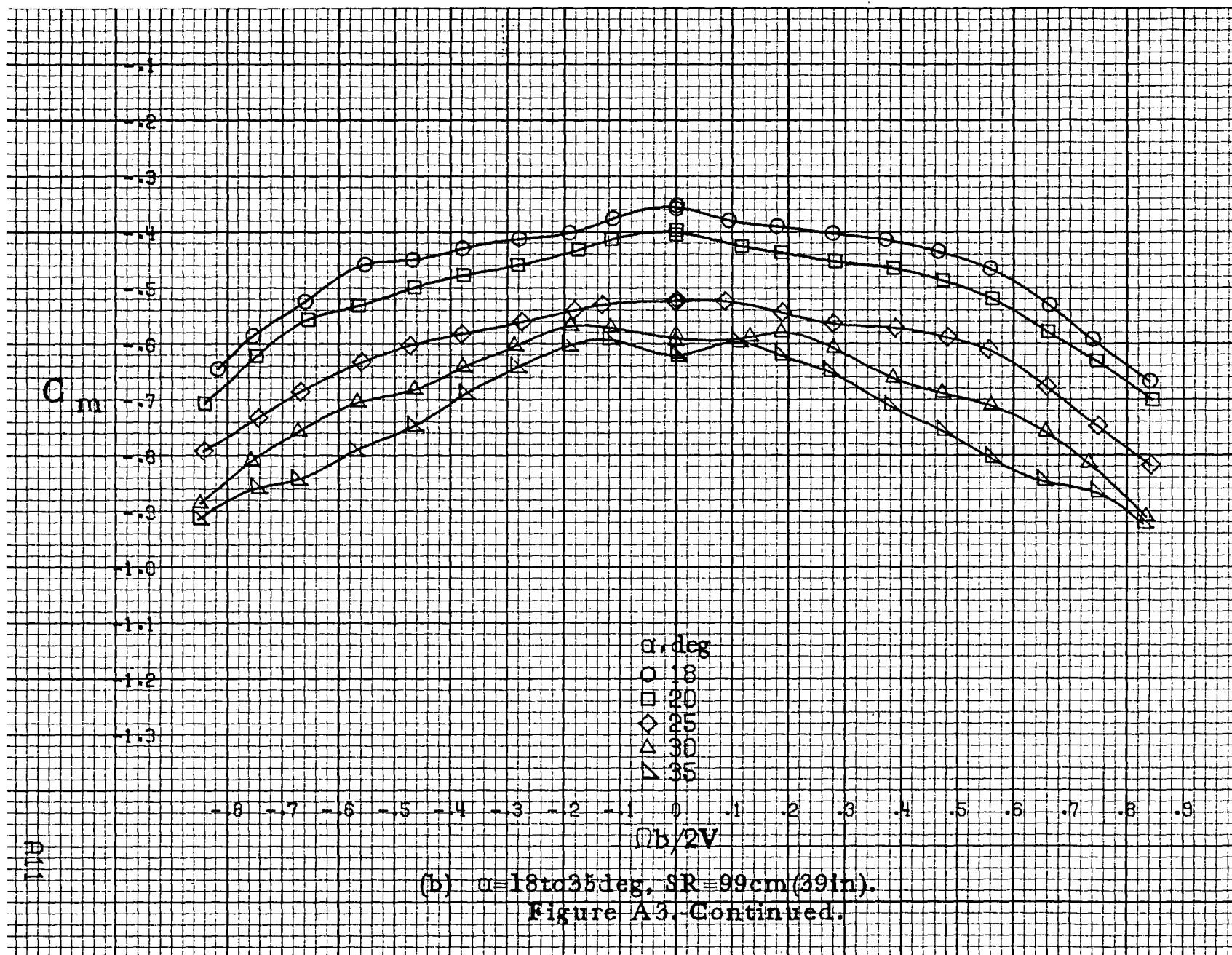




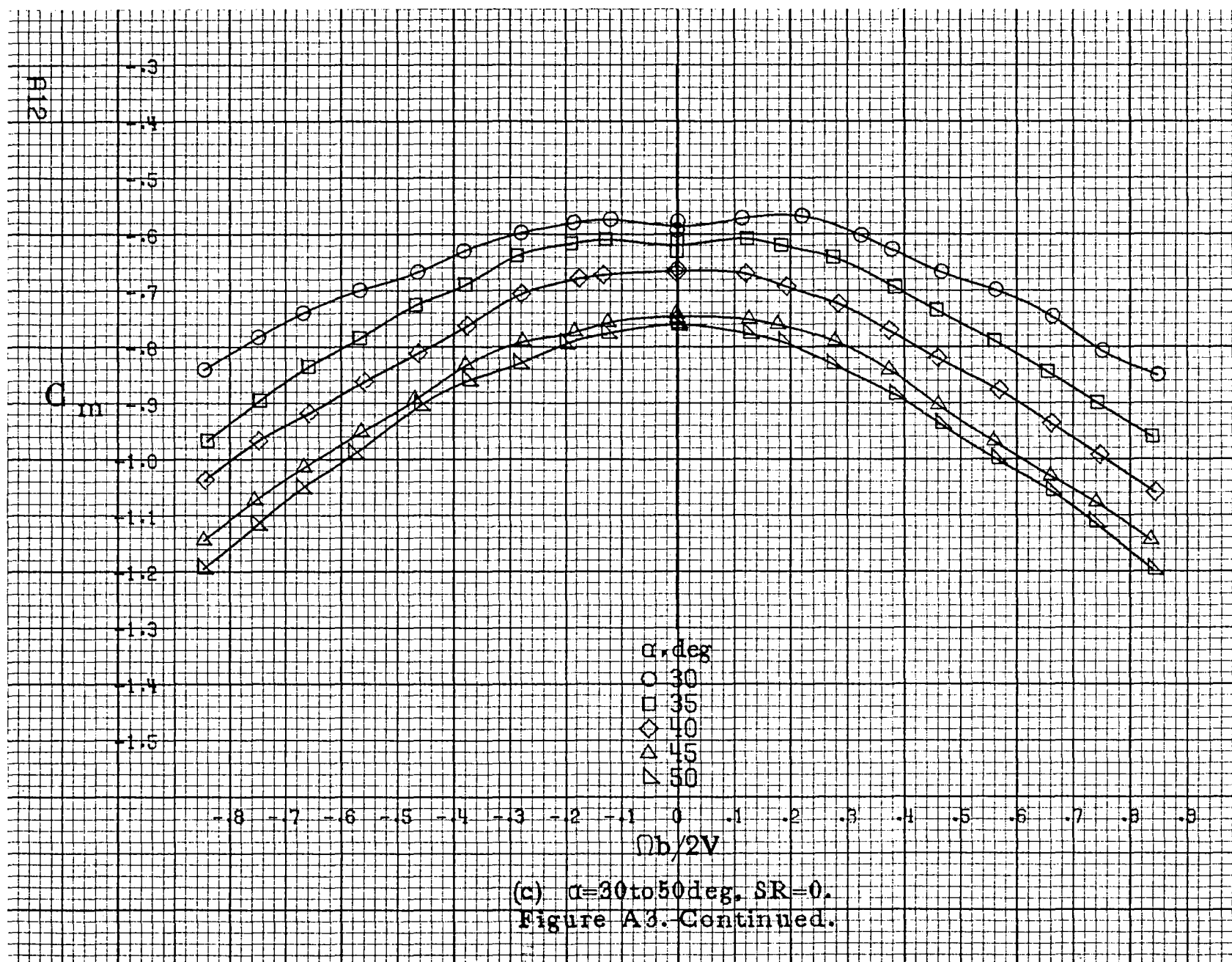


(a)  $\alpha = 8$  to  $16^\circ$ ,  $SR = 99 \text{ cm (39 in.)}$ .

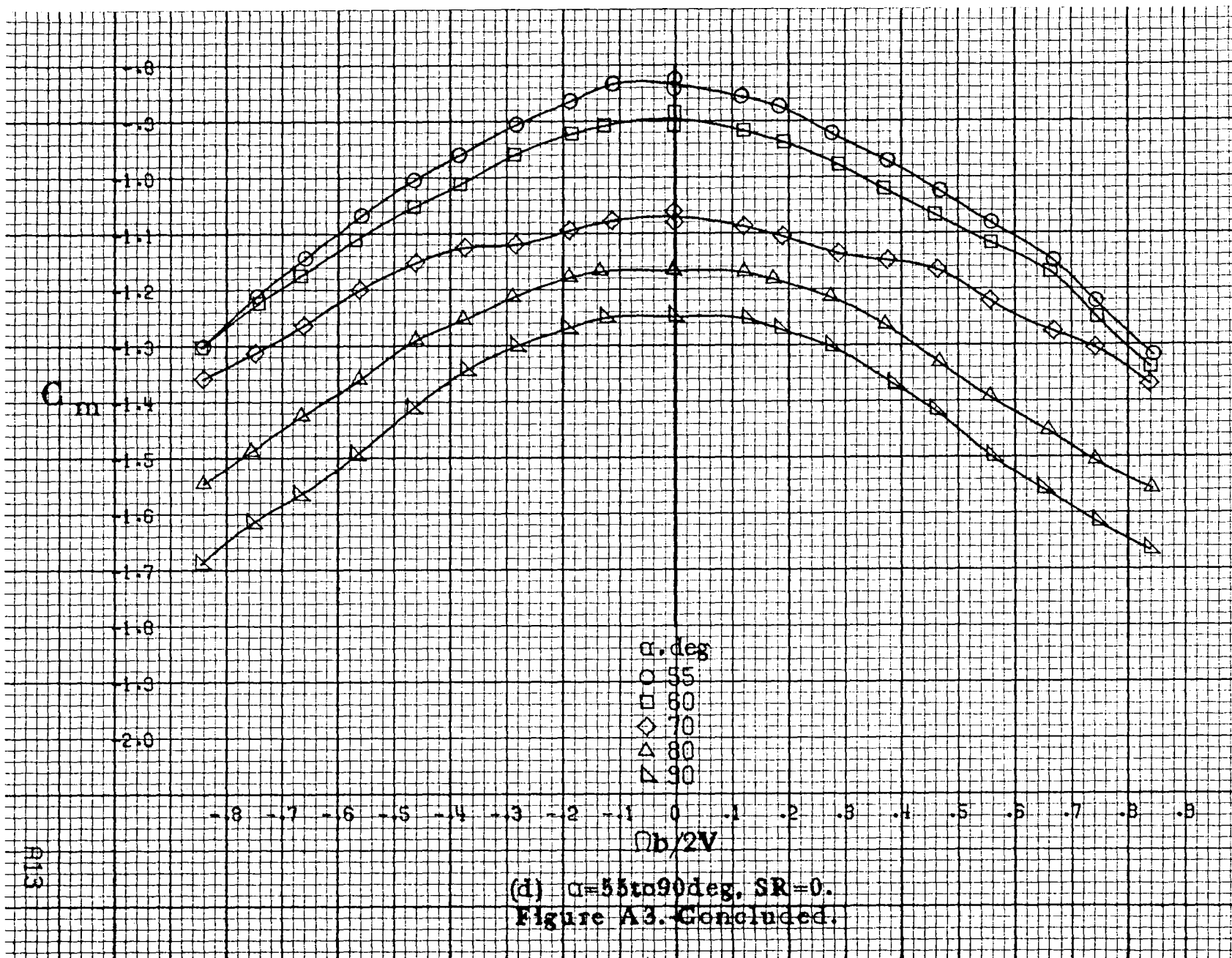
Figure A3.-Effect of rotation rate and angle of attack on pitching-moment coefficient for basic configuration.  $\delta_a = 0^\circ$ ,  $\delta_z = 0^\circ$ ,  $\delta_r = 0^\circ$ ,  $\beta = 0^\circ$ .

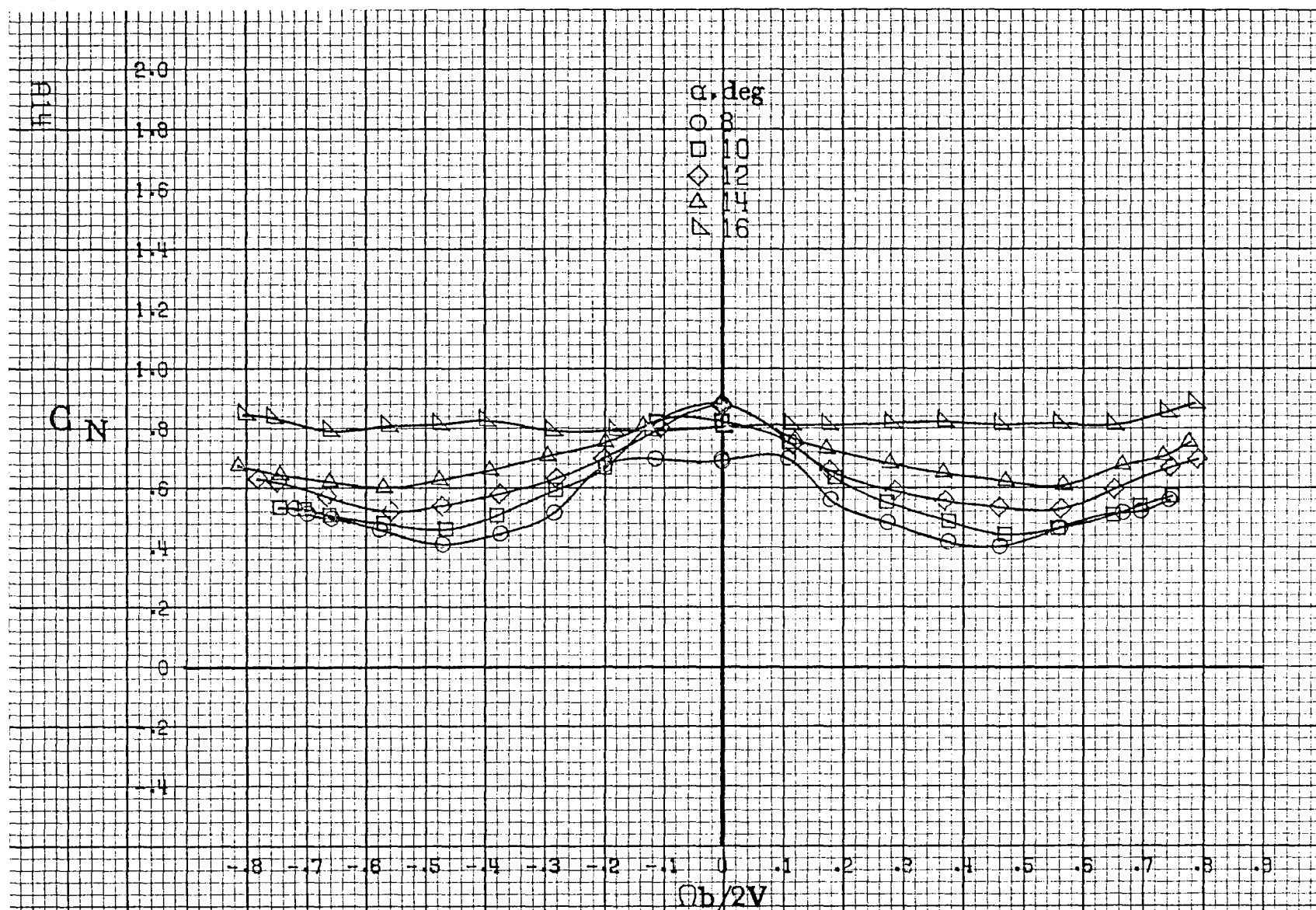






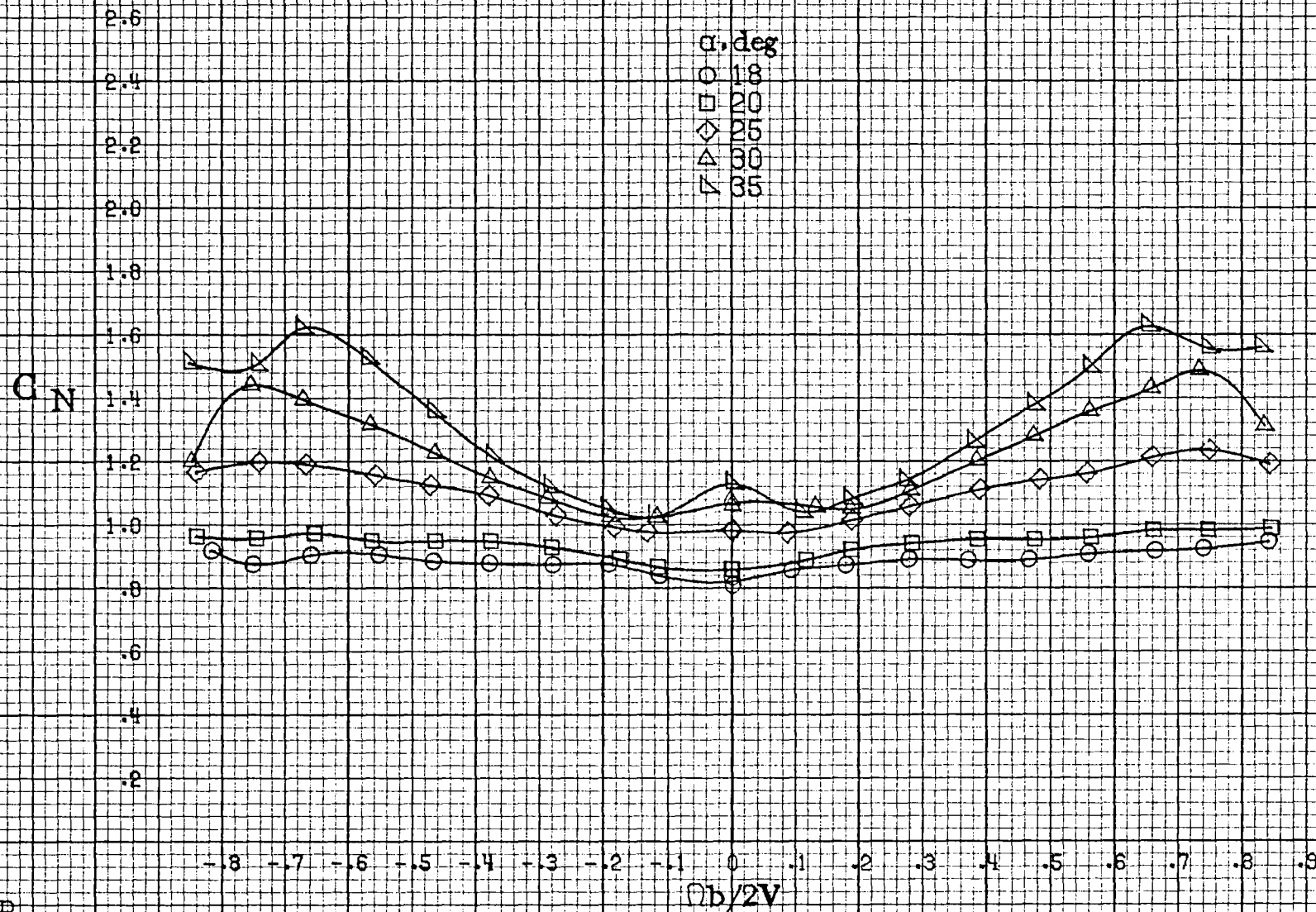




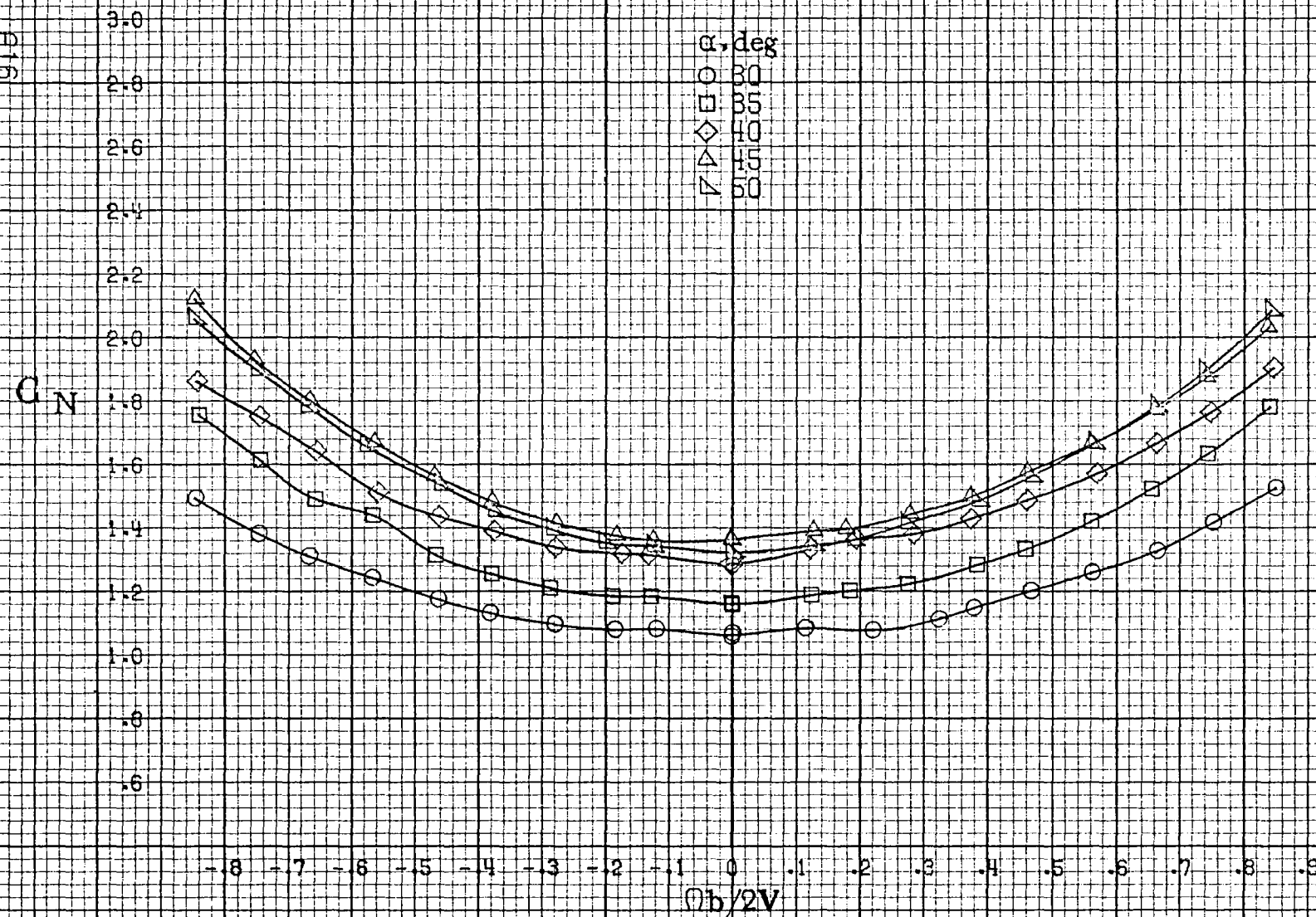


(a)  $\alpha = 8$  to  $16$  deg,  $SR = 99$  cm (39 in).

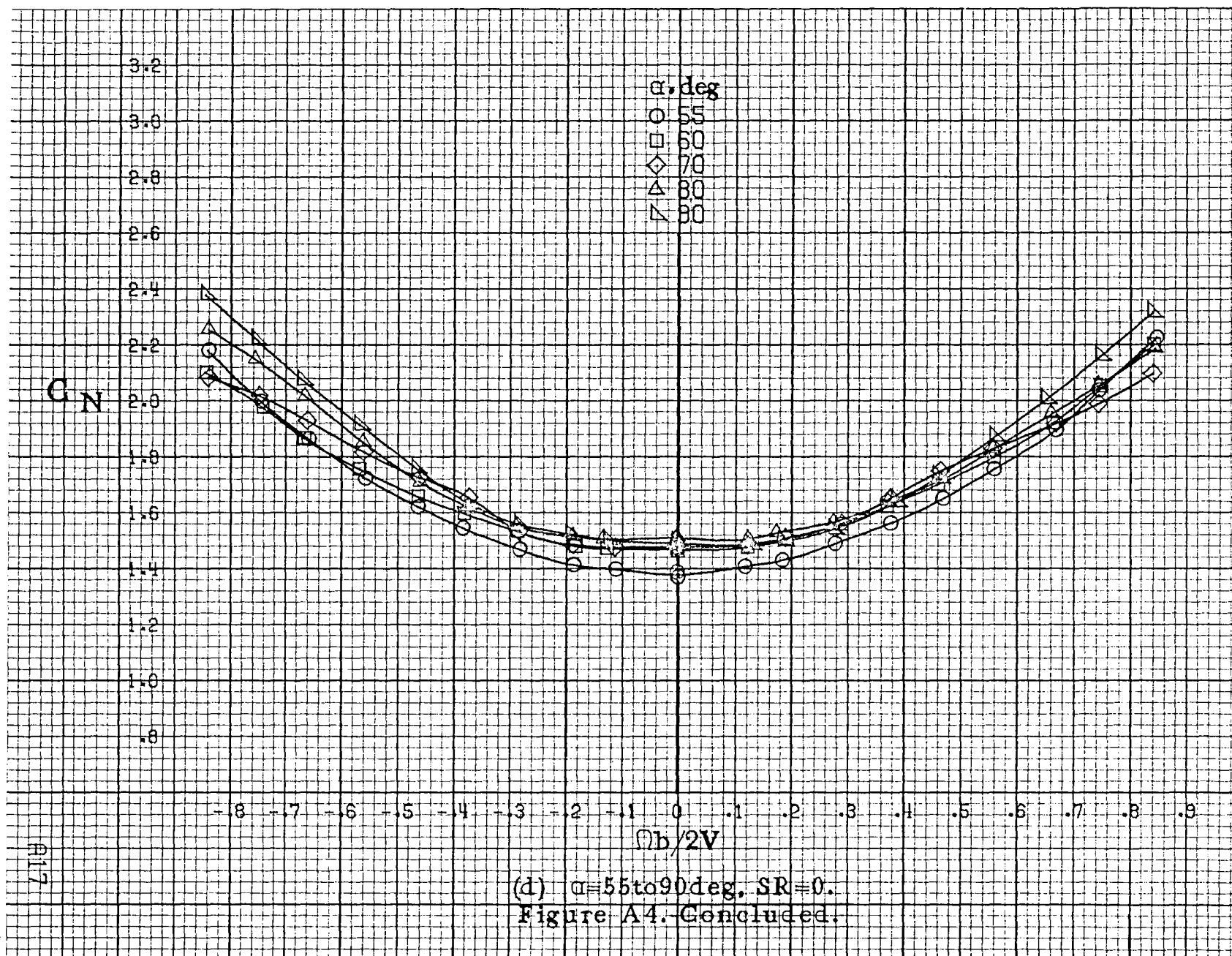
Figure A4. Effect of rotation rate and angle of attack on normal-force coefficient for basic configuration.  $\delta_a = 0^\circ$ ,  $\delta_r = 0^\circ$ ,  $\delta_z = 0^\circ$ ,  $\beta = 0^\circ$ .

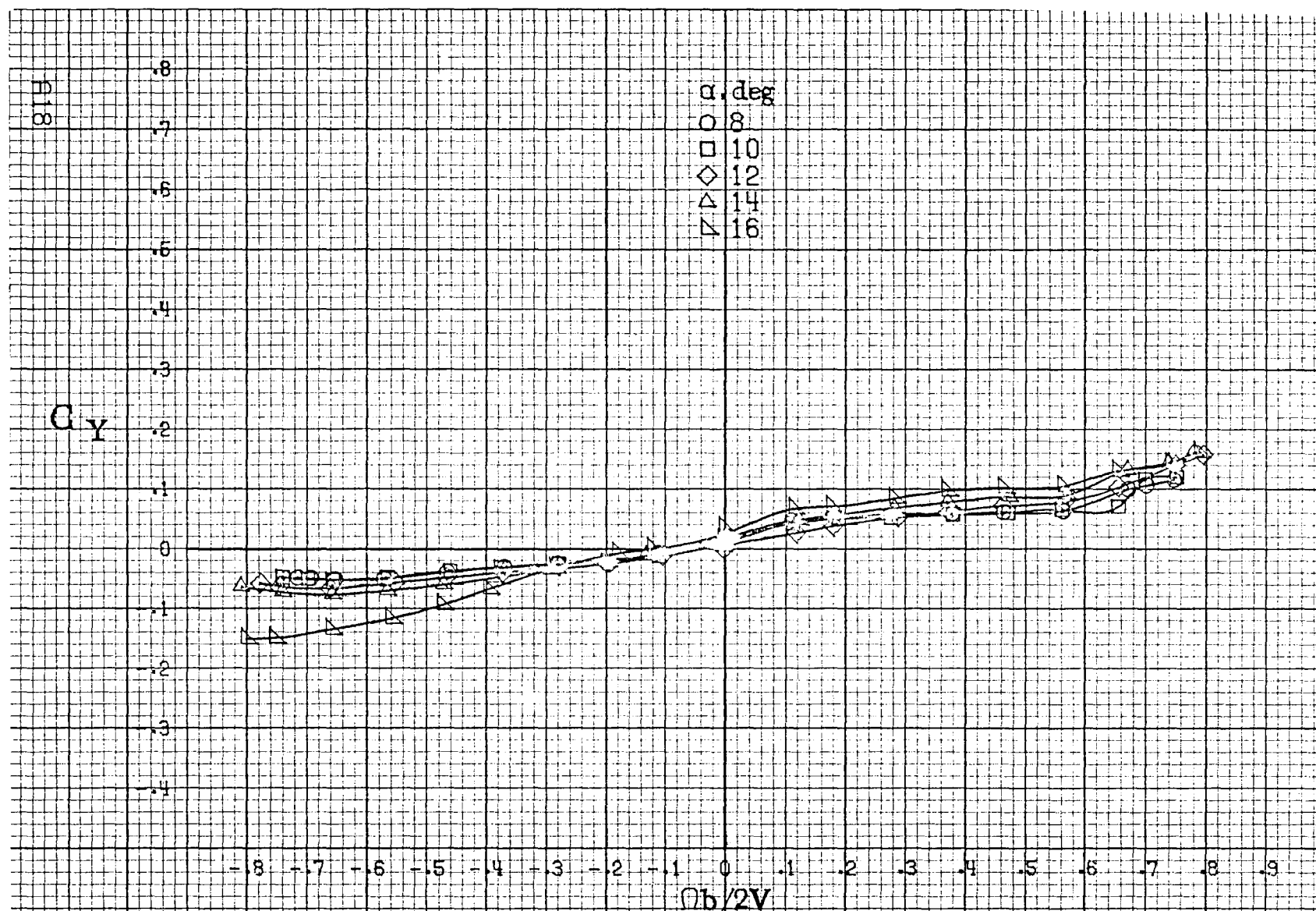


(b)  $\alpha=18$  to  $35$  deg,  $SR=99$  cm (39 in).  
Figure A4-Continued.



(c)  $\alpha=30$  to  $50$  deg,  $SR=0$ .  
Figure A4. Continued.

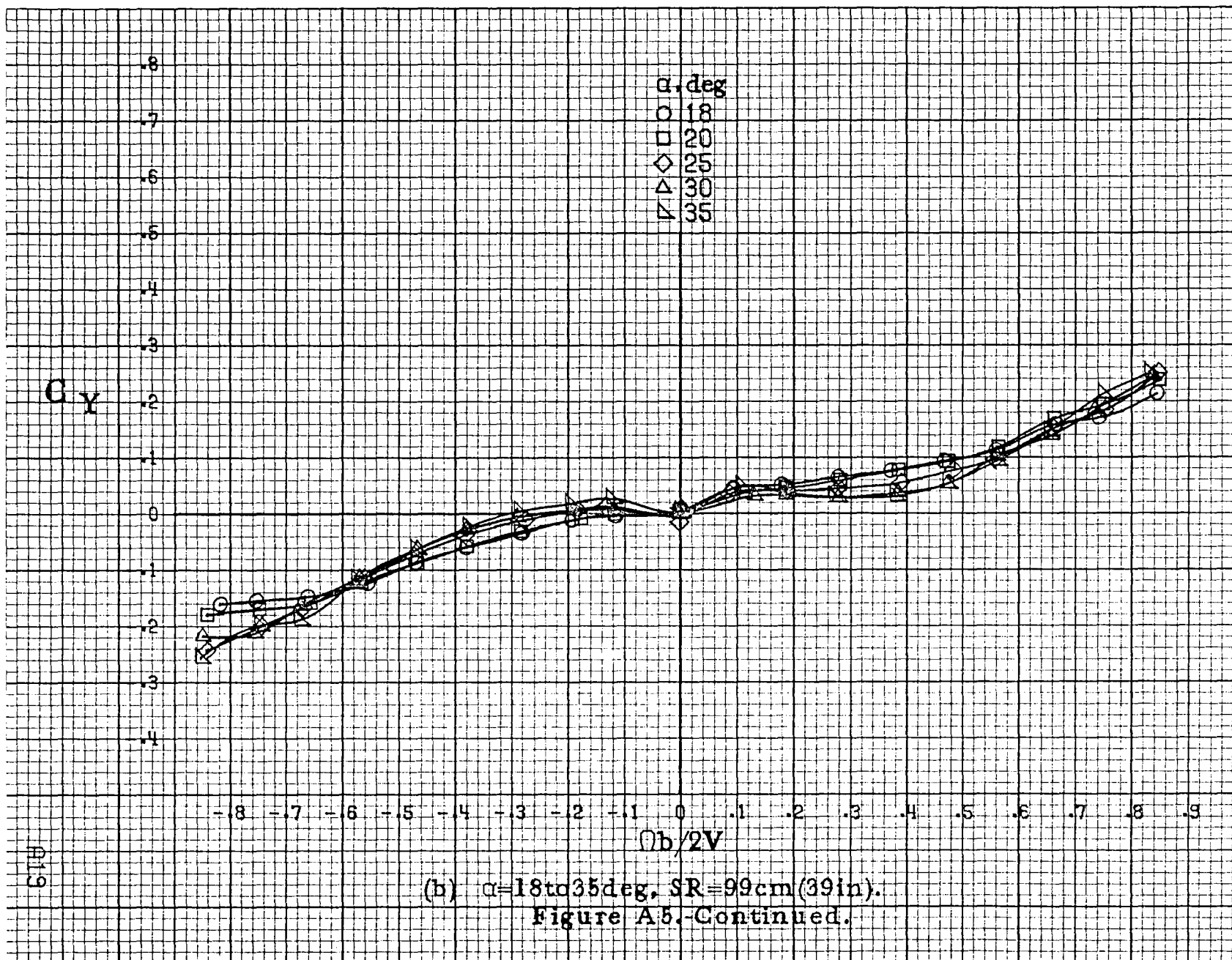


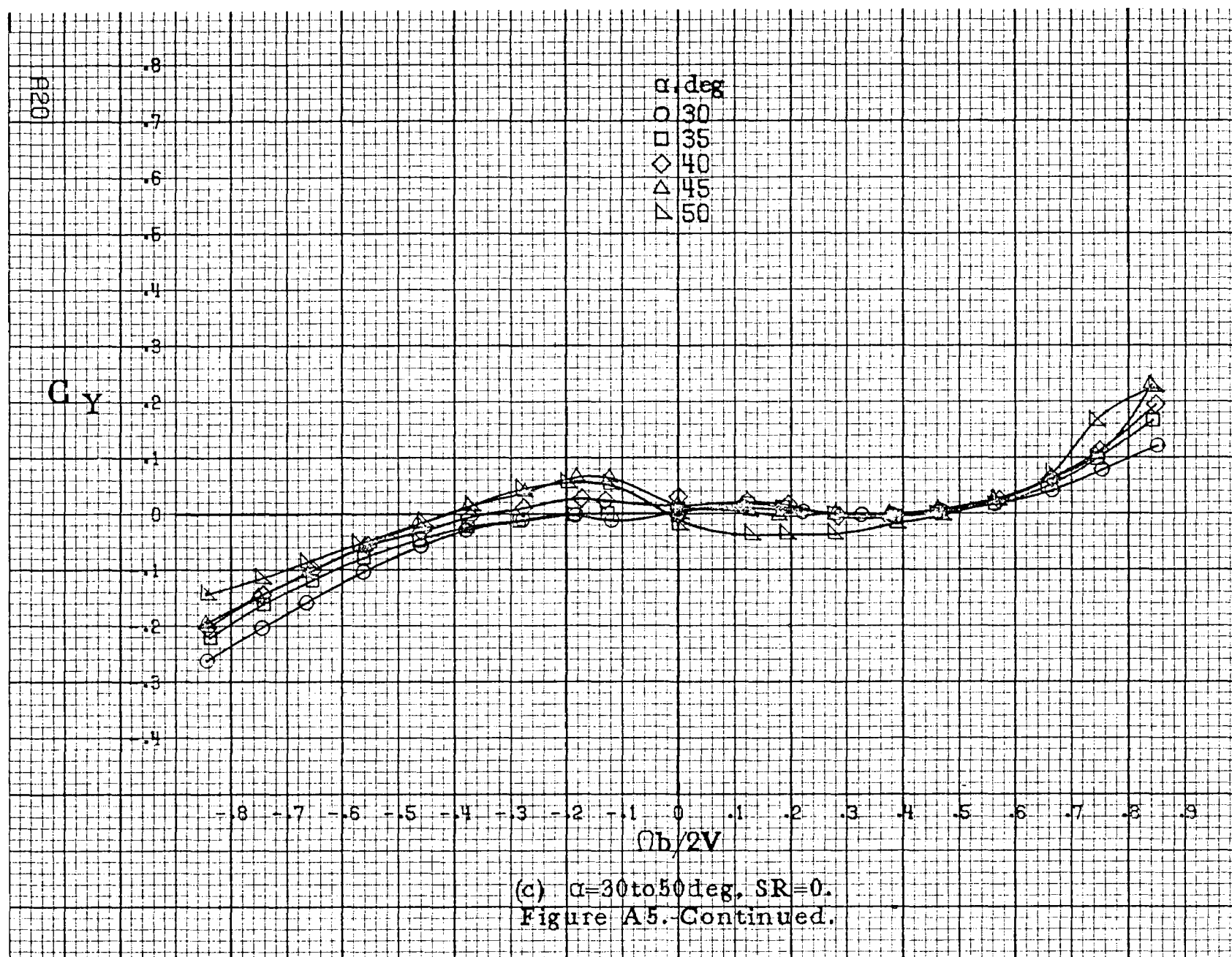


(a)  $\alpha=8$  to  $16^\circ$ ,  $SR=99\text{cm}(39\text{in})$ .

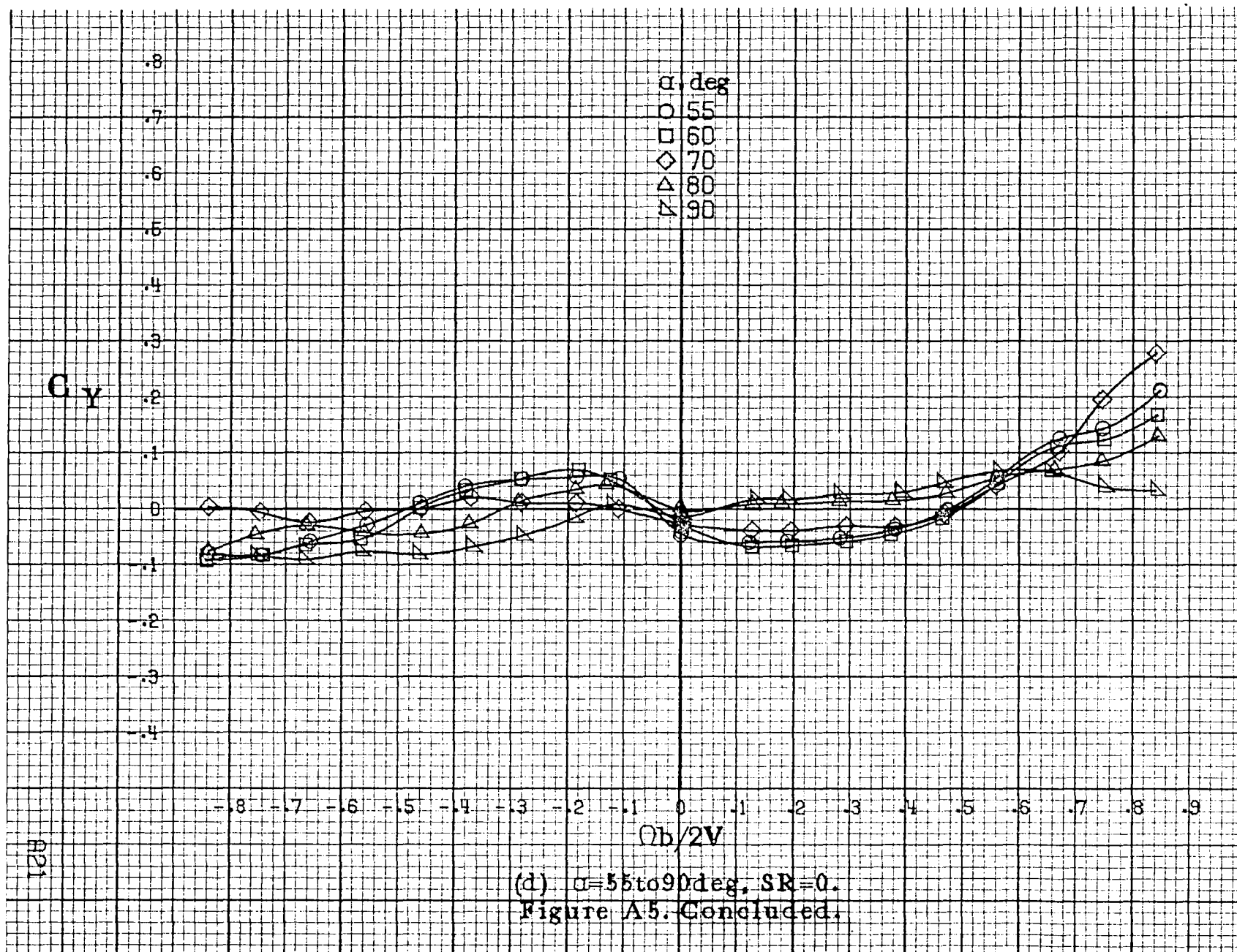
Figure A5.-Effect of rotation rate and angle of attack on side-force coefficient for basic configuration.  $\delta_e=0^\circ$ ,  $\delta_a=0^\circ$ ,  $\delta_r=0^\circ$ ,  $\beta=0^\circ$ .

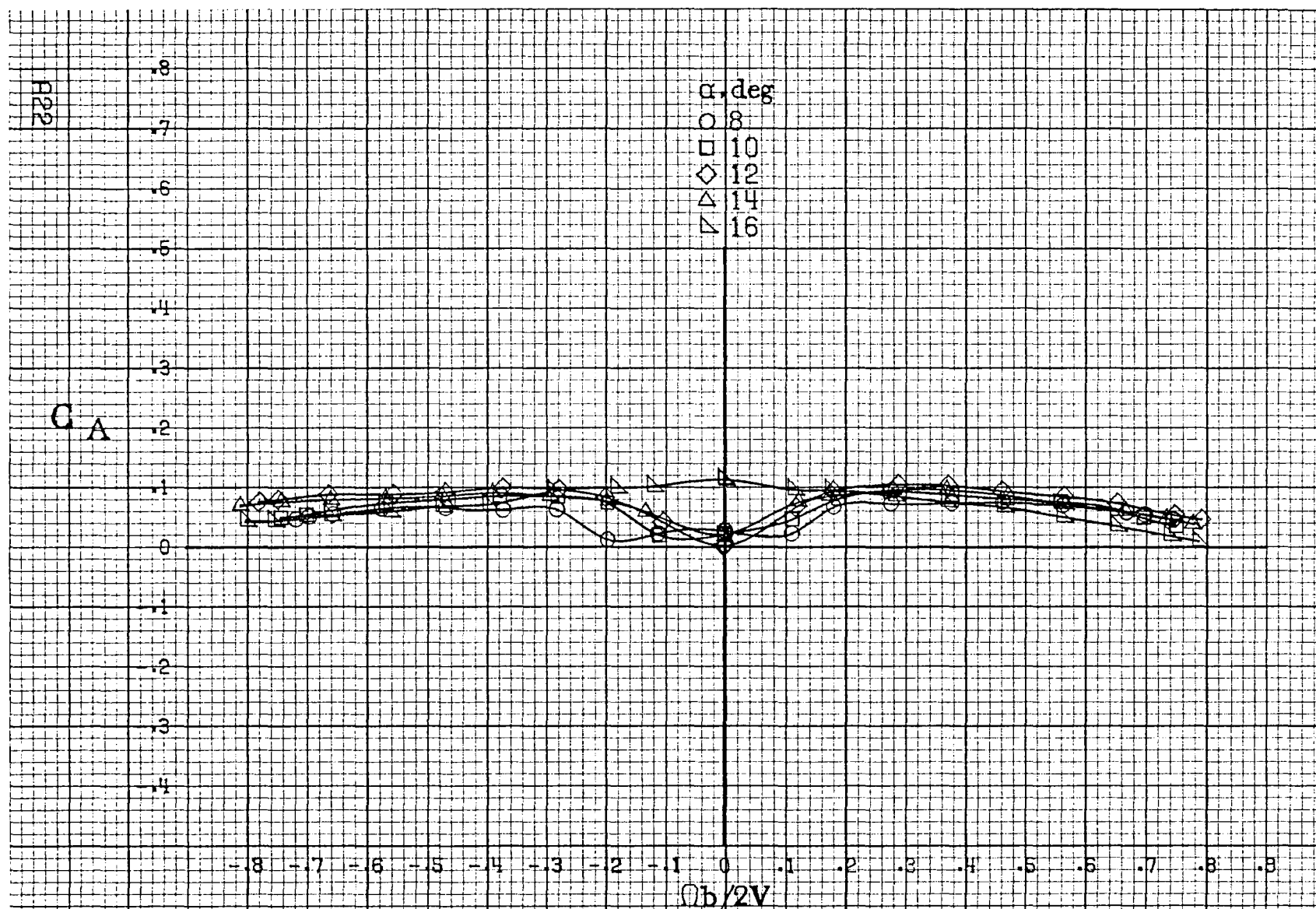






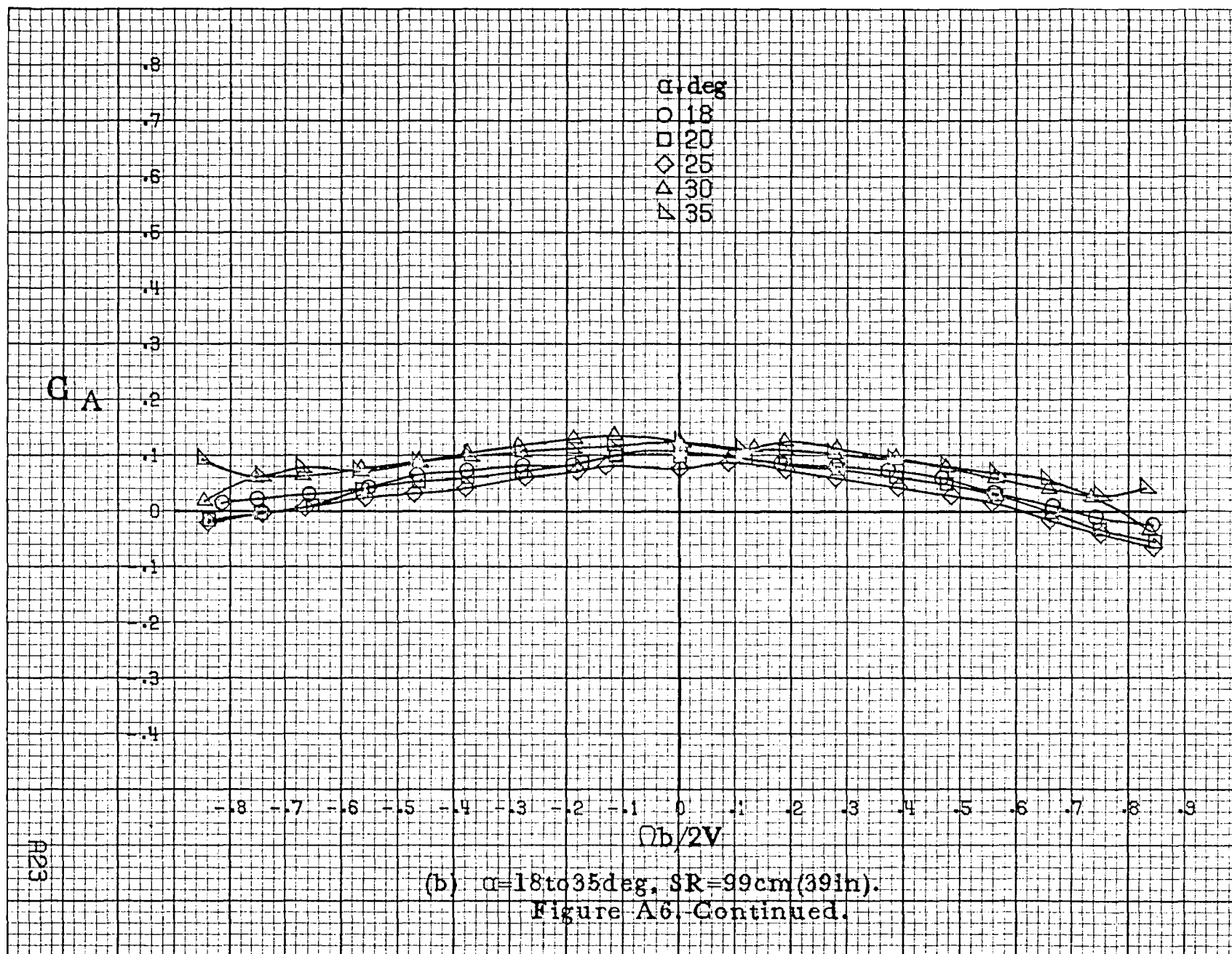


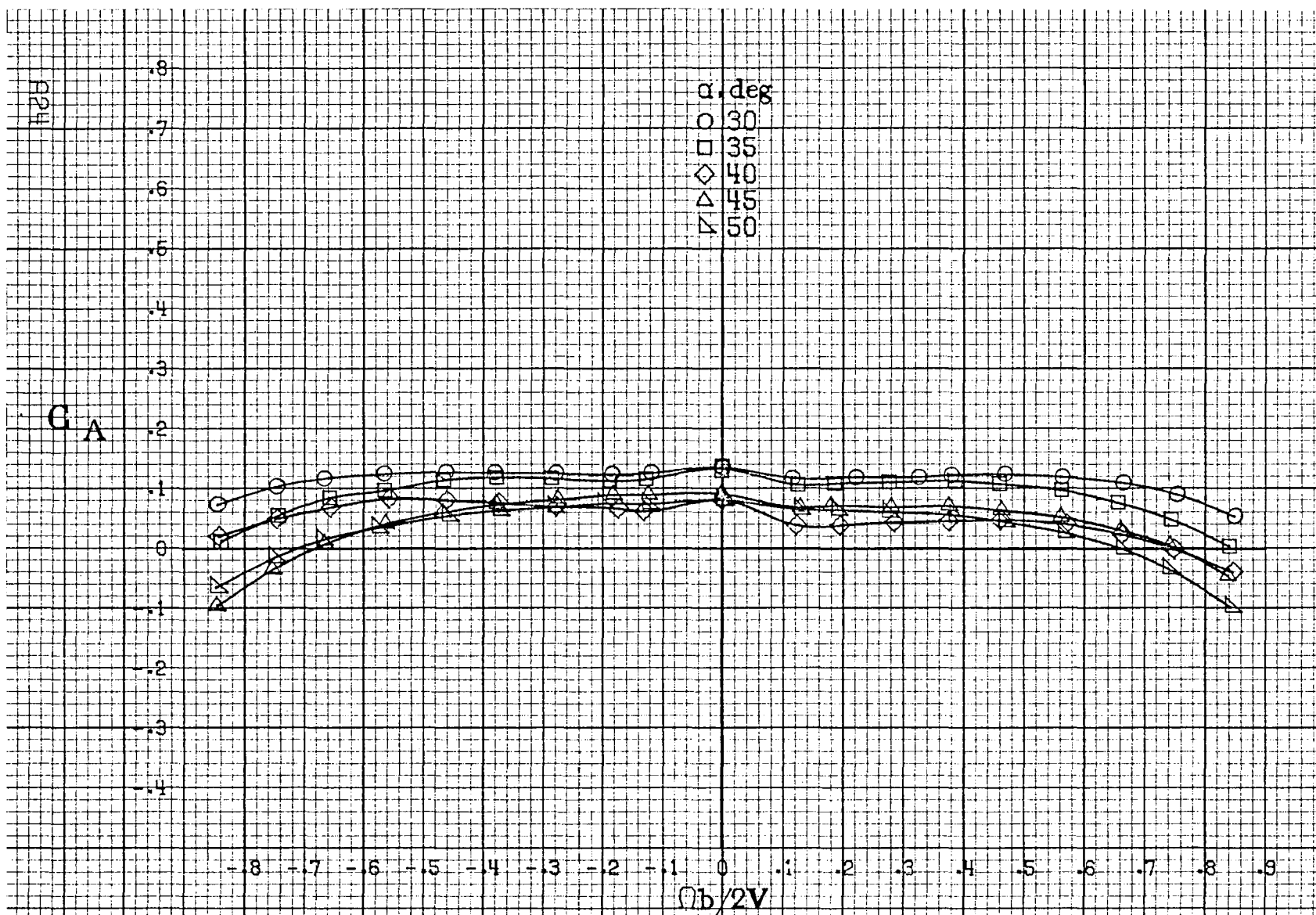




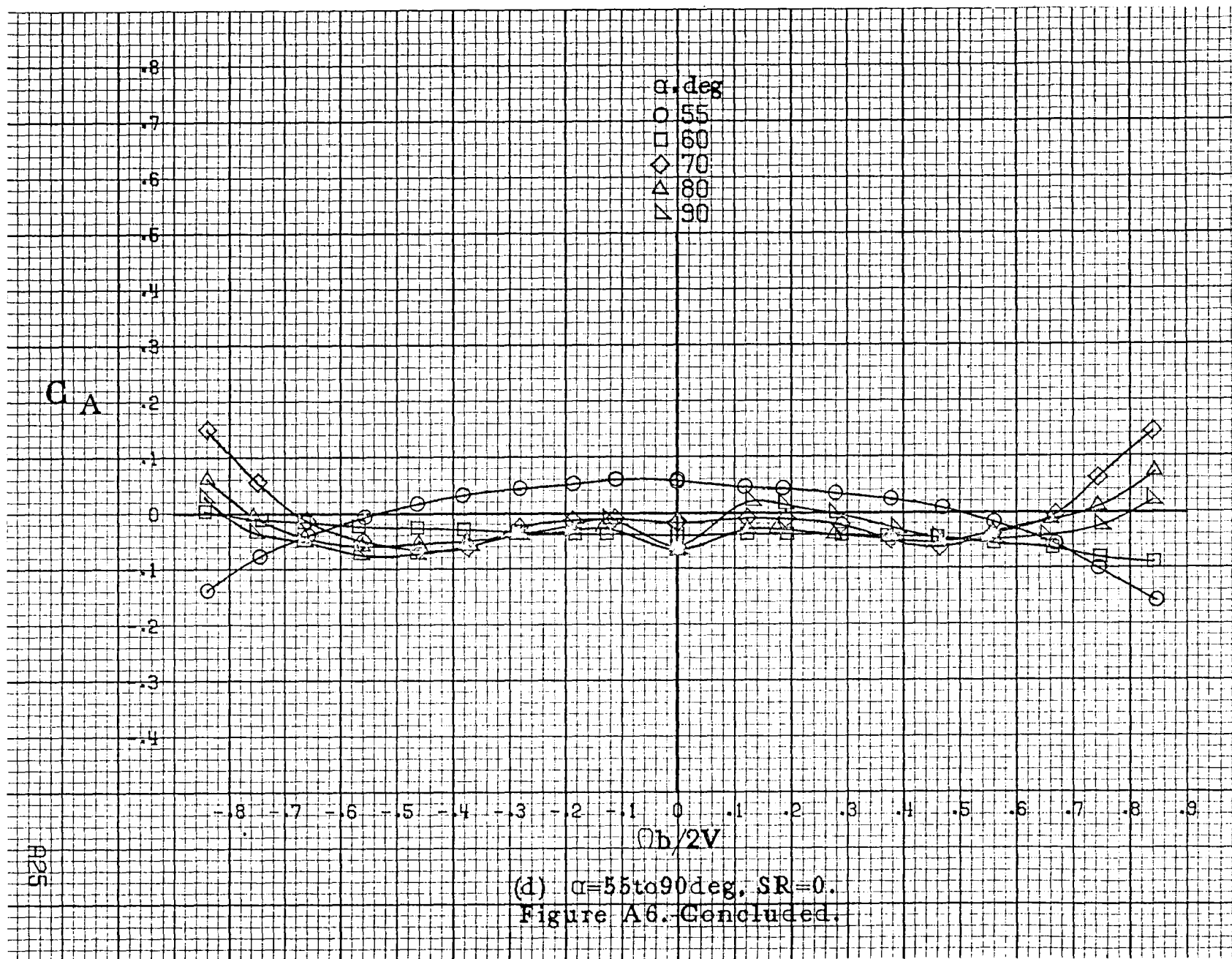
(a)  $\alpha=8\text{ to }16^\circ$ ,  $SR=99\text{cm}(39\text{in})$ .

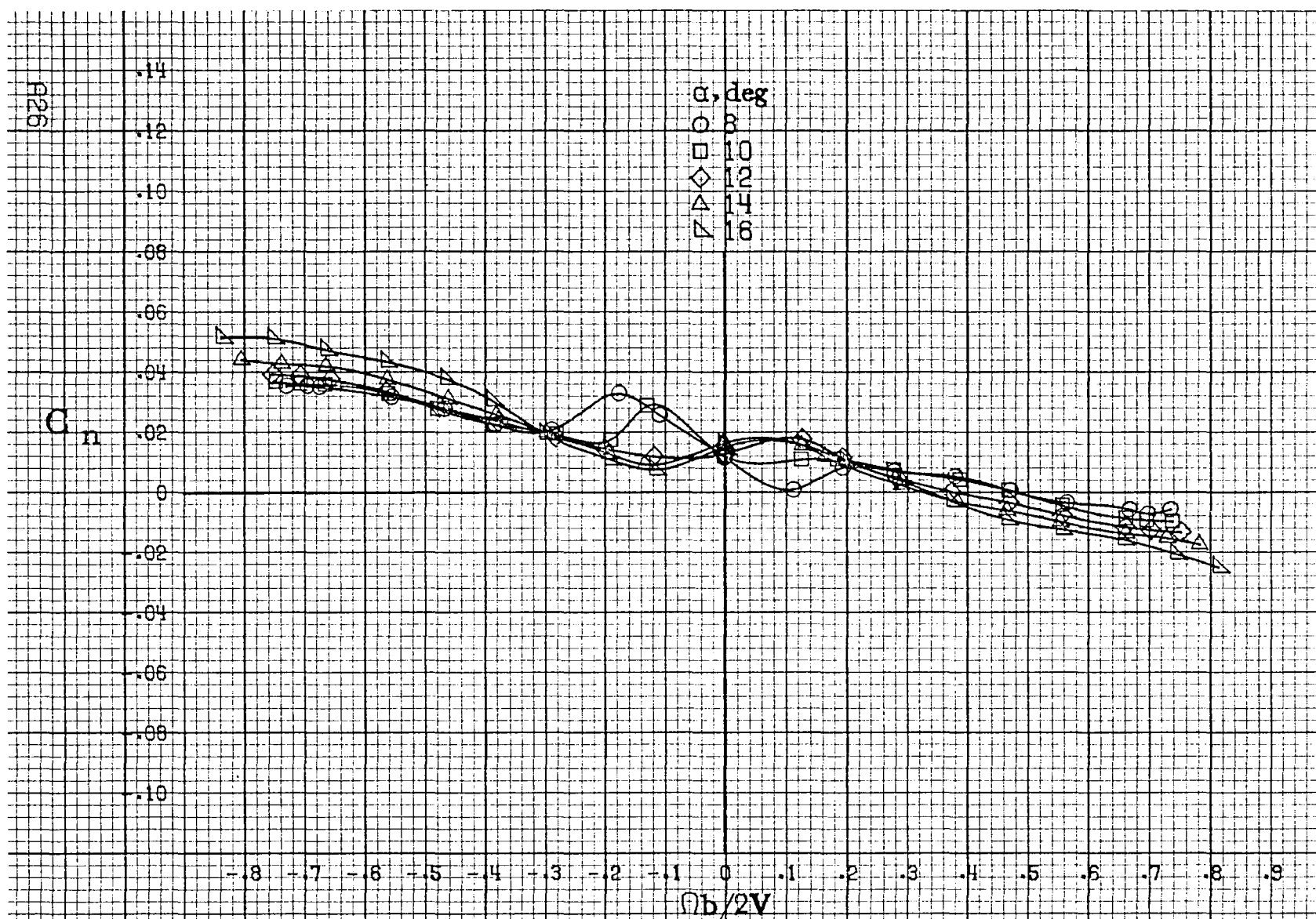
Figure A6. Effect of rotation rate and angle of attack on axial force coefficient for basic configuration.  $\delta_e=0^\circ$ ,  $\delta_a=0^\circ$ ,  $\delta_r=0^\circ$ ,  $\beta=0^\circ$ .





(a)  $\alpha=30$  to  $50^\circ$ ,  $SR=0$ .  
Figure A6.-Continued.

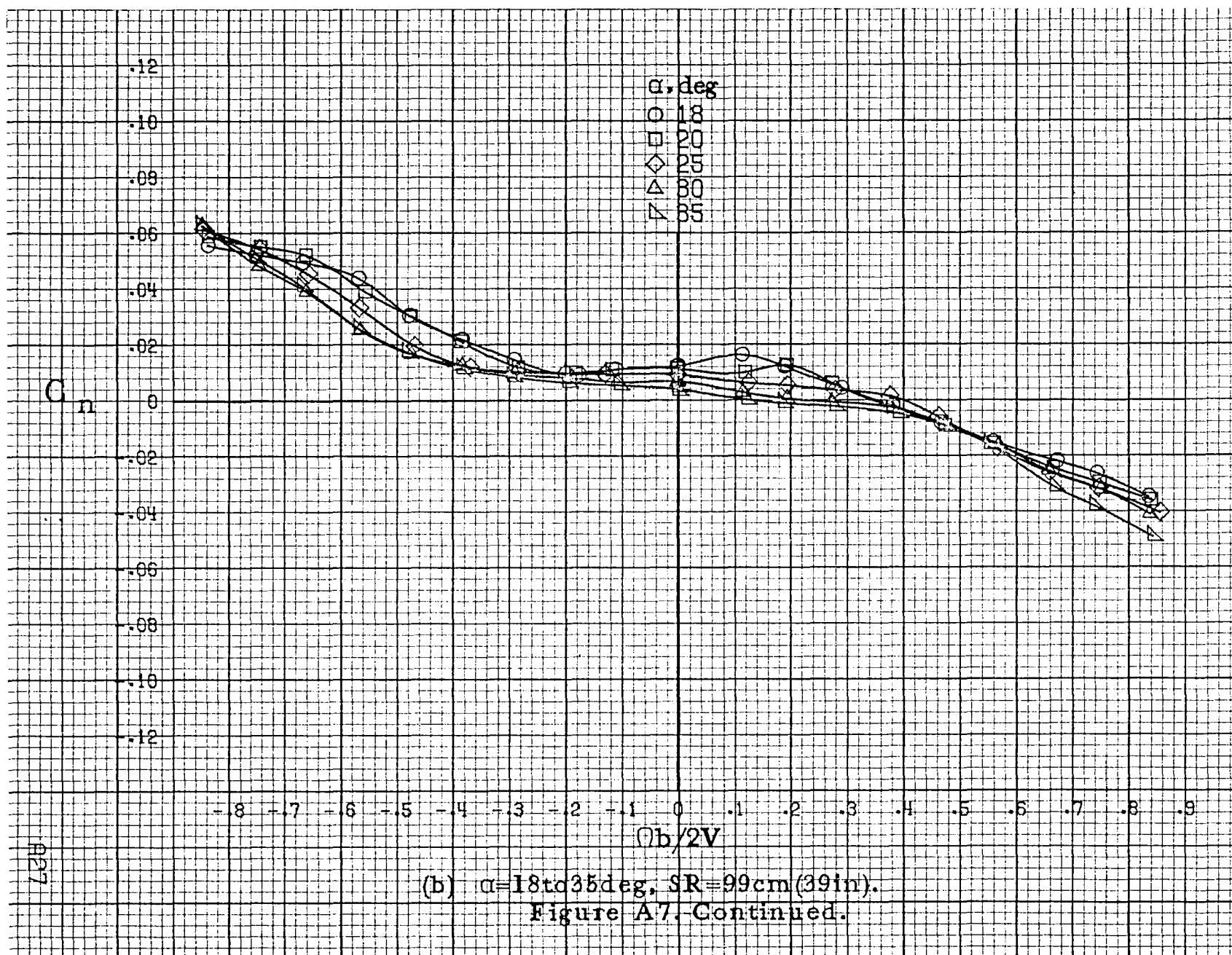


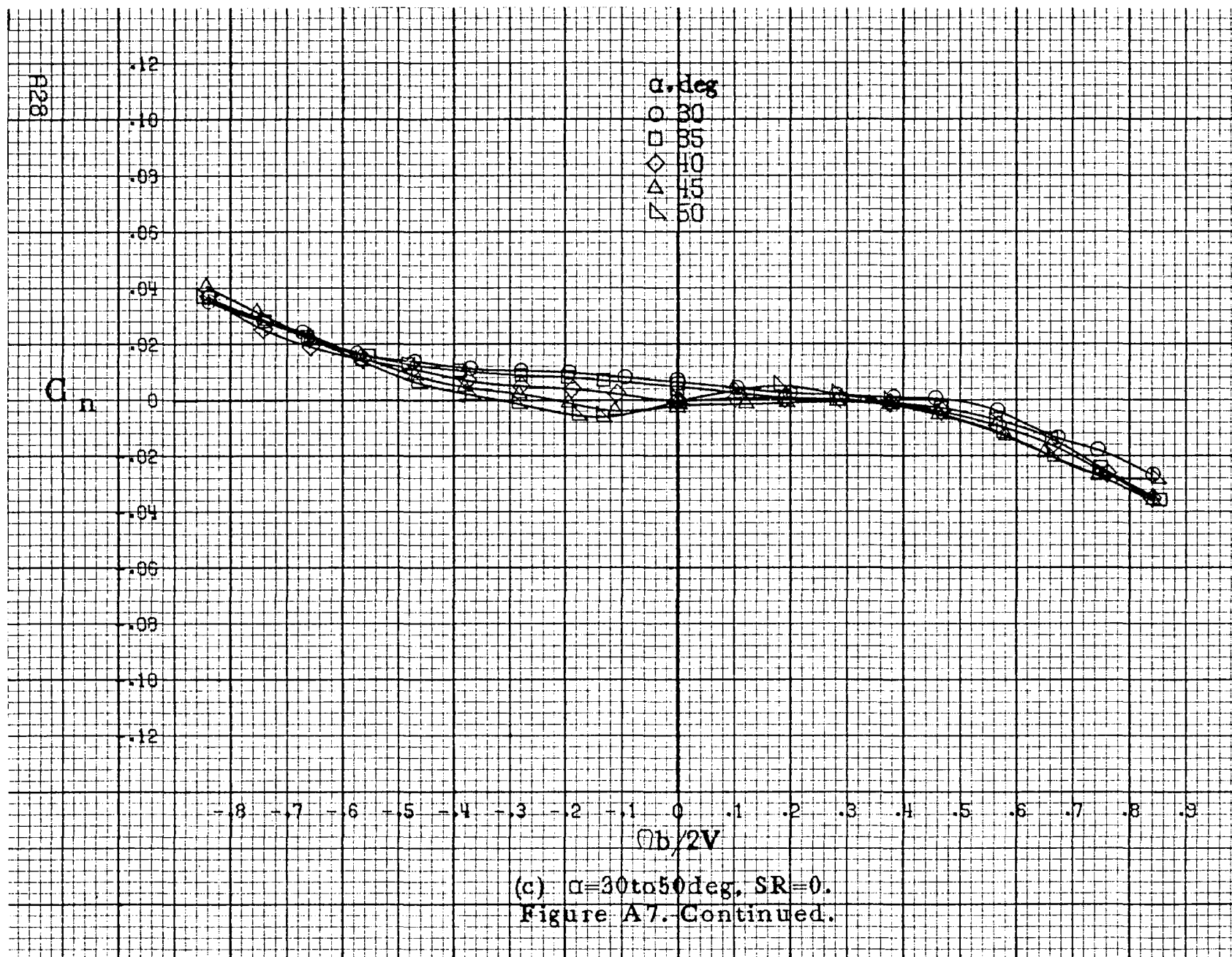


(a)  $\alpha=8$  to  $16^\circ$ ,  $SR=99\text{cm}(39\text{in})$ .

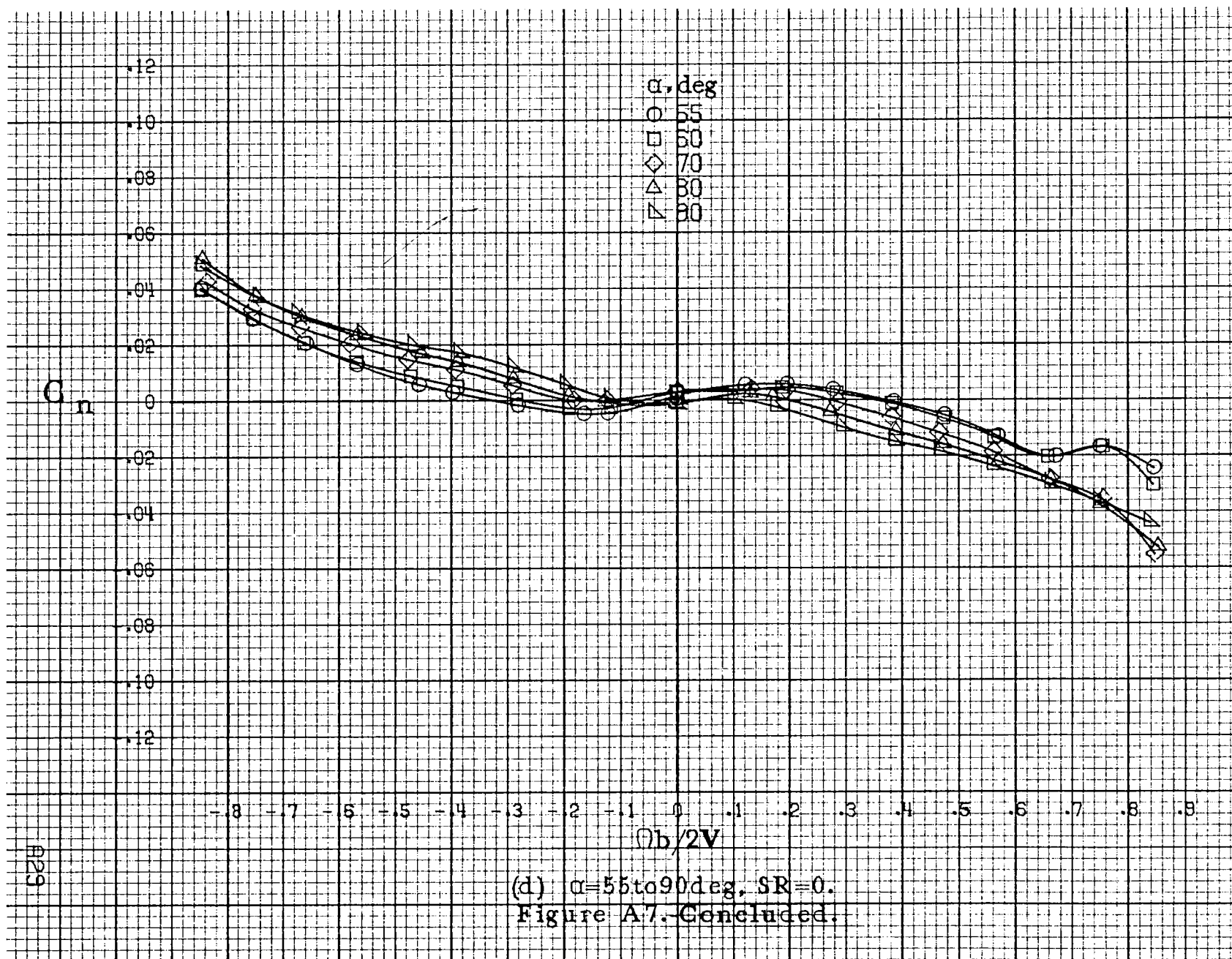
Figure A7.-Effect of rotation rate and angle of attack on yawing-moment coefficient for basic configuration.  $\delta_a=0^\circ$ ,  $\delta_r=0^\circ$ ,  $\delta_t=-25^\circ$ ,  $\beta=0^\circ$ .

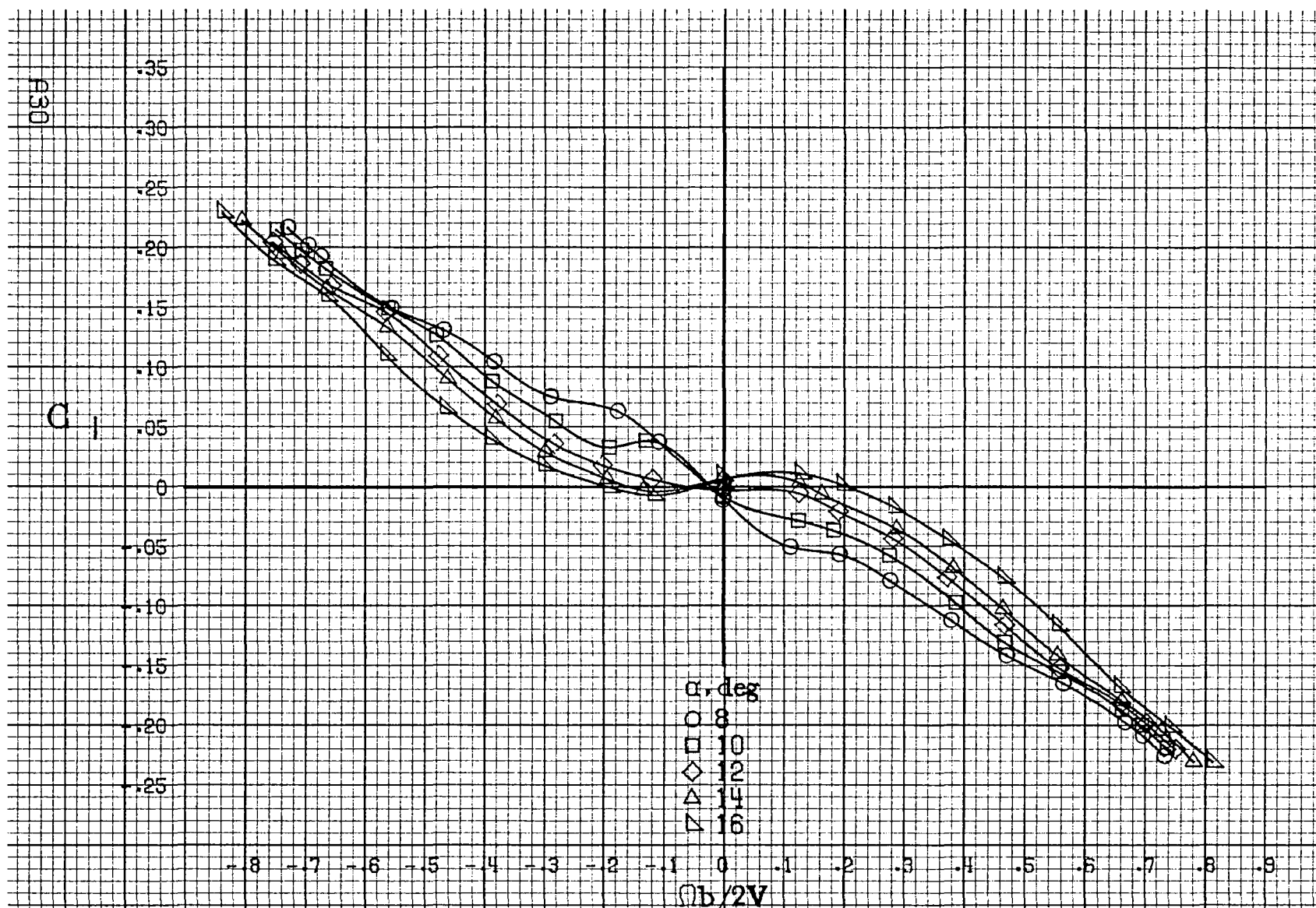






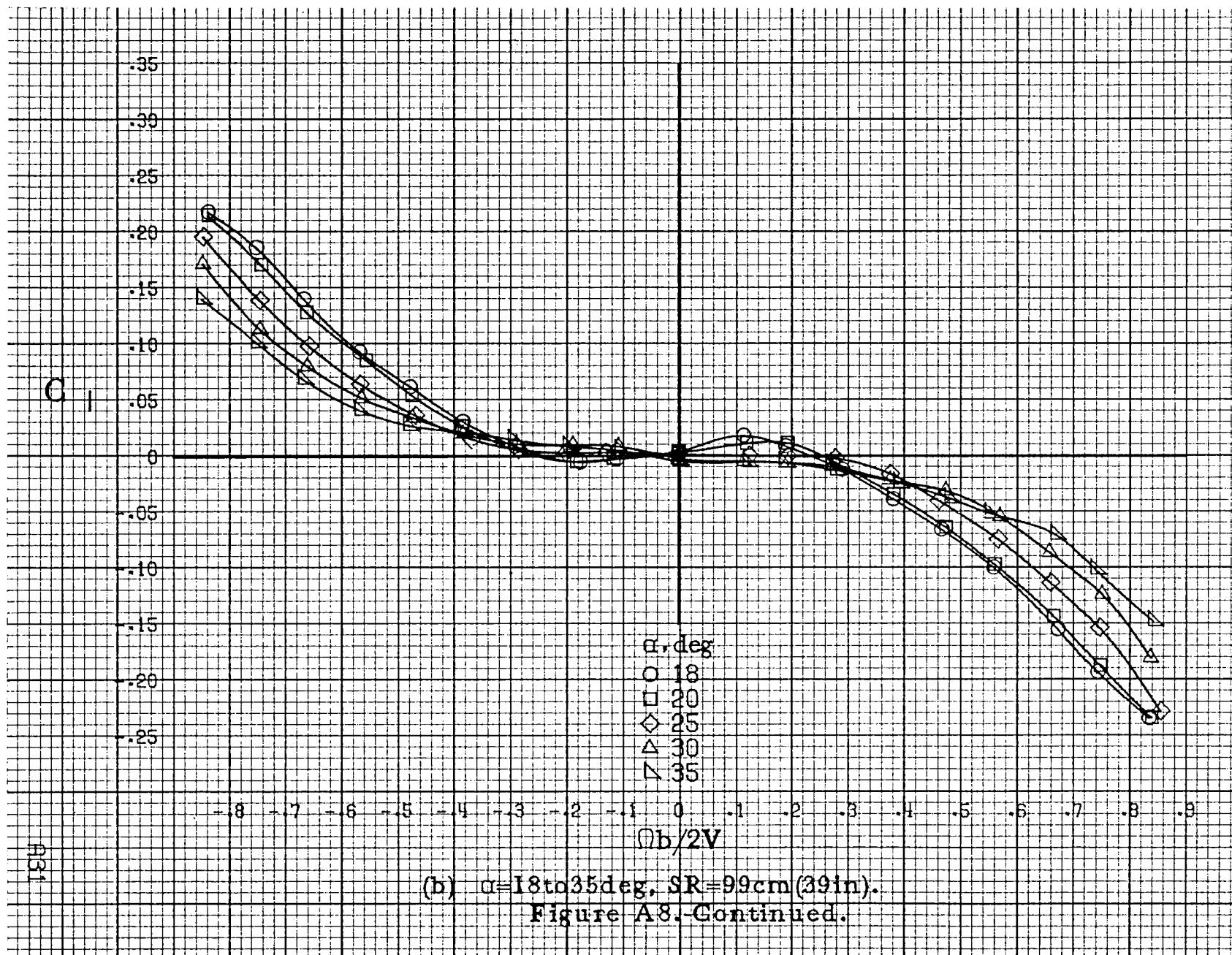


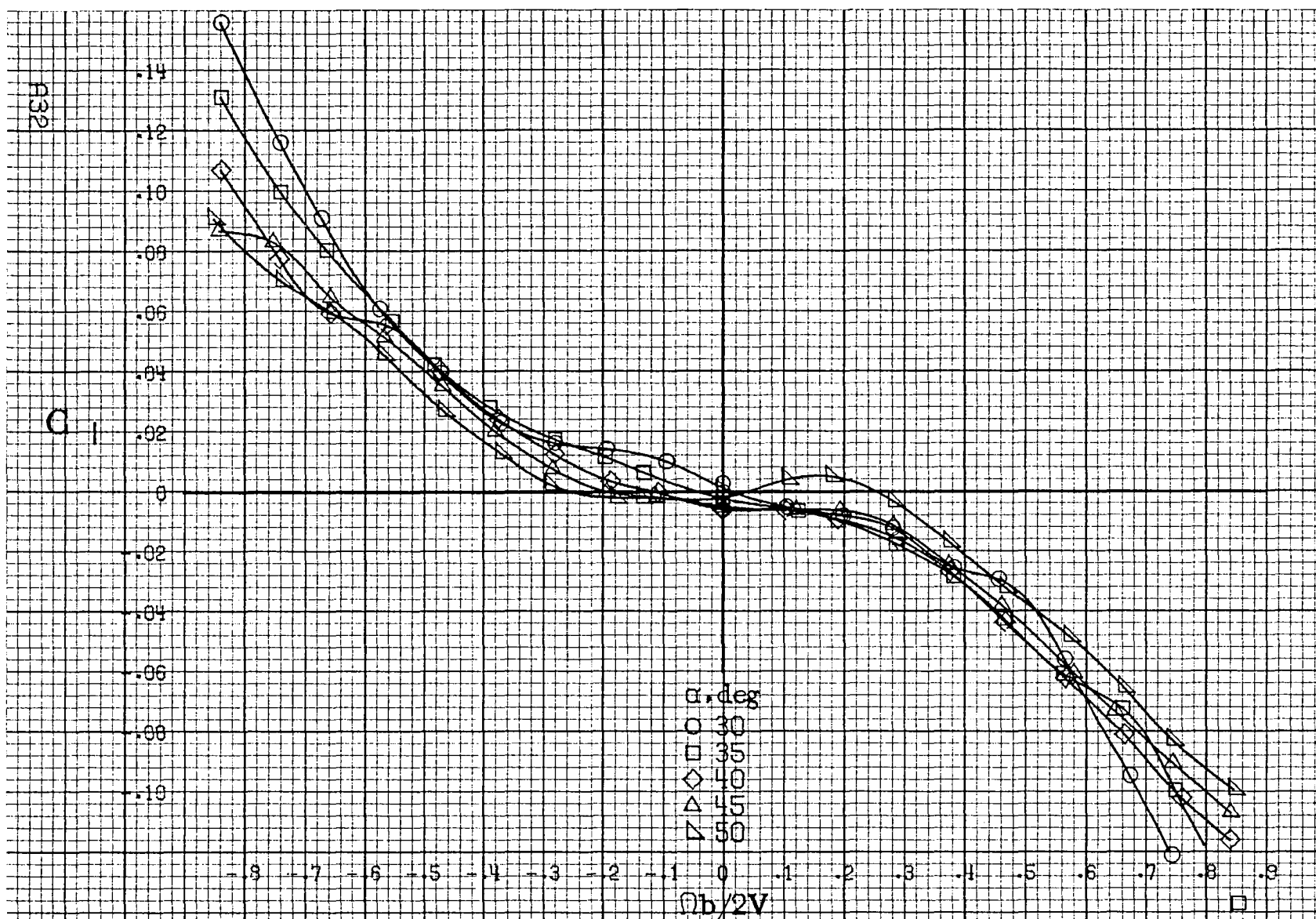




(a)  $\alpha=8$  to  $16^\circ$ ,  $SR=99\text{cm}(39\text{in})$ .

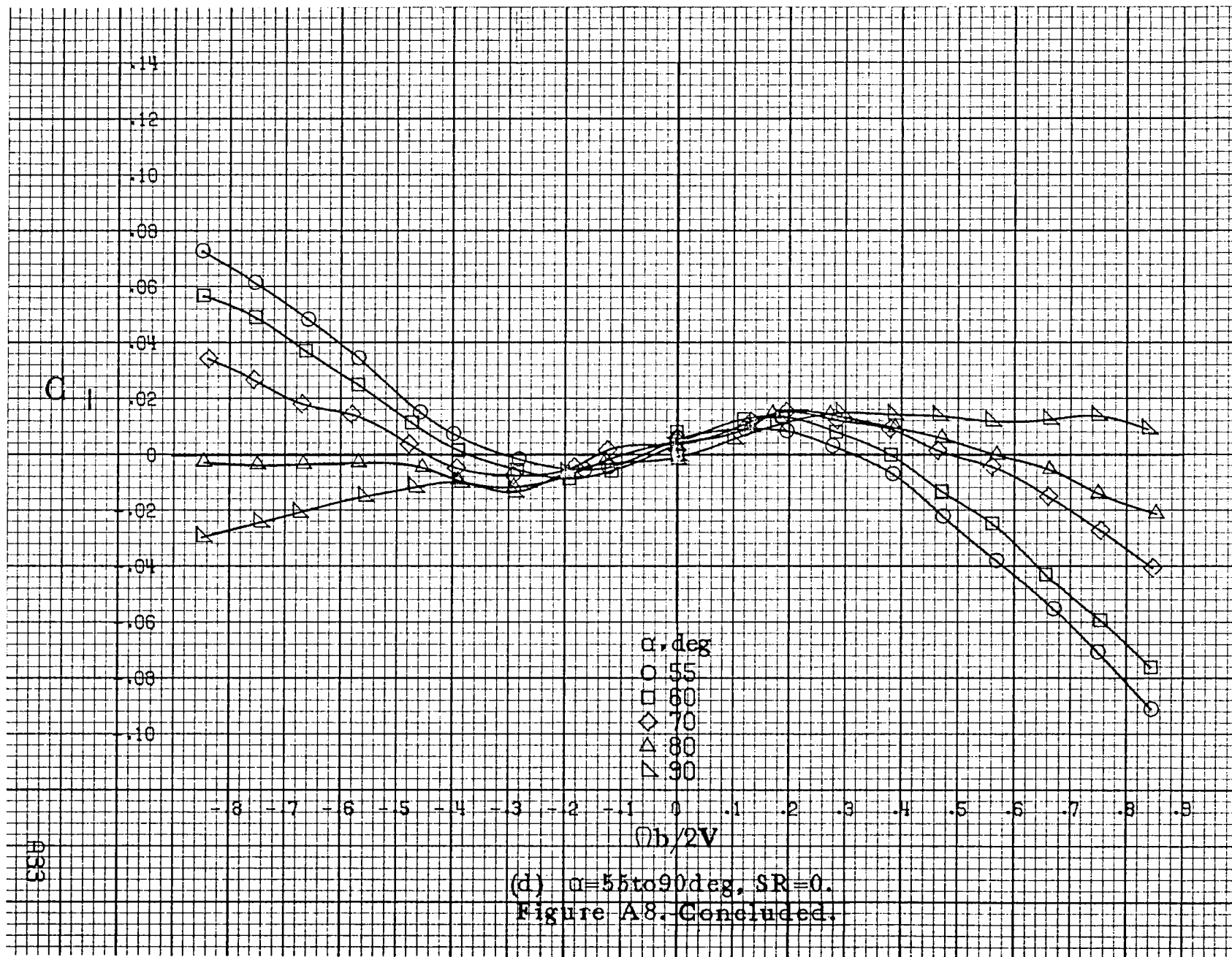
Figure A8.-Effect of rotation rate and angle of attack on rolling-moment coefficient for basic configuration.  $\delta_a=0^\circ$ ,  $\delta_z=0^\circ$ ,  $\delta_r=-25^\circ$ ,  $\beta=0^\circ$ .

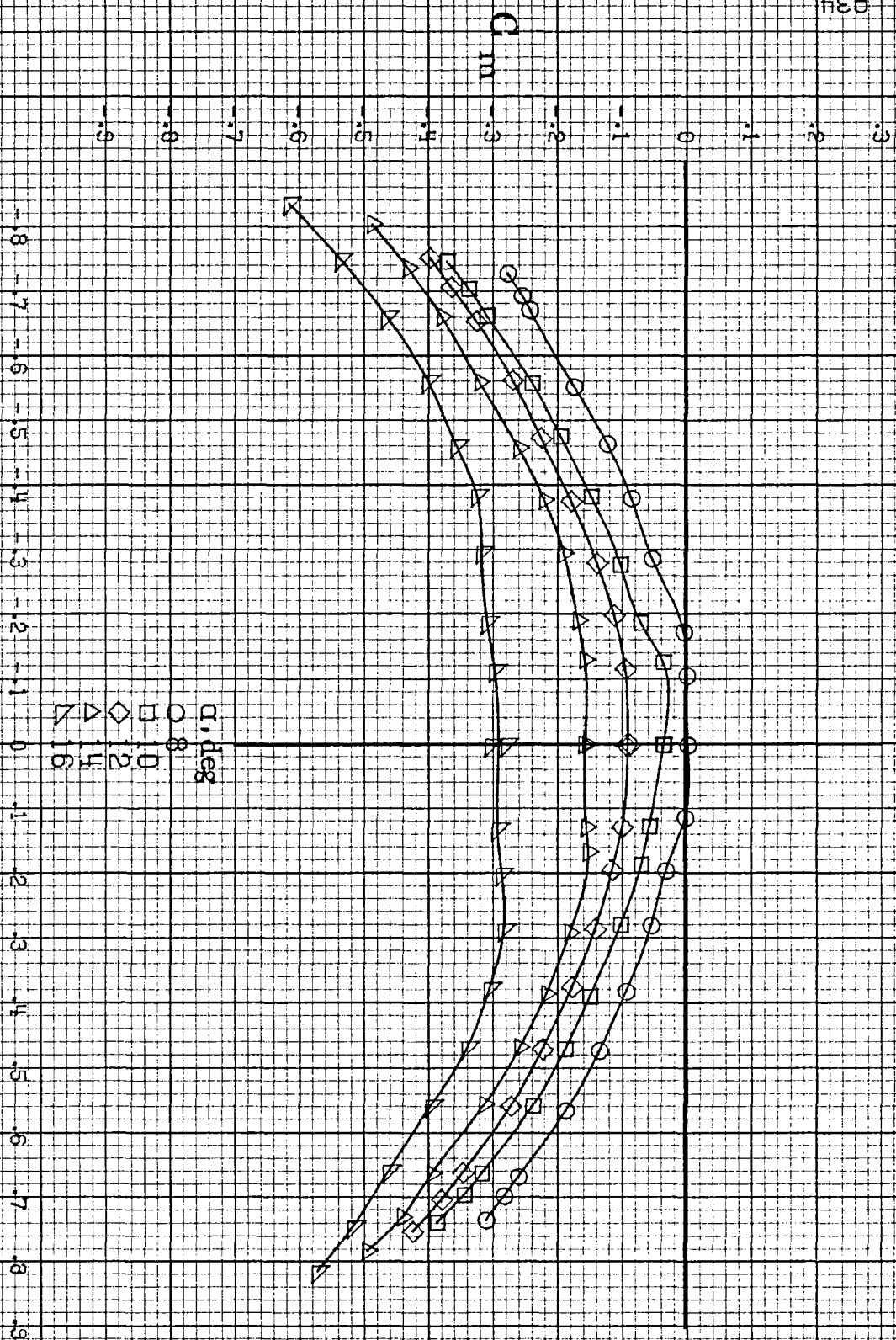




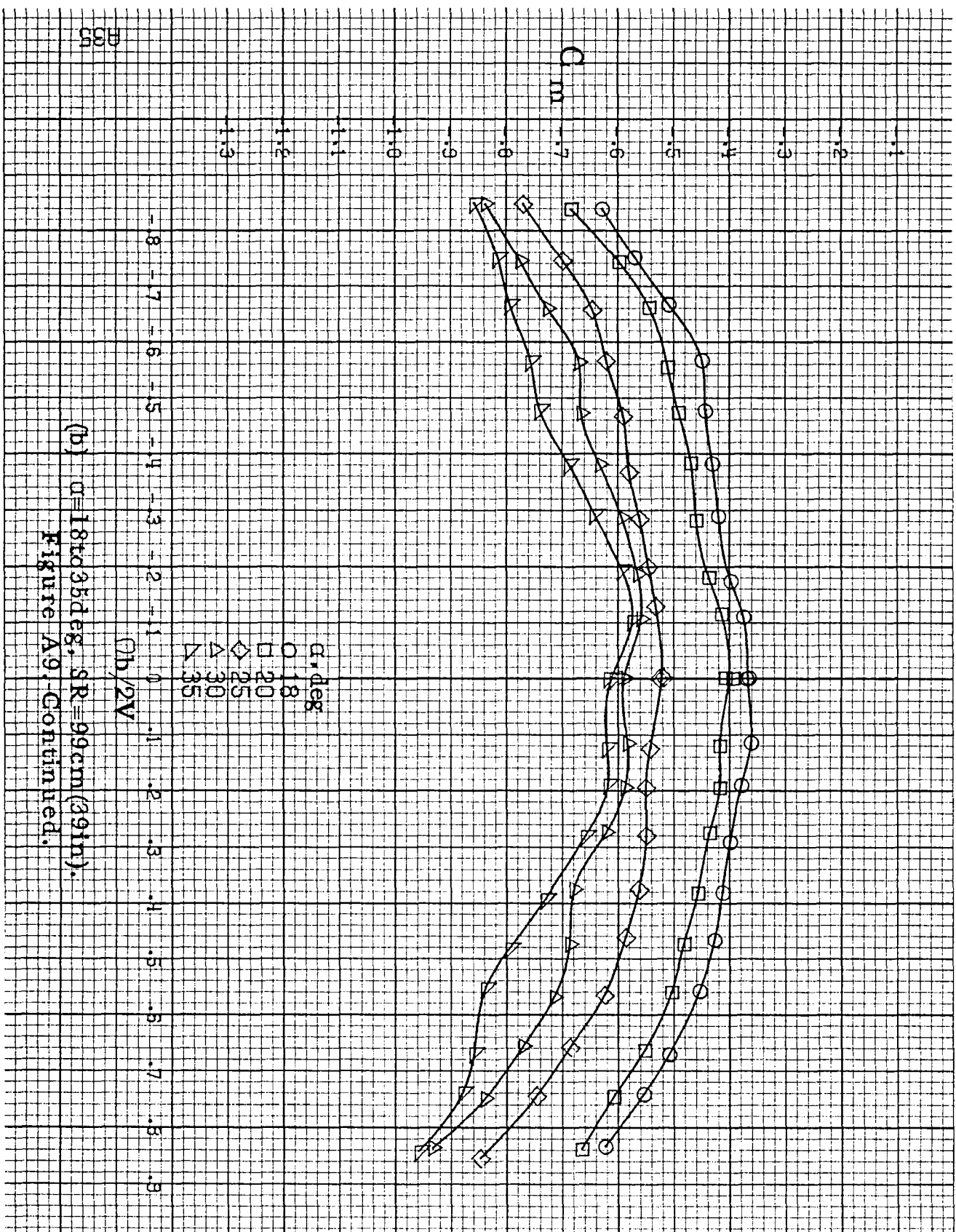
(c)  $\alpha=30$  to  $50$  deg,  $SR=0$ .

Figure A8. Continued.

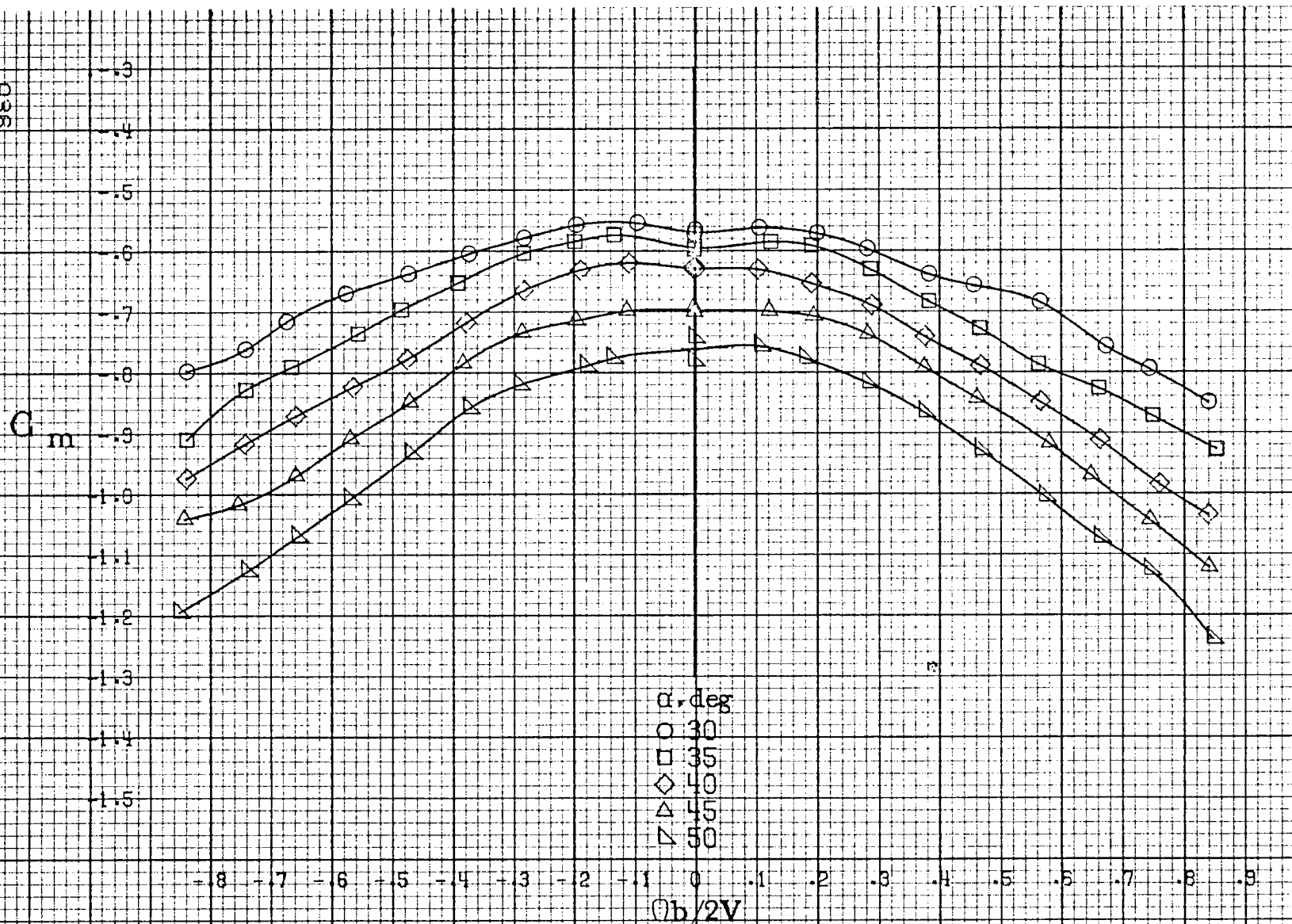




(a)  $G=8$  to  $16 \text{ deg}$ ,  $SR=99 \text{ cm (39 in)}$ .  
 Figure A9. Effect of rotation rate and angle of attack on pitching-moment coefficient for basic configuration.  $\delta_e=0^\circ$ ,  $\delta_a=0^\circ$ ,  $\delta_r=-25^\circ$ ,  $\beta=0^\circ$ .

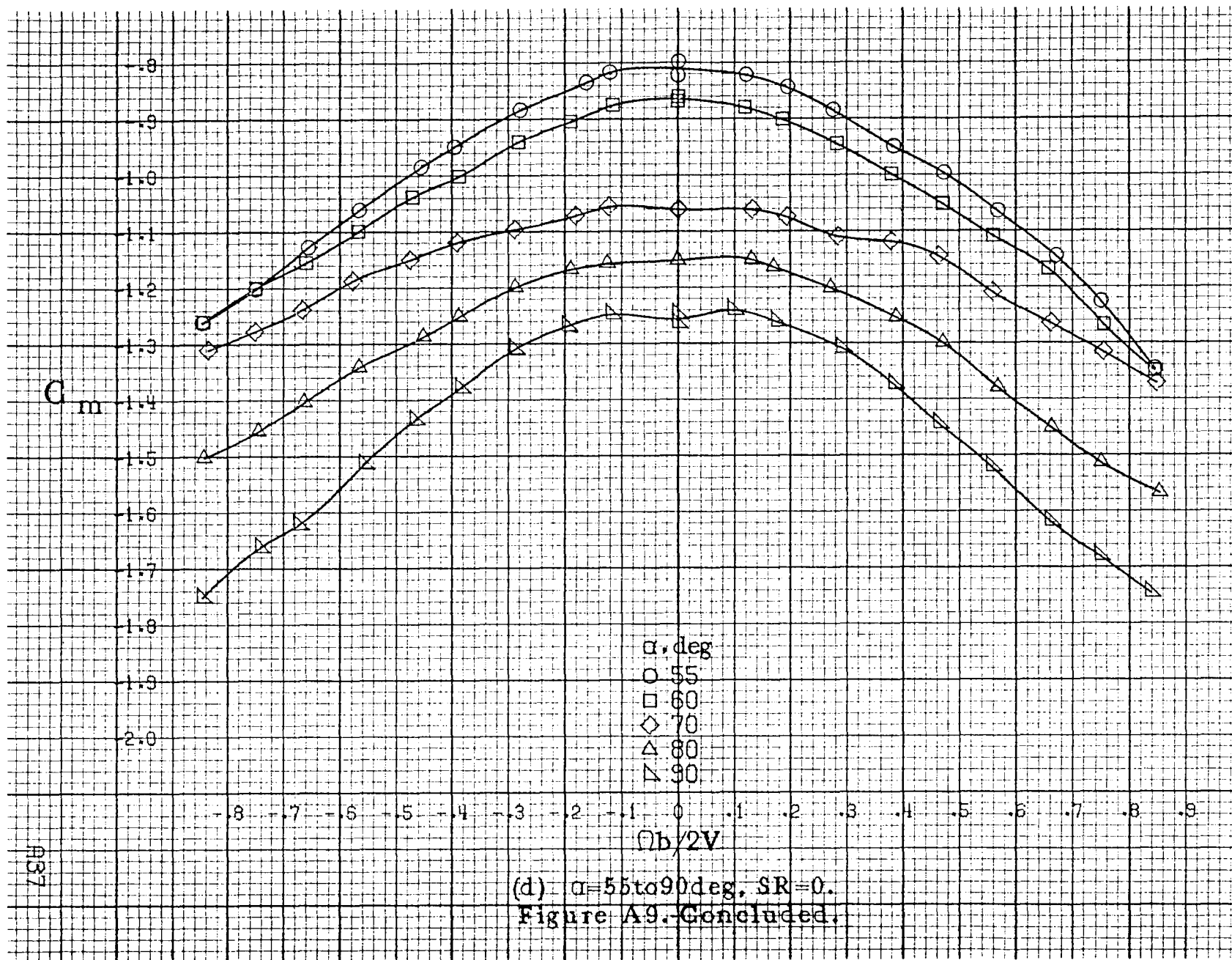


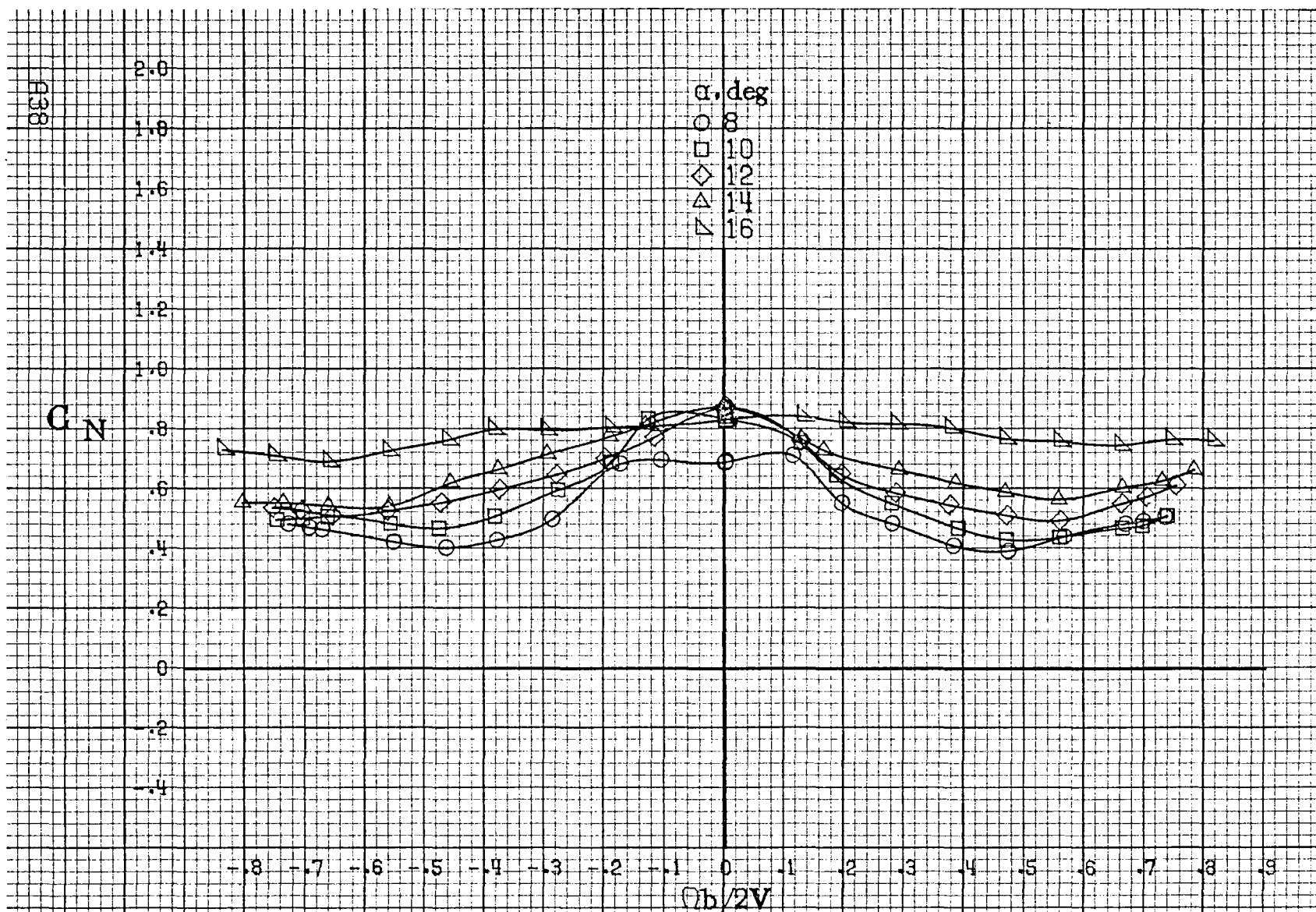




(c)  $\alpha = 30$  to  $50^\circ$ ,  $SR = 0$ .  
Figure A9. Continued.

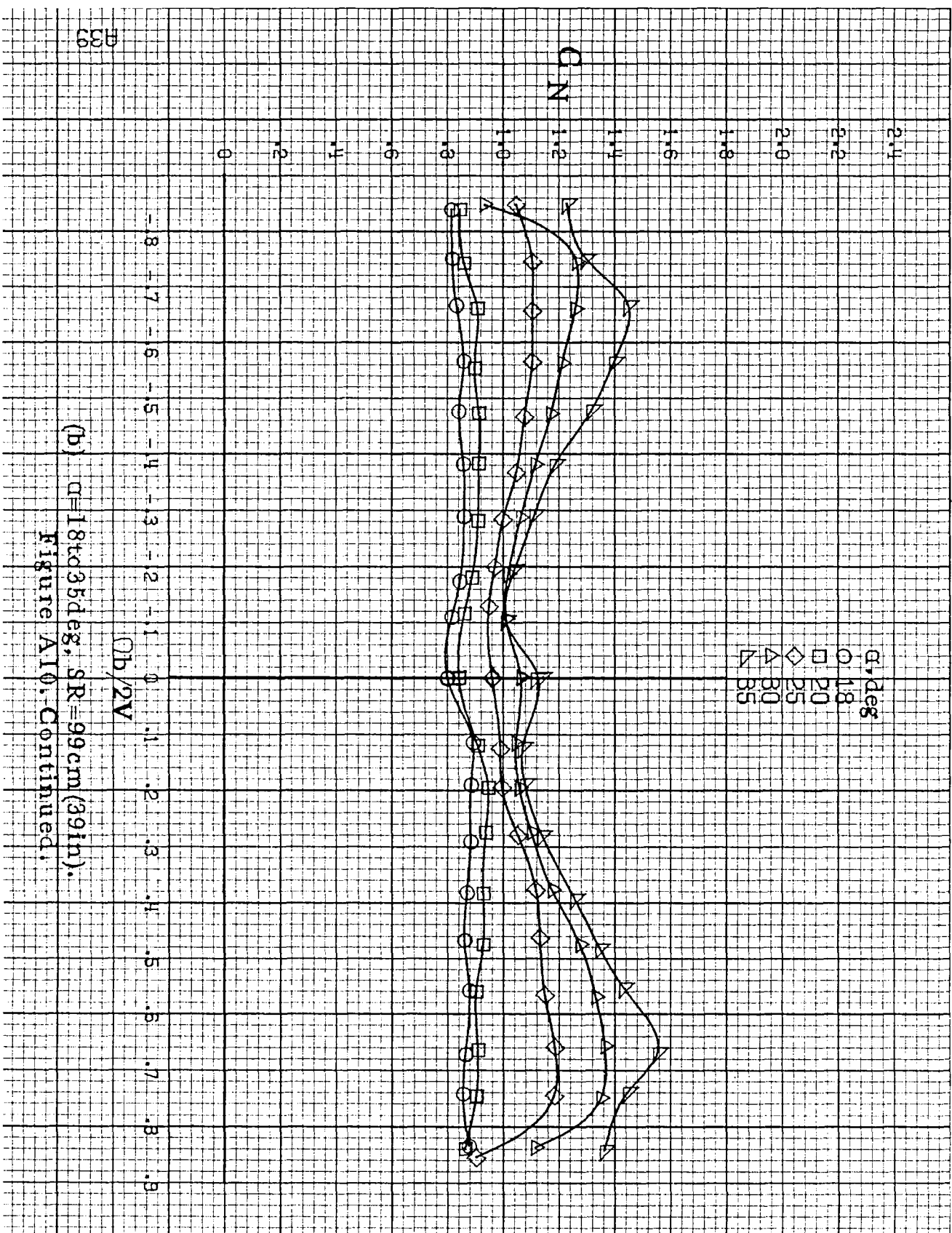






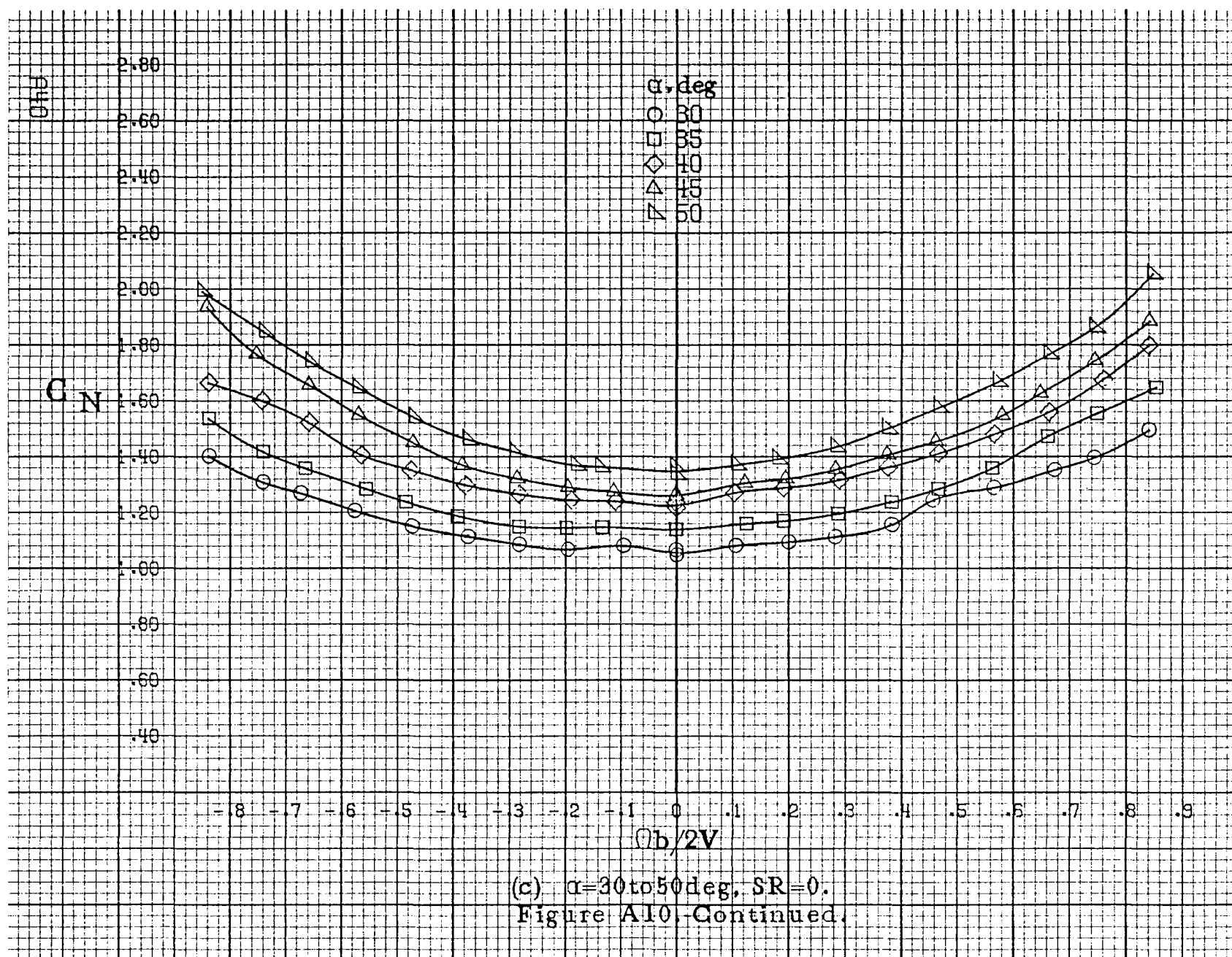
(a)  $\alpha=8\text{ to }16\text{deg}$ ,  $SR=99\text{cm}(39\text{in})$ .

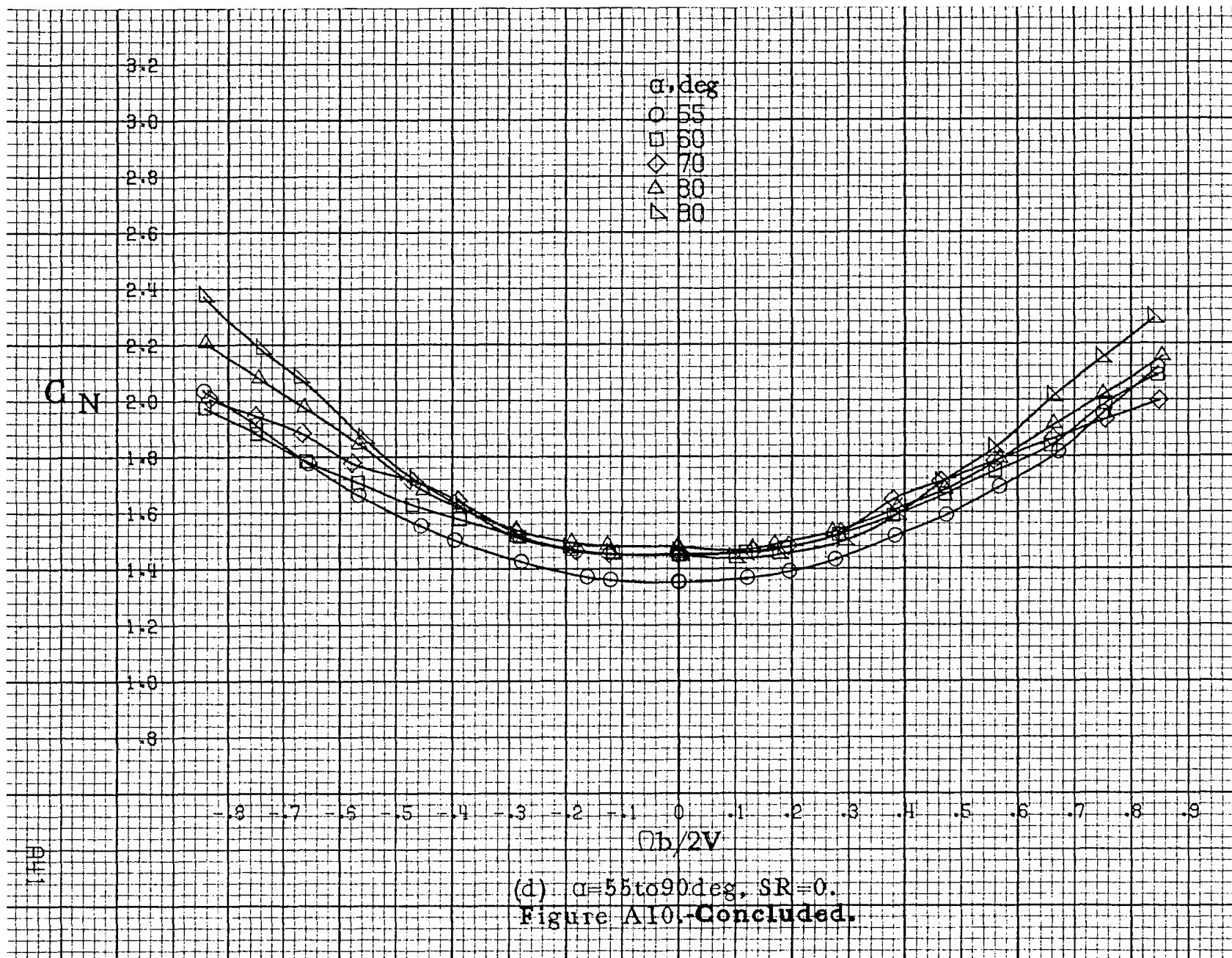
Figure A10.-Effect of rotation rate and angle of attack on normal-force coefficient for basic configuration.  $\delta_e=0^\circ$ ,  $\delta_a=0^\circ$ ,  $\delta_r=-25^\circ$ ,  $\beta=0^\circ$ .

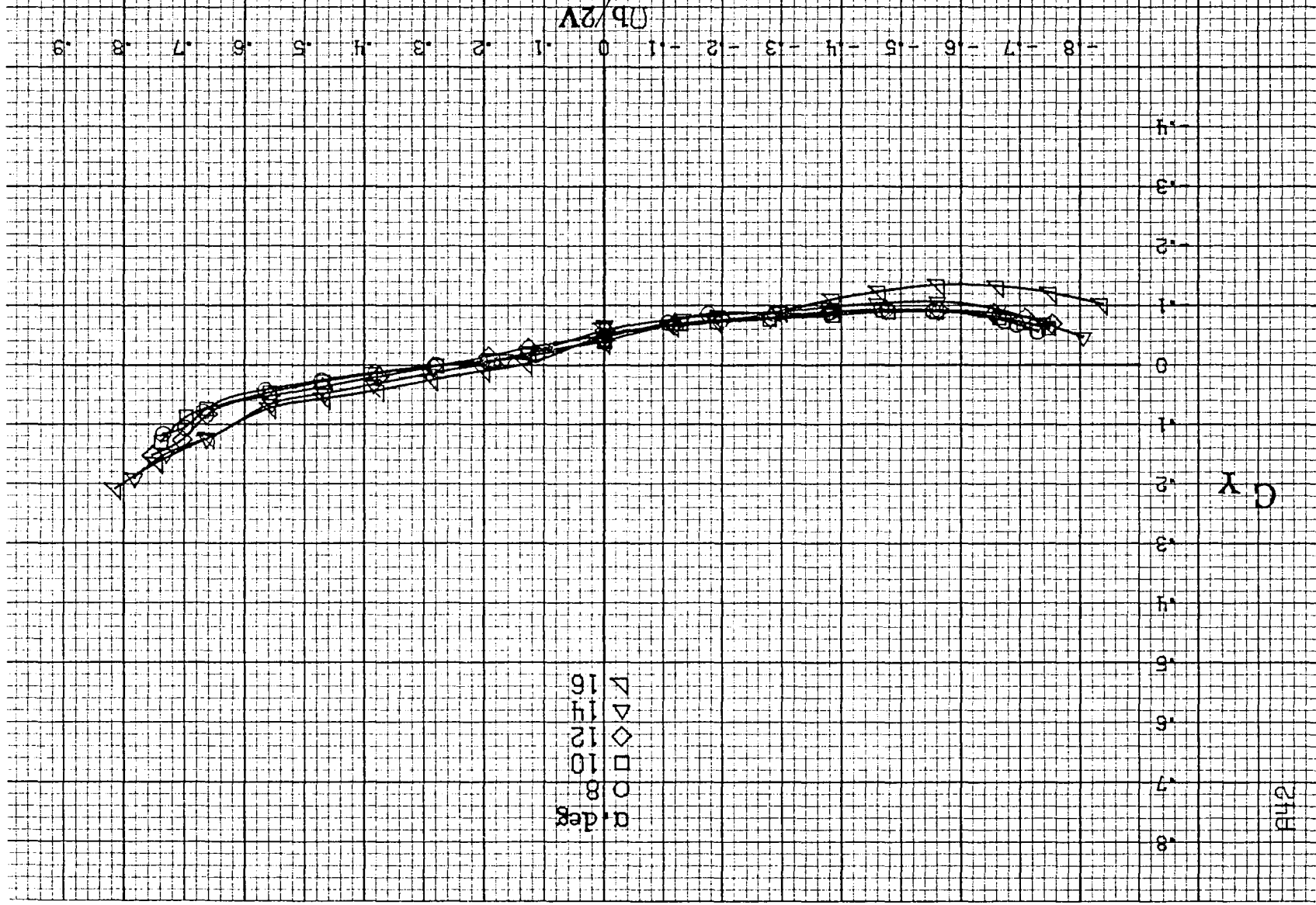


(b)  $\alpha = 18$  to  $35$  deg,  $SR = 99 \text{ cm (39 in.)}$ .

Figure A10. Continued.

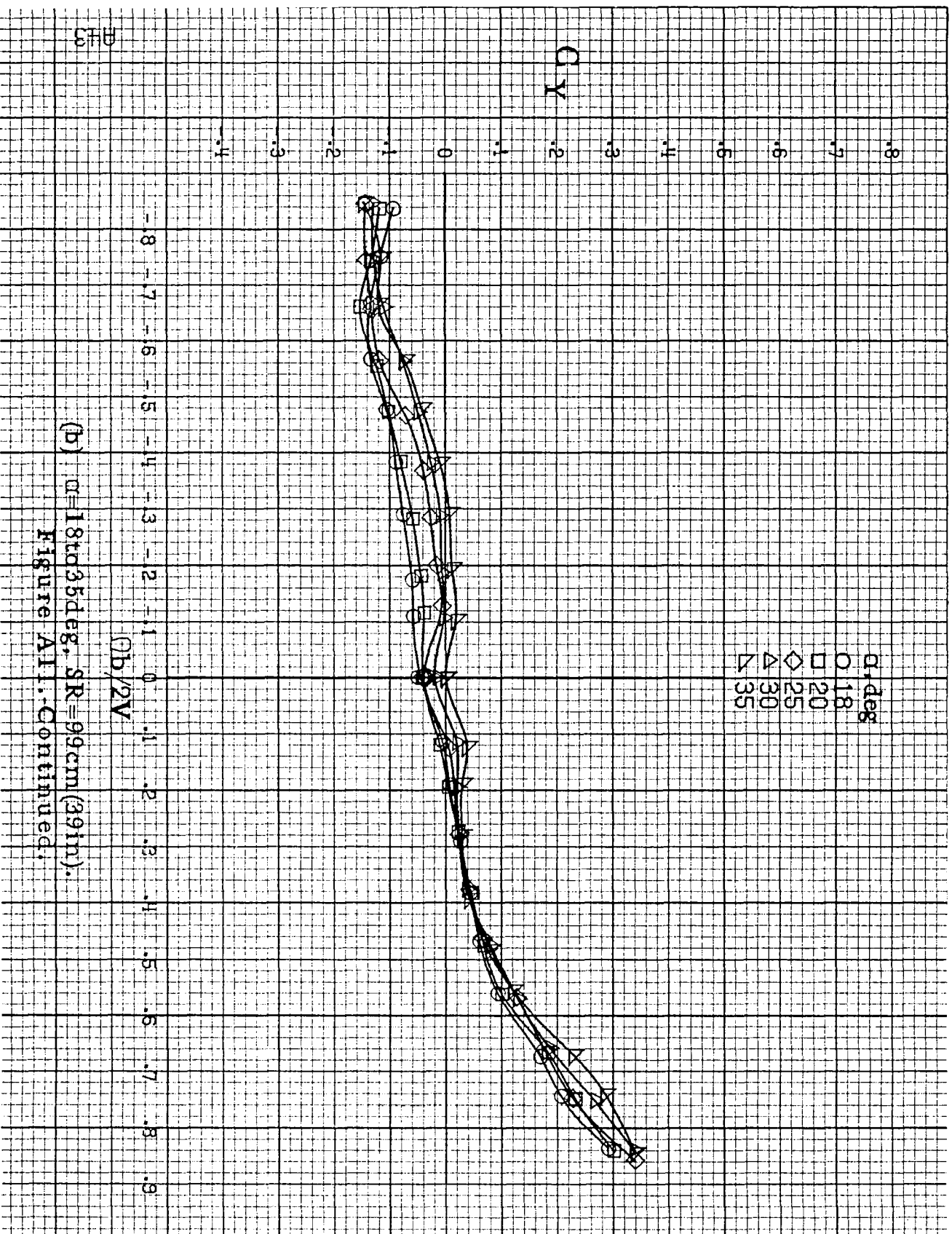




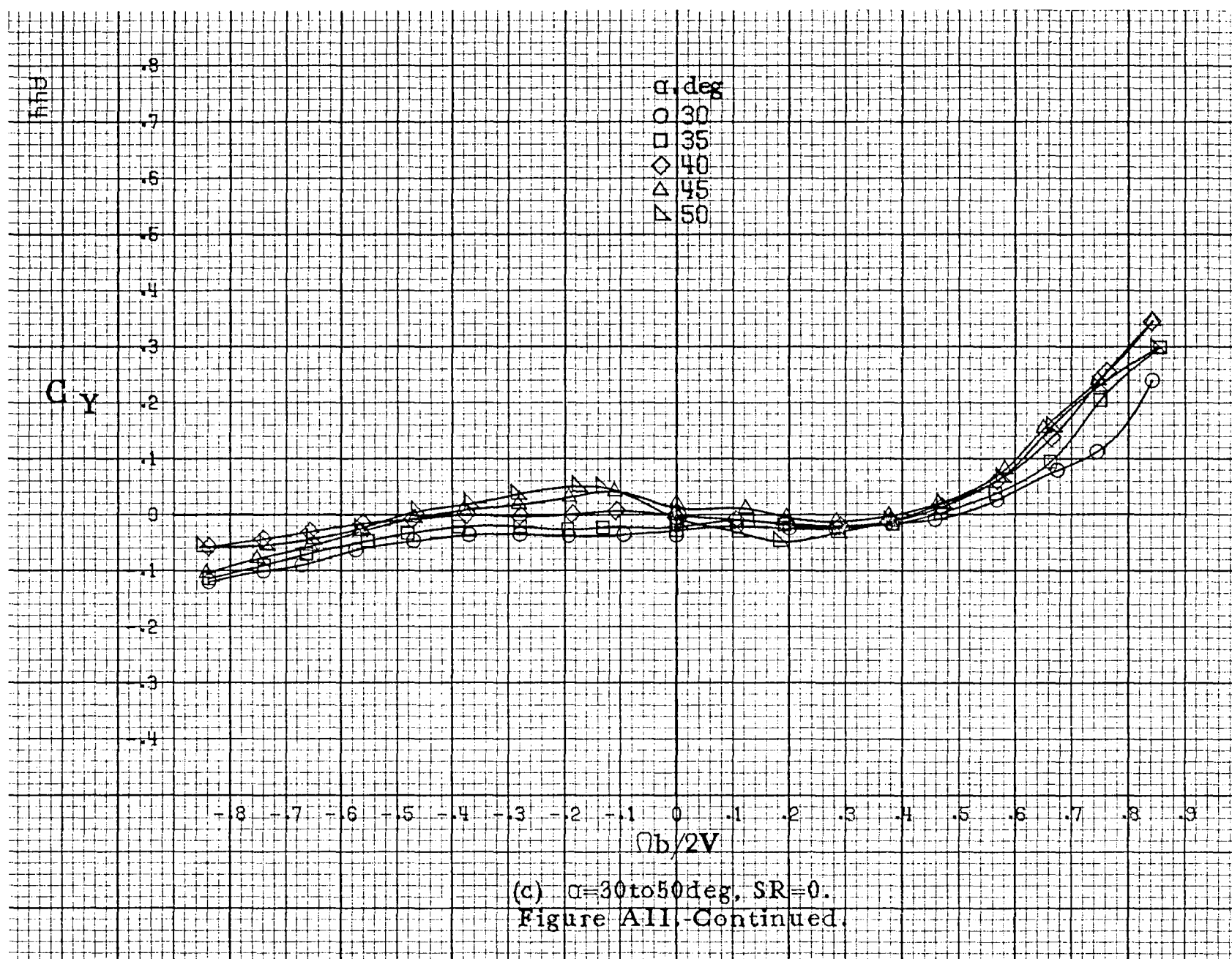


(a)  $d=8$  to  $16$  deg,  $SR=99$  cm (39 in).  
 Figure A11. Effect of rotation rate and angle of attack on side-force coefficient for basic configuration.  $\delta\alpha=0^\circ$ ,  $\delta\alpha=0^\circ$ ,  $\delta\alpha=-25^\circ$ ,  $\delta\alpha=0^\circ$ .

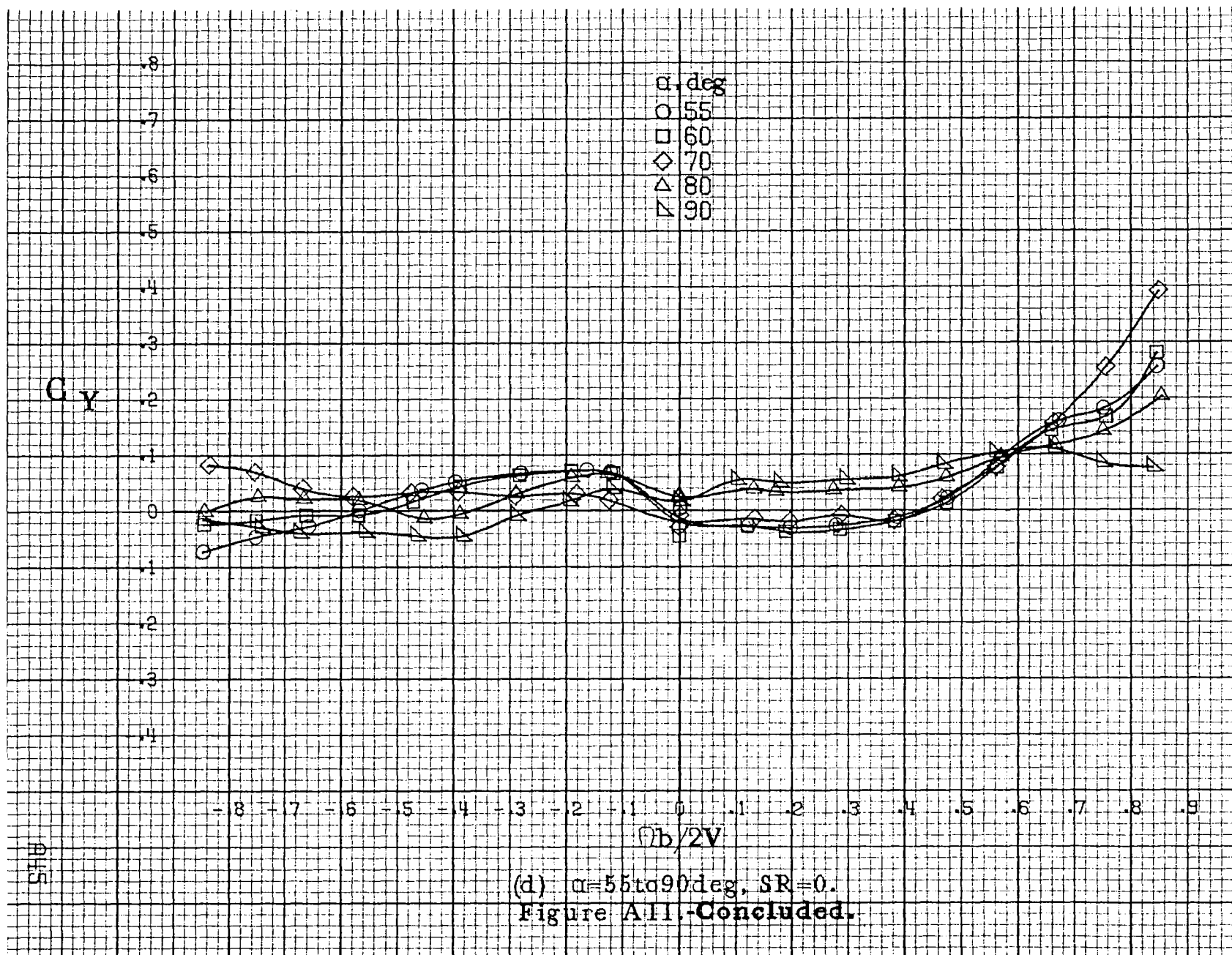


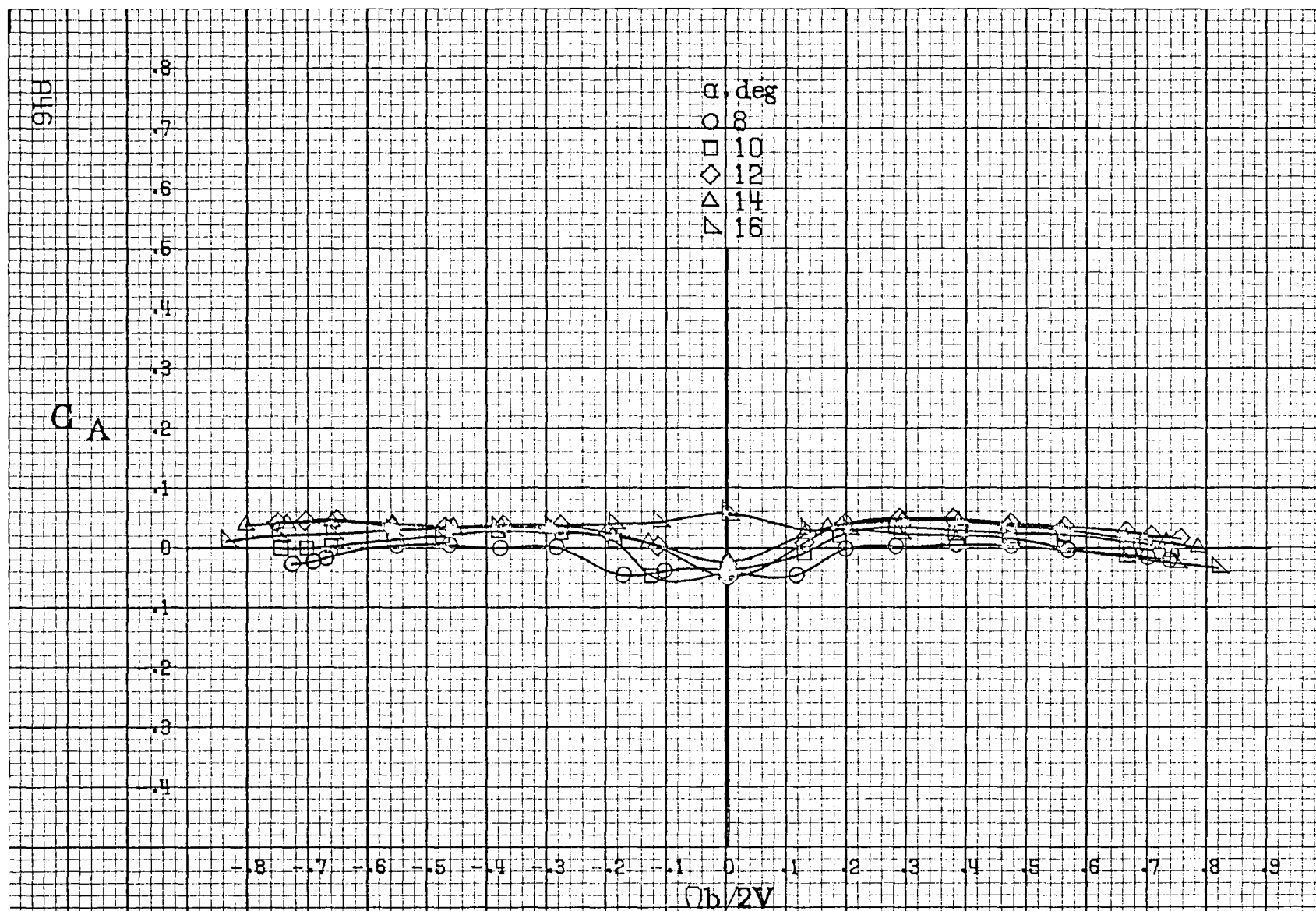


(b)  $\alpha = 18$  to  $35$  deg,  $SR = 99$  cm (39 in).  
Figure A11. Continued.



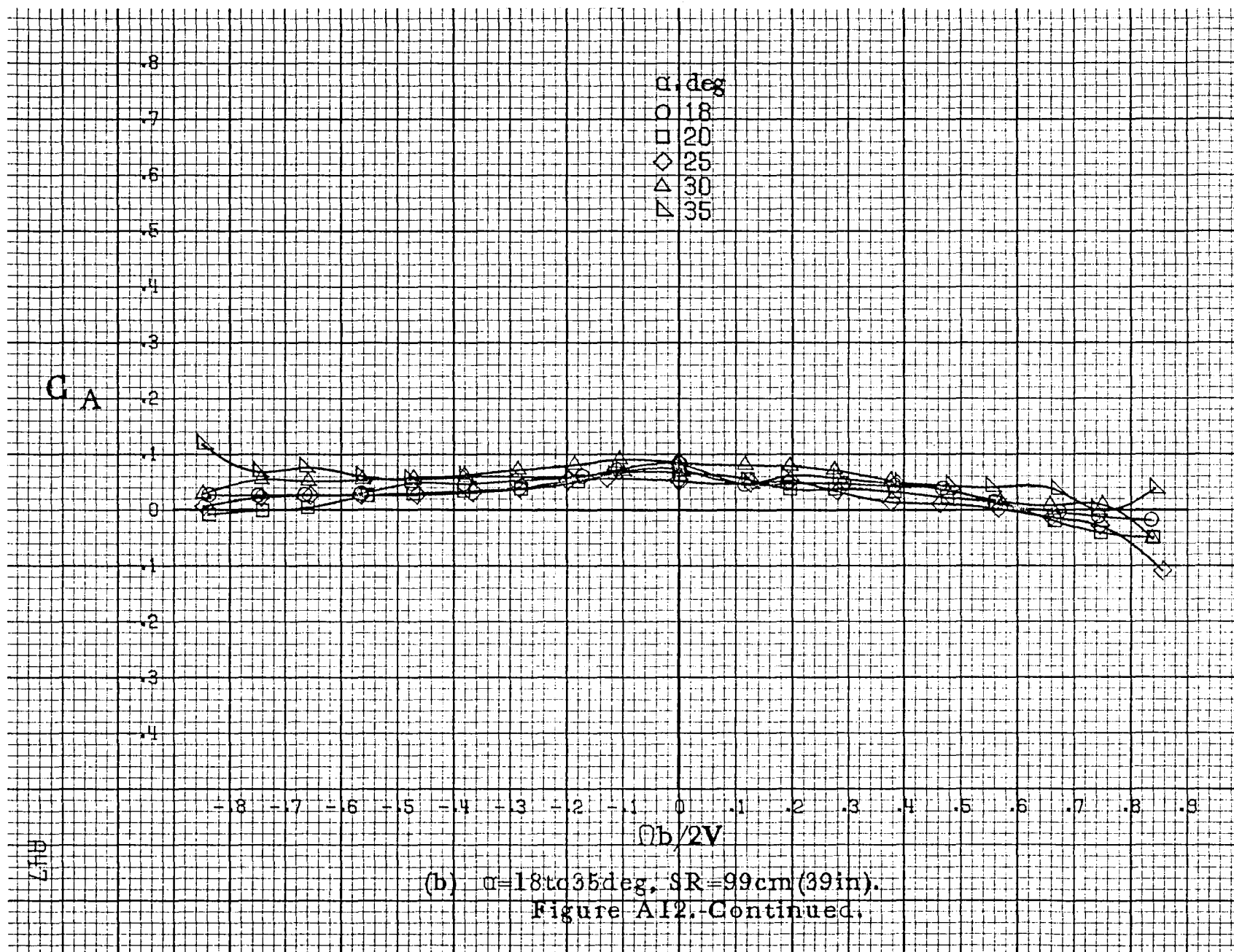


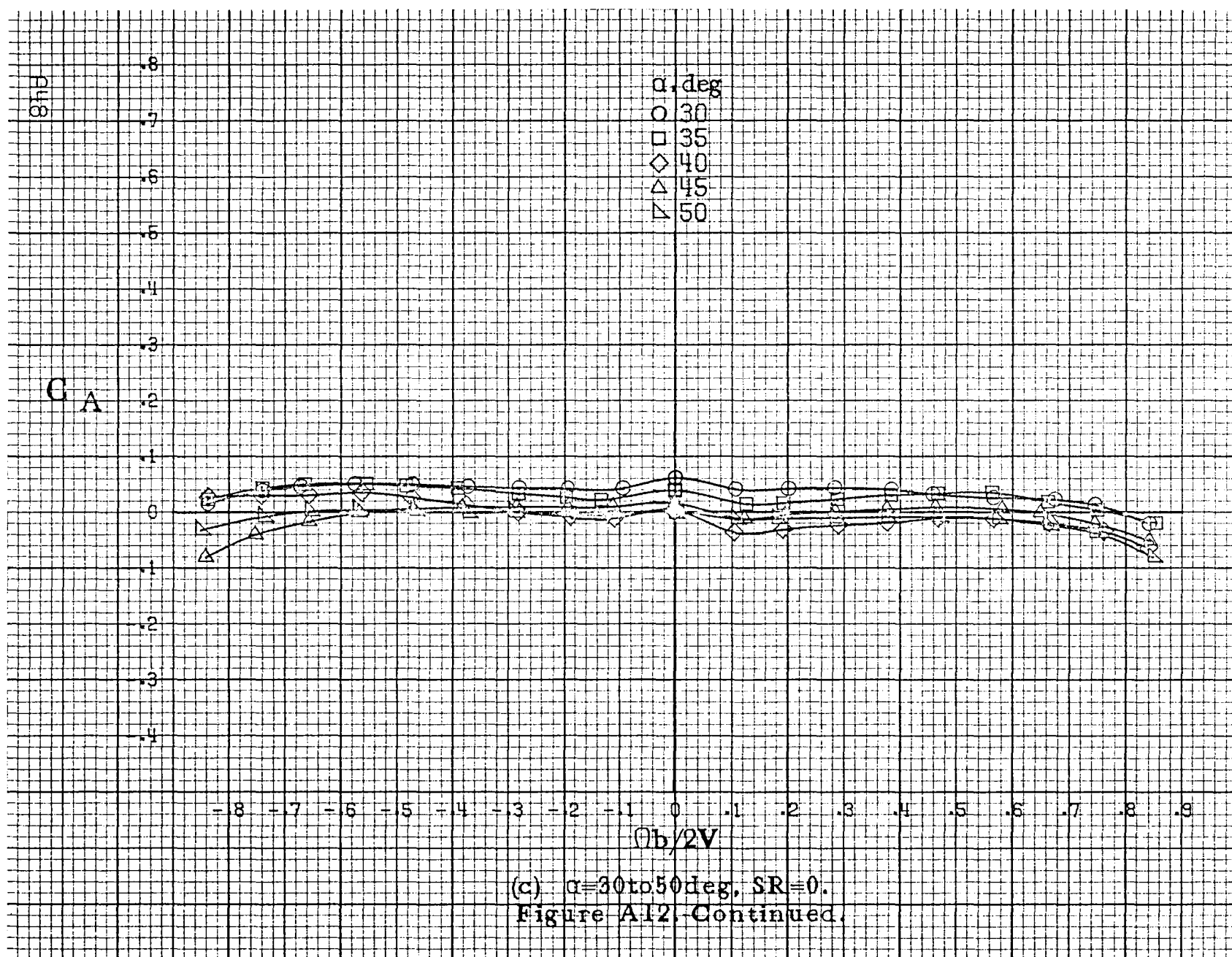


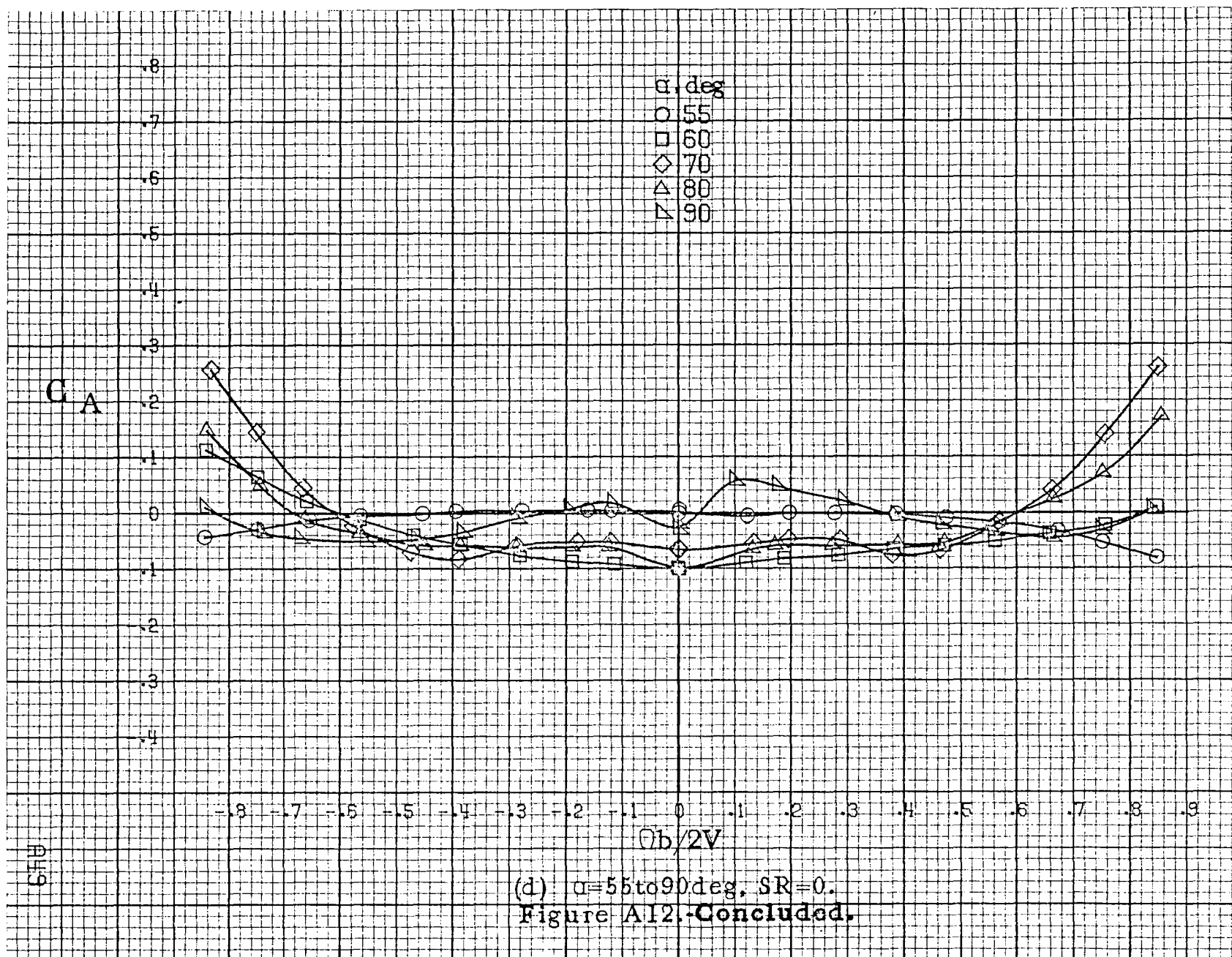


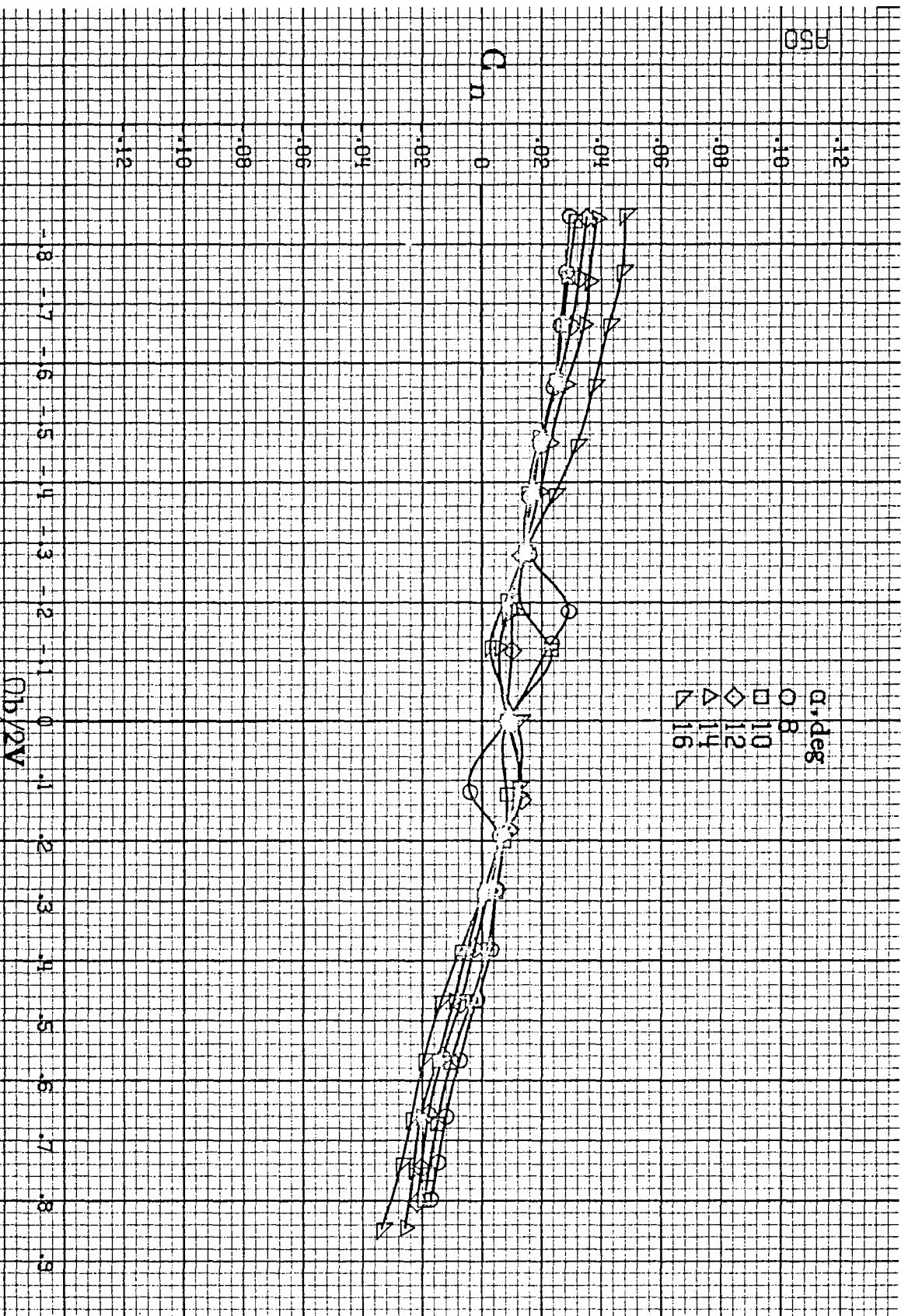
(a)  $\alpha = 8$  to  $16$  deg,  $SR = 99$  cm (39 in).

Figure A12. Effect of rotation rate and angle of attack on axial force coefficient for basic configuration.  $\delta_a = 0^\circ$ ,  $\delta_s = 0^\circ$ ,  $\delta_r = -25^\circ$ ,  $\beta = 0^\circ$ .



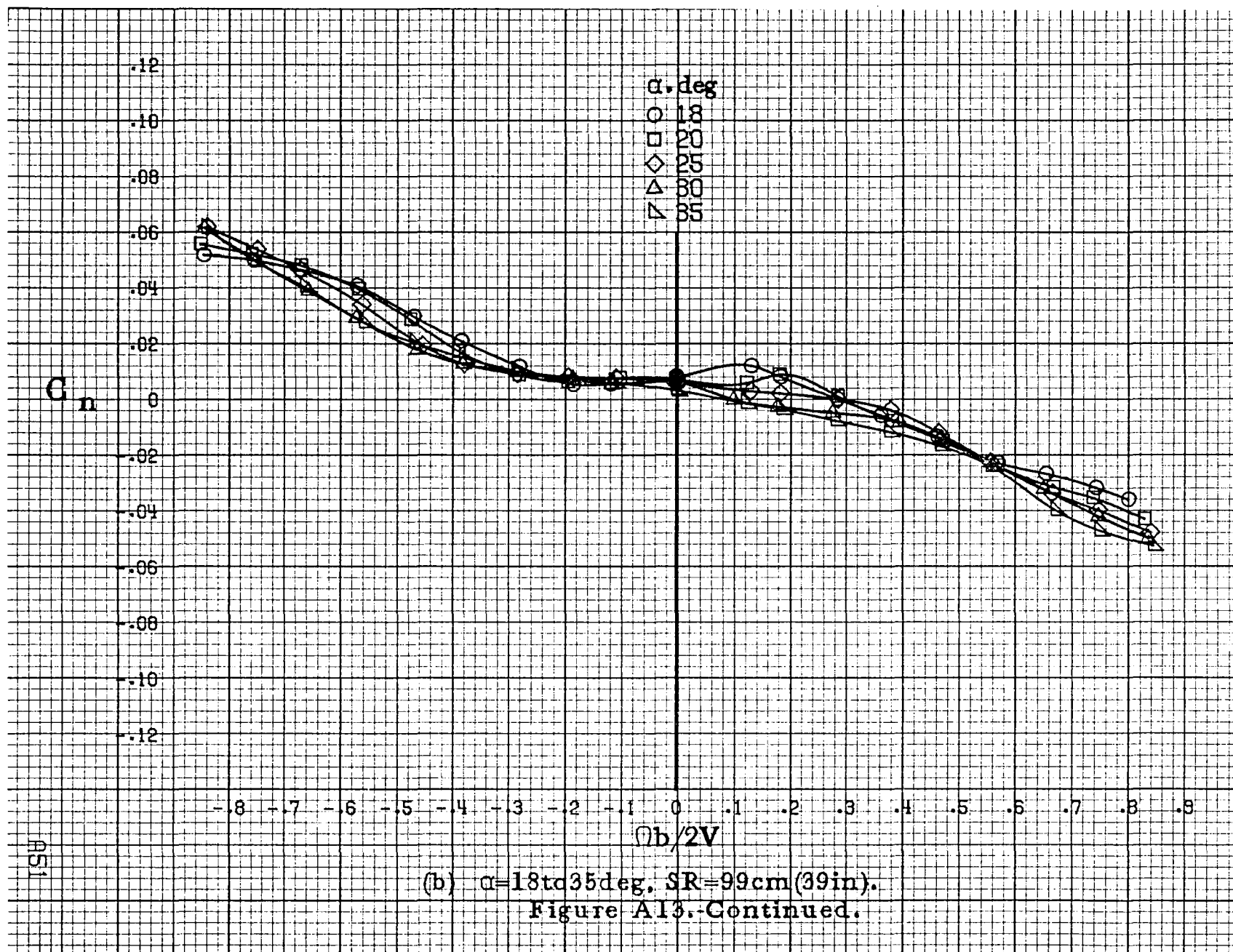


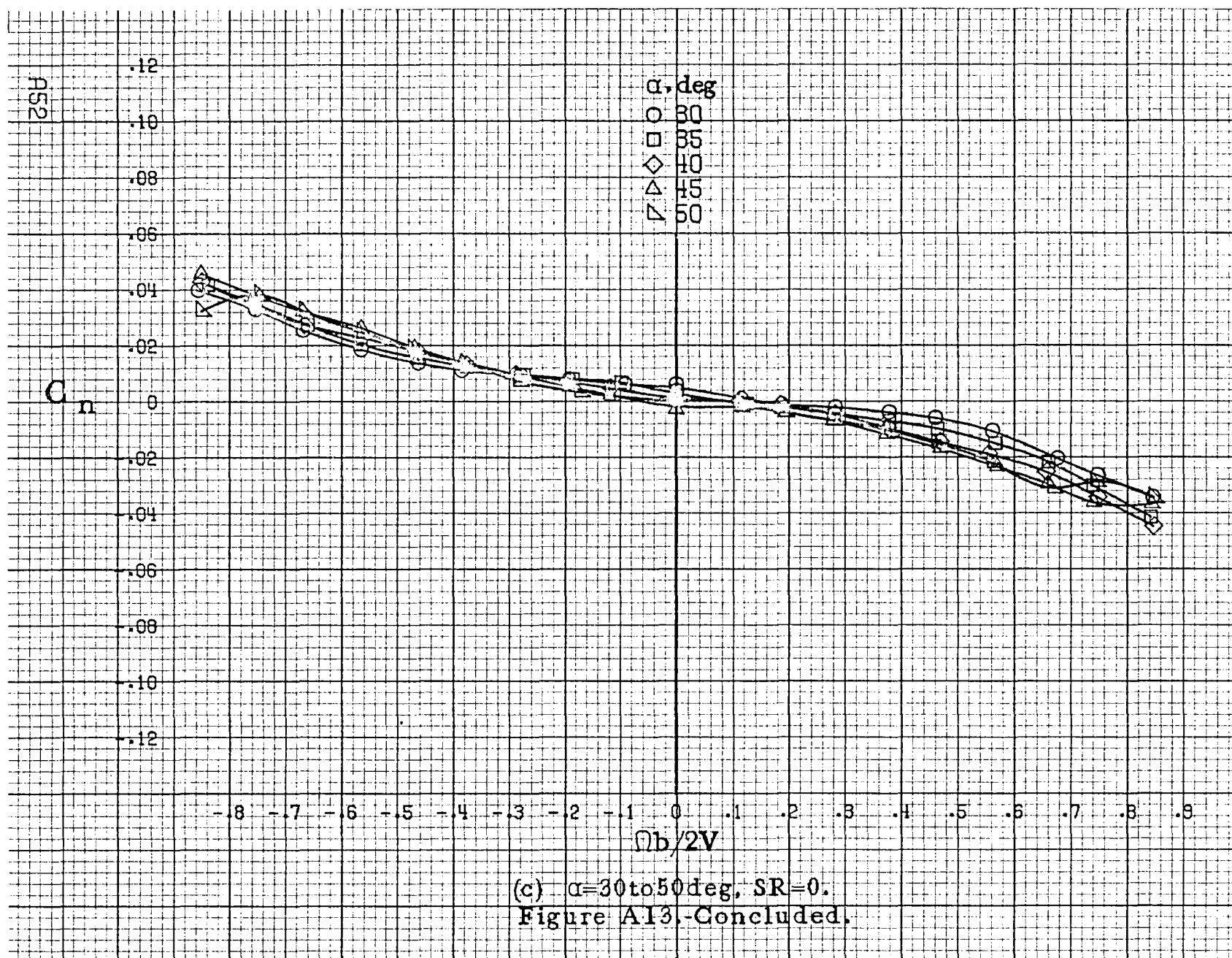




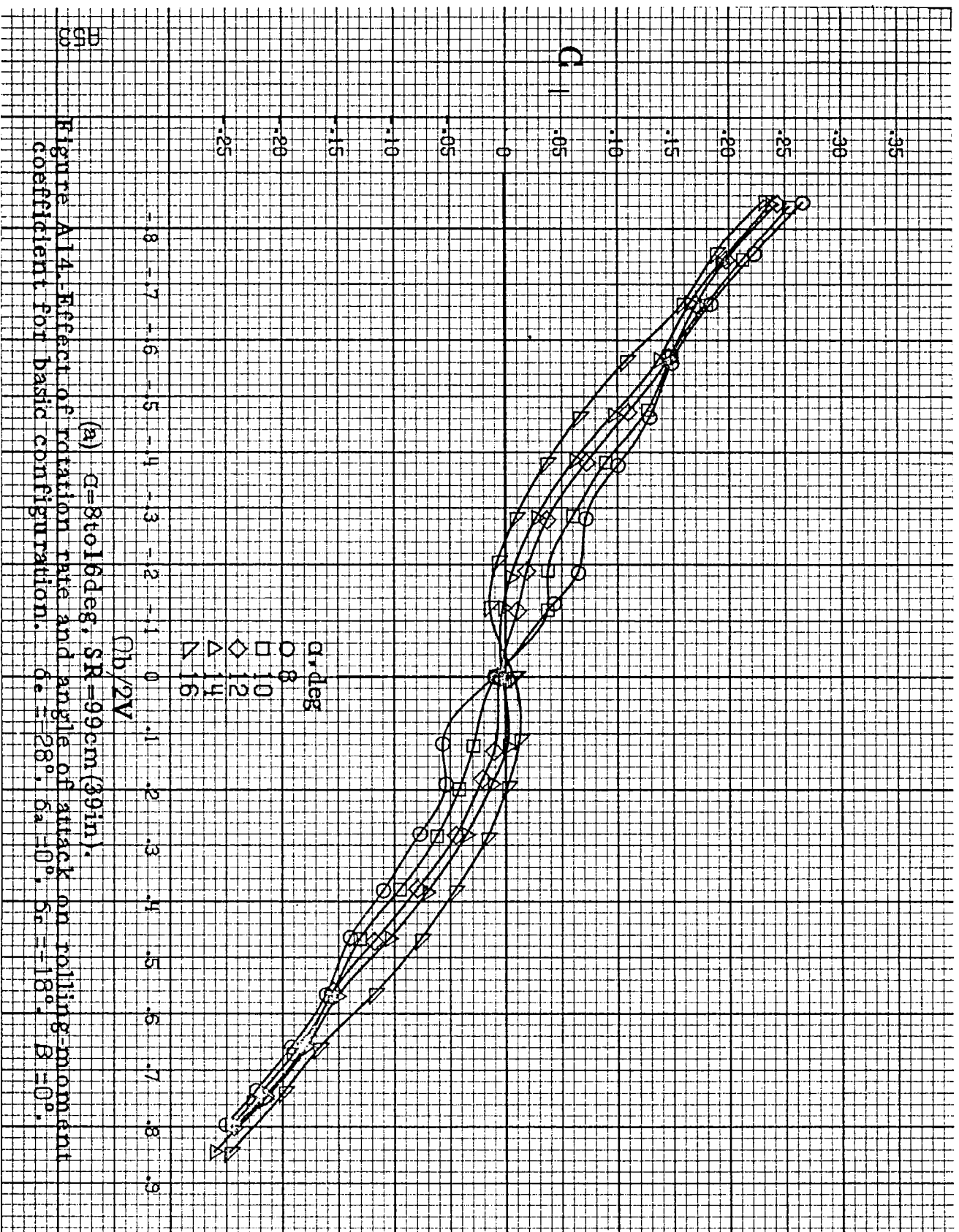
(a)  $G=8$  to  $16$  deg,  $SR=99$  cm (39 in).

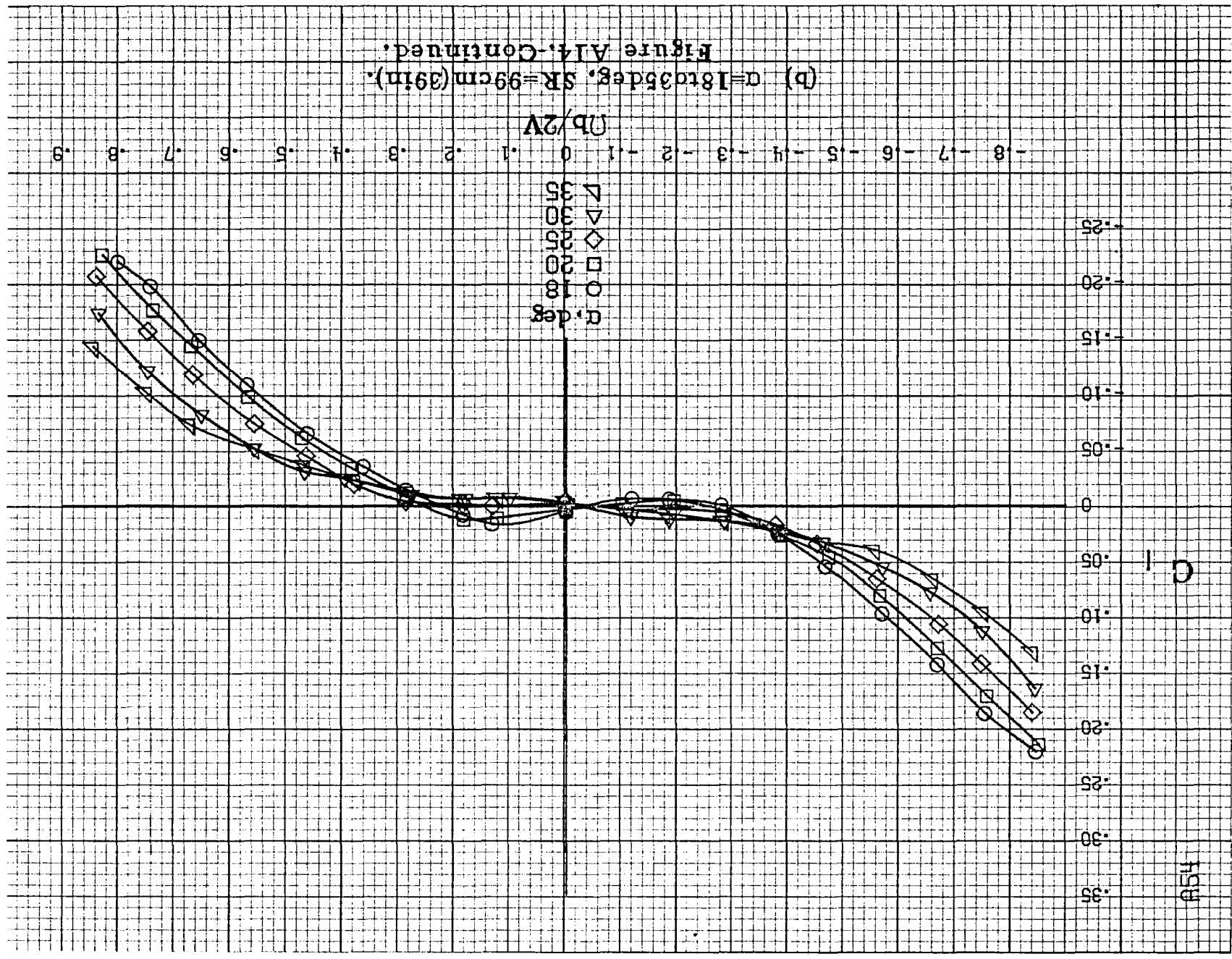












(b)  $\alpha=18$  to  $35^\circ$ ,  $SR=99\text{cm}$  (39in).  
Figure A14. Continued.

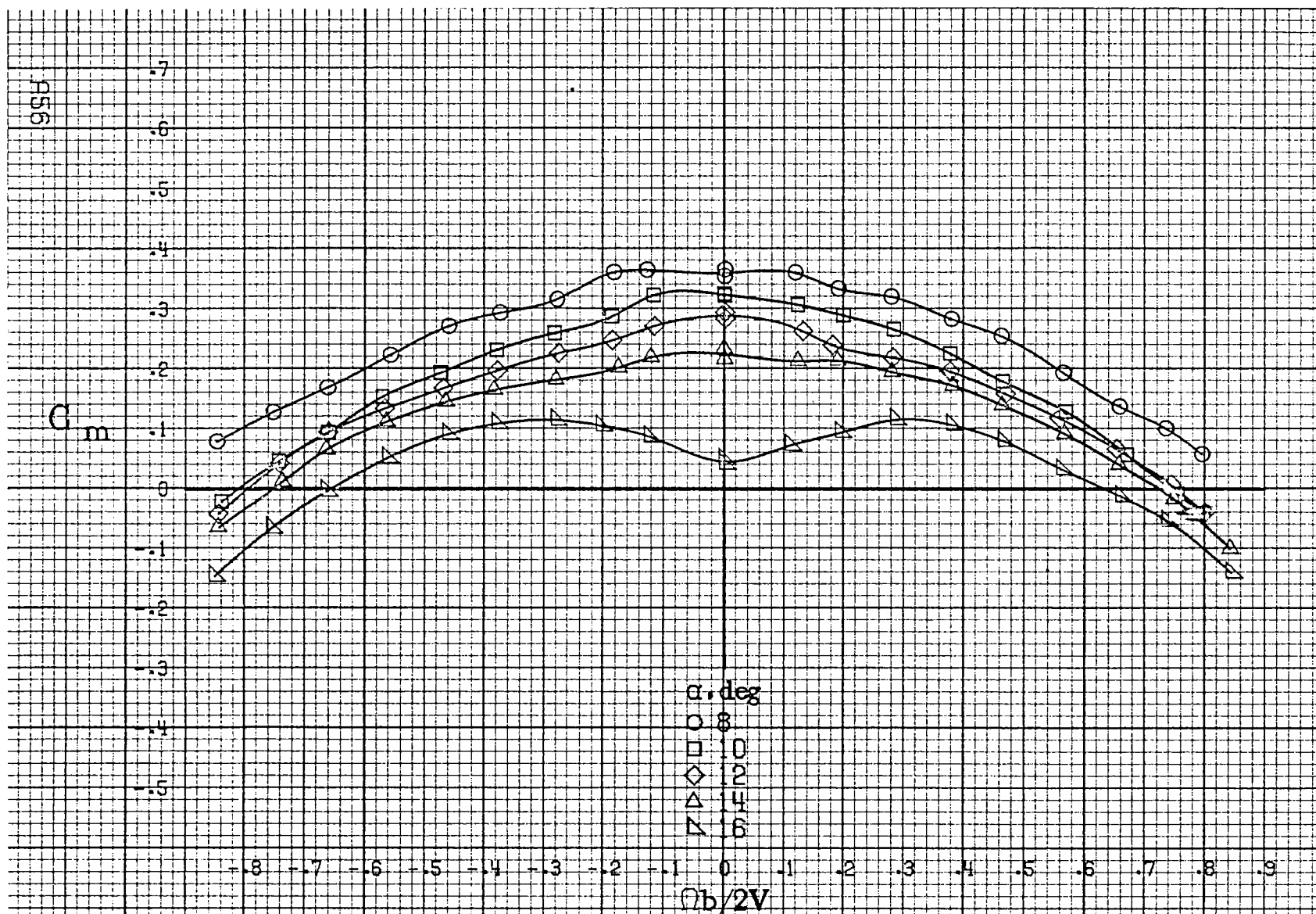
C<sub>I</sub>

.35  
.30  
.25  
.20  
.15  
.10  
.05  
0  
-.05  
-.10  
-.15  
-.20  
-.25

$\alpha$ , deg  
○ 30  
□ 35  
◇ 40  
△ 45  
▽ 50

-.8 -.7 -.6 -.5 -.4 -.3 -.2 -.1 0 .1 .2 .3 .4 .5 .6 .7 .8  
 $\eta b/2V$

(c)  $\alpha=30$  to  $50$  deg,  $SR=0$ .  
Figure A14. Concluded.



(a)  $\alpha = 8$  to  $16$  deg, SR = 99 cm (39 in).

Figure A15. Effect of rotation rate and angle of attack on pitching-moment coefficient for basic configuration.  $\delta_a = -28^\circ$ ,  $\delta_a = 0^\circ$ ,  $\delta_r = -18^\circ$ .  $\beta = 0^\circ$ .

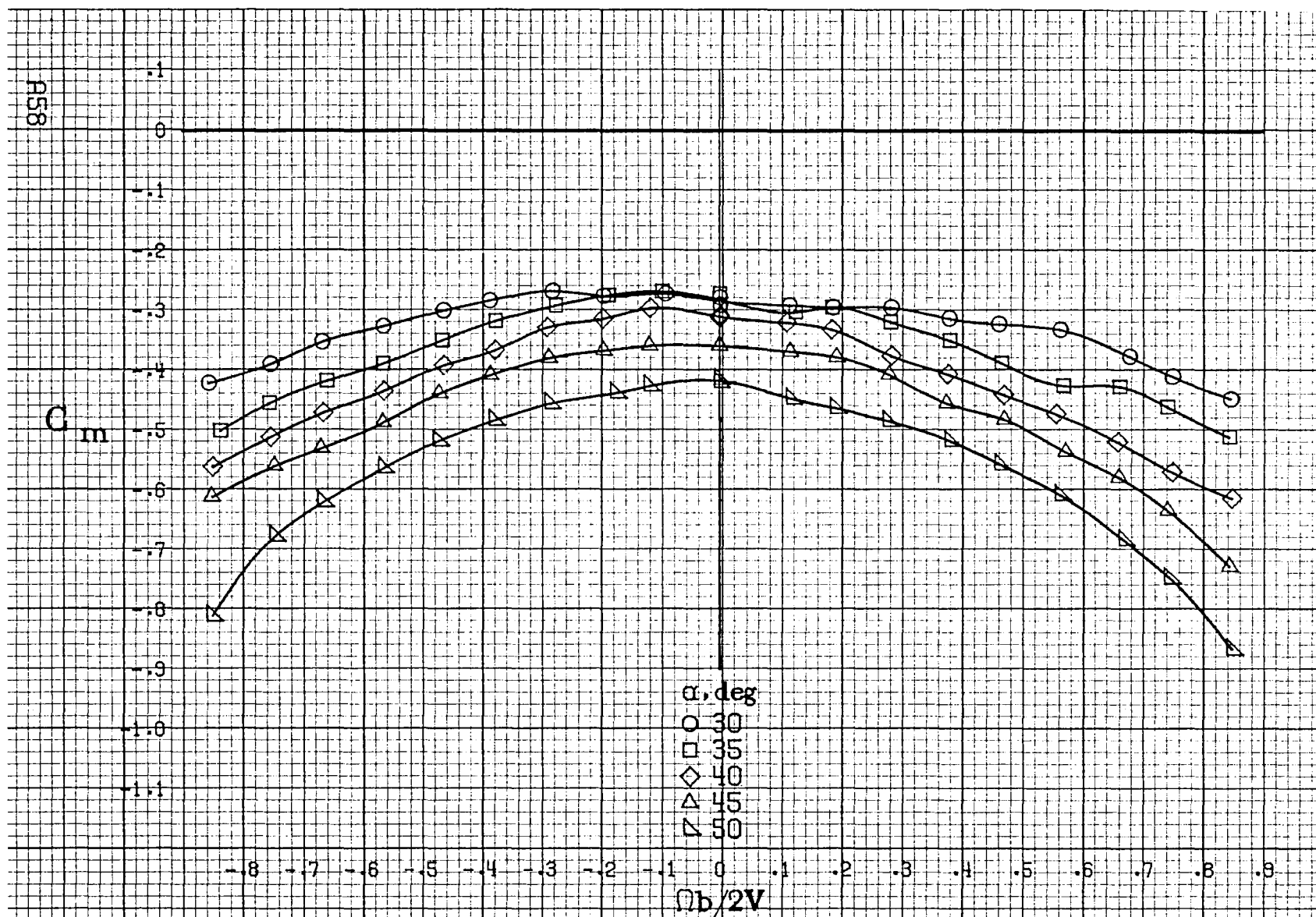
$C_m$

.3  
.2  
.1  
0  
-.1  
-.2  
-.3  
-.4  
-.5  
-.6  
-.7  
-.8  
-.9

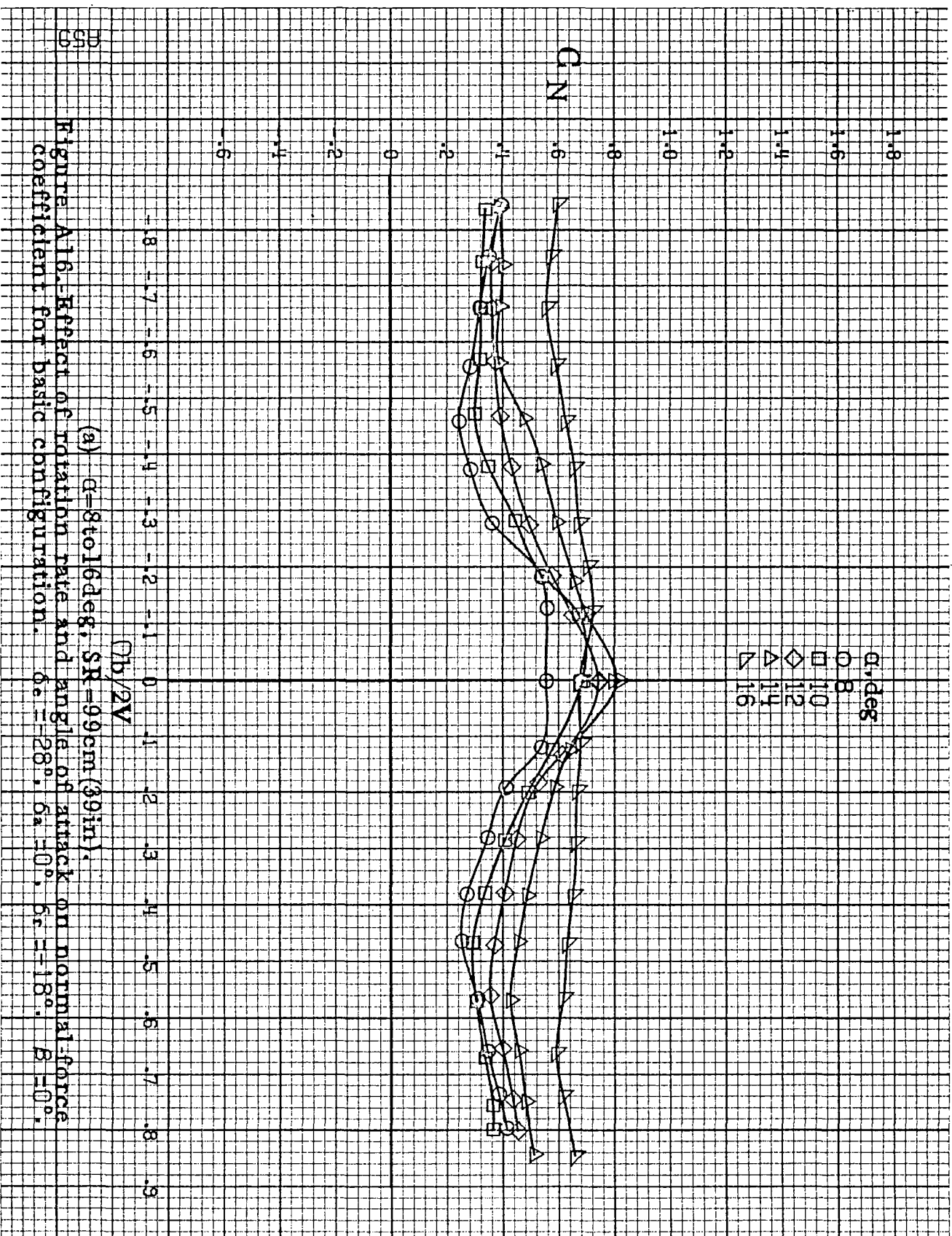
$\alpha$ , deg  
○ 18  
□ 20  
◇ 25  
△ 30  
▽ 35

-.8 -.7 -.6 -.5 -.4 -.3 -.2 -.1 0 .1 .2 .3 .4 .5 .6 .7 .8 .9  
 $nb/2V$

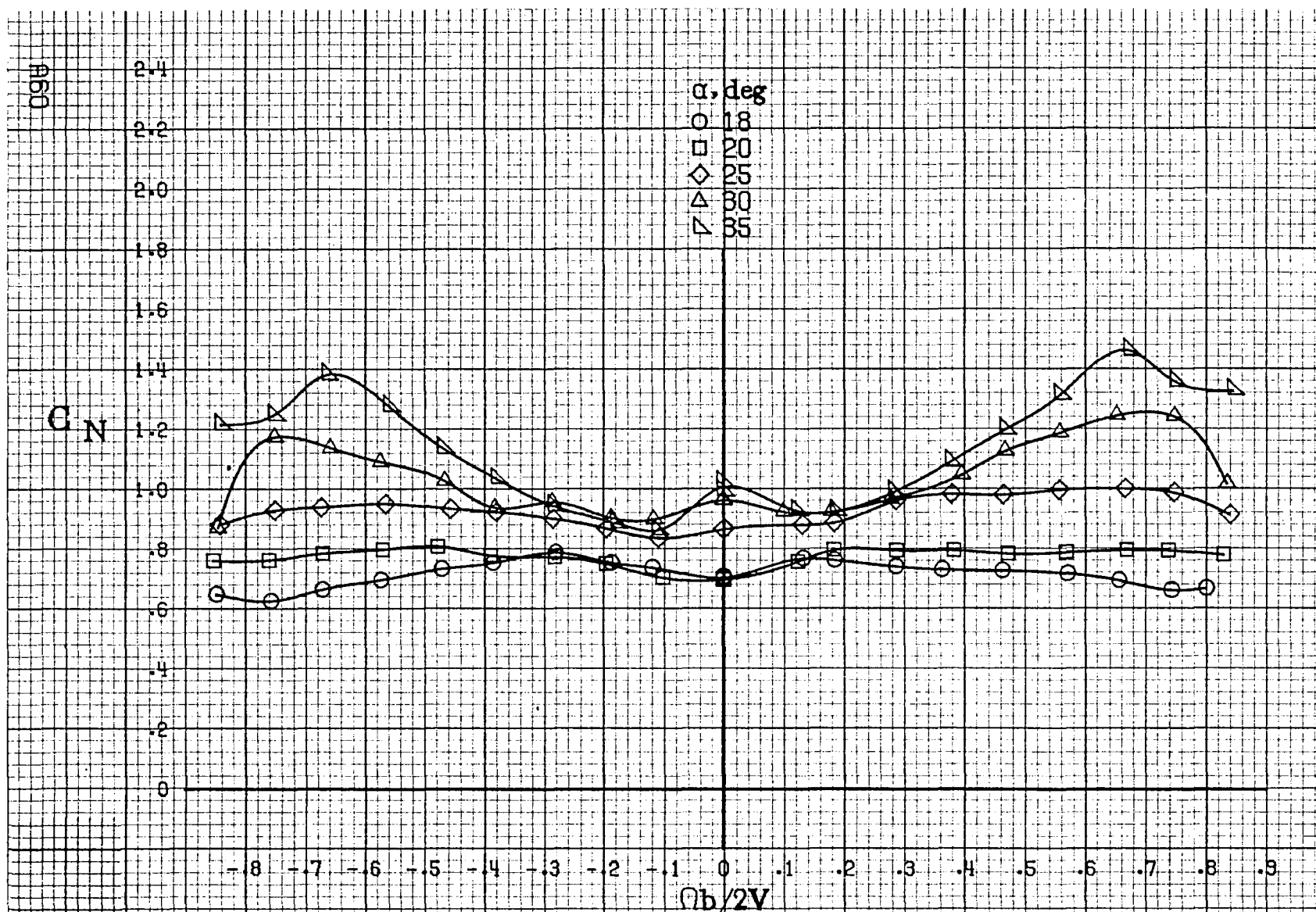
(b)  $\alpha=18$  to  $35$  deg.  $SR=99$  cm (39 in).  
Figure A15.-Continued.



(c)  $\alpha=30$  to  $50^\circ$ ,  $SR=0$ .  
Figure A15-Concluded.



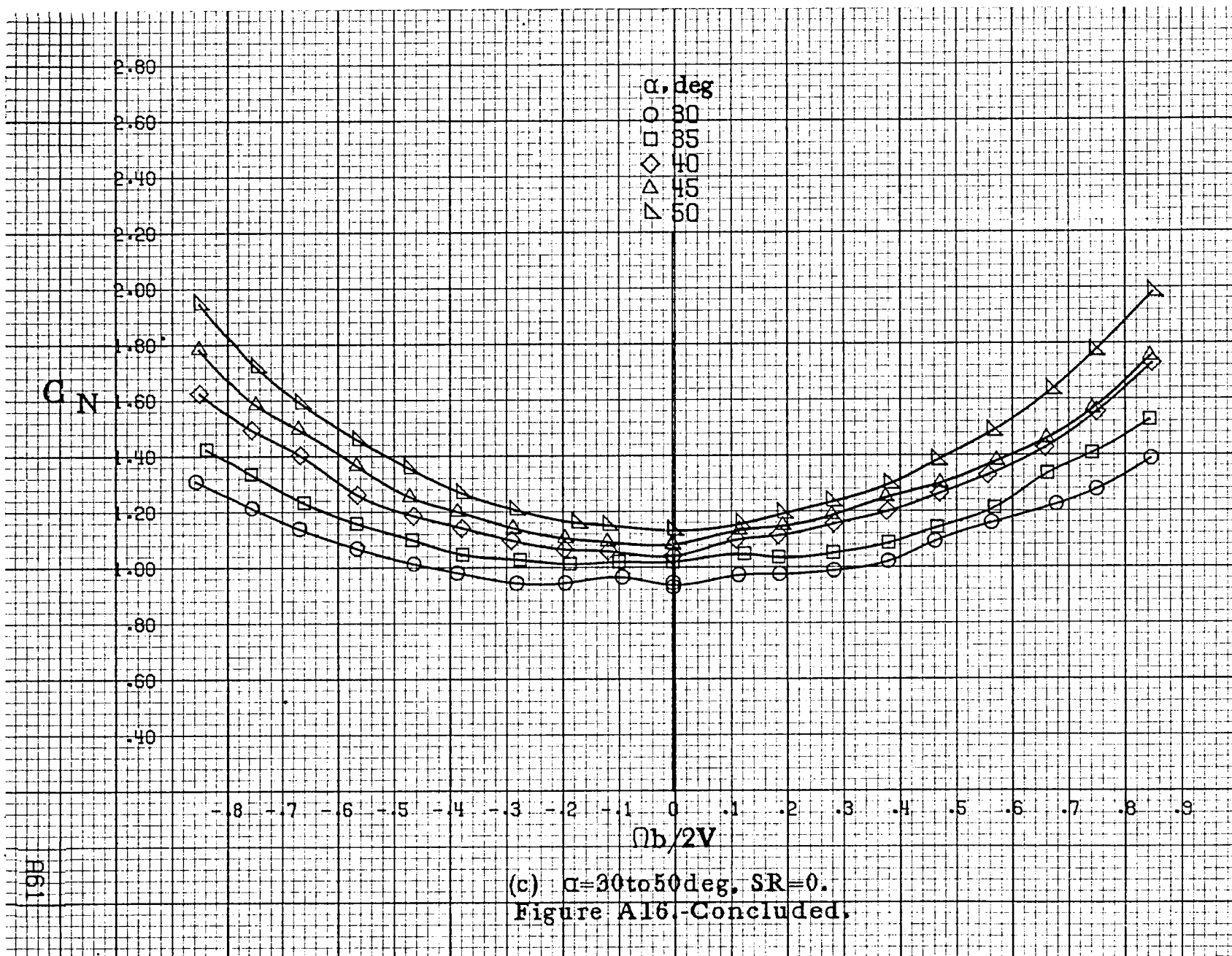


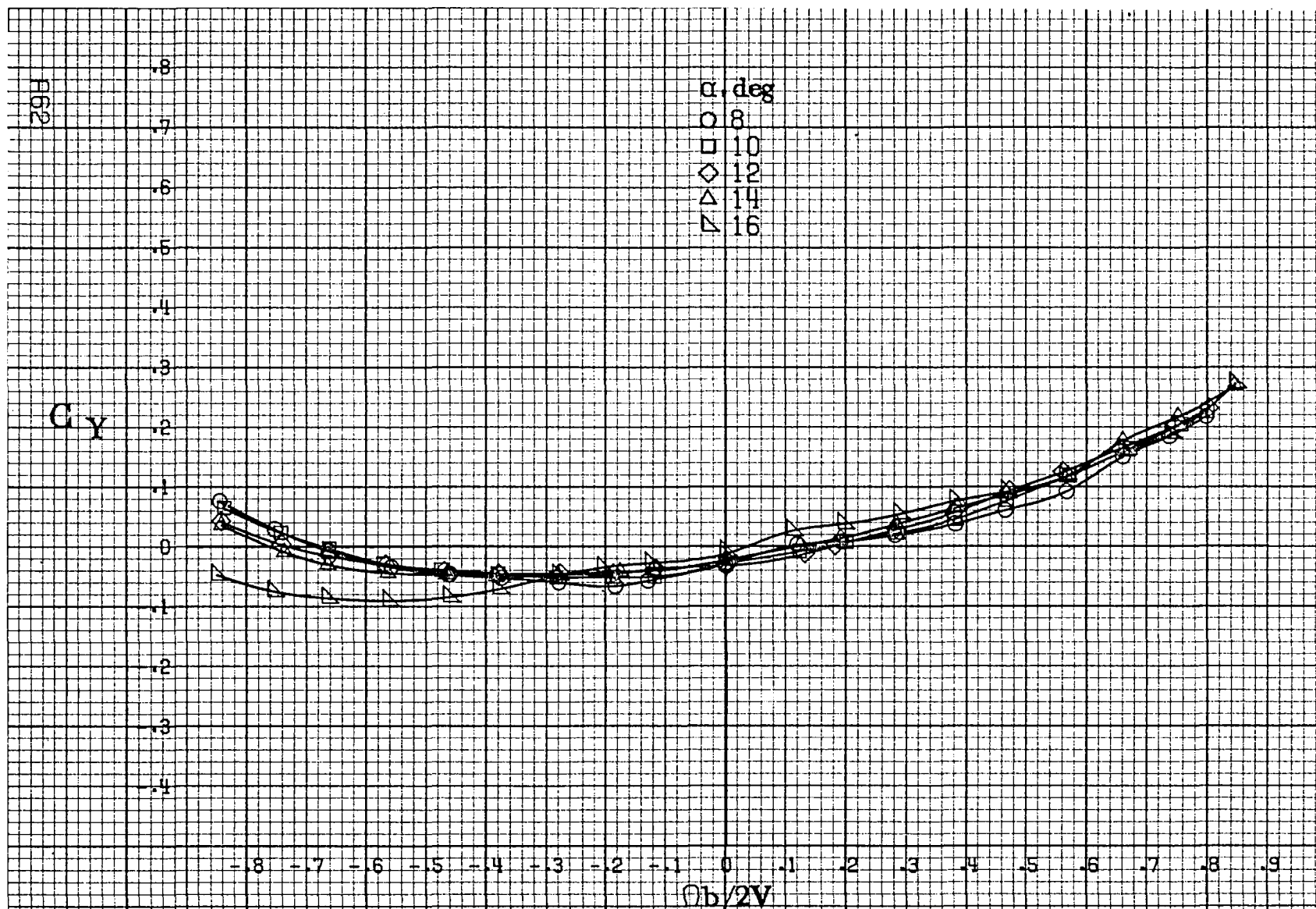


(b)  $\alpha = 18$  to  $35$  deg,  $SR = 99$  cm (39 in).

Figure A16.-Continued.

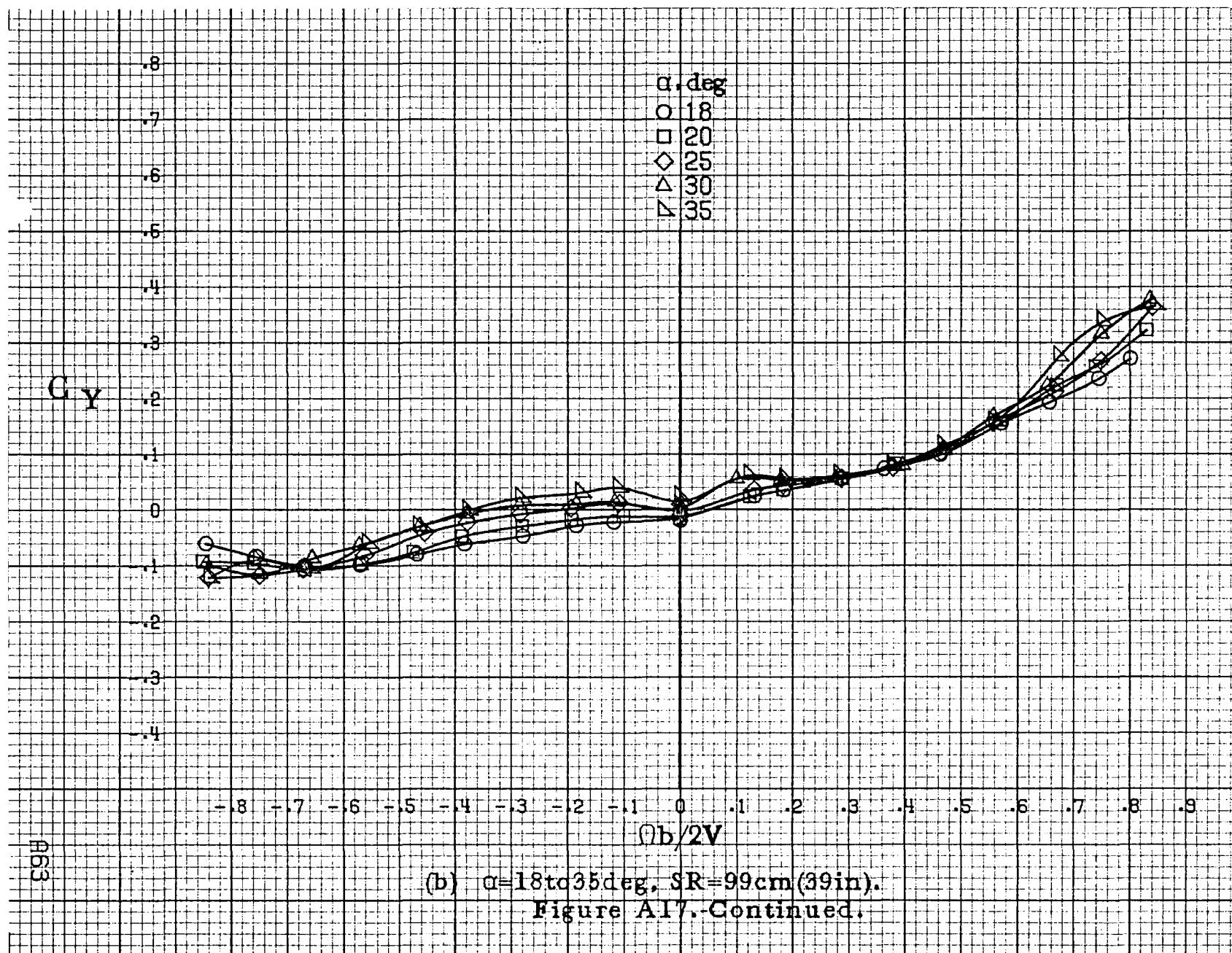


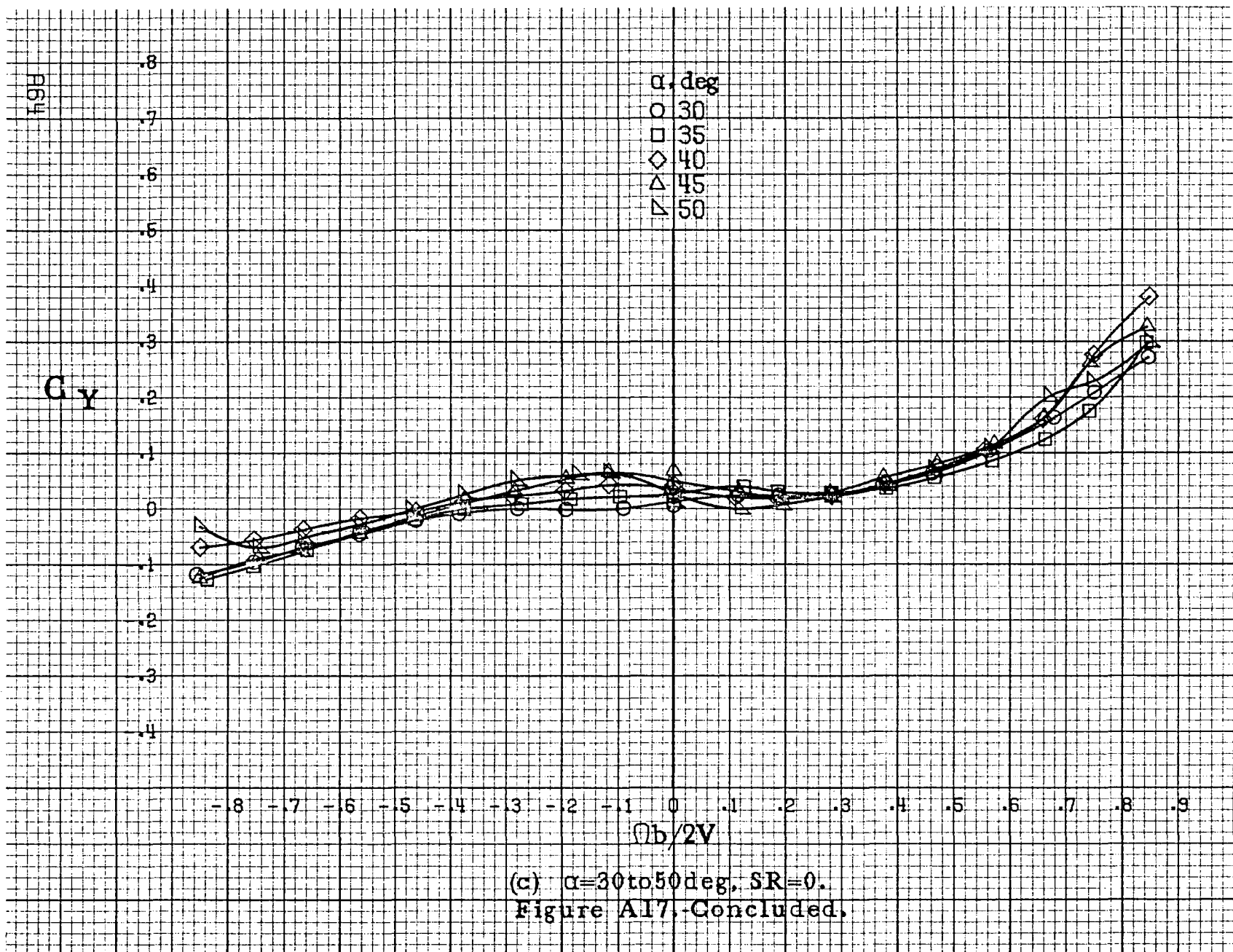


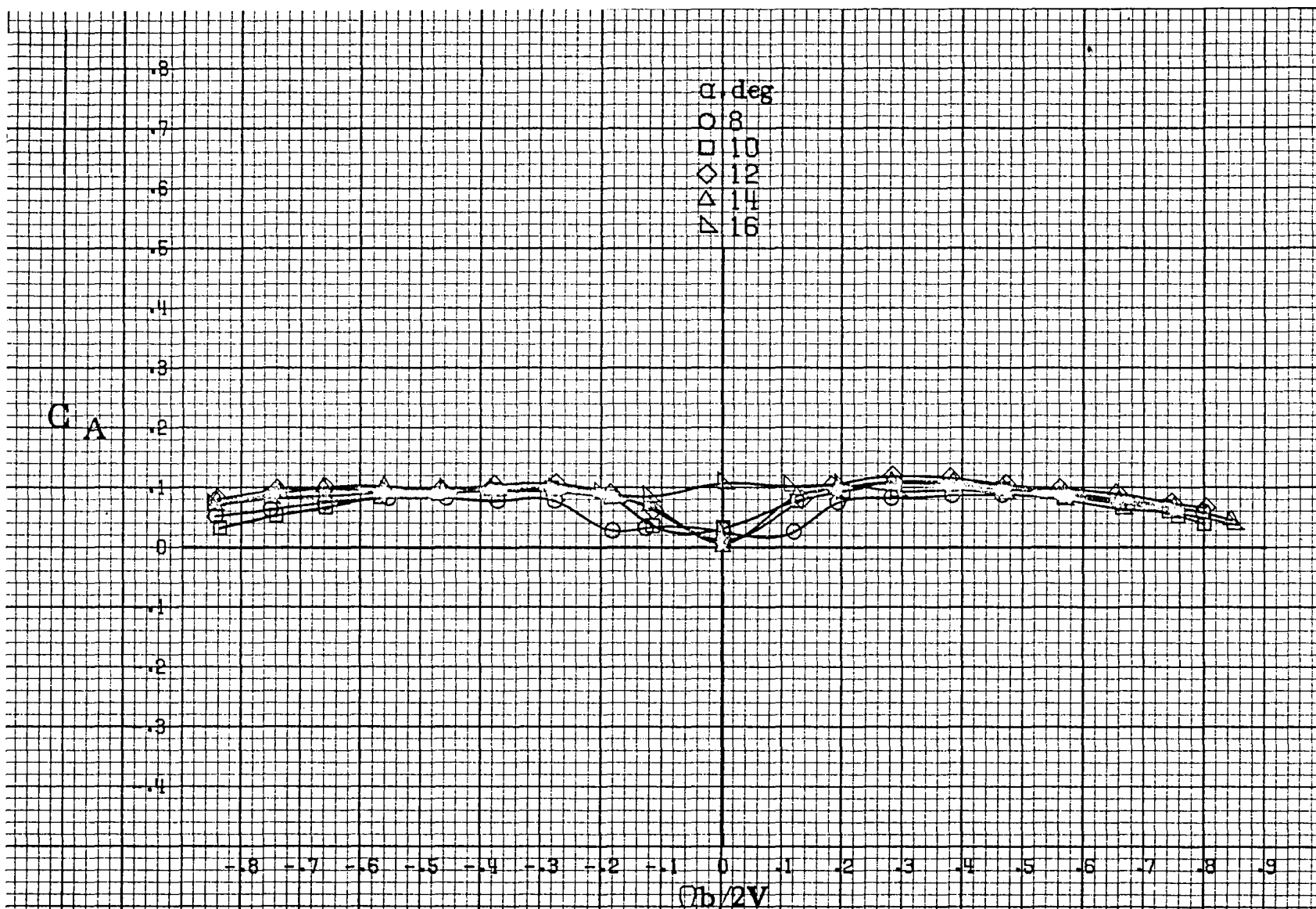


(a)  $\alpha=8\text{ to }16\text{deg}$ ,  $SR=99\text{cm}(39\text{in})$ .

Figure A17.-Effect of rotation rate and angle of attack on side force coefficient for basic configuration.  $\delta_e = -28^\circ$ ,  $\delta_a = 0^\circ$ ,  $\delta_r = -18^\circ$ .  $\beta = 0^\circ$ .

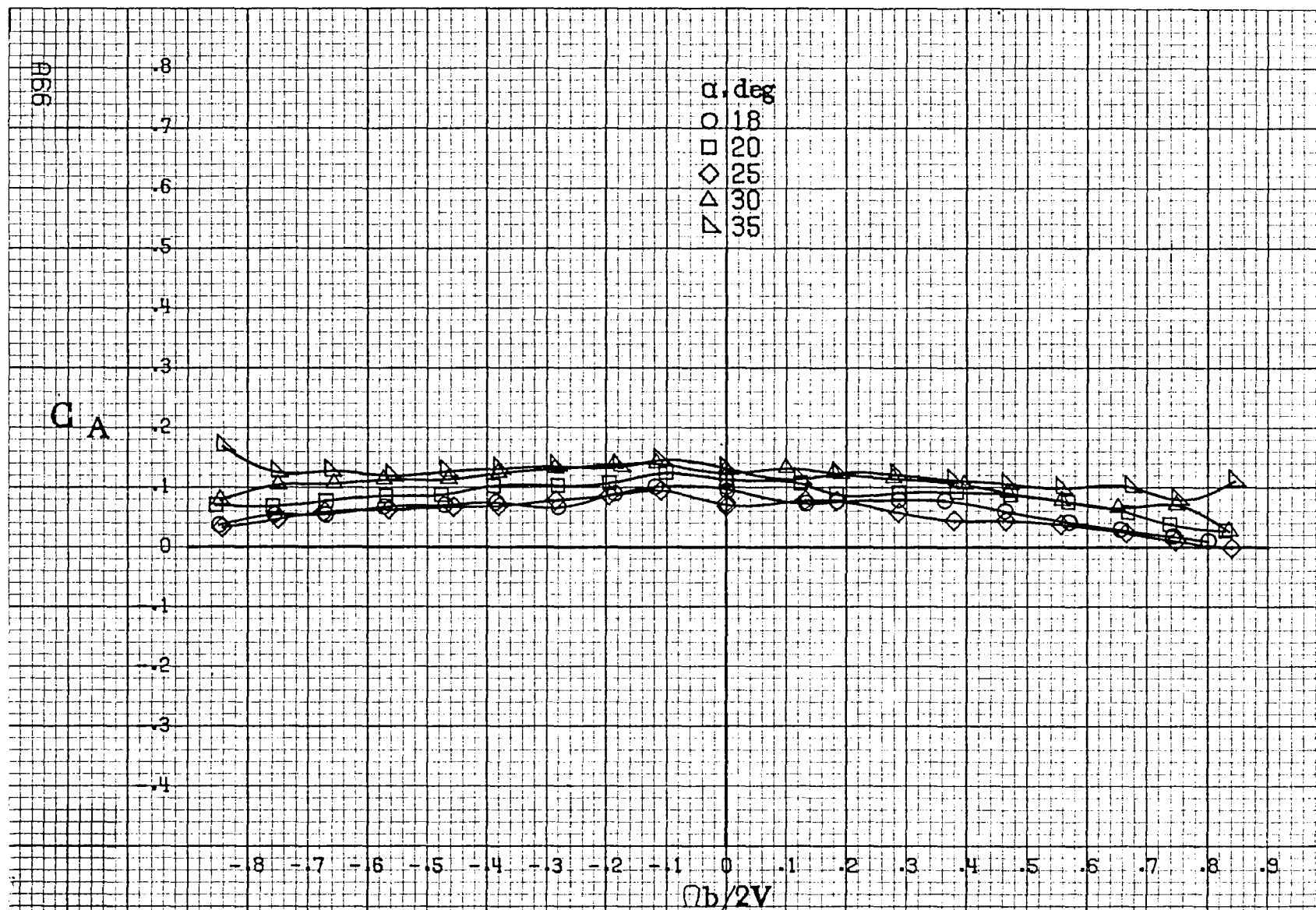




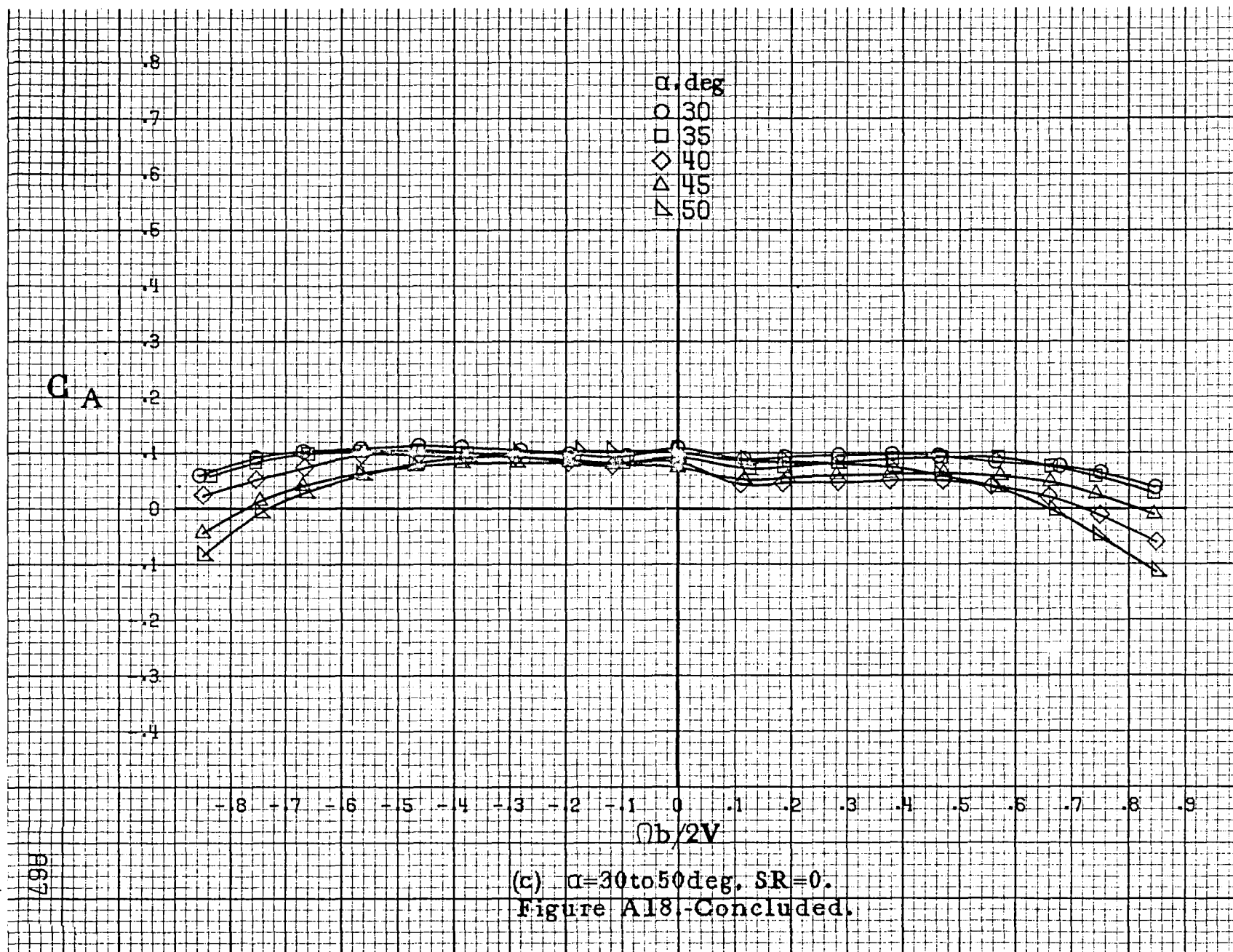


(a)  $\alpha = 8$  to  $16^\circ$ ,  $SR = 99 \text{ cm (39 in.)}$ .

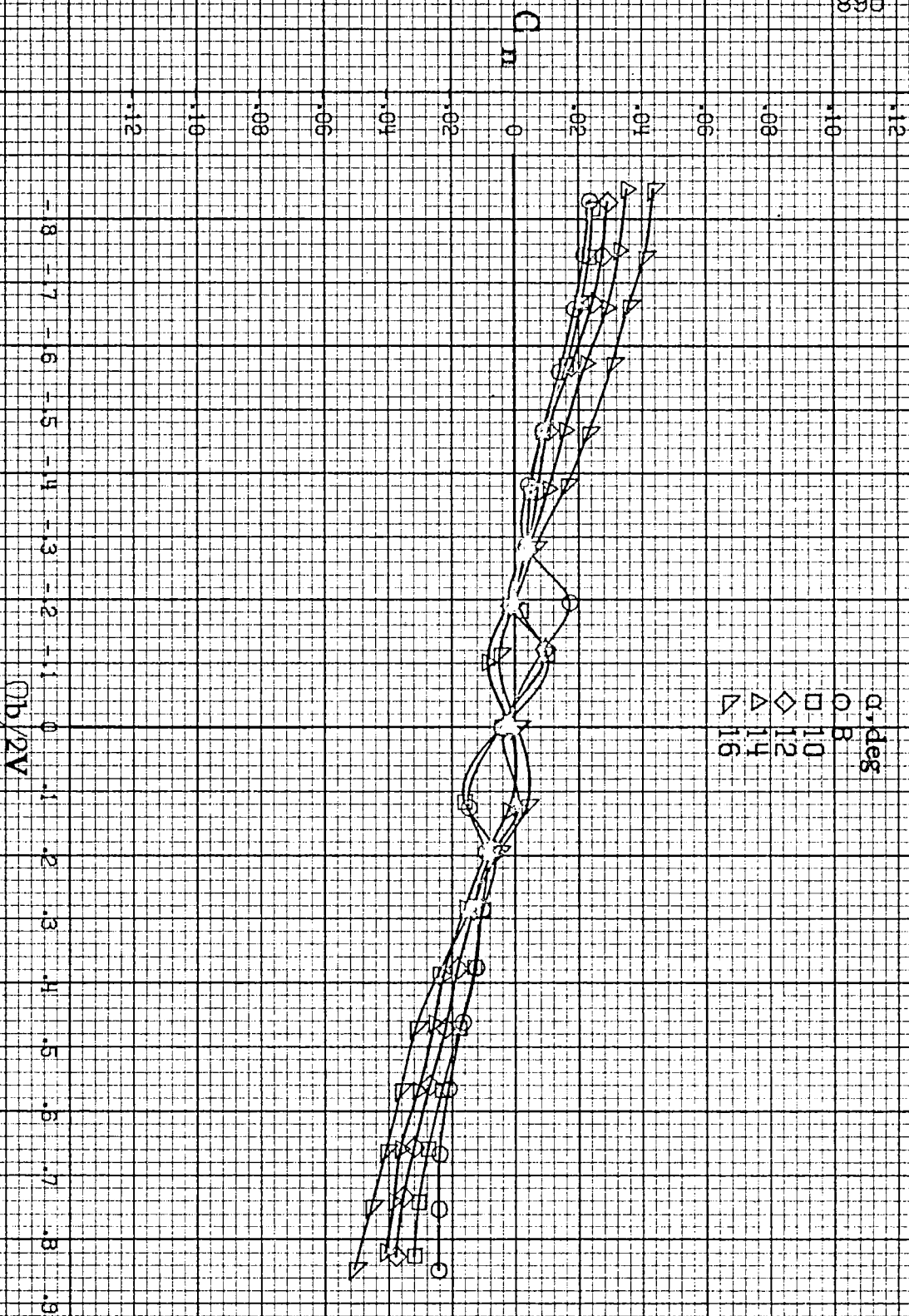
Figure A18.-Effect of rotation rate and angle of attack on axial force coefficient for basic configuration.  $\delta_a = -28^\circ$ ,  $\delta_s = 10^\circ$ ,  $\delta_r = -16^\circ$ .  $\beta = 0^\circ$ .



(b)  $\alpha=18$  to  $35^\circ$ ,  $SR=99\text{cm}(39\text{in})$ .  
Figure A18.-Continued.



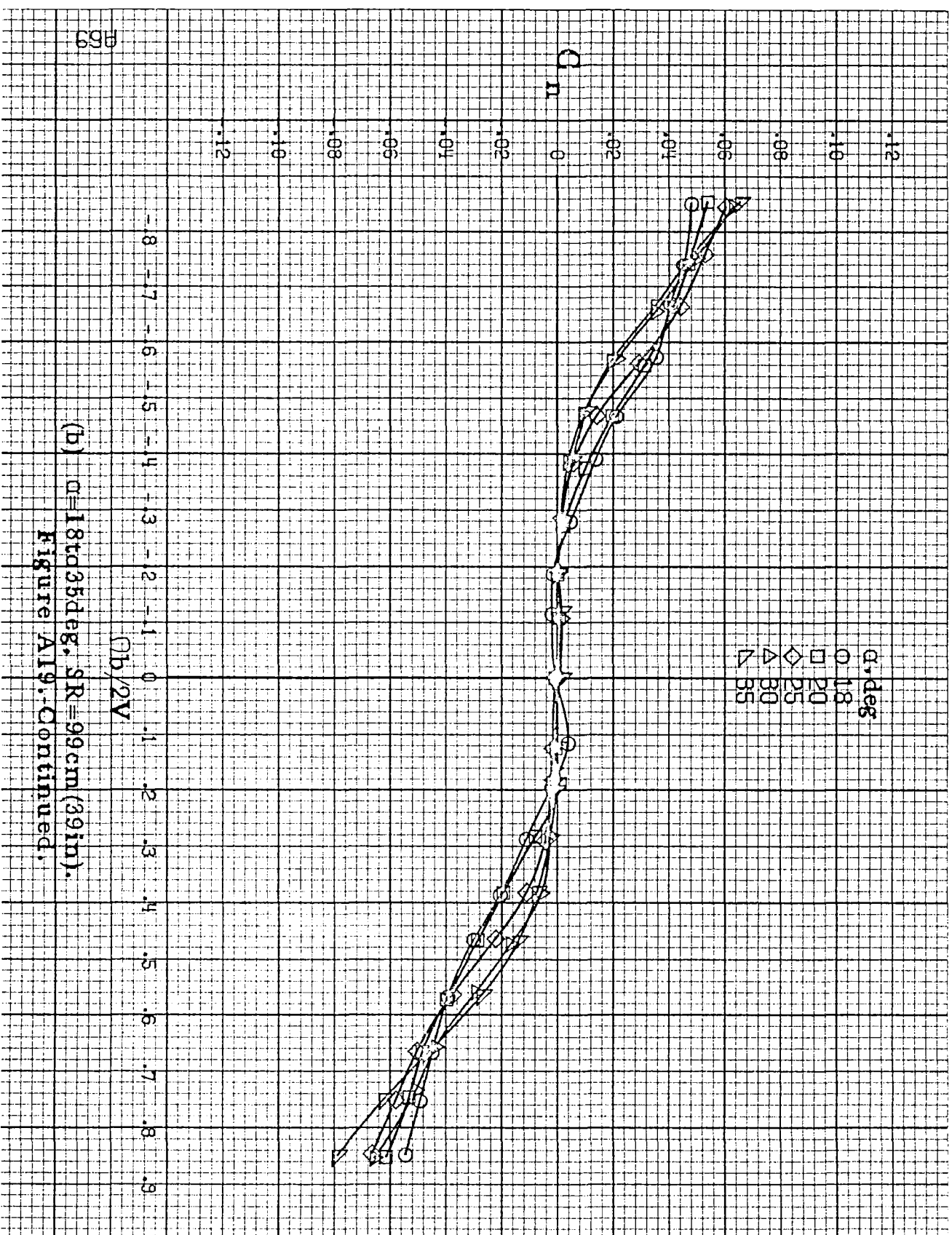




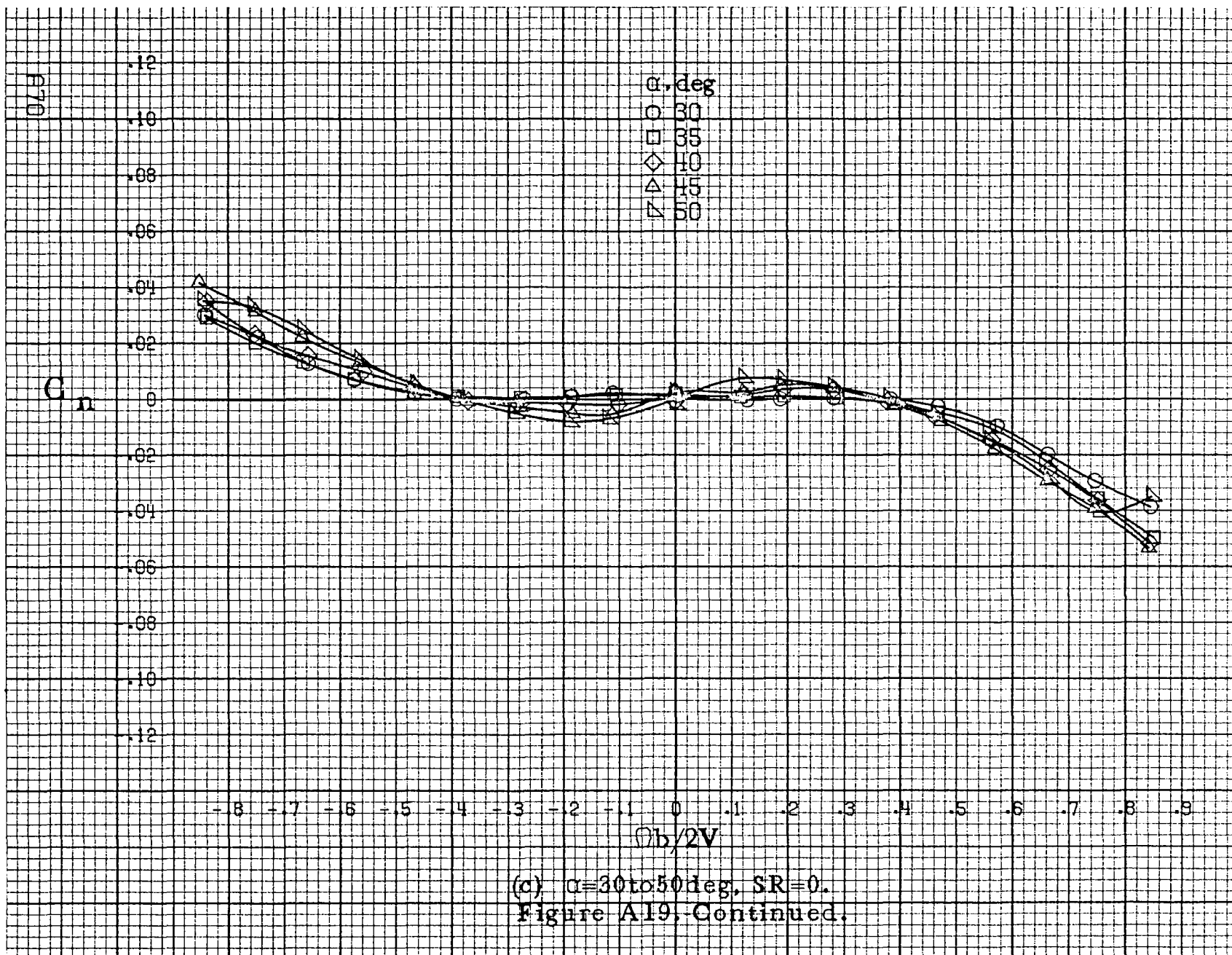
(a)  $C=8$  to  $16$  deg,  $SR=99$  cm (39 in).

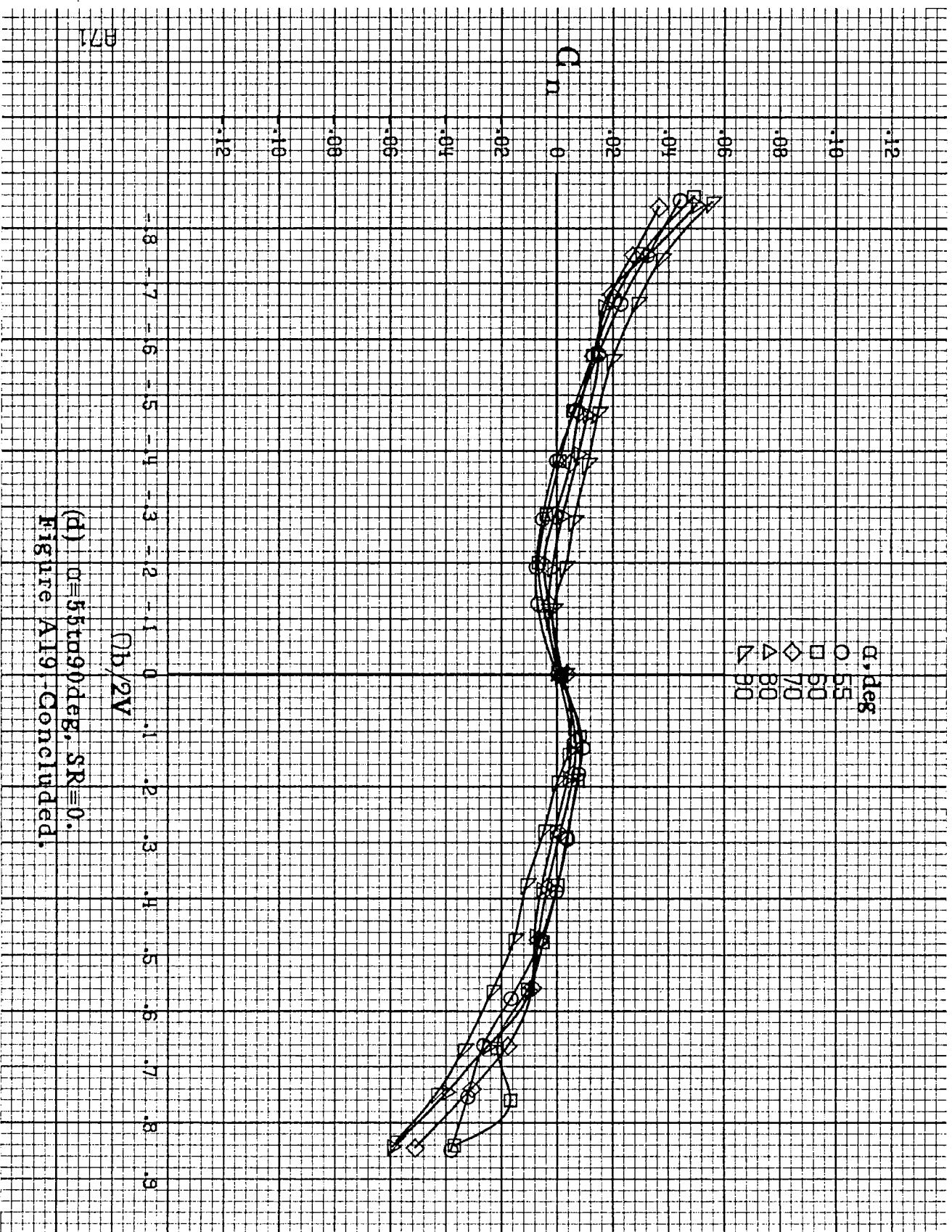
Figure A19. Effect of rotation rate and angle of attack on yawing moment coefficient for no. 1 horizontal tail configuration.  $\delta_e = 0^\circ$ ,  $\delta_a = 0^\circ$ ,  $\delta_r = 0^\circ$ .





(b)  $\alpha=18$  to  $35^\circ$ ,  $SR=99\text{ cm (39 in.)}$ .  
Figure A19. Continued.

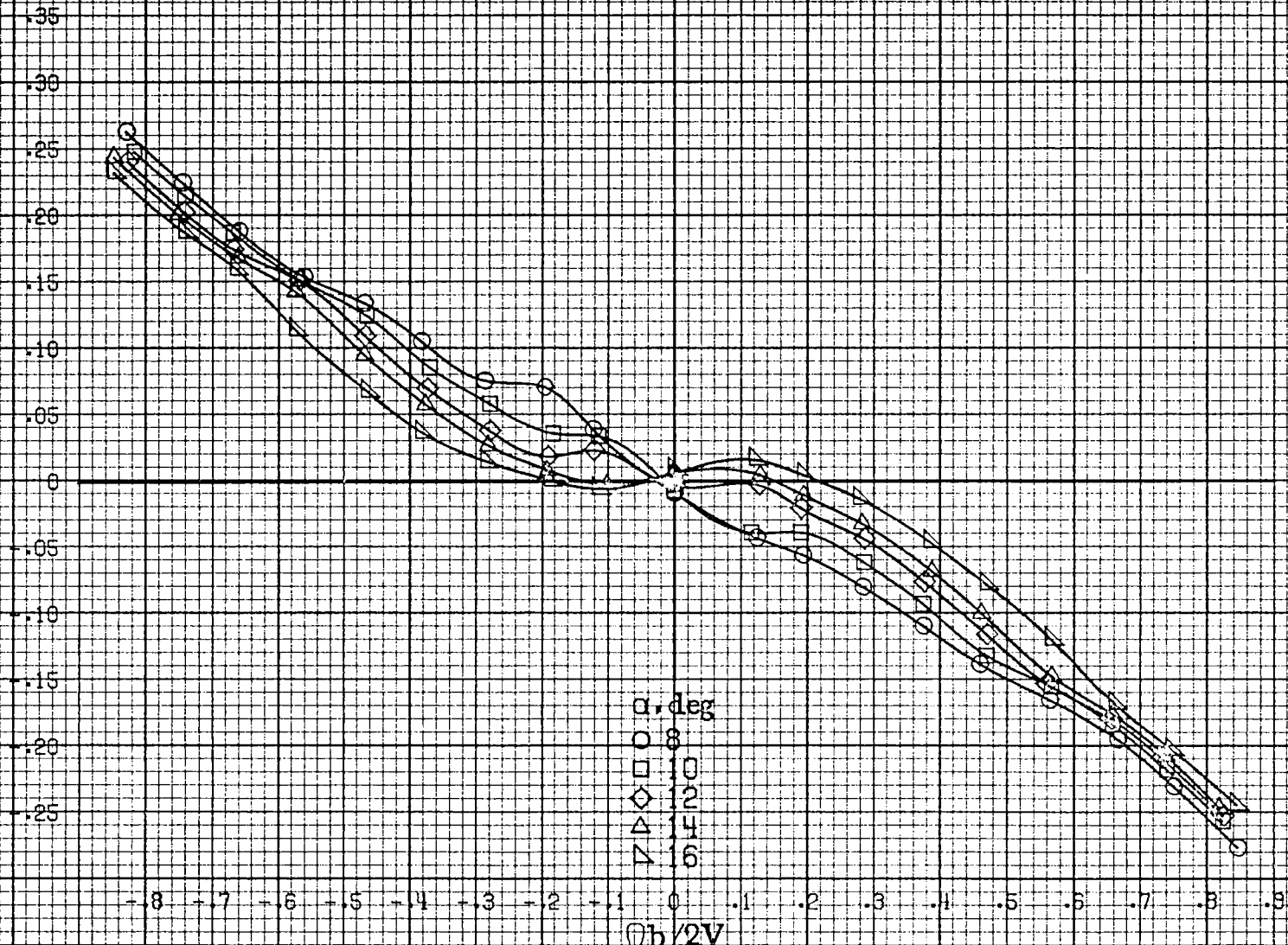




(d)  $\alpha = 55$  to  $90$  deg,  $SR \equiv 0$ .  
 Figure A19-Concluded.

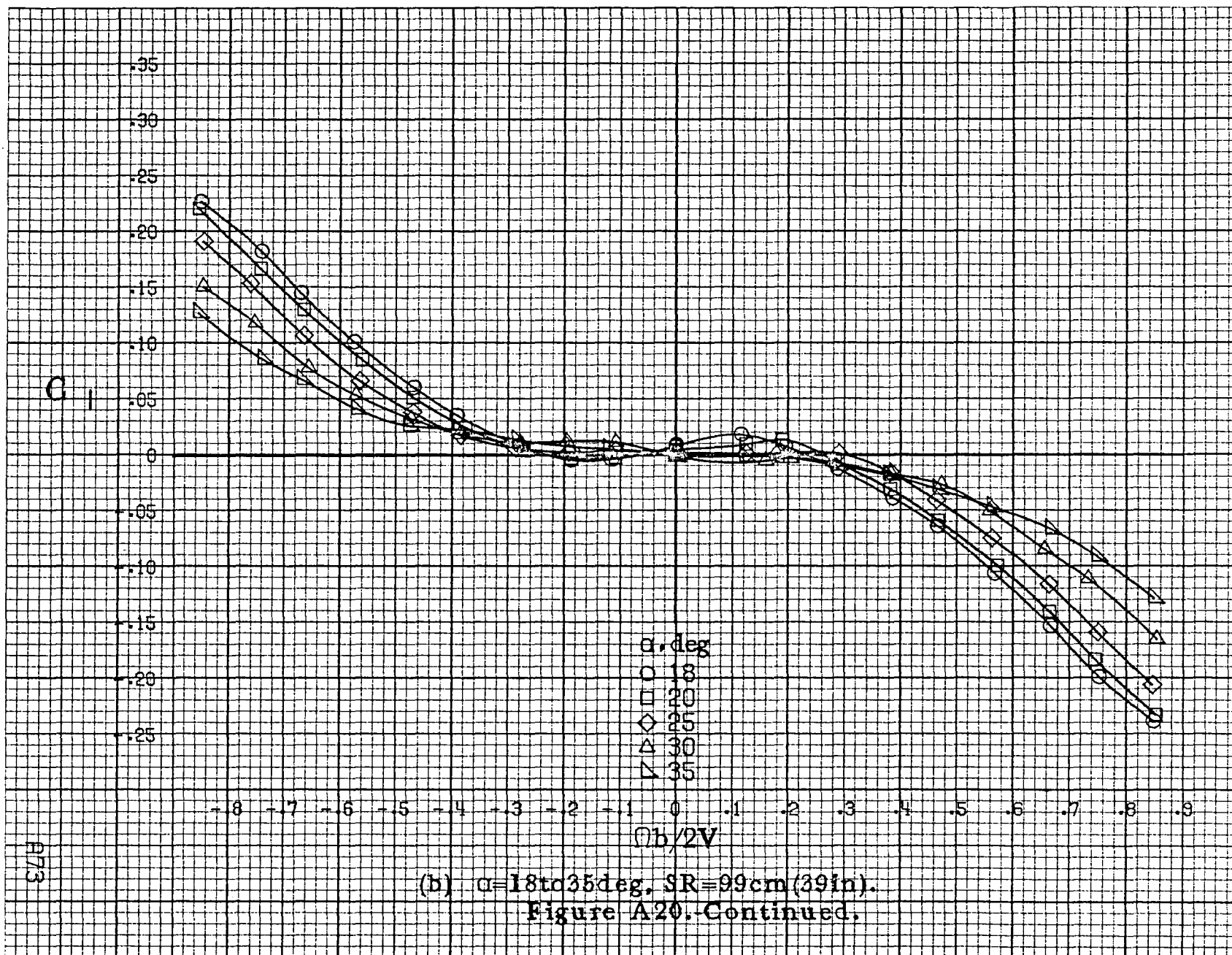
872

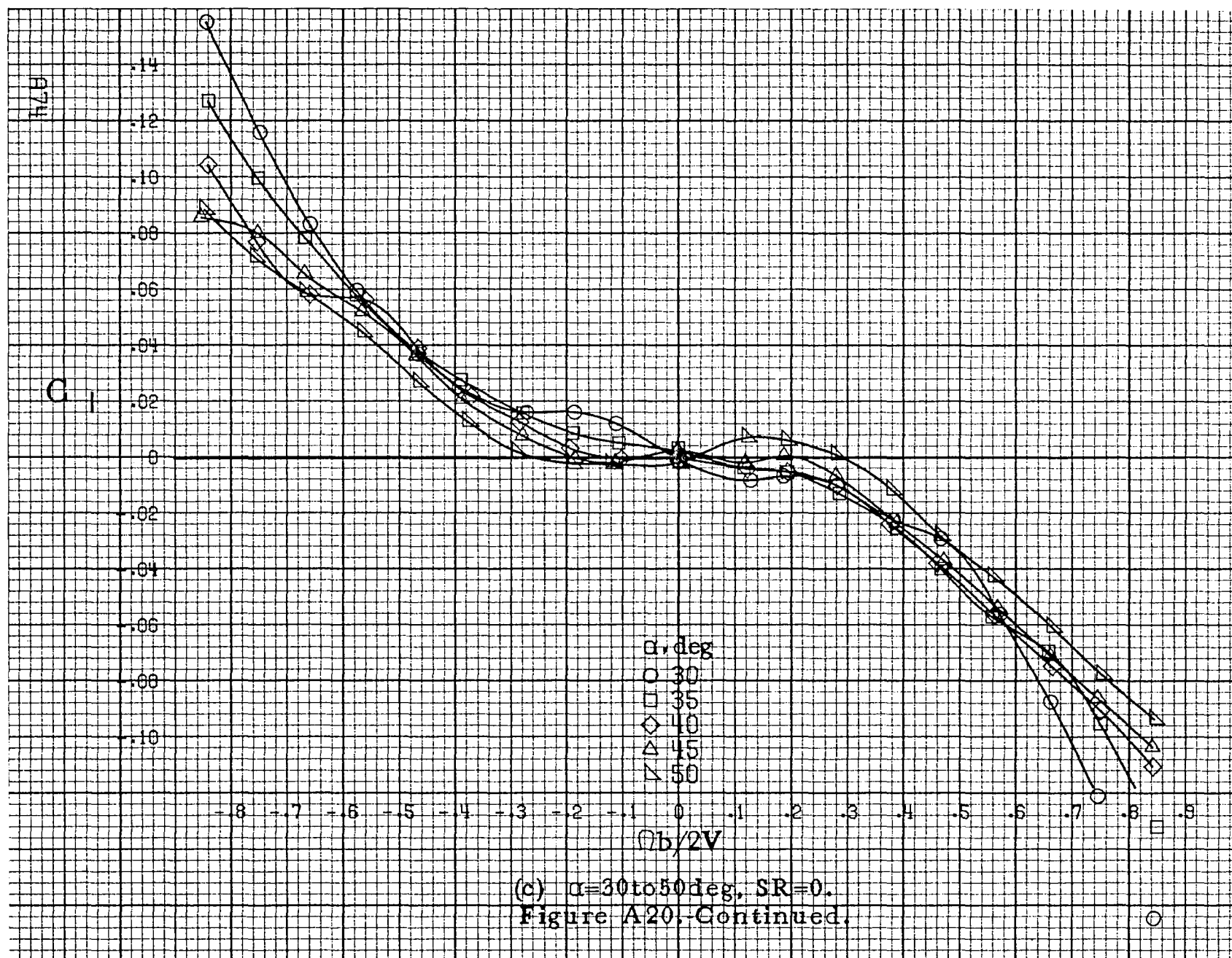
$C_l$

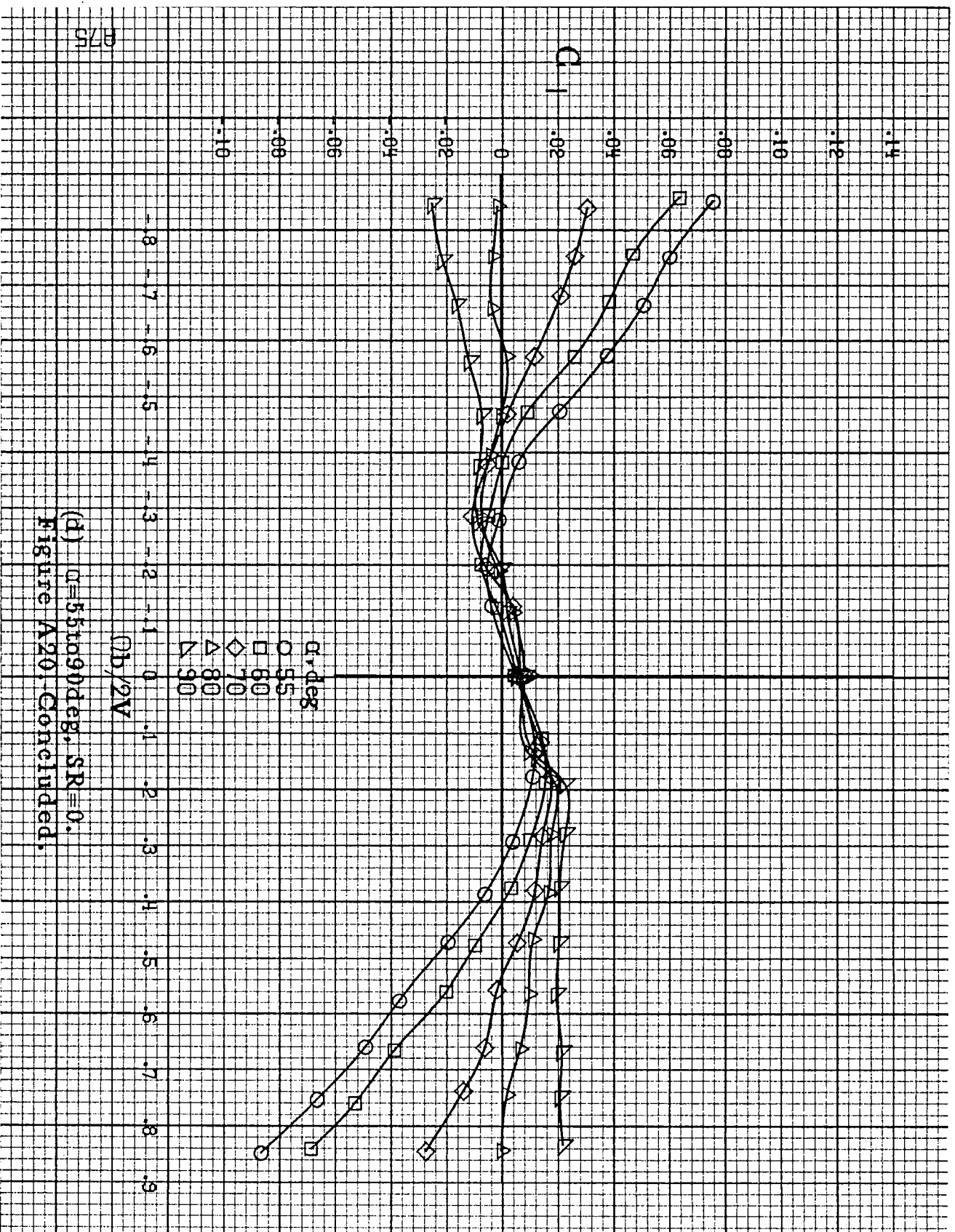


(a)  $\alpha = 8$  to  $16^\circ$ ,  $SR = 99 \text{ cm (39 in.)}$ .

Figure A20.-Effect of rotation rate and angle of attack on rolling-moment coefficient for no. 1 horizontal tail configuration.  $\delta_e = 0^\circ$ ,  $\delta_a = 0^\circ$ ,  $\delta_r = 0^\circ$ ,  $\delta = 0^\circ$ .

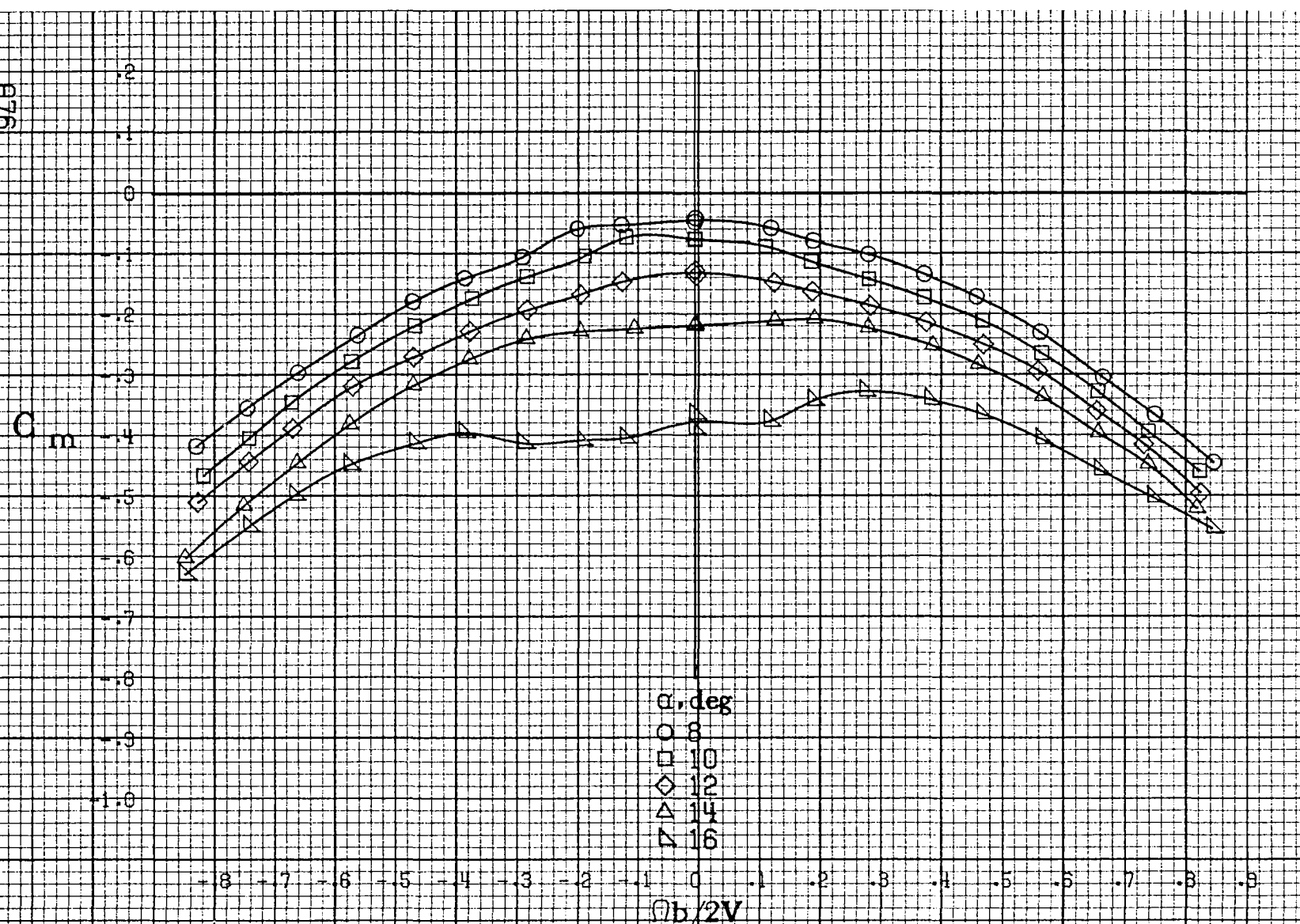






(d)  $C=55$  to  $90^\circ$ ,  $SR=0$ .  
Figure A20, Concluded,

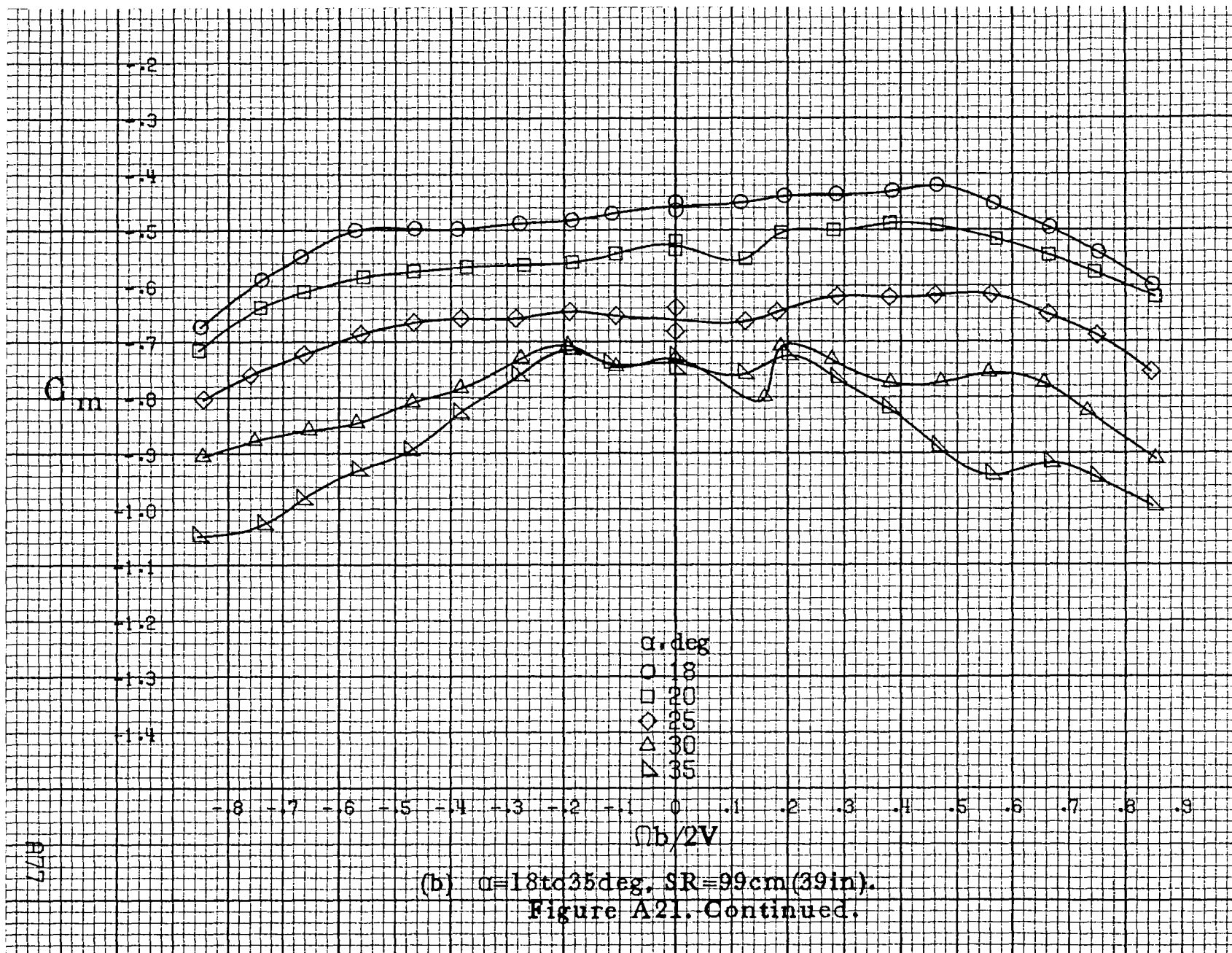


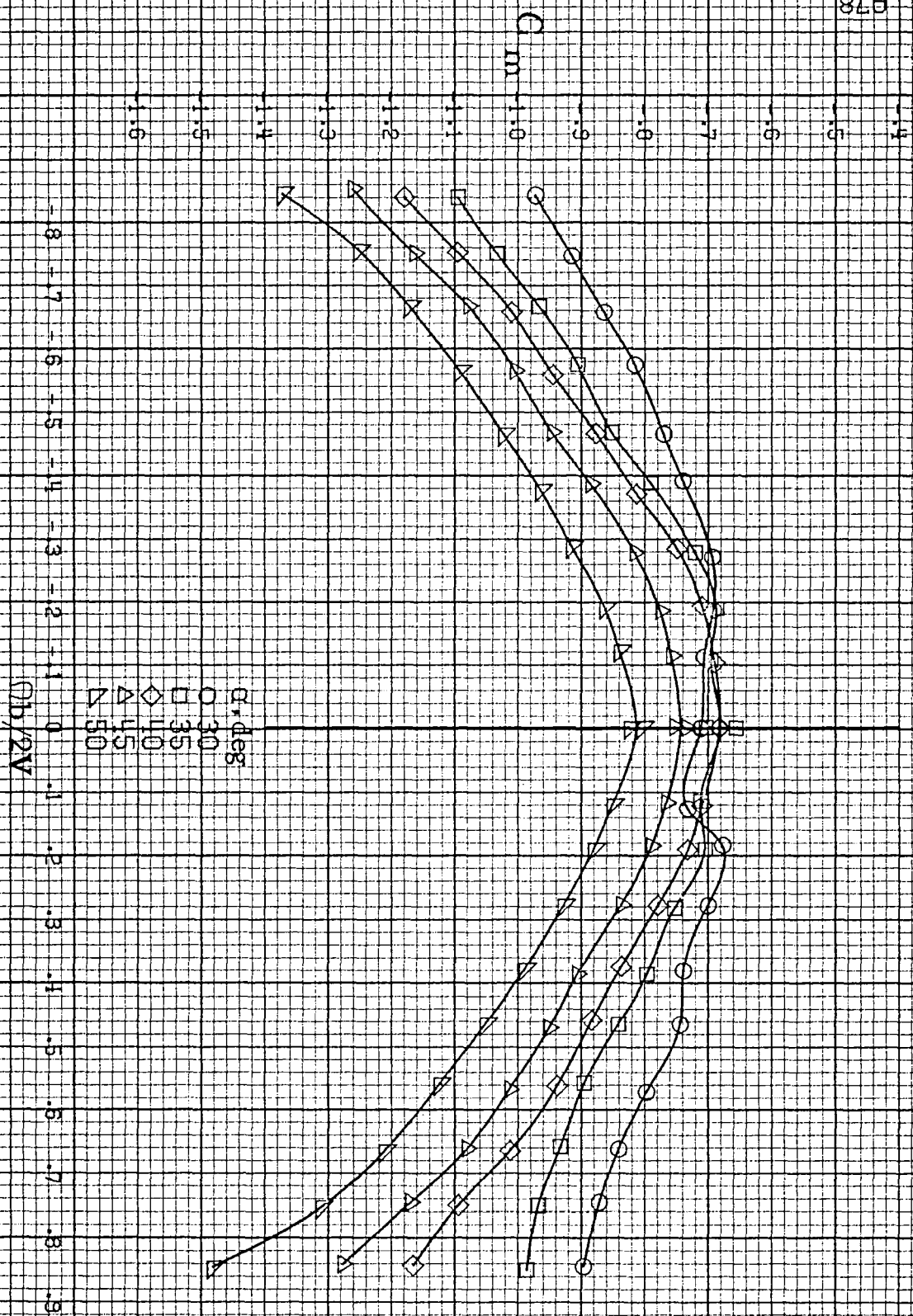


(a)  $\alpha = 8$  to  $16^\circ$ ,  $SR = 99 \text{ cm (39 in.)}$ .

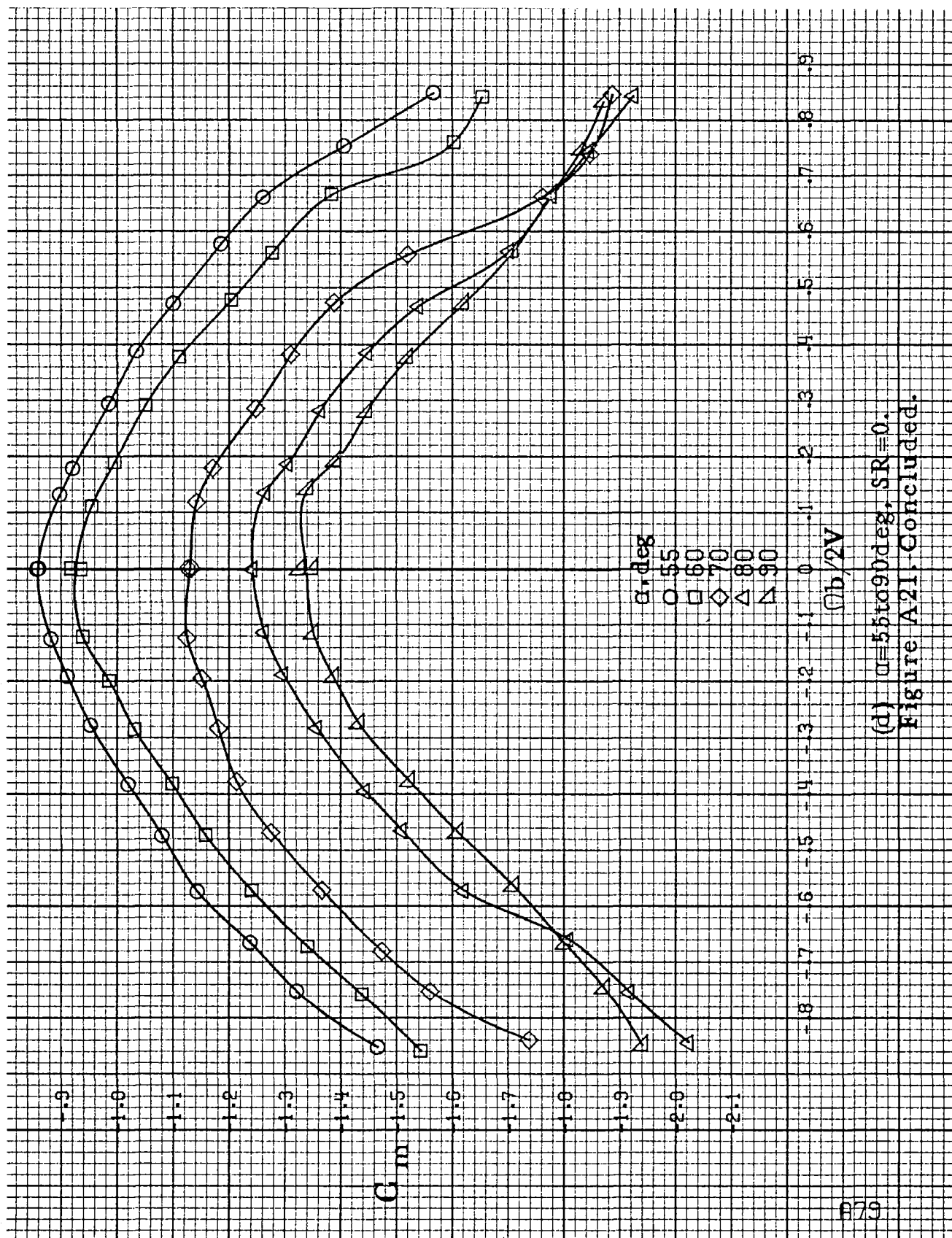
Figure A21. Effect of rotation rate and angle of attack on pitching-moment coefficient for no. 1 horizontal tail configuration.  $\delta_e = 0^\circ$ ,  $\delta_a = 0^\circ$ ,  $\delta_r = 0^\circ$ ,  $\beta = 0^\circ$ .



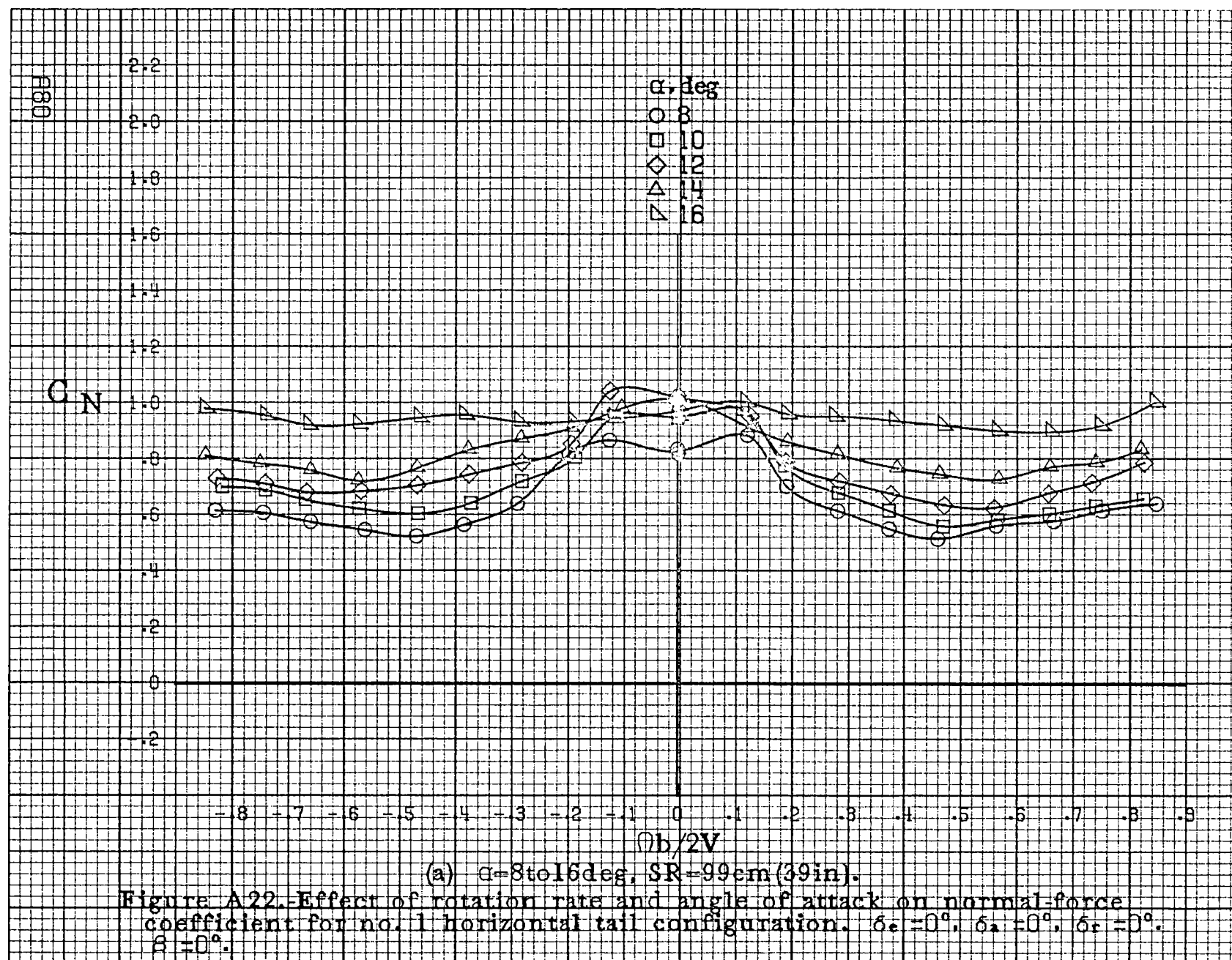


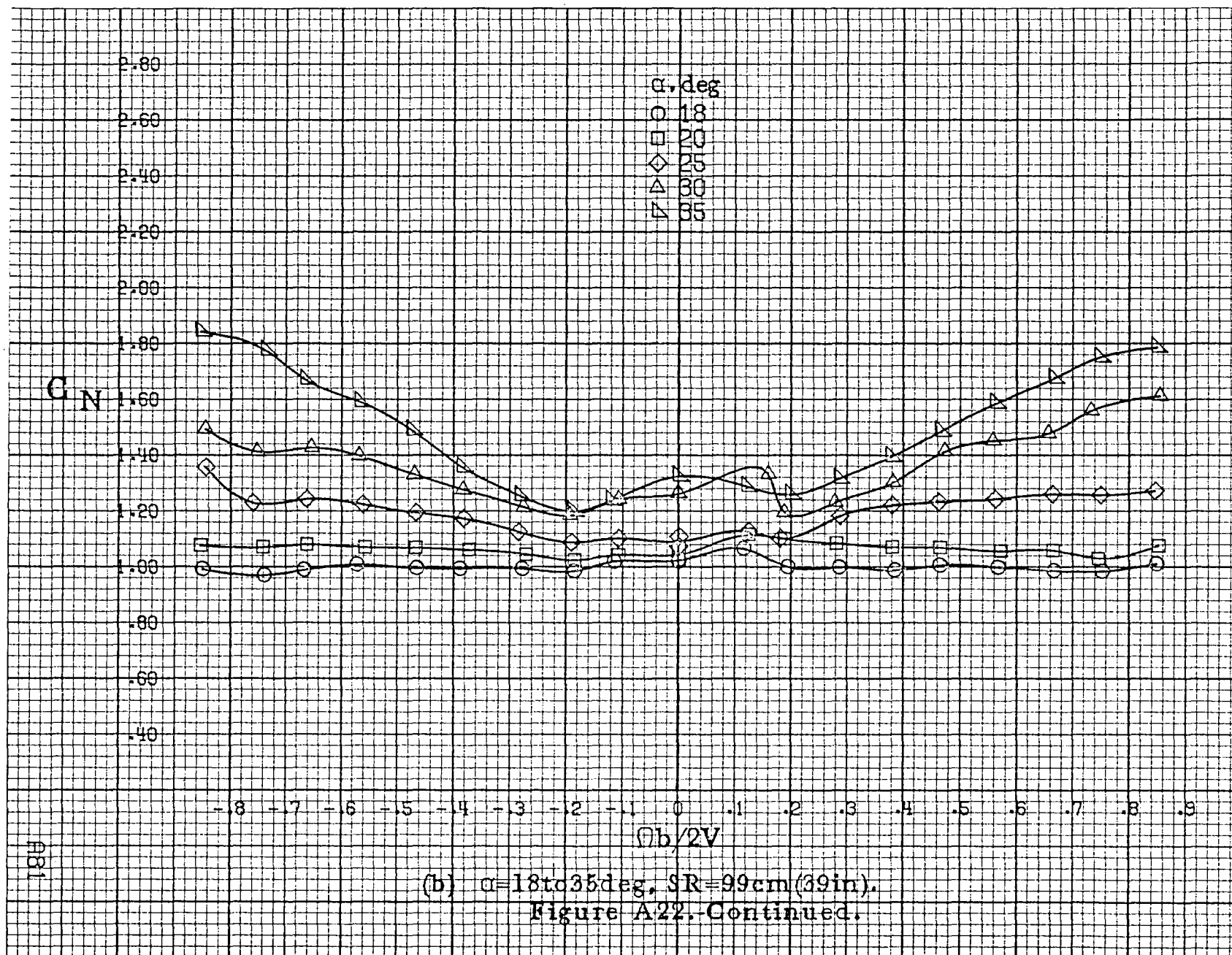


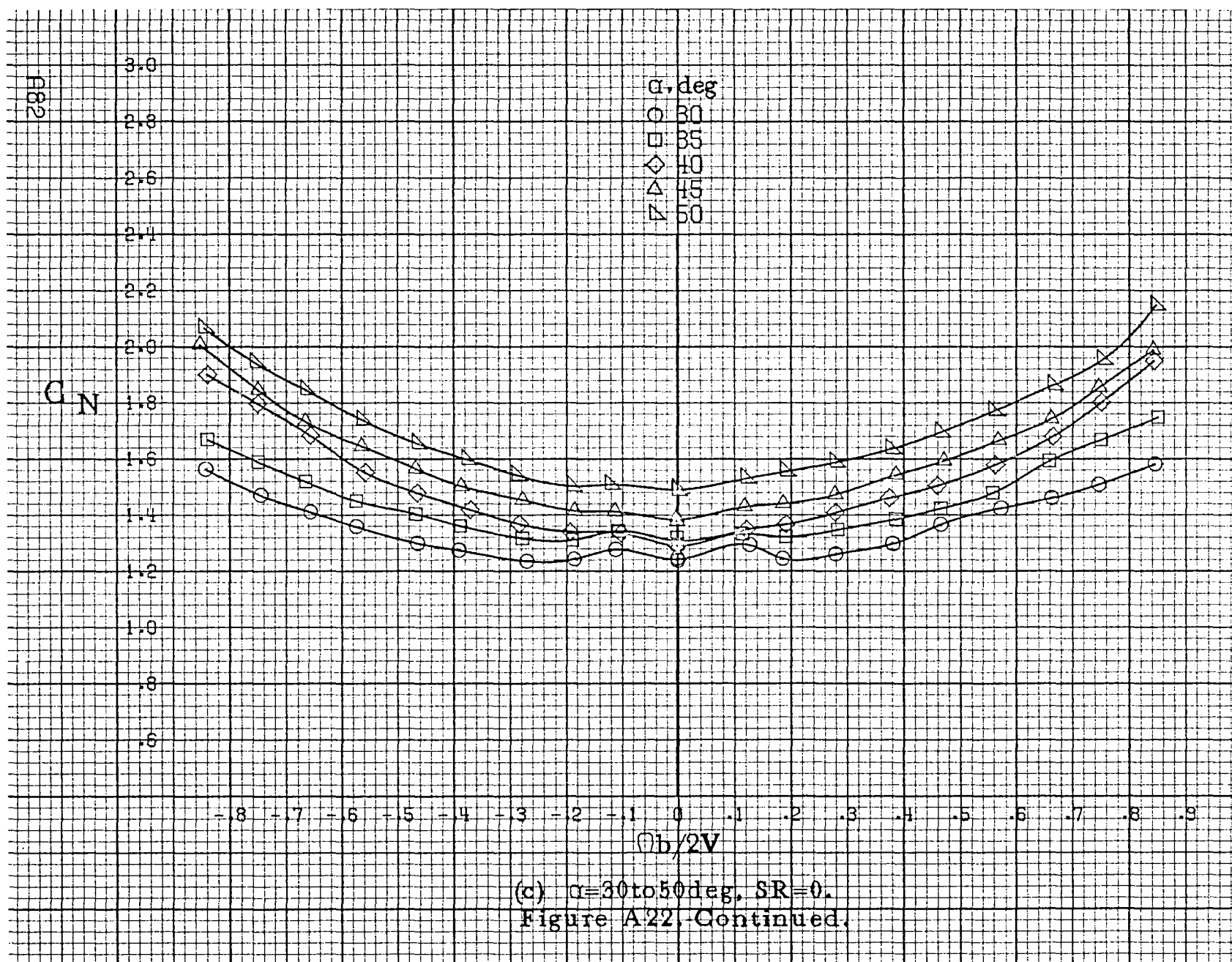
(c)  $\alpha = 30$  to  $50$  deg,  $SR = 0$ ,  
Figure A21, Continued.



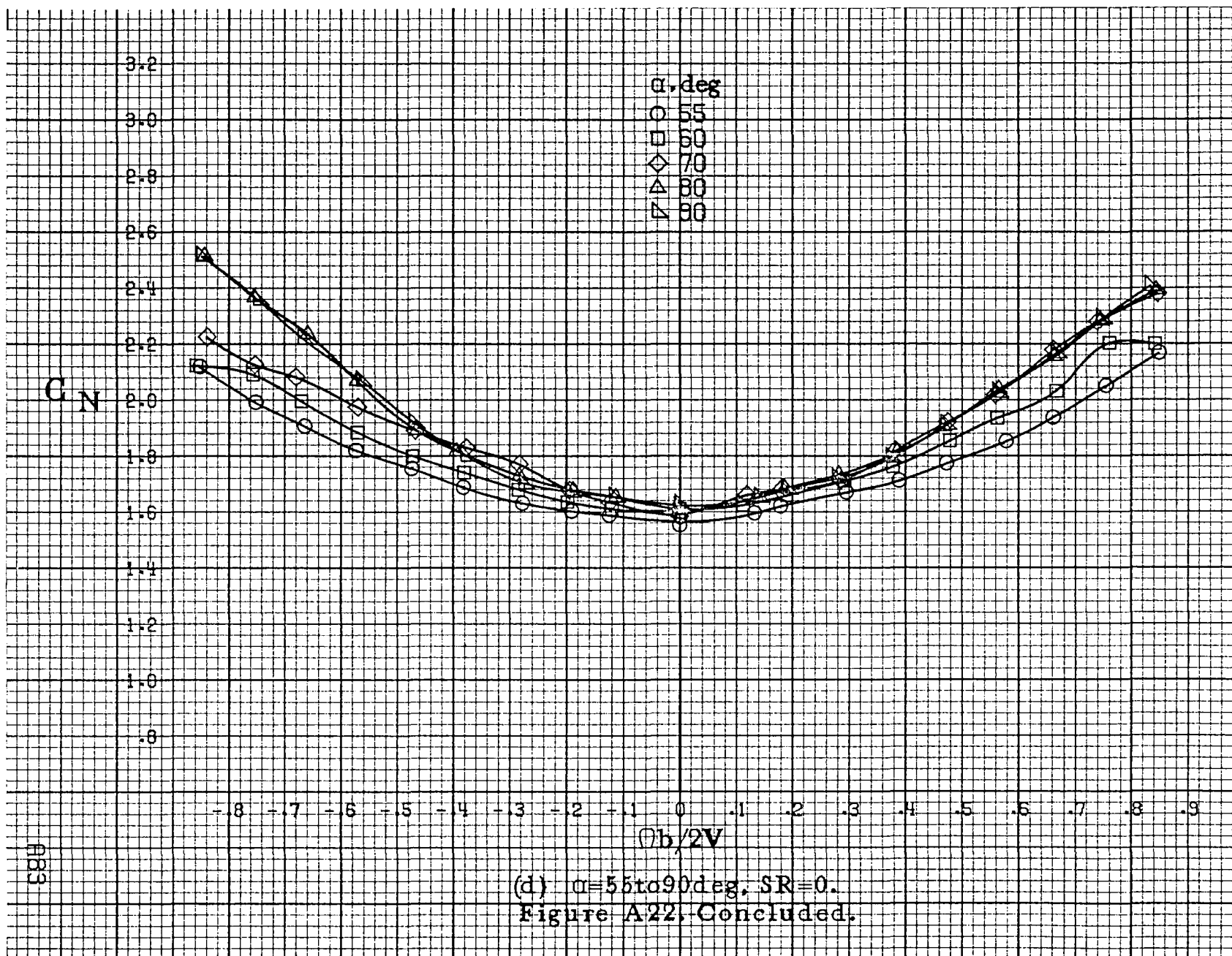
(d)  $\alpha=55$  to  $90^\circ$ ,  $SR=0$ .  
Figure A21. Concluded.

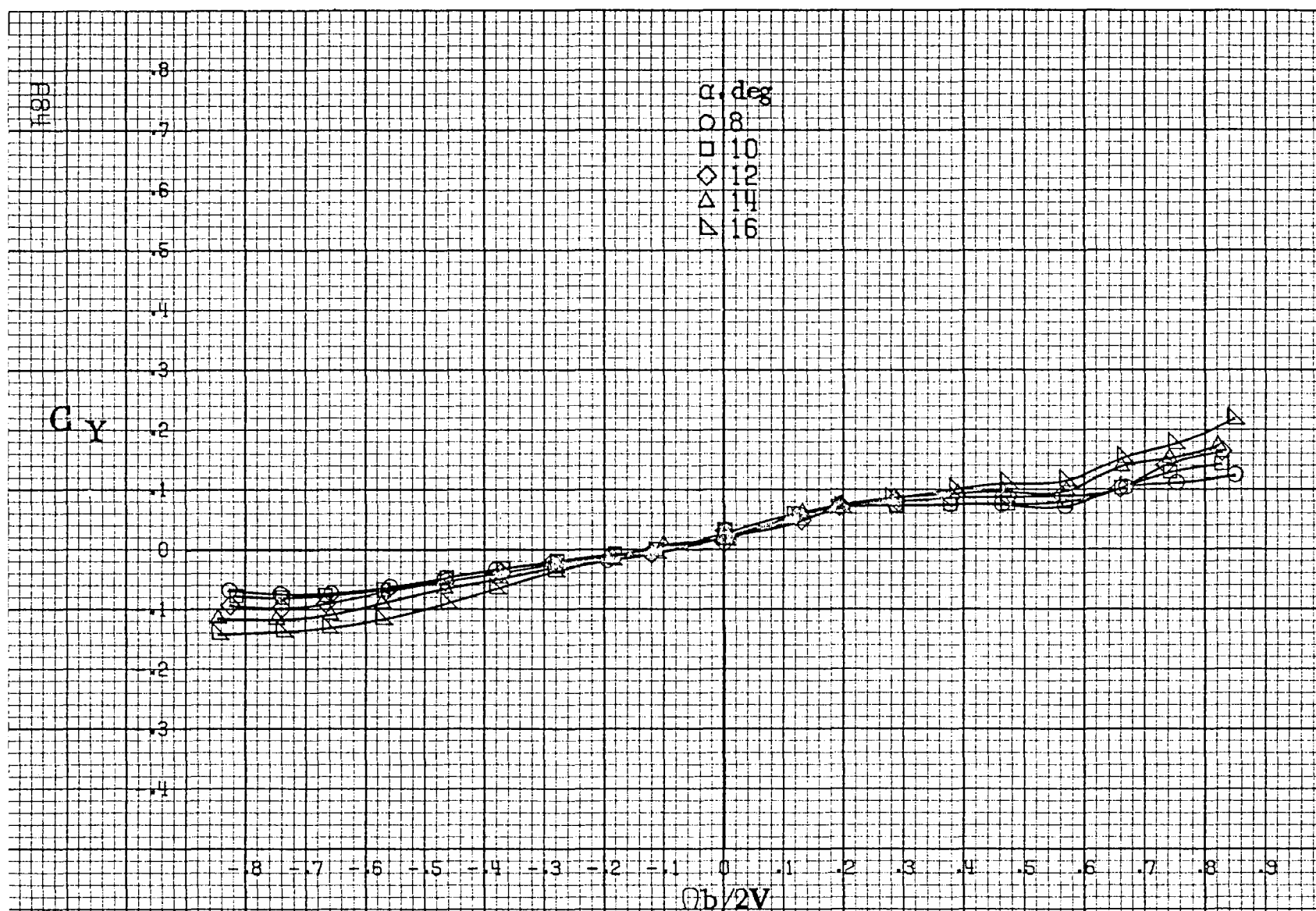








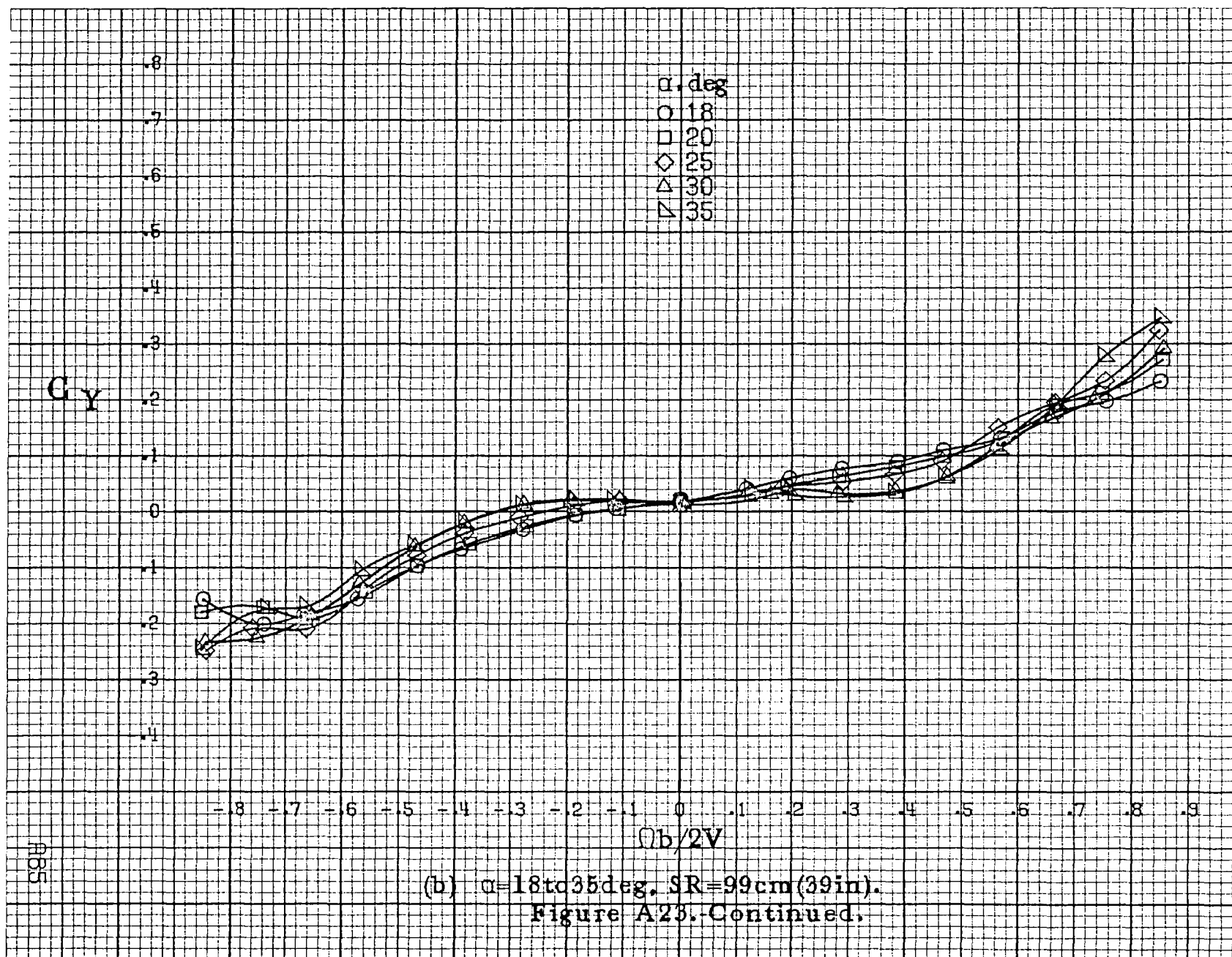


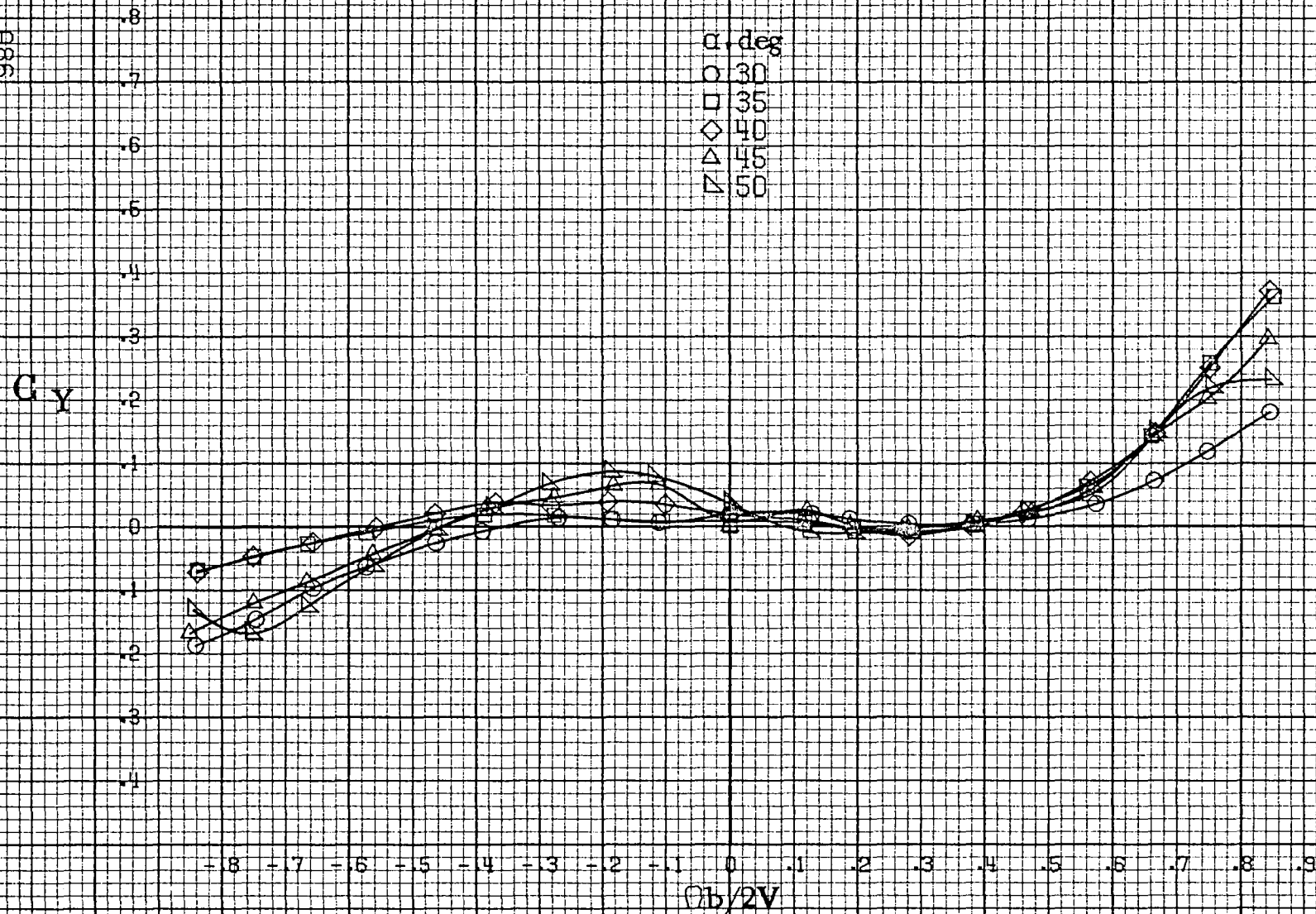


(a)  $\alpha = 8$  to  $16^\circ$ ,  $SR = 99\text{cm}(39\text{in})$ .

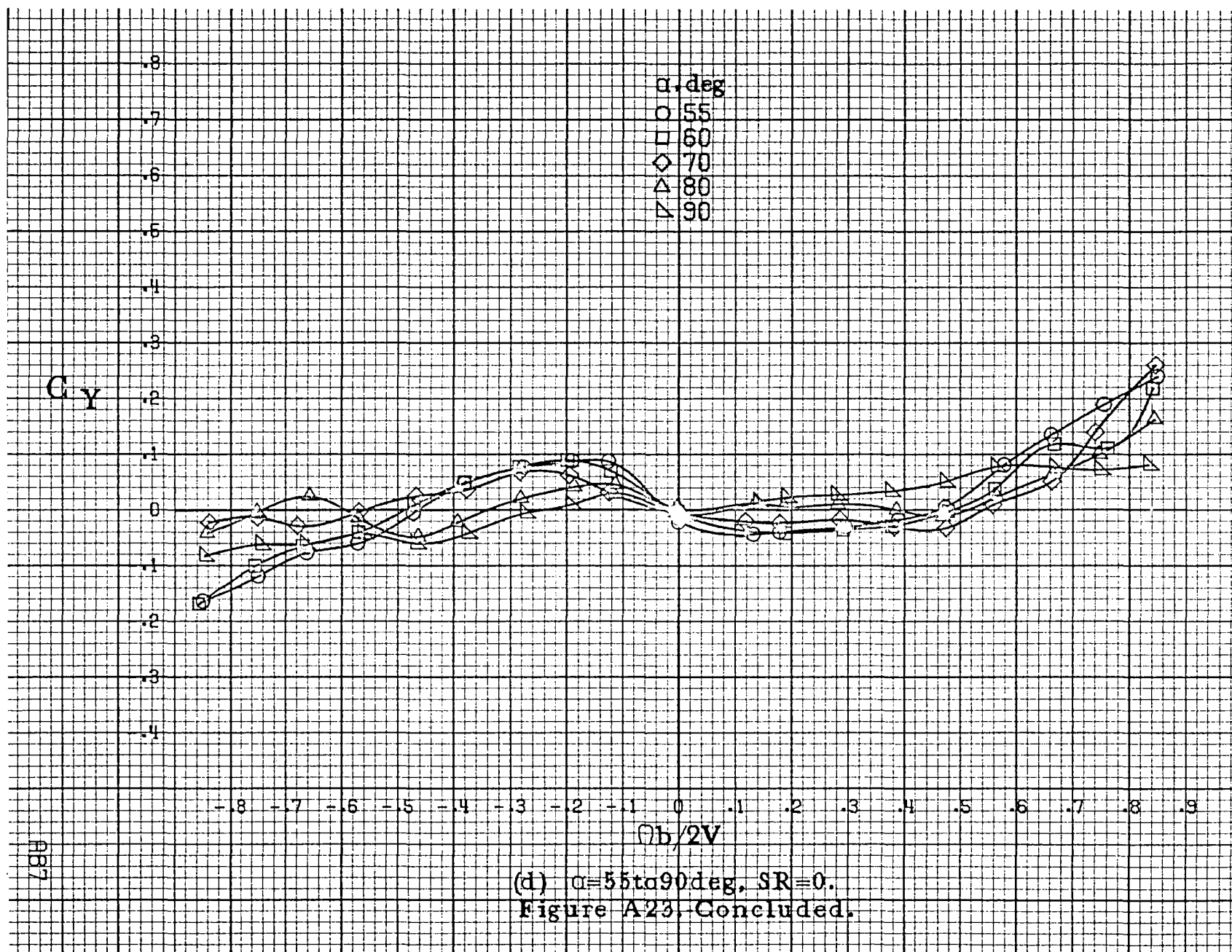
Figure A23.-Effect of rotation rate and angle of attack on side-force coefficient for no. 1 horizontal tail configuration.  $\delta_e = 0^\circ$ ,  $\delta_a = 0^\circ$ ,  $\delta_r = 0^\circ$ .  $\beta = 0^\circ$ .

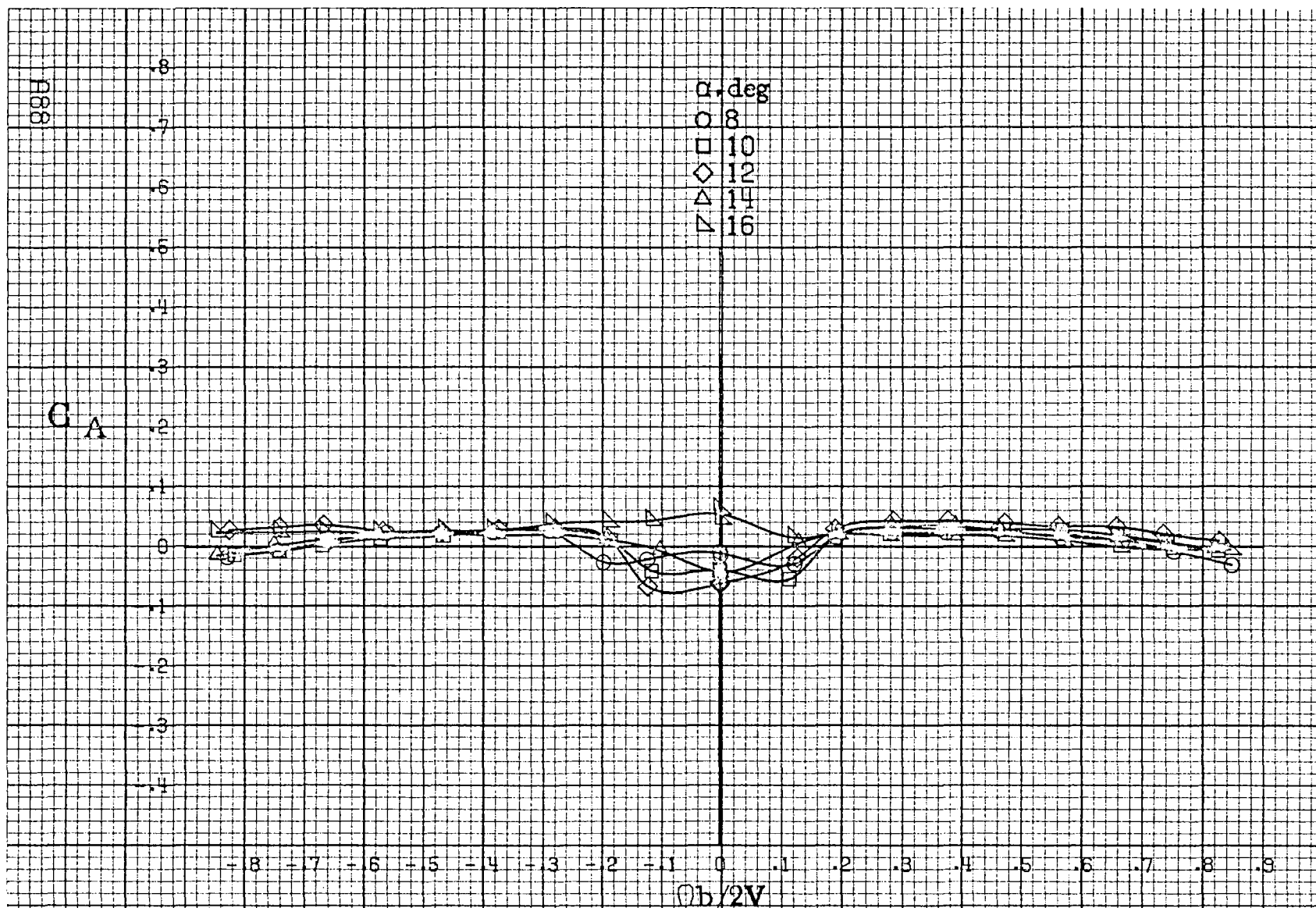






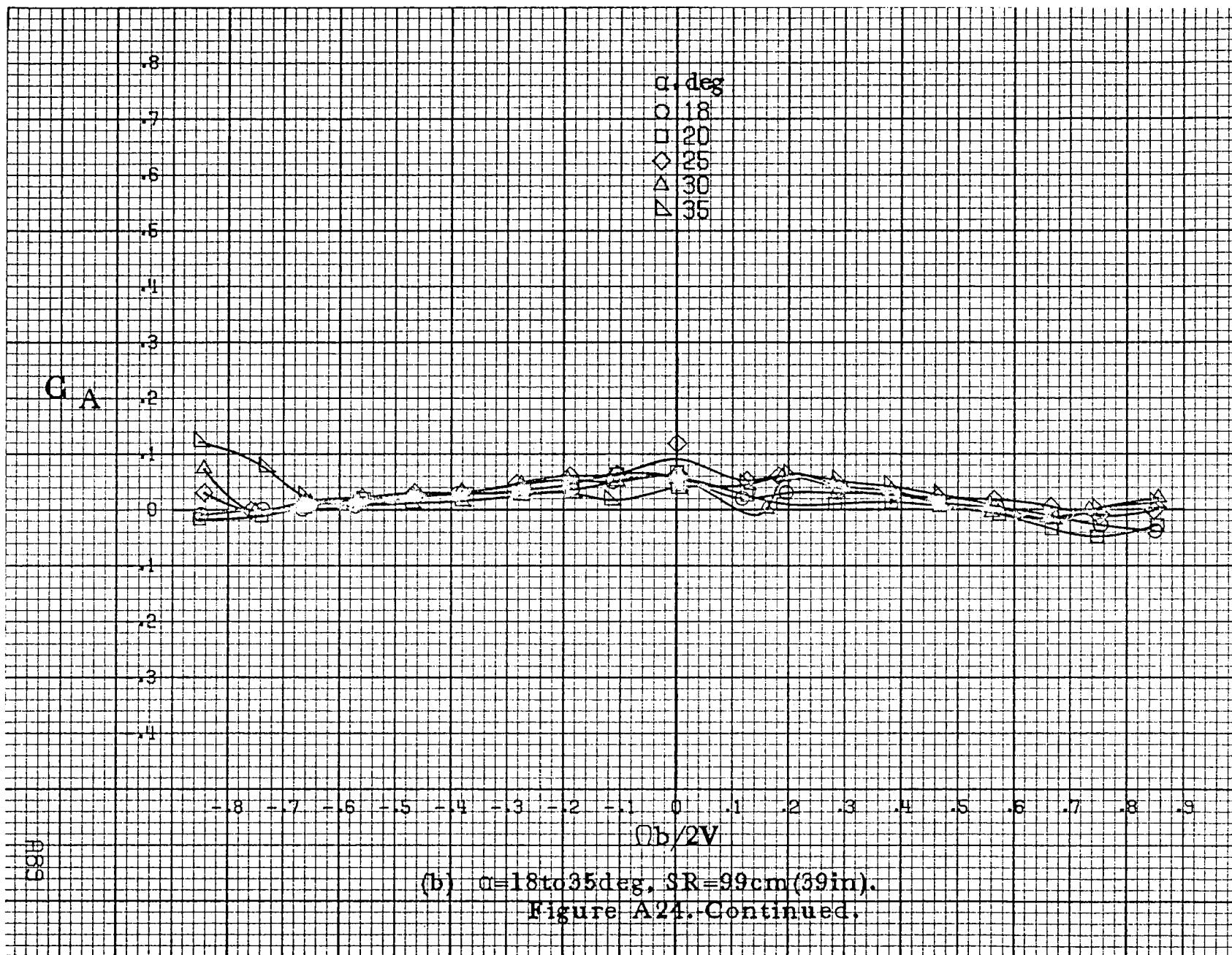
(c)  $\alpha=30$  to  $50^\circ$ ,  $SR=0$ .  
Figure A23. Continued.

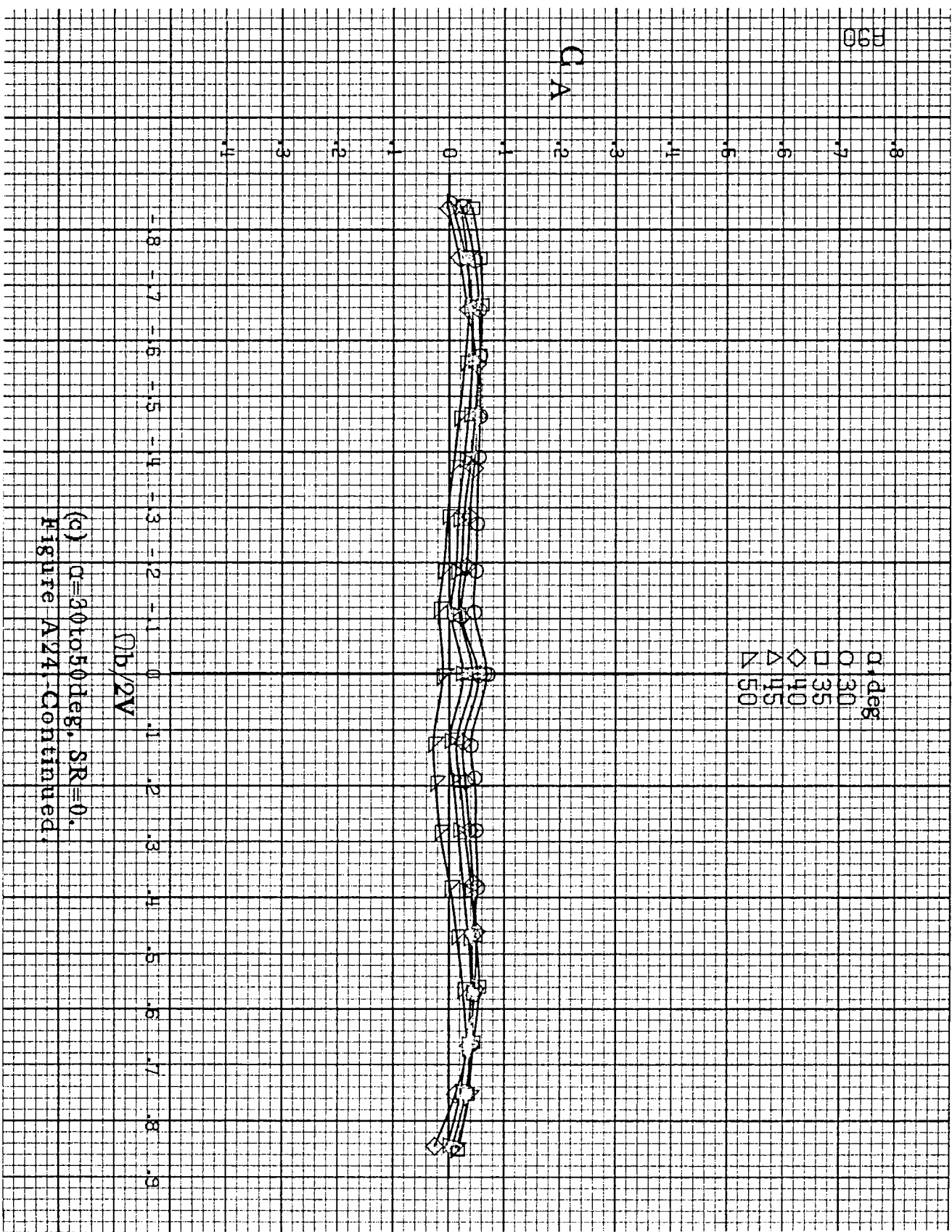




(a)  $\alpha = 8 \text{ to } 16 \text{ deg}$ ,  $SR = 99 \text{ cm (39 in)}$ .

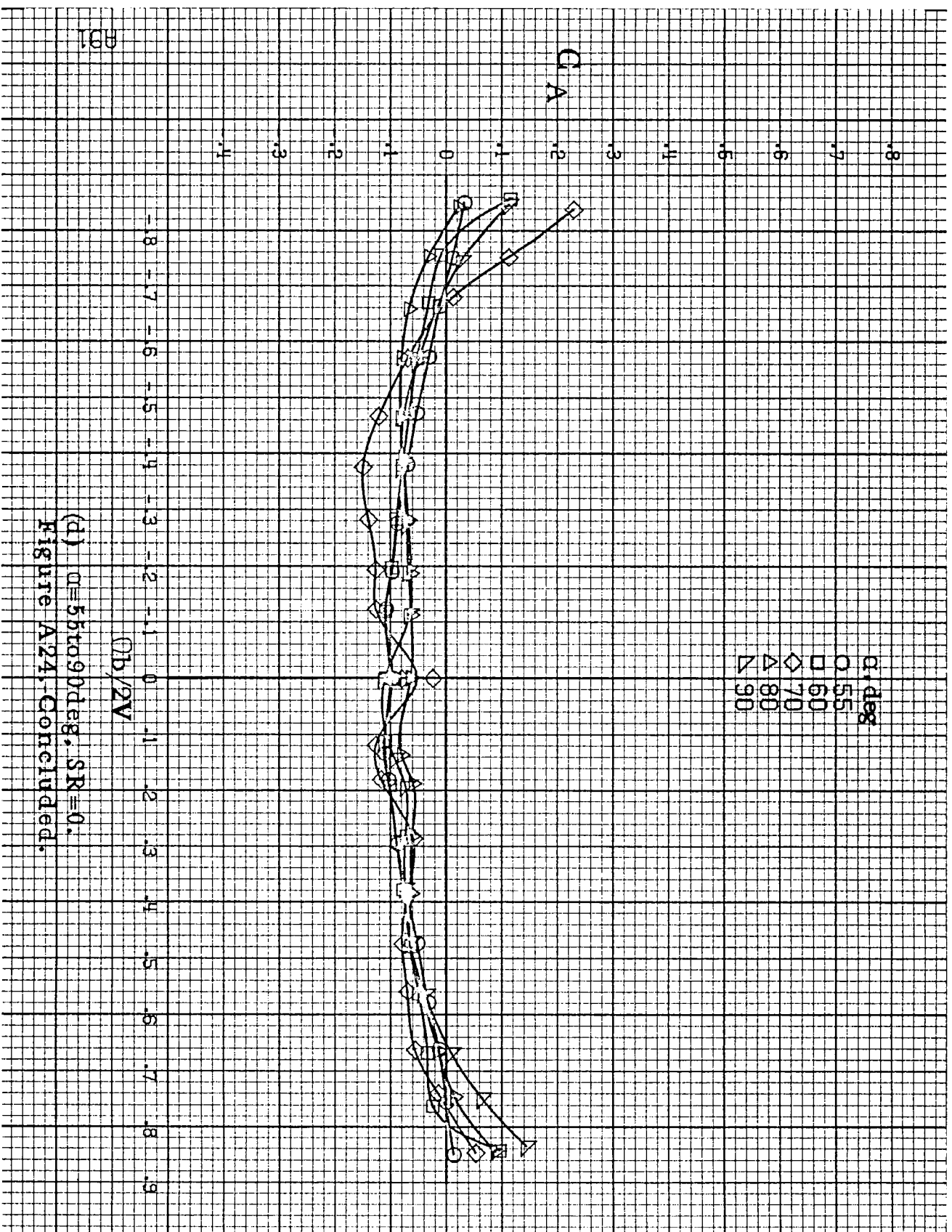
Figure A24. Effect of rotation rate and angle of attack on axial-force coefficient for no. 1 horizontal tail configuration.  $\delta_e = 0^\circ$ ,  $\delta_a = 0^\circ$ ,  $\delta_r = 0^\circ$ .  $\beta = 0^\circ$ .





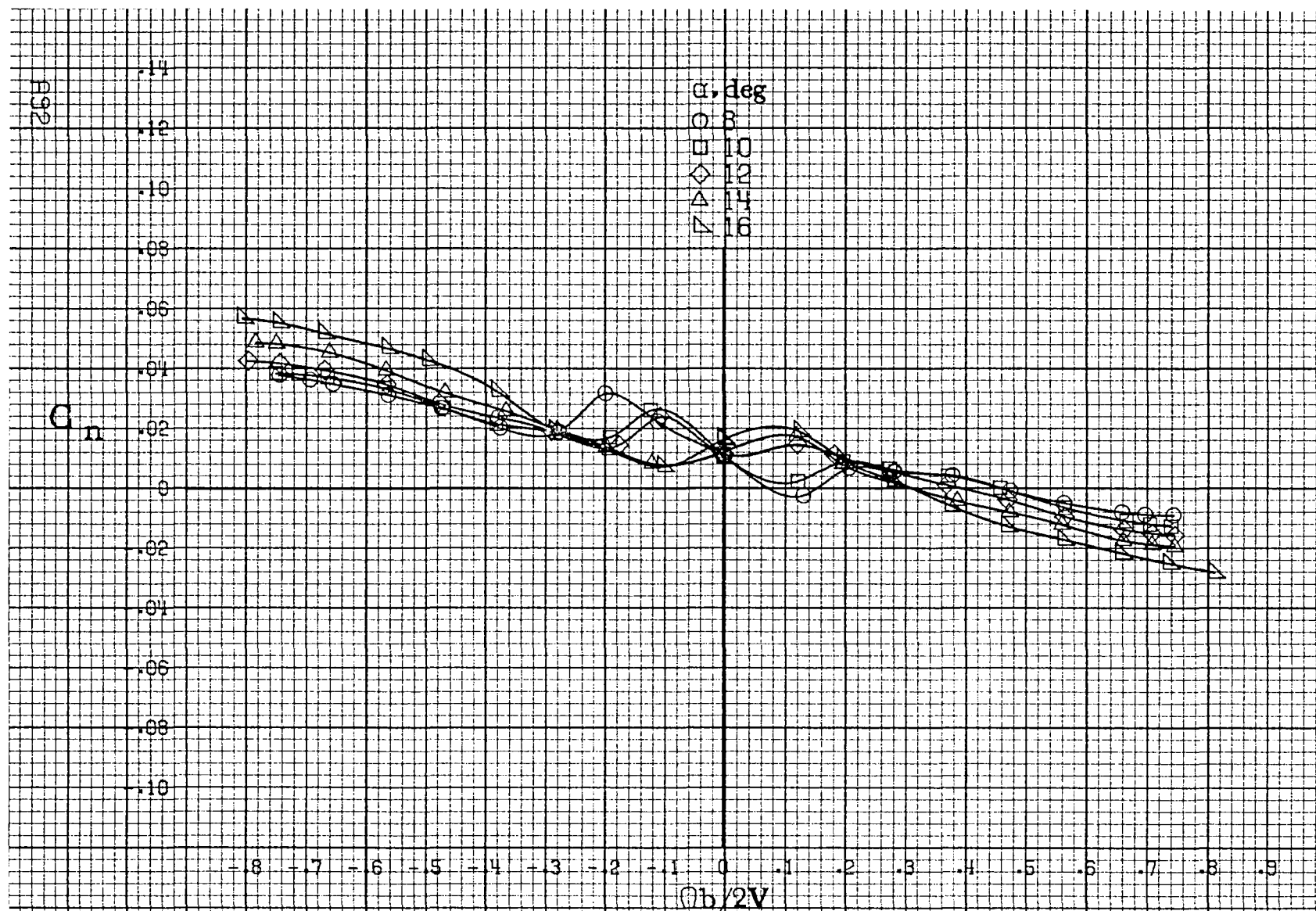
(c)  $C=30$  to  $50$  deg,  $SR=0$ .  
Figure A24, Continued.

(7b) 2V



(d)  $\alpha = 55$  to  $90$  deg,  $SR = 0$ .  
Figure A24, Concluded.

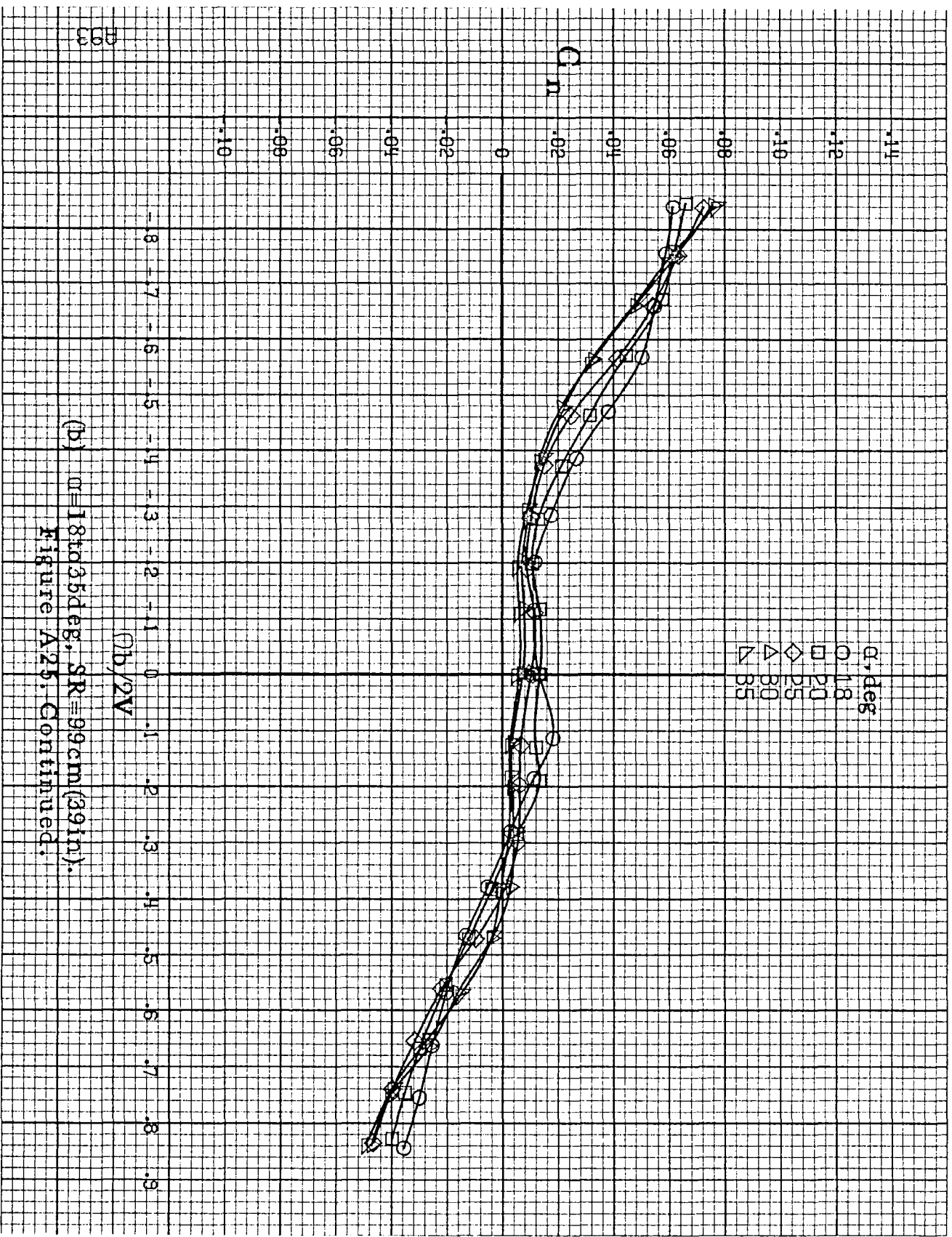




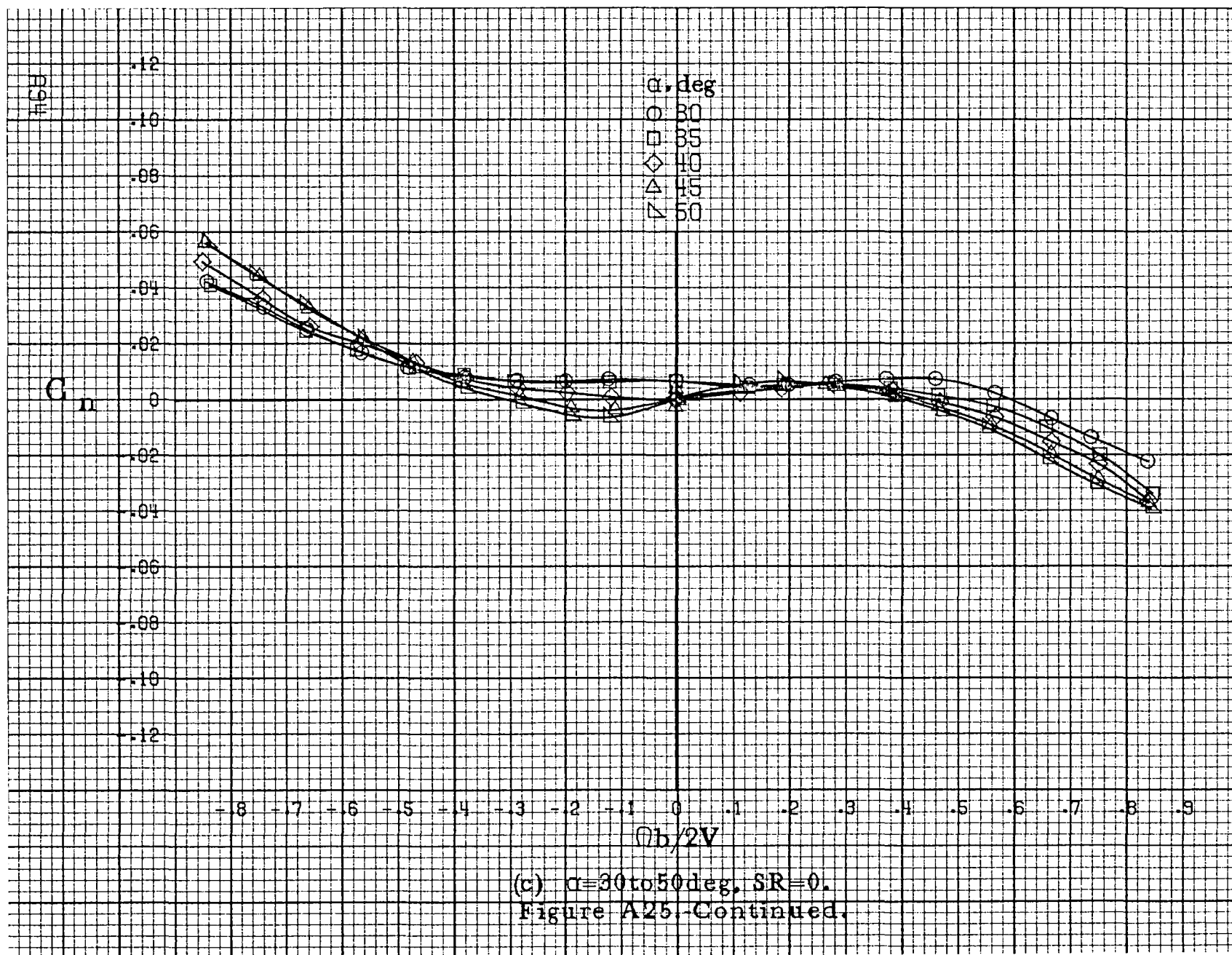
(a)  $\alpha=8$  to  $16^\circ$ , SR=99cm (39in).

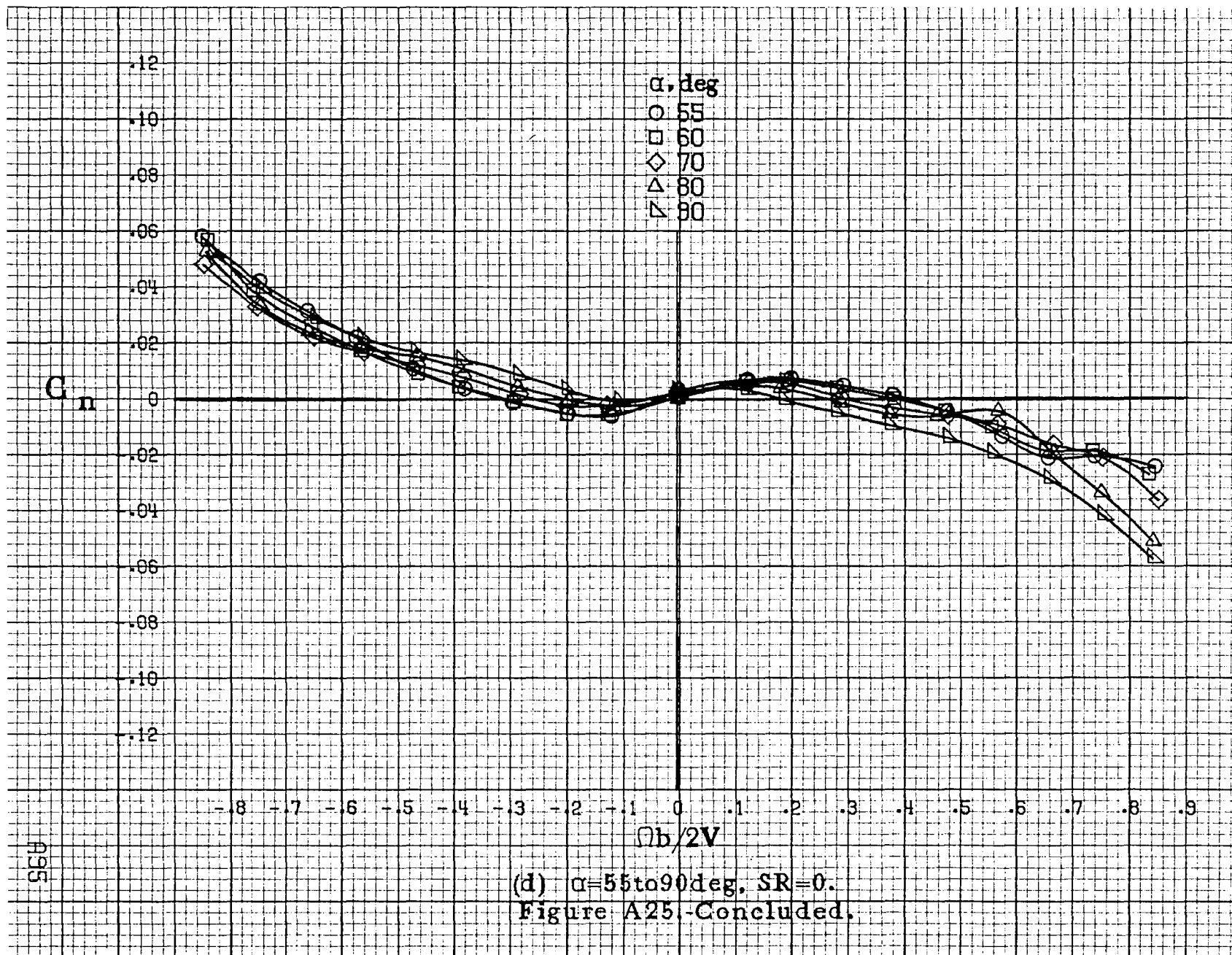
Figure A25. Effect of rotation rate and angle of attack on yawing-moment coefficient for no. 1 horizontal tail configuration.  $\delta_e=0^\circ$ ,  $\delta_a=0^\circ$ ,  $\delta_r=-25^\circ$ ,  $\beta=0^\circ$ .

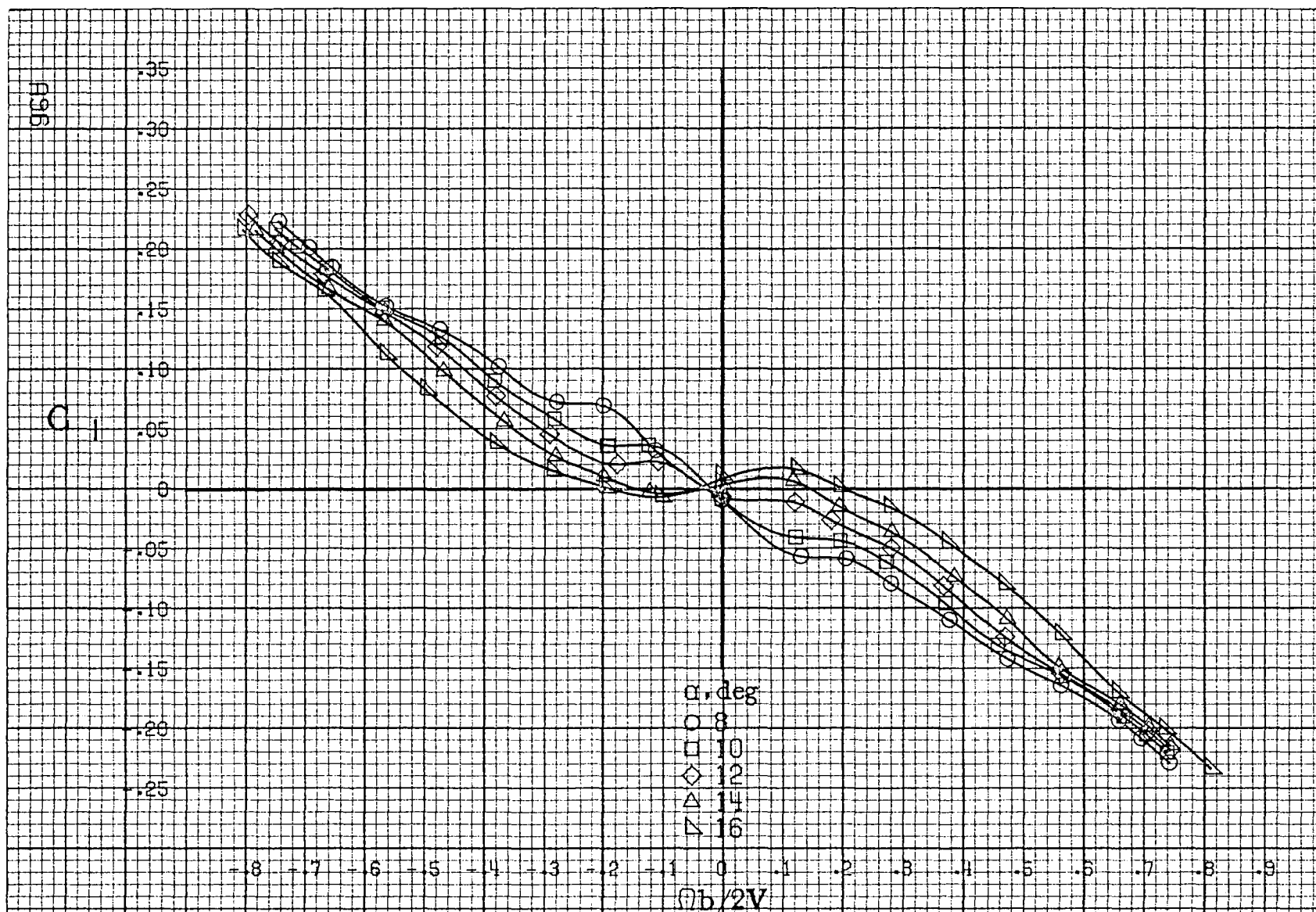




(b)  $\alpha = 18$  to  $35$  deg,  $SR = 99 \text{ cm (39 in.)}$ .  
Figure A25. Continued.







(a)  $\alpha=8$  to  $16^\circ$ ,  $SR=99\text{cm}(39\text{in})$ .

Figure A26.-Effect of rotation rate and angle of attack on rolling-moment coefficient for no. 1 horizontal tail configuration.  $\delta_e=0^\circ$ ,  $\delta_a=0^\circ$ ,  $\delta_r=25^\circ$ ,  $\beta=0^\circ$ .

$C_1$

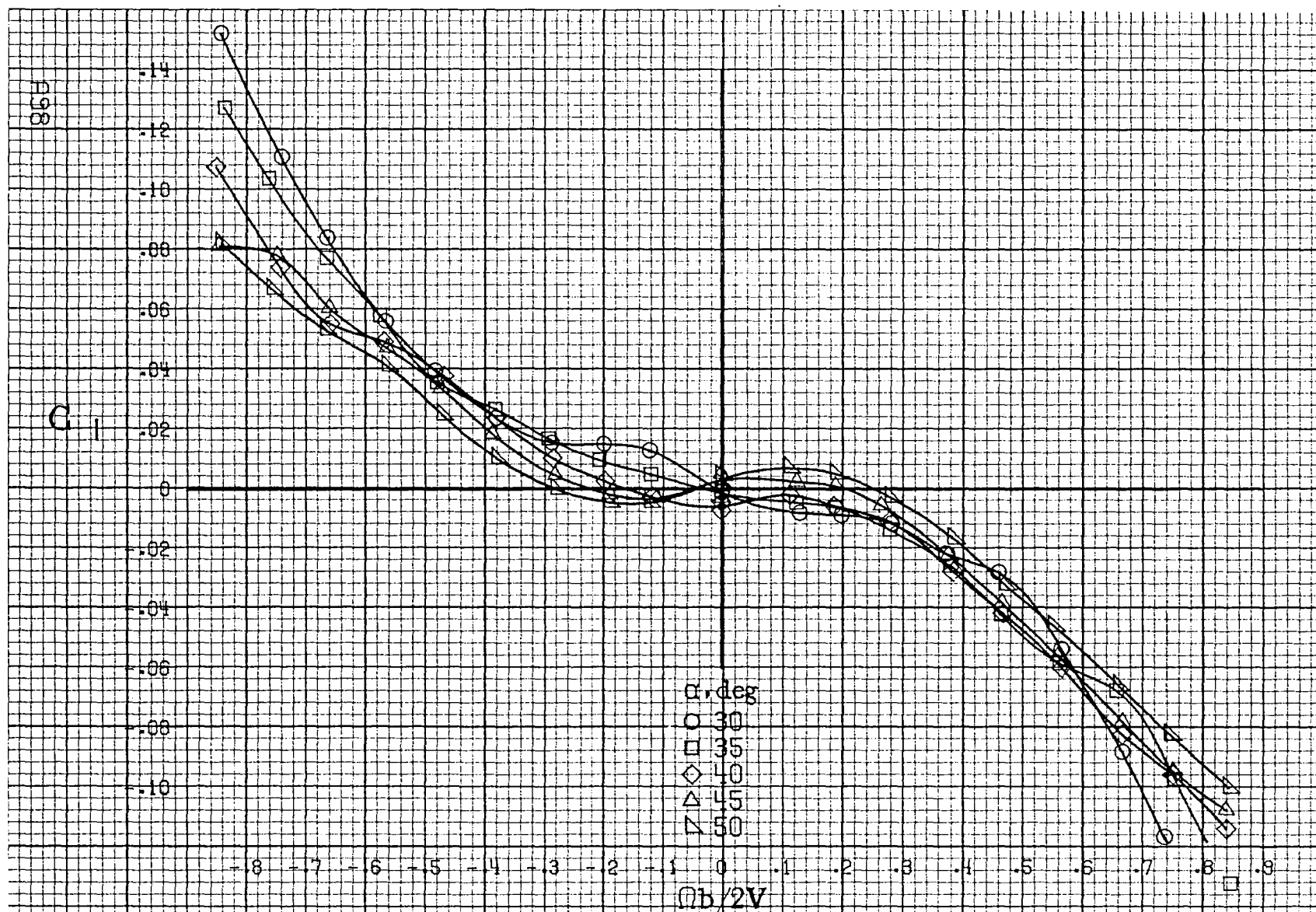
.35  
.30  
.25  
.20  
.15  
.10  
.05  
0  
-.05  
-.10  
-.15  
-.20  
-.25

$\alpha$ , deg  
○ 18  
□ 20  
◇ 25  
△ 30  
▽ 35

$\Omega b/2V$

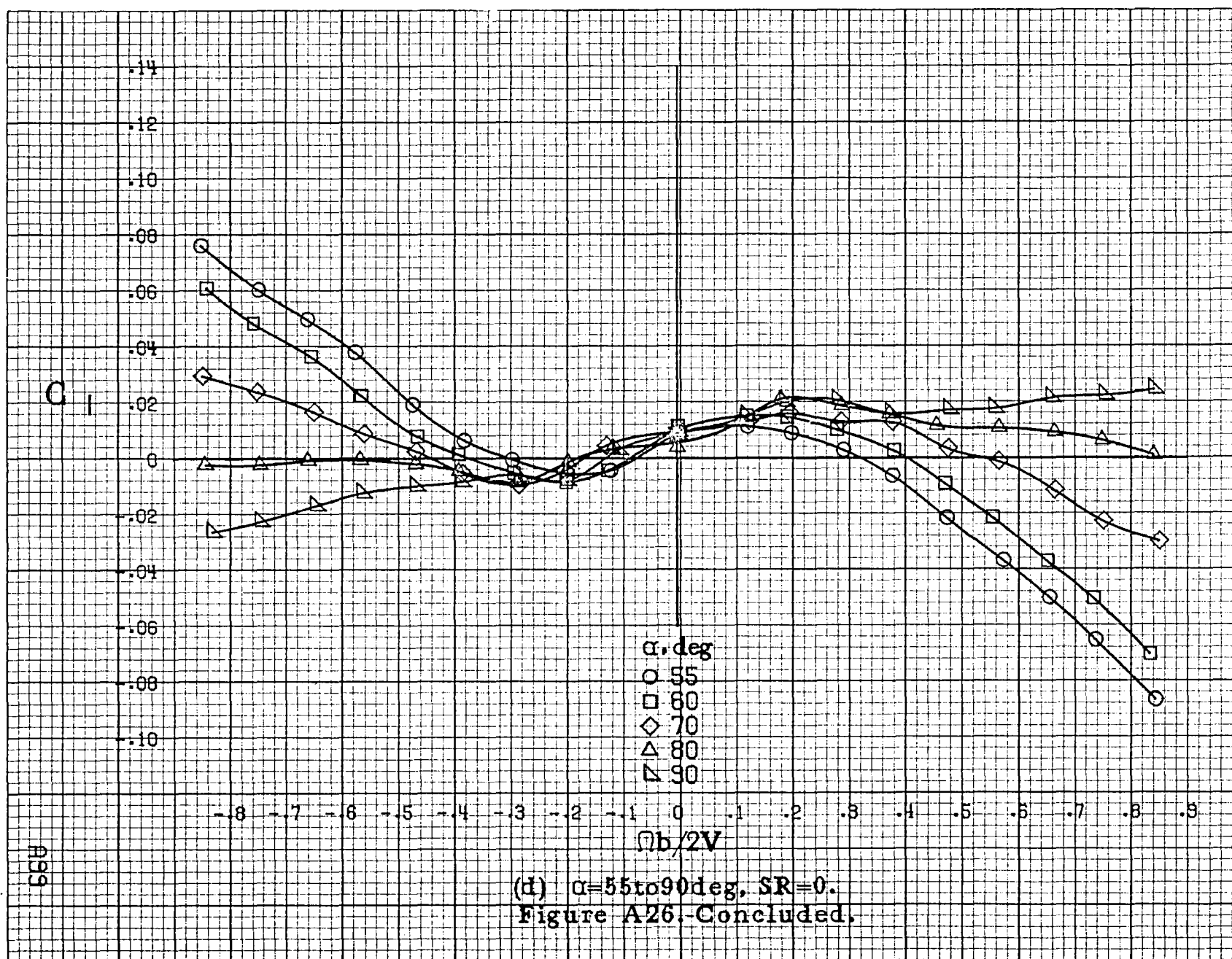
-.8 -.7 -.6 -.5 -.4 -.3 -.2 -.1 0 .1 .2 .3 .4 .5 .6 .7 .8 .9

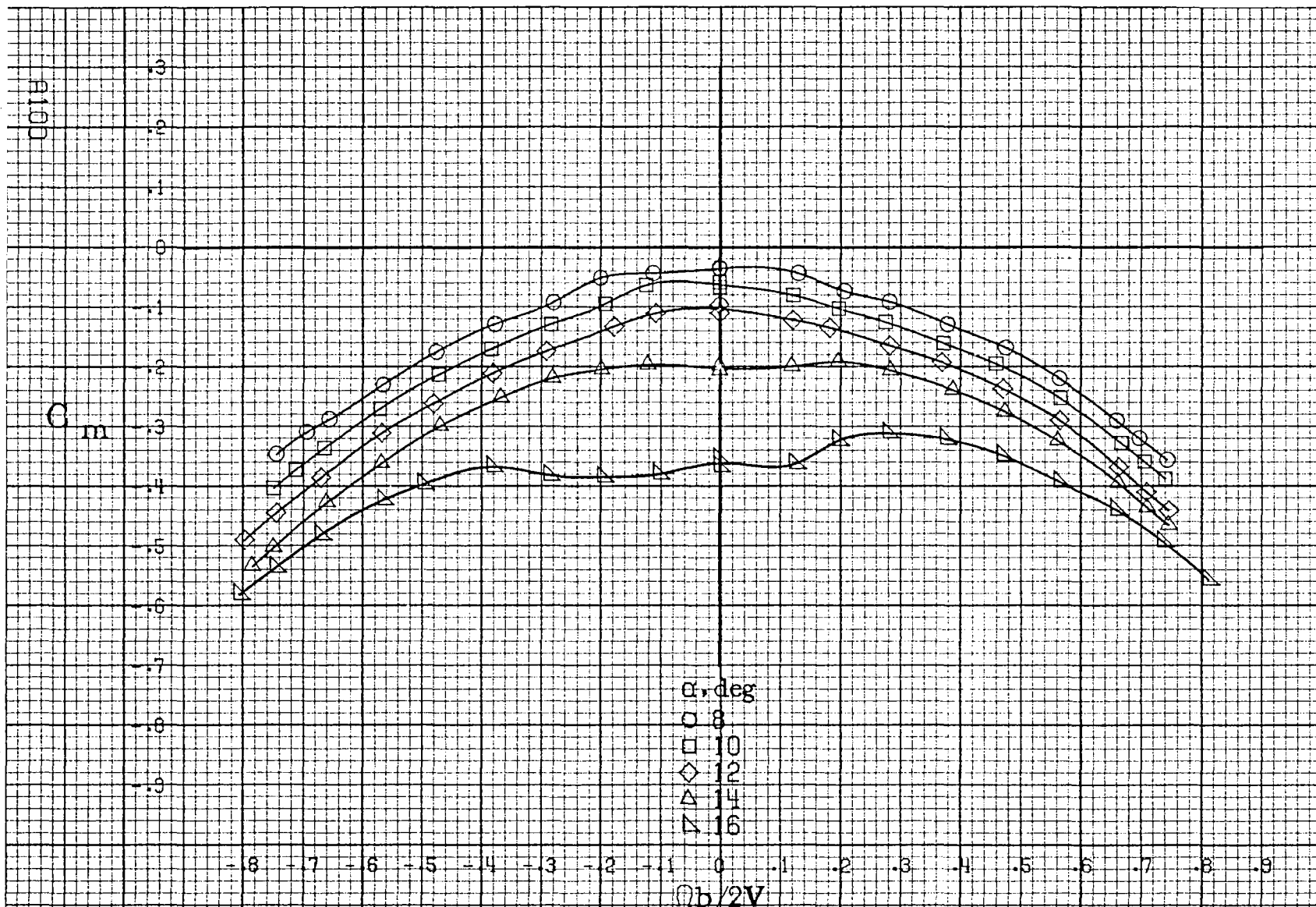
(b)  $\alpha=18$  to  $35$  deg,  $SR=99$  cm (39 in).  
Figure A26. Continued.



(c)  $\alpha = 30$  to  $50^\circ$ ,  $SR = 0$ .  
Figure A26. Continued.



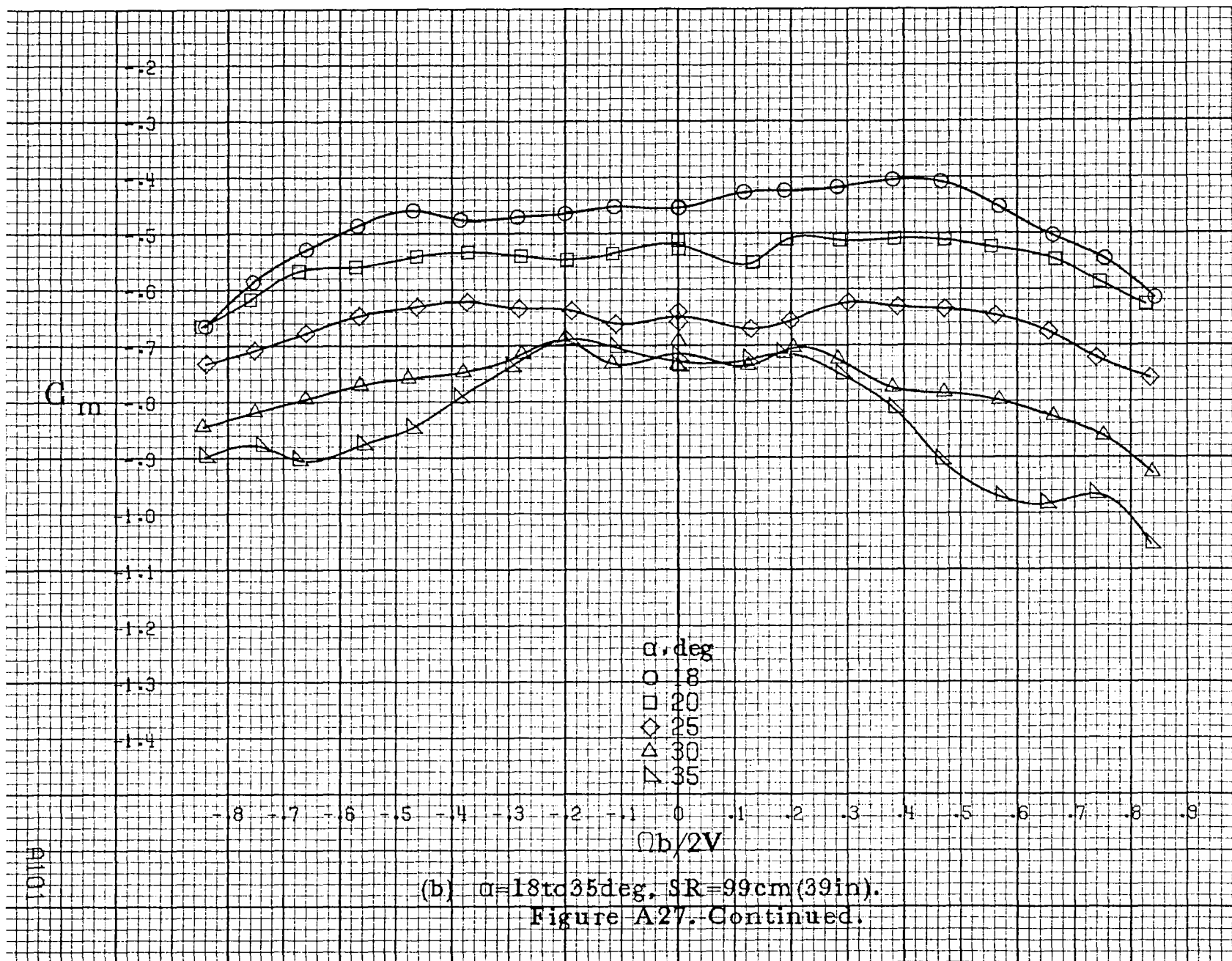


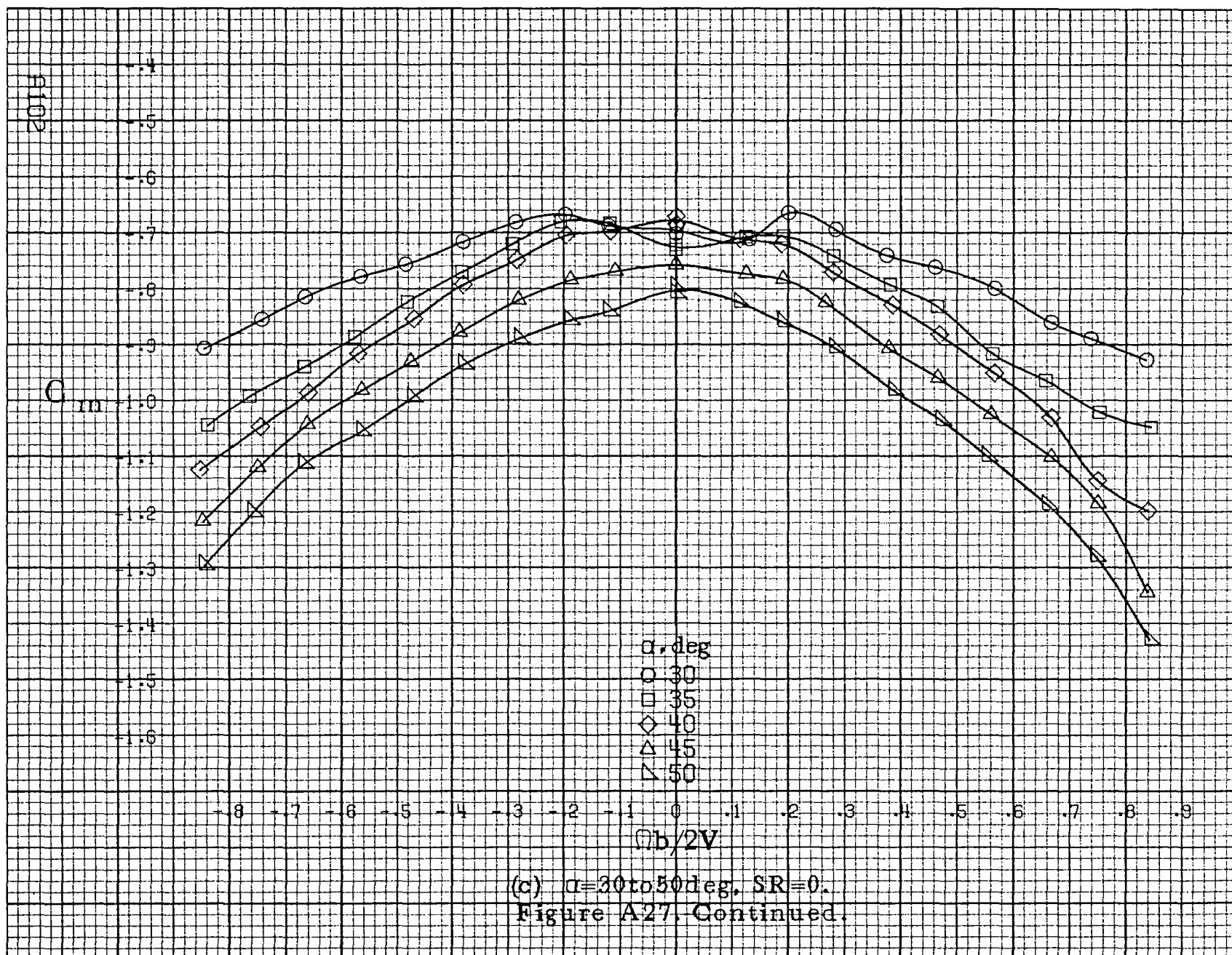


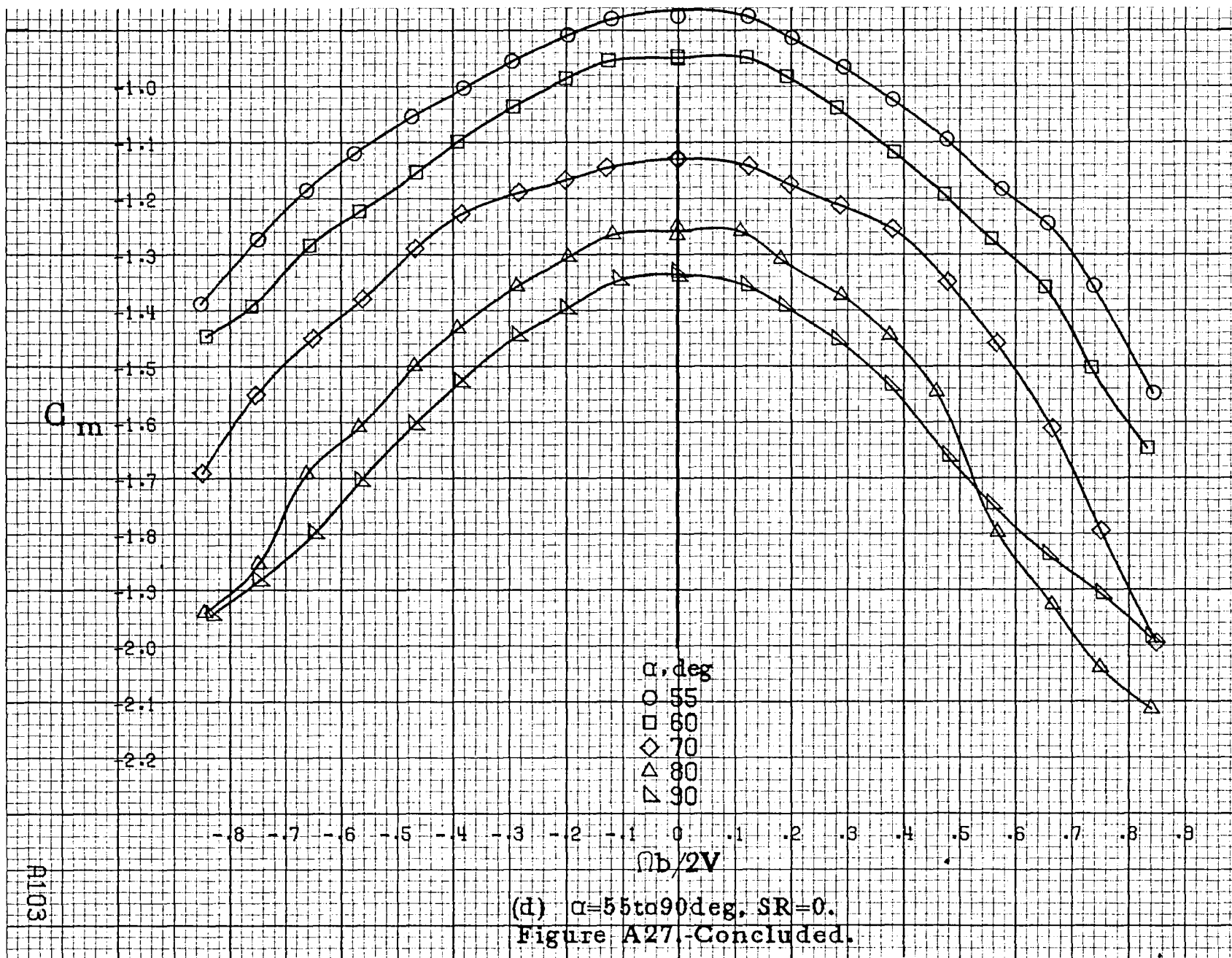
(a)  $\alpha = 8$  to  $16$  deg,  $SR = 99$  cm (39 in).

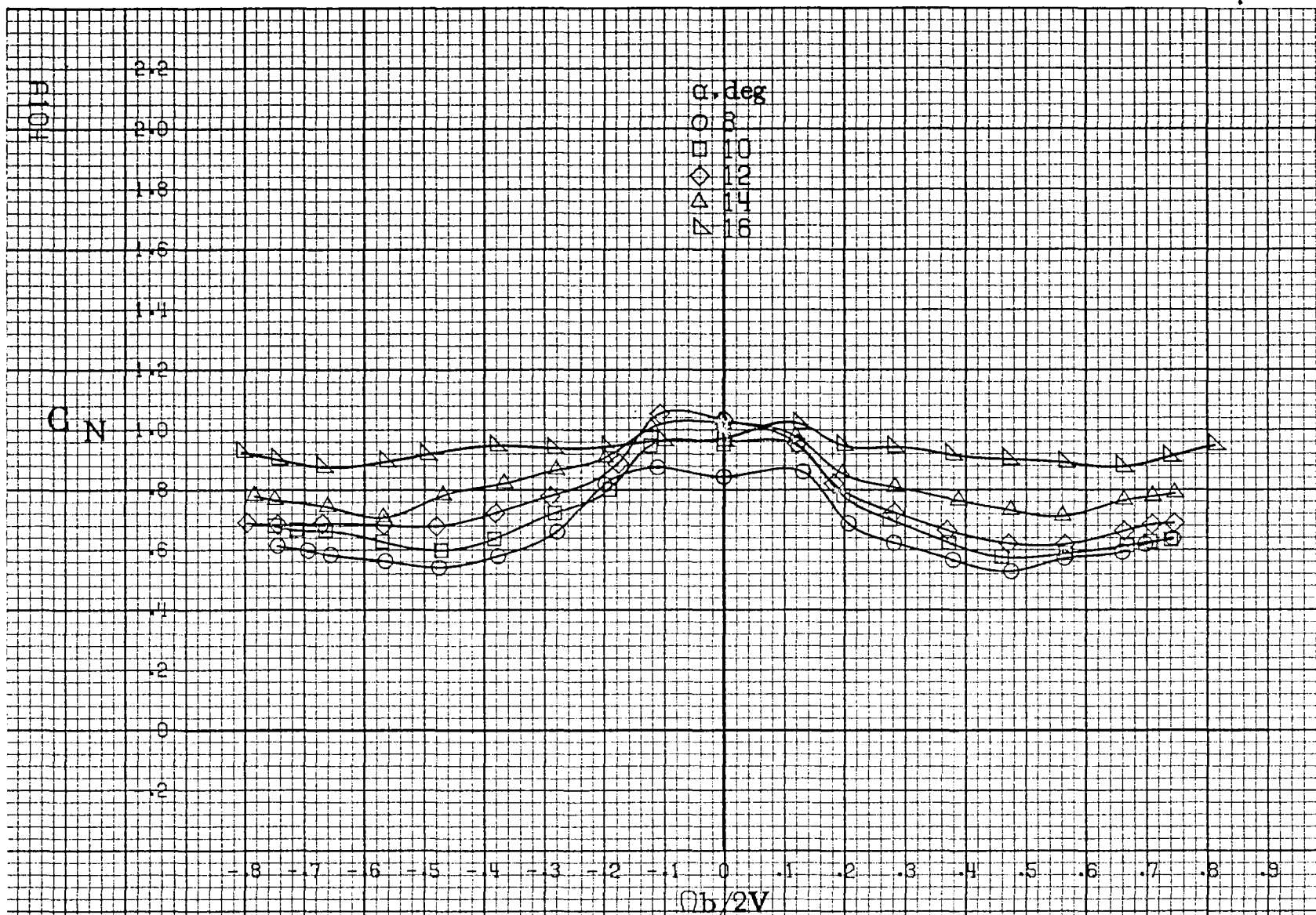
Figure A27. Effect of rotation rate and angle of attack on pitching-moment coefficient for no. 1 horizontal tail configuration.  $\delta_e = 0^\circ$ ,  $\delta_a = 0^\circ$ ,  $\delta_r = -25^\circ$ ,  $B = 0^\circ$ .





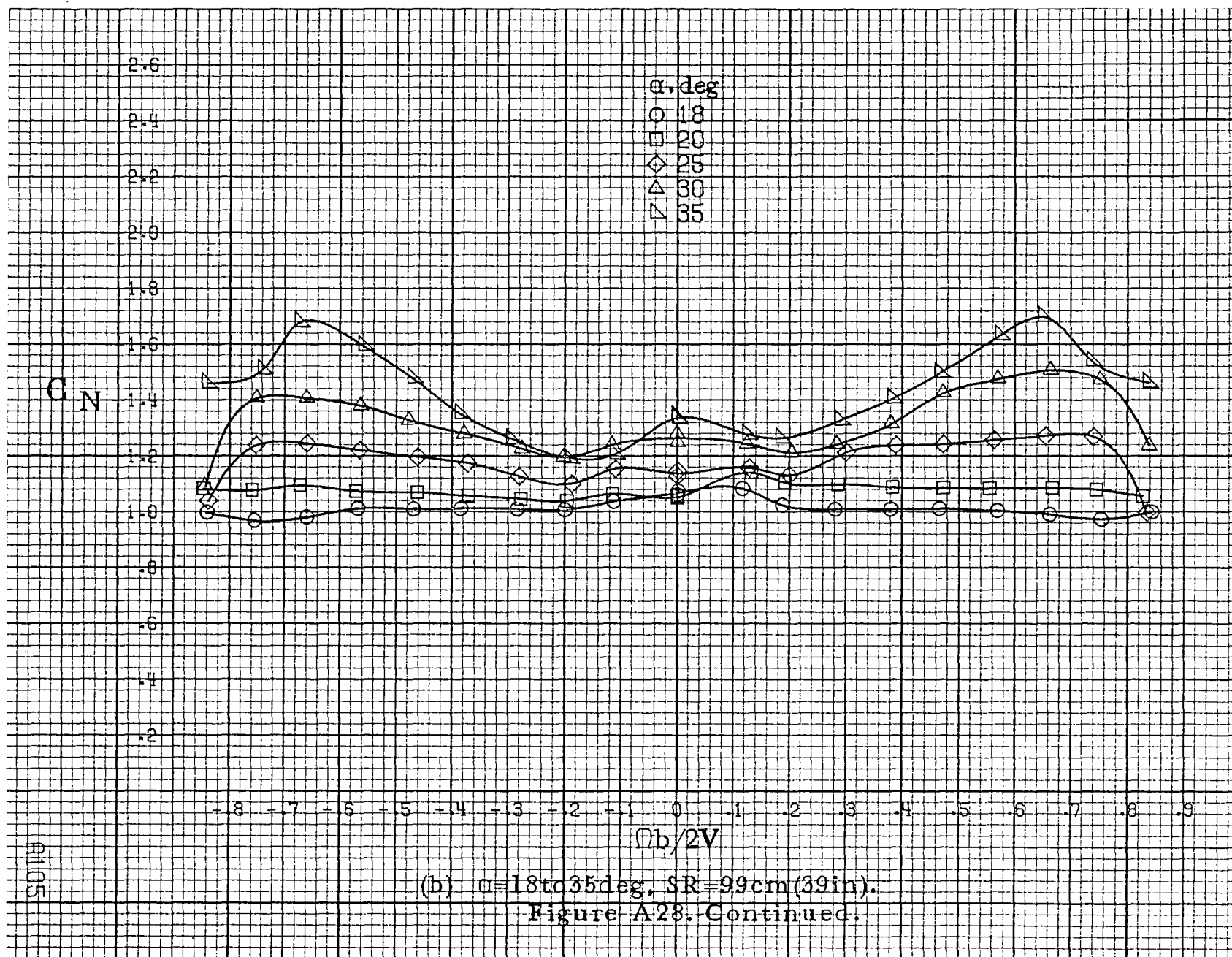


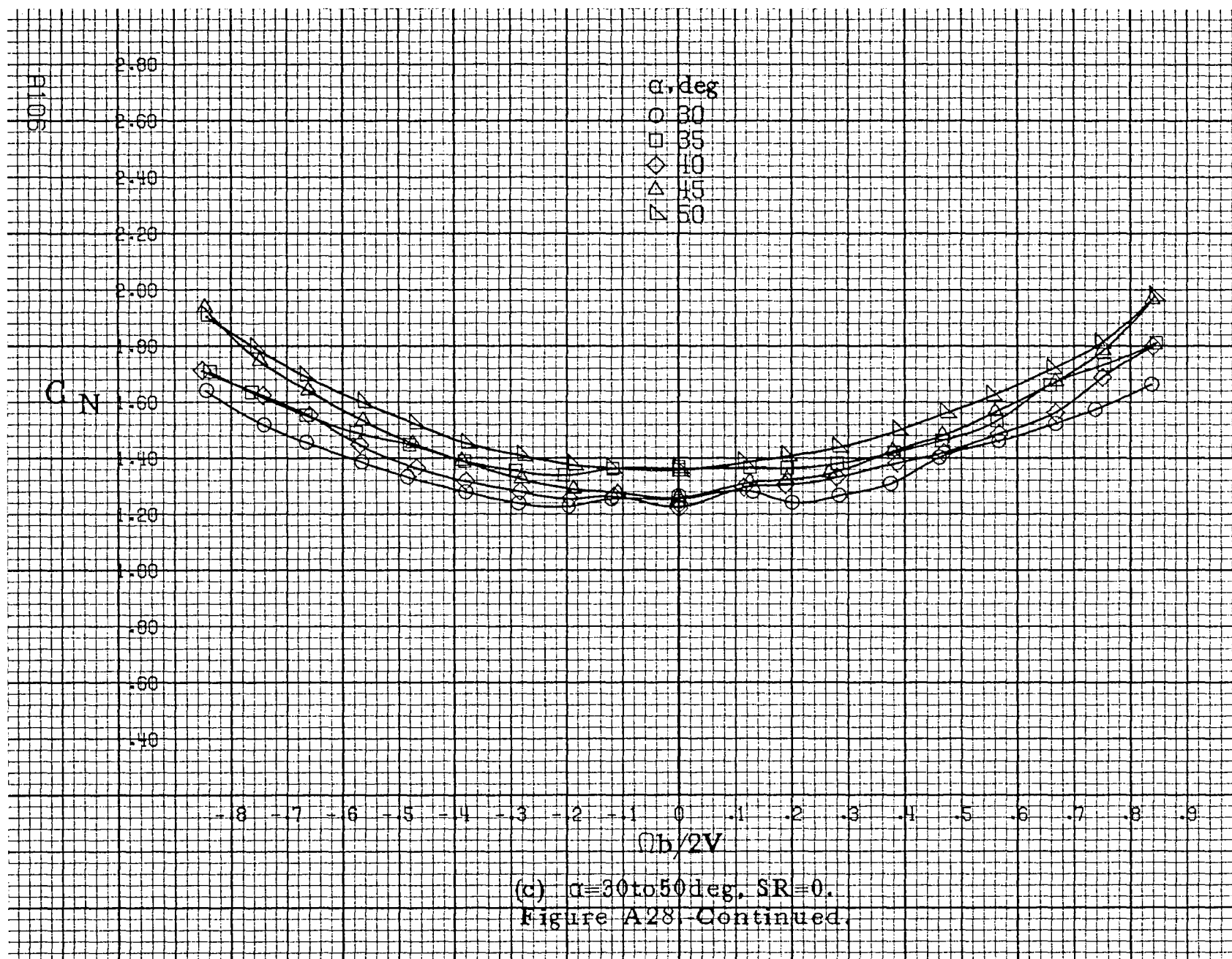




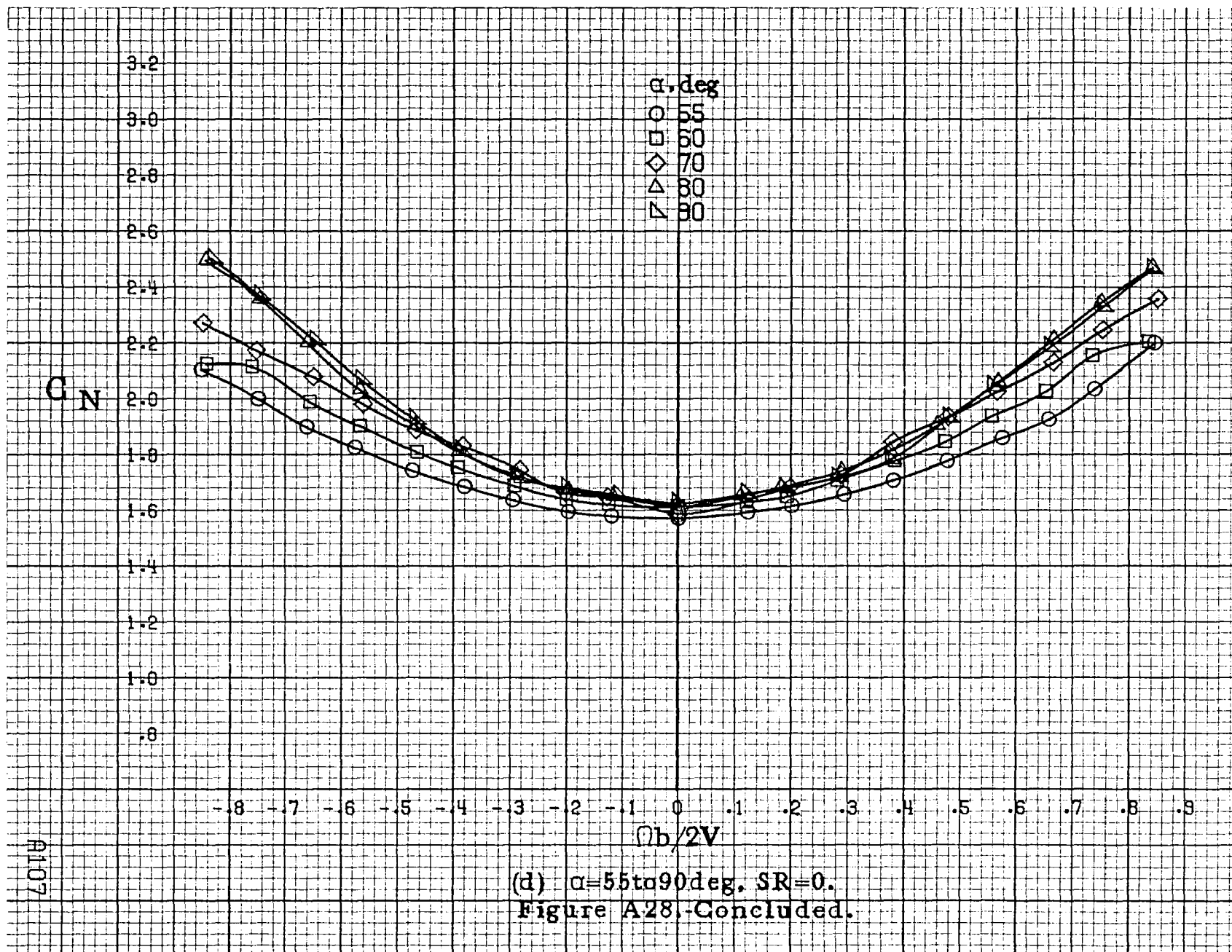
(a)  $\alpha = 8$  to  $16^\circ$ ,  $SR = 99 \text{ cm (39 in.)}$ .

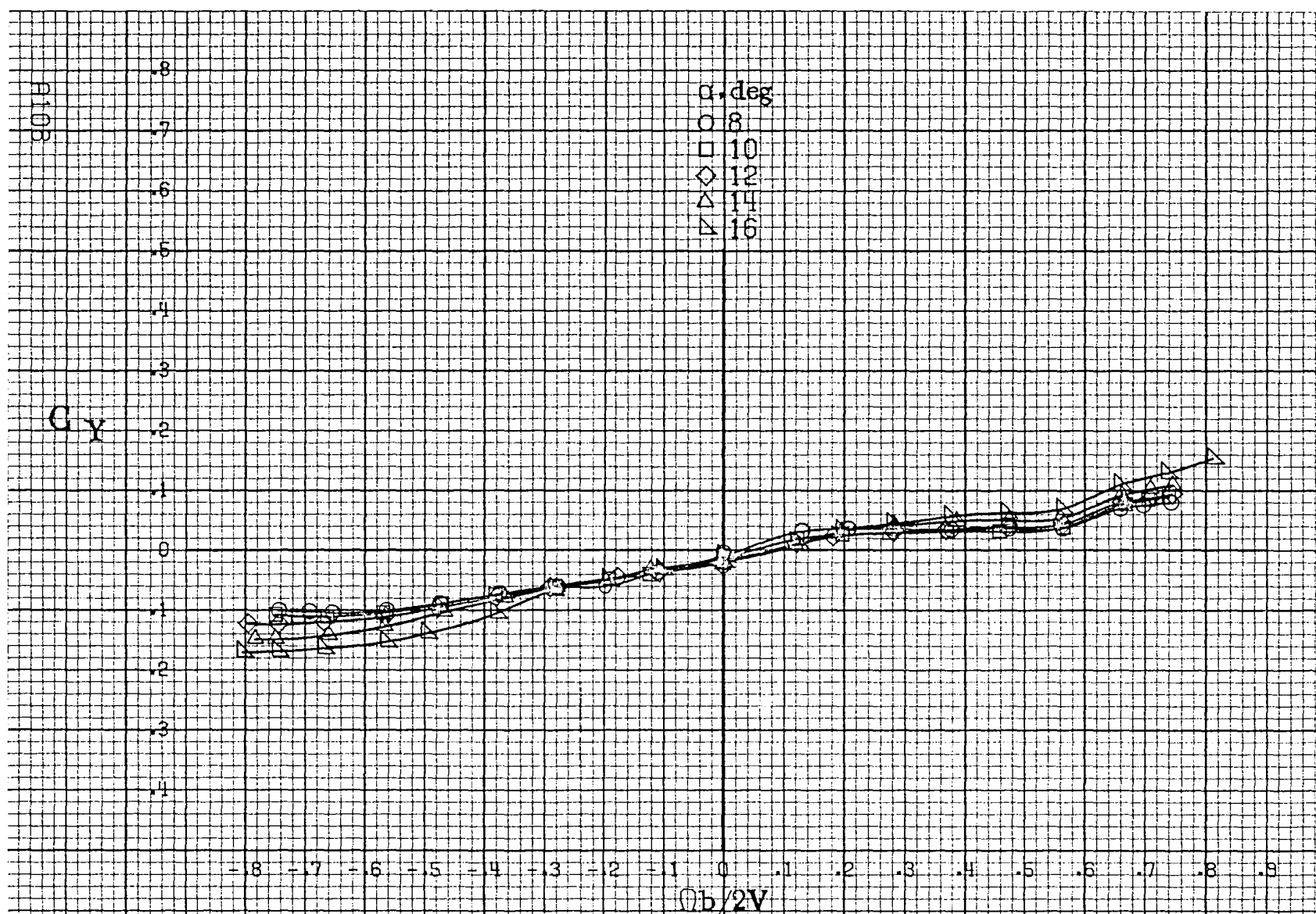
Figure A28. Effect of rotation rate and angle of attack on normal force coefficient for no. 1 horizontal tail configuration.  $\delta_e = 0^\circ$ ,  $\delta_a = 0^\circ$ ,  $\delta_r = 25^\circ$ .  $\beta = 0^\circ$ .







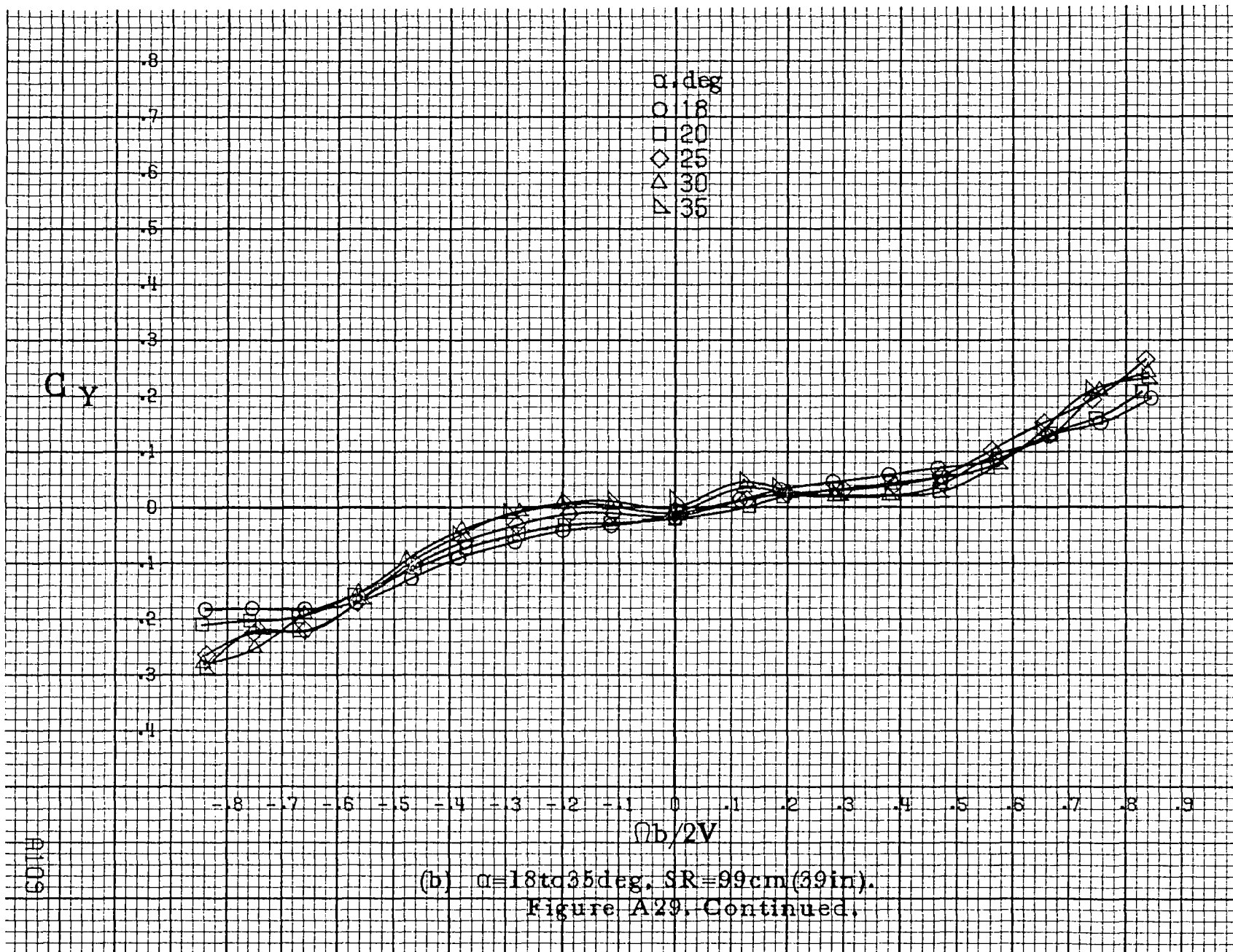


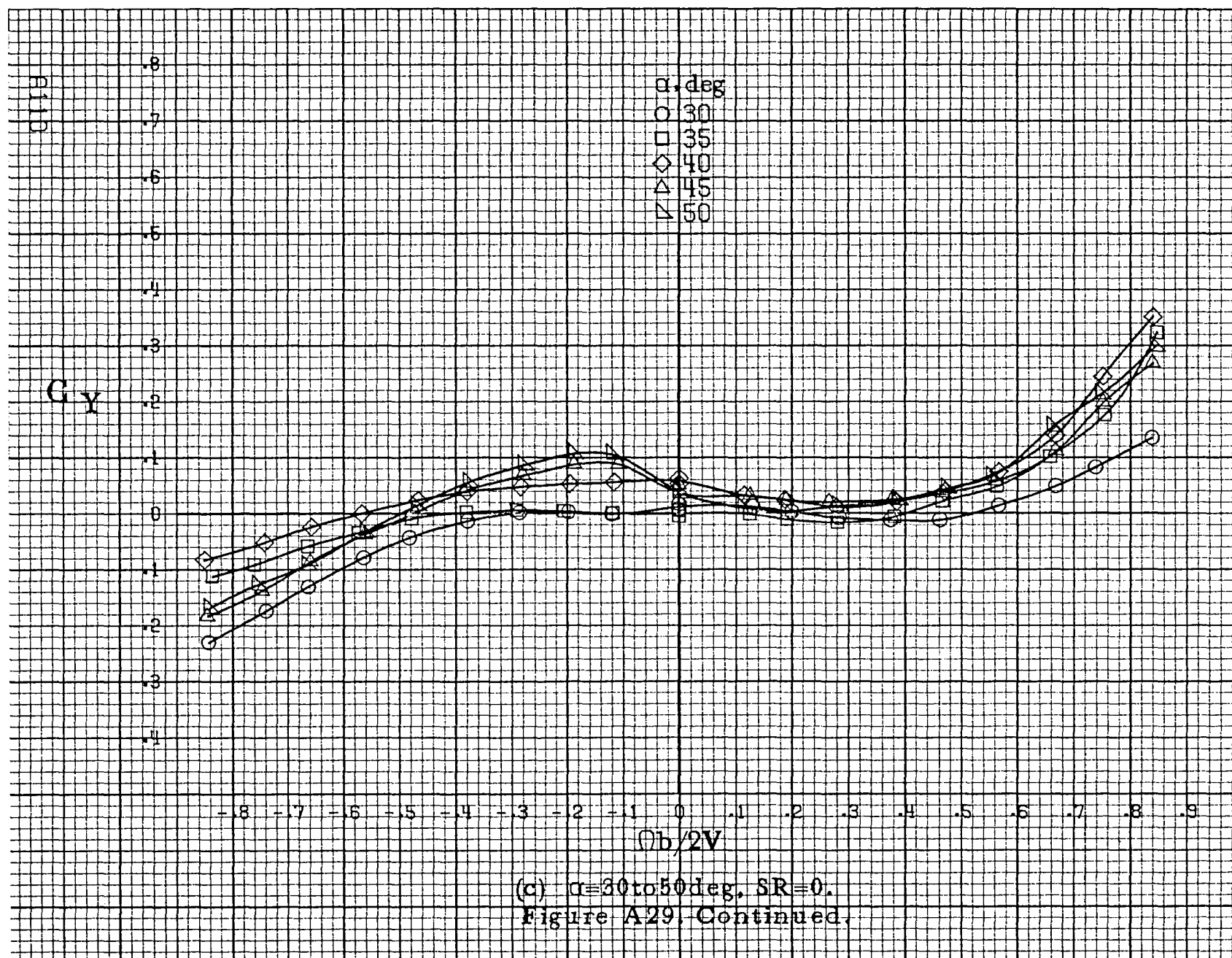


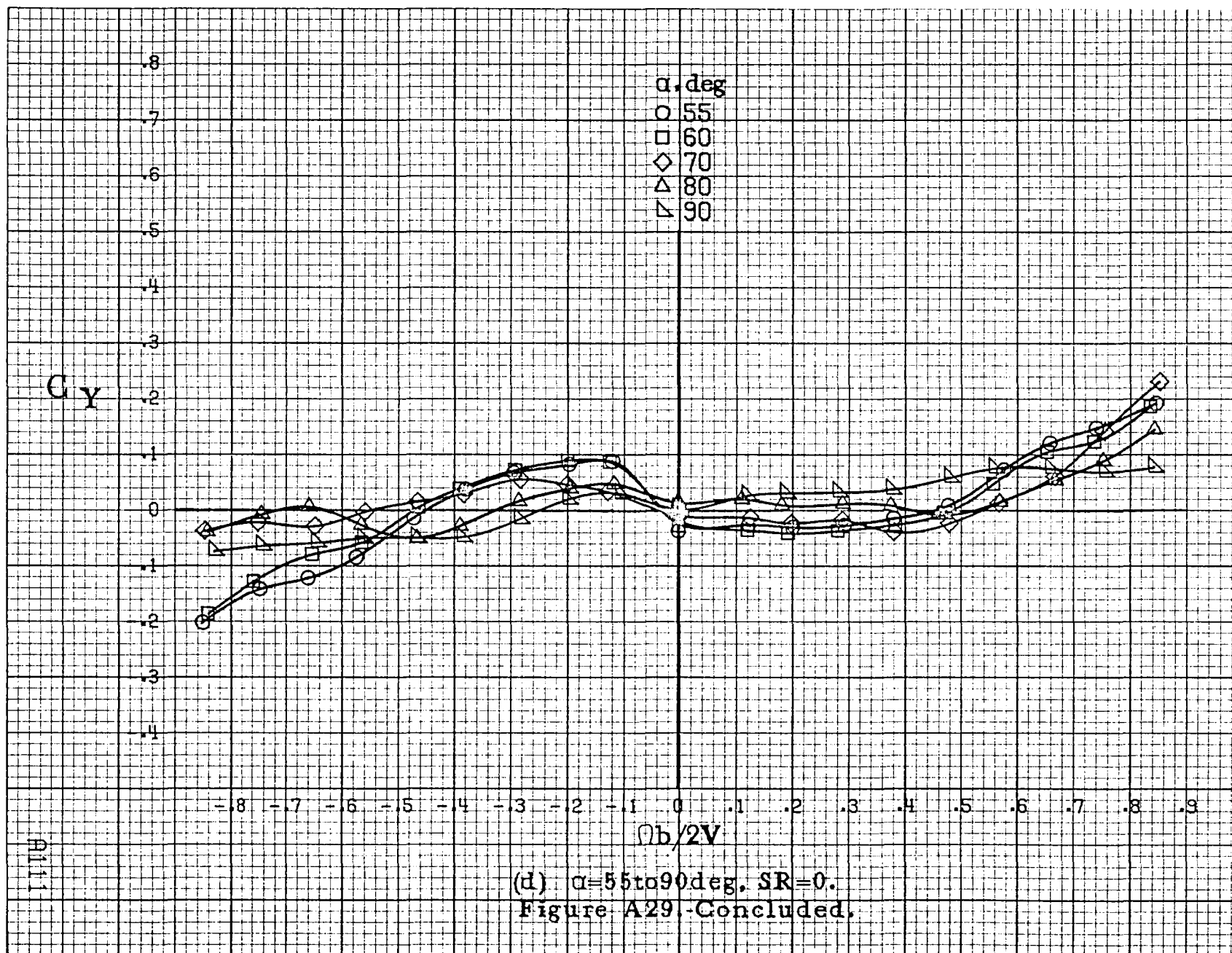
(a)  $\alpha=8$  to  $16^\circ$ ,  $SR=99\text{cm}(39\text{in})$ .

Figure A29. Effect of rotation rate and angle of attack on side-force coefficient for no. 1 horizontal tail configuration.  $\delta_e = 0^\circ$ ,  $\delta_a = 0^\circ$ ,  $\delta_r = -25^\circ$ ,  $\beta = 0^\circ$ .

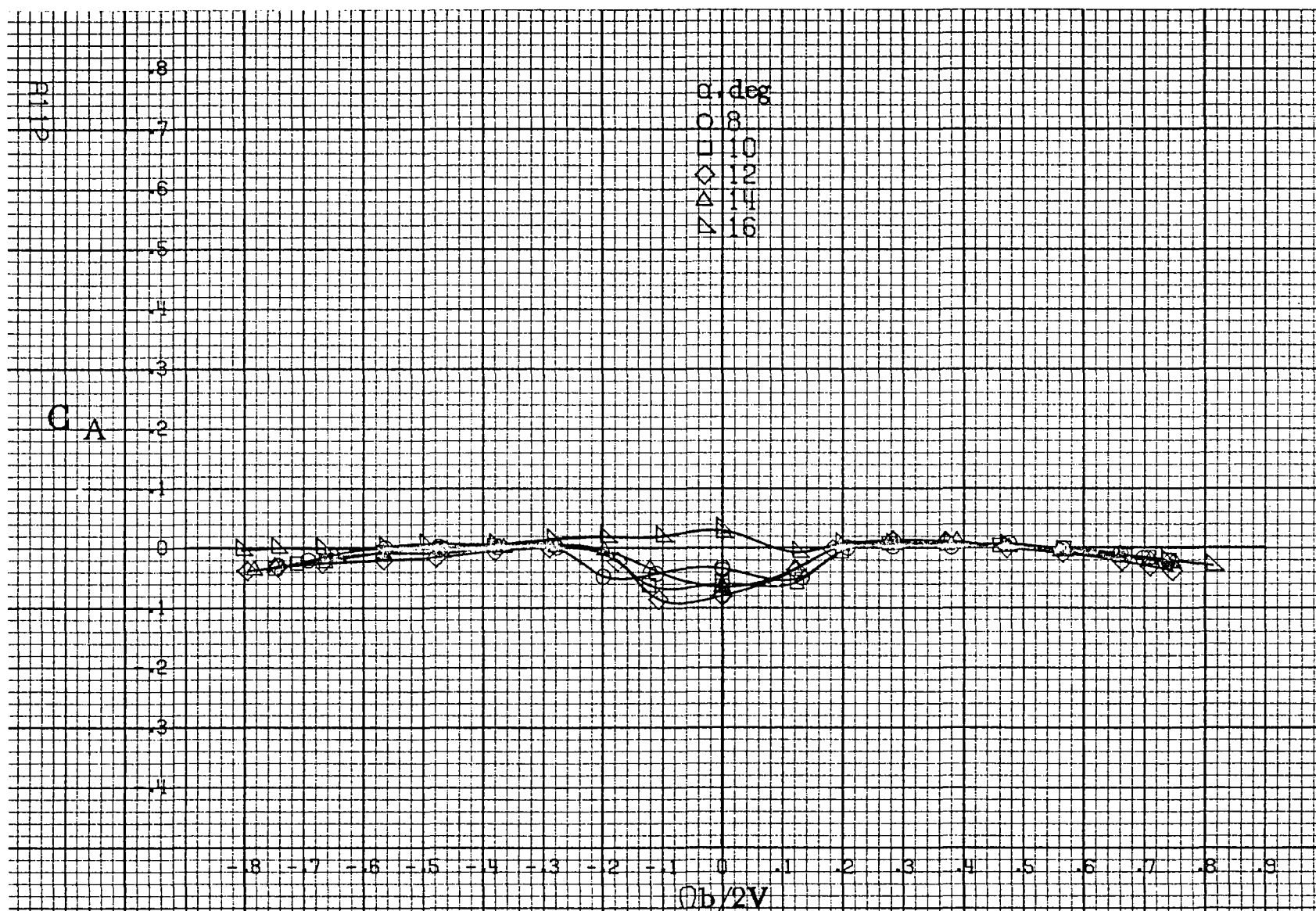






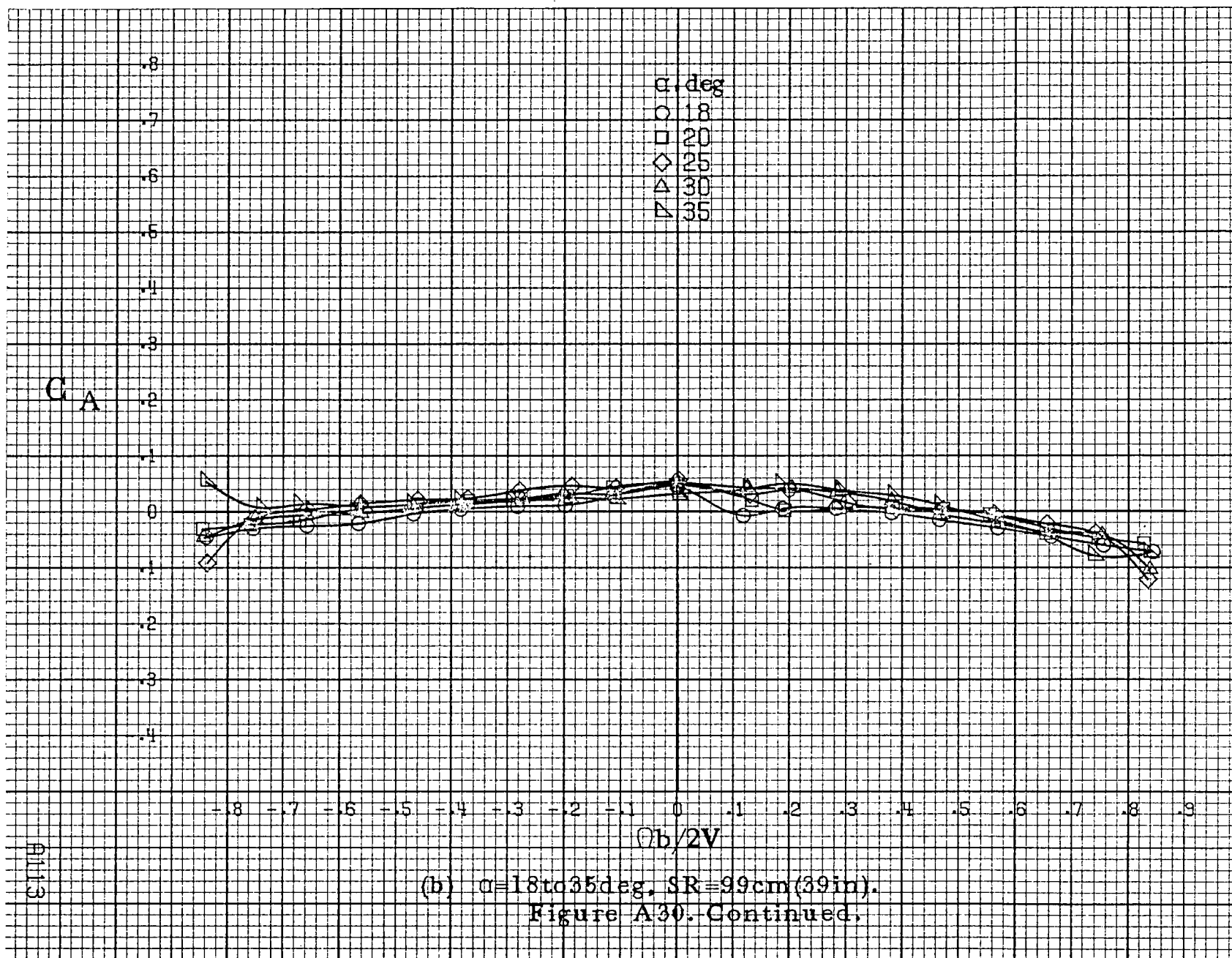


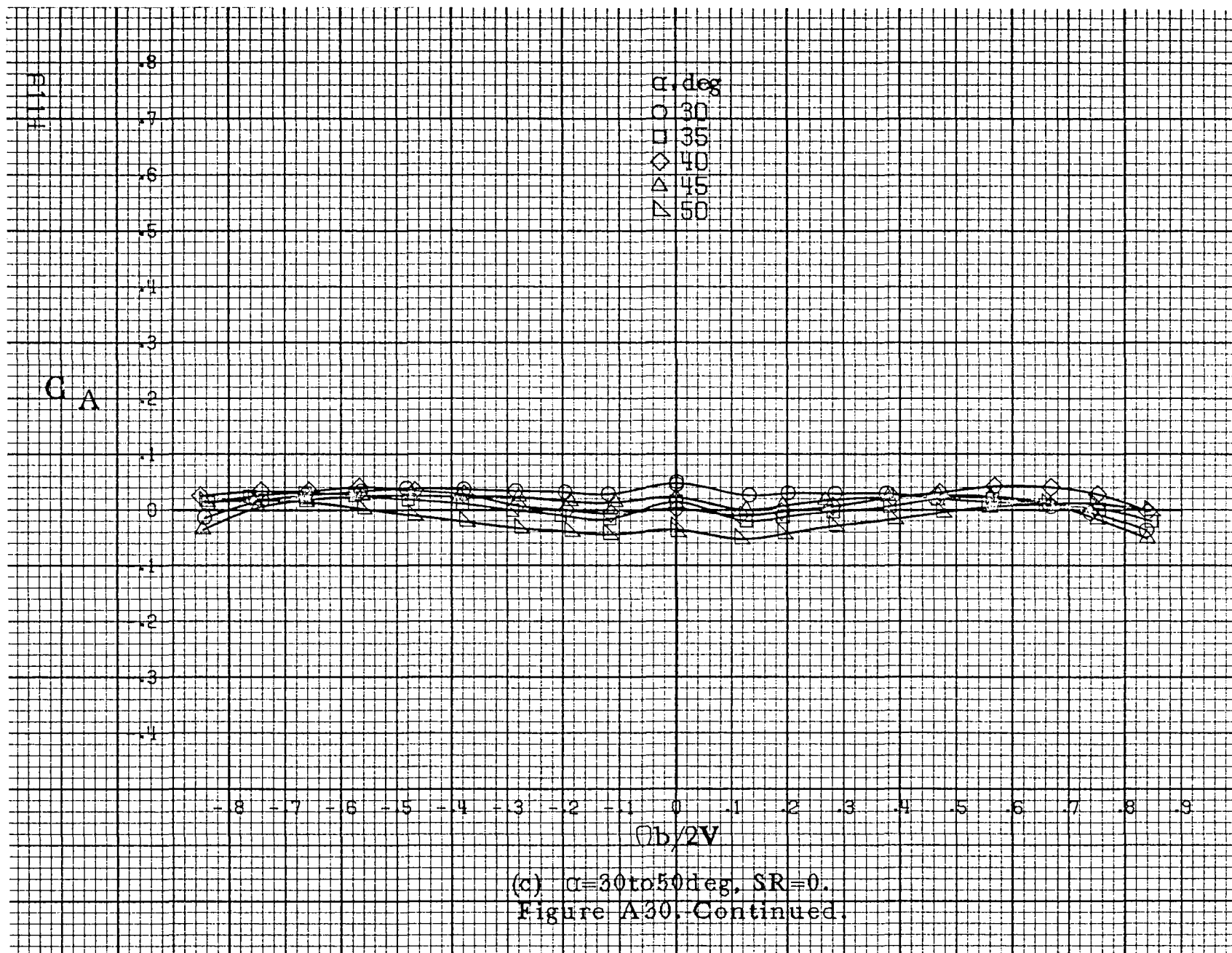
(d)  $\alpha=55$  to  $90^\circ$ ,  $SR=0$ .  
Figure A29.-Concluded.



(a)  $\alpha = 8$  to  $16^\circ$ ,  $SR = 99 \text{ cm (39 in)}$ .

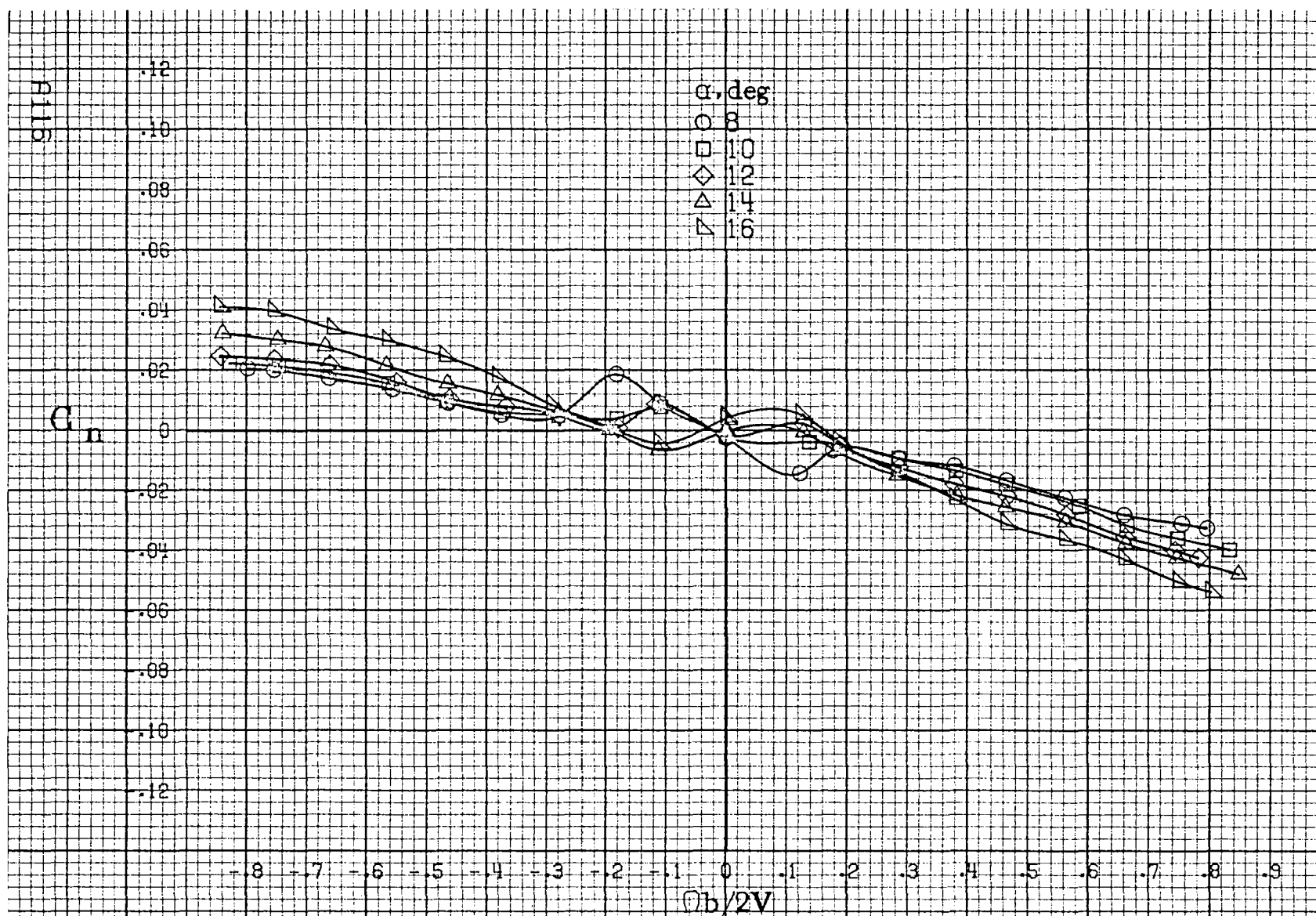
Figure A30. Effect of rotation rate and angle of attack on axial force coefficient for no. 1 horizontal tail configuration.  $\delta_e = 0^\circ$ ,  $\delta_a = 0^\circ$ ,  $\delta_r = 25^\circ$ .  $\beta = 0^\circ$ .







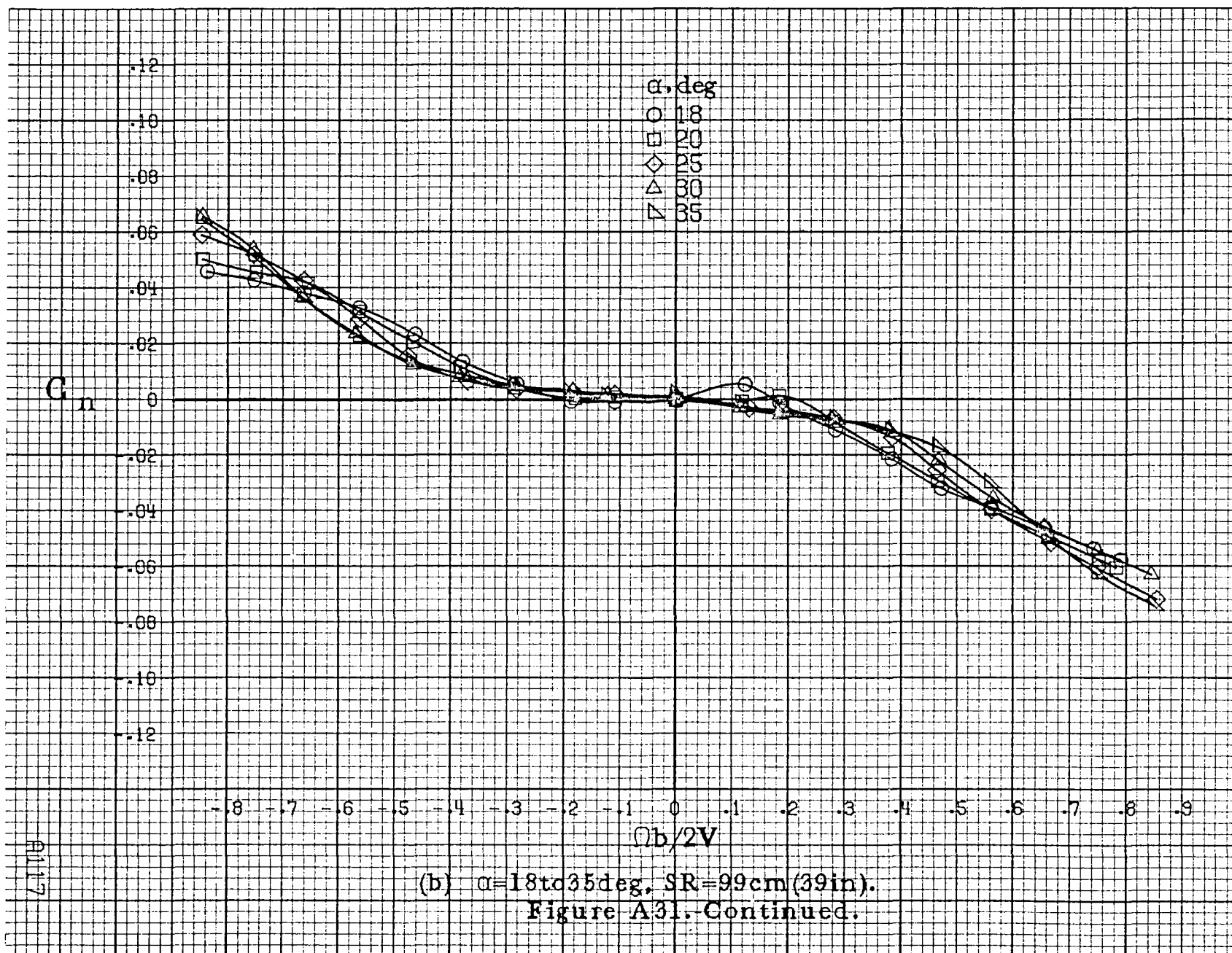


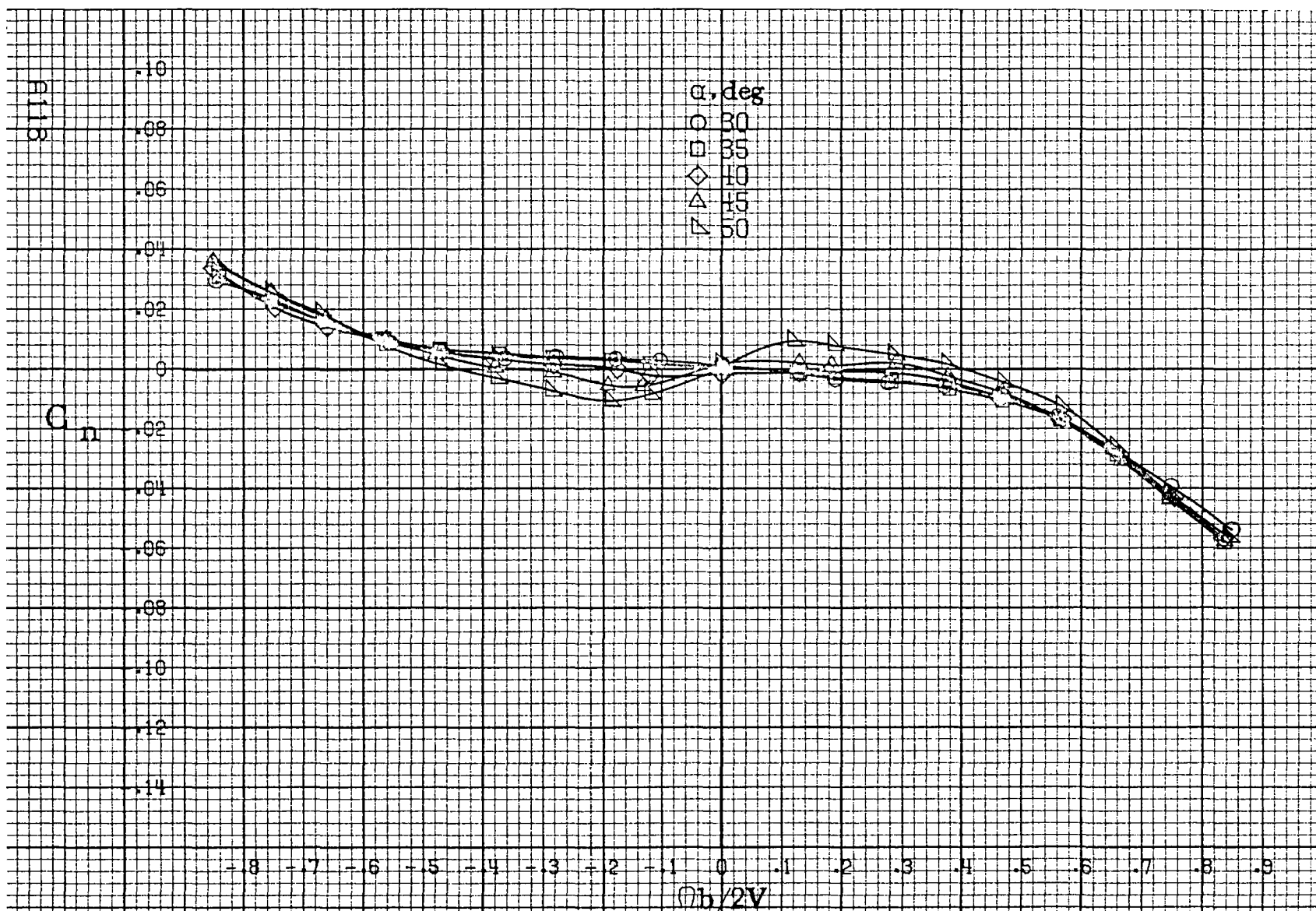


(a)  $\alpha = 8$  to  $16^\circ$ ,  $SR = 99 \text{ cm (39 in.)}$ .

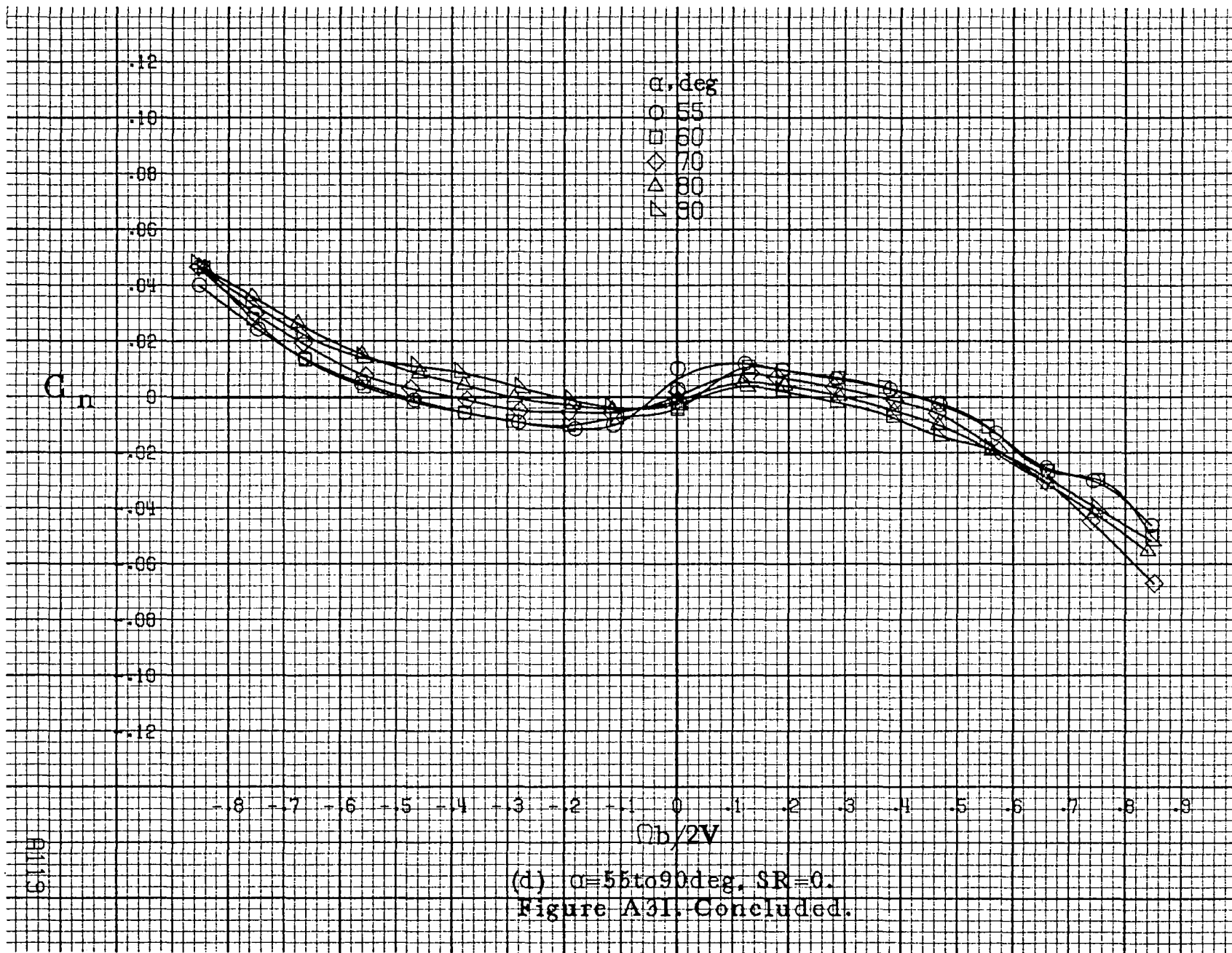
Figure A31. Effect of rotation rate and angle of attack on yawing moment coefficient for no. 2 horizontal tail configuration.  $\delta_e = 0^\circ$ ,  $\delta_a = 0^\circ$ ,  $\delta_r = 0^\circ$ ,  $\beta = 0^\circ$ .

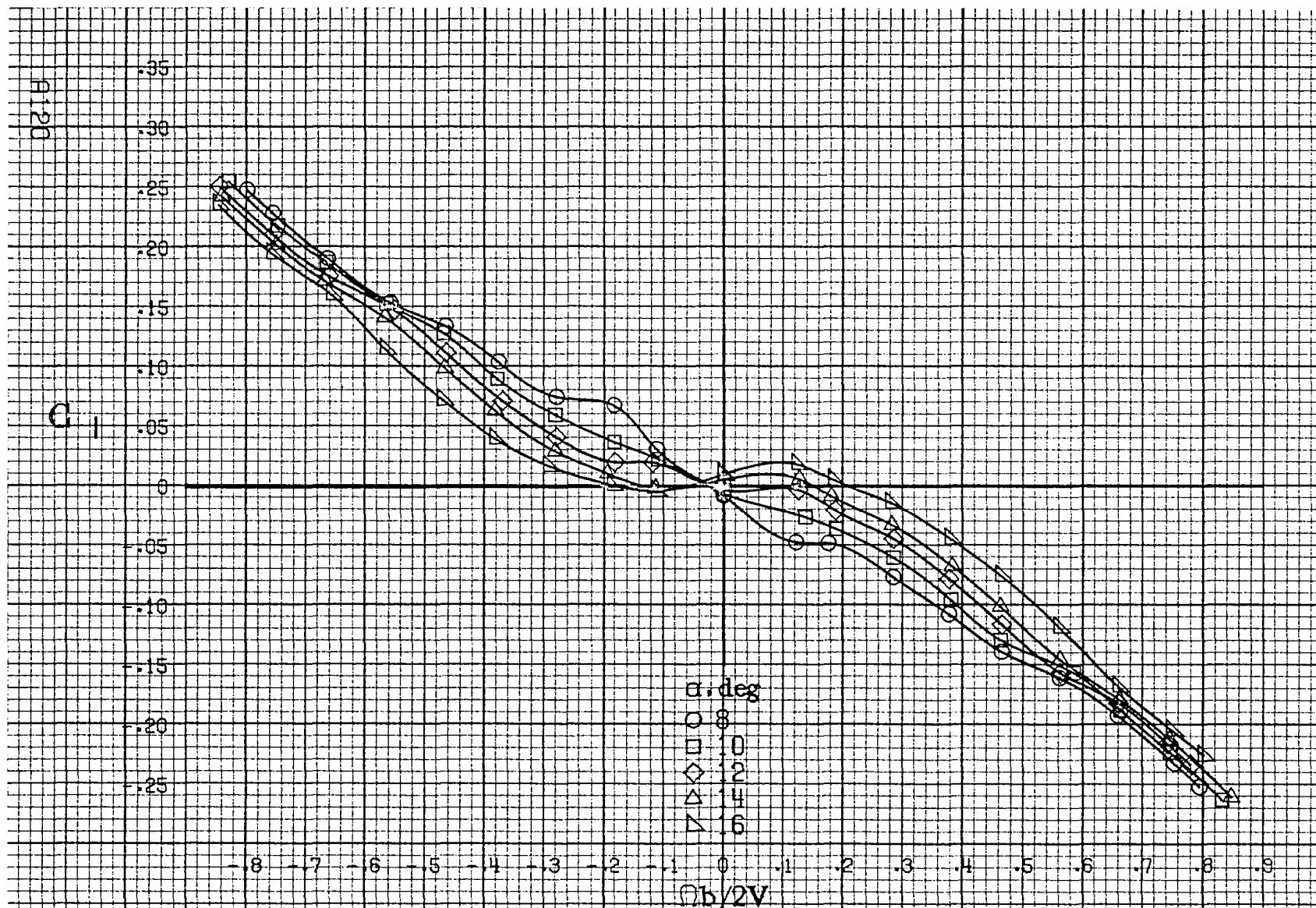






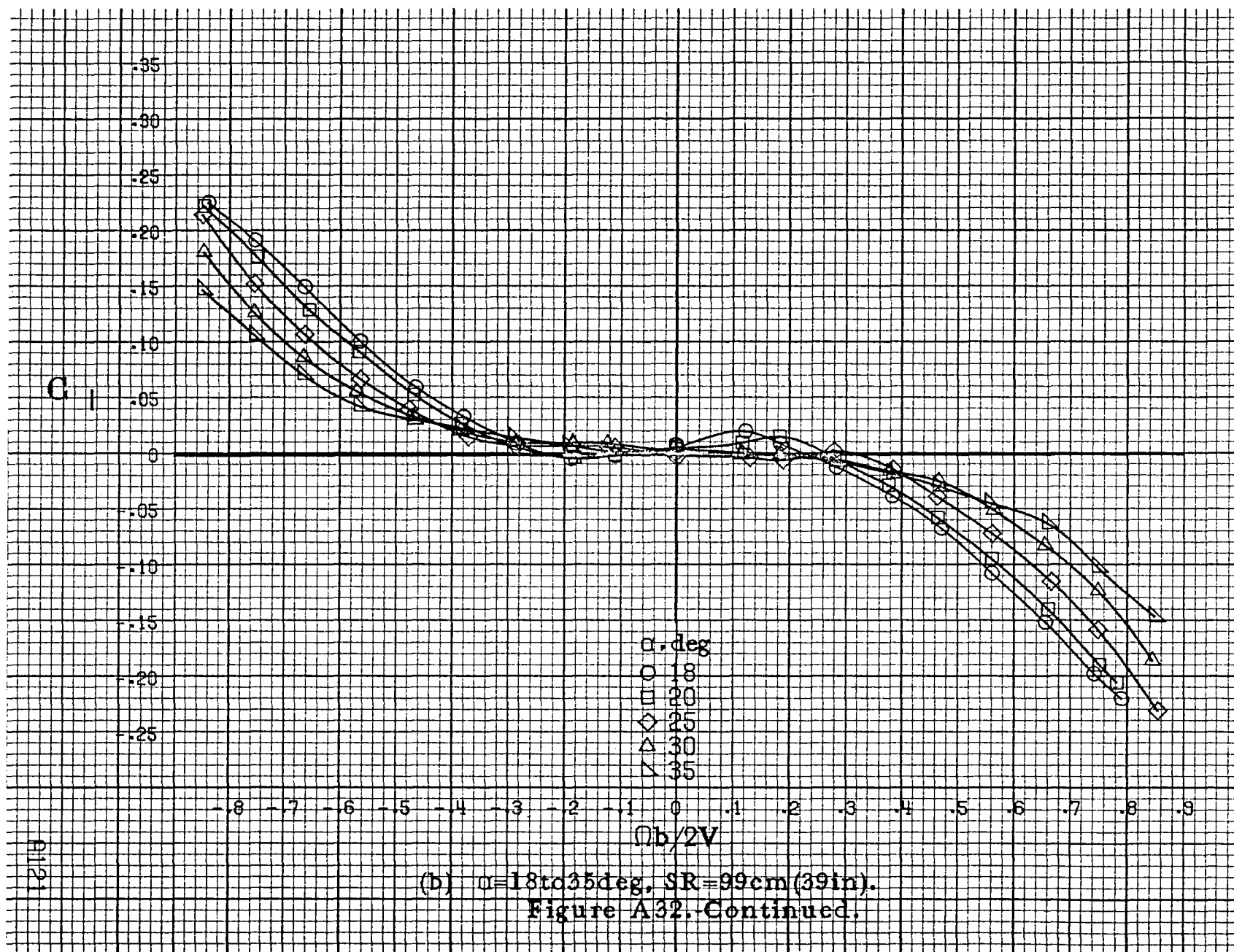
(c)  $\alpha=30$  to  $50$  deg.  $SR=0$ .  
Figure A31, Continued.

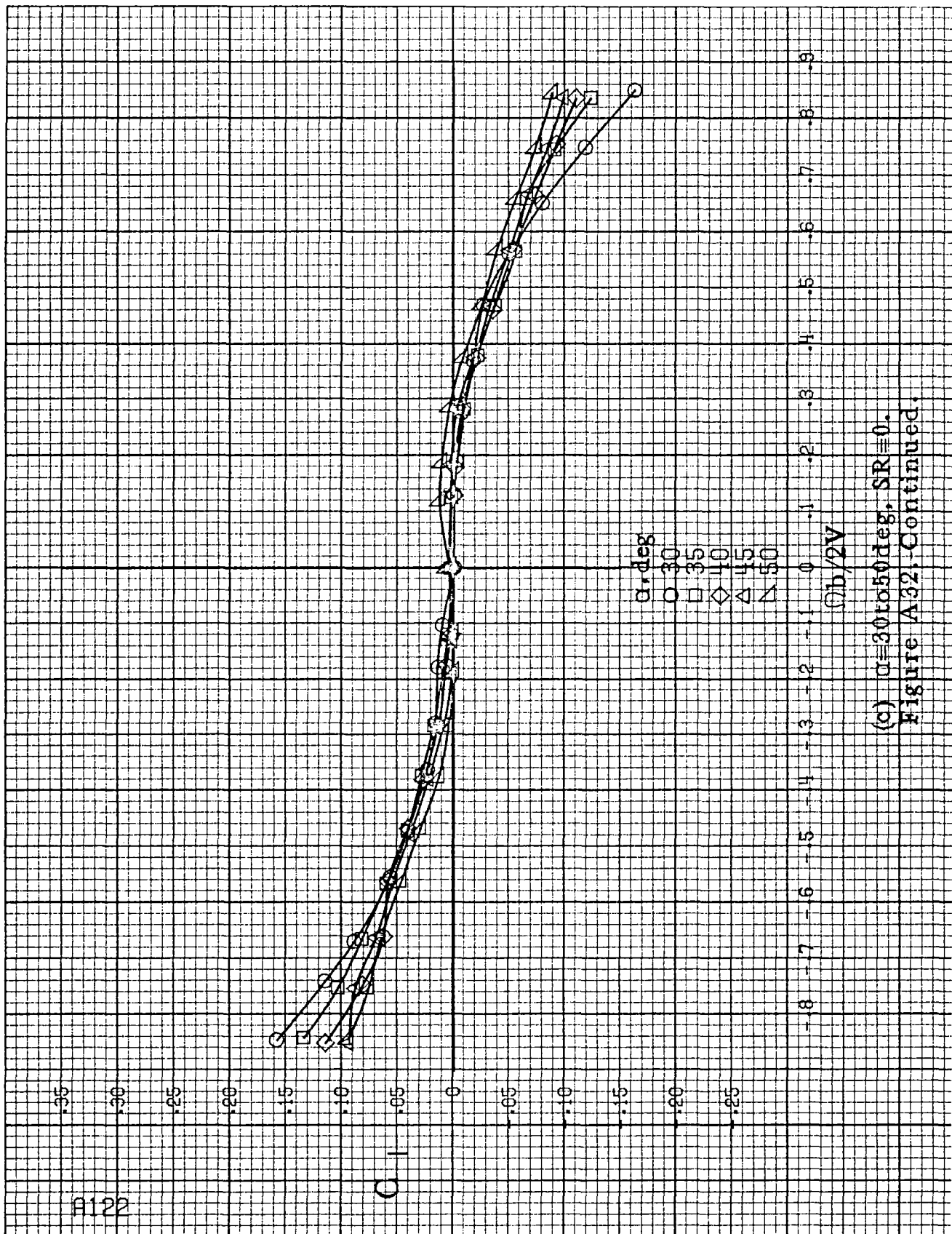




(a)  $\alpha=8$  to  $16$  deg,  $SR=99\text{cm}(39\text{in})$ .

Figure A32. Effect of rotation rate and angle of attack on rolling-moment coefficient for no. 2 horizontal tail configuration.  $\delta_e=0^\circ$ ,  $\delta_a=0^\circ$ ,  $\delta_r=0^\circ$ ,  $\beta=0^\circ$ .





C<sub>1</sub>

-0.14  
-0.12  
-0.10  
-0.08  
-0.06  
-0.04  
-0.02  
0  
-0.02  
-0.04  
-0.06  
-0.08  
-0.10

$\alpha$ , deg  
○ 55  
□ 60  
◇ 70  
△ 80  
▽ 90

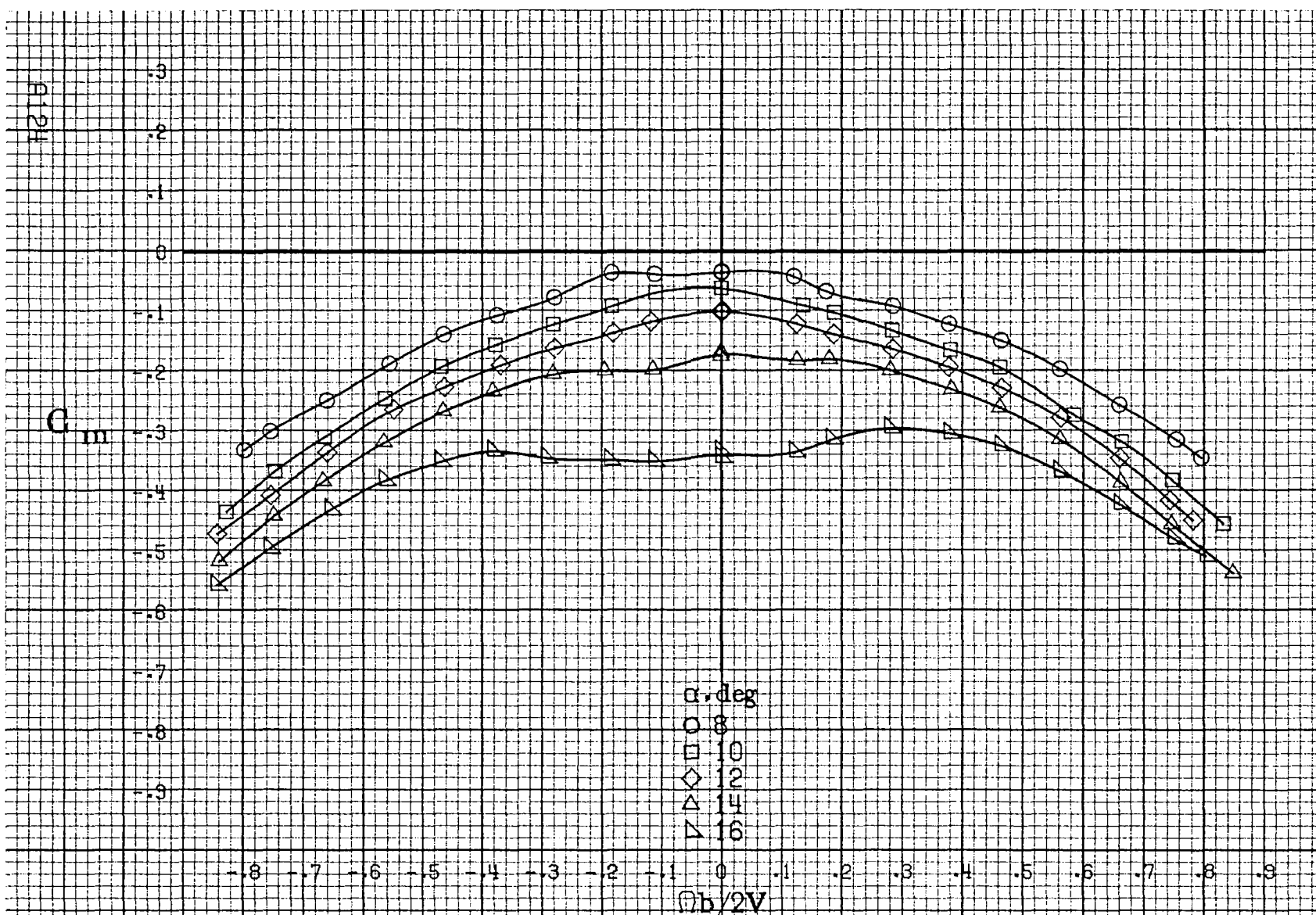
-0.8 -0.7 -0.6 -0.5 -0.4 -0.3 -0.2 -0.1 0 0.1 0.2 0.3 0.4 0.5 0.6 0.7 0.8 0.9

$\Omega b/2V$

(d)  $\alpha=55$  to  $90$  deg,  $SR=0$ .  
Figure A32. Concluded.

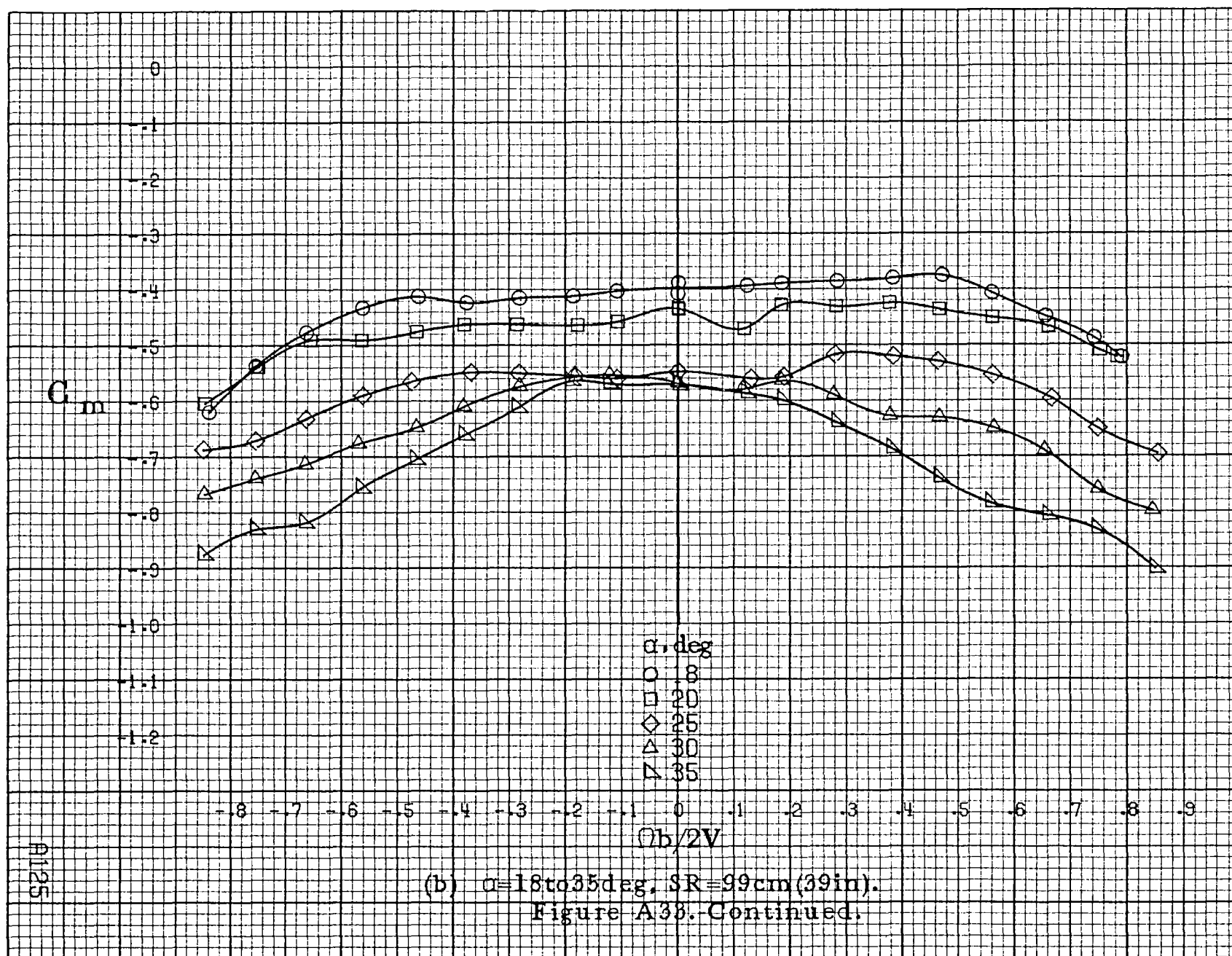
A123

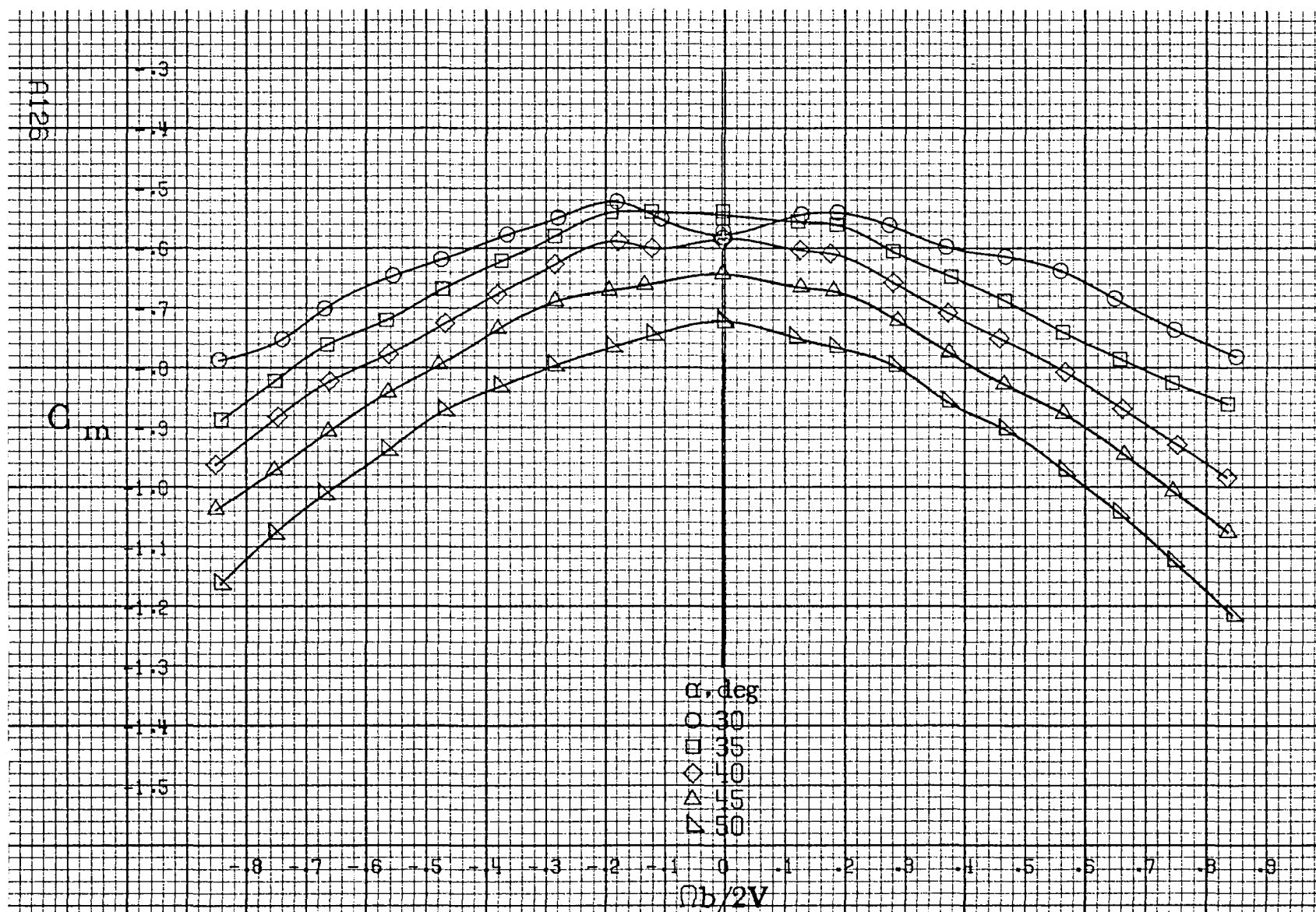




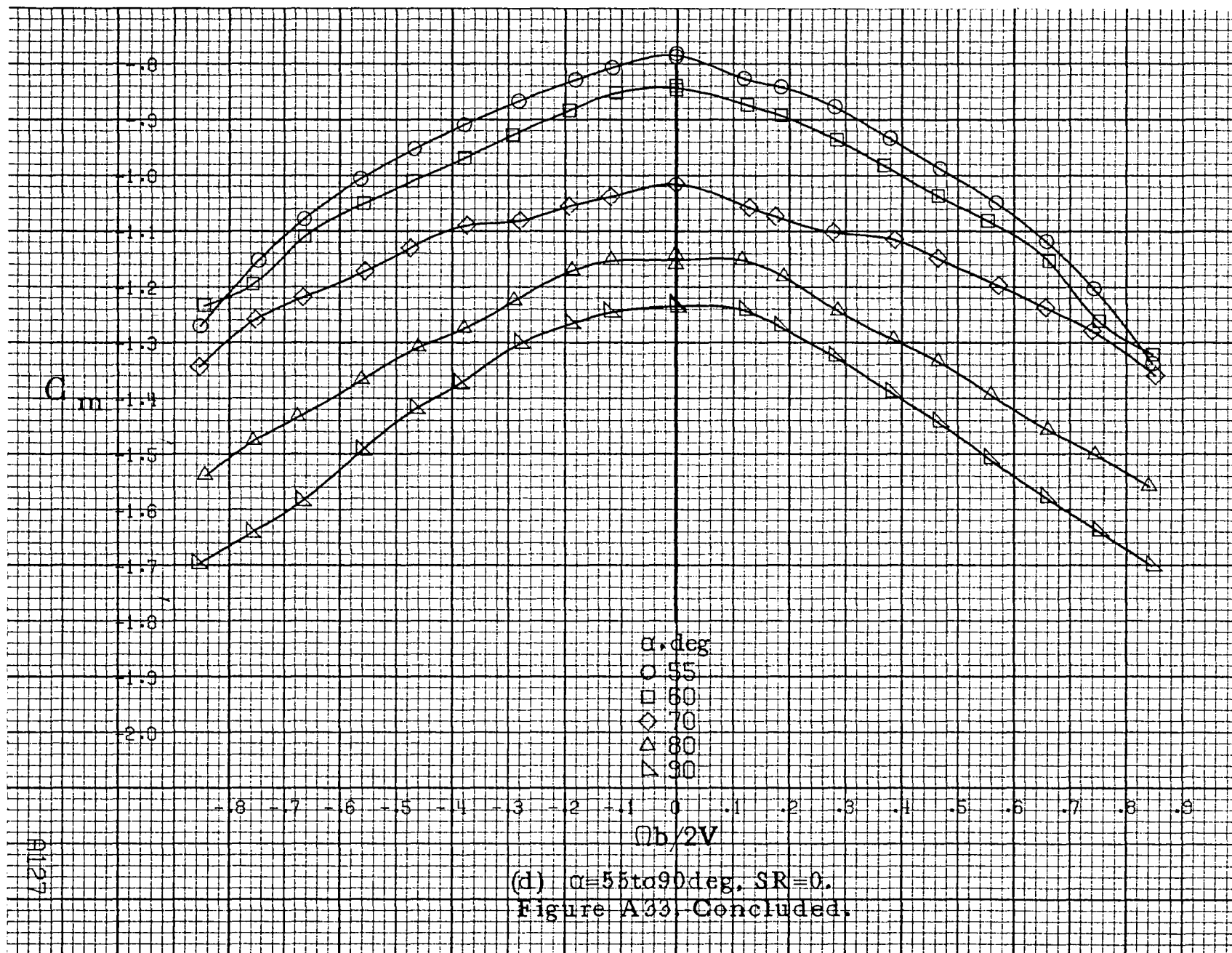
(a)  $\alpha = 8$  to  $16$  deg,  $SR = 99$  cm (39 in).

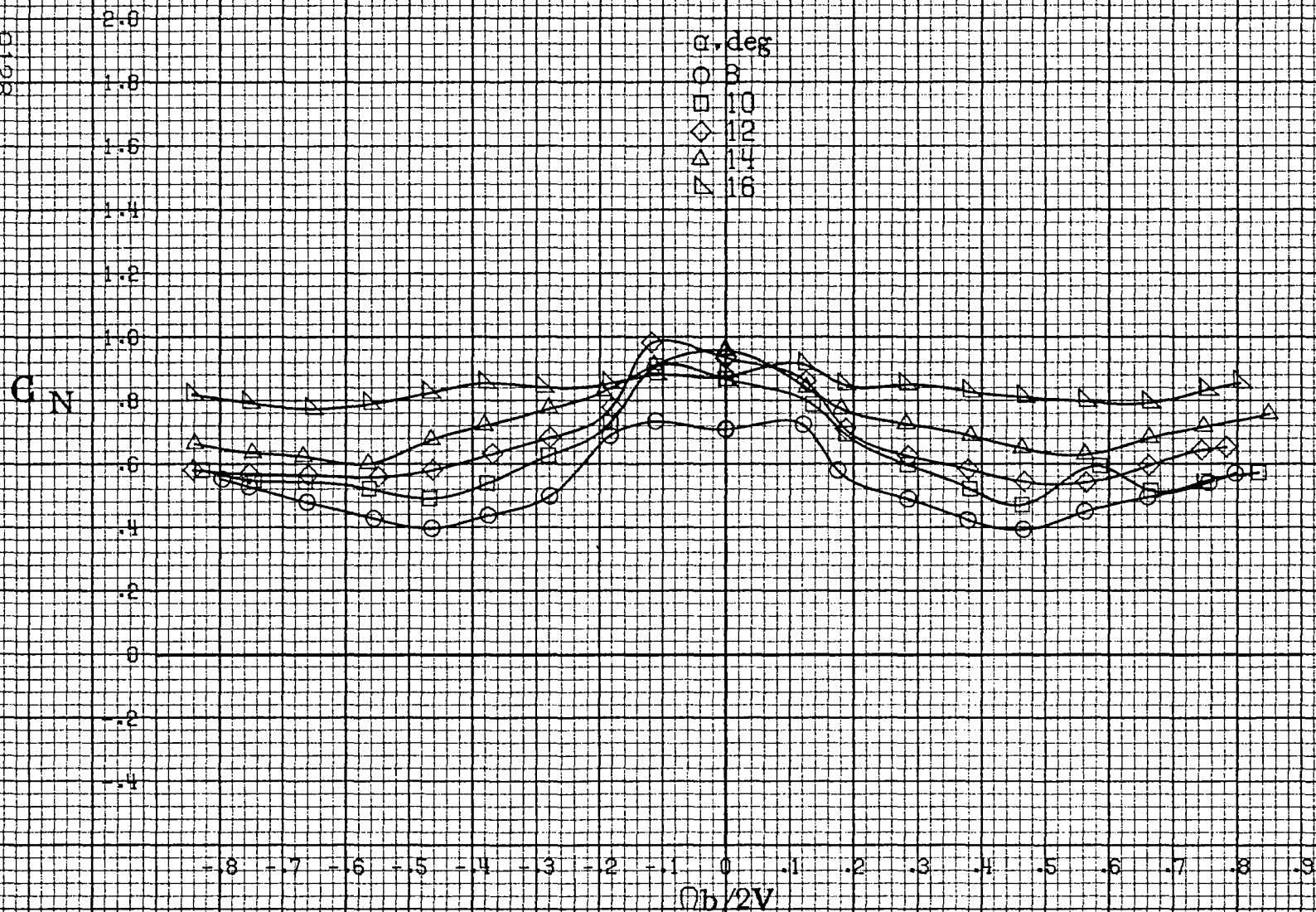
Figure A33.-Effect of rotation rate and angle of attack on pitching-moment coefficient for no. 2 horizontal tail configuration.  $\delta_e = 0^\circ$ ,  $\delta_a = 0^\circ$ ,  $\delta_r = 0^\circ$ ,  $\delta = 0^\circ$ .





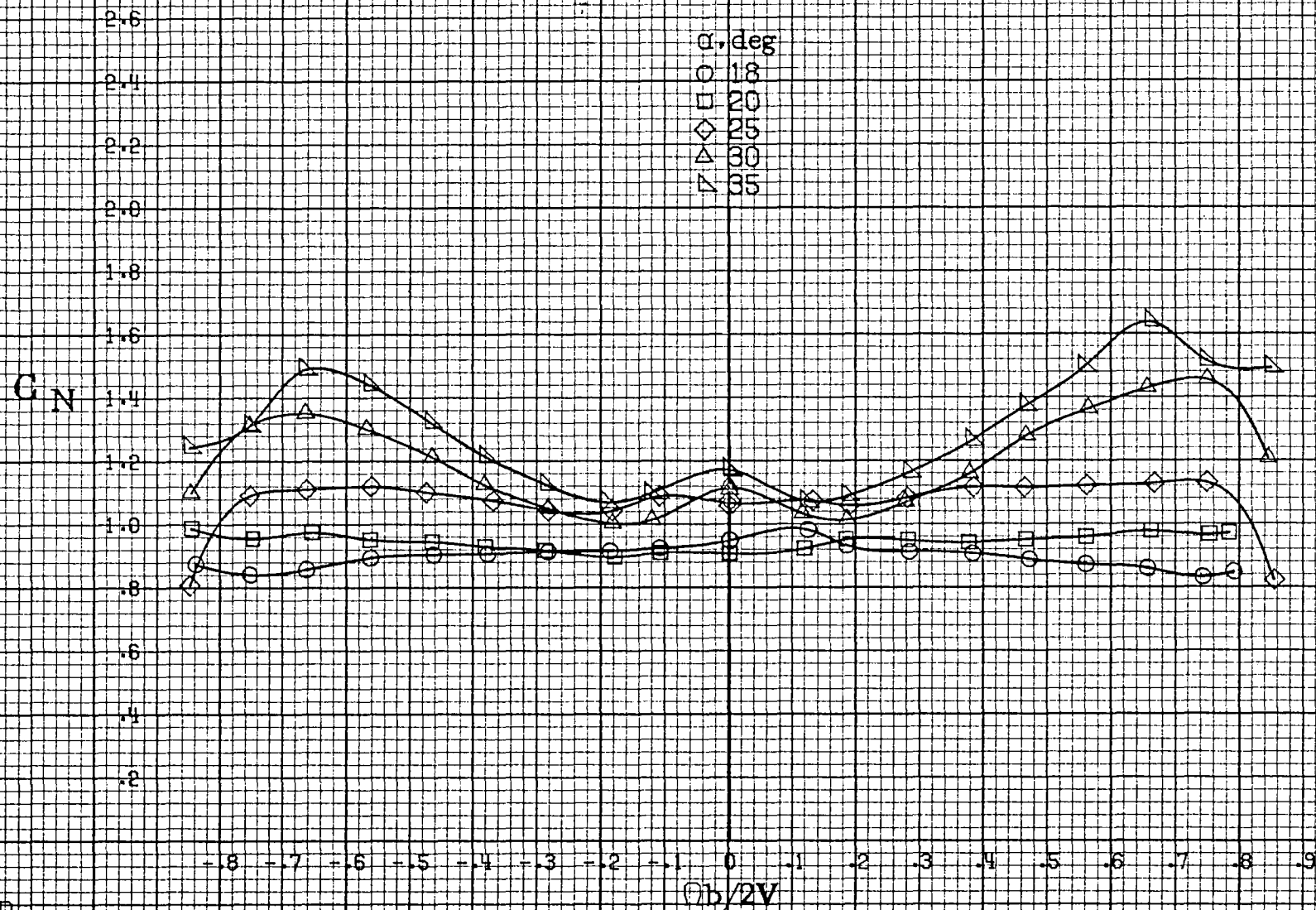
(c)  $\alpha=30$  to  $50^\circ$ ,  $SR=0$ .  
Figure A33. Continued.





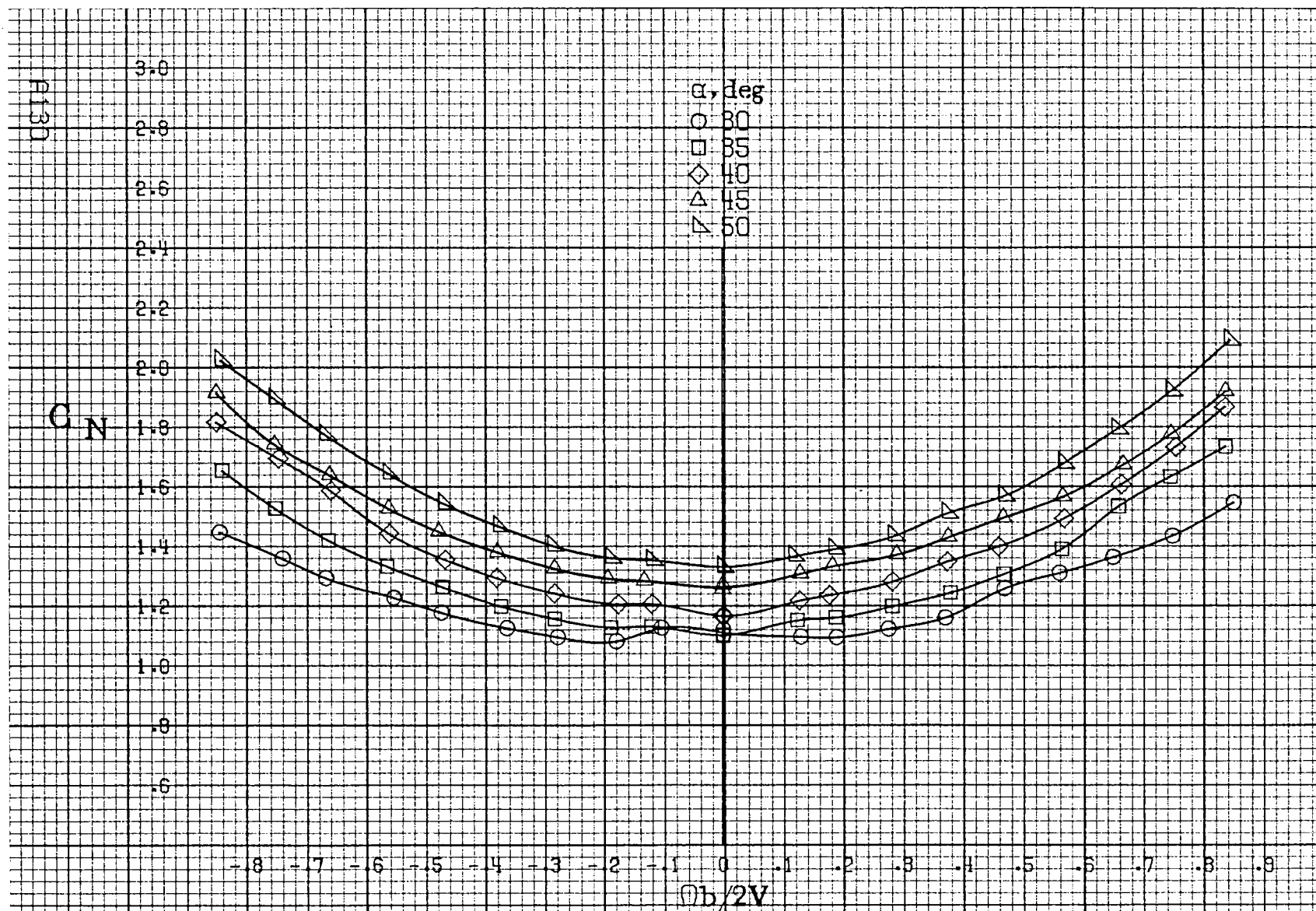
(a)  $\alpha = 8$  to  $16$  deg,  $SR = 99$  cm (39 in).

Figure A34. Effect of rotation rate and angle of attack on normal force coefficient for no. 2 horizontal tail configuration.  $\delta_e = 0^\circ$ ,  $\delta_a = 0^\circ$ ,  $\delta_r = 0^\circ$ ,  $\beta = 0^\circ$ .



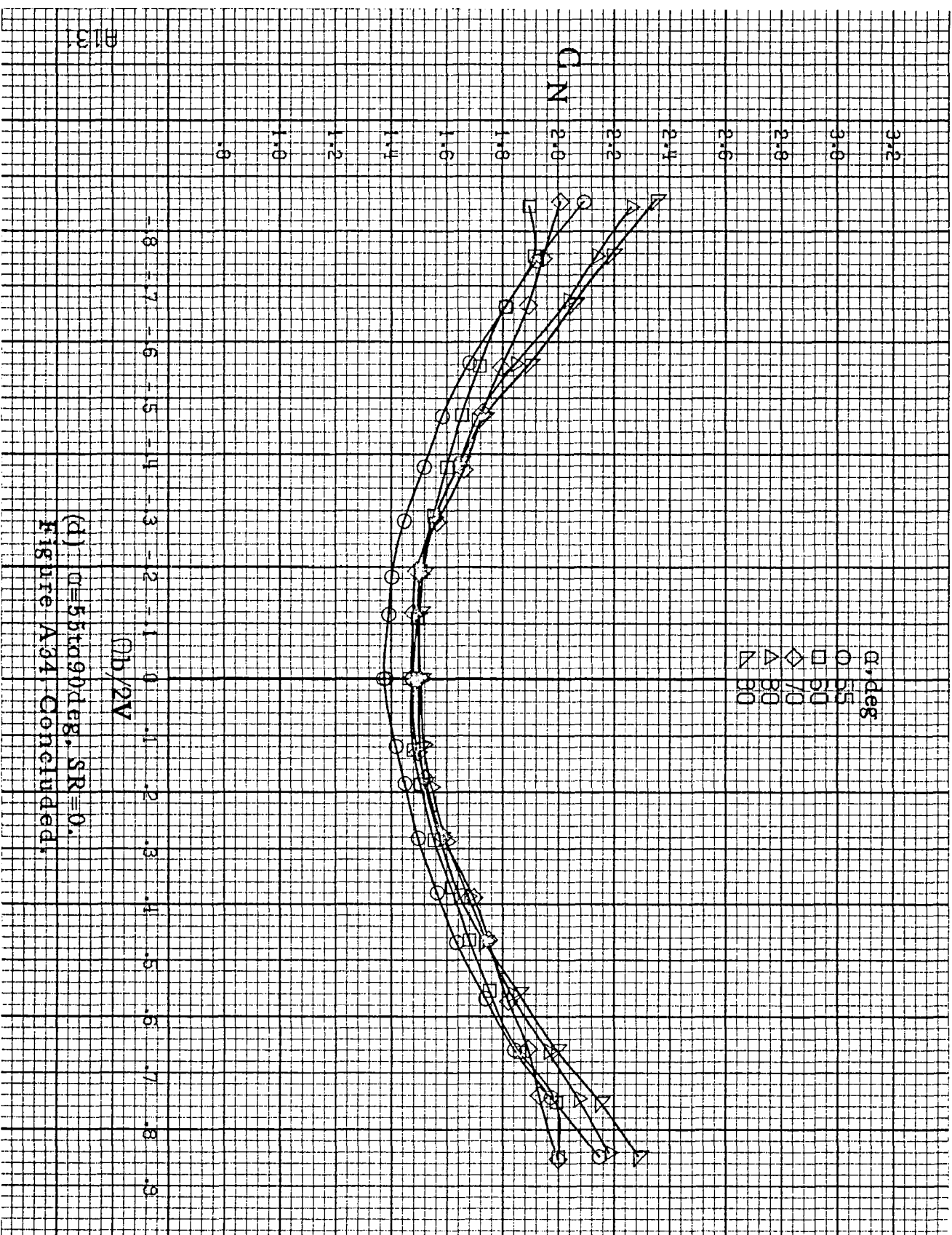
(b)  $\alpha=18$  to  $35$  deg,  $SR=99$  cm (39 in).  
Figure A34. Continued.



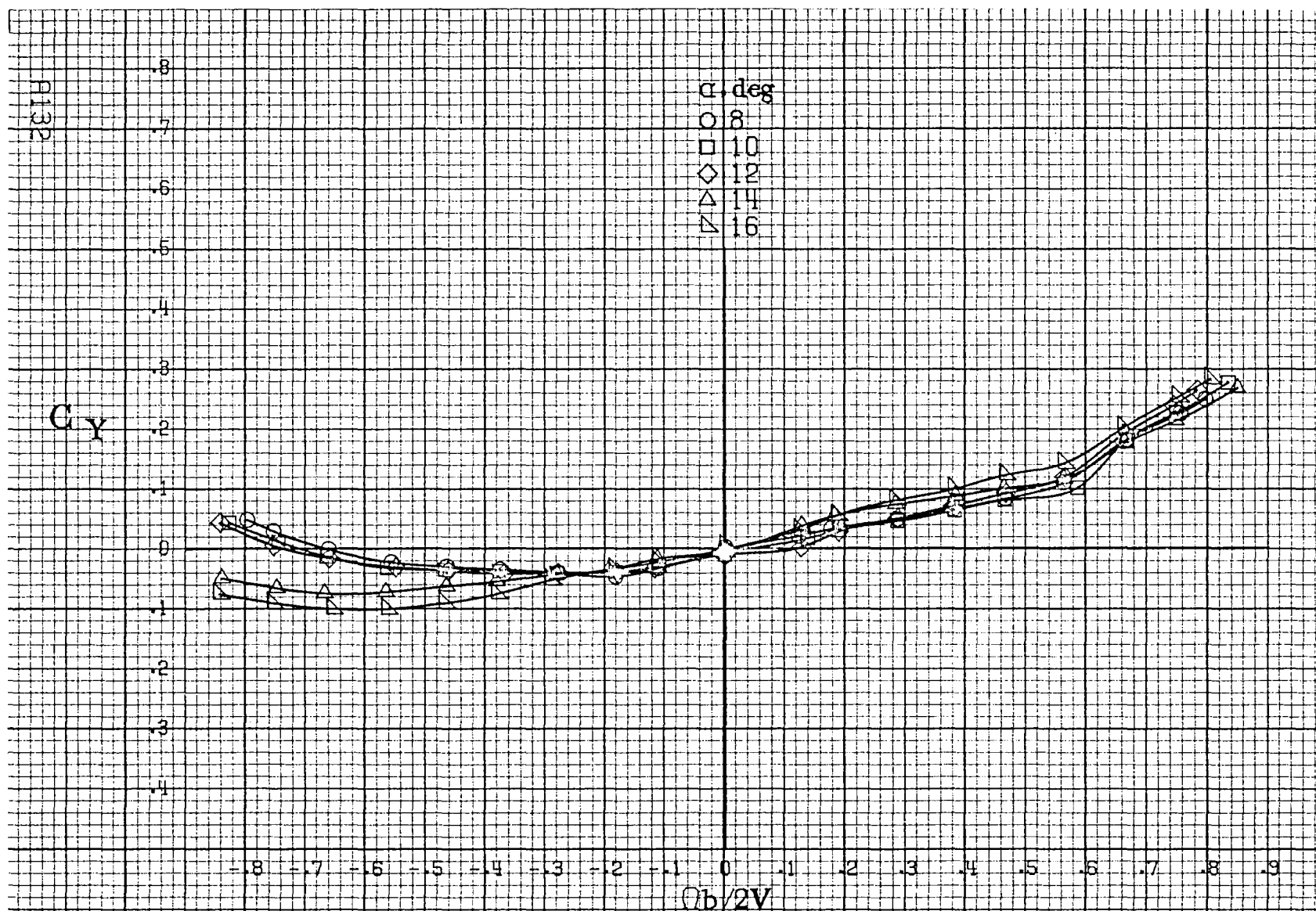


(c)  $\alpha = 30$  to  $50^\circ$ ,  $SR = 0$ .  
Figure A34-Continued.



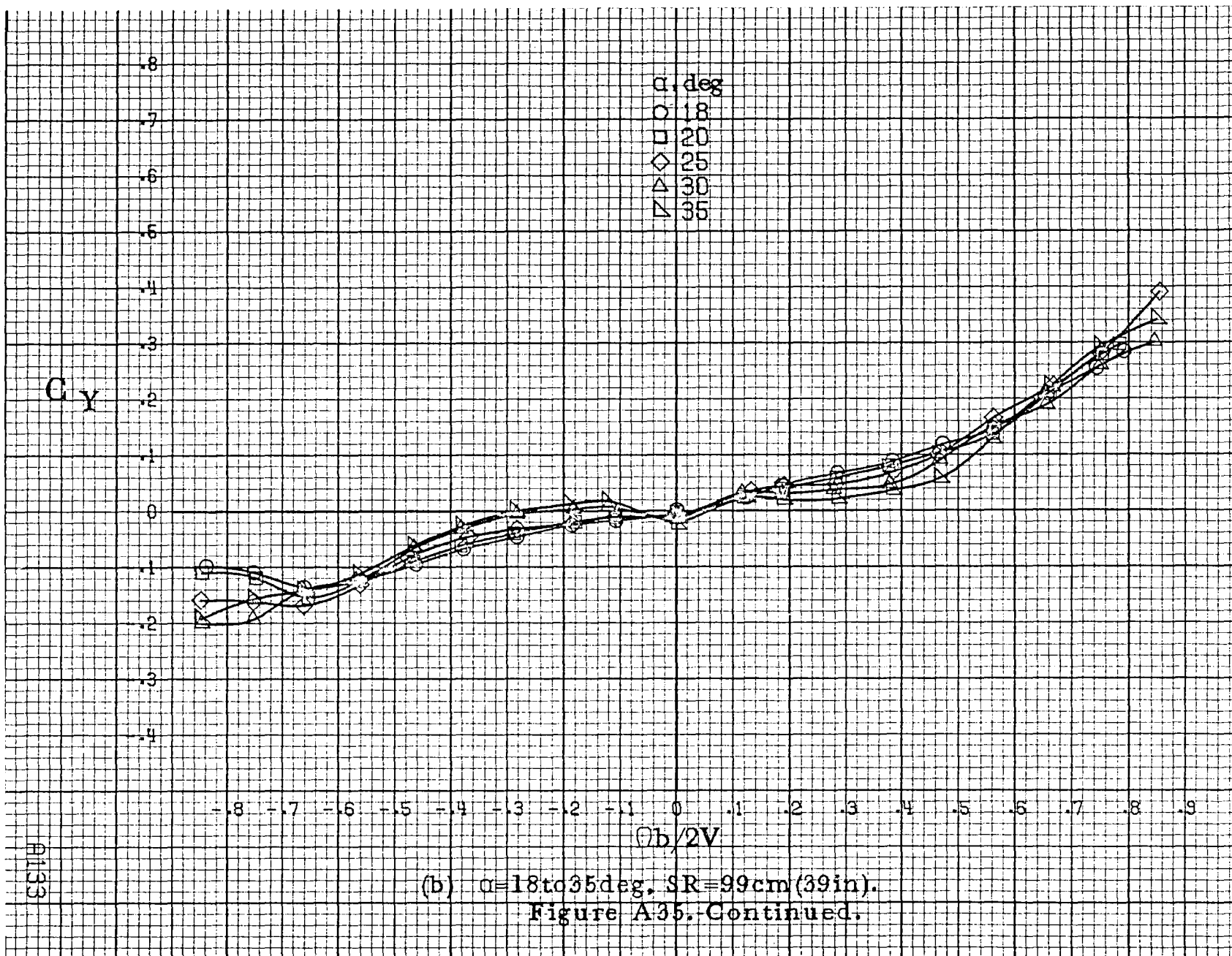


(d)  $\alpha=55$  to  $90$  deg.  $SR=0$ .  
Figure A34. Concluded.



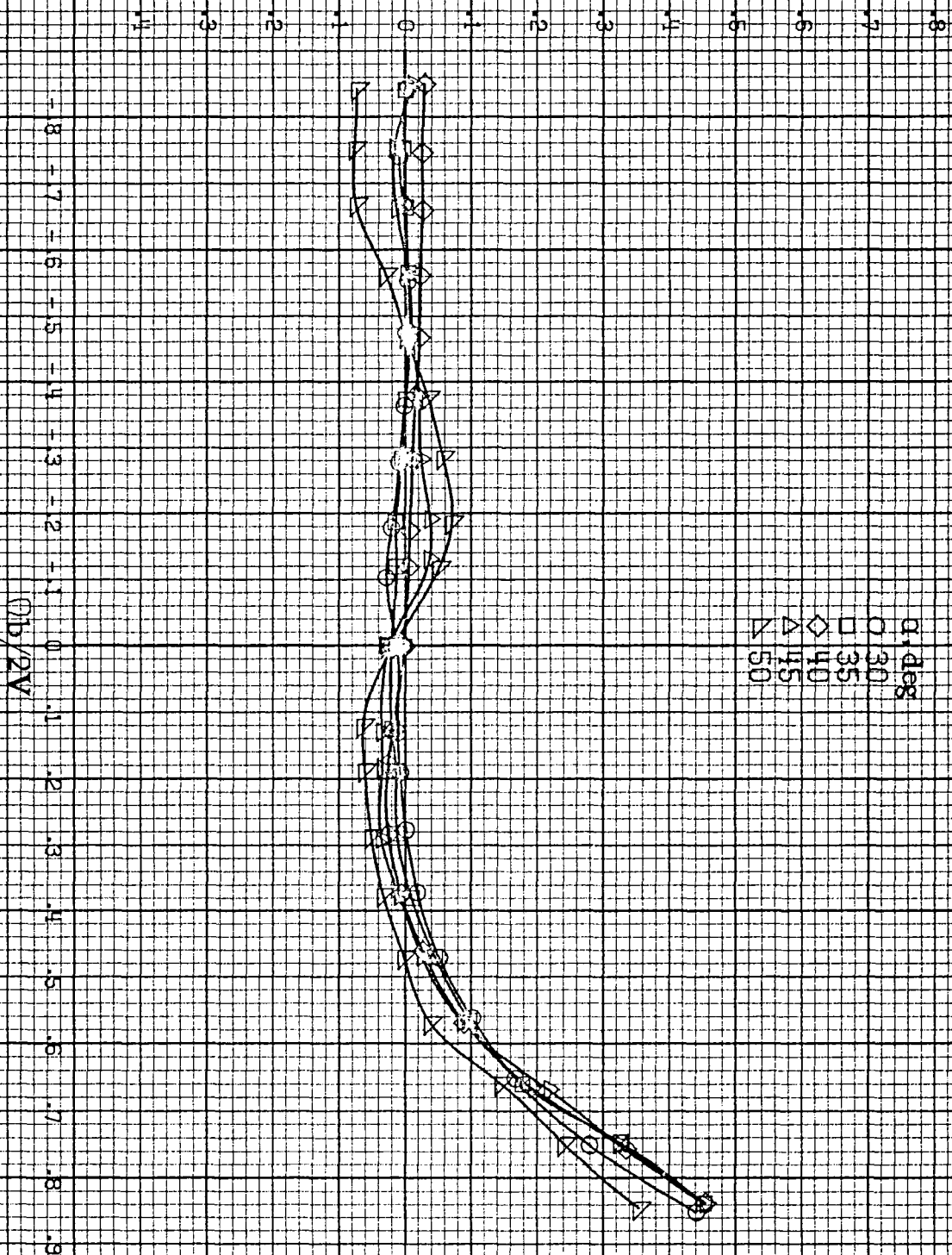
(a)  $\alpha = 8$  to  $16^\circ$ ,  $SR = 99 \text{ cm (39 in.)}$ .

Figure A35.-Effect of rotation rate and angle of attack on side-force coefficient for no. 2 horizontal tail configuration.  $\delta_a = 0^\circ$ ,  $\delta_e = 0^\circ$ ,  $\delta_r = 0^\circ$ ,  $\beta = 0^\circ$ .



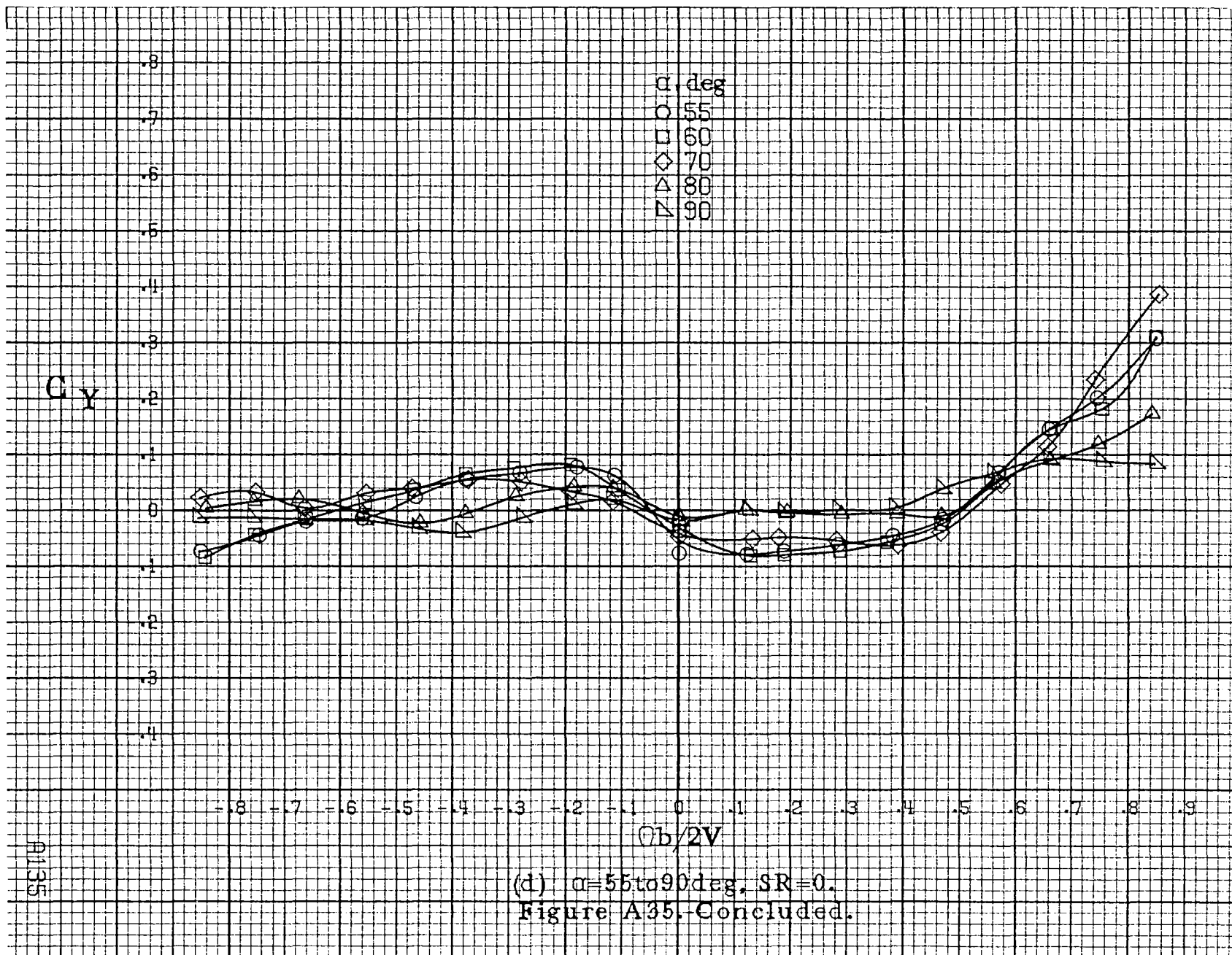
B134

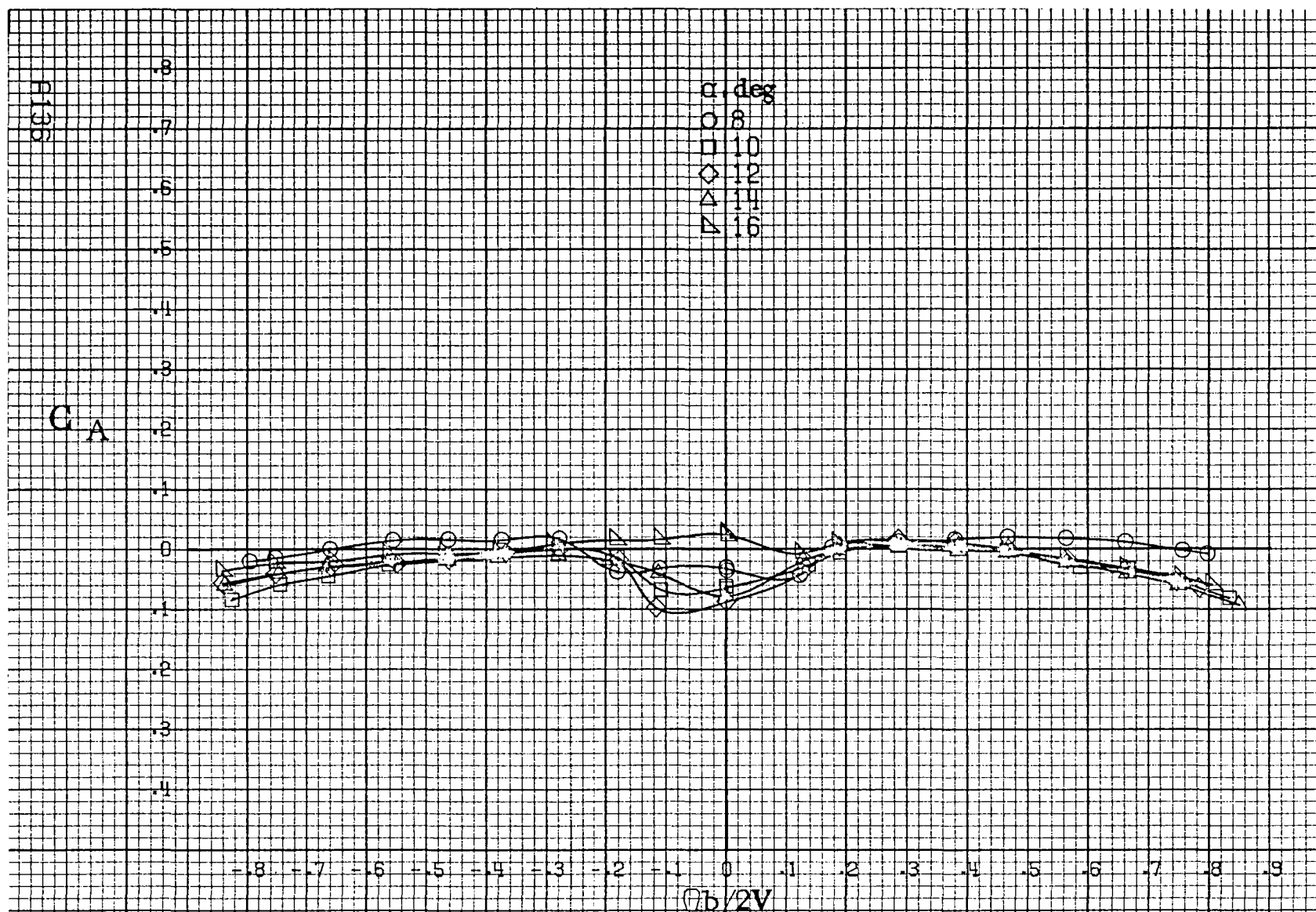
$C_Y$



$Ob/2V$

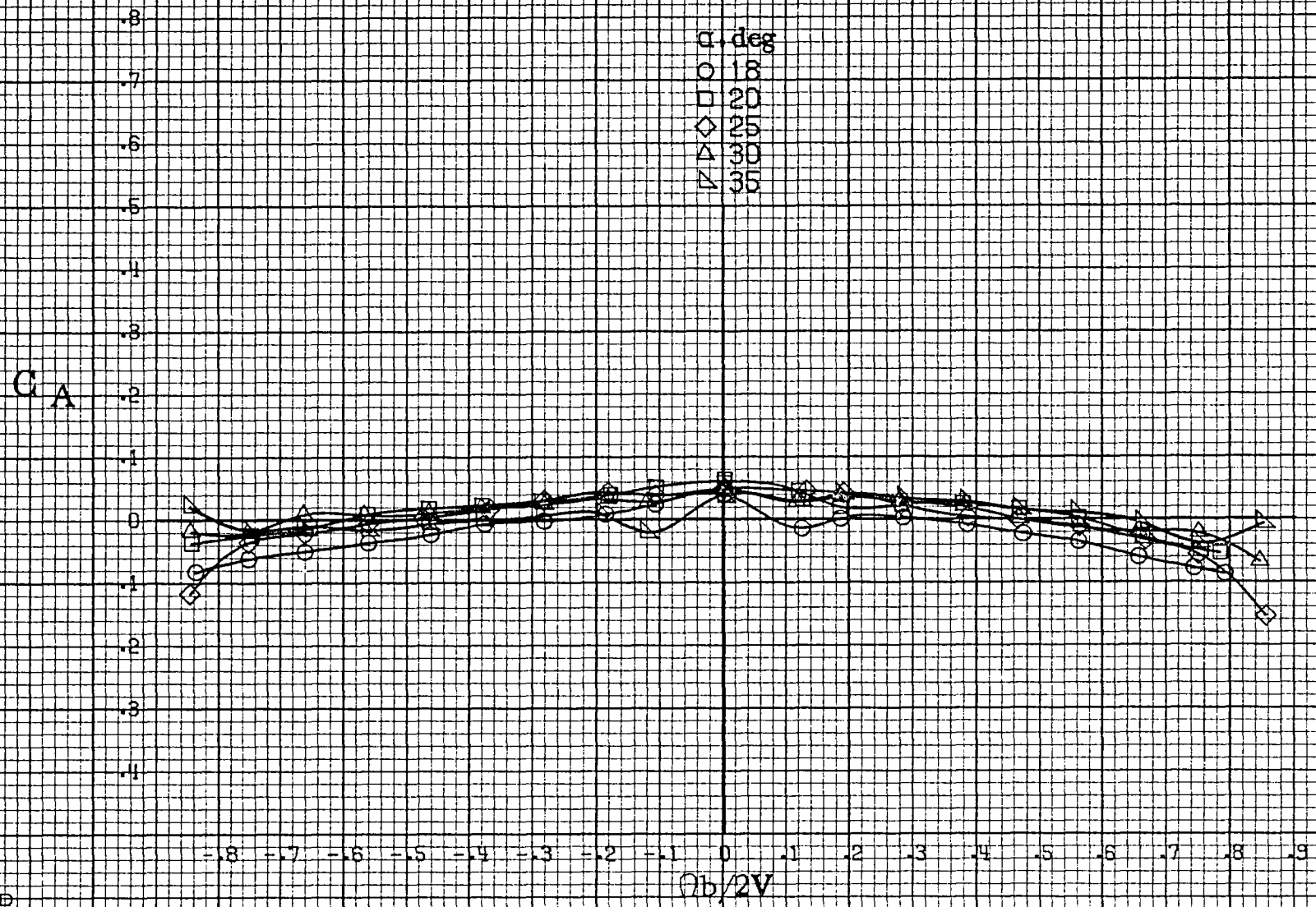
(c)  $\alpha=30$  to  $50$  deg,  $SR=0$ .  
Figure A35, Continued.





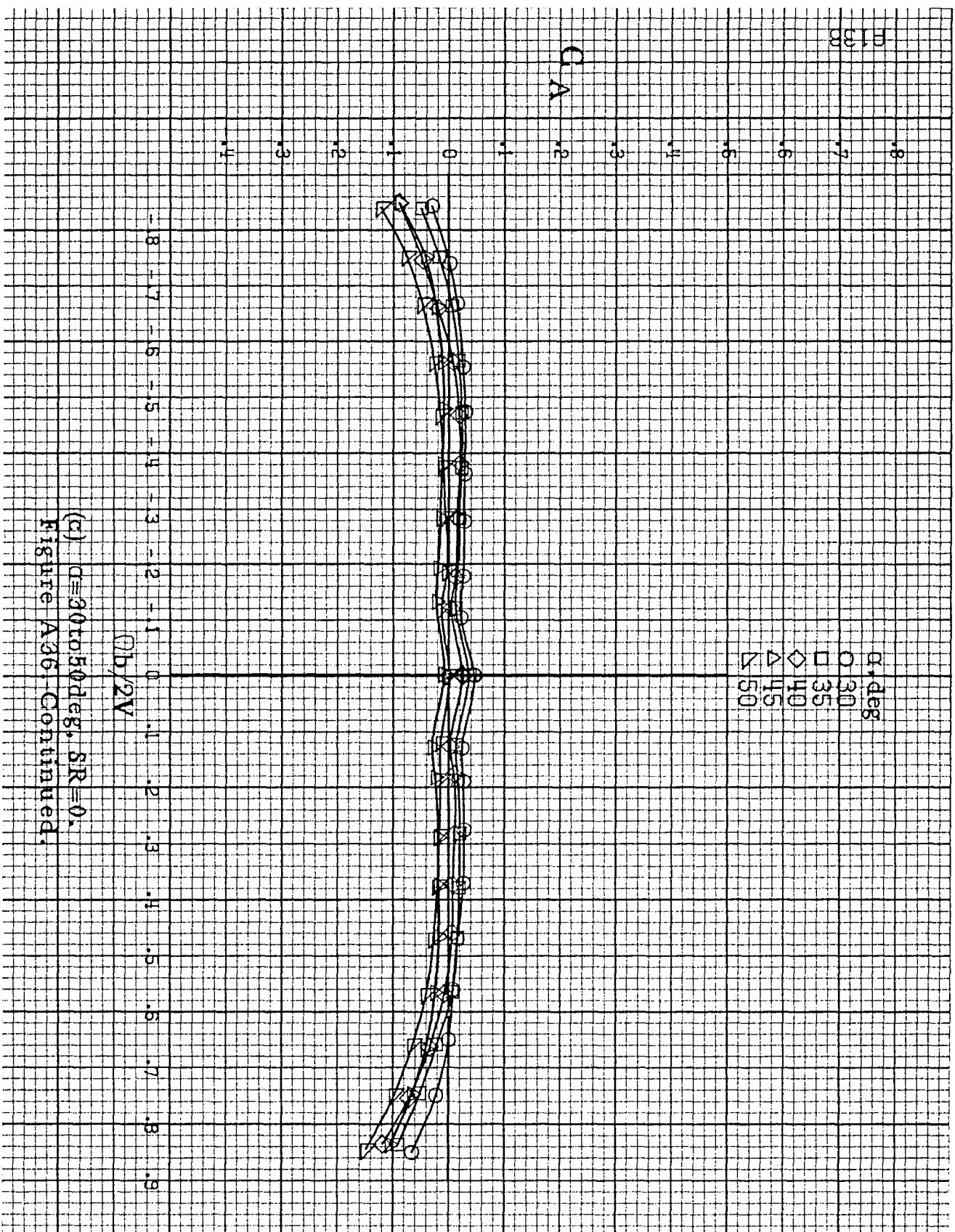
(a)  $\alpha = 8$  to  $16^\circ$ ,  $SR = 99 \text{ cm (39 in.)}$ .

Figure A36.-Effect of rotation rate and angle of attack on axial force coefficient for no. 2 horizontal tail configuration.  $\delta_a = 0^\circ$ ,  $\delta_z = 0^\circ$ ,  $\delta_r = 0^\circ$ ,  $\beta = 0^\circ$ .

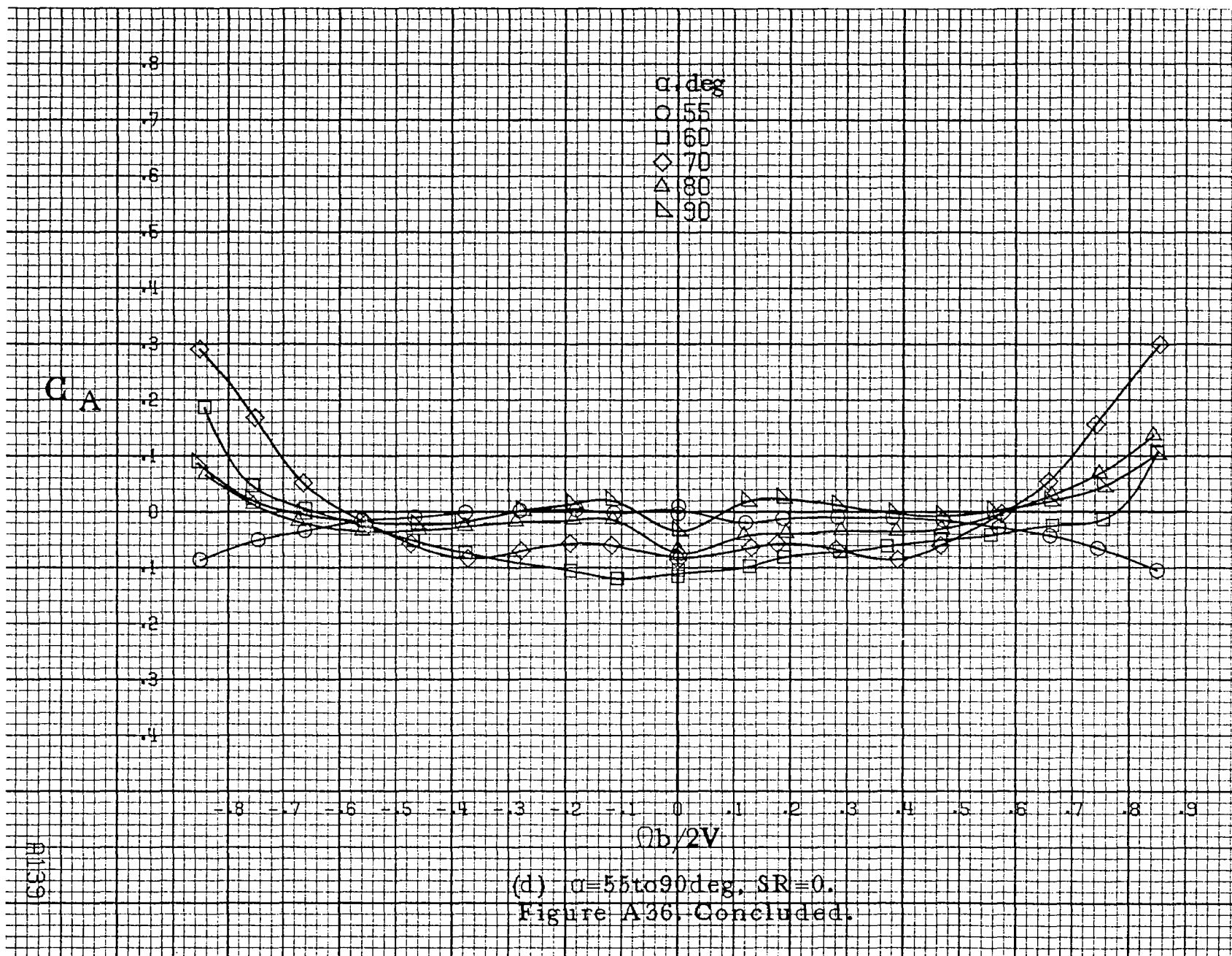


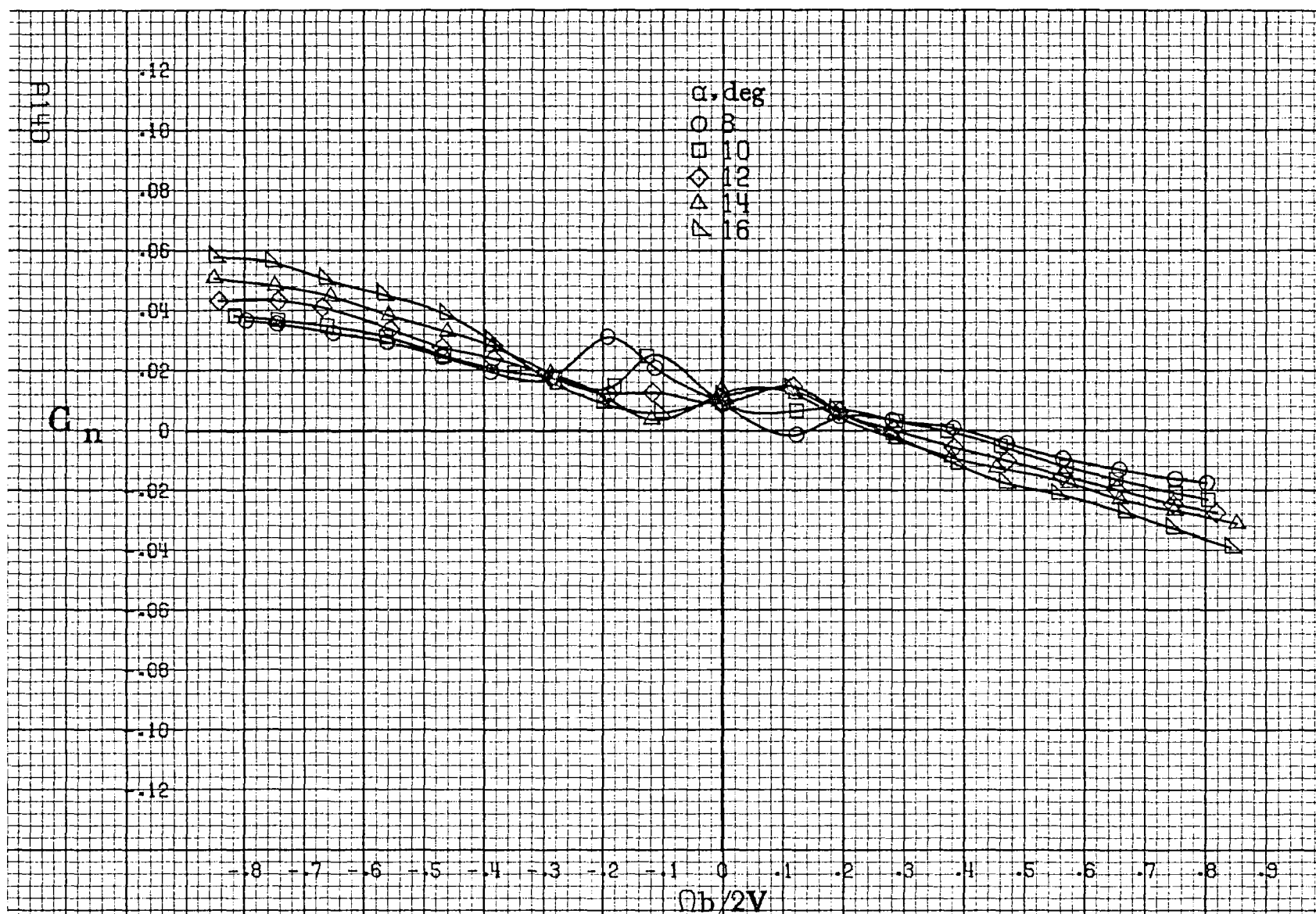
(b)  $\alpha=18$  to  $35^\circ$ ,  $SR=99\text{cm}(39\text{in})$ .  
Figure A36. Continued.





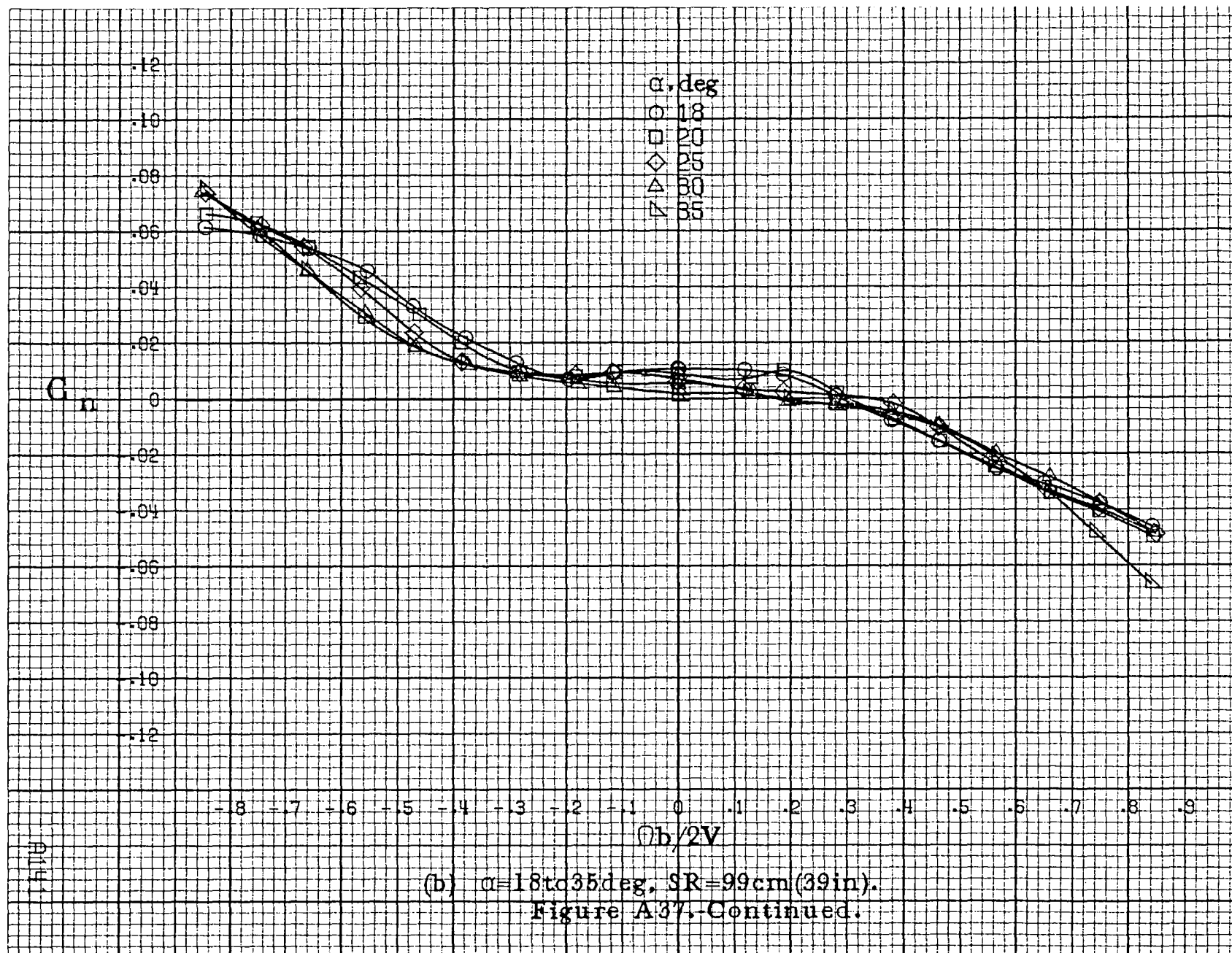
(c)  $\alpha=30$  to  $50$  deg,  $5R=0$ ,  
Figure A36, Continued.

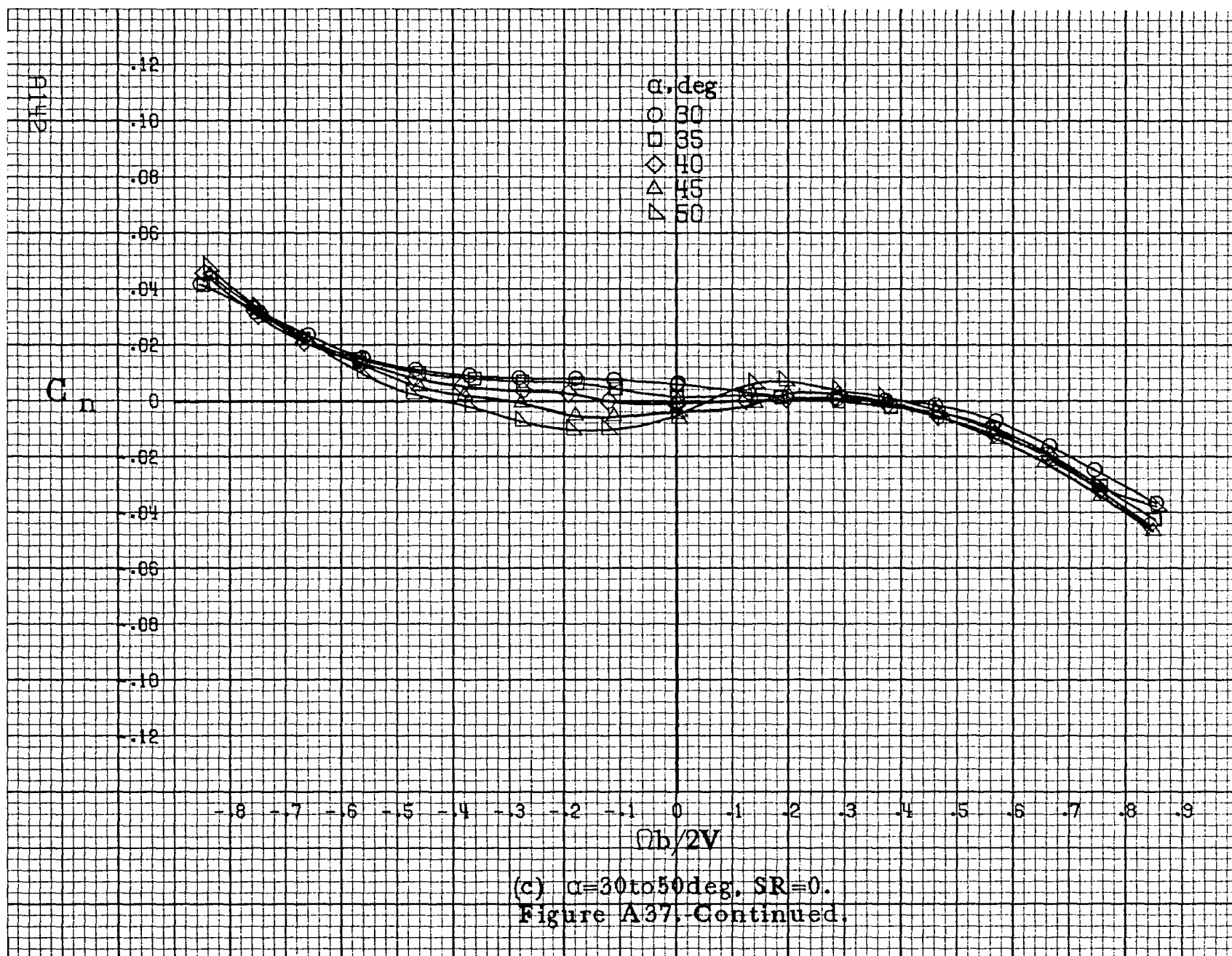


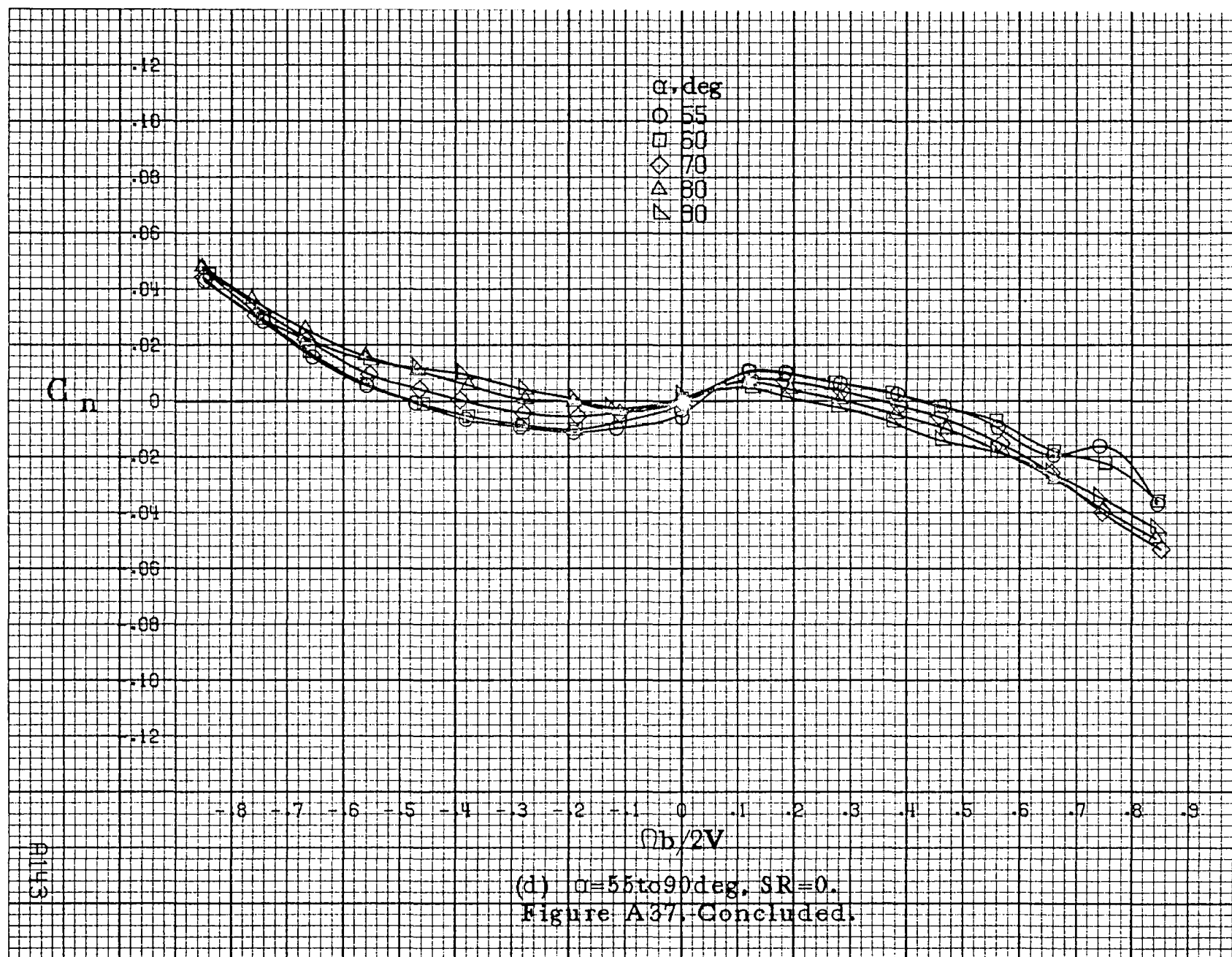


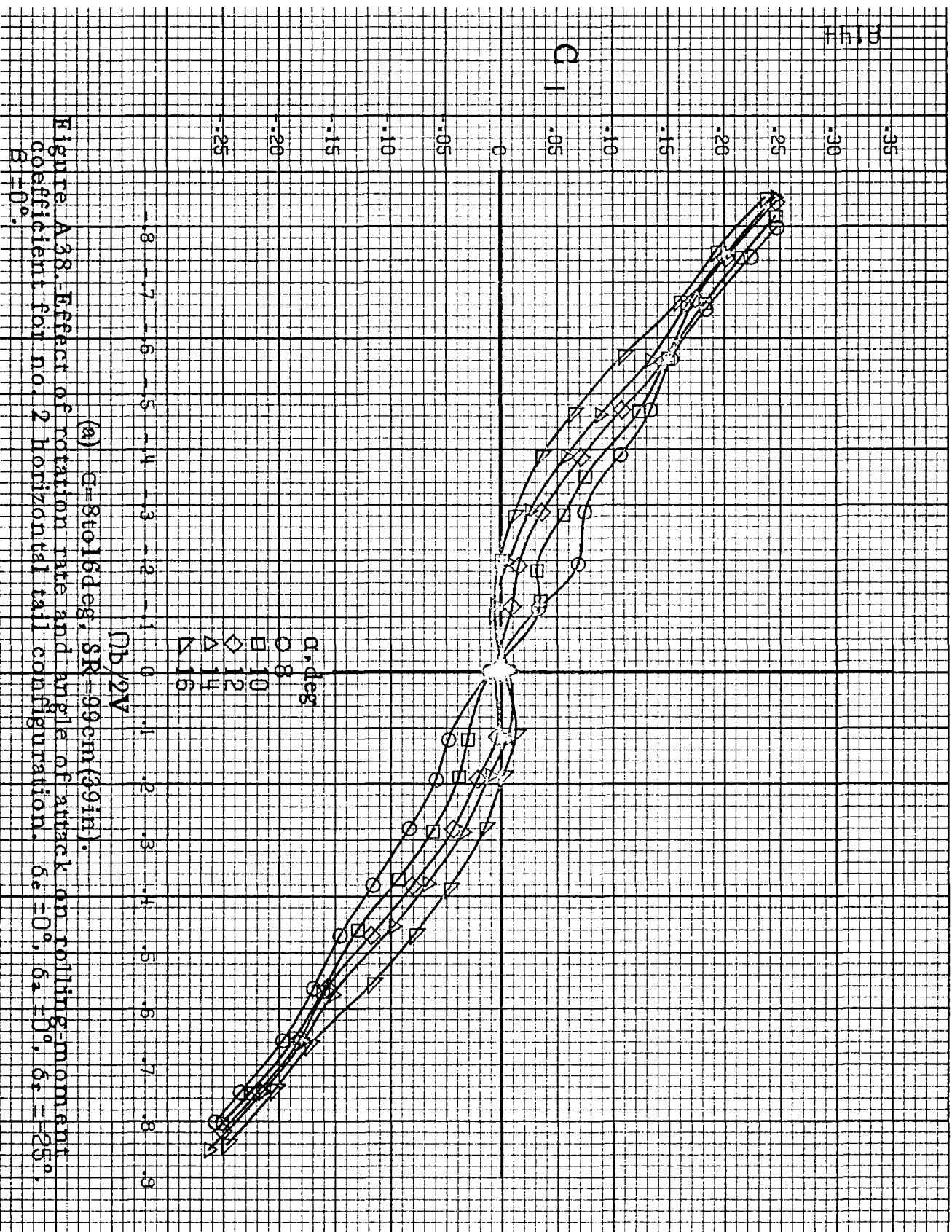
(a)  $\alpha=8$  to  $16^\circ$ ,  $SR=99\text{cm}(39\text{in})$ .

Figure A37.-Effect of rotation rate and angle of attack on yawing-moment coefficient for no. 2 horizontal tail configuration.  $\delta_e=0^\circ$ ,  $\delta_a=0^\circ$ ,  $\delta_r=-25^\circ$ ,  $\beta=0^\circ$ .





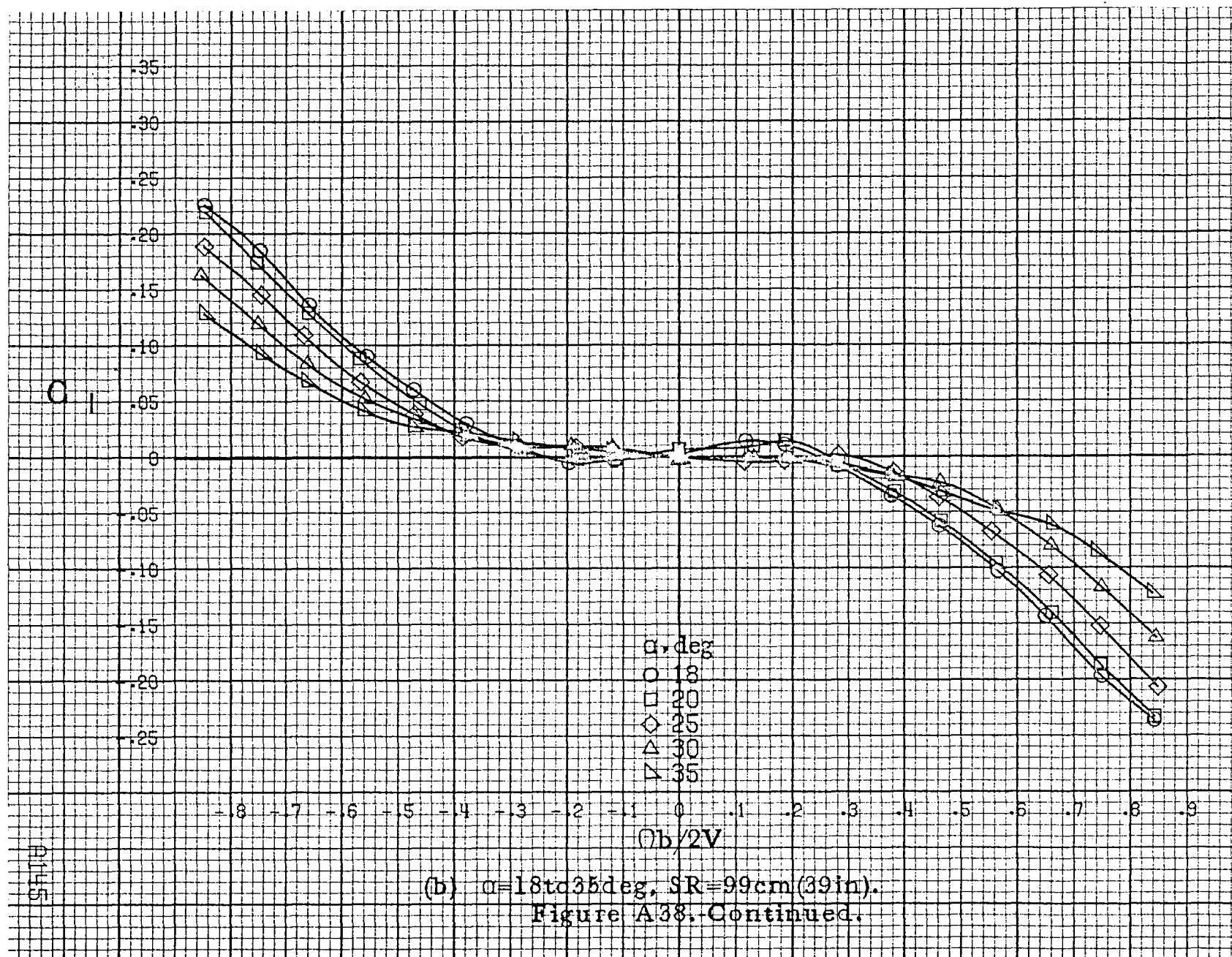


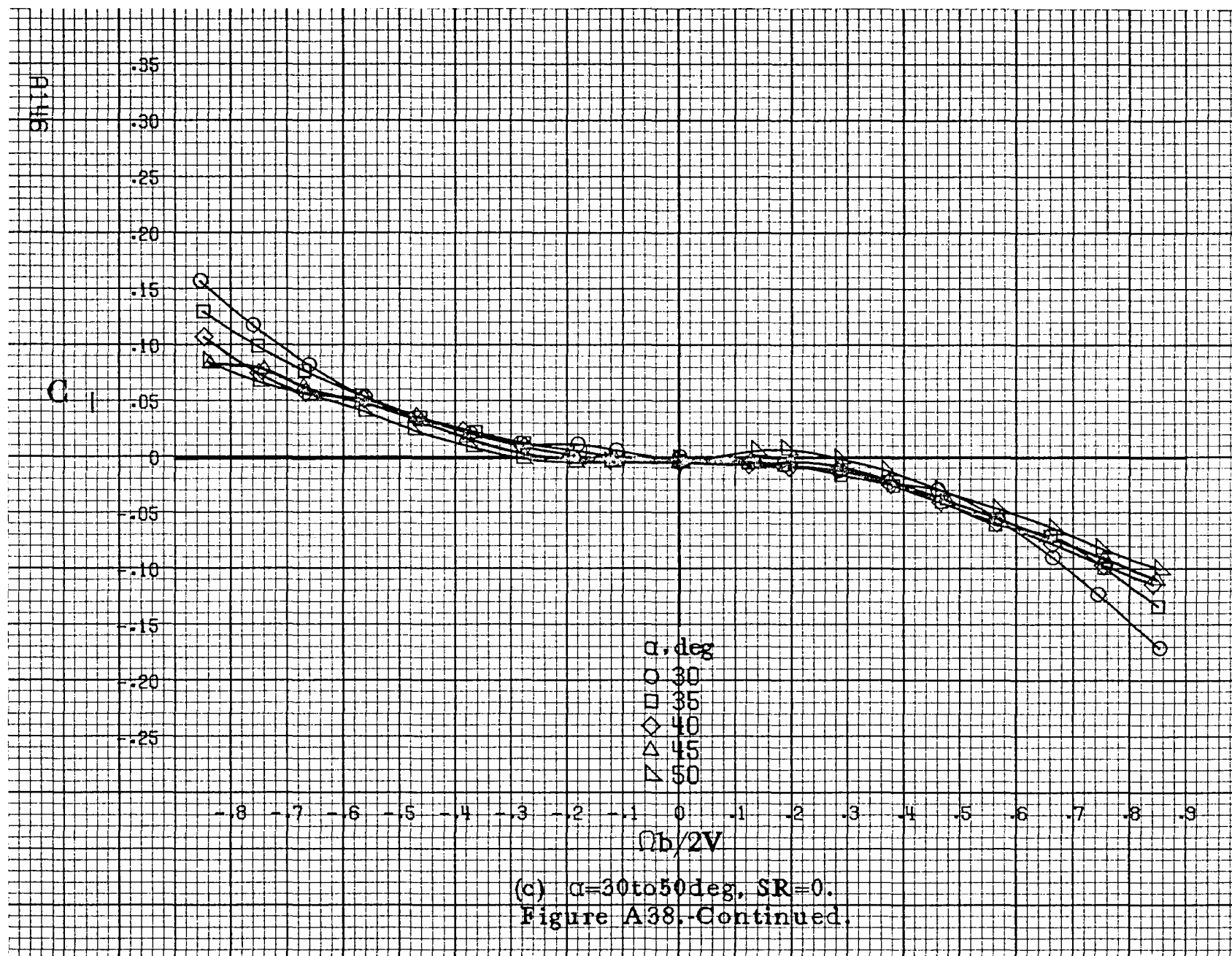


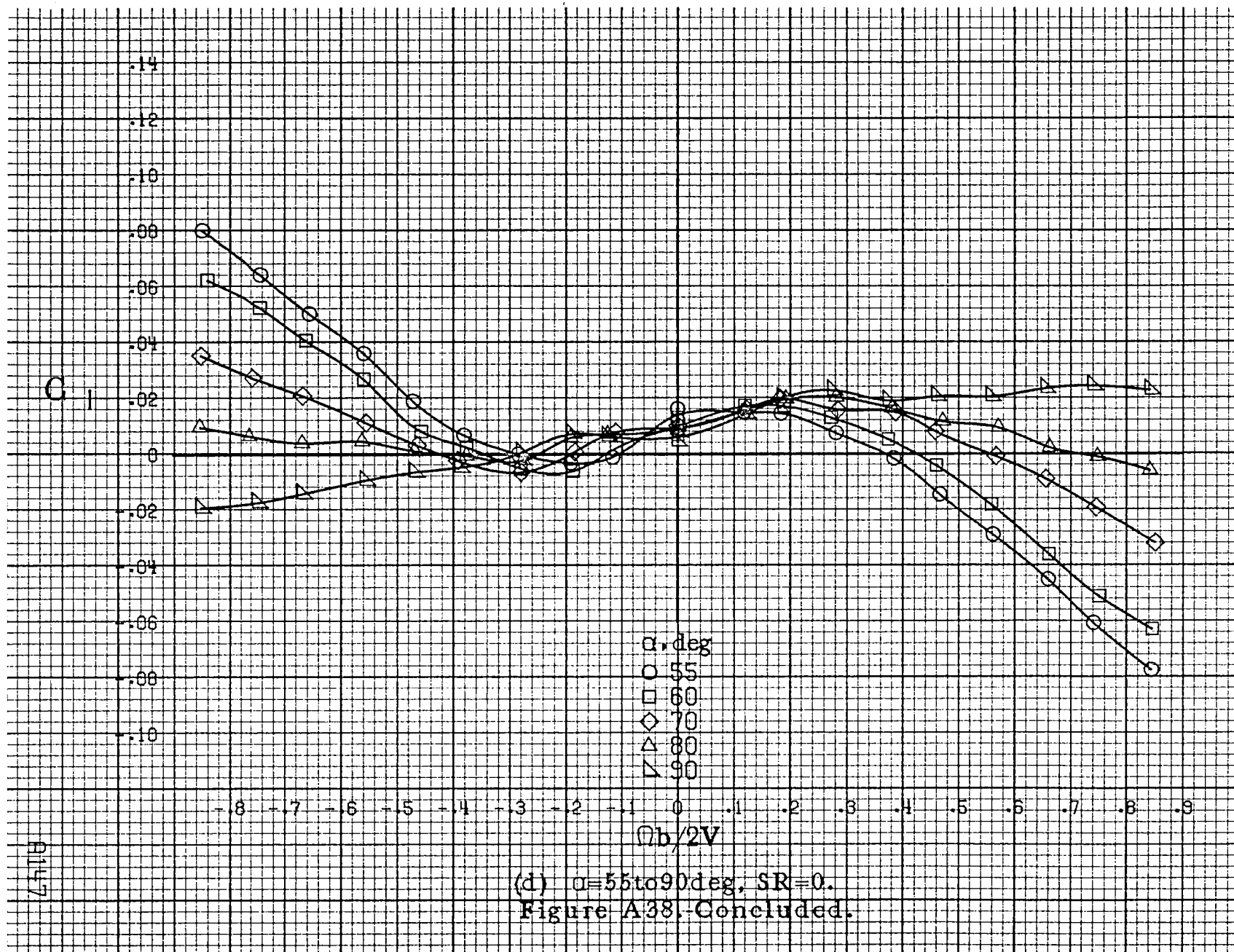
(a)  $G=8$  to  $16$  deg,  $SR=99$  cm (39 in).

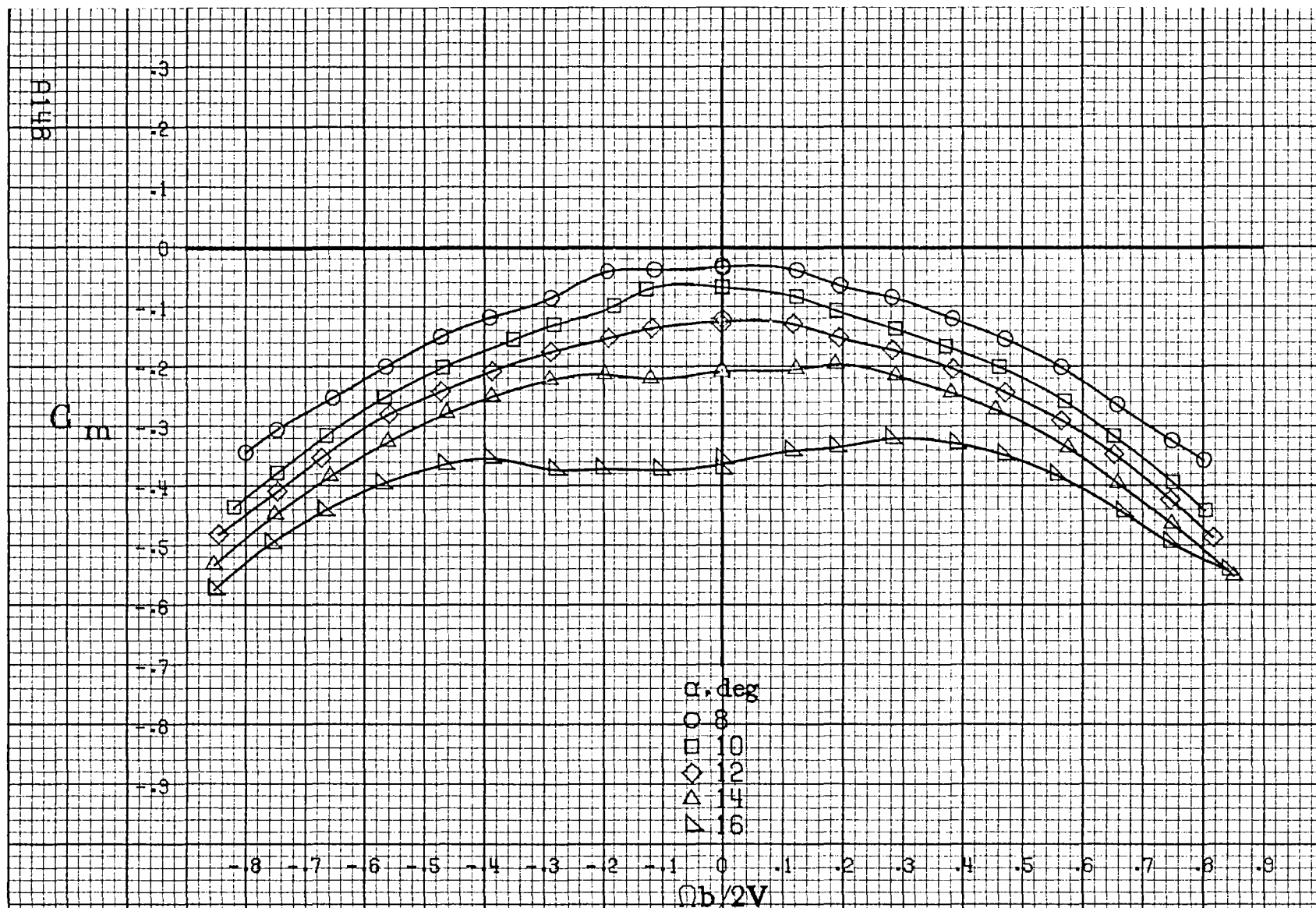
Figure A38.-Effect of rotation rate and angle of attack on rolling-moment coefficient for no. 2 horizontal tail configuration.  $\delta_e=0^\circ$ ,  $\delta_a=0^\circ$ ,  $\delta_r=25^\circ$ ,  $B=0^\circ$ .





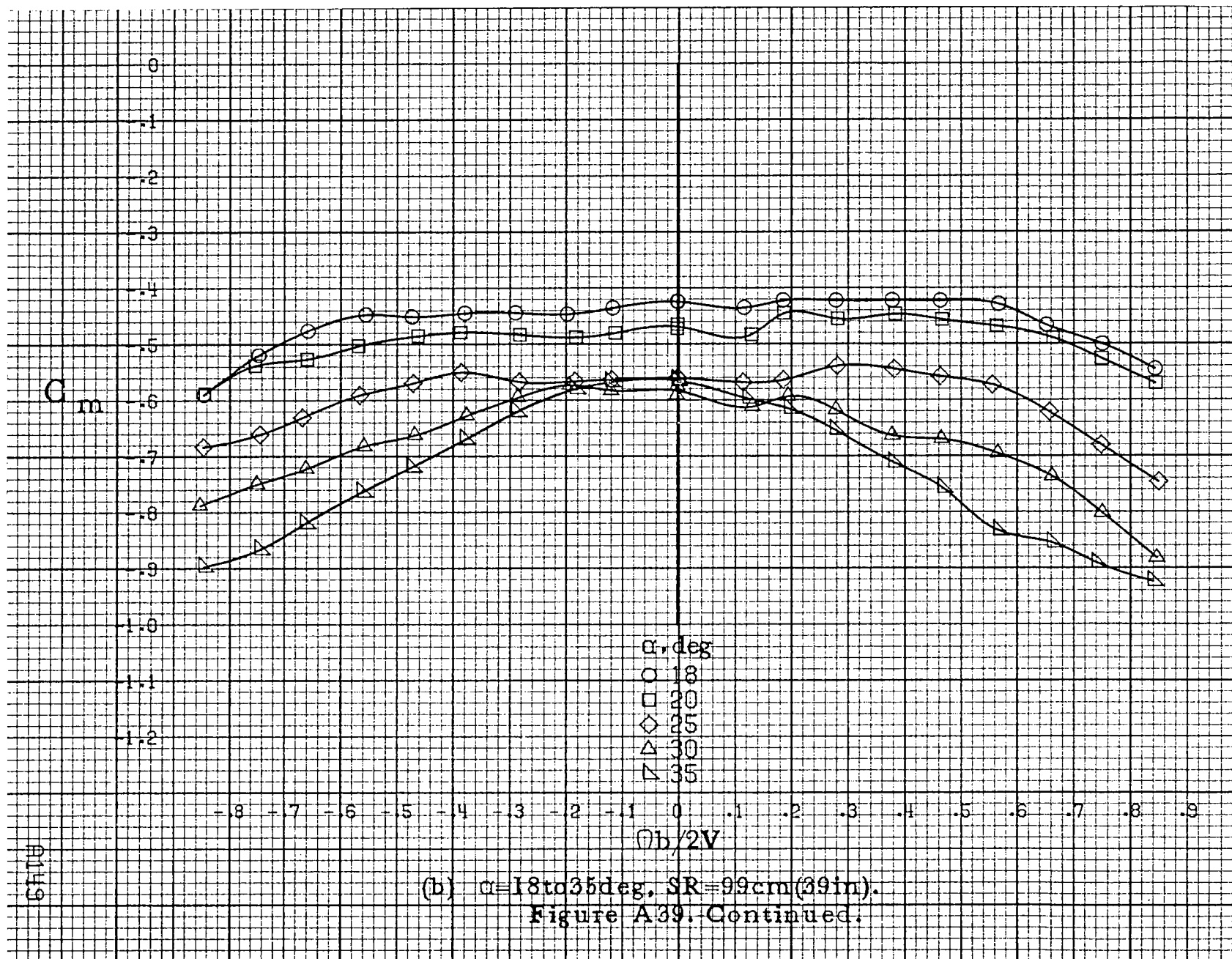


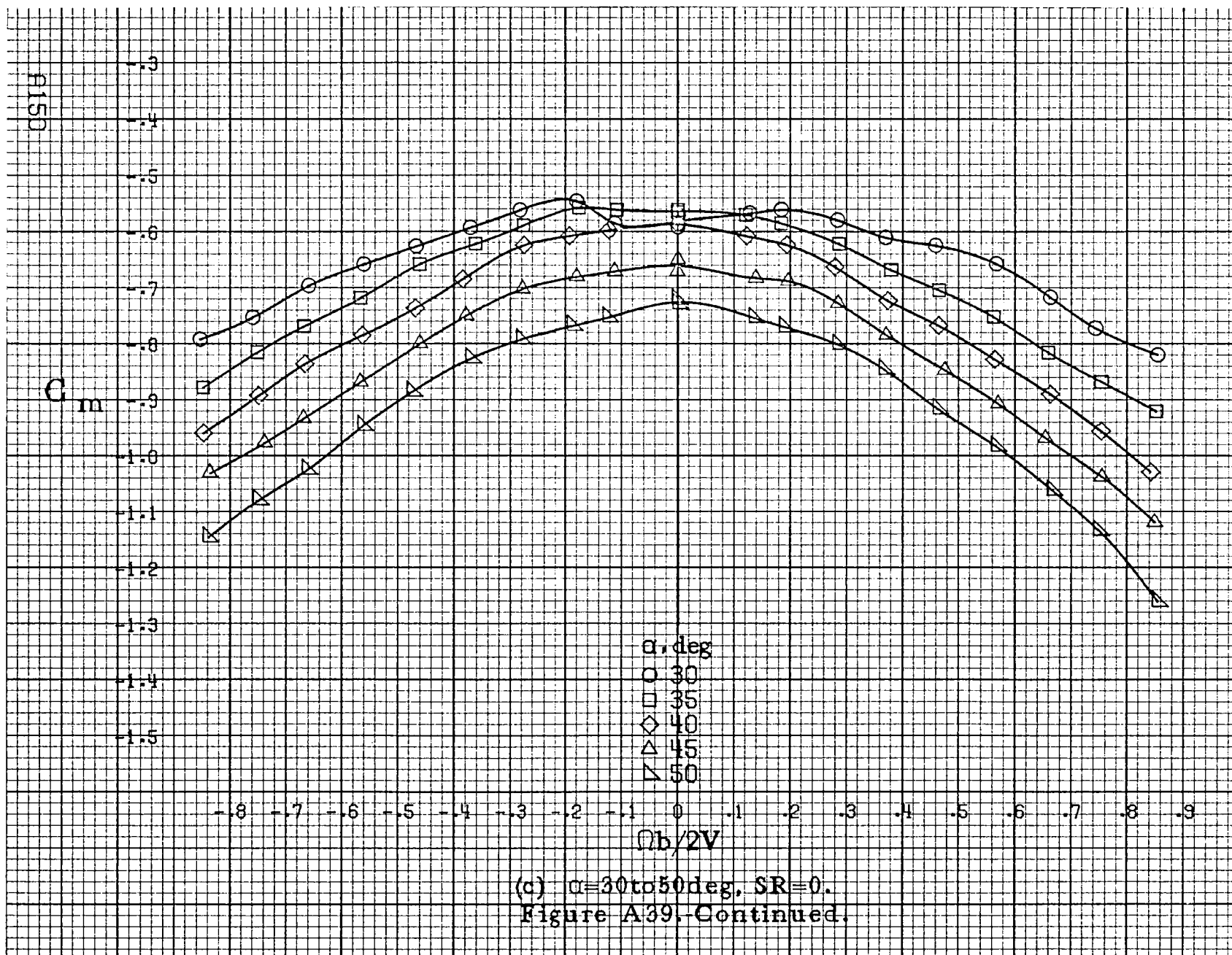


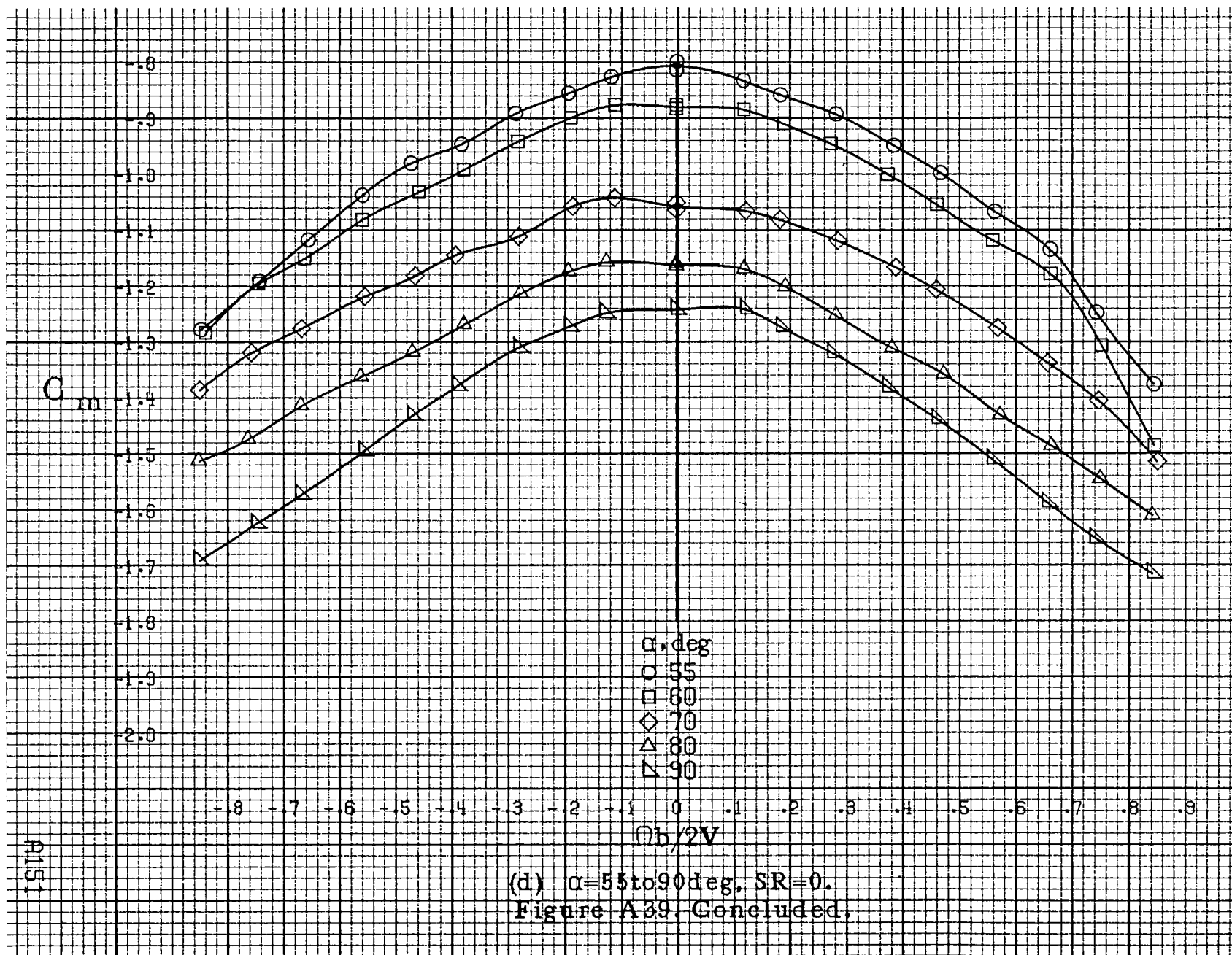


(a)  $\alpha=8$  to  $16^\circ$ ,  $SR=99\text{cm}(39\text{in})$ .

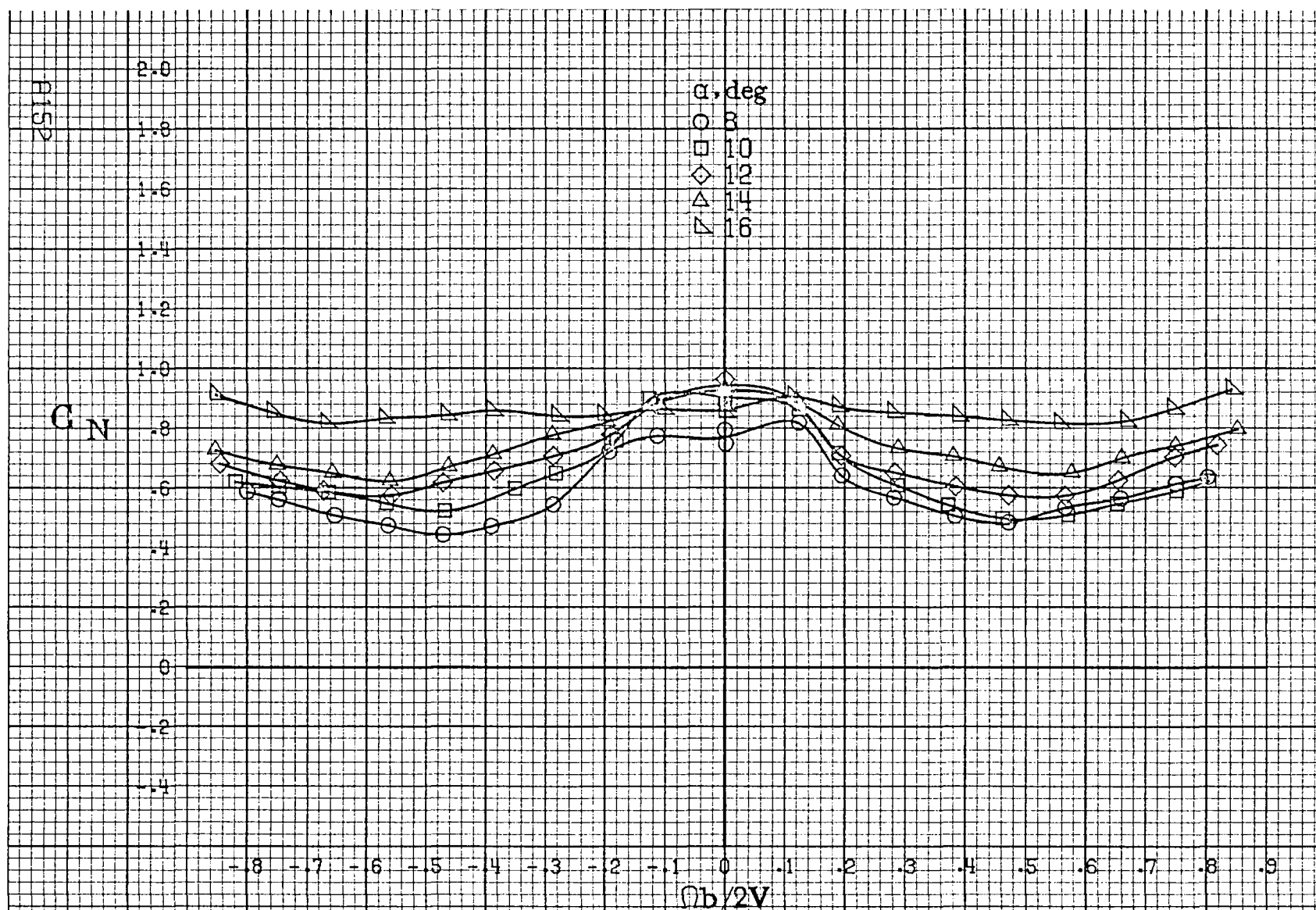
Figure A39. Effect of rotation rate and angle of attack on pitching-moment coefficient for no. 2 horizontal tail configuration.  $\delta_e = 0^\circ$ ,  $\delta_a = 0^\circ$ ,  $\delta_r = -25^\circ$ ,  $\delta = 0^\circ$ .





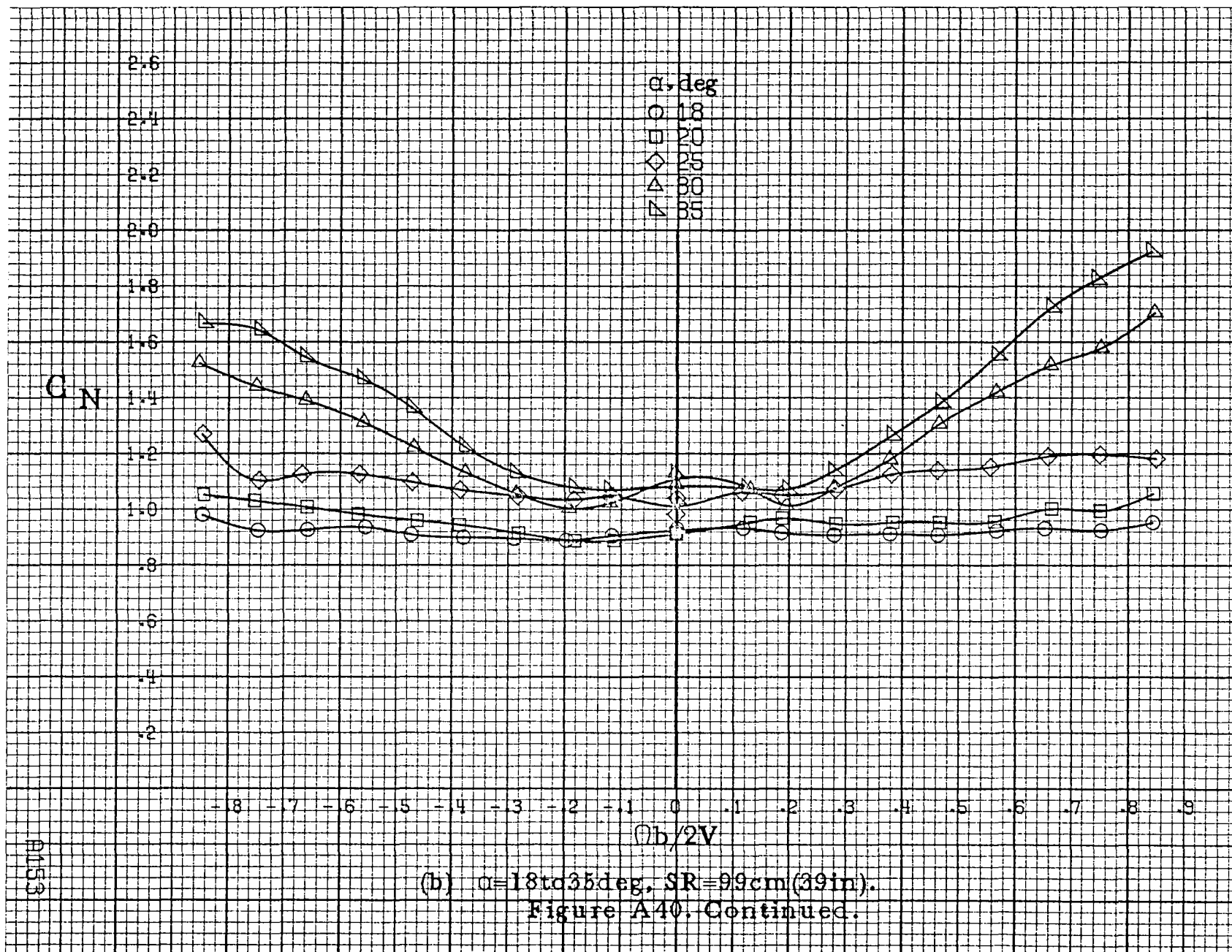


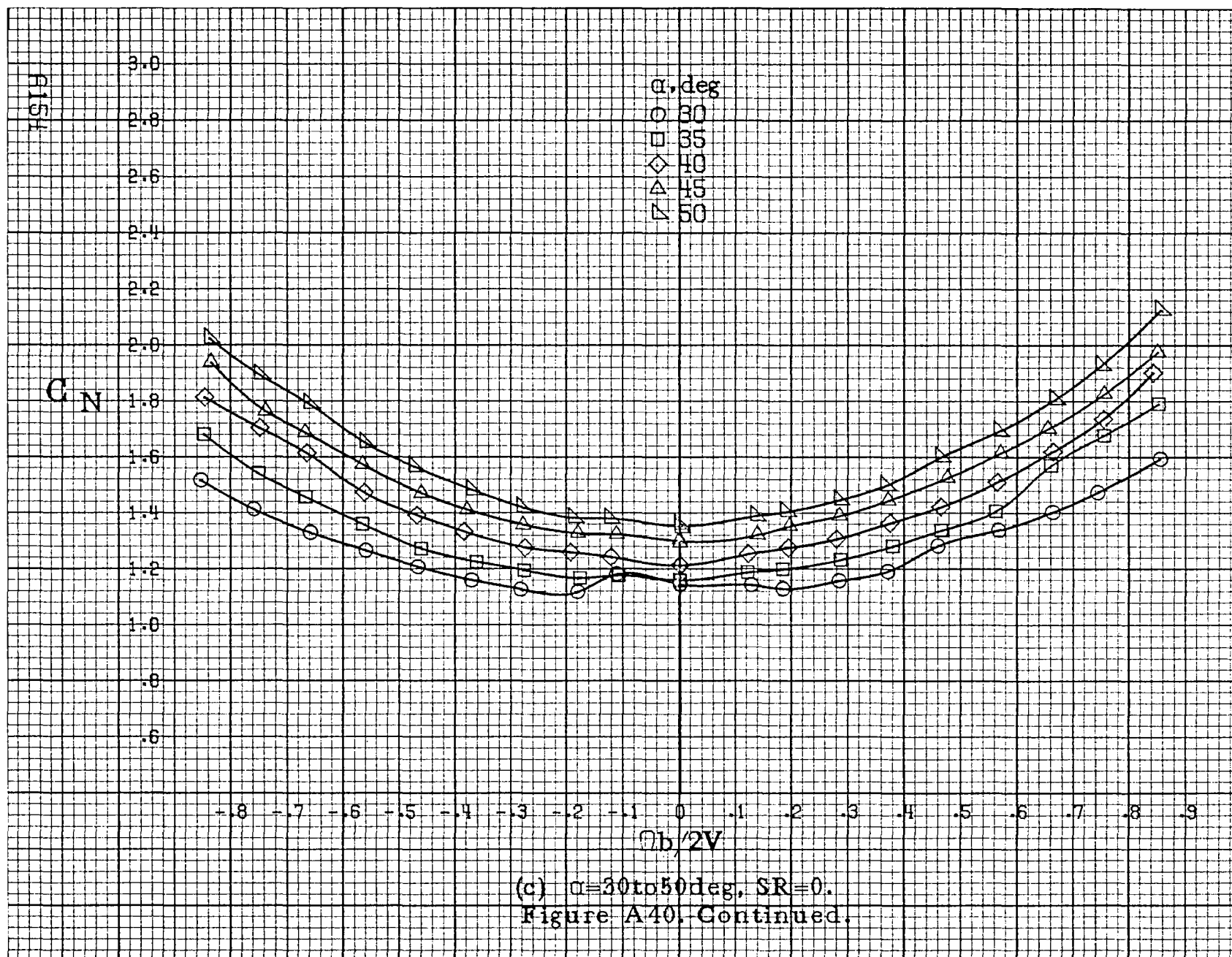


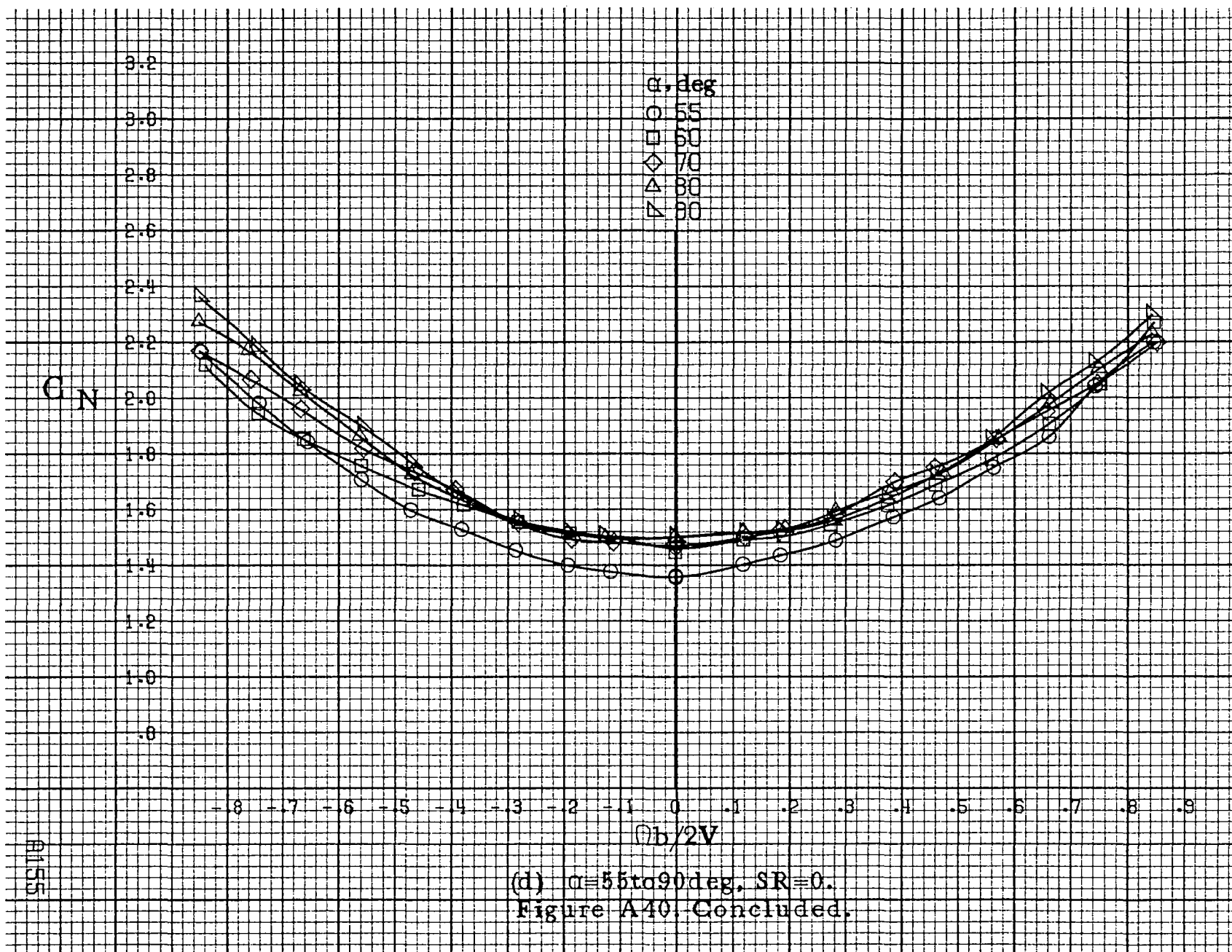


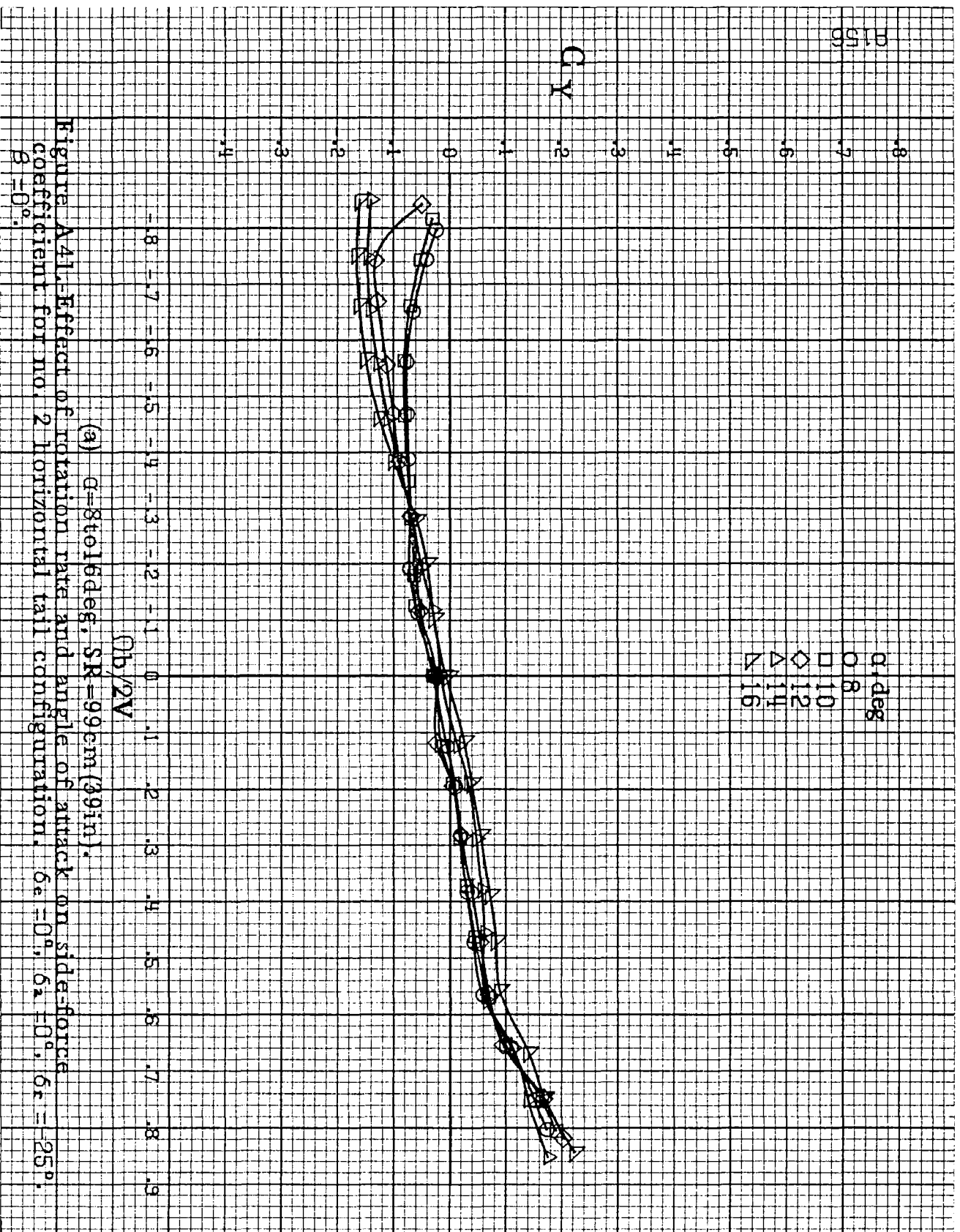
(a)  $\alpha=8$  to  $16^\circ$ ,  $SR=99\text{cm}(39\text{in})$ .

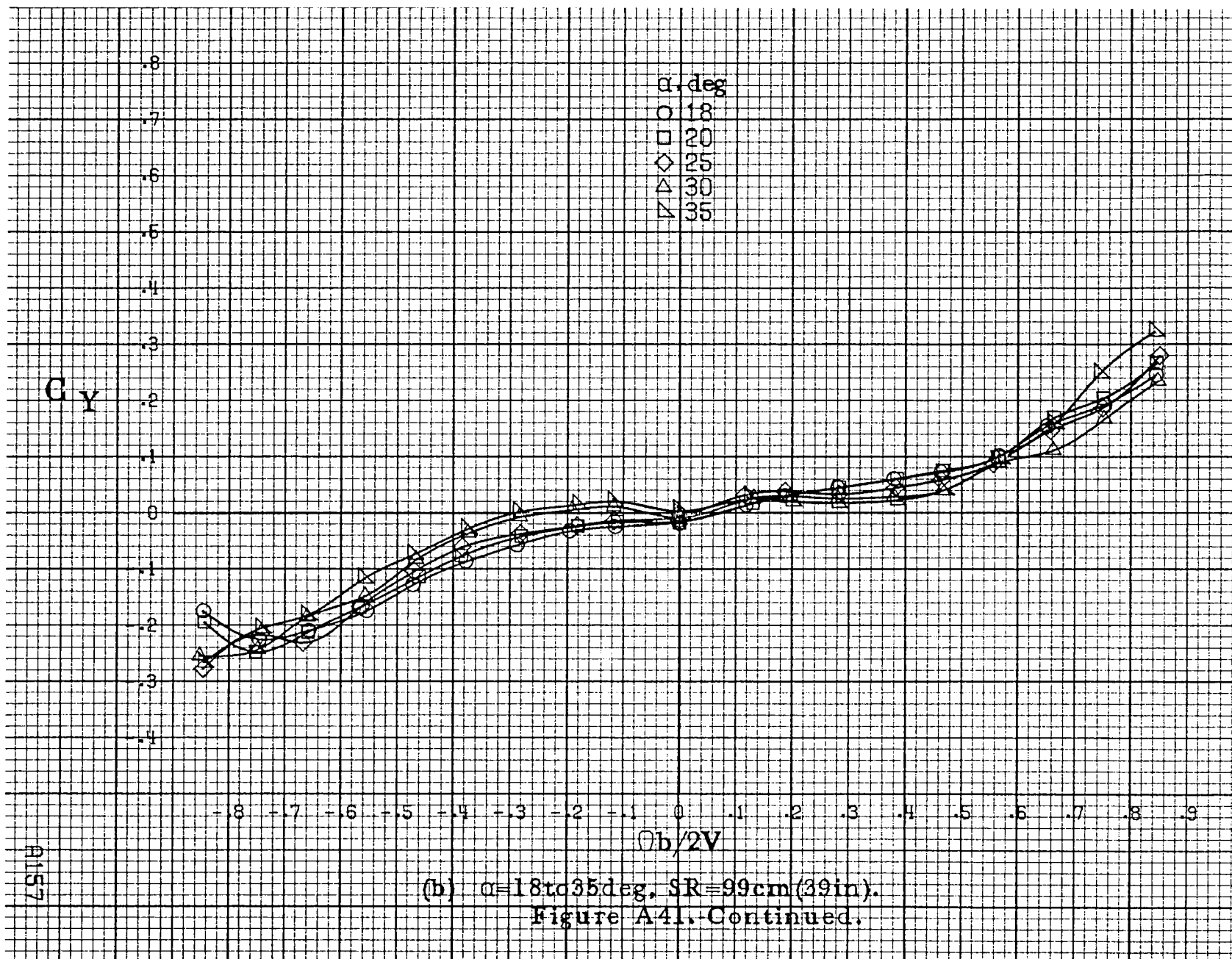
Figure A40. Effect of rotation rate and angle of attack on normal-force coefficient for no. 2 horizontal tail configuration.  $\delta_e = 0^\circ$ ,  $\delta_a = 0^\circ$ ,  $\delta_r = -25^\circ$ ,  $\beta = 0^\circ$ .

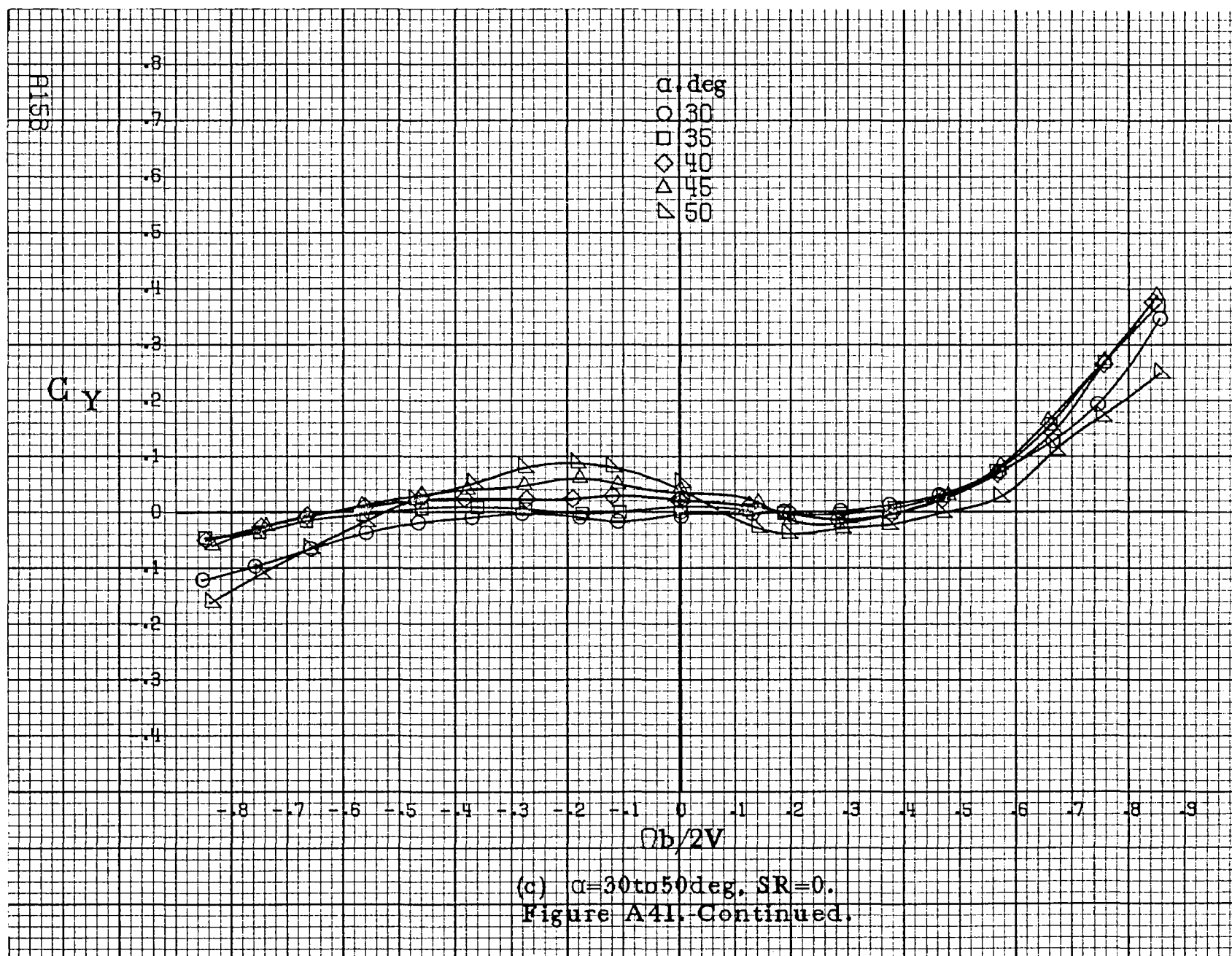




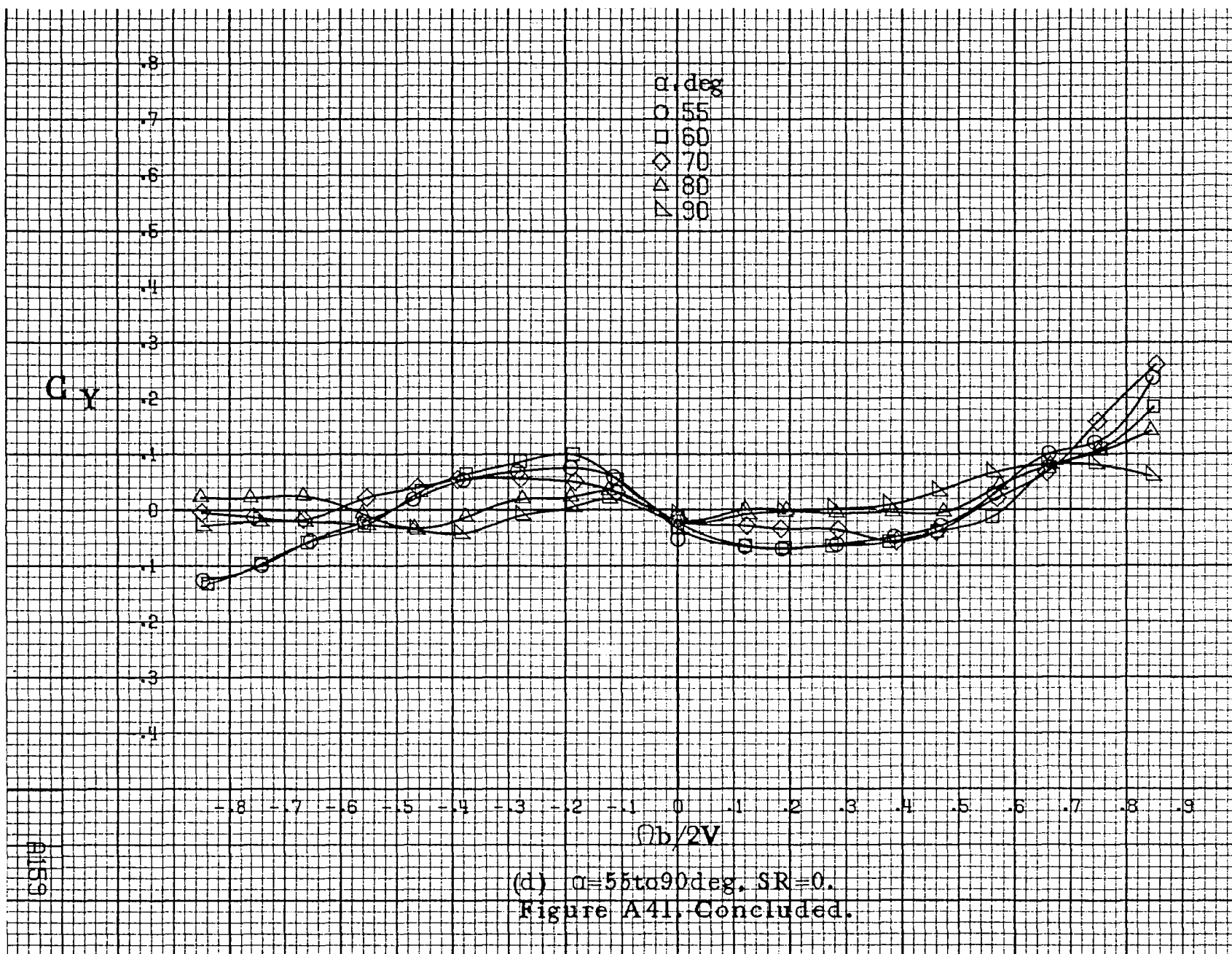


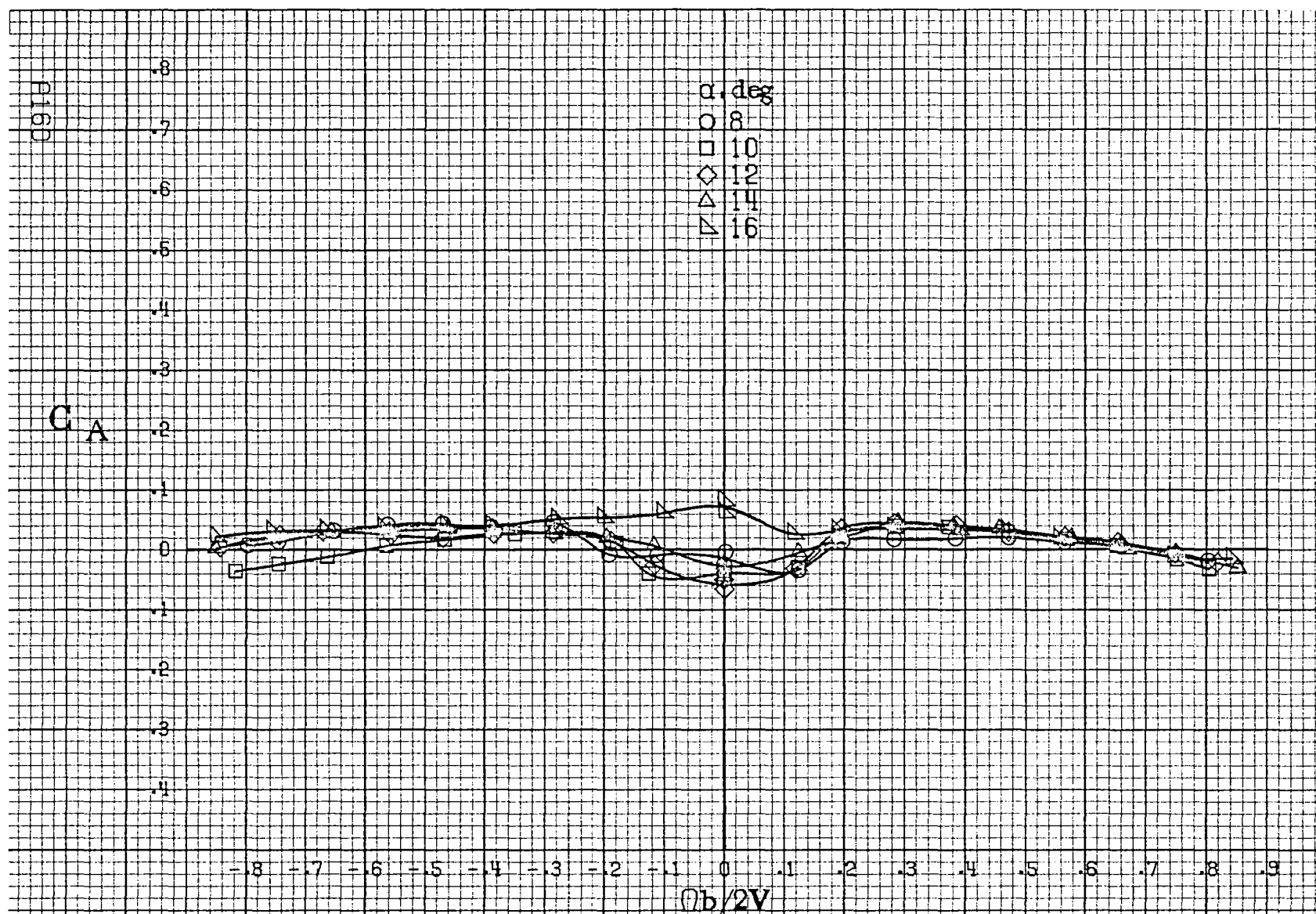






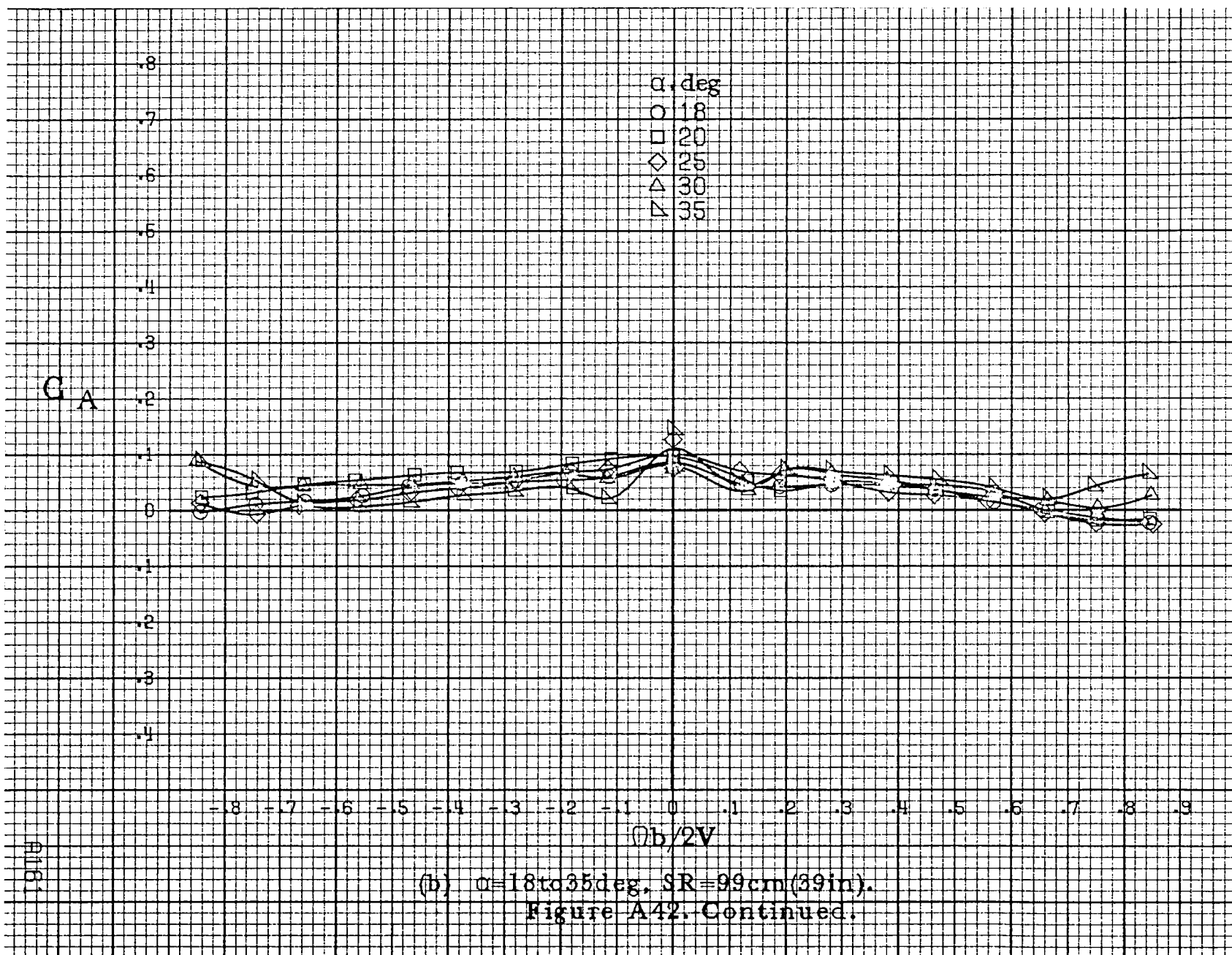






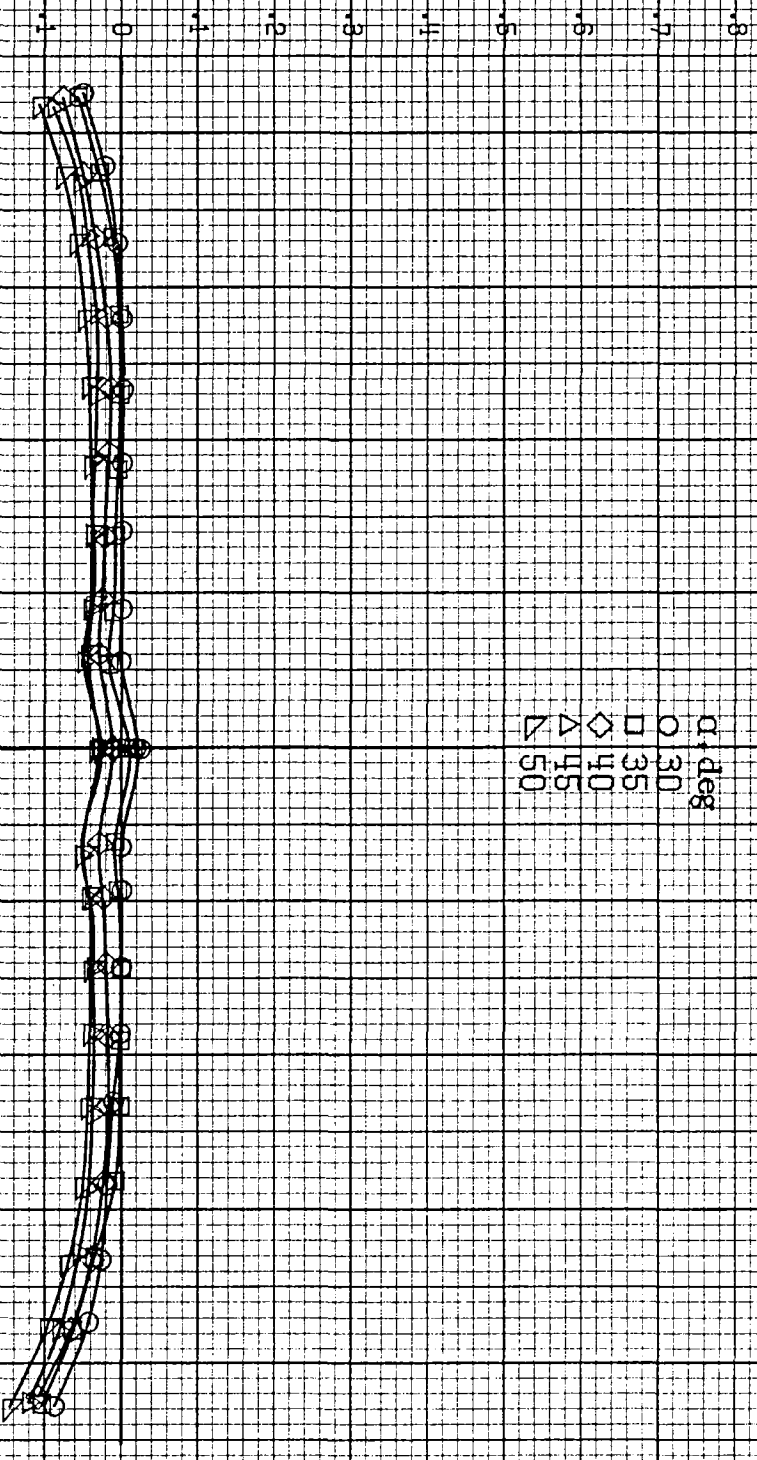
(a)  $\alpha = 8$  to  $16^\circ$ ,  $SR = 99 \text{ cm (39 in)}$ .

Figure A42.-Effect of rotation rate and angle of attack on axial force coefficient for no. 2 horizontal tail configuration.  $\delta_a = 0^\circ$ ,  $\delta_s = 0^\circ$ ,  $\delta_z = -25^\circ$ ,  $\theta = 0^\circ$ .



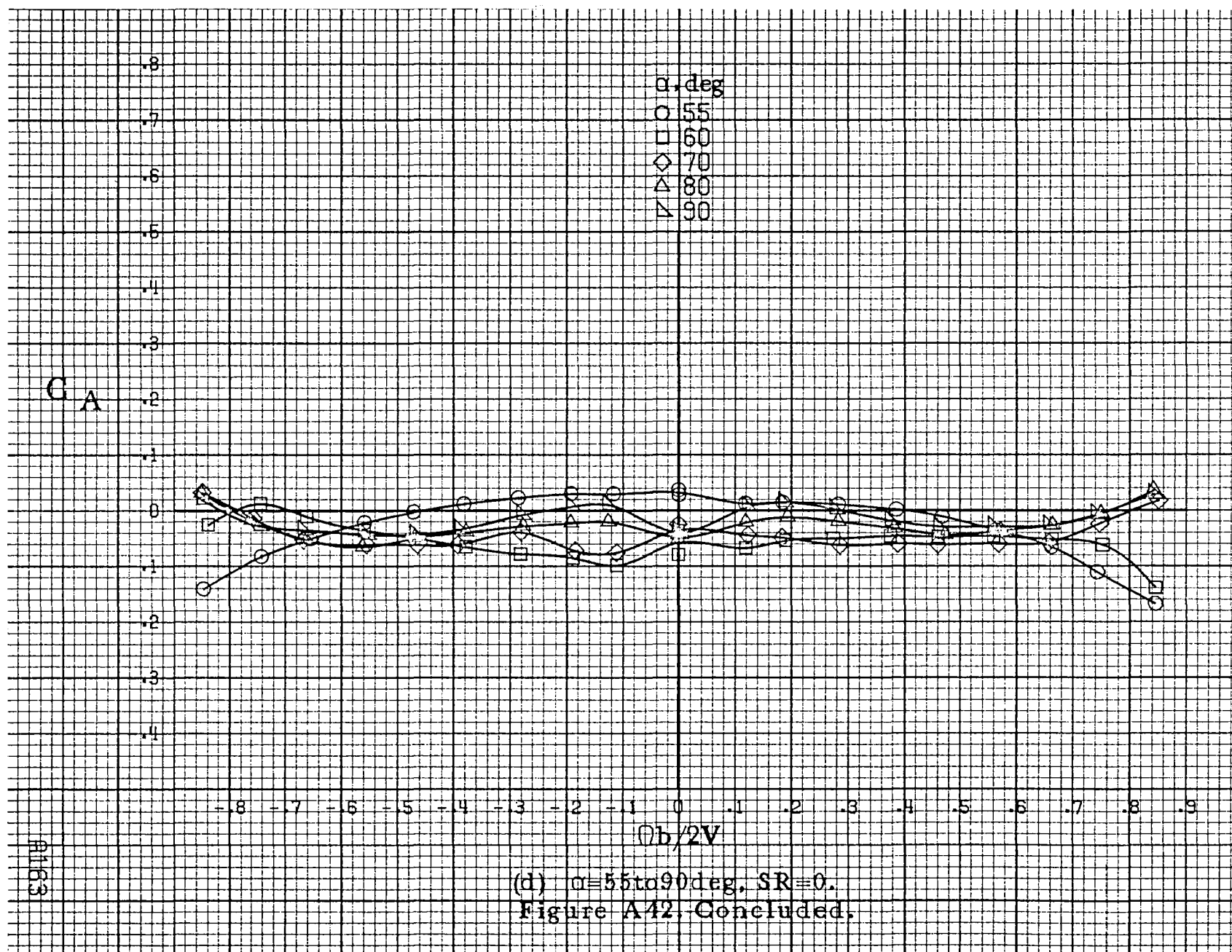
8162

GA

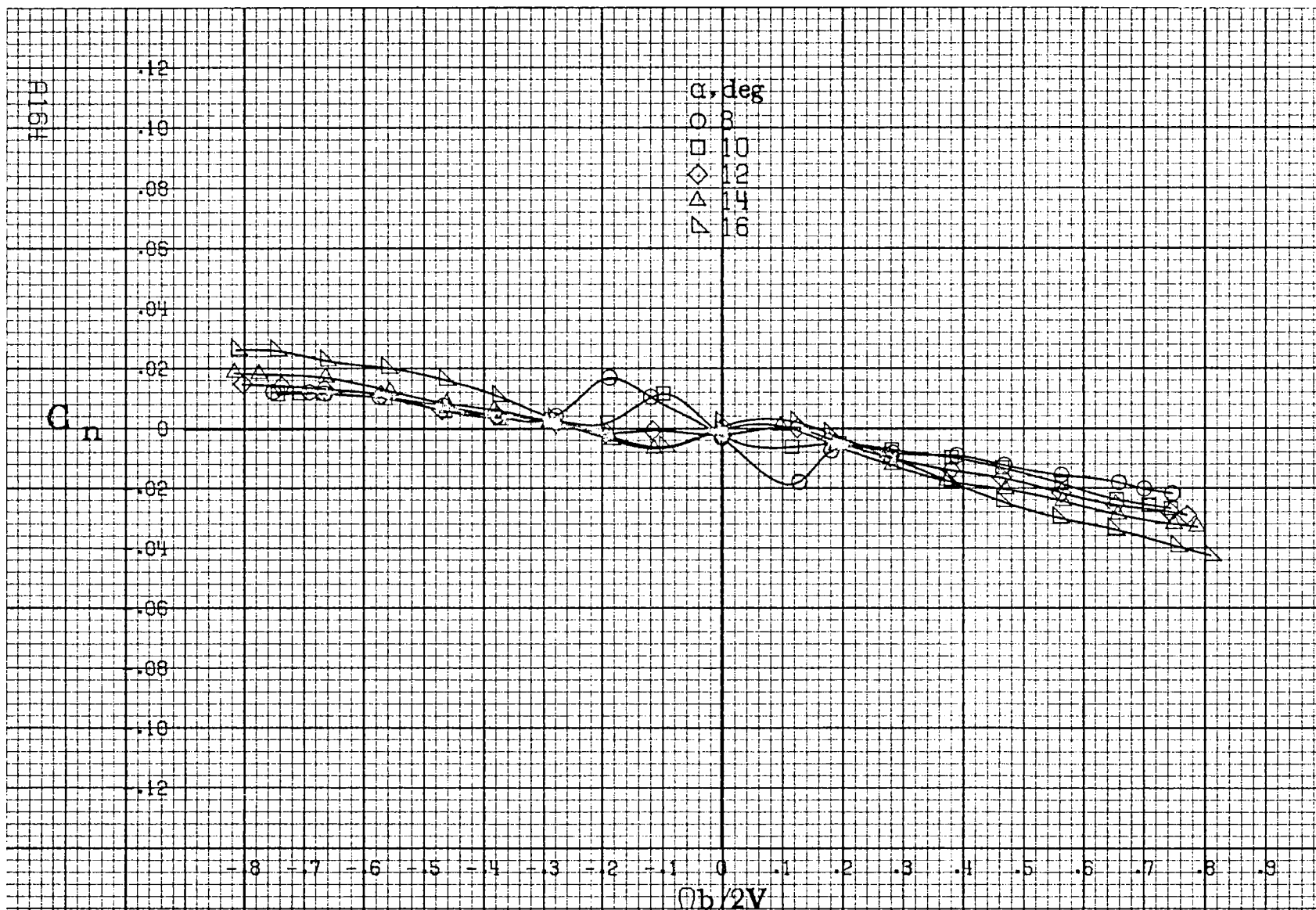


Ob/2V

(c)  $\alpha=30$  to  $50$  deg,  $SR=0$ .  
Figure A42. Continued.

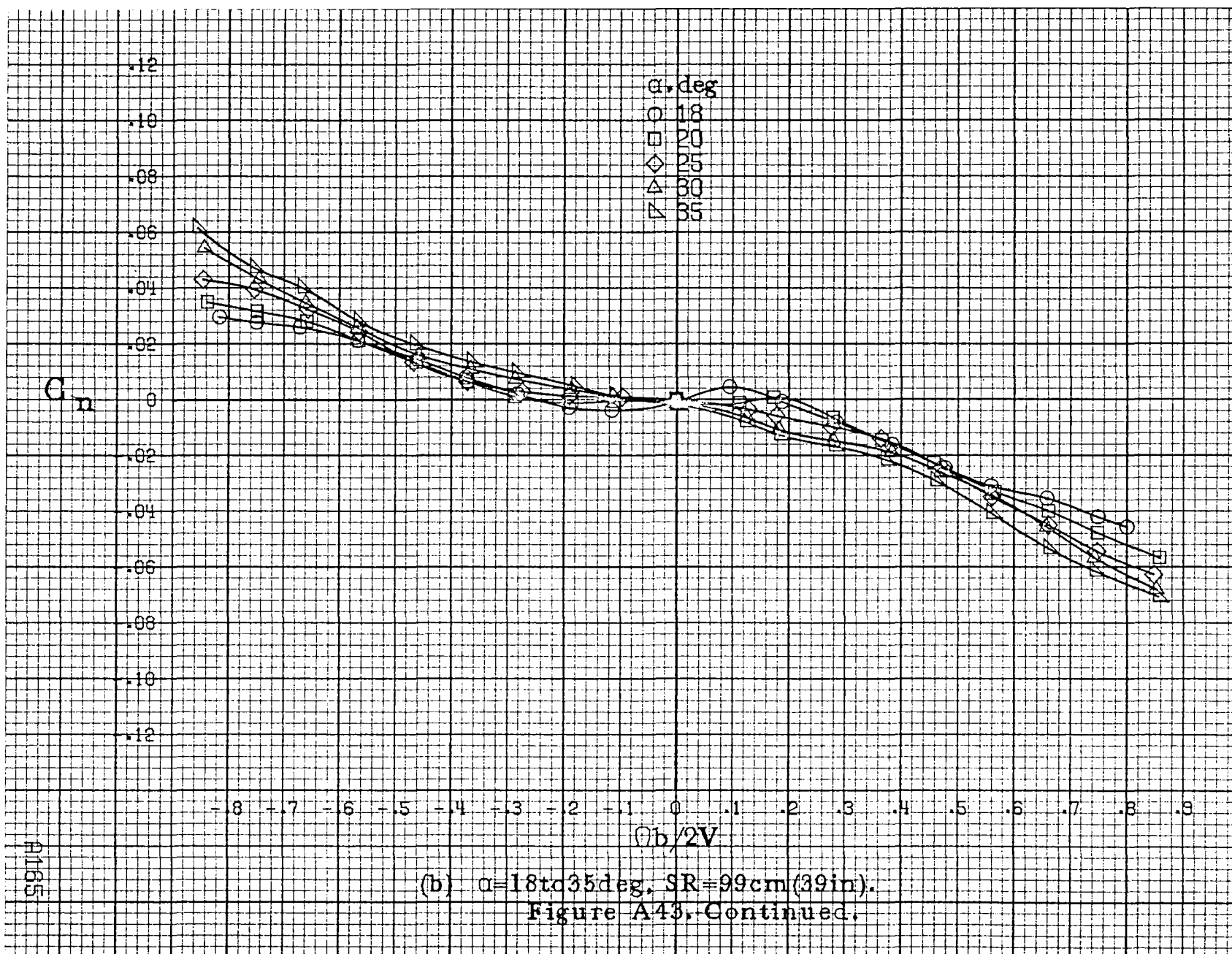


(d)  $\alpha=55$  to  $90^\circ$ ,  $SR=0$ .  
Figure A42. Concluded.

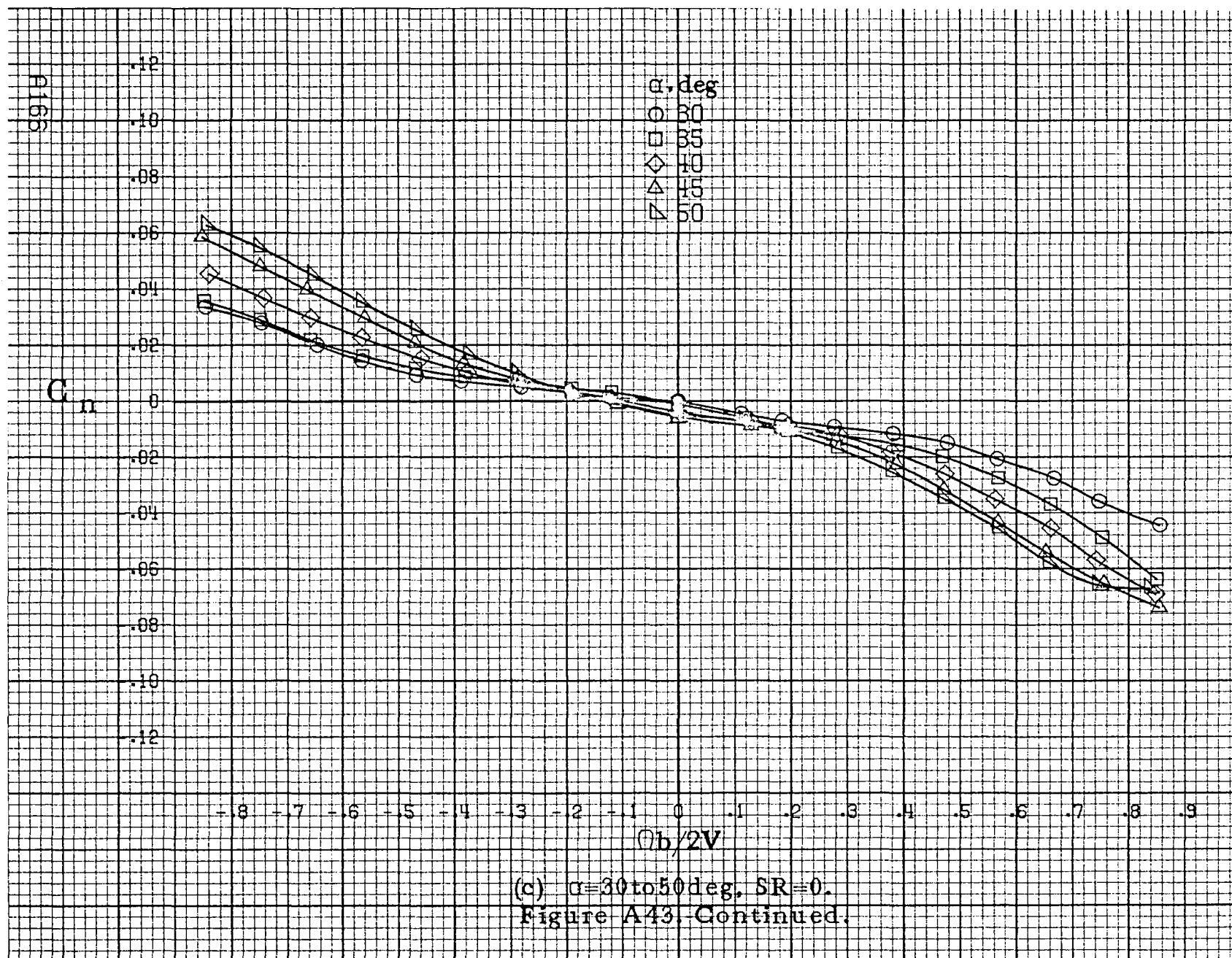


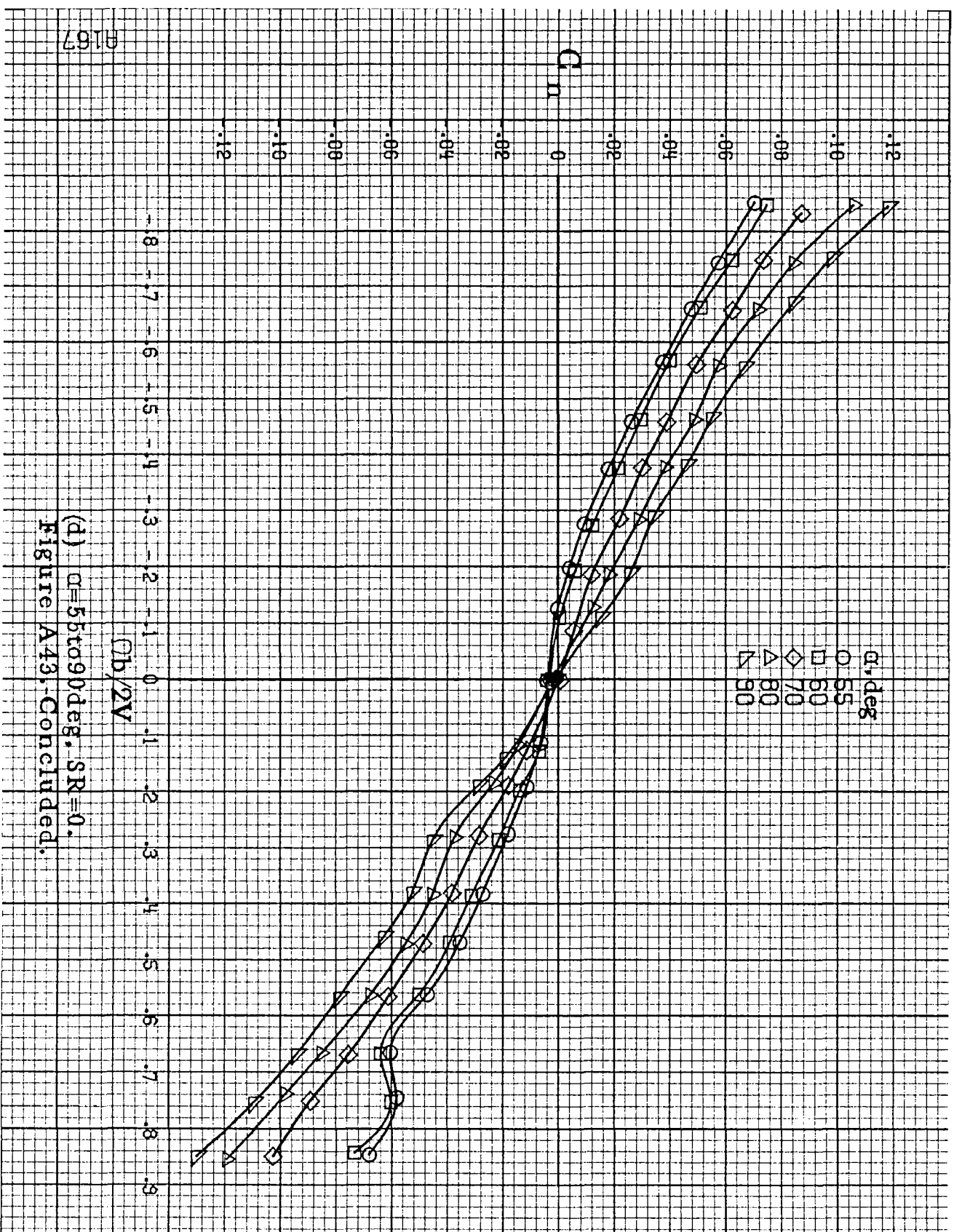
(a)  $\alpha=8$  to  $16^\circ$ ,  $SR=99\text{cm}(39\text{in})$ .

Figure A43. Effect of rotation rate and angle of attack on yawing-moment coefficient for T-tail configuration.  $\delta_e=0^\circ$ ,  $\delta_a=0^\circ$ ,  $\delta_r=0^\circ$ ,  $\beta=0^\circ$ .

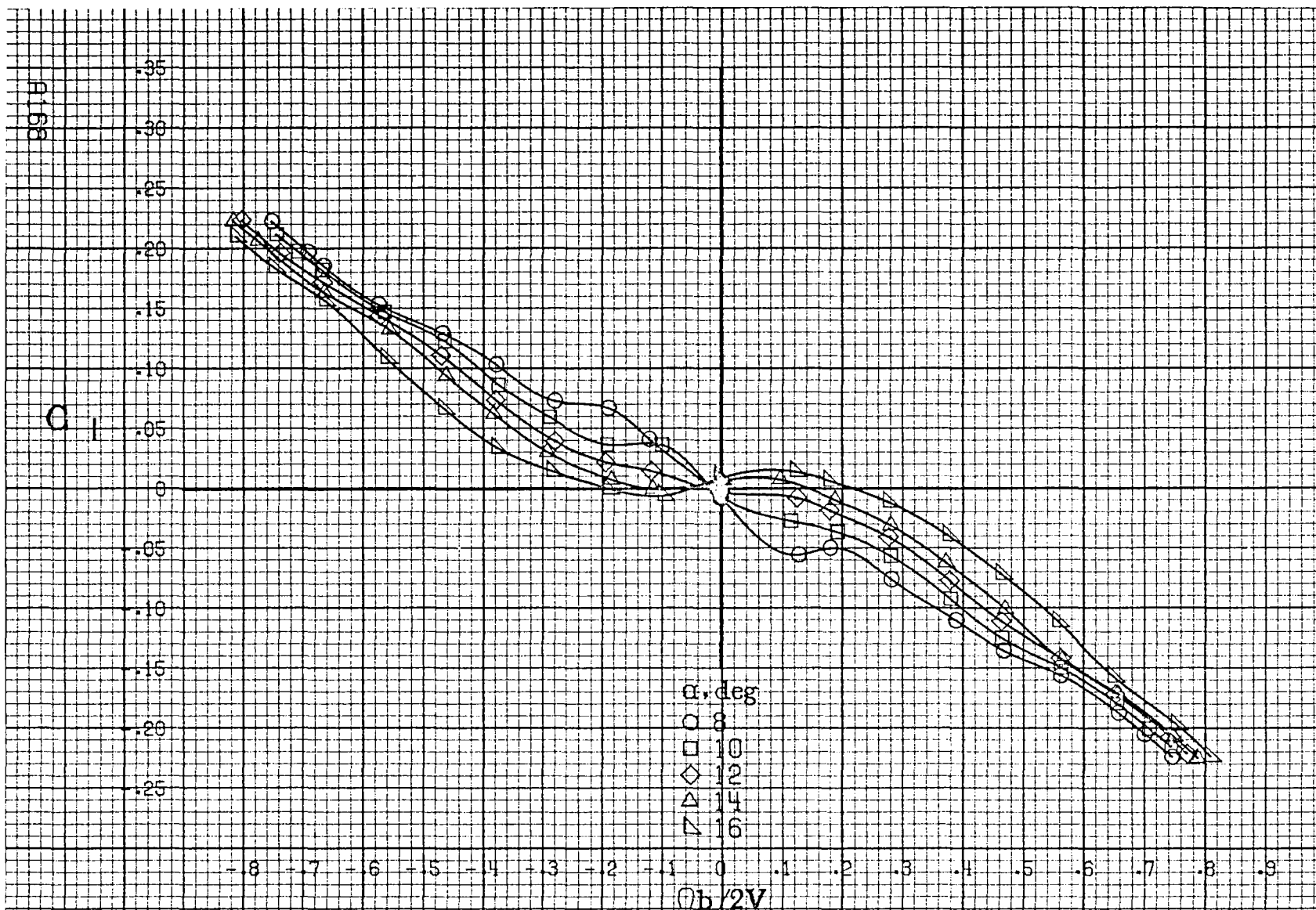








(d)  $\alpha=55$  to  $90$  deg.  $SR=0$ .  
Figure A43.-Concluded.



(a)  $\alpha=8\text{ to }16\text{deg}$ ,  $SR=99\text{cm}(39\text{in})$ .

Figure A44. Effect of rotation rate and angle of attack on rolling-moment coefficient for T-tail configuration.  $\delta_e=0^\circ$ ,  $\delta_a=0^\circ$ ,  $\delta_r=0^\circ$ ,  $\beta=0^\circ$ .

C<sub>II</sub>

.35  
.30  
.25  
.20  
.15  
.10  
.05  
0  
-.05  
-.10  
-.15  
-.20  
-.25

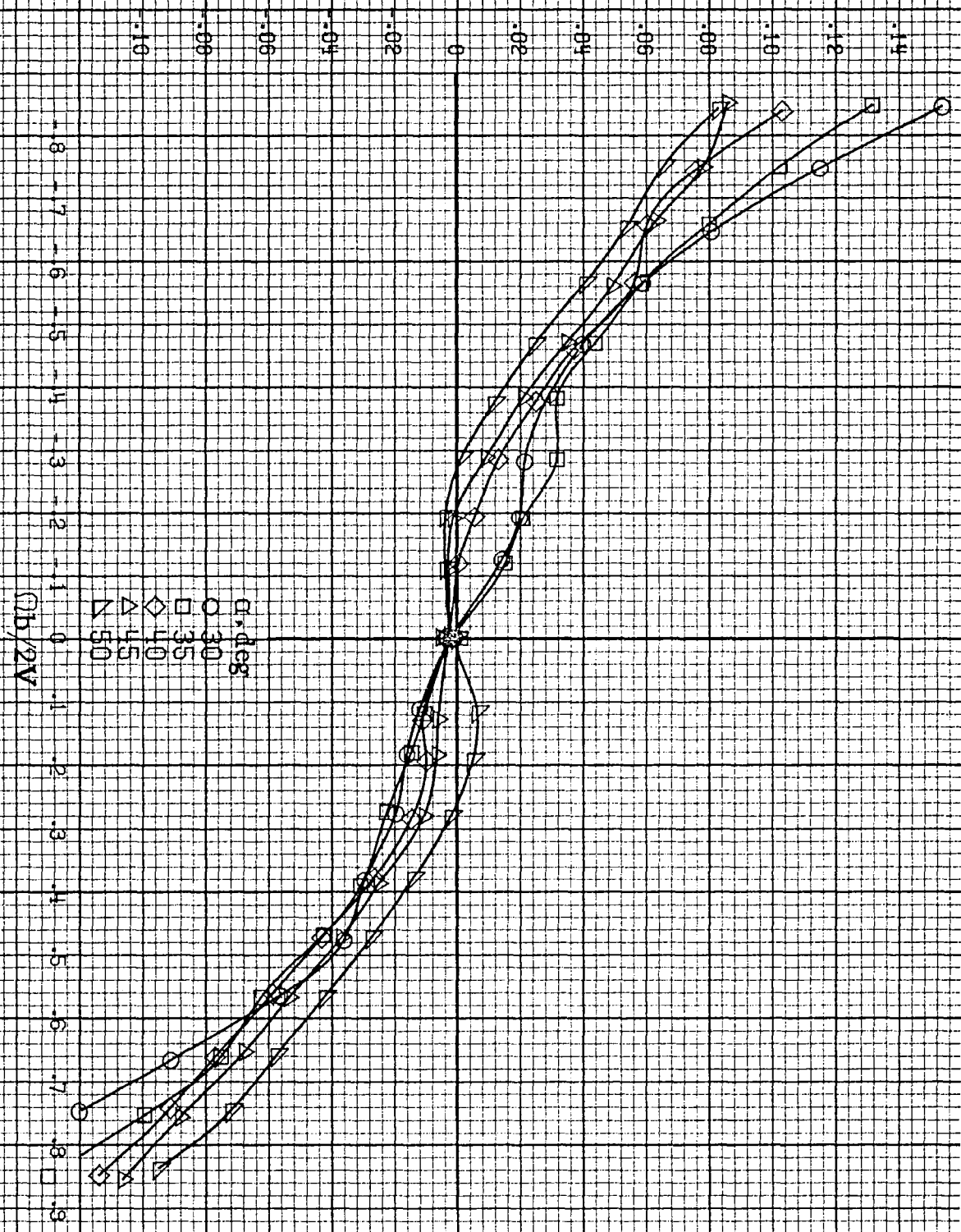
$\alpha$ , deg  
○ 18  
□ 20  
◇ 25  
△ 30  
▽ 35

-8 -7 -6 -5 -4 -3 -2 -1 0 .1 .2 .3 .4 .5 .6 .7 .8 .9  
 $\Omega b/2V$

(b)  $\alpha=18$  to  $35$  deg, SR=99cm(39in).  
Figure A44. Continued.

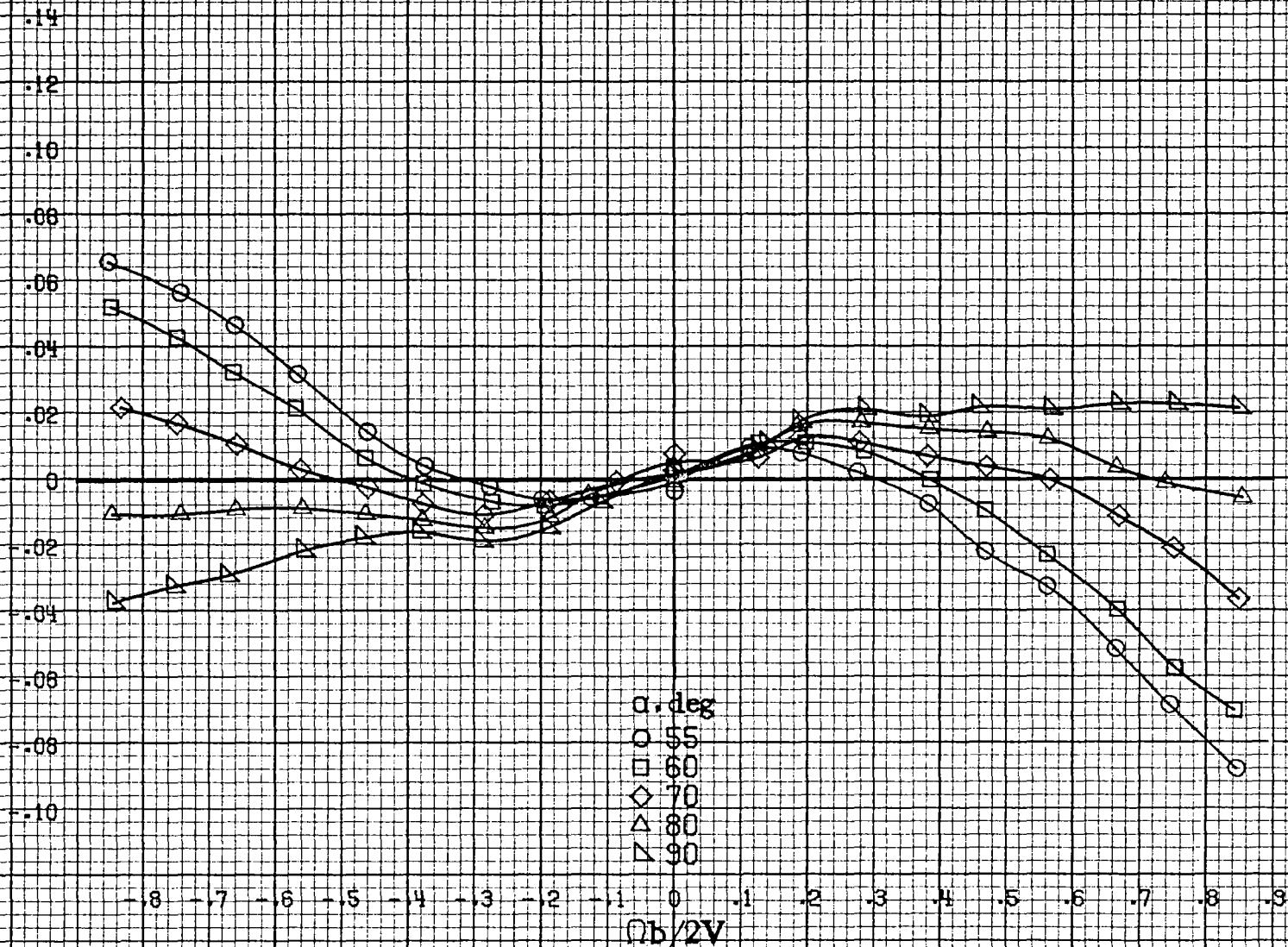
A169

C



(c)  $\alpha=30$  to  $50$  deg,  $SR=0$ .  
Figure A44: Continued.

G<sub>1</sub>



(d)  $\alpha = 55$  to  $90$  deg,  $SR = 0$ .  
Figure A44. Concluded.



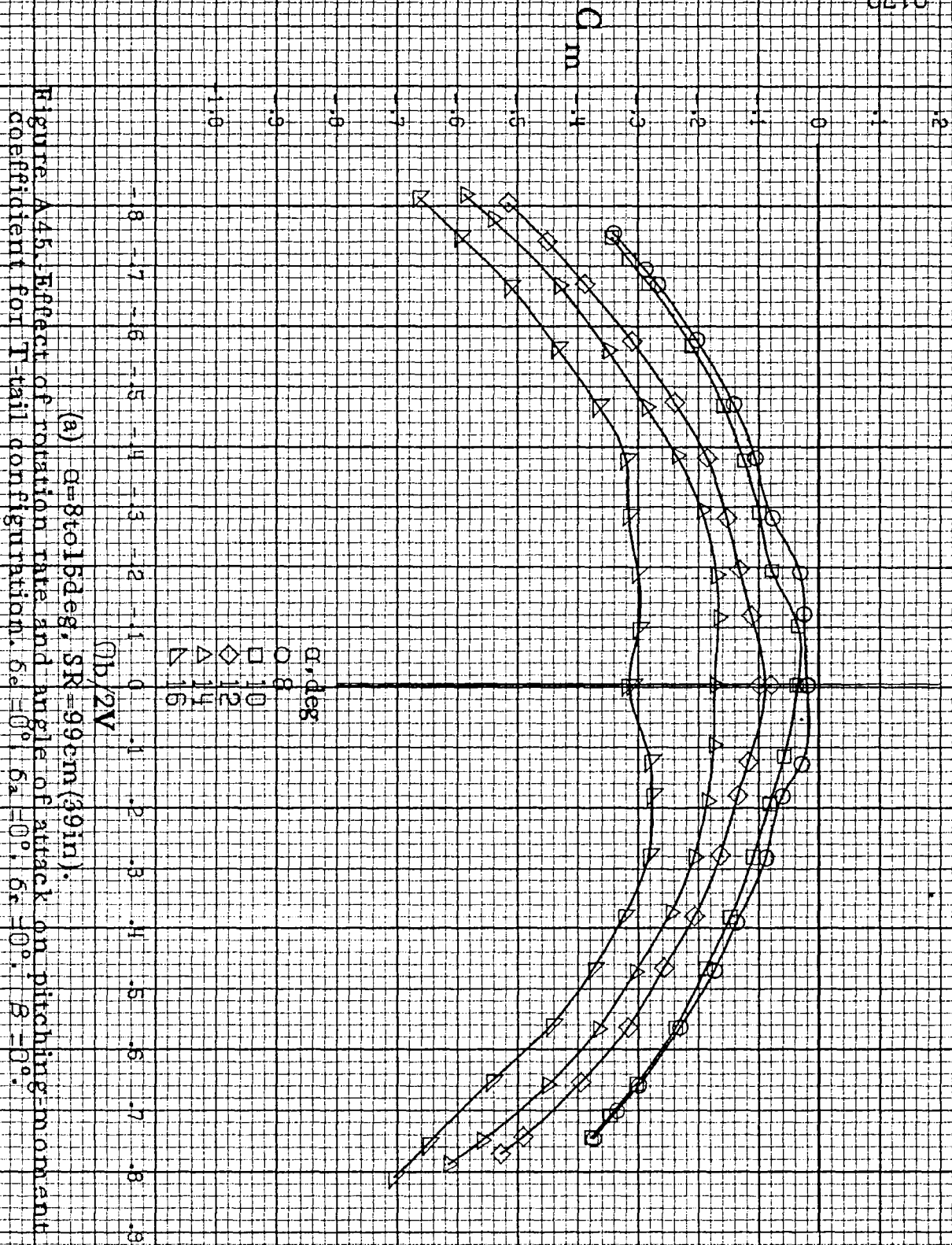
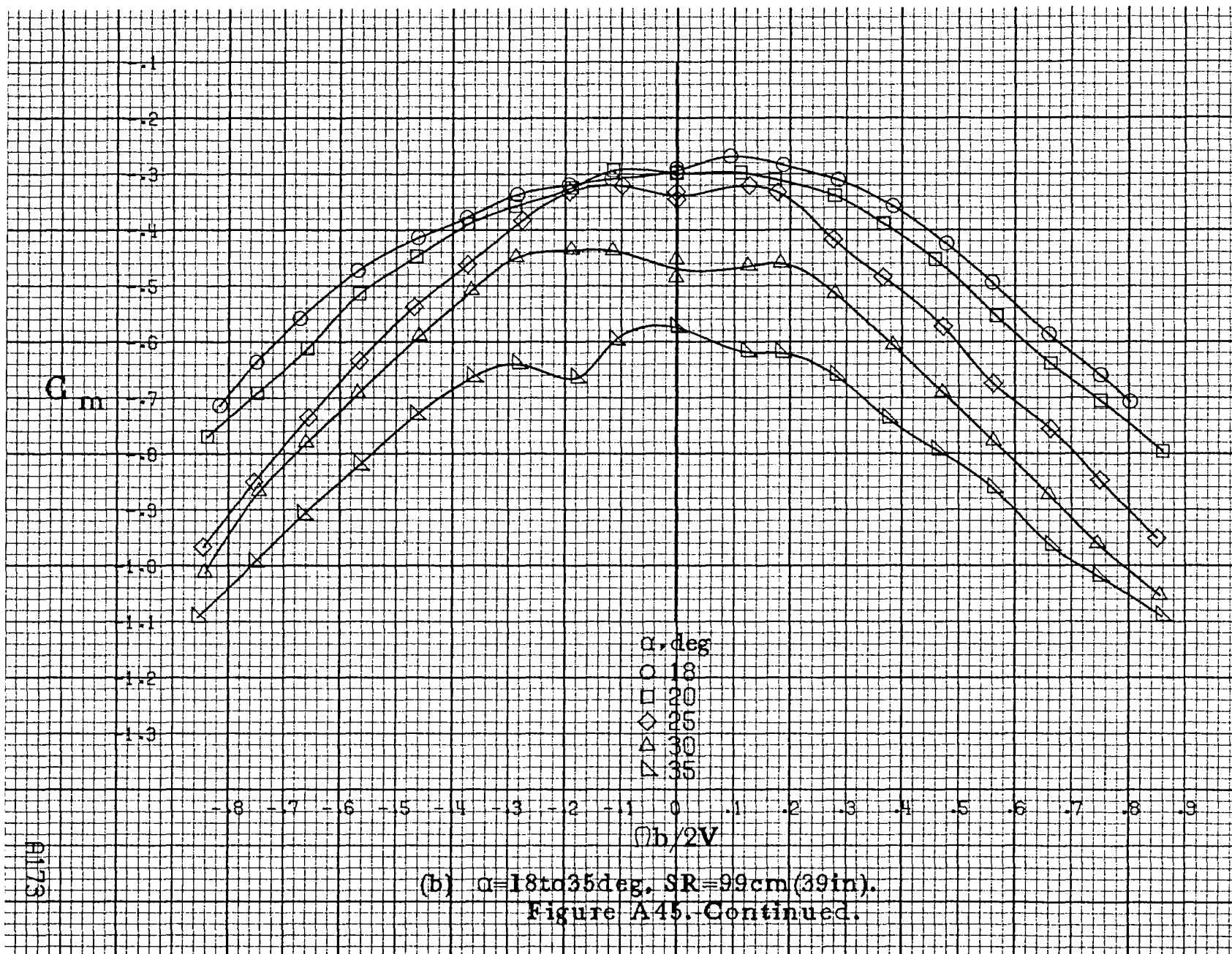
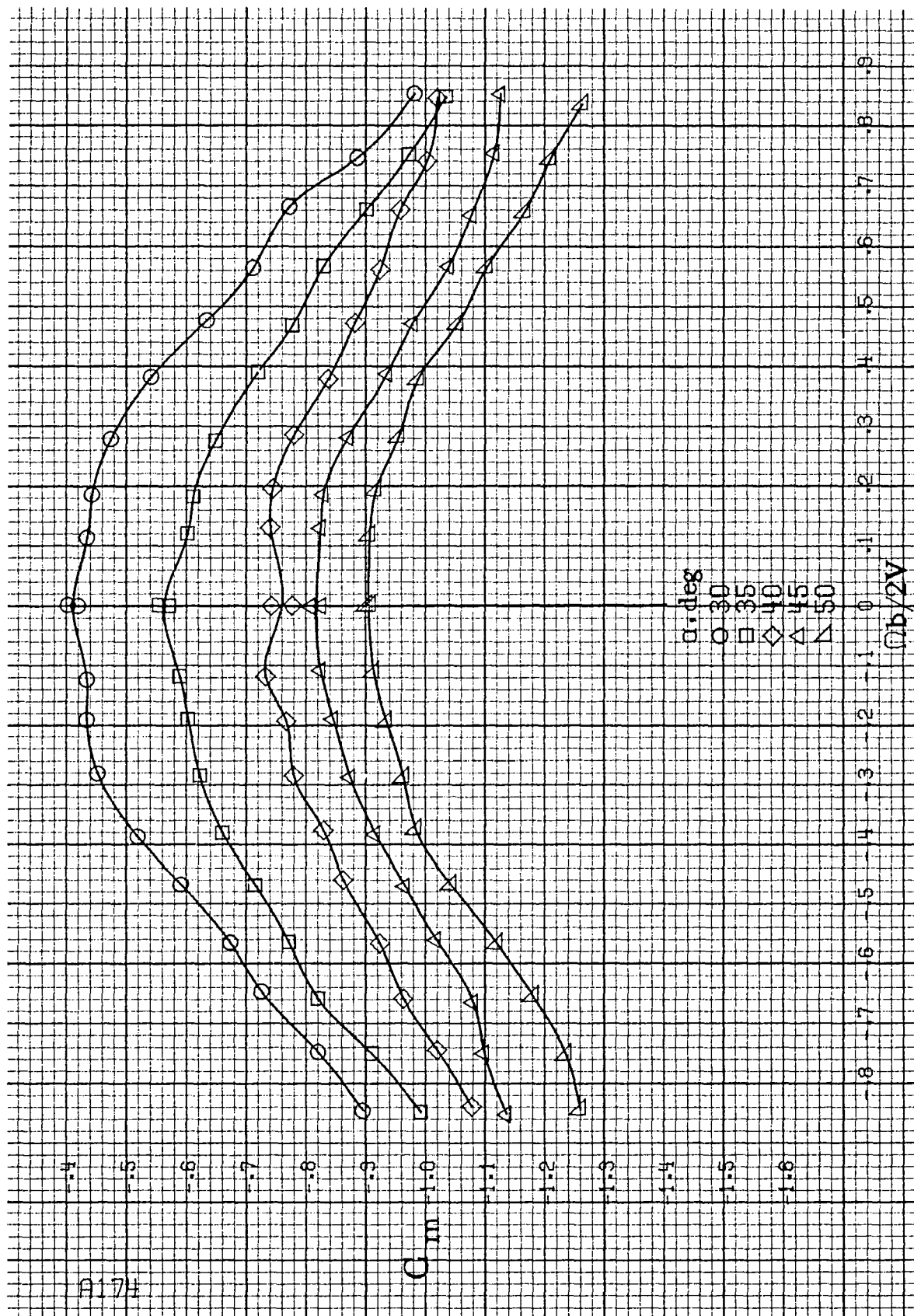


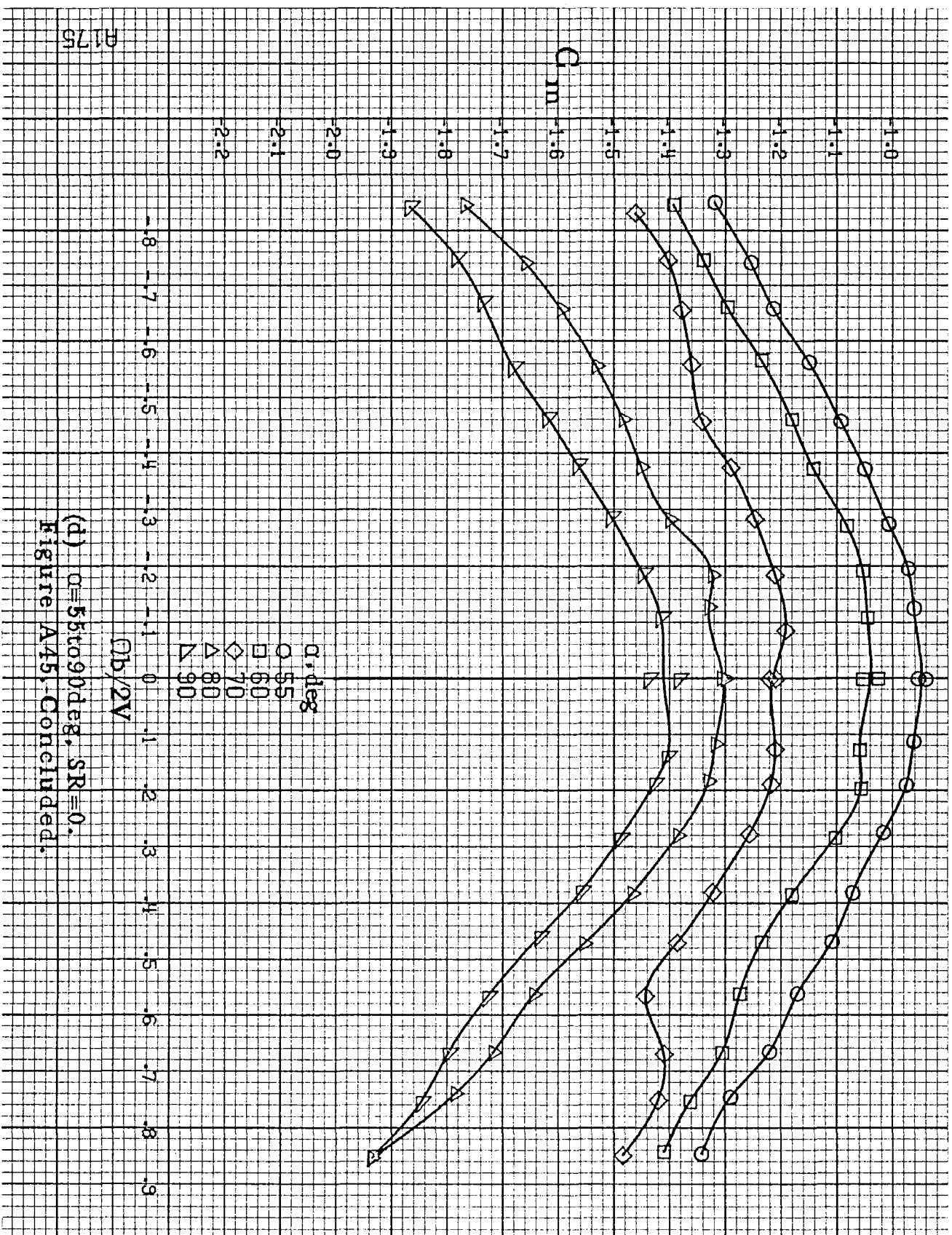
Figure A45. Effect of rotation rate and angle of attack on pitching-moment coefficient for T-tail configuration.  $\delta_e = 0^\circ$ ,  $\delta_a = 0^\circ$ ,  $\delta_r = 0^\circ$ ,  $\beta = 0^\circ$ .



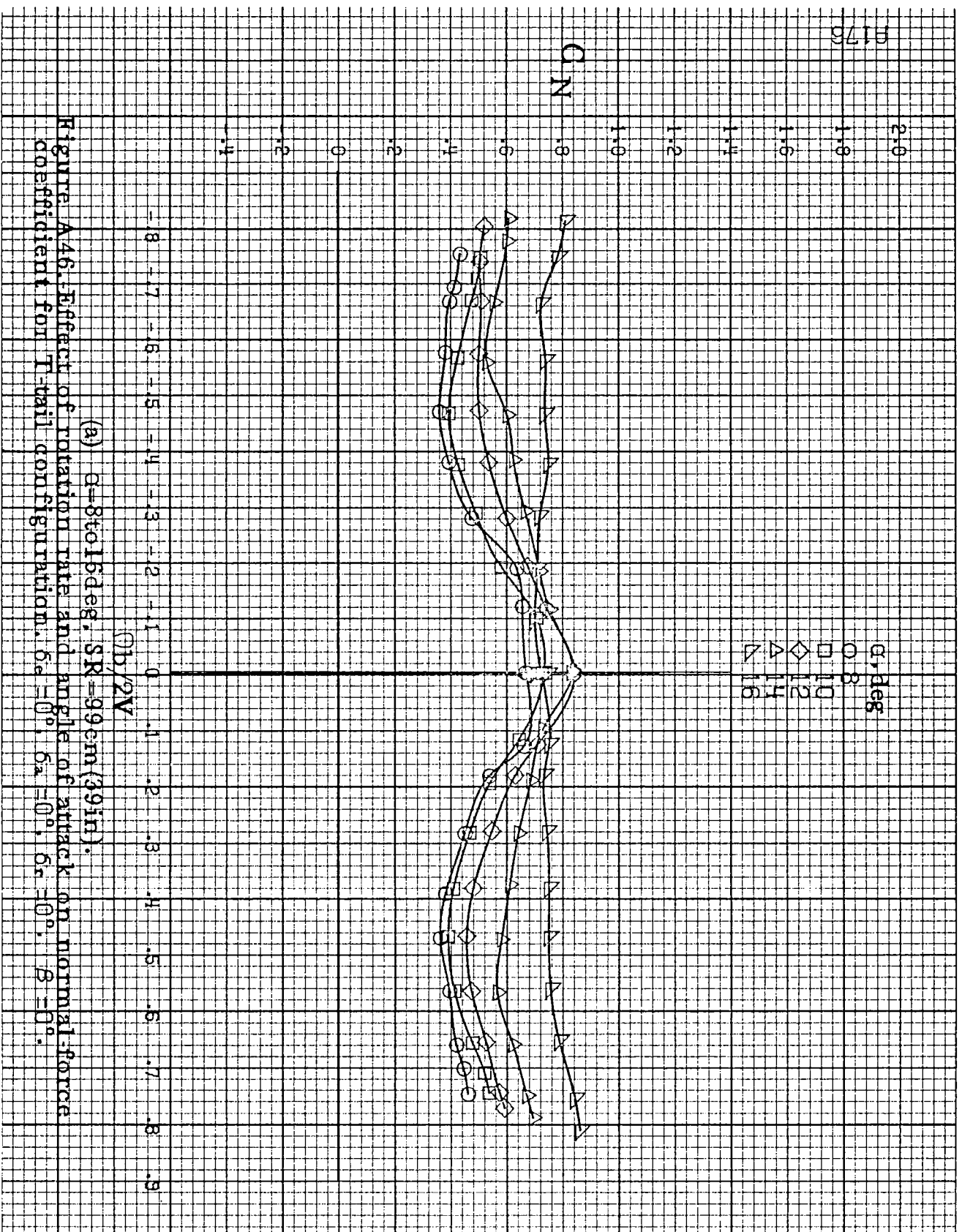


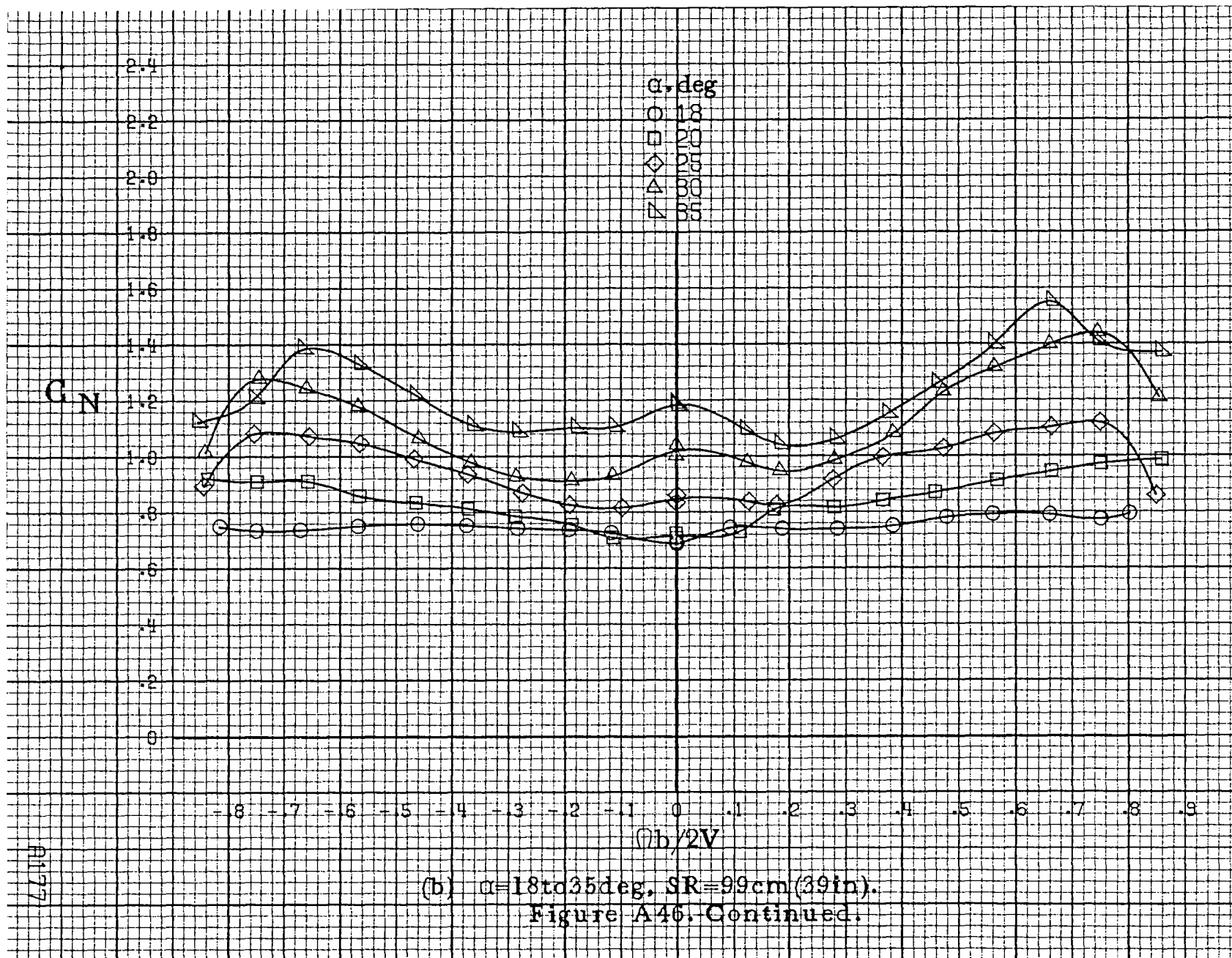


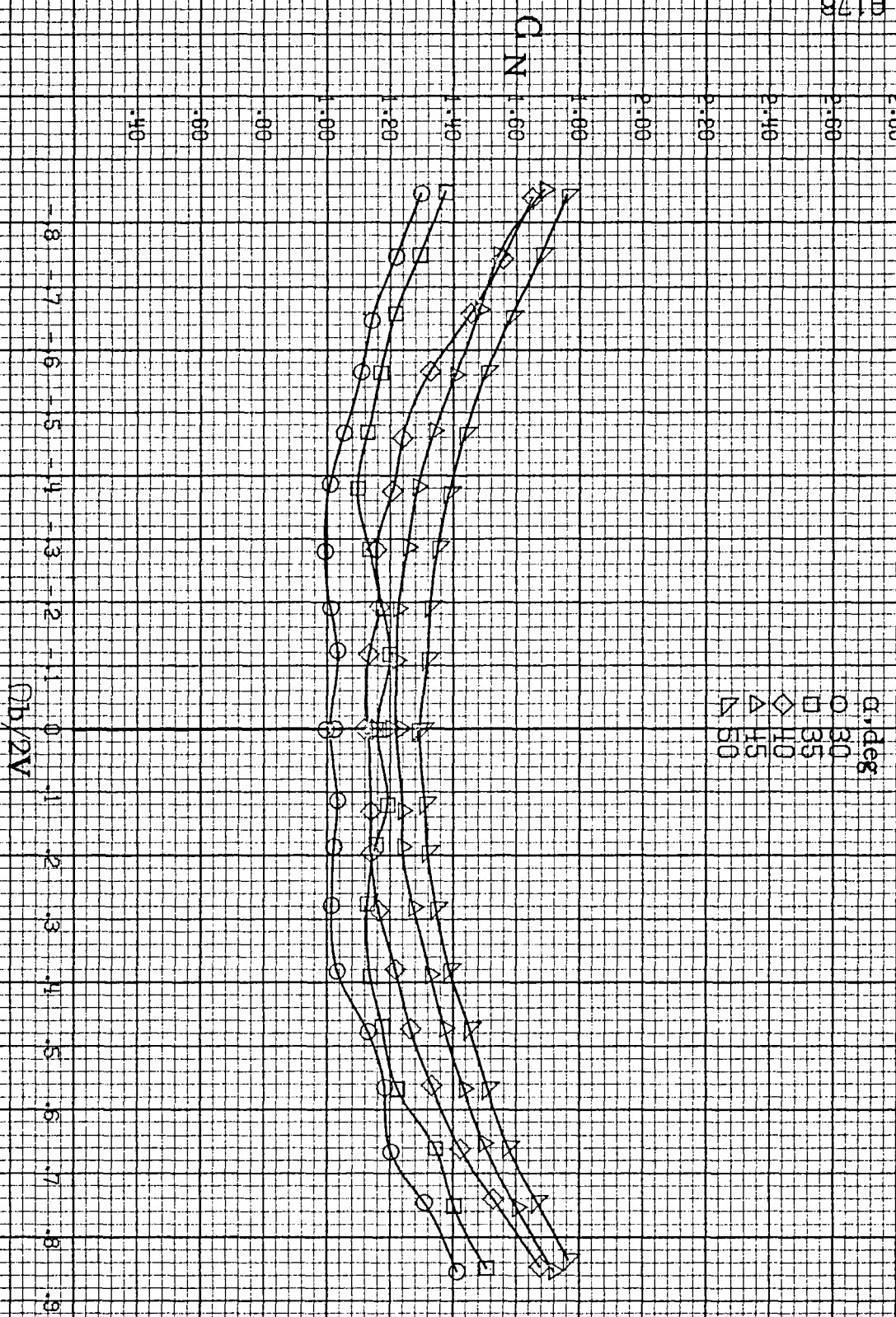
(c)  $\alpha=30$  to  $50$  deg,  $SR=0$ .  
Figure A45, Continued.



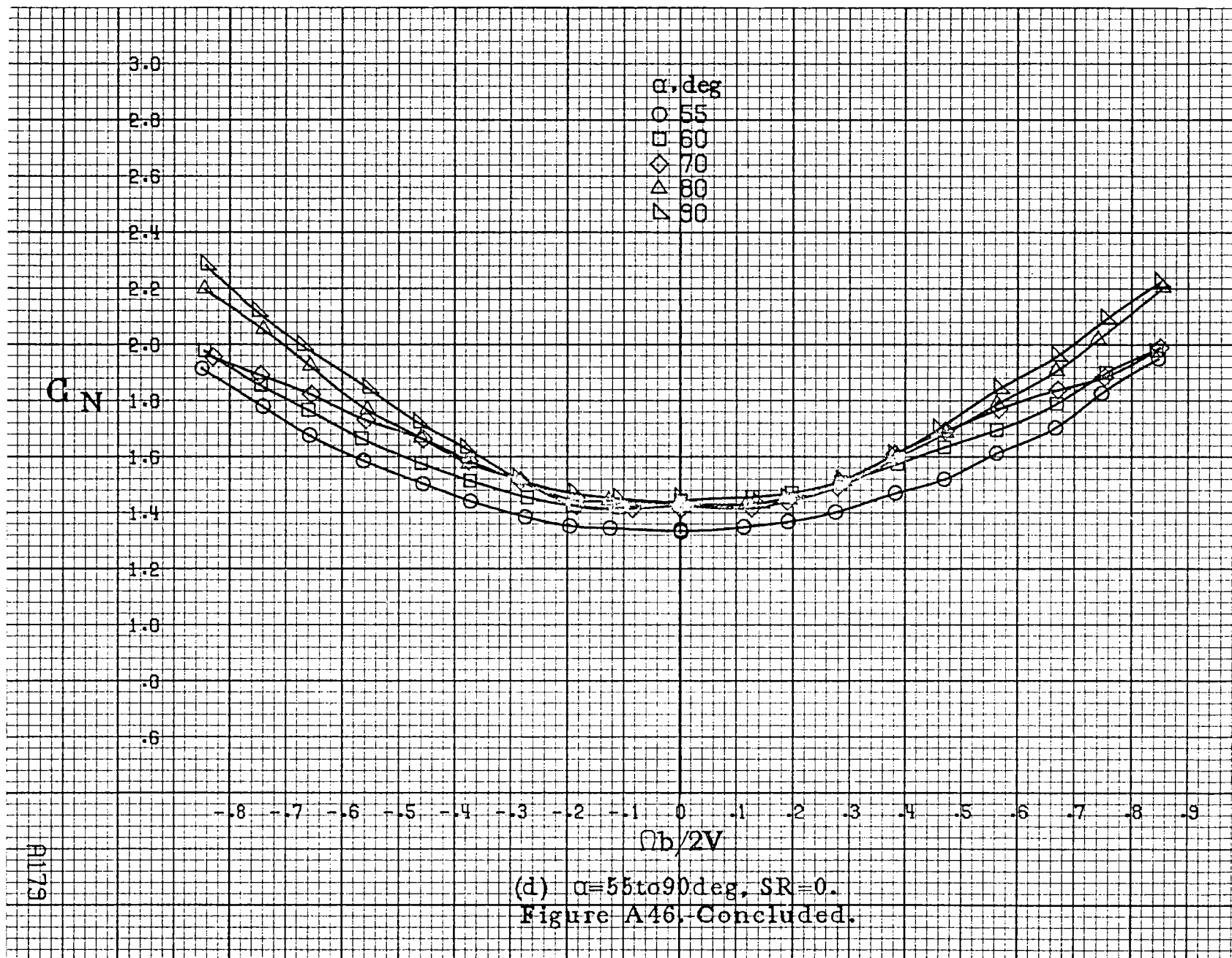
(d)  $C=55$  to  $90$  deg,  $SR=0$ .  
Figure A45, Concluded.



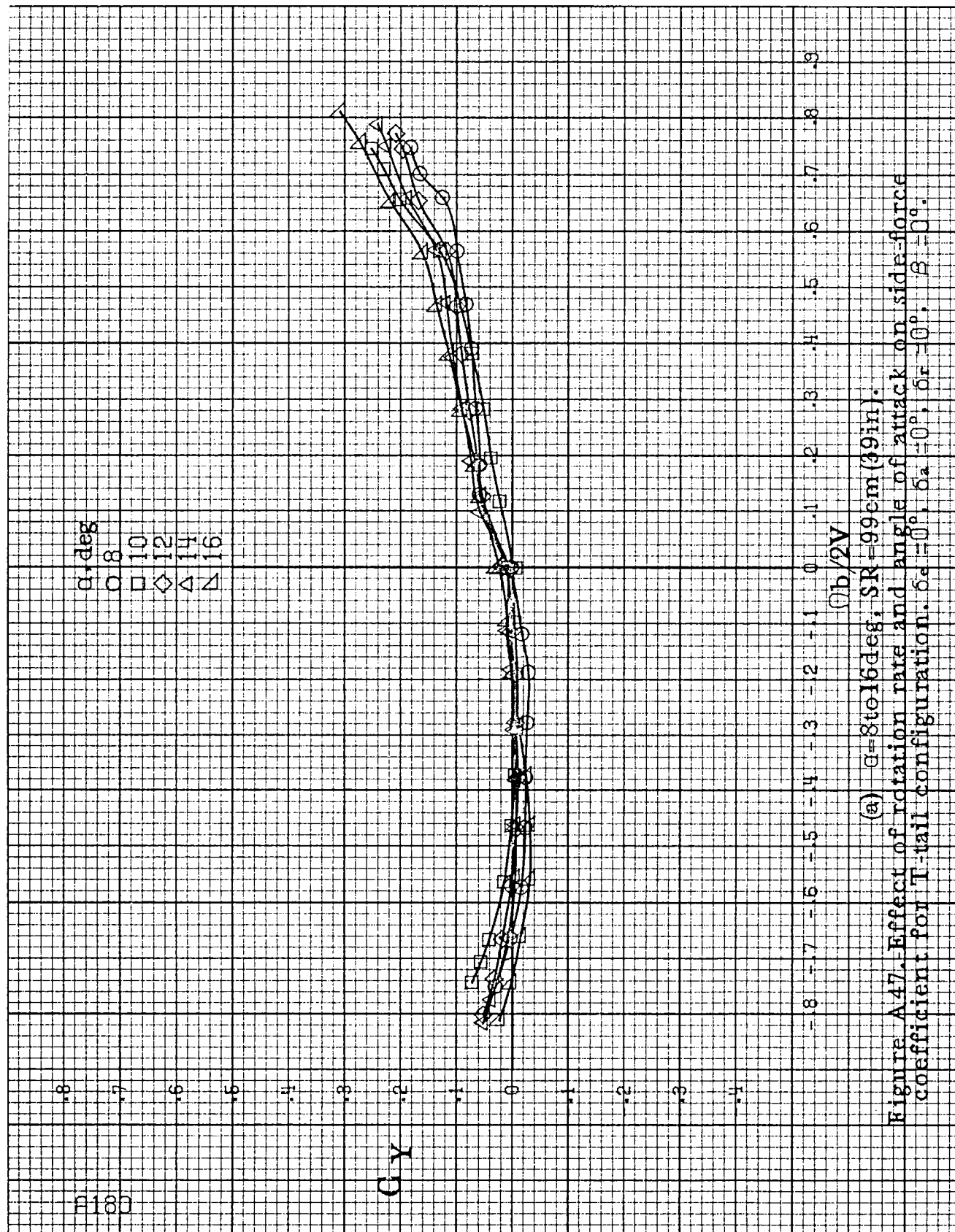


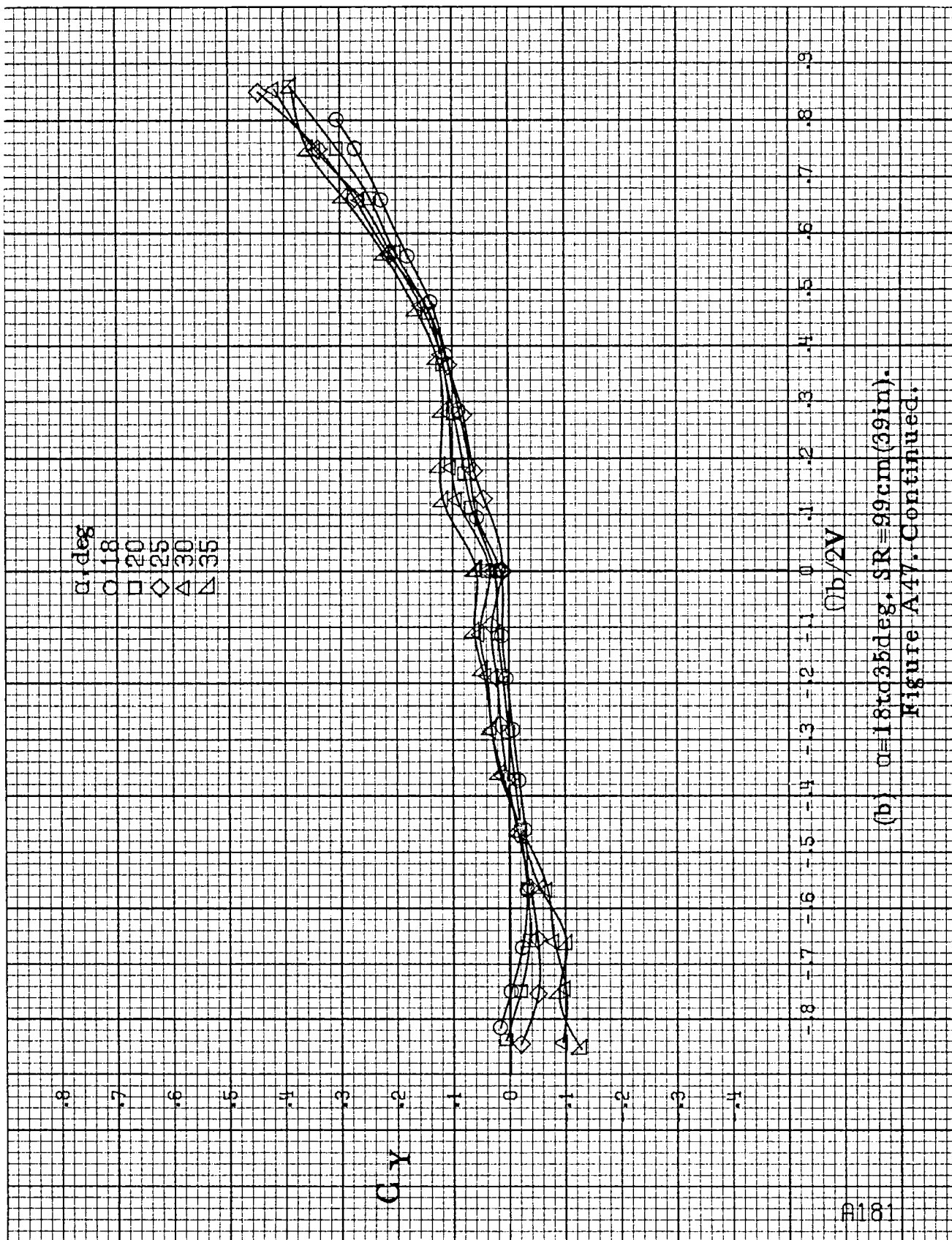


(c)  $\alpha = 30$  to  $50^\circ$ ,  $SR = 0$ .  
Figure A46, Continued.



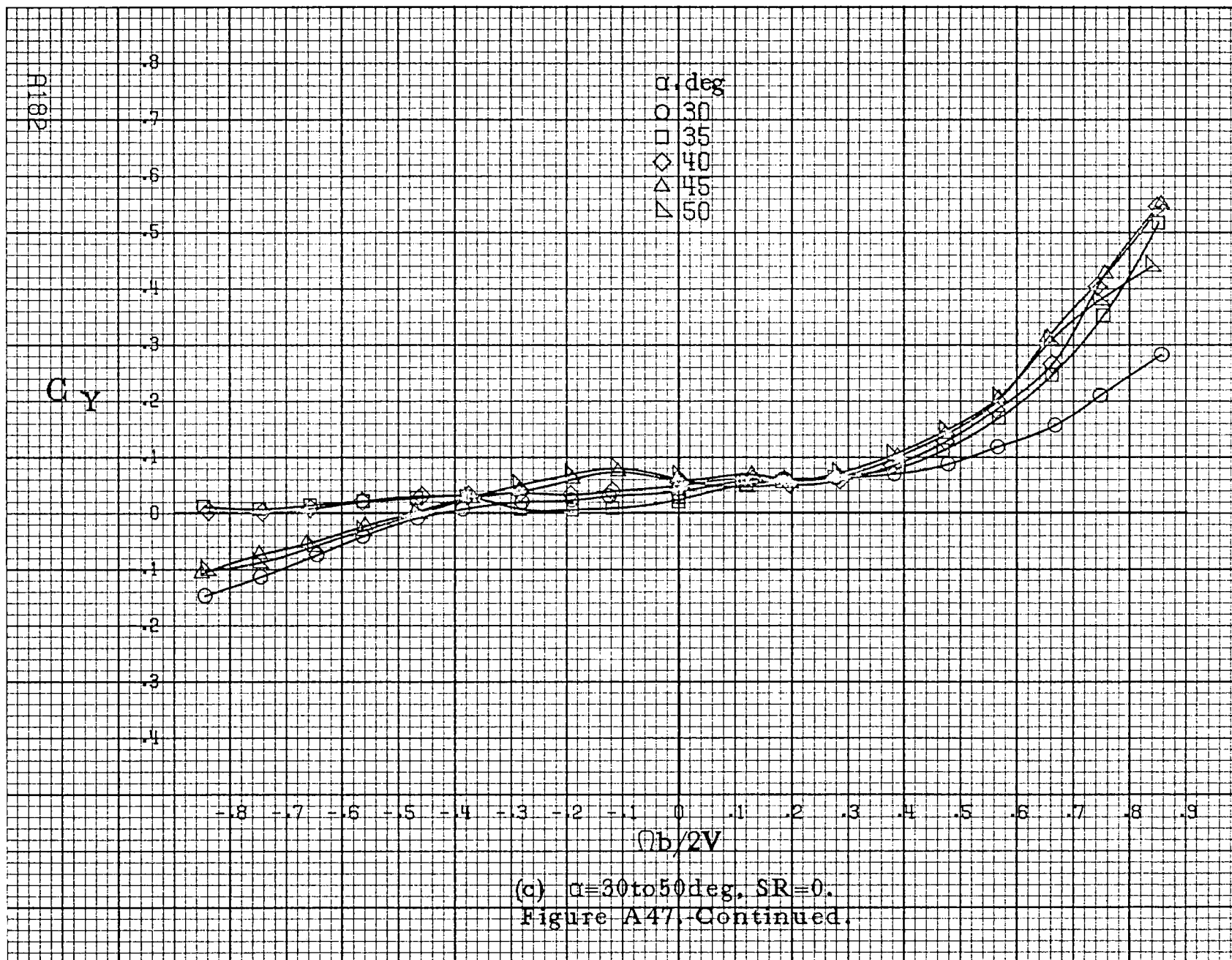


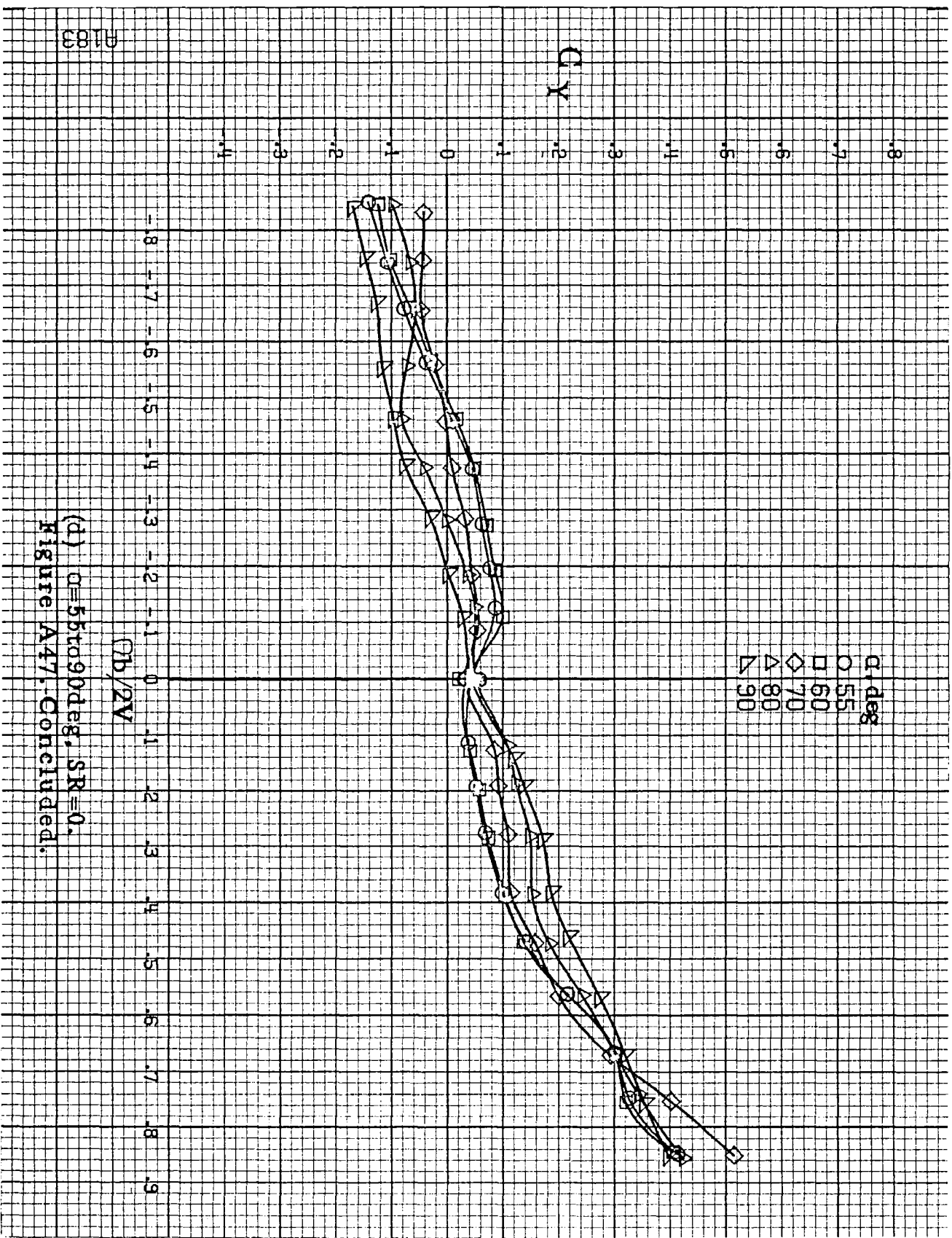




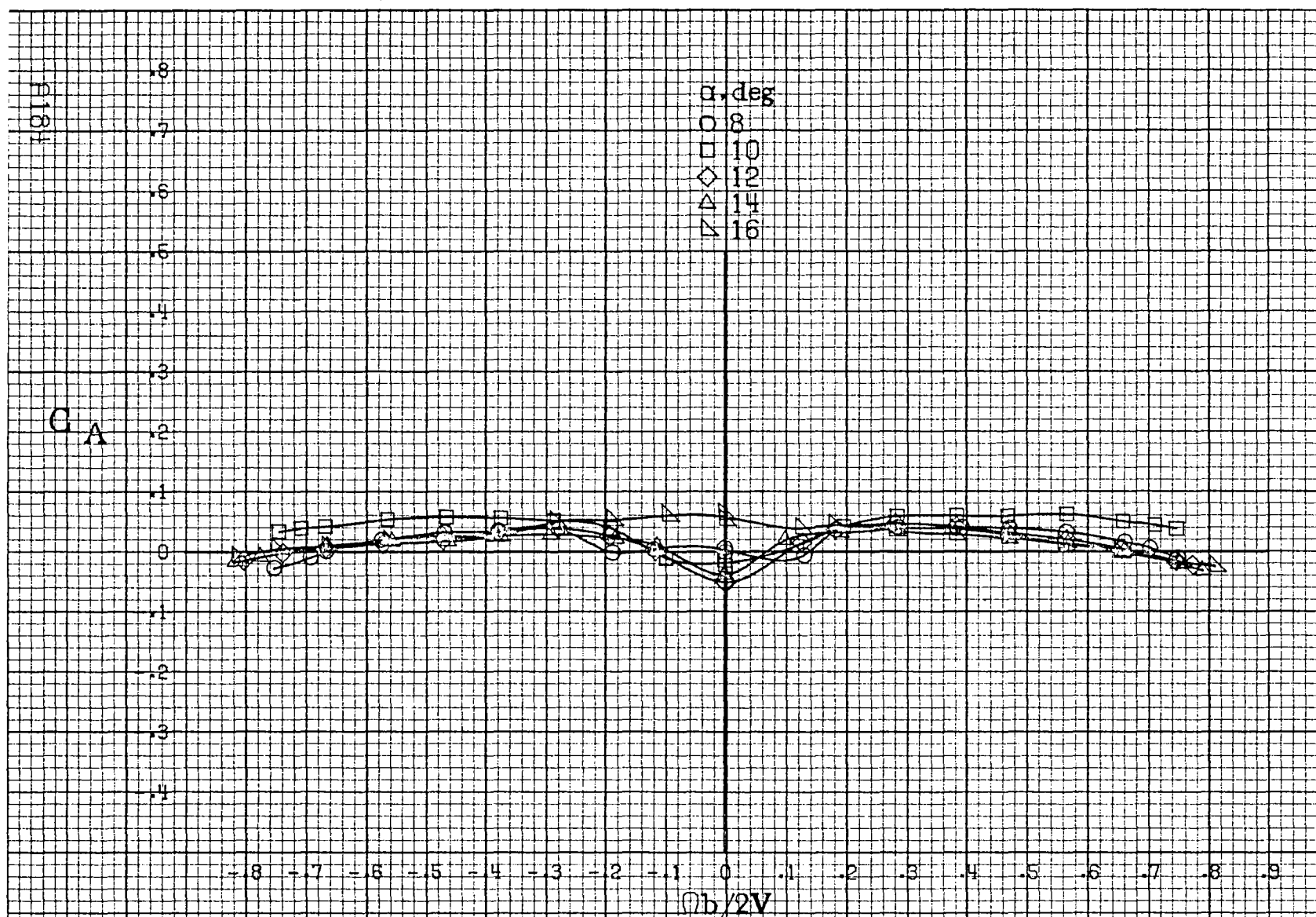
(b)  $\alpha = 18$  to  $35^\circ$ ,  $SR = 99\text{cm}$  (39in).

Figure A47. Continued.



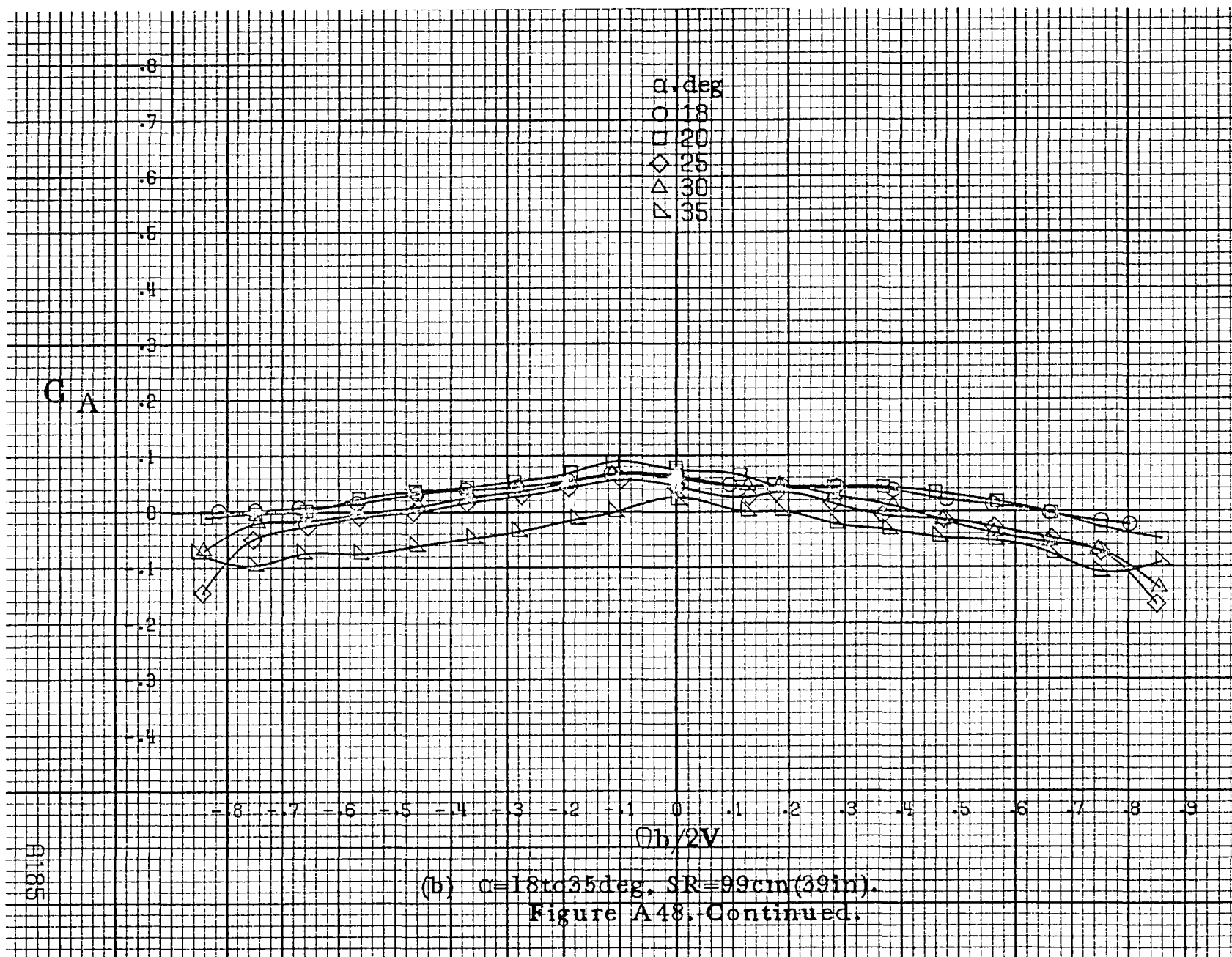


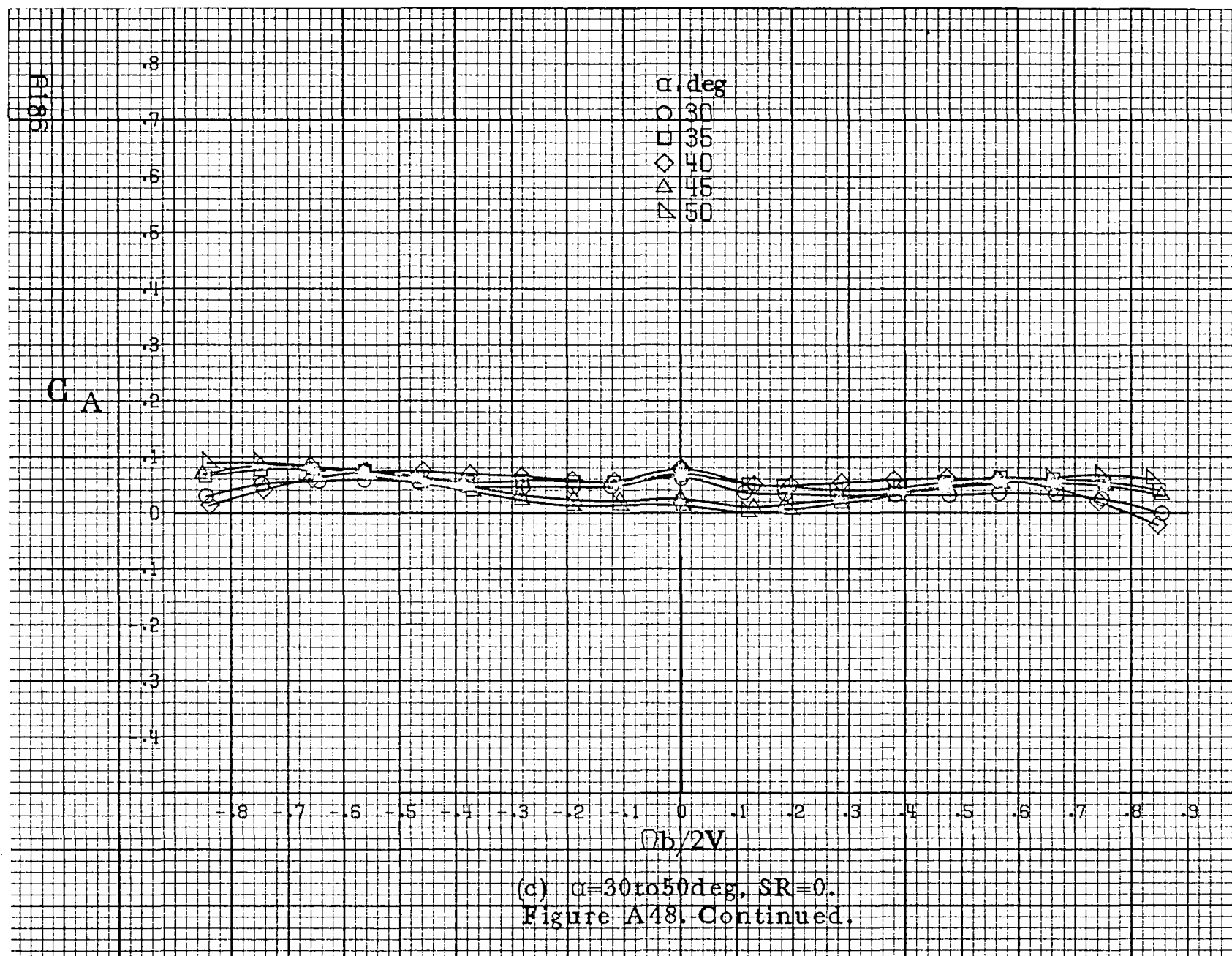
(d)  $\alpha = 55$  to  $90^\circ$ ,  $SR = 0$ .  
Figure A47. Concluded.



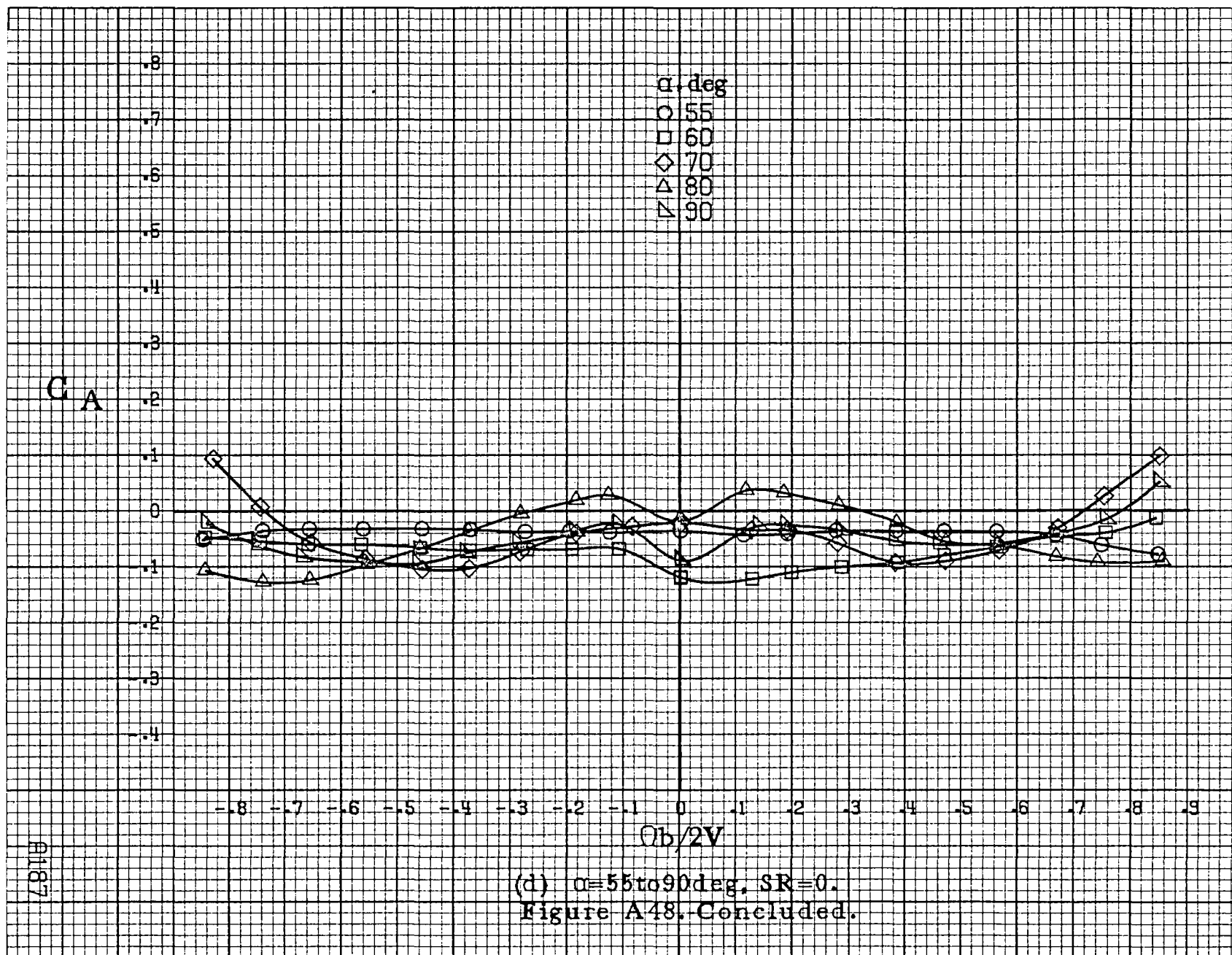
(a)  $\alpha = 8$  to  $16^\circ$ ,  $SR = 99 \text{ cm (39 in.)}$ .

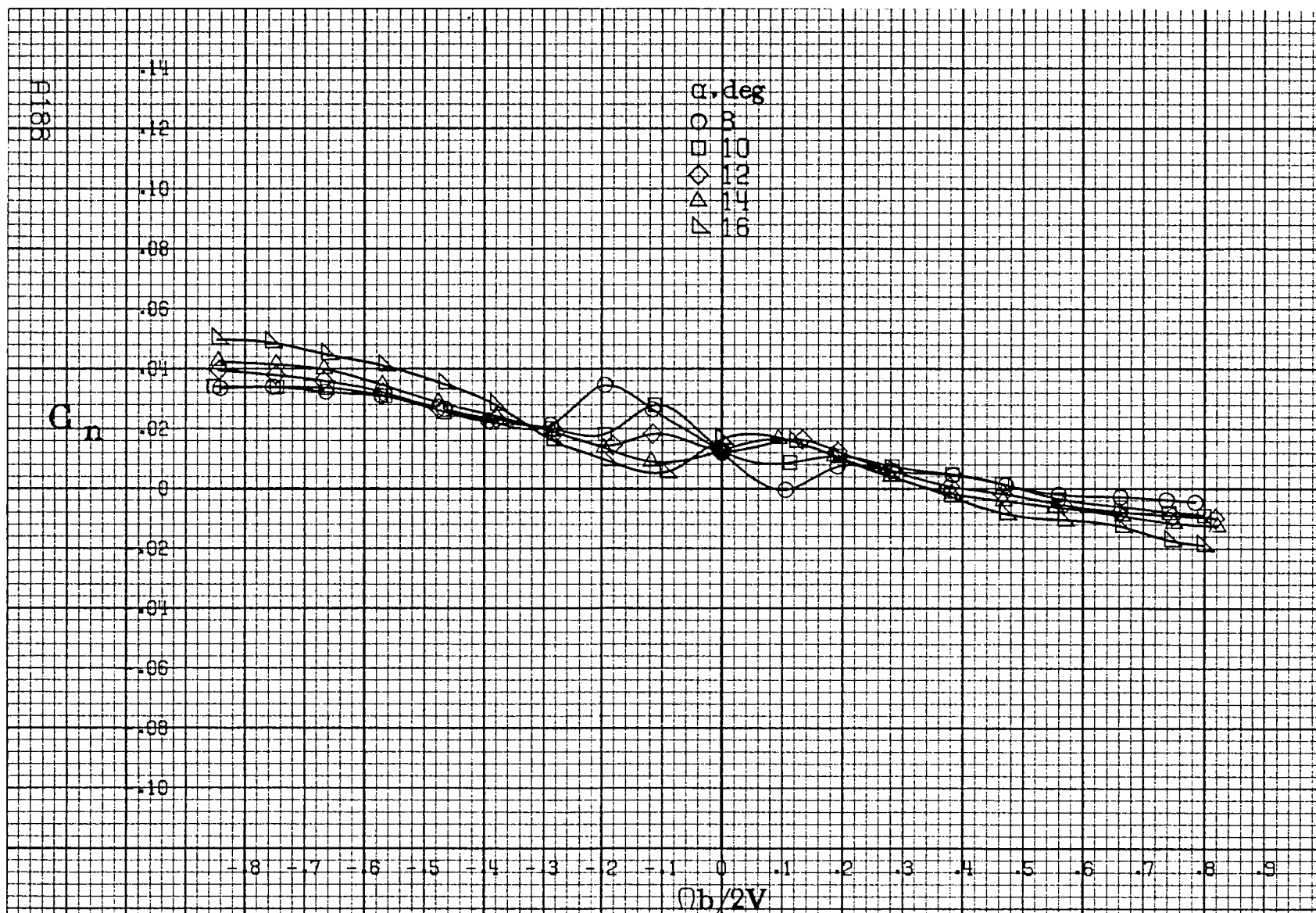
Figure A48. Effect of rotation rate and angle of attack on axial-force coefficient for T-tail configuration.  $\delta_e = 0^\circ$ ,  $\delta_a = 0^\circ$ ,  $\delta_r = 0^\circ$ ,  $\beta = 0^\circ$ .





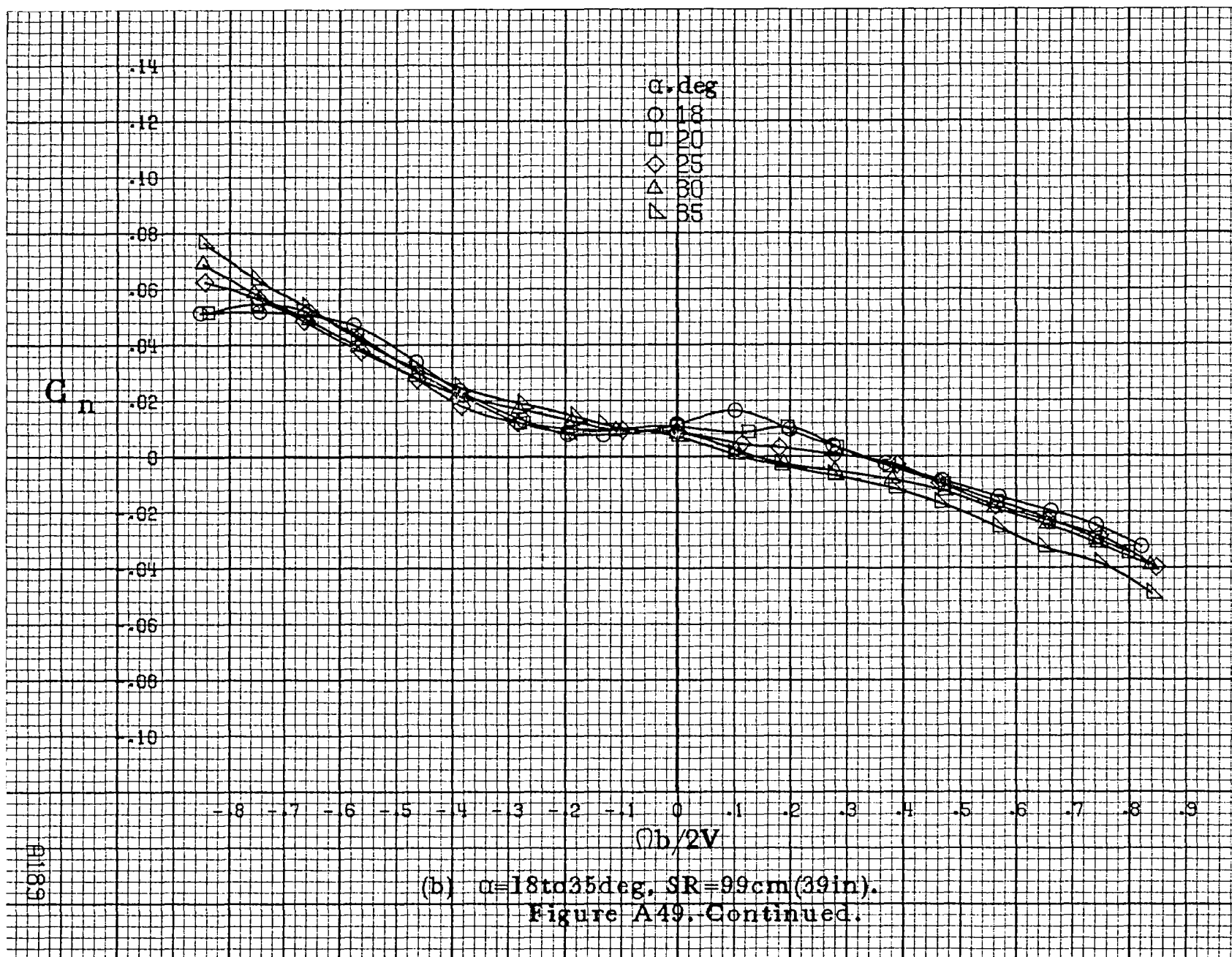


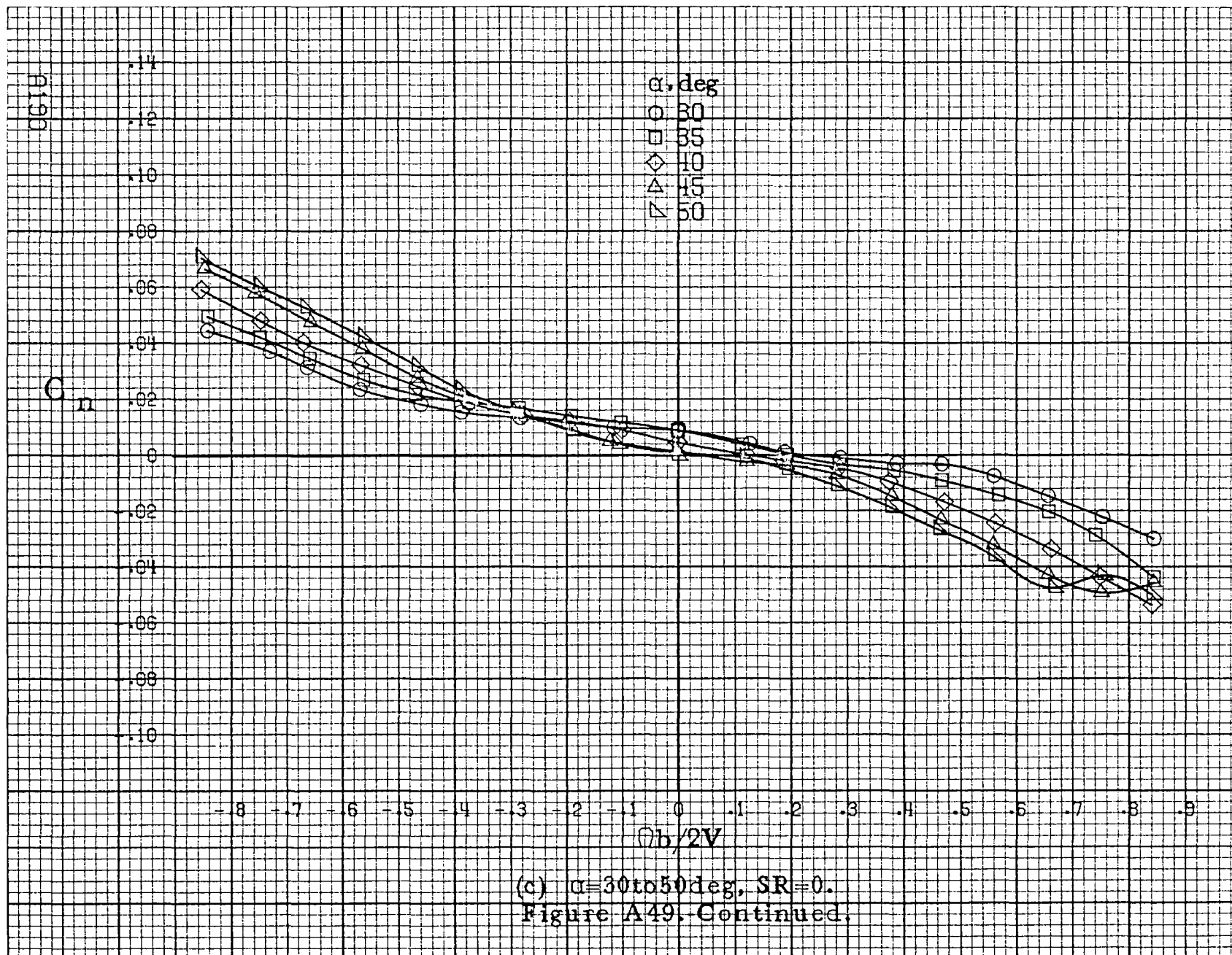


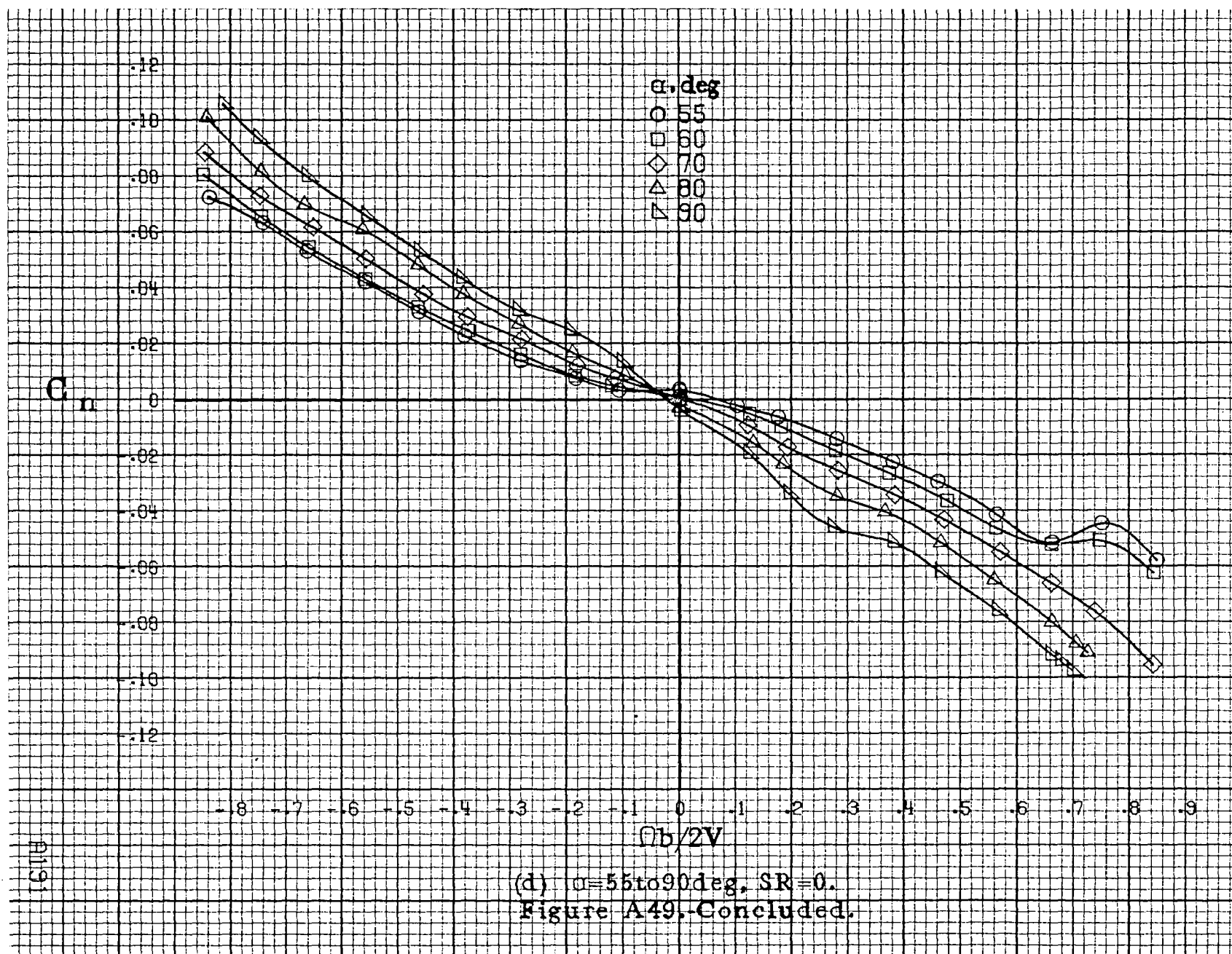


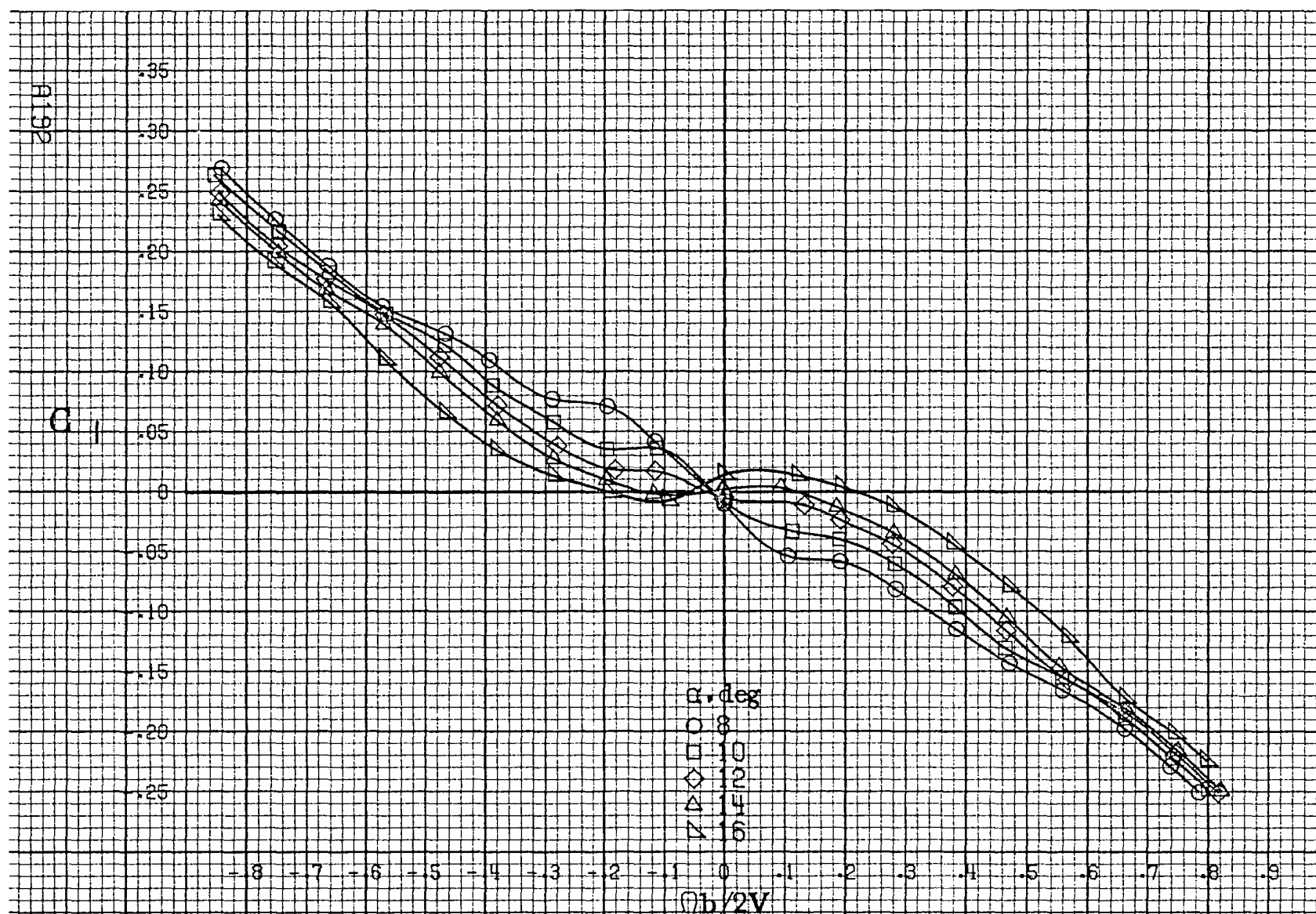
(a)  $\alpha=8$  to  $16^\circ$ ,  $SR=99\text{cm}(39\text{in})$ .

Figure A49. Effect of rotation rate and angle of attack on yawing-moment coefficient for T-tail configuration.  $\delta_e=0^\circ$ ,  $\delta_a=0^\circ$ ,  $\delta_r=-25^\circ$ .  $\beta=0^\circ$ .



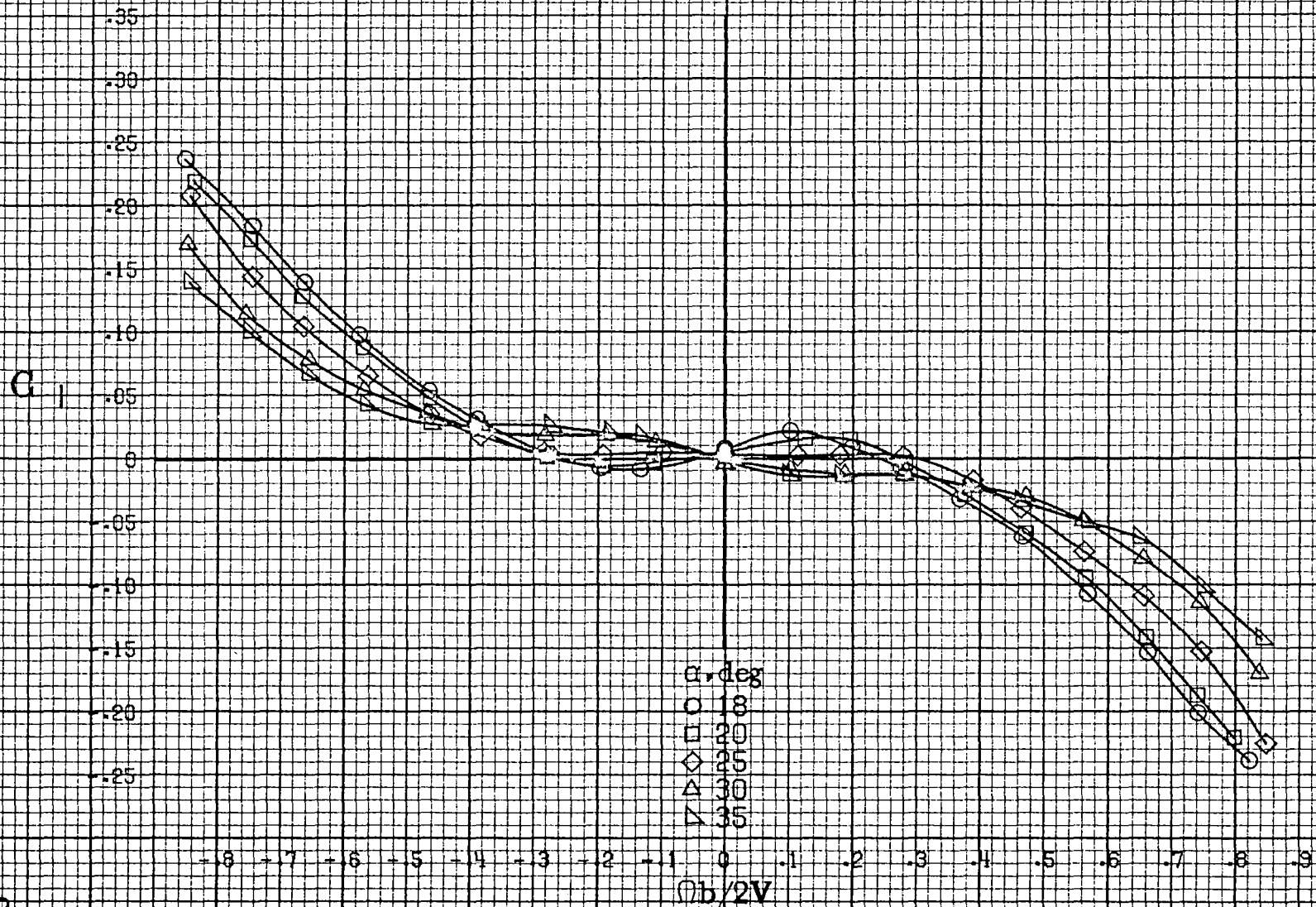






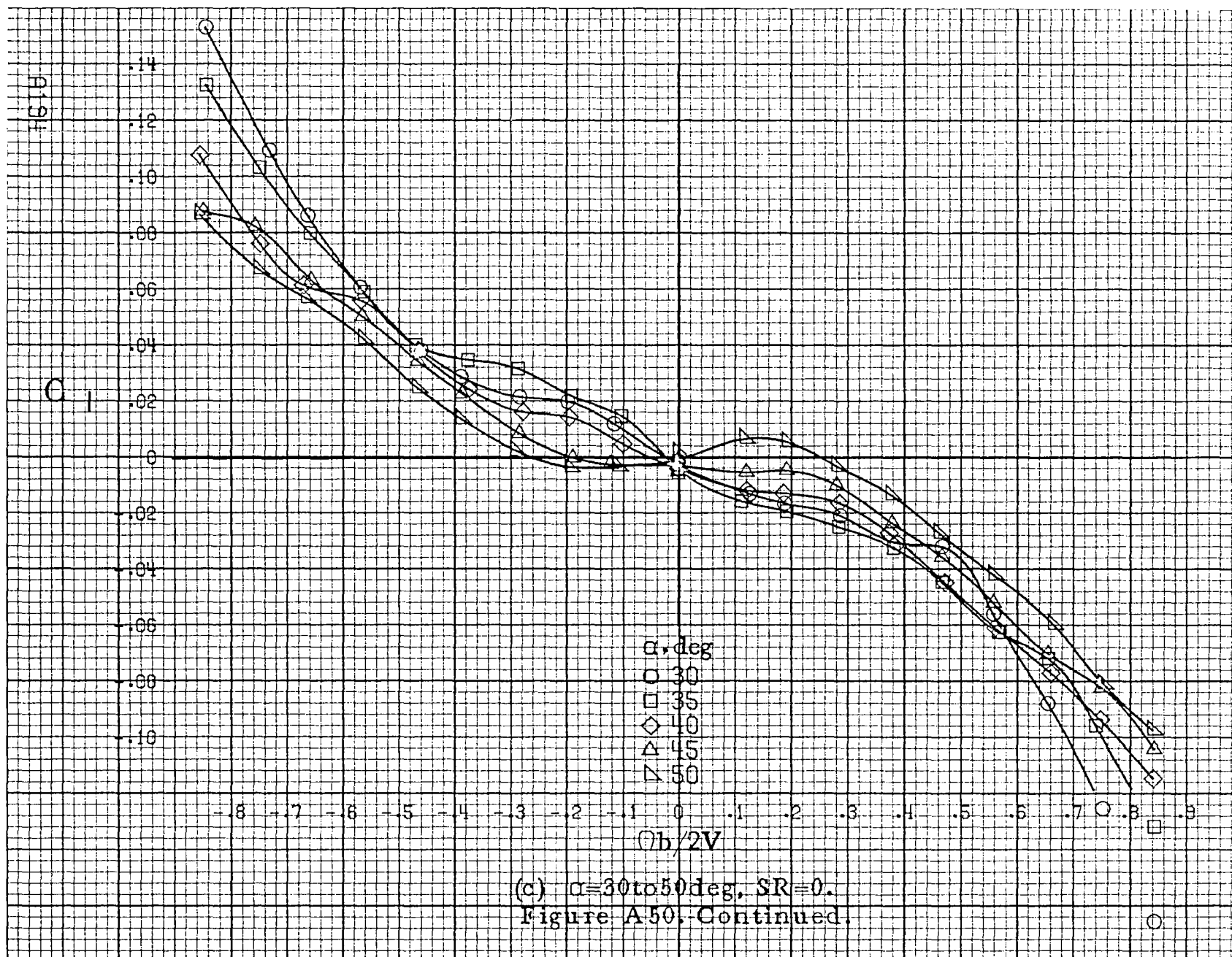
(a)  $\alpha = 8 \text{ to } 16 \text{ deg}$ ,  $SR = 99 \text{ cm (39 in)}$ .

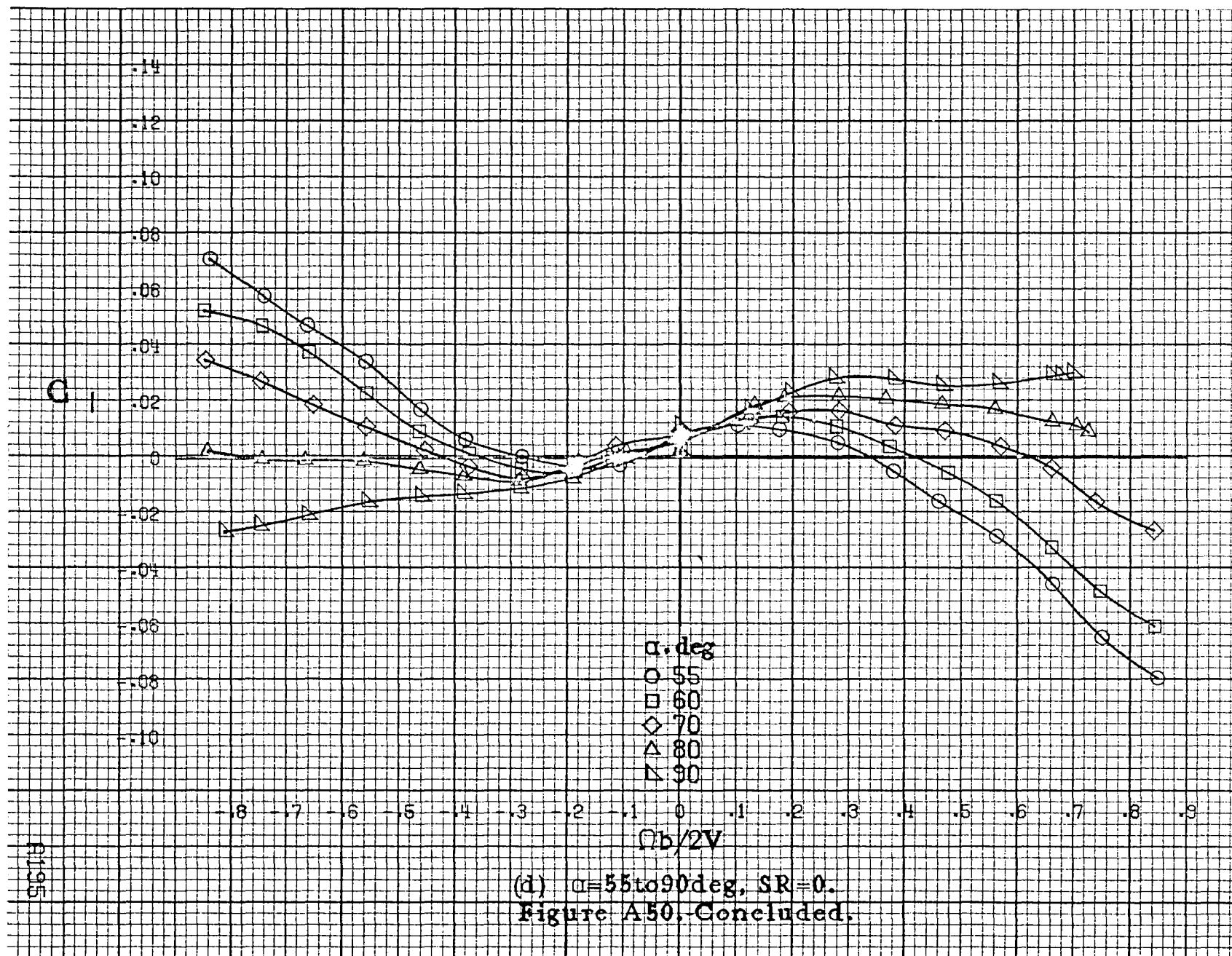
Figure A50. Effect of rotation rate and angle of attack on rolling-moment coefficient for T-tail configuration.  $\delta a = 0^\circ$ ,  $\delta a = 0^\circ$ ,  $\delta r = -25^\circ$ ,  $\beta = 0^\circ$ .

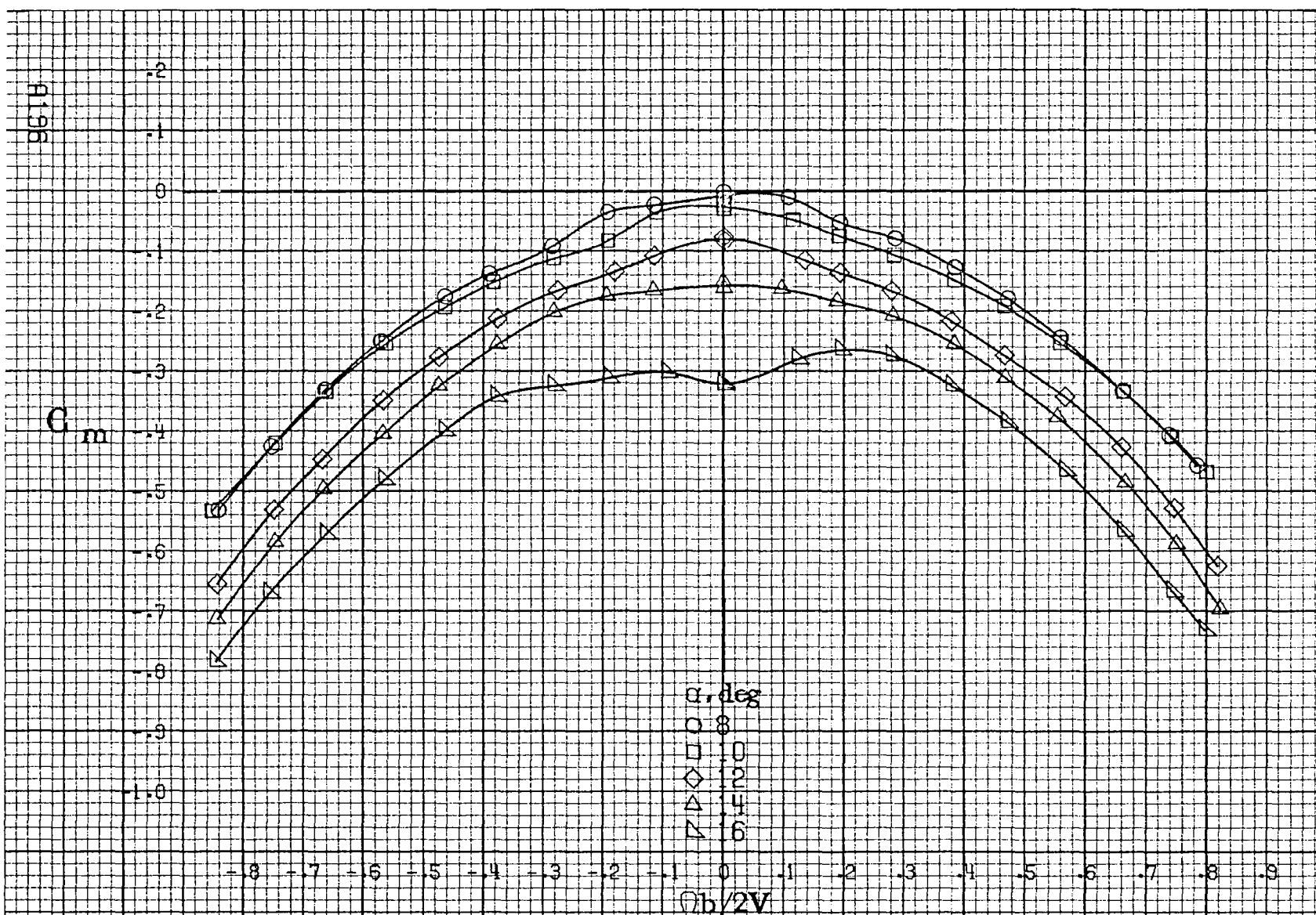


(b)  $\alpha=18$  to  $35$  deg,  $SR=99$  cm (39 in).  
Figure A50. Continued.



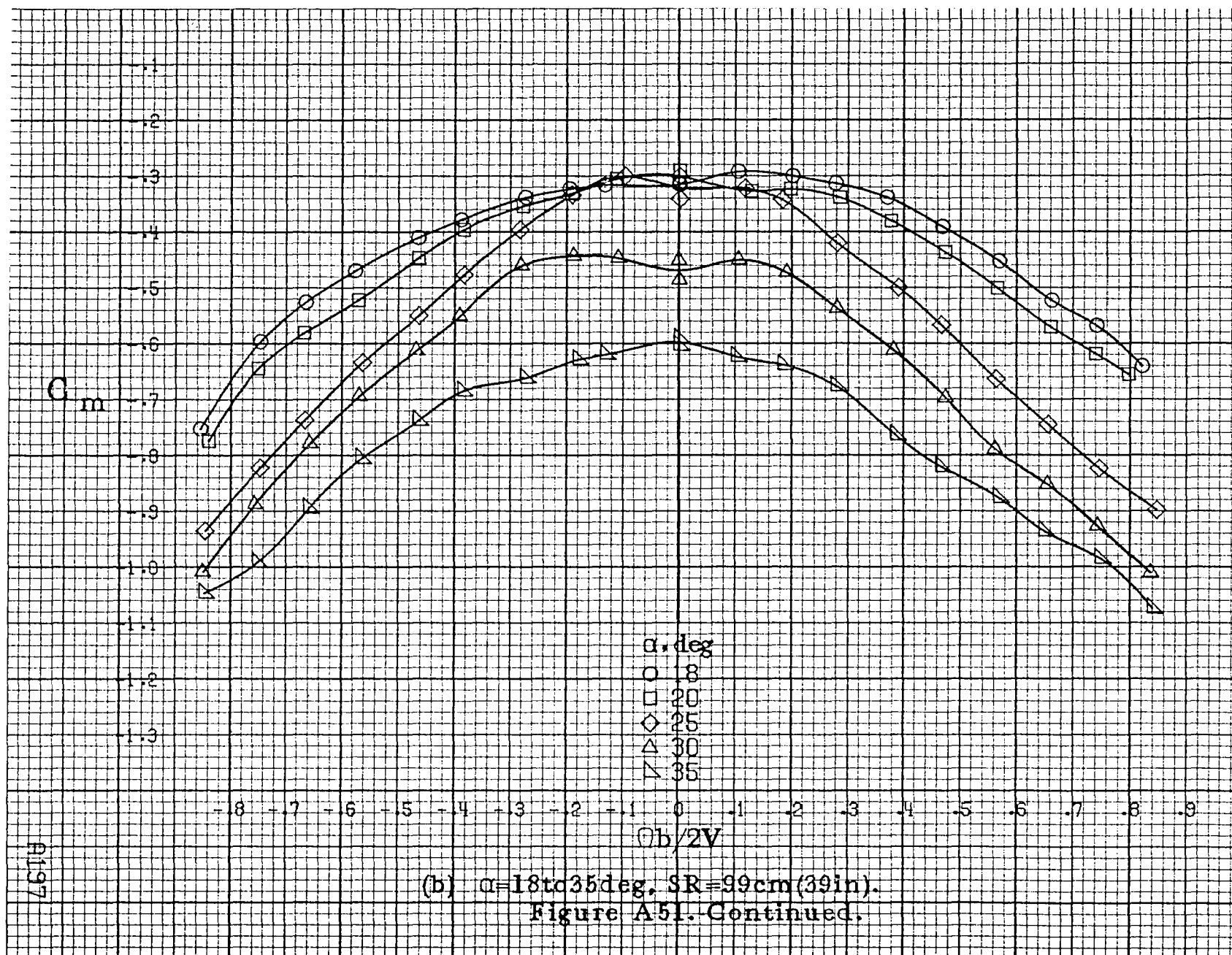


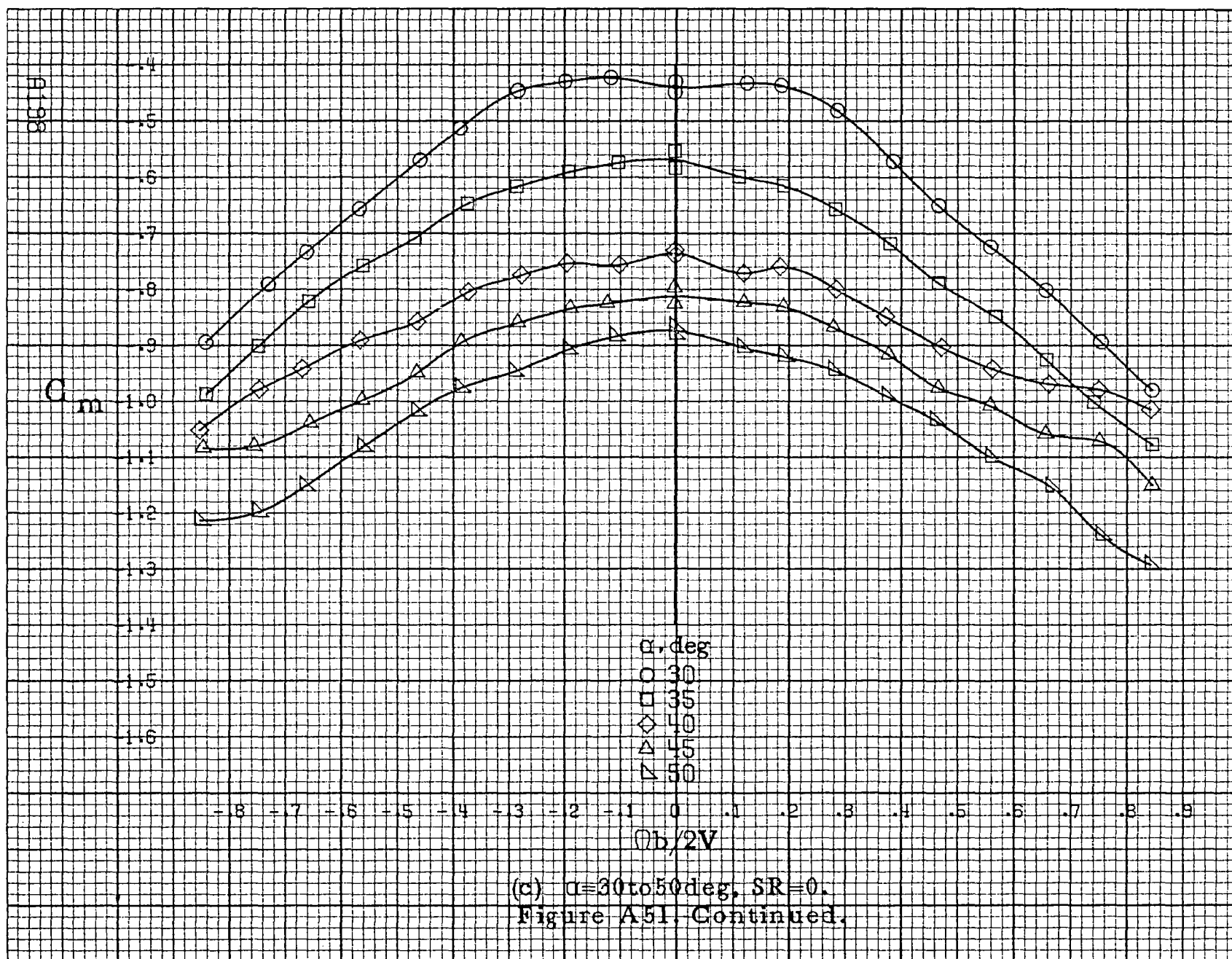




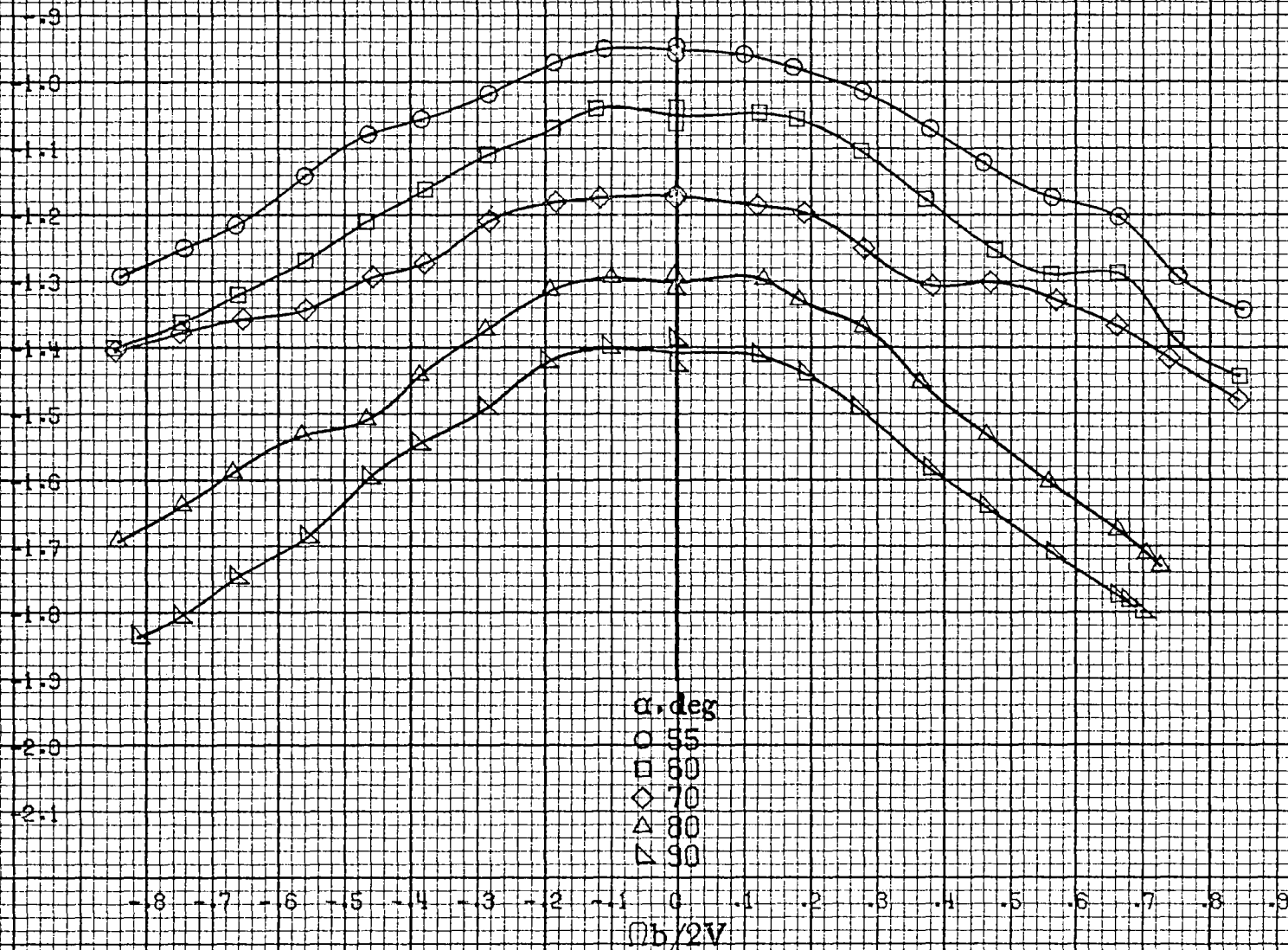
(a)  $\alpha = 8$  to  $16^\circ$ ,  $SR = 99\text{cm}$  (39 in).

Figure A51. Effect of rotation rate and angle of attack on pitching-moment coefficient for T-tail configuration.  $\delta a = 0^\circ$ ,  $\delta a = 0^\circ$ ,  $\delta r = -25^\circ$ ,  $\beta = 0^\circ$ .



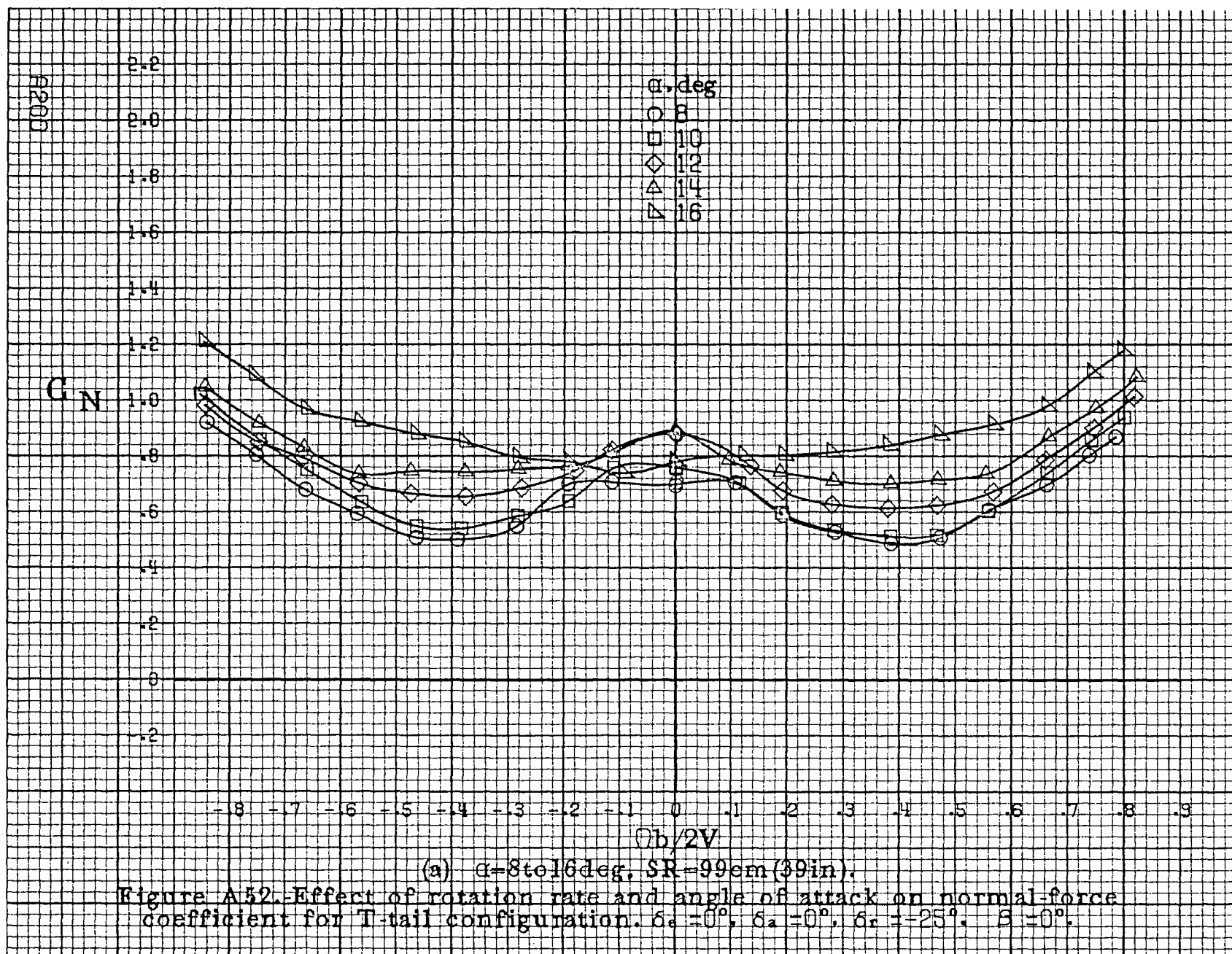


$C_m$

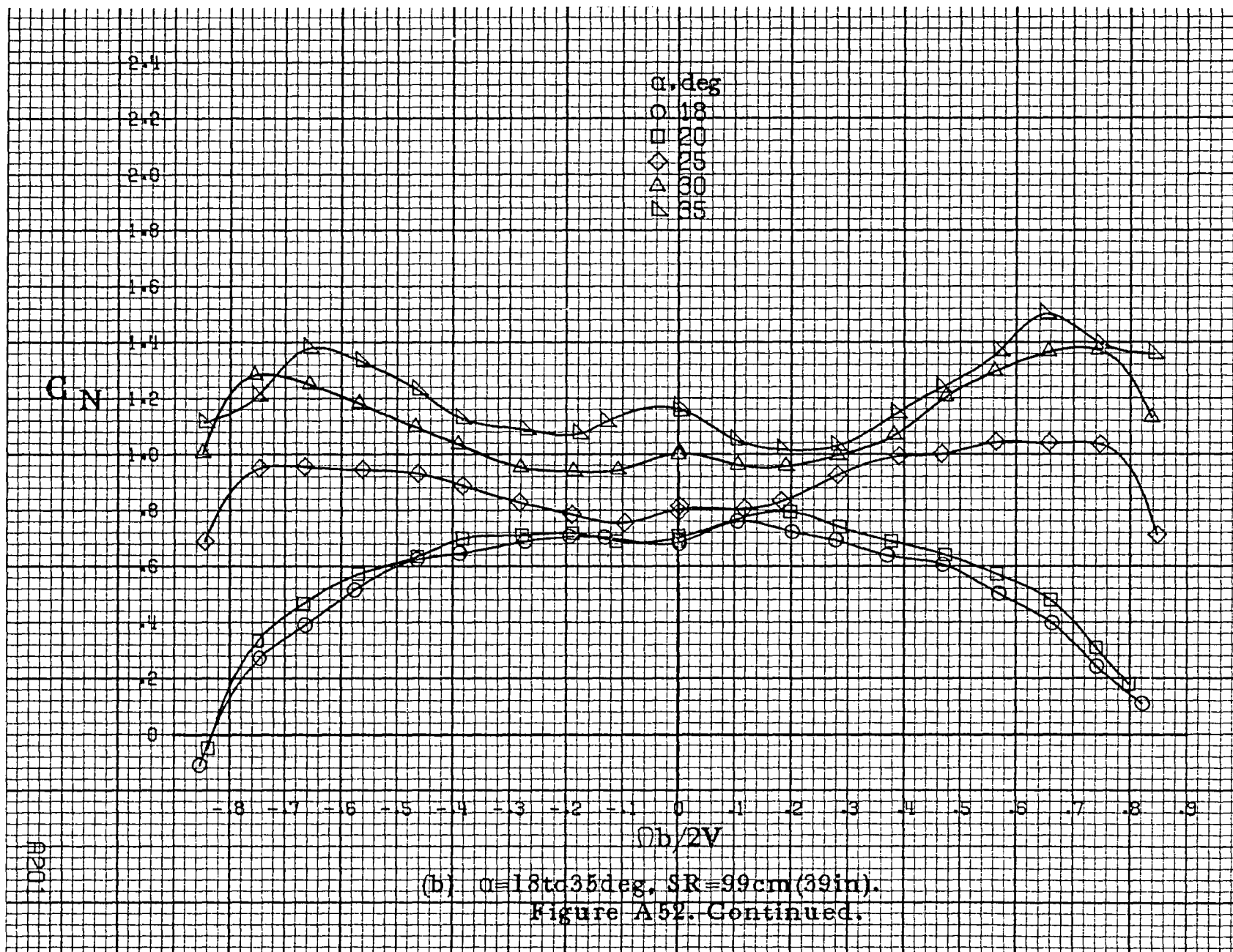


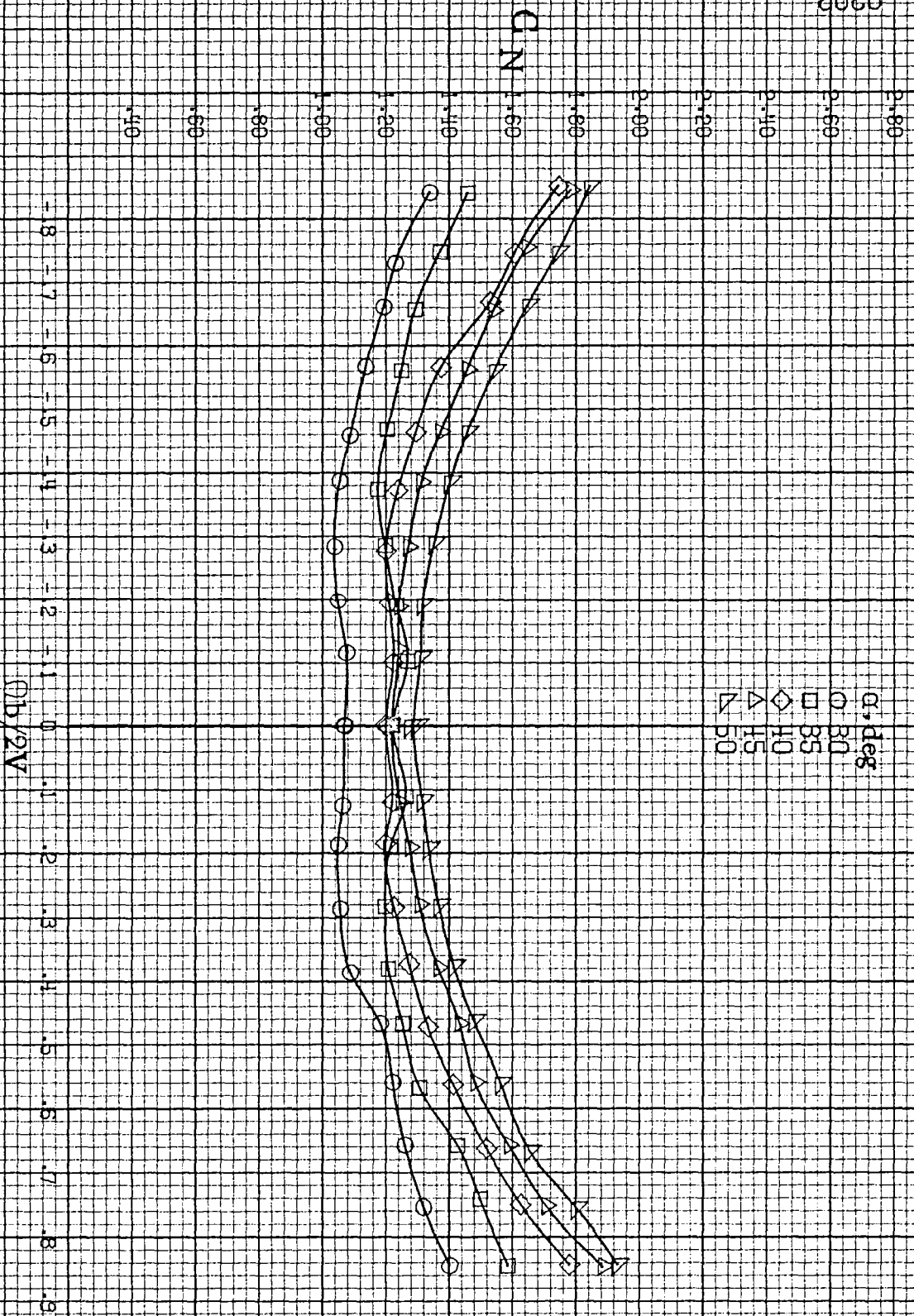
(d)  $\alpha = 55$  to  $90^\circ$ ,  $SR = 0$ .  
Figure A51. Concluded.



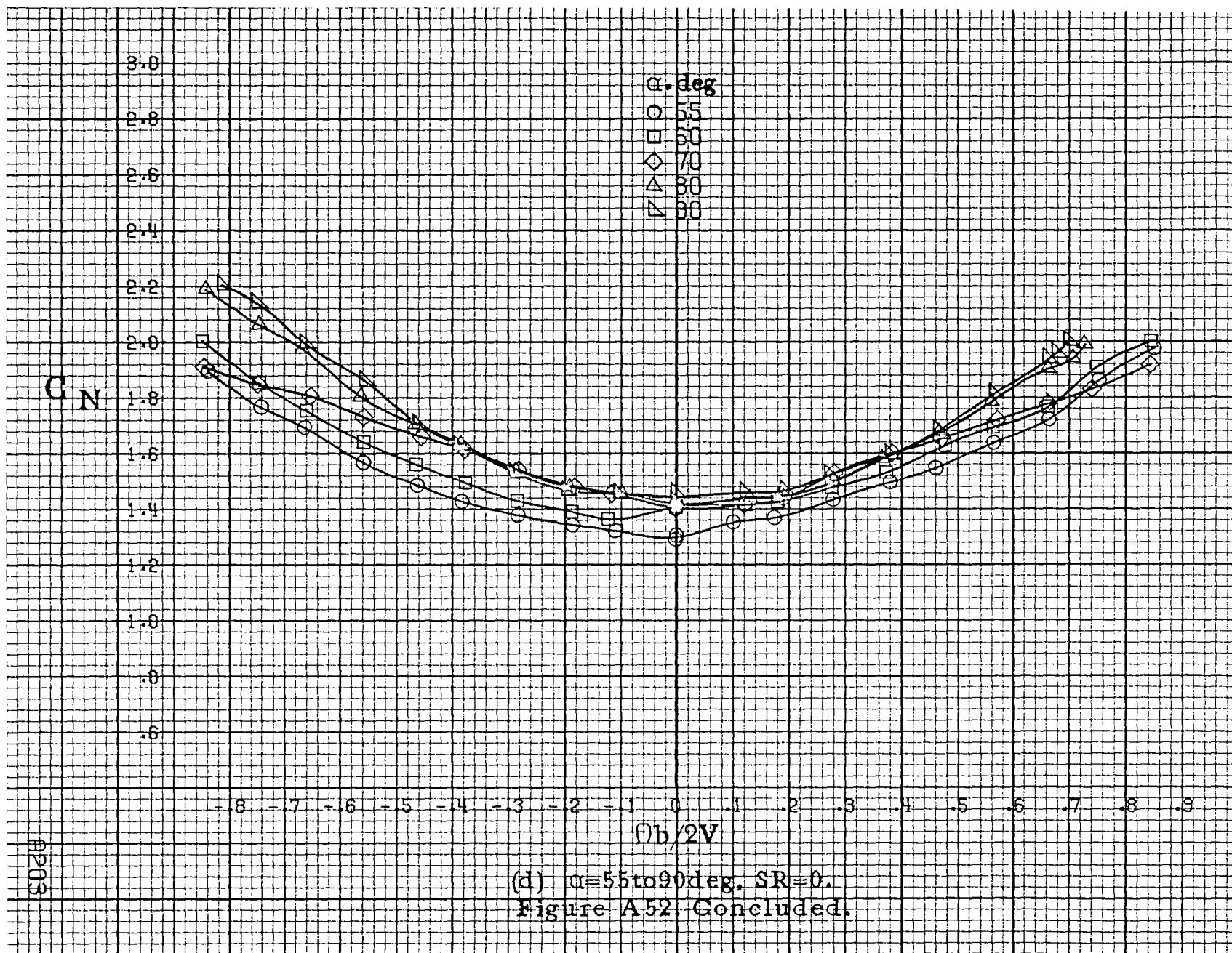


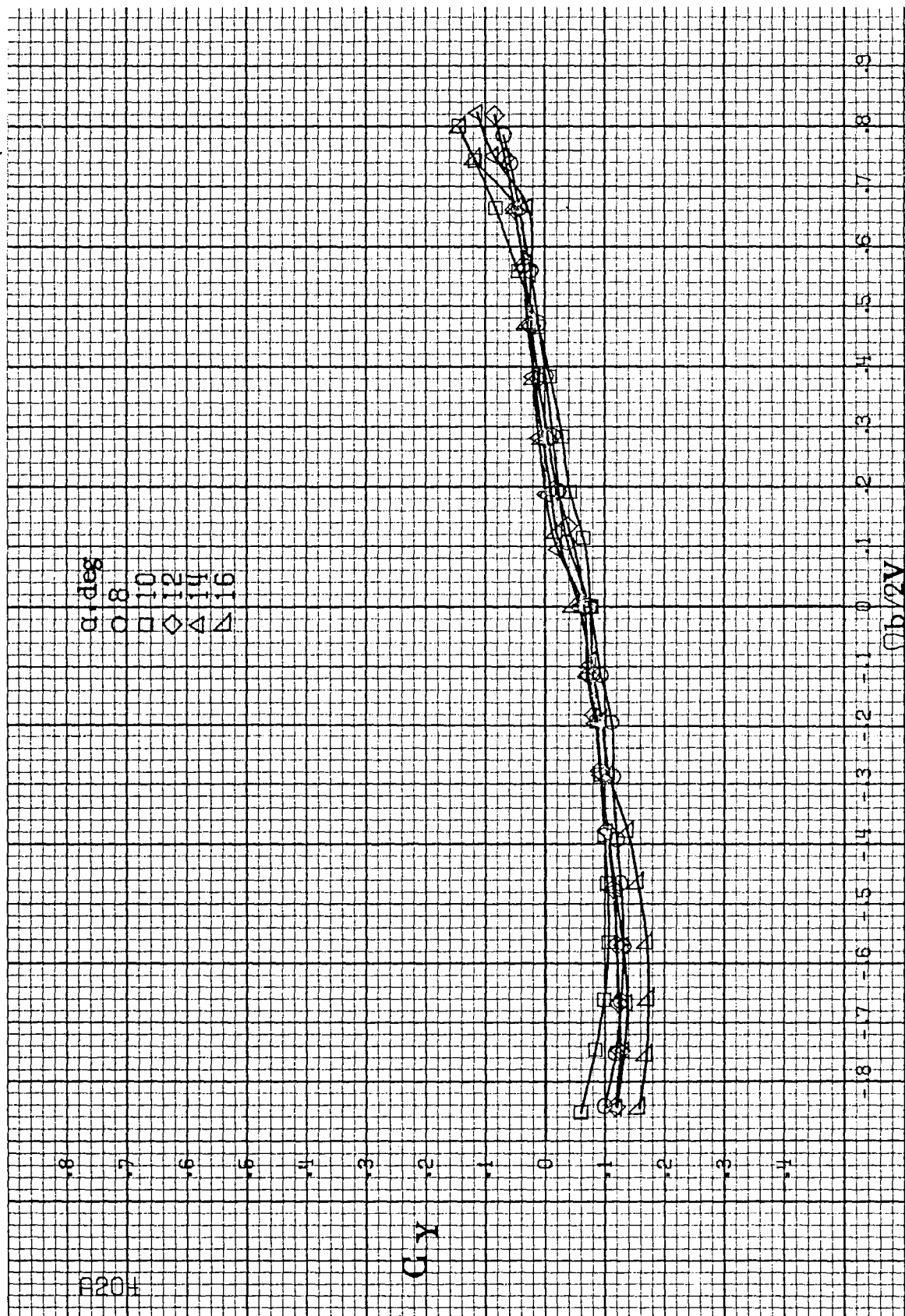




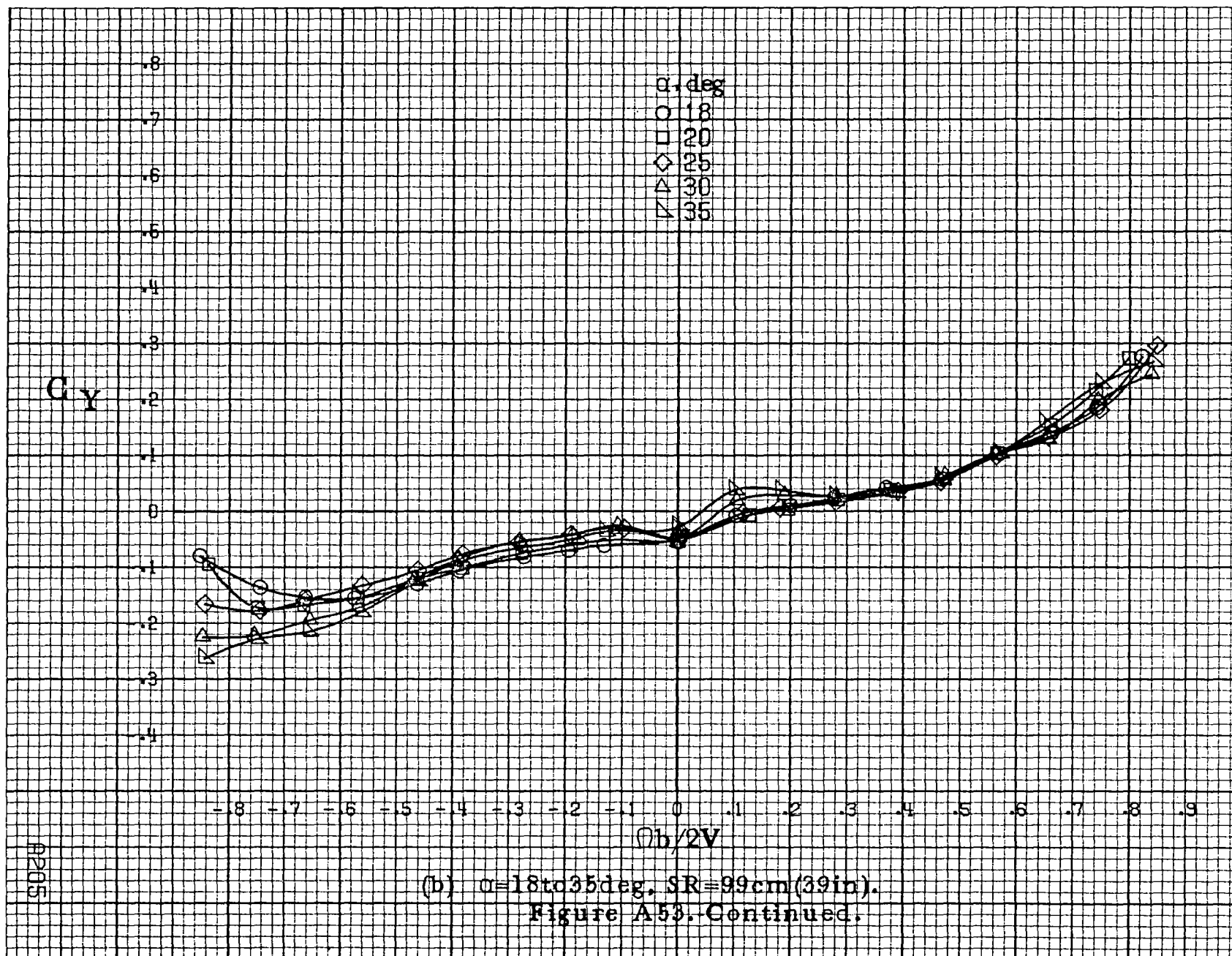


(d)  $\alpha = 30$  to  $50$  deg,  $SR = 0$ .  
Figure A52, Continued.

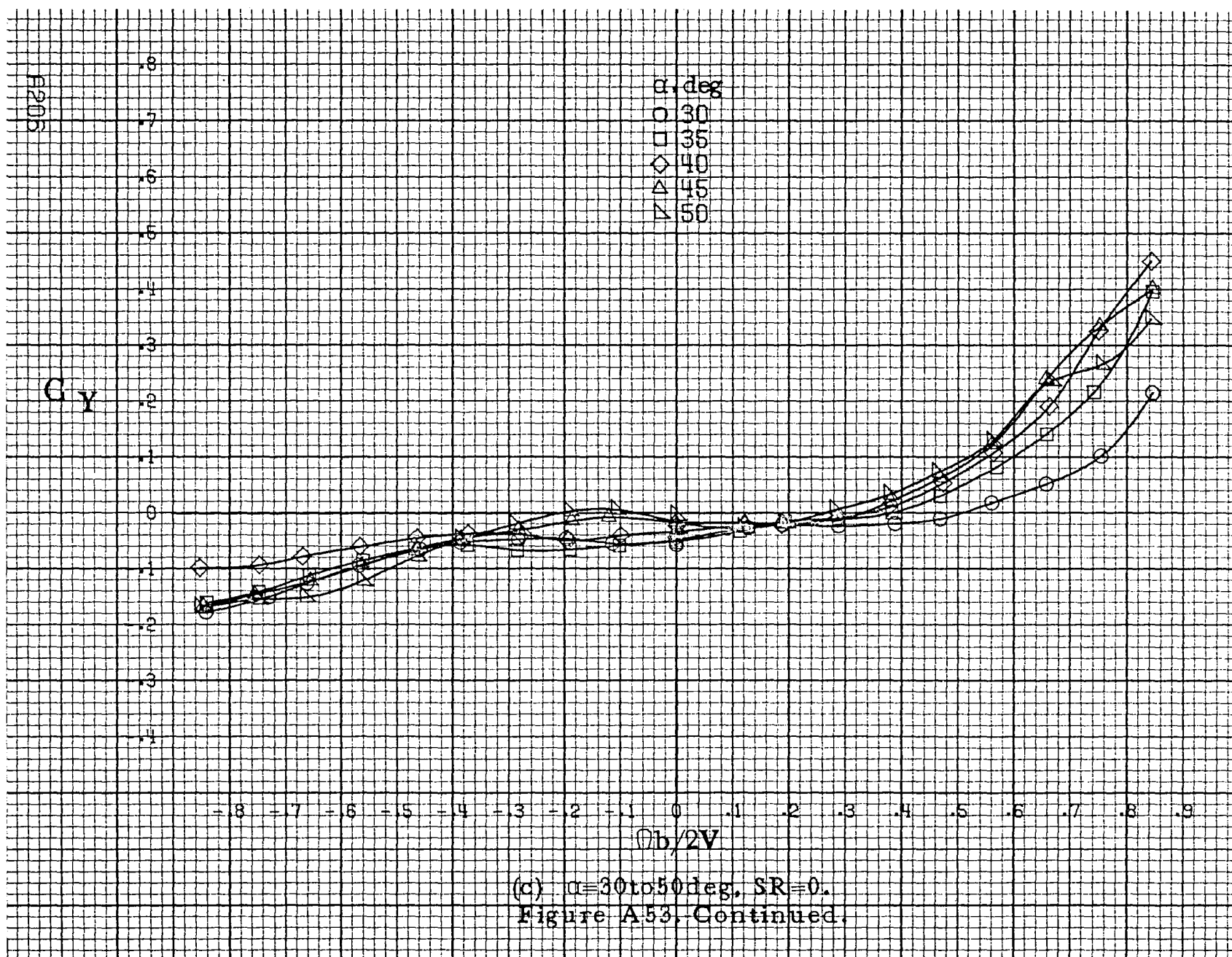




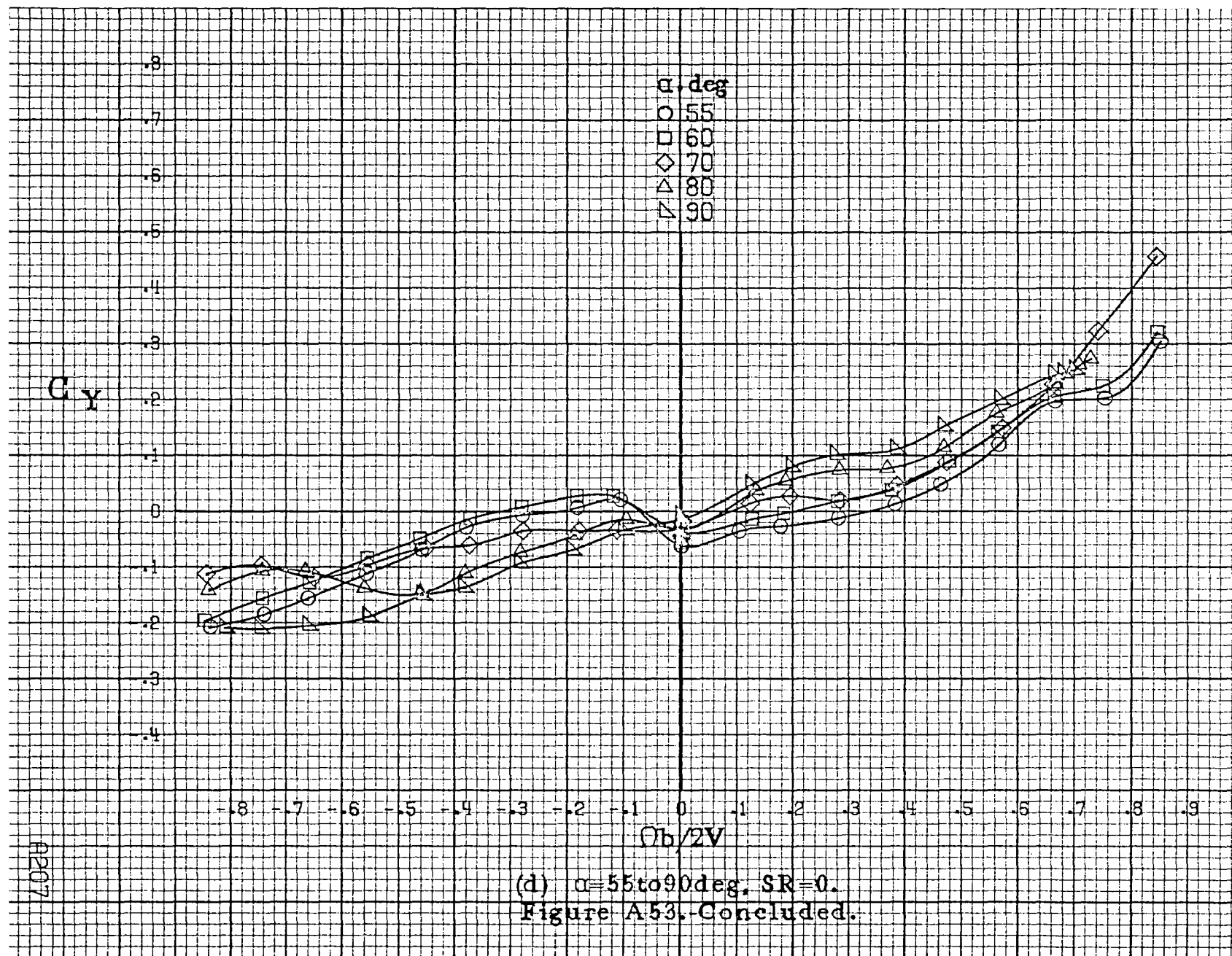
(a)  $\alpha = 8$  to  $16$  deg,  $SR = 99$  cm (39 in).  
 Figure A53. Effect of rotation rate and angle of attack on side-force coefficient for T-tail configuration.  $\delta_a = 0^\circ$ ,  $\delta_r = 25^\circ$ ,  $\beta = 0^\circ$ .



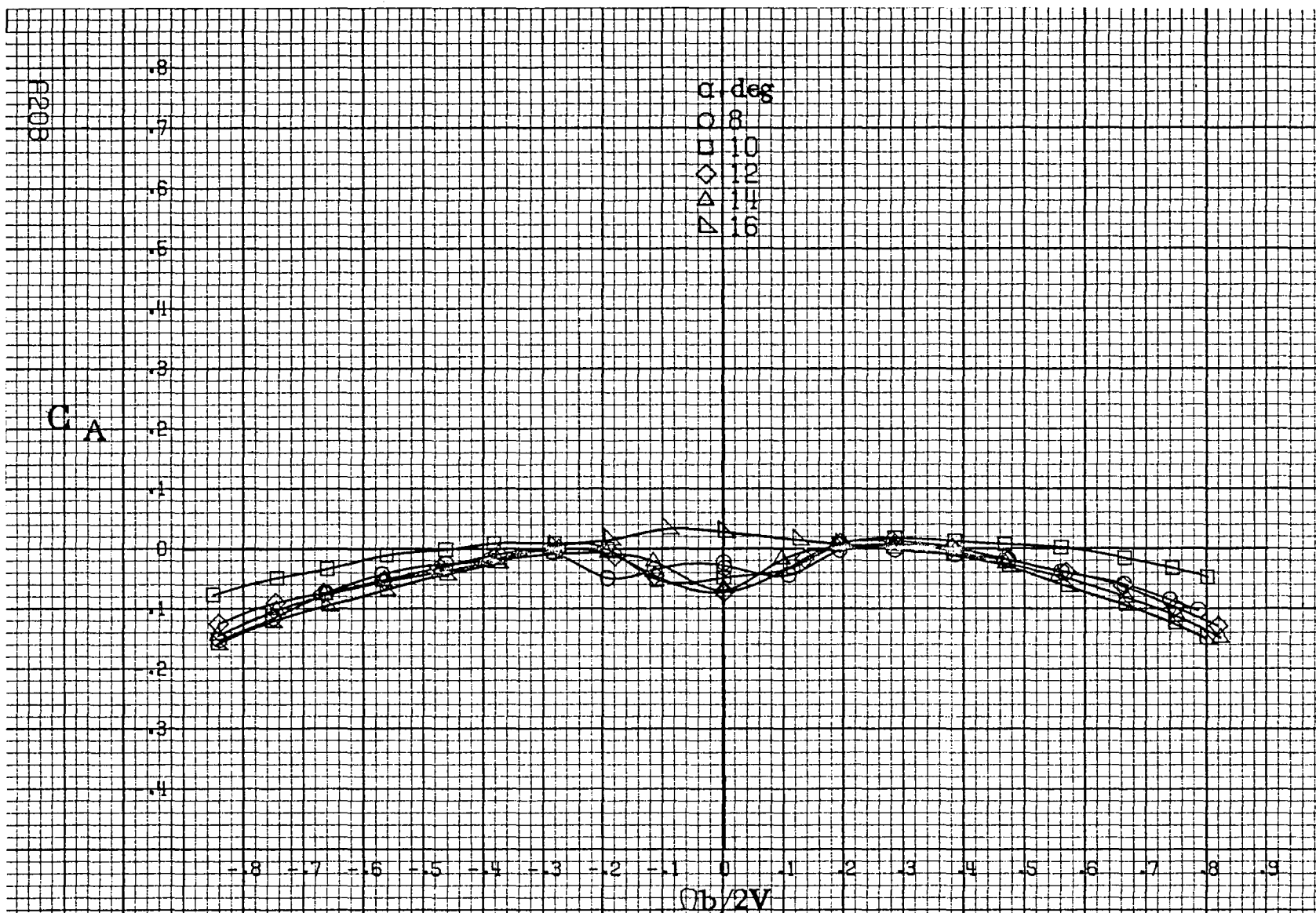
(b)  $\alpha=18$  to  $35^\circ$ ,  $SR=99\text{cm}(39\text{in})$ .  
Figure A53. Continued.











(a)  $\alpha=8$  to  $16^\circ$ ,  $SR=99\text{cm}(39\text{in})$ .

Figure A54. Effect of rotation rate and angle of attack on axial force coefficient for T-tail configuration.  $\delta_a = 0^\circ$ ,  $\delta_e = 0^\circ$ ,  $\delta_r = -25^\circ$ ,  $\delta = 0^\circ$ .

$C_A$

$\alpha, \text{deg}$   
 ○ 18  
 □ 20  
 ◇ 25  
 △ 30  
 ▽ 35

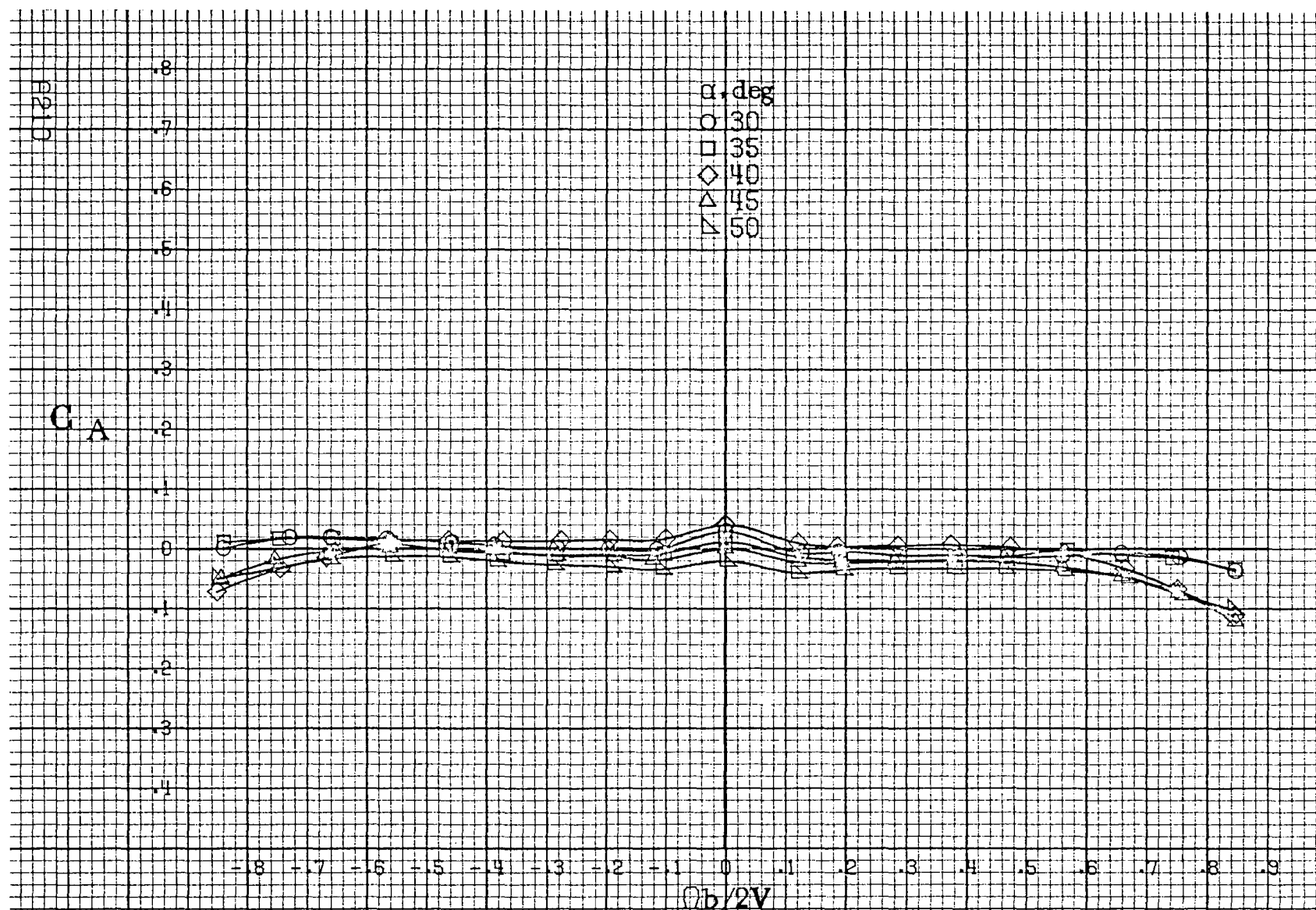
.8  
.7  
.6  
.5  
.4  
.3  
.2  
.1  
0  
-1  
-2  
-3  
-4

-0.8 -0.7 -0.6 -0.5 -0.4 -0.3 -0.2 -0.1 0 0.1 0.2 0.3 0.4 0.5 0.6 0.7 0.8 0.9

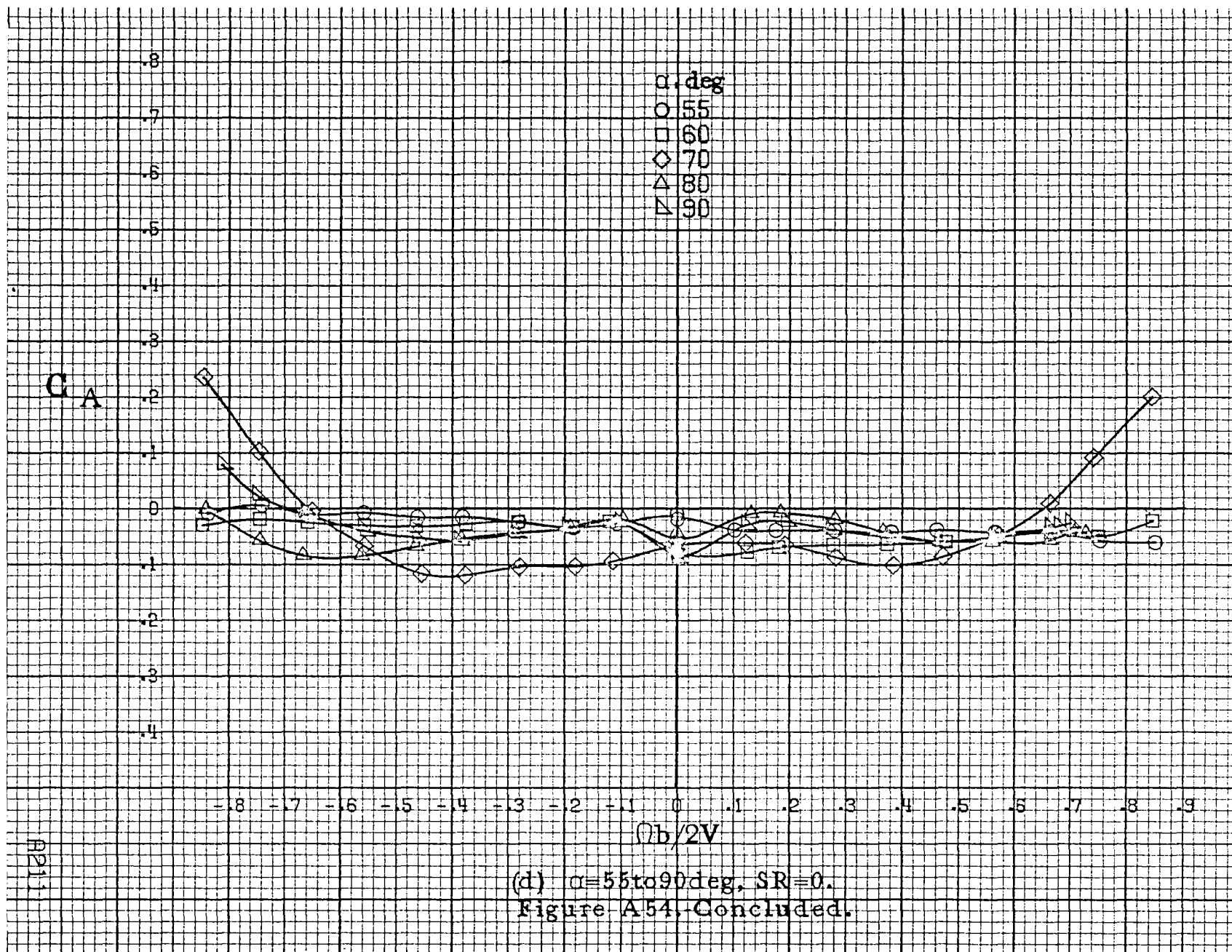
$Ob/2V$

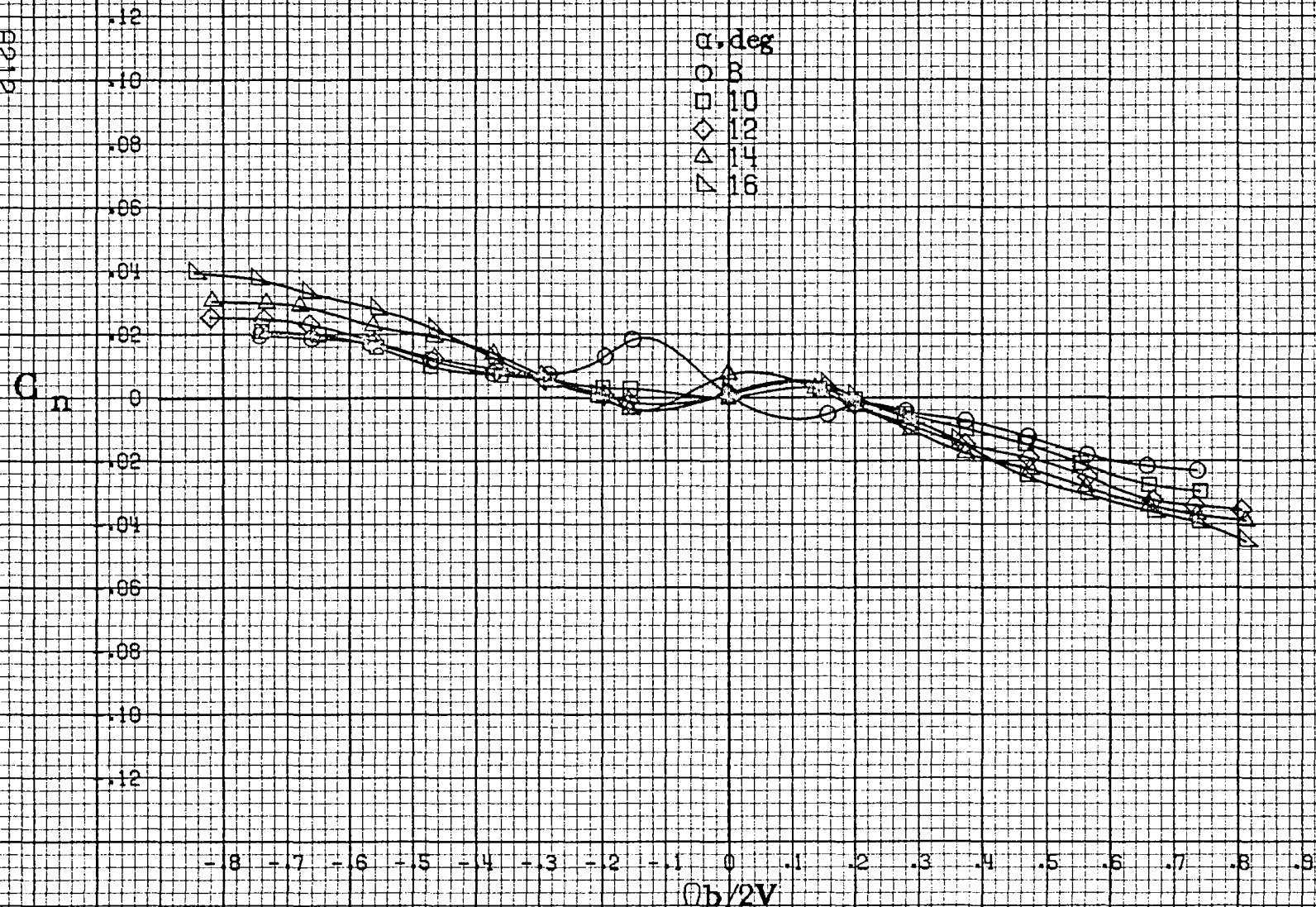
(b)  $\alpha=18$  to  $35$  deg,  $SR=99\text{cm}(39\text{in})$ .  
 Figure A54. Continued.

A209



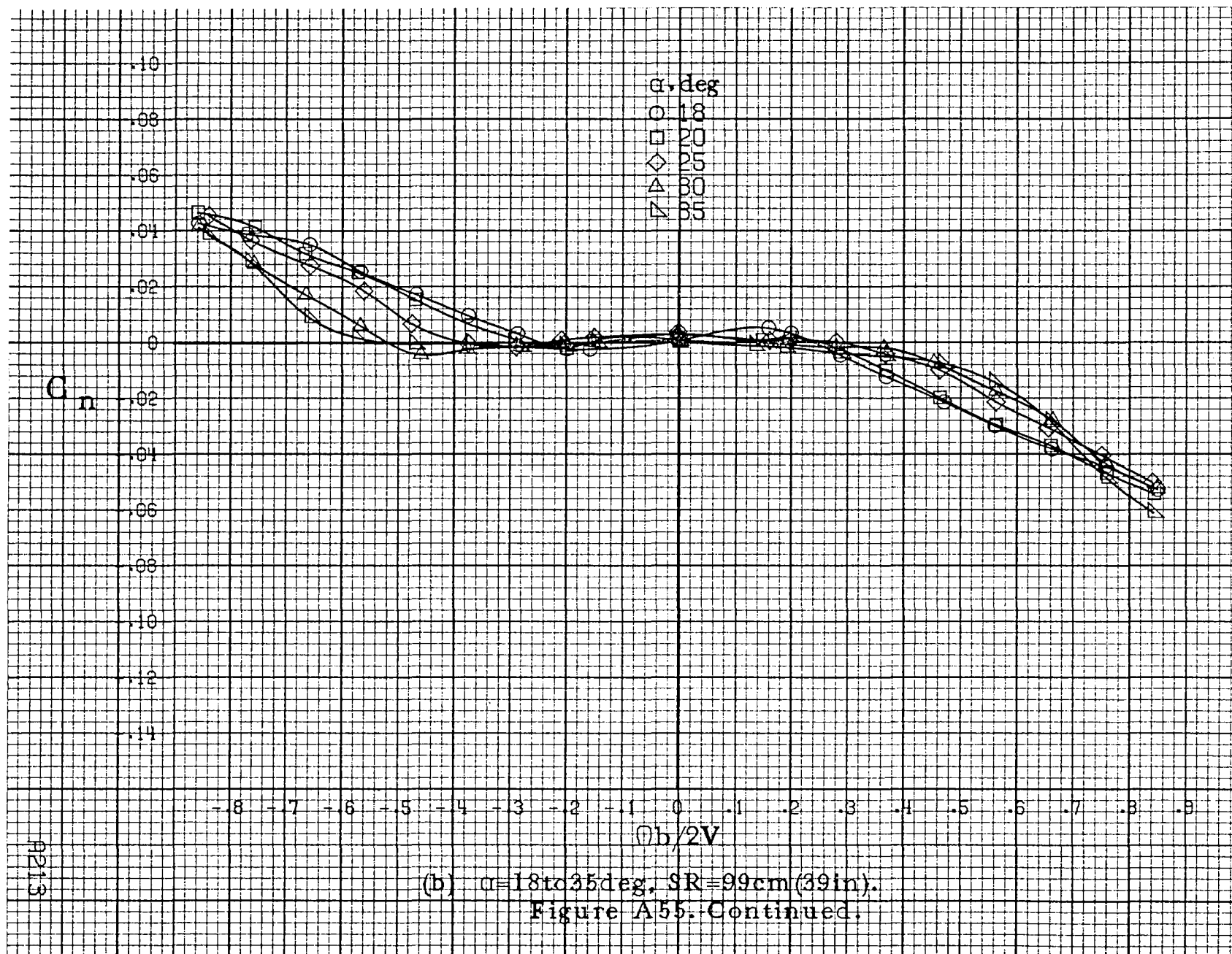
(c)  $\alpha=30$  to  $50^\circ$ ,  $SR=0$ .  
Figure A54. Continued.

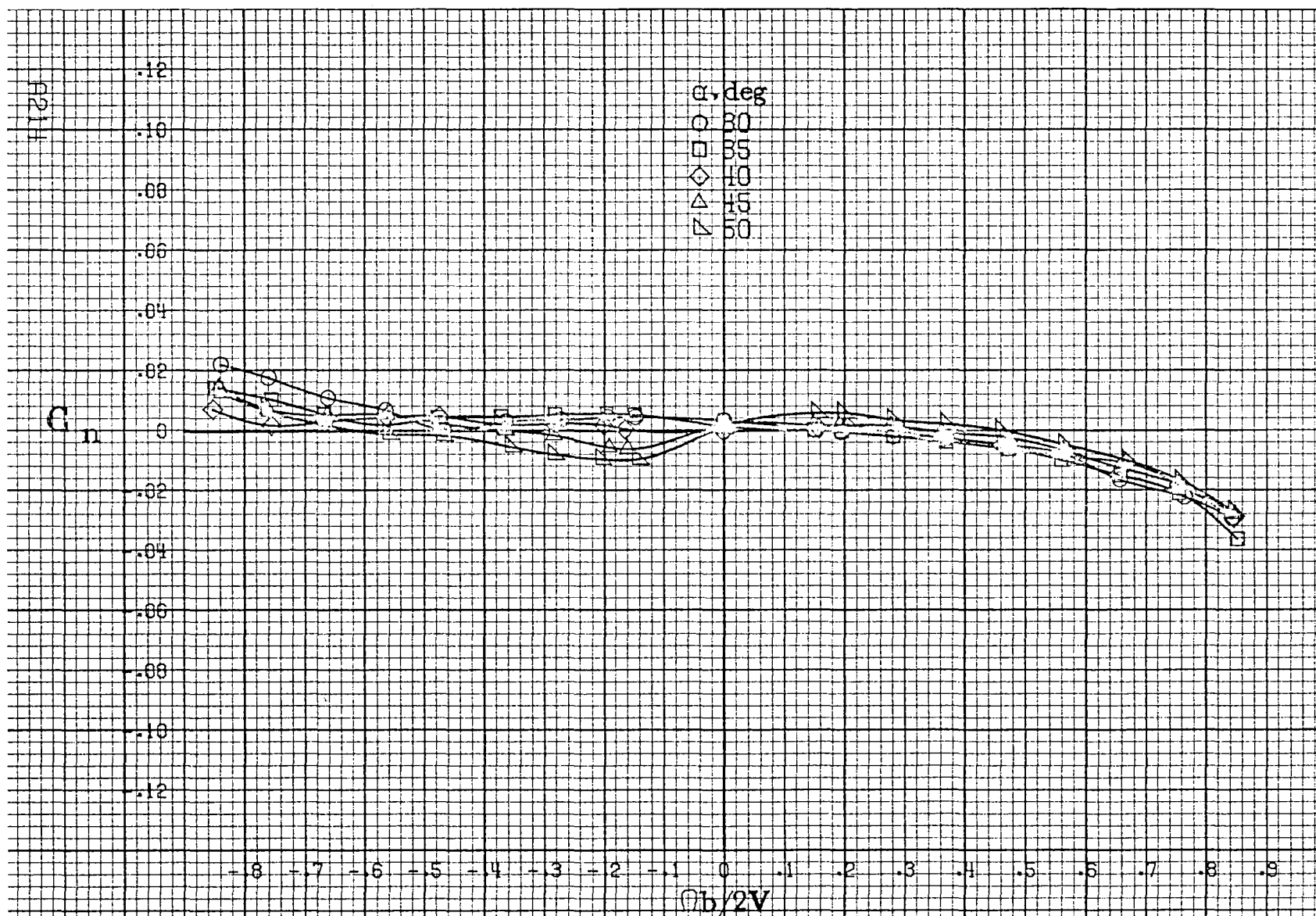




(a)  $\alpha=8$  to  $16$  deg,  $SR=99$  cm (39 in).

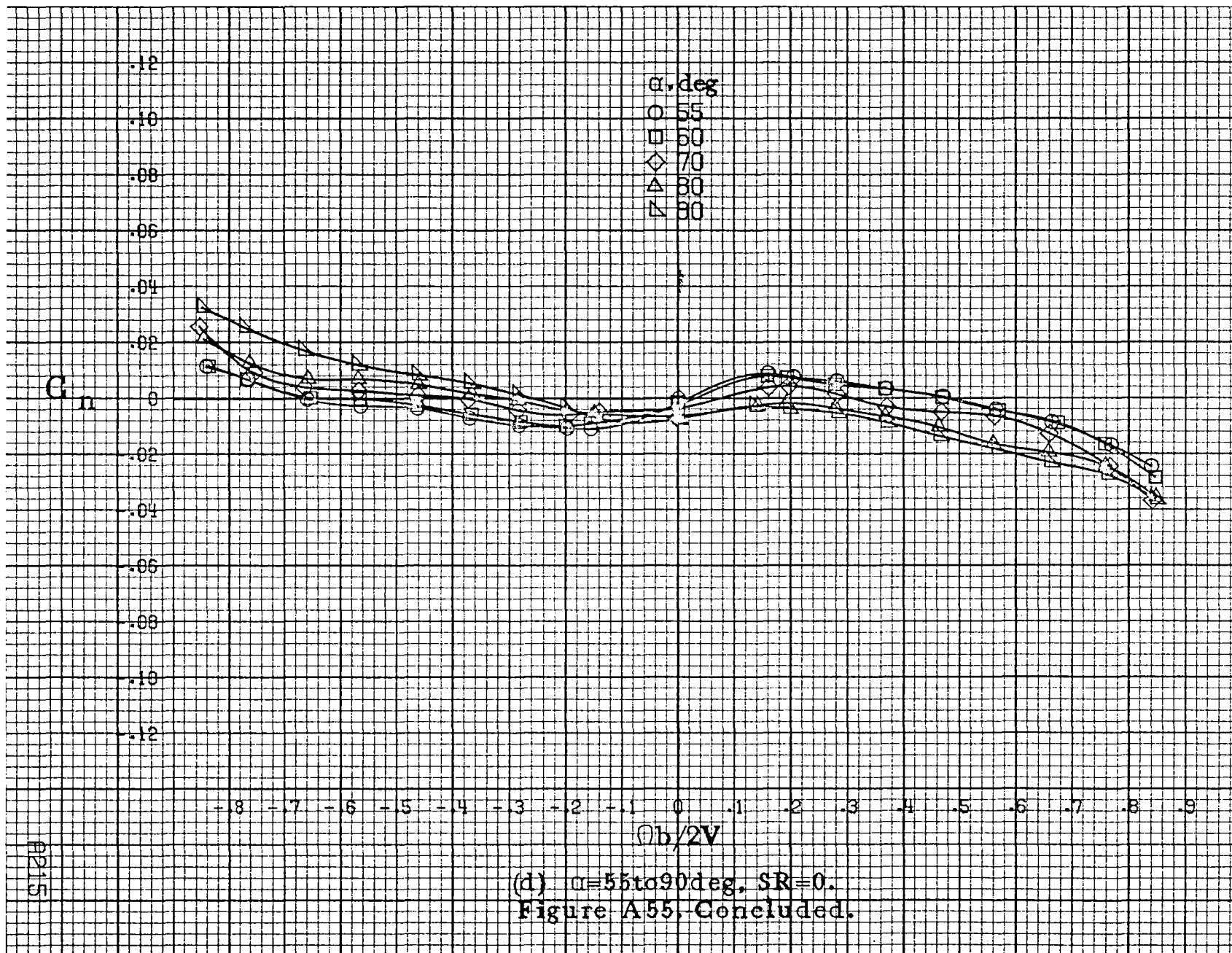
Figure A55. Effect of rotation rate and angle of attack on yawing-moment coefficient for configuration having sharp-edged fuselage bottom aft of wing TE.  $\delta_a=0^\circ$ ,  $\delta_s=0^\circ$ ,  $\delta_r=0^\circ$ ,  $\beta=0^\circ$ .





(c)  $\alpha=30$  to  $50$  deg,  $SR=0$ .  
Figure A55. Continued.





$C_l$

.35  
.30  
.25  
.20  
.15  
.10  
.05  
0  
-.05  
-.10  
-.15  
-.20  
-.25

$\alpha$ , deg  
○ 8  
□ 10  
◇ 12  
△ 14  
▽ 16

-8 -7 -6 -5 -4 -3 -2 -1 0 .1 .2 .3 .4 .5 .6 .7 .8 .9  
 $\Omega b/2V$

(a)  $\alpha=8$  to  $16$  deg,  $SR=99$  cm (39 in).

Figure A56. Effect of rotation rate and angle of attack on rolling-moment coefficient for configuration having sharp-edged fuselage bottom aft of wing TE.  $\delta_a=0^\circ$ ,  $\delta_h=0^\circ$ ,  $\delta_r=0^\circ$ ,  $\beta=0^\circ$ .

C<sub>1</sub>

.35  
.30  
.25  
.20  
.15  
.10  
.05  
0  
-.05  
-.10  
-.15  
-.20  
-.25

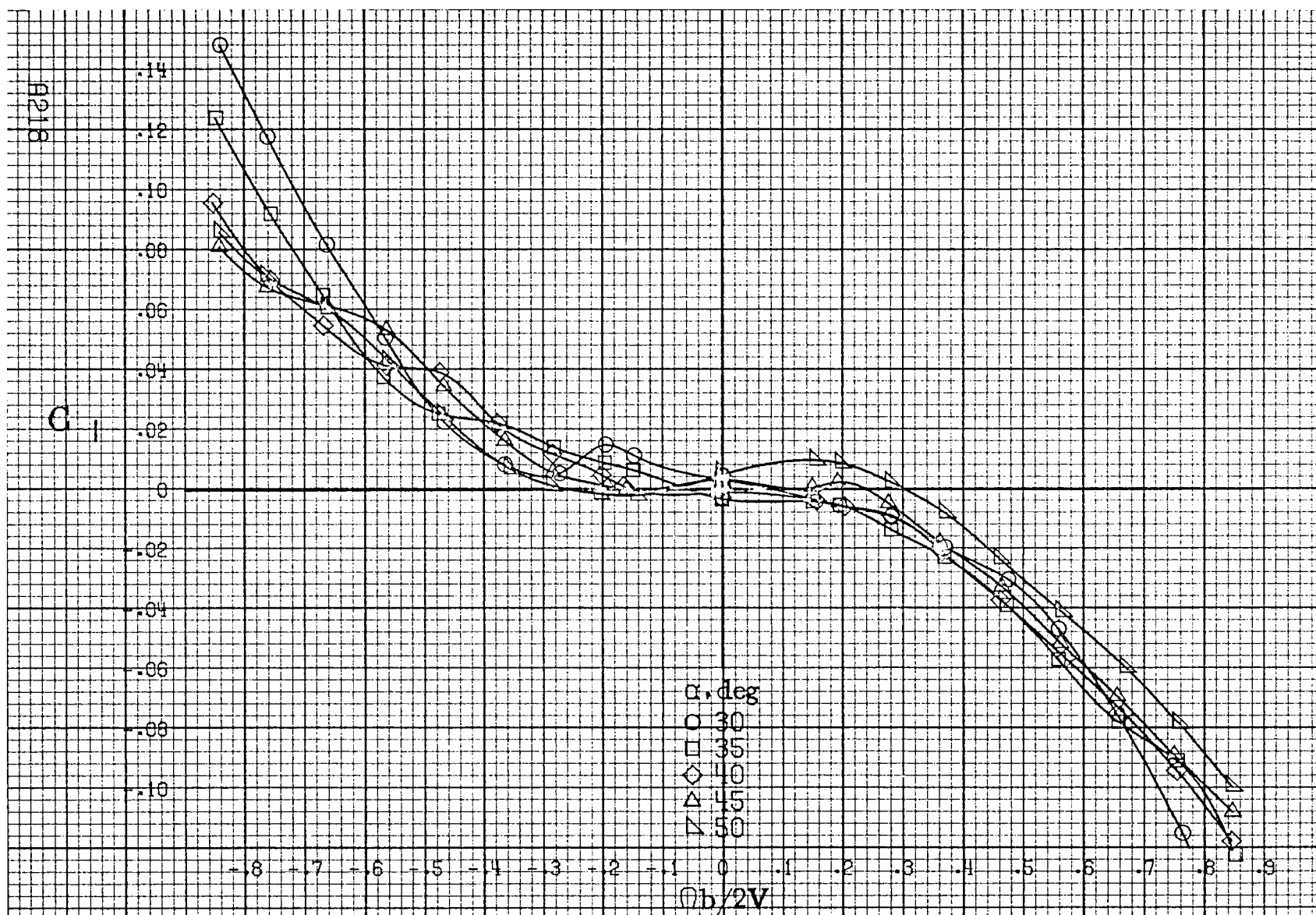
-.8 -.7 -.6 -.5 -.4 -.3 -.2 -.1 0 .1 .2 .3 .4 .5 .6 .7 .8 .9

$\alpha, \text{deg}$   
○ 18  
□ 20  
◇ 25  
△ 30  
▽ 35

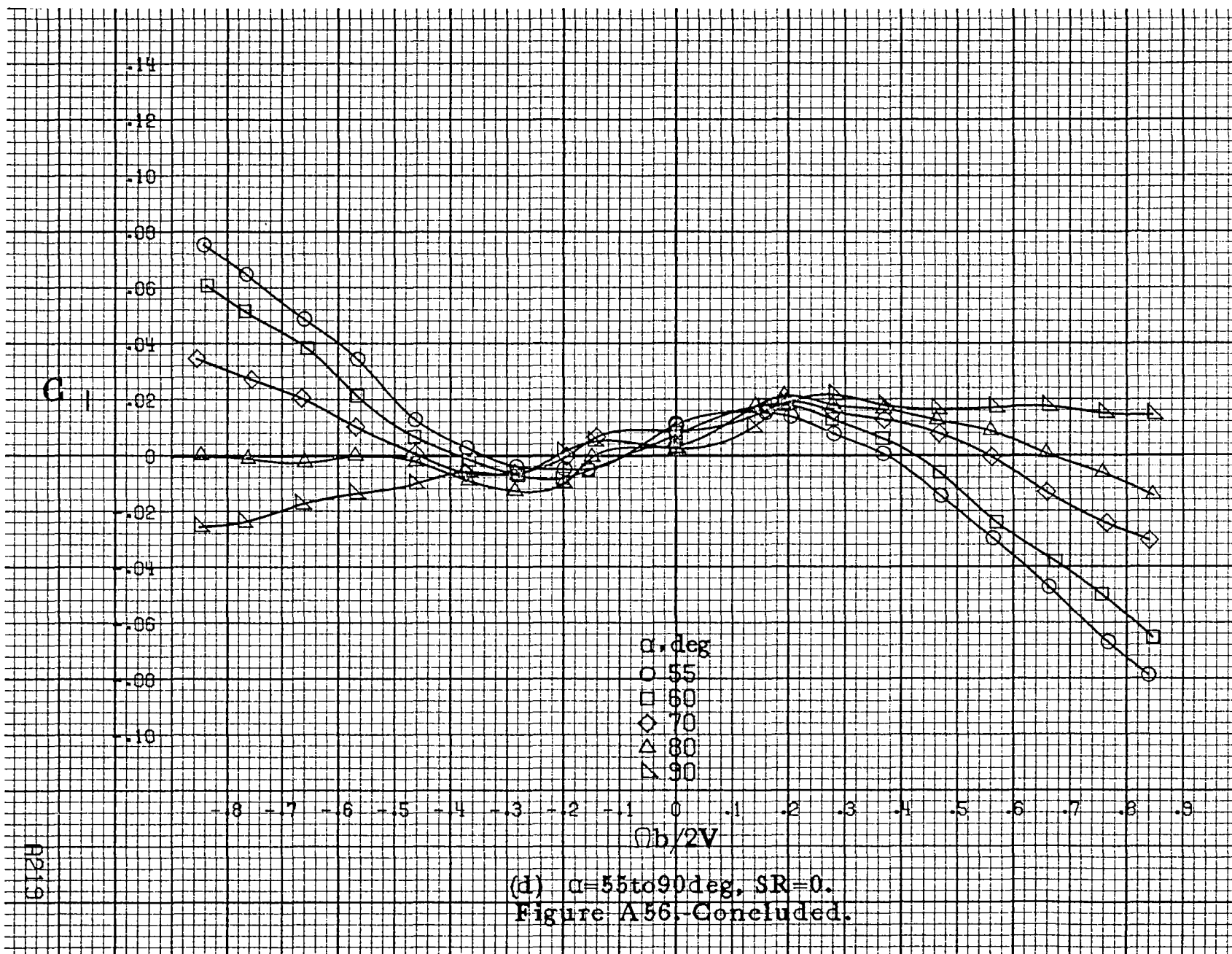
$b/2V$

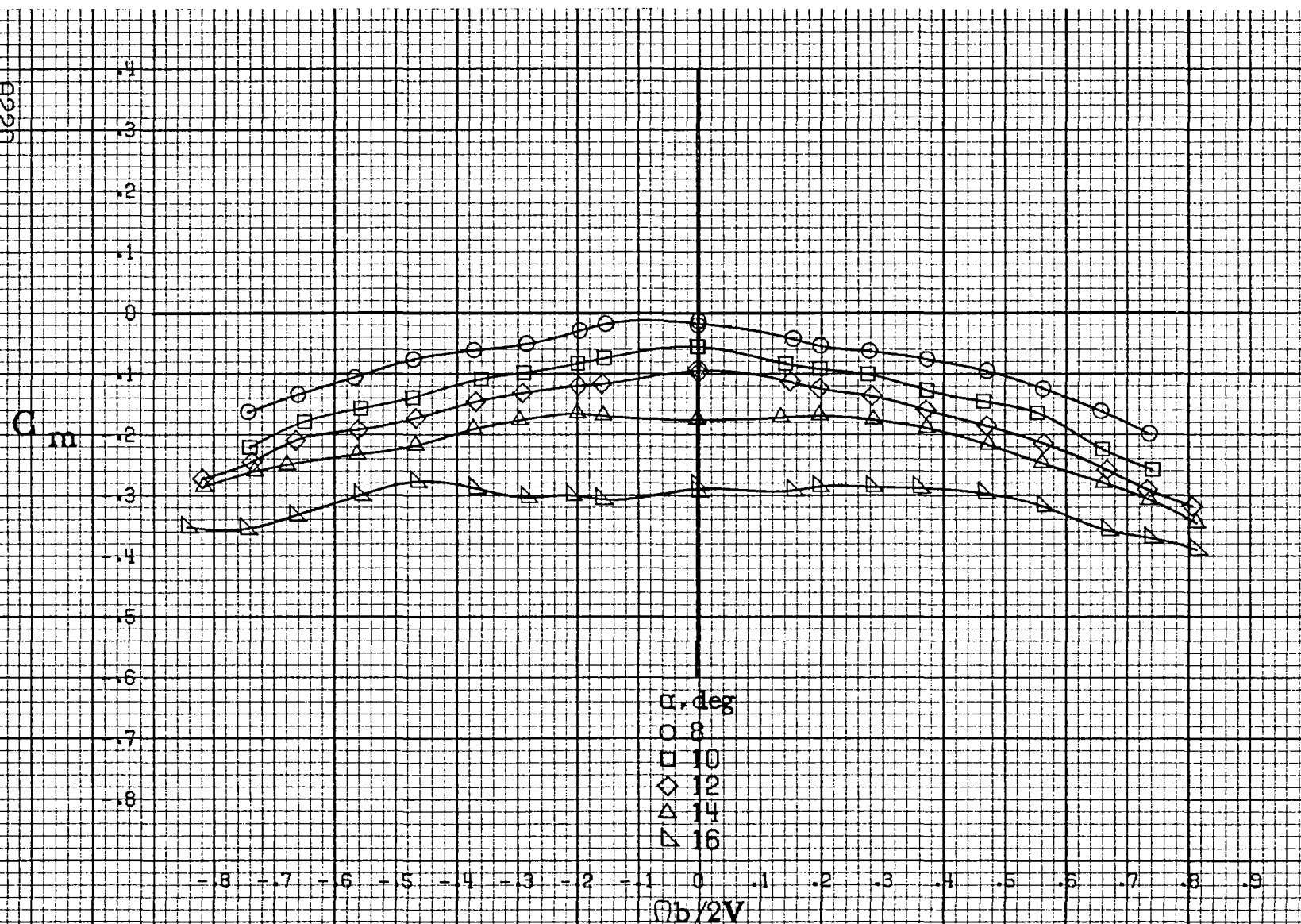
(b)  $\alpha=18$  to  $35$  deg,  $SR=99\text{cm}(39\text{in})$ .  
Figure A56. Continued.

A217



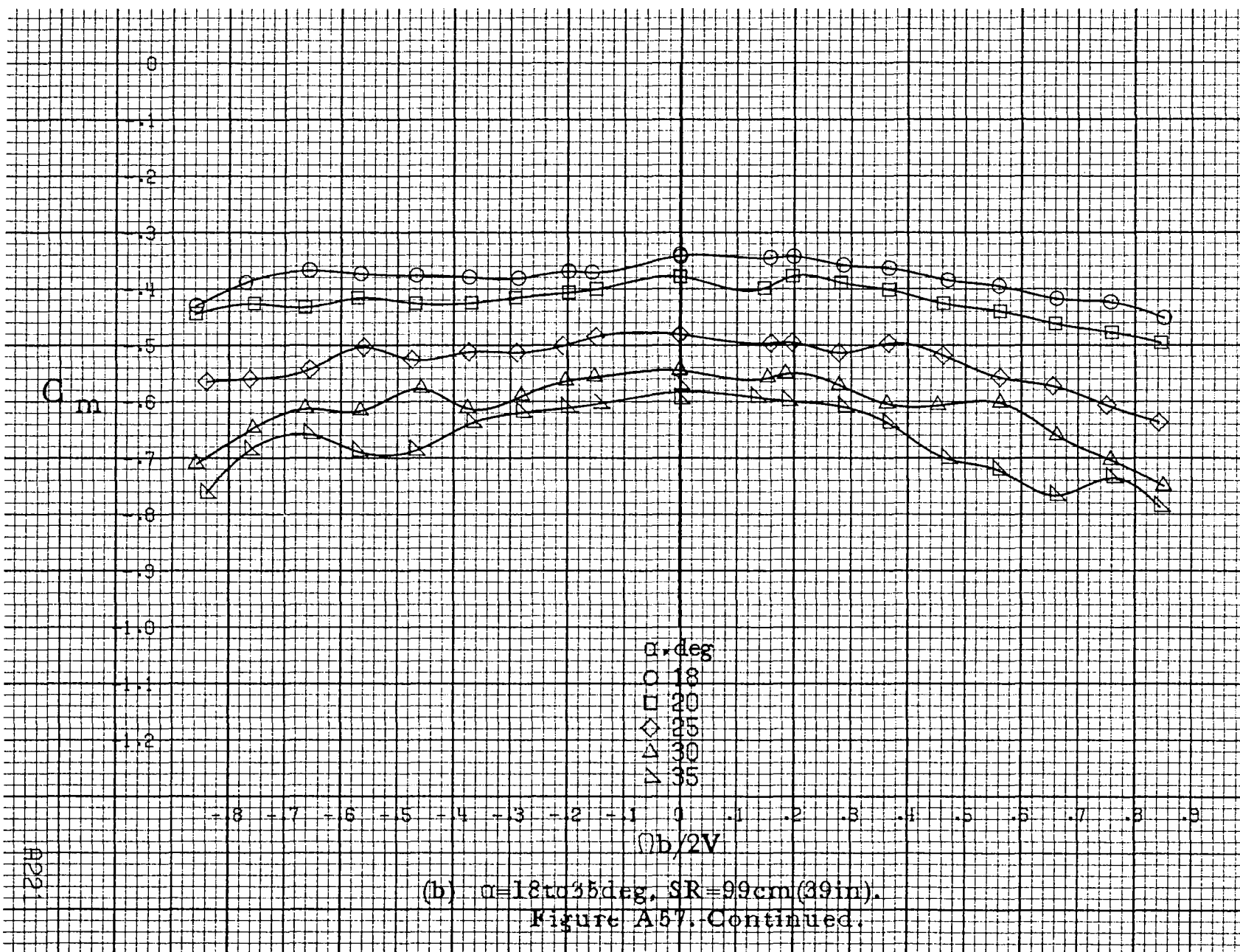
(c)  $\alpha=30$  to  $50$  deg,  $SR=0$ .  
Figure A56. Continued.





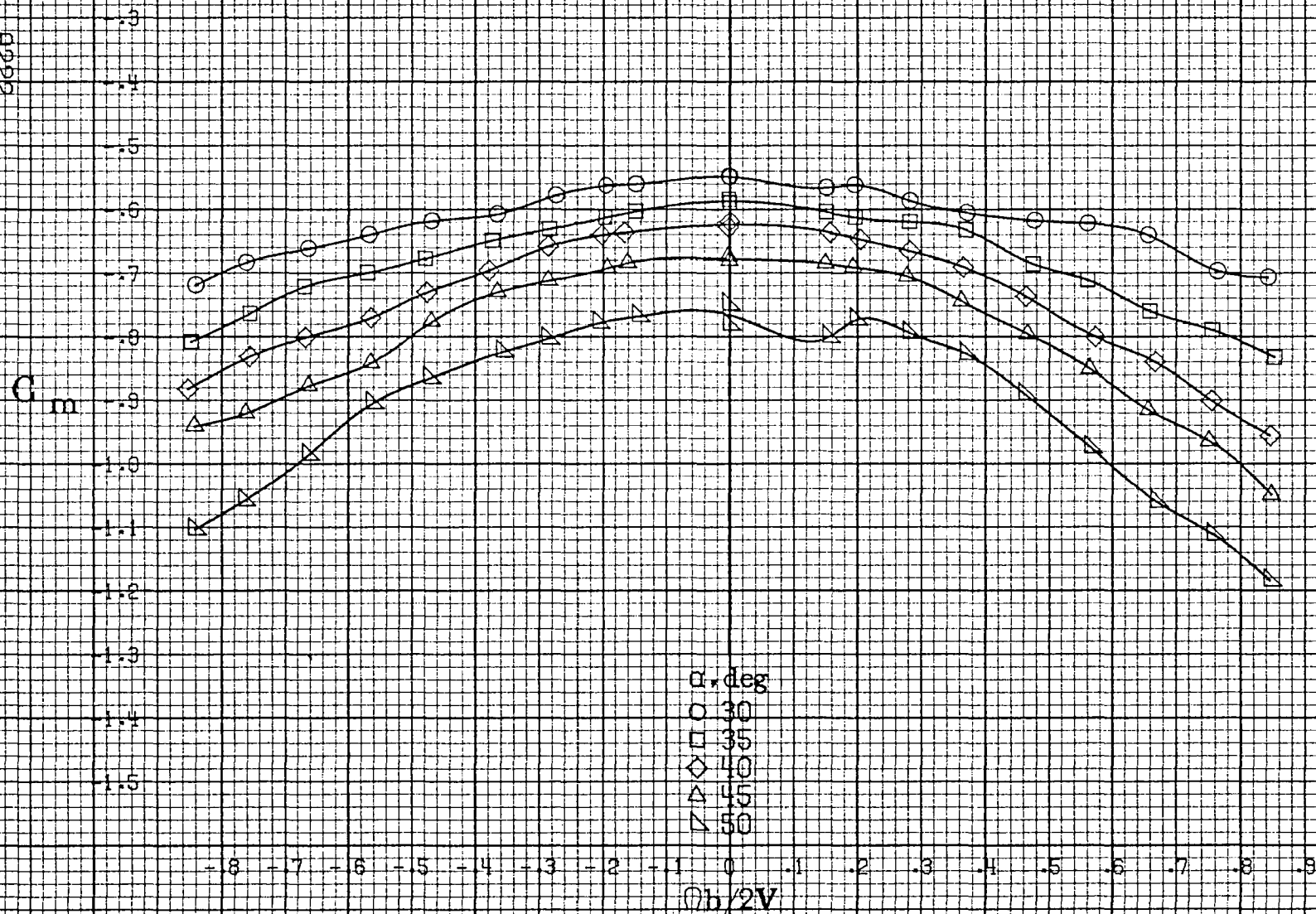
(a)  $\alpha = 8$  to  $16^\circ$ ,  $SR = 99\text{cm}(39\text{in})$ .

Figure A.57.-Effect of rotation rate and angle of attack on pitching-moment coefficient for configuration having sharp-edged fuselage bottom aft of wing T.E.  $\delta_a = 0^\circ$ ,  $\delta_e = 0^\circ$ ,  $\delta_r = 0^\circ$ ,  $\beta = 0^\circ$ .

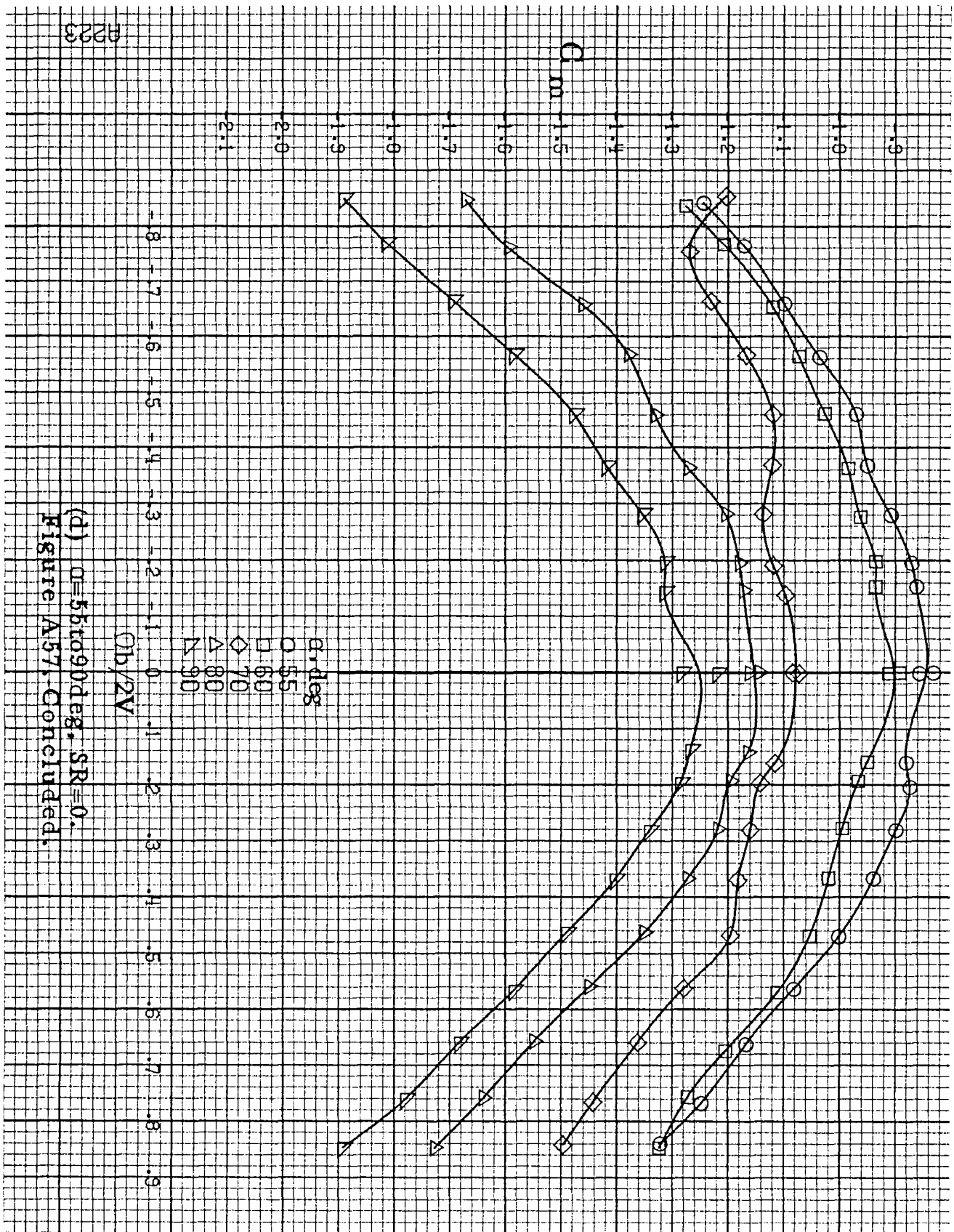




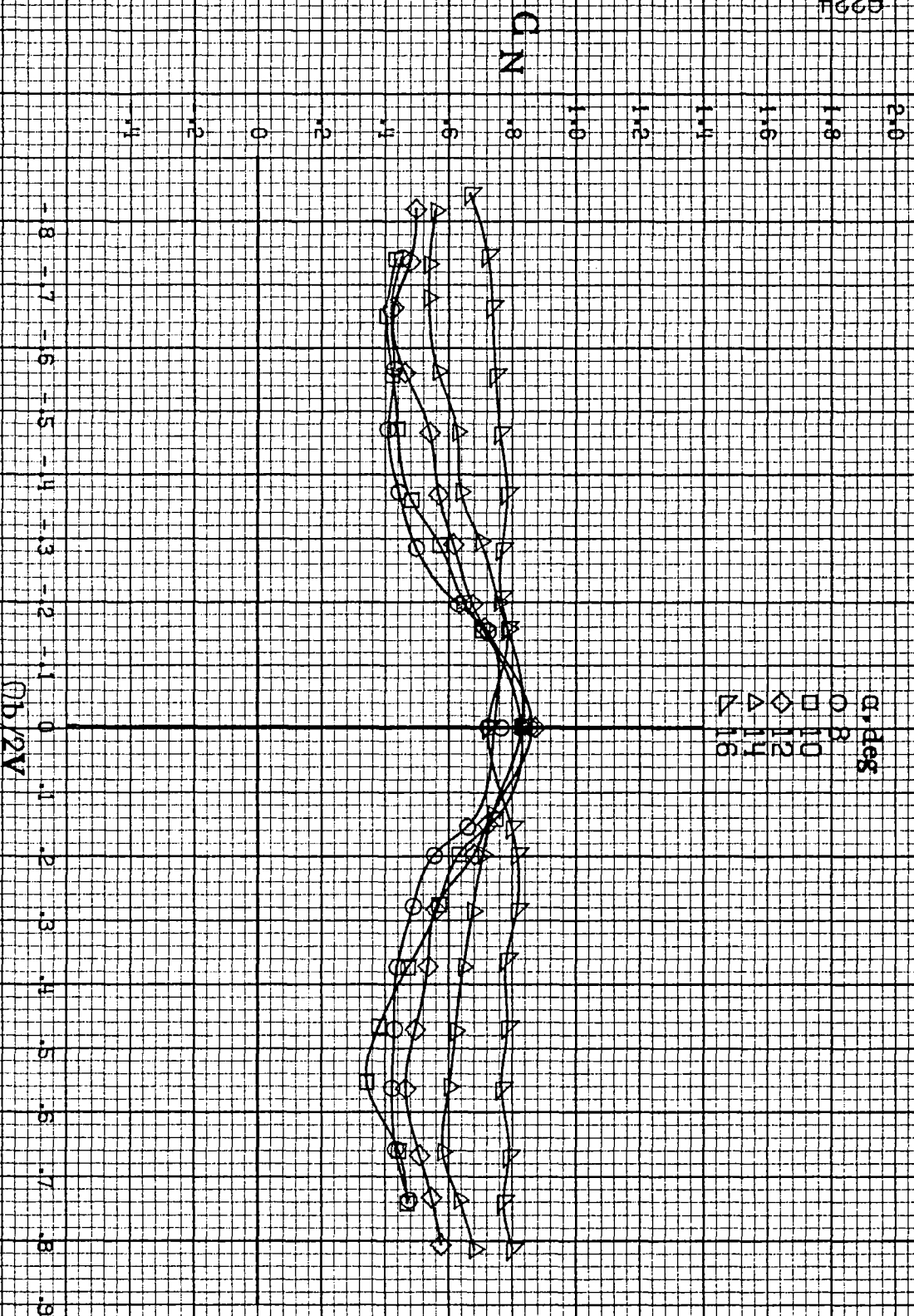
B222



(c)  $\alpha=30$  to  $50^\circ$ ,  $SR=0$ .  
Figure A57. Continued.



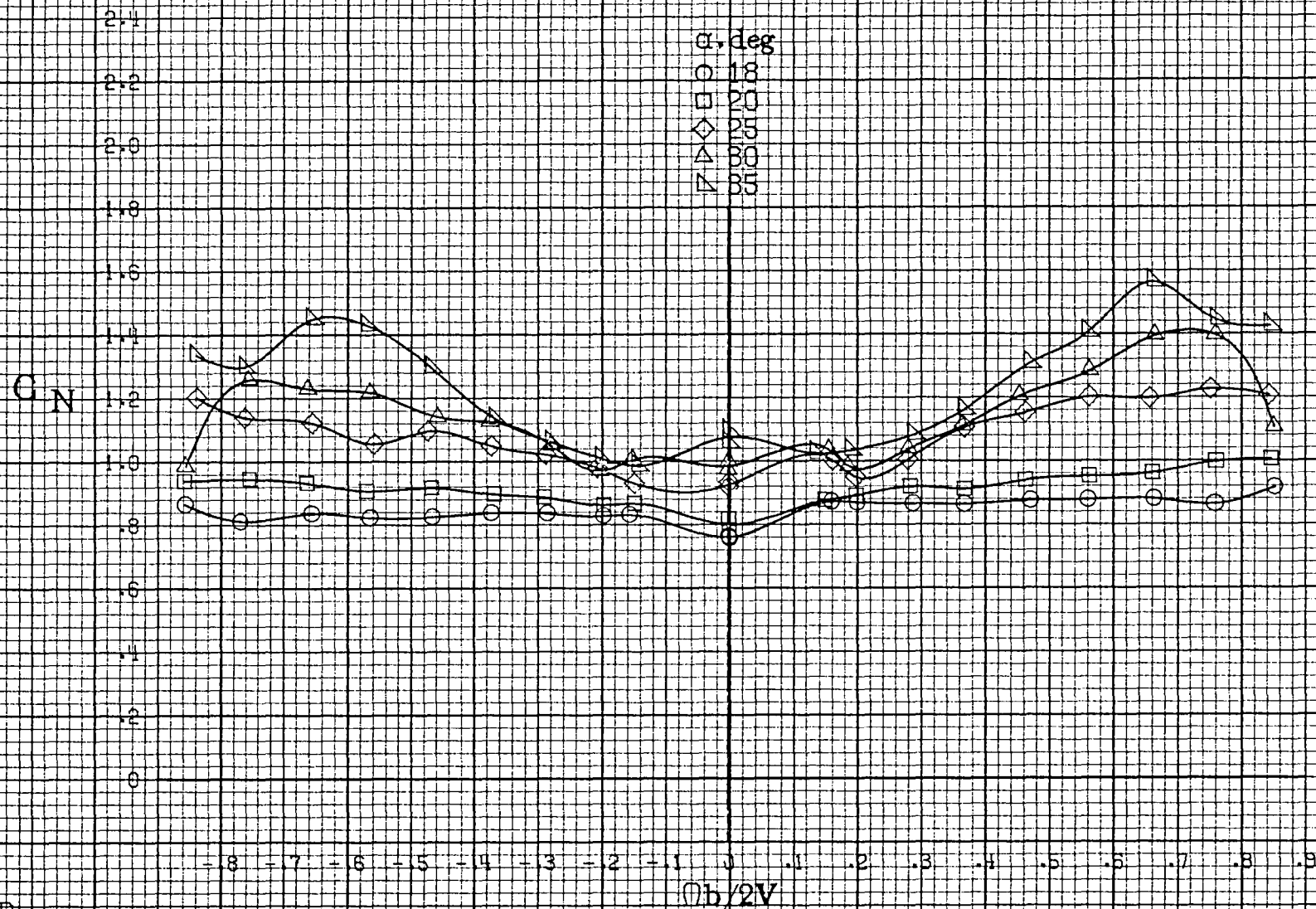
(d)  $\alpha=55$  to  $90^\circ$ ,  $SR=0$ .  
Figure A57. Concluded.



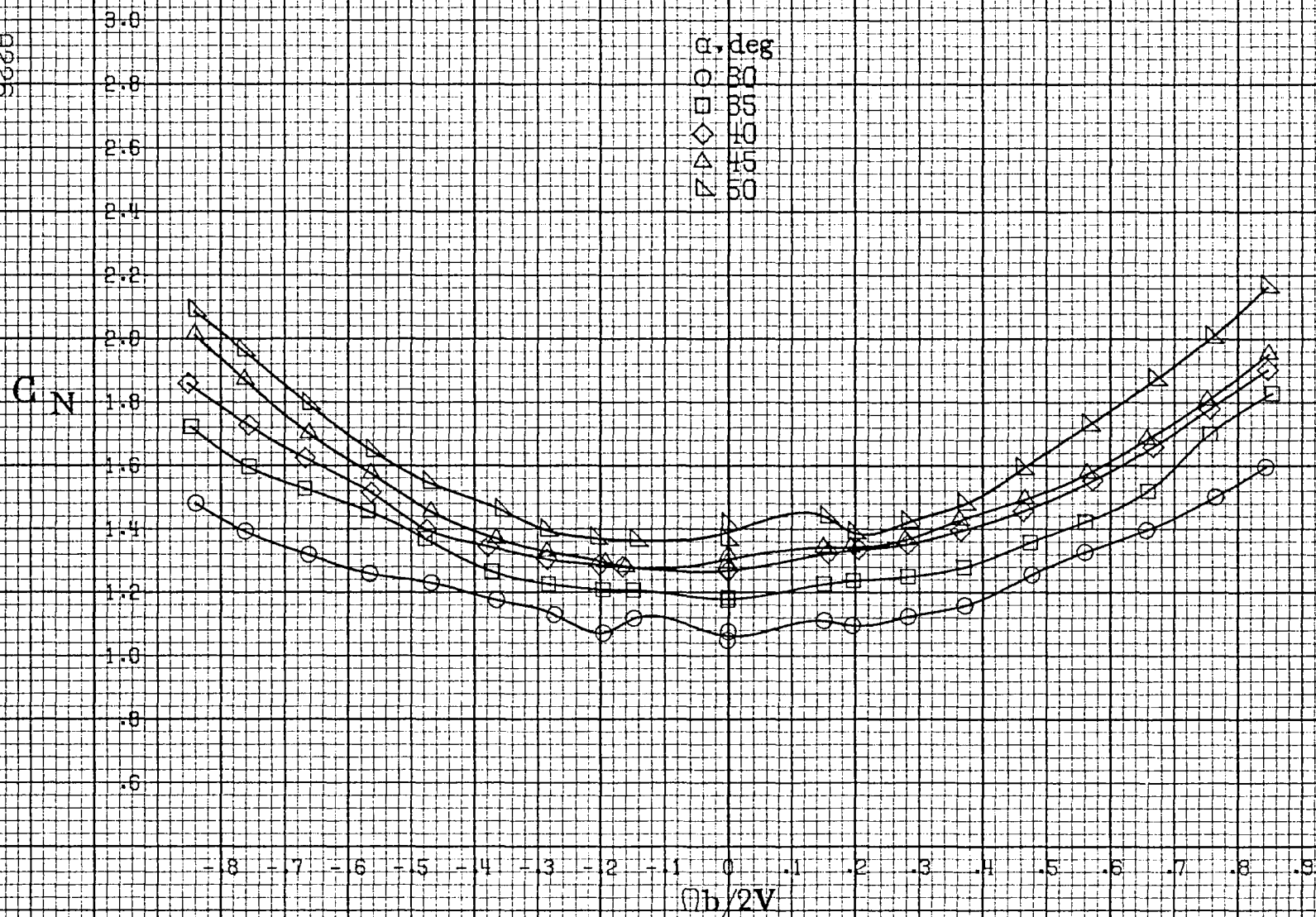
(a)  $\alpha=8$  to  $16^\circ$ ,  $SR=99\text{ cm (39 in.)}$ .

Figure A58. Effect of rotation rate and angle of attack on normal force coefficient for configuration having sharp-edged fuselage bottom aft of wing

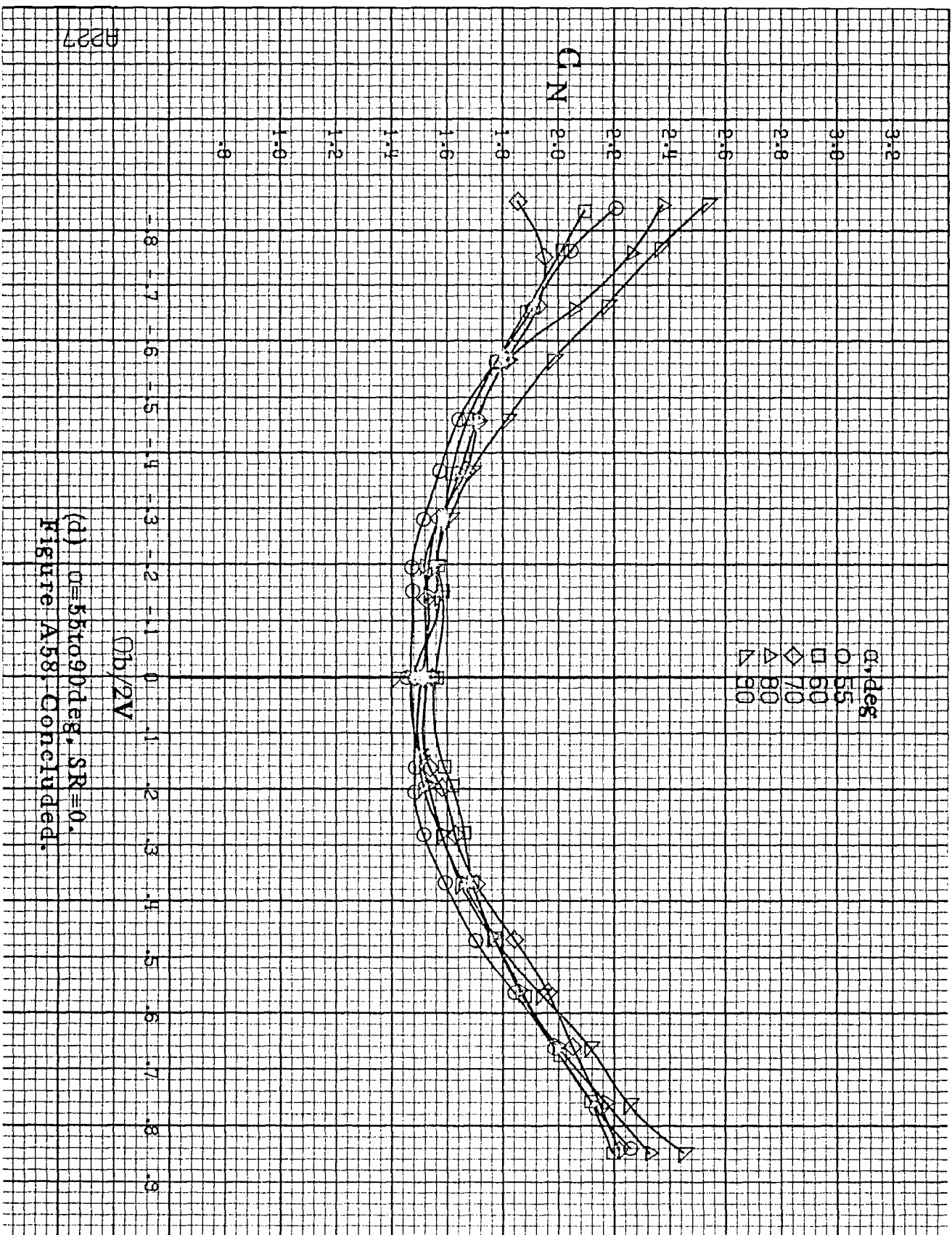
TE.  $\delta_a=0^\circ$ ,  $\delta_r=0^\circ$ ,  $\delta_s=0^\circ$ ,  $\beta=0^\circ$ .



(b)  $\alpha = 18$  to  $35$  deg.  $SR = 99$  cm (39 in.).  
Figure A58. Continued.

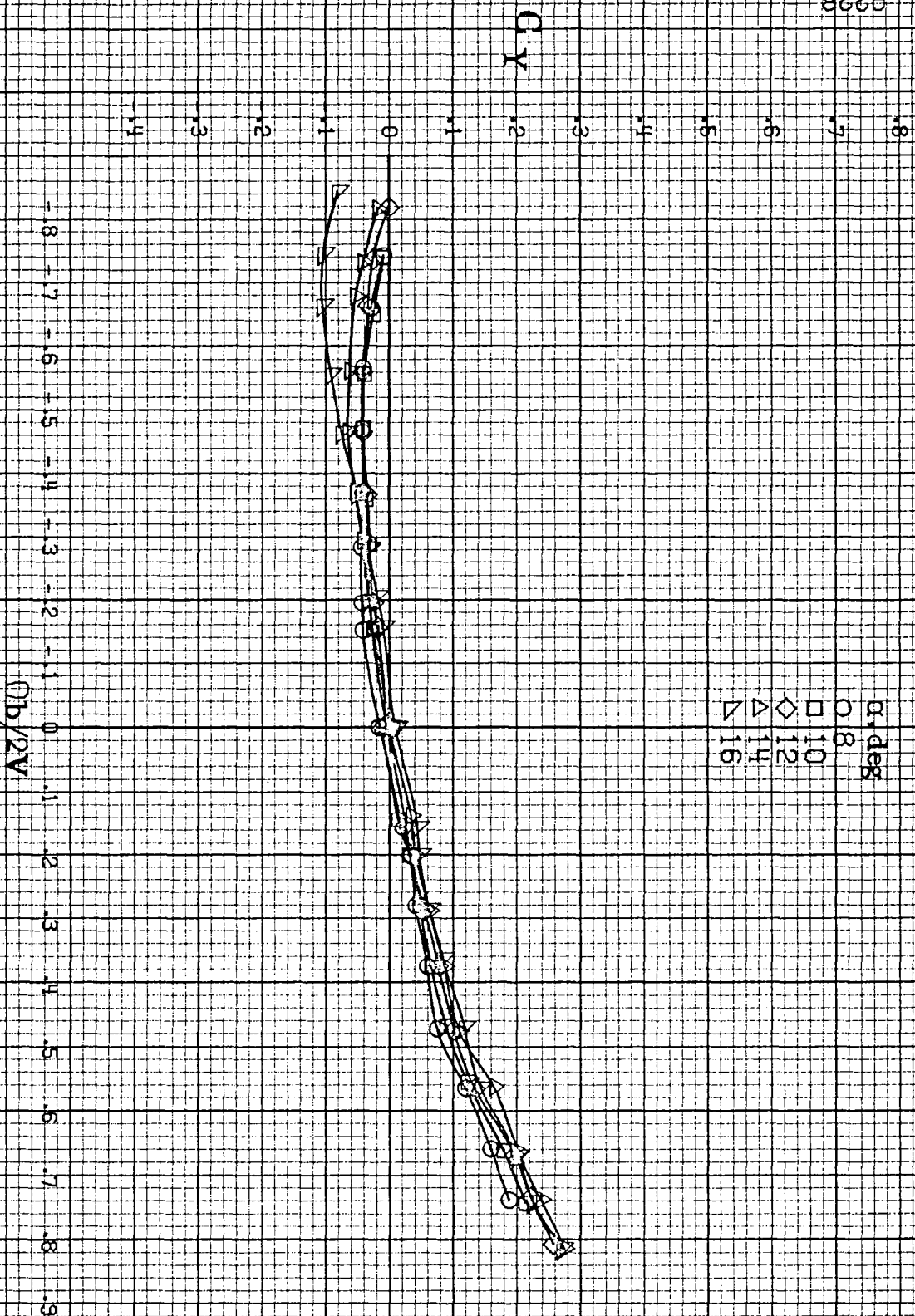


(c)  $\alpha=30$  to  $50$  deg,  $SR=0$ .  
Figure A58. Continued.



(d)  $\alpha = 55$  to  $90$  deg,  $SR = 0$ .  
 Figure A.58. Concluded.

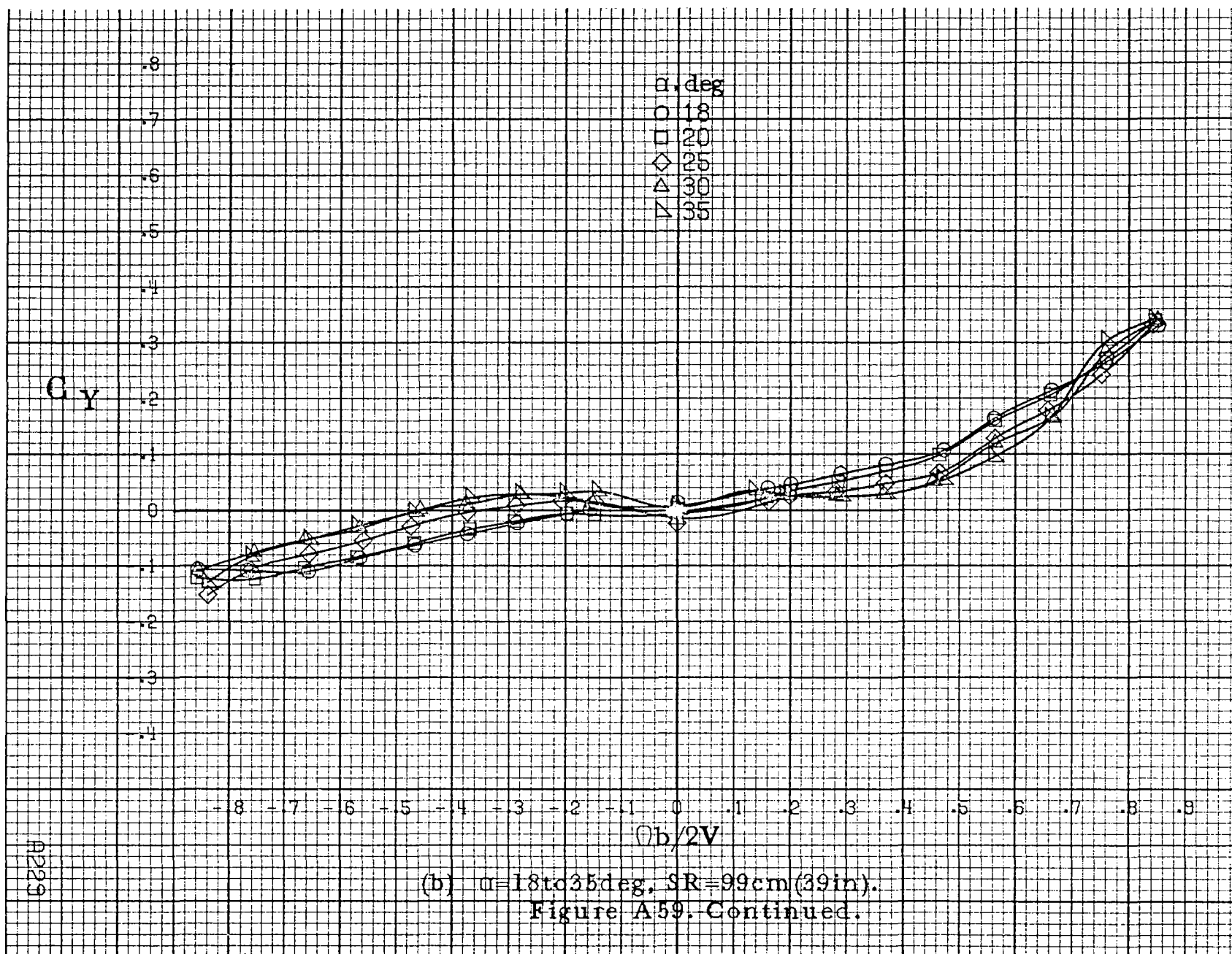




(a)  $\alpha = 8$  to  $16^\circ$ ,  $SR = 99 \text{ cm (39 in.)}$ .

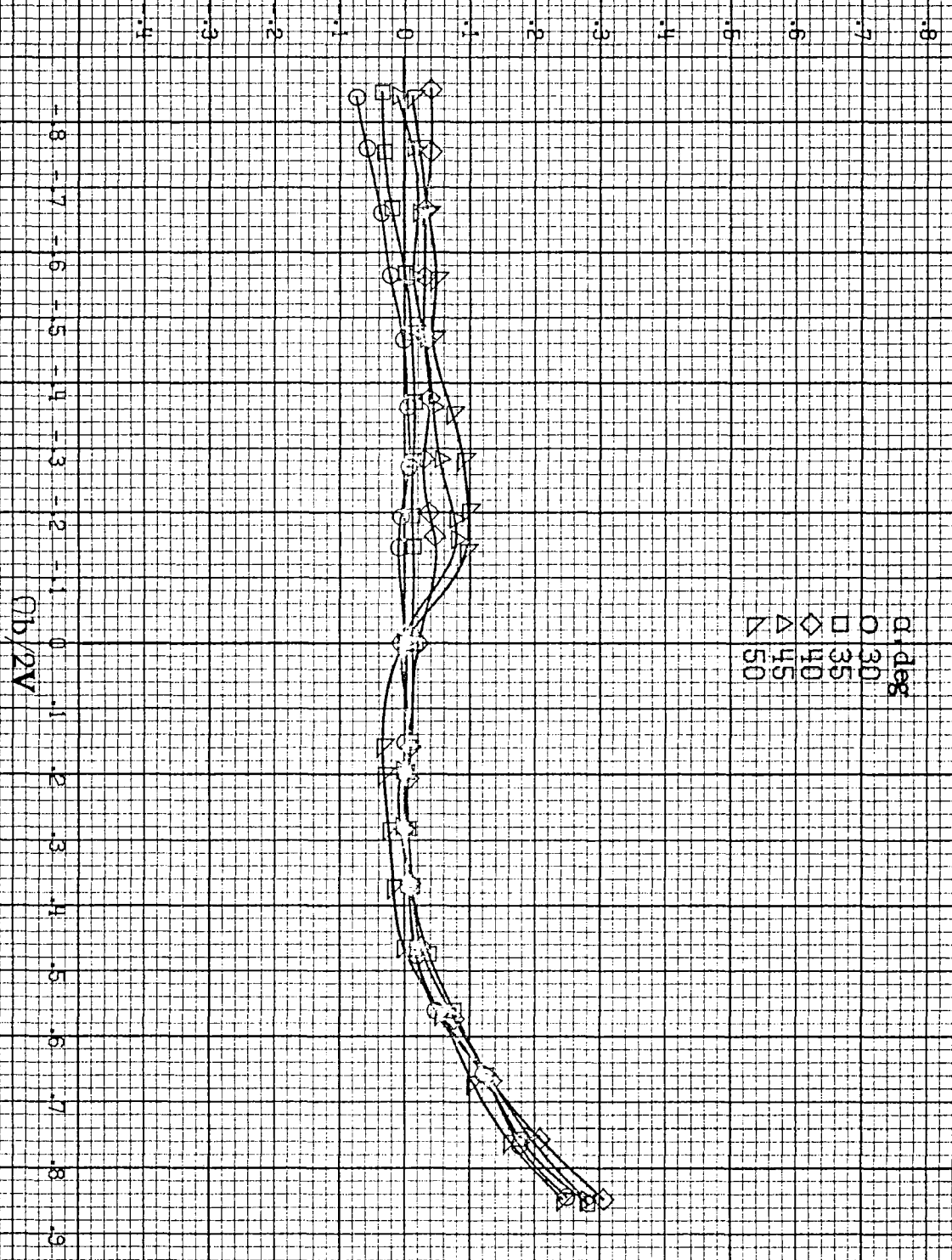
Figure A.59. Effect of rotation rate and angle of attack on side-force coefficient for configuration having sharp-edged fuselage bottom aft of wing TE.  $\delta_a = 0^\circ$ ,  $\delta_r = 0^\circ$ ,  $\delta_i = 0^\circ$ ,  $\beta = 0^\circ$ .



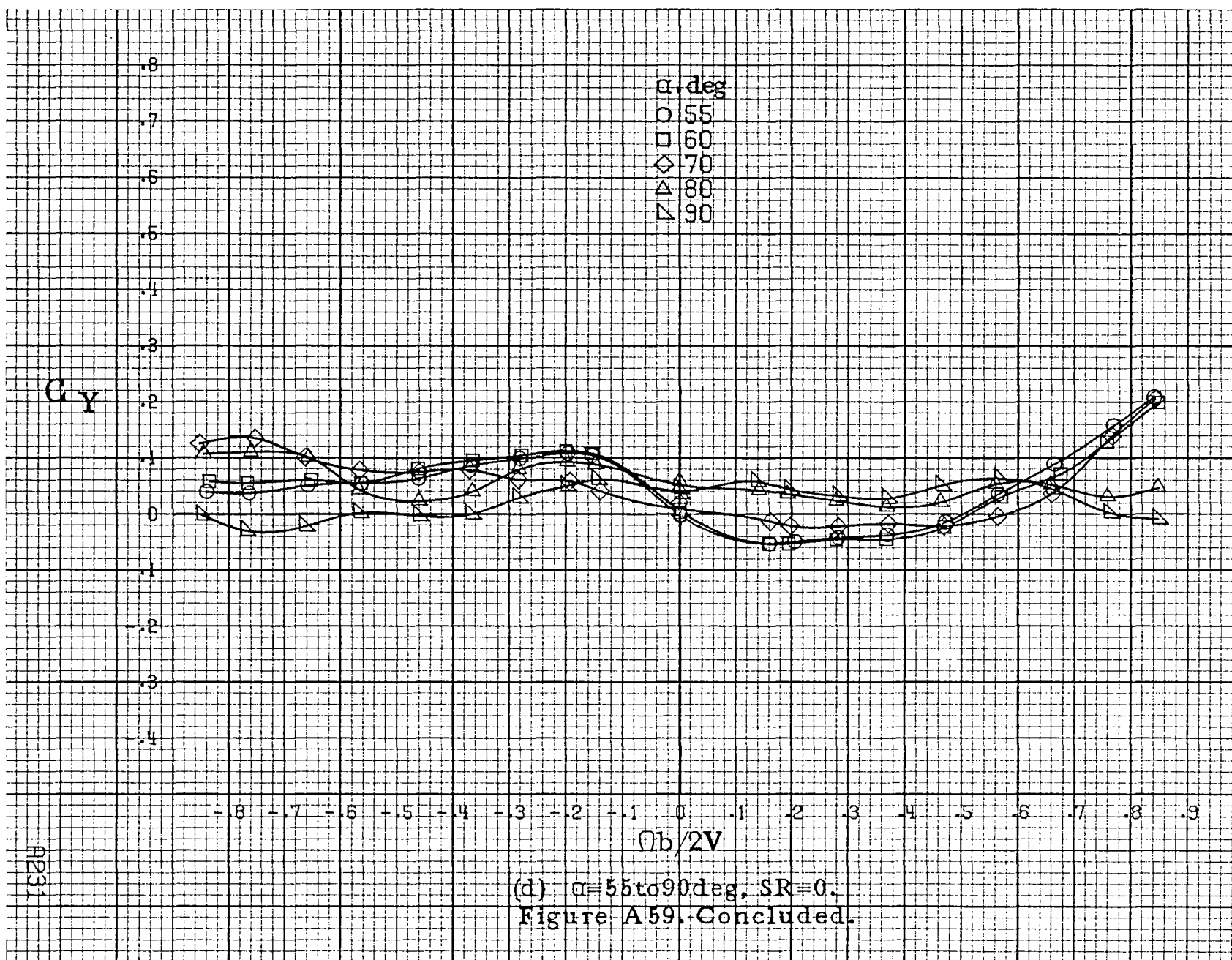


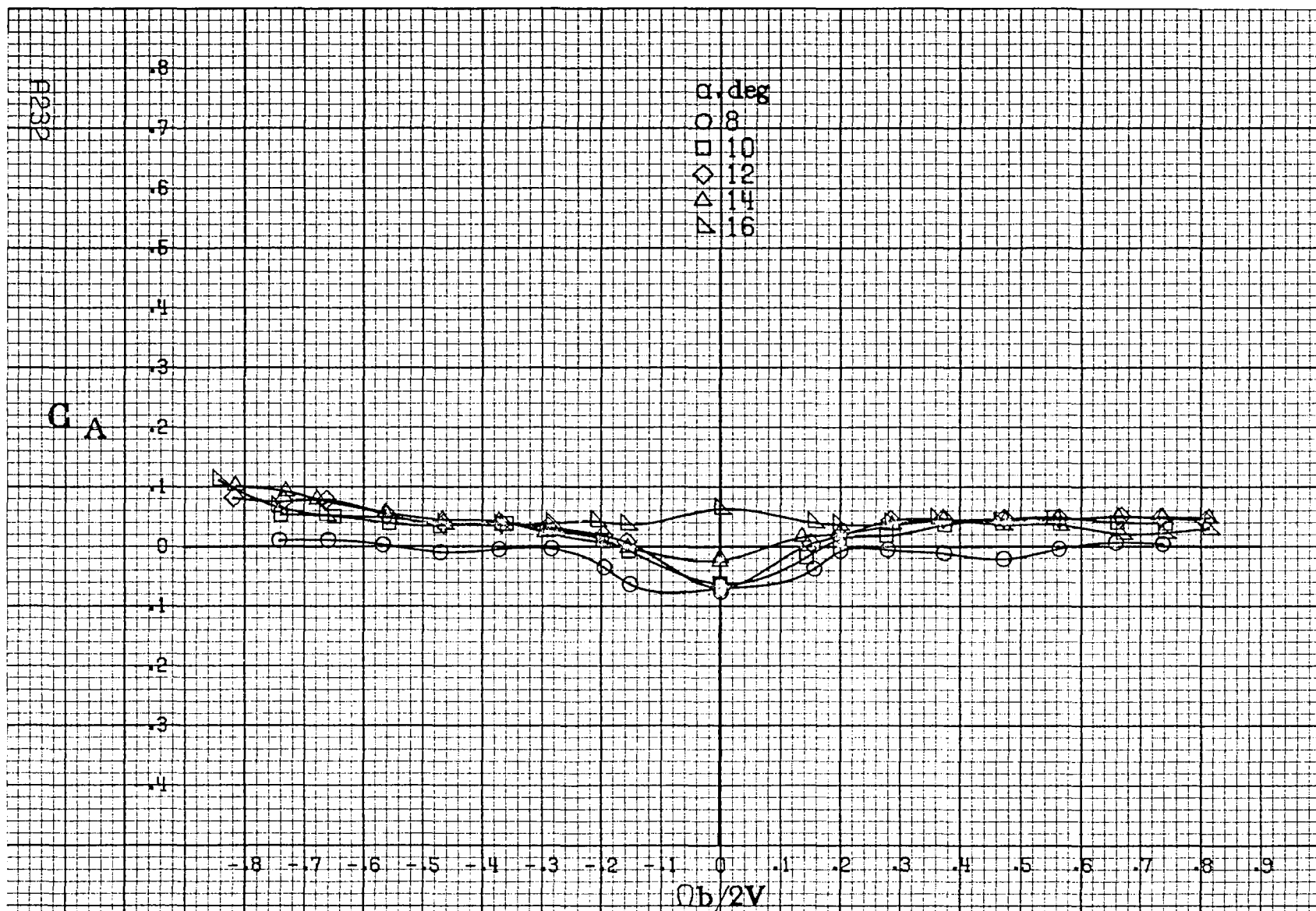
H230

C<sub>y</sub>



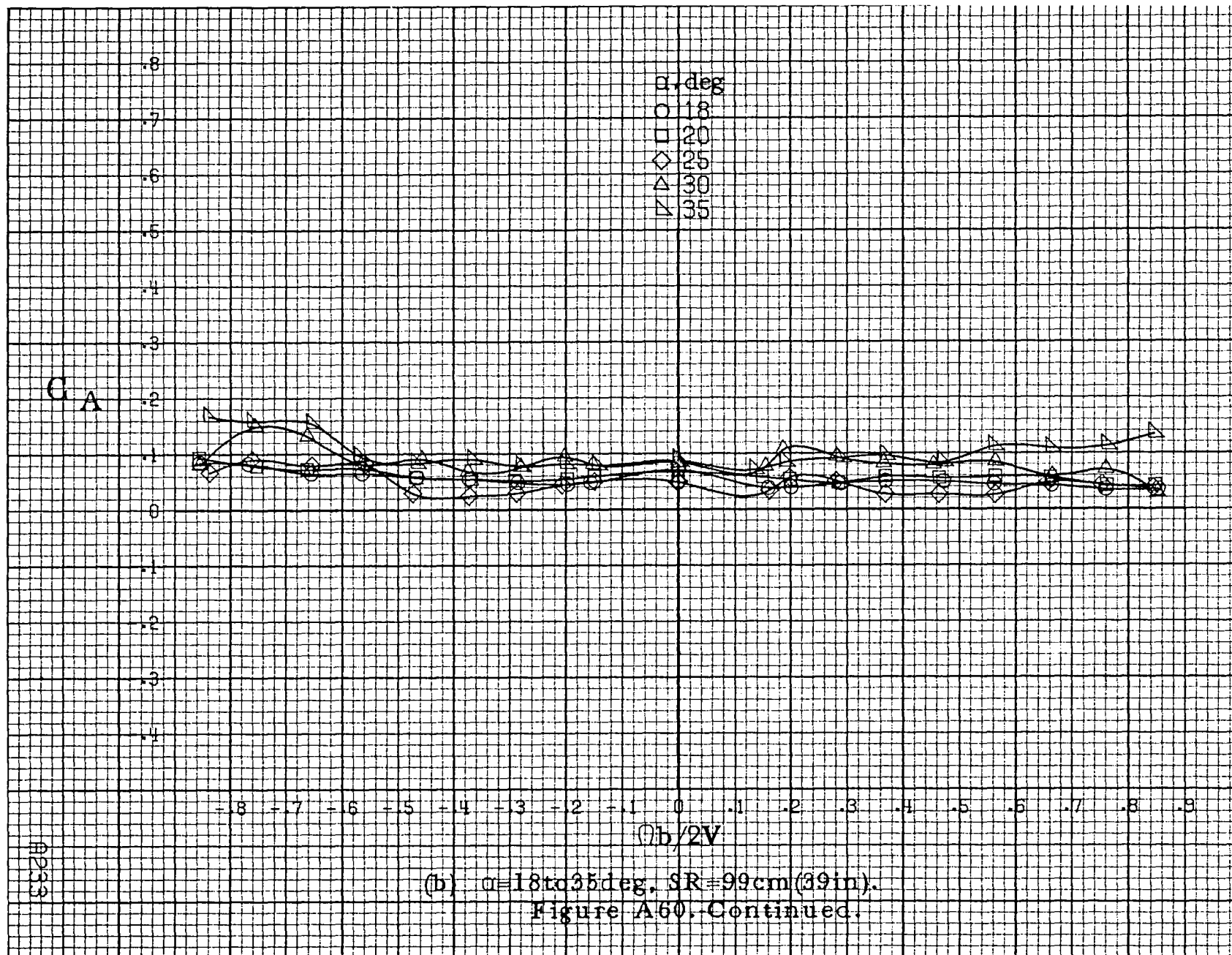
(c)  $\alpha = 30$  to  $50$  deg,  $SR = 0$ .  
Figure A59. Continued.

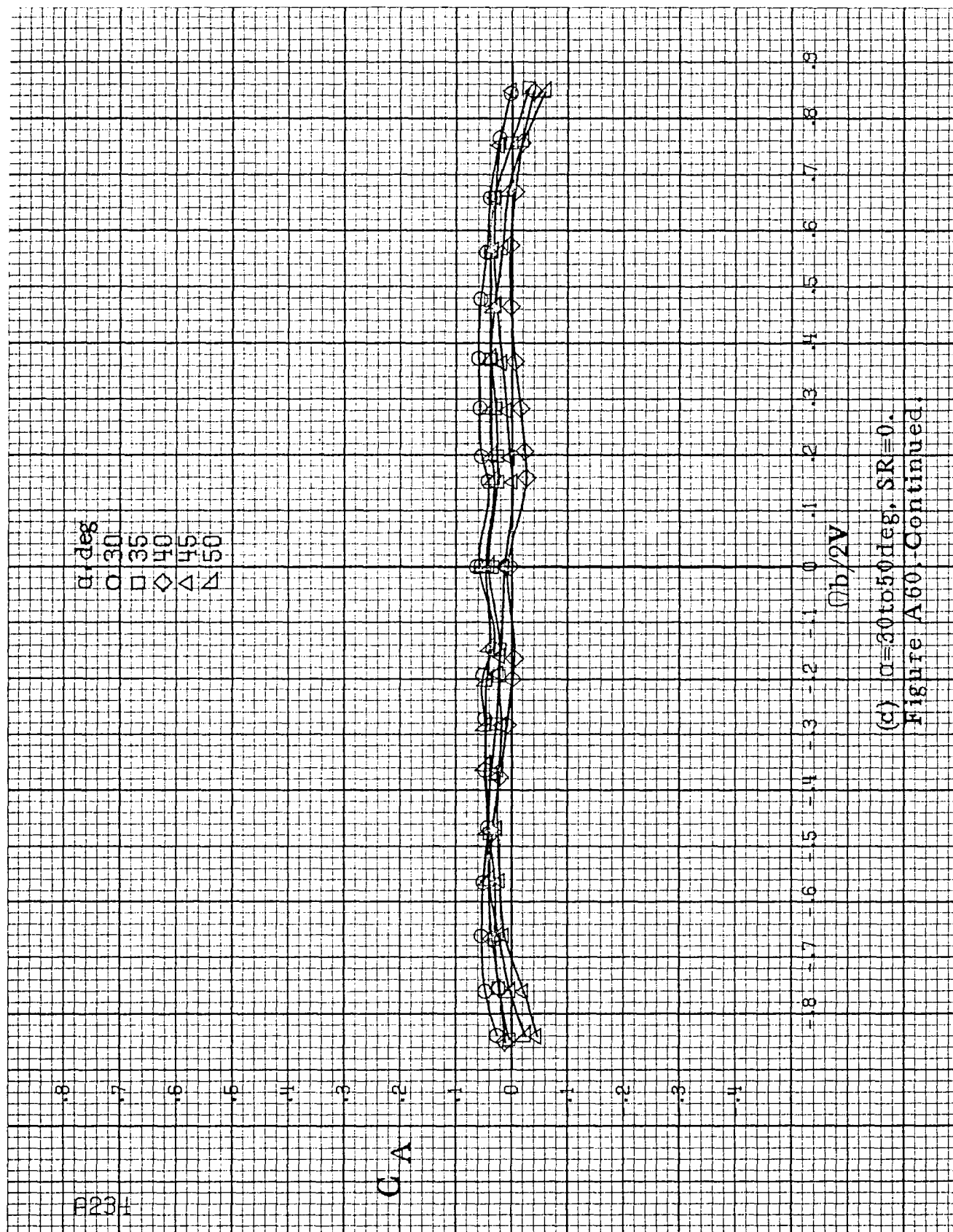




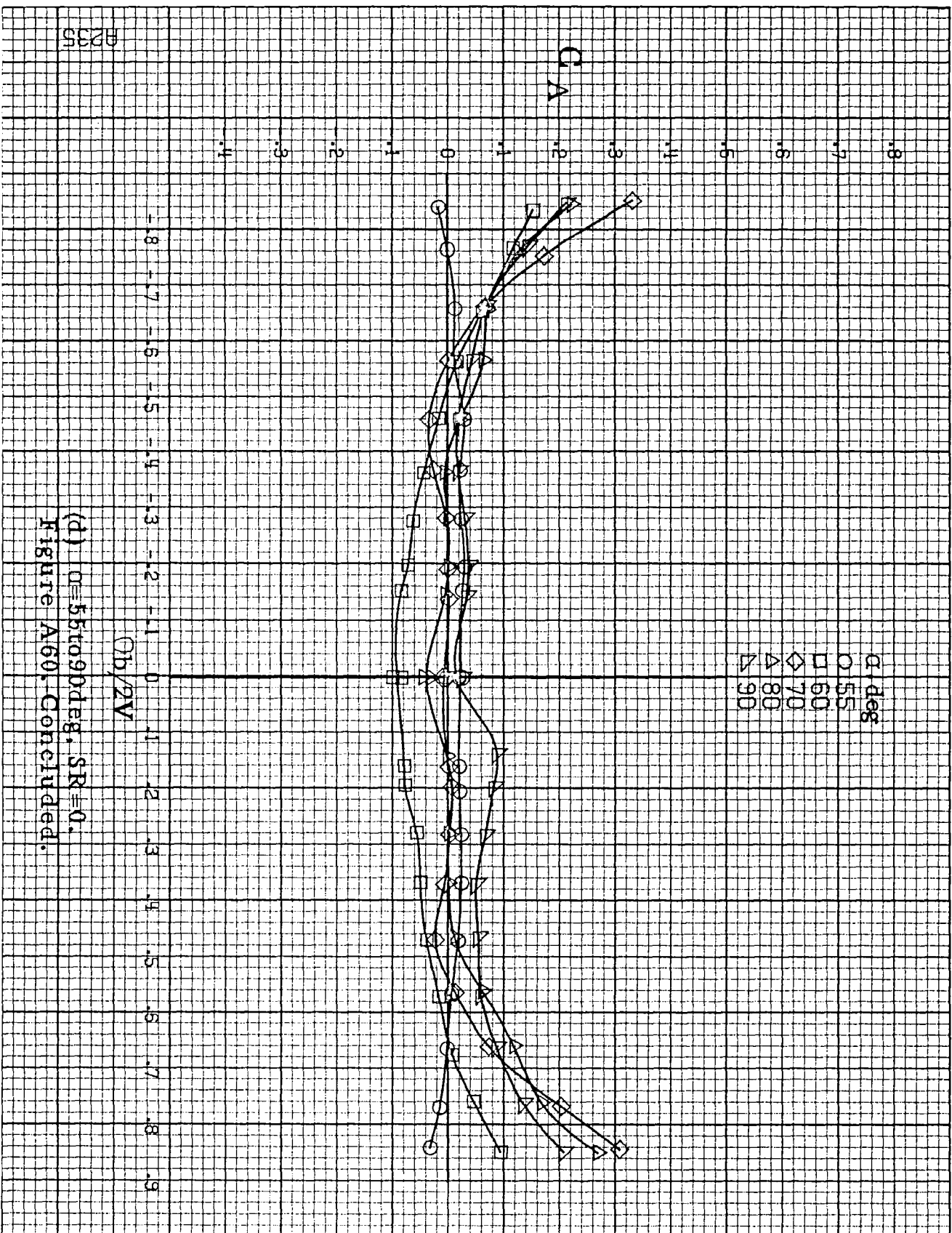
(a)  $\alpha = 8 \text{ to } 16 \text{ deg}$ ,  $SR = 99 \text{ cm (39 in)}$ .

Figure A60. Effect of rotation rate and angle of attack on axial-force coefficient for configuration having sharp-edged fuselage bottom aft of wing T.E.  $\delta_e = 0^\circ$ ,  $\delta_a = 0^\circ$ ,  $\delta_r = 0^\circ$ ,  $\beta = 0^\circ$ .



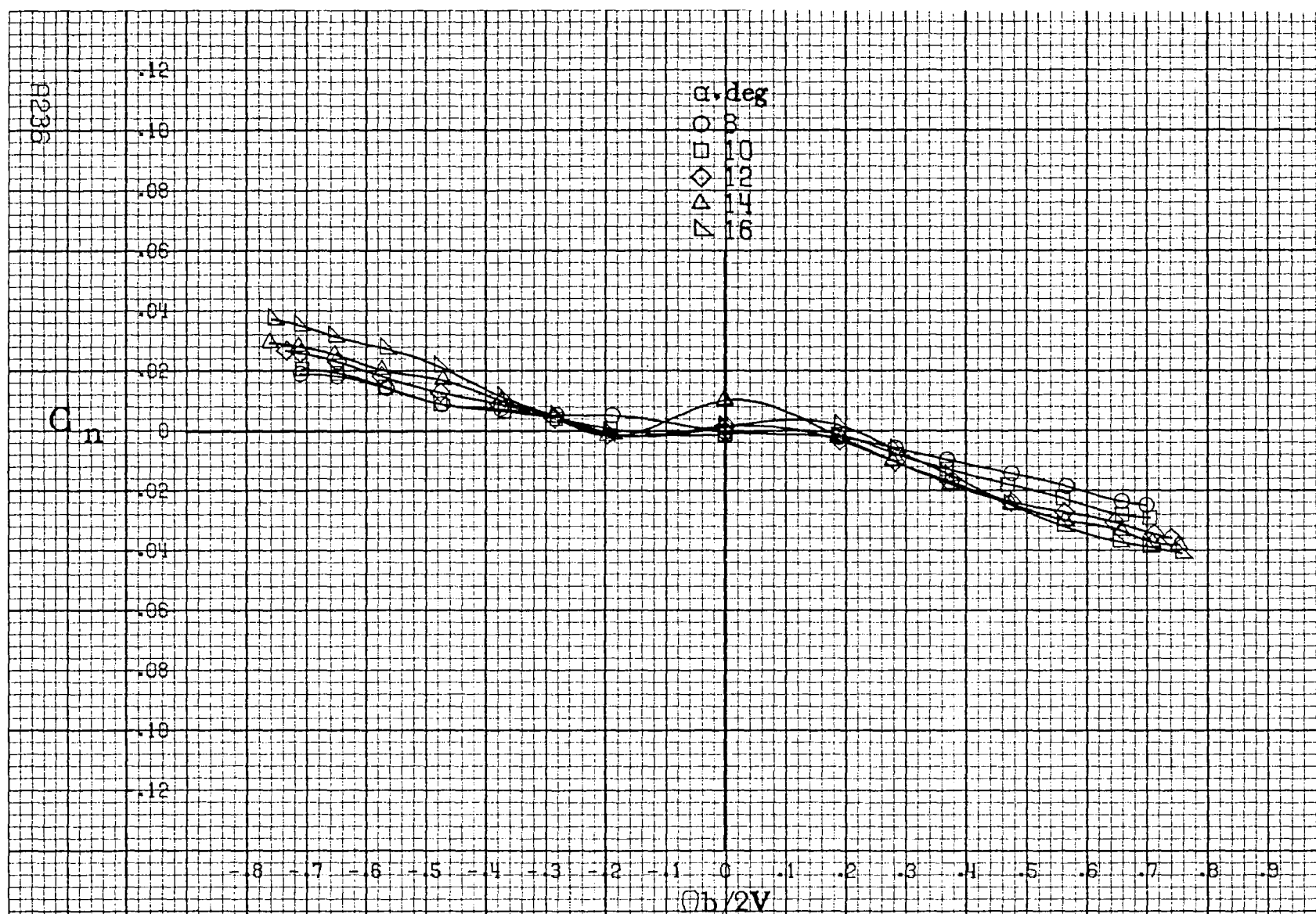






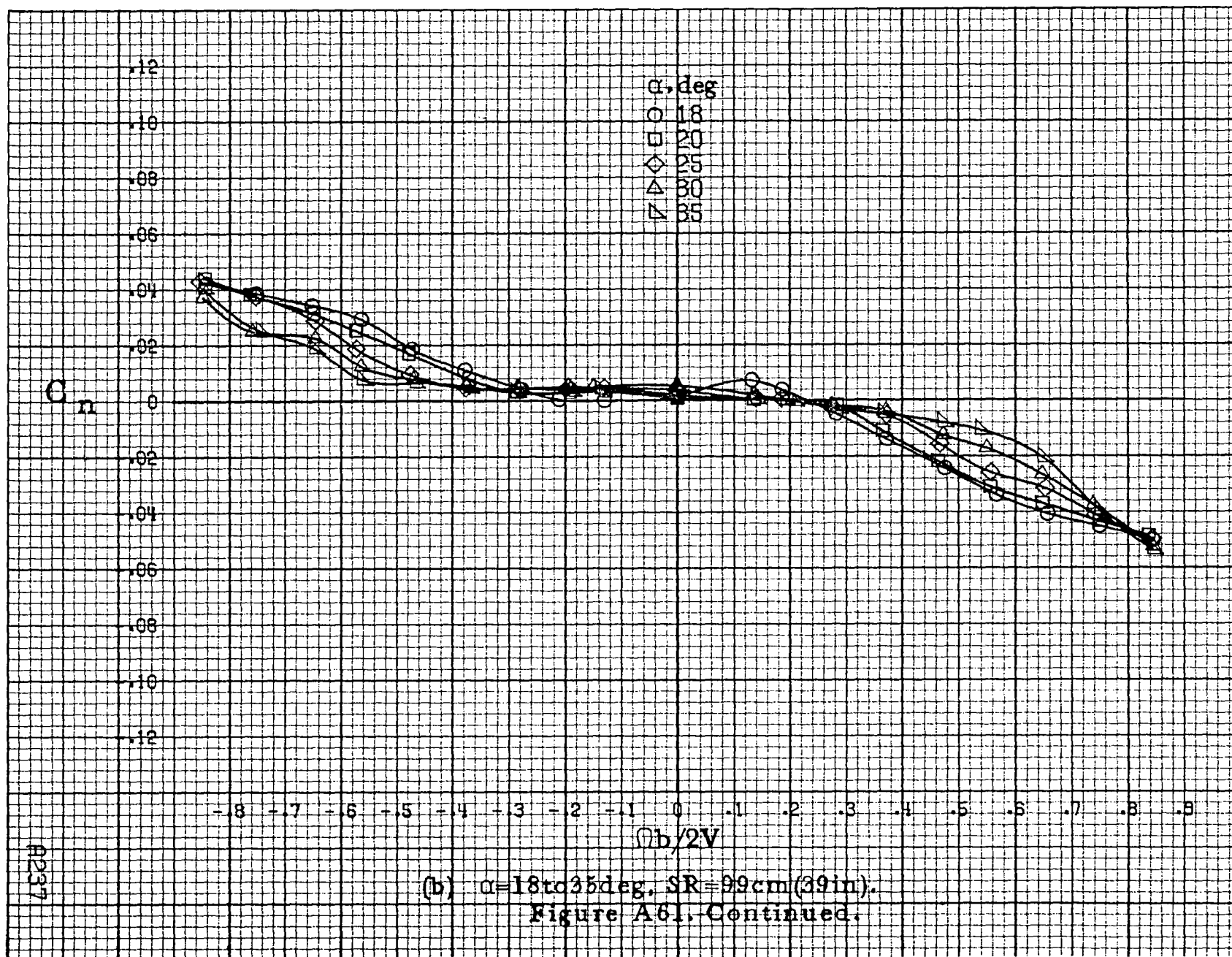
(d)  $\alpha=55$  to  $90$  deg,  $SR=0$ .  
Figure A60. Concluded.



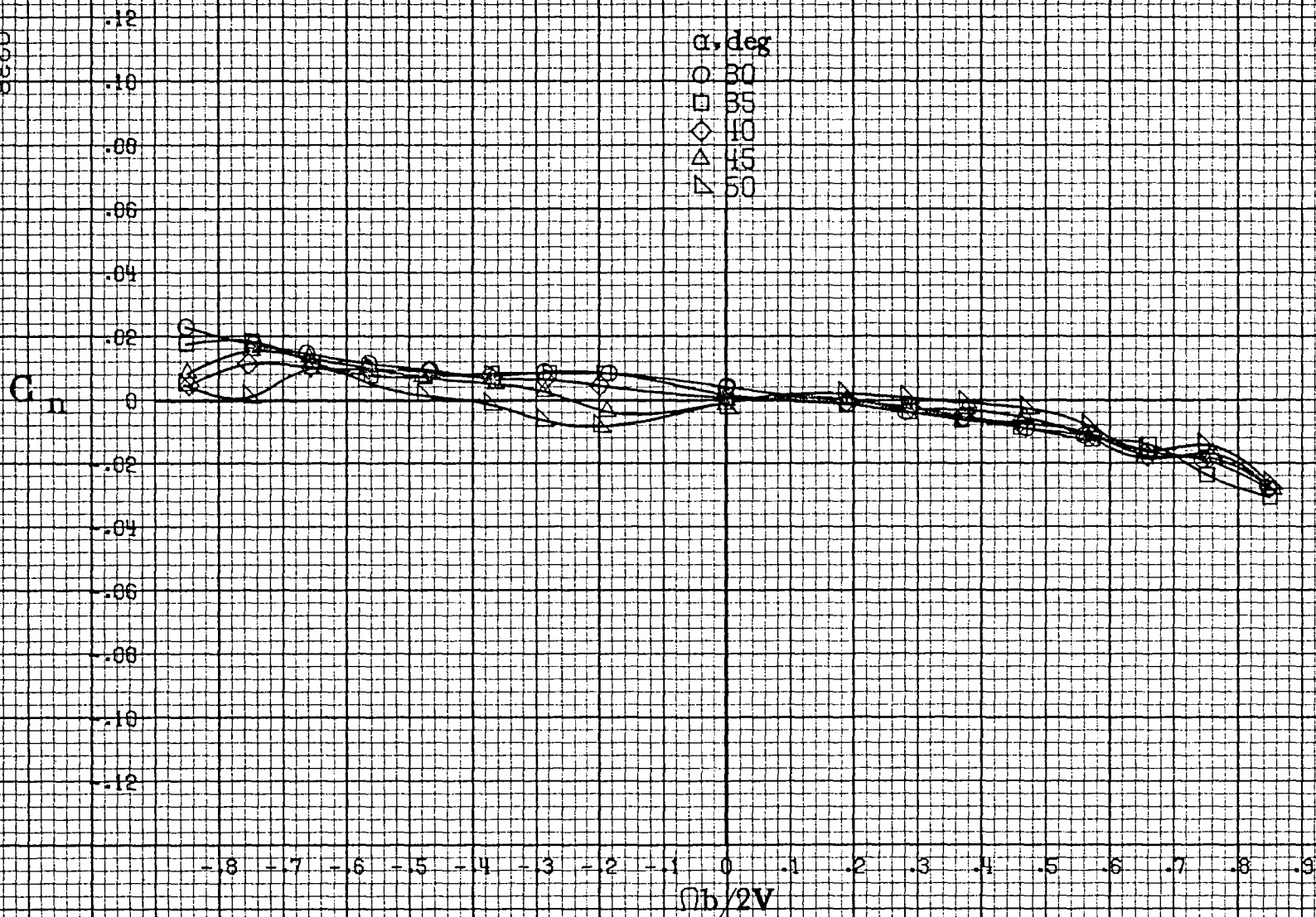


(a)  $\alpha=8$  to  $16^\circ$ ,  $SR=99\text{cm}(39\text{in})$ .

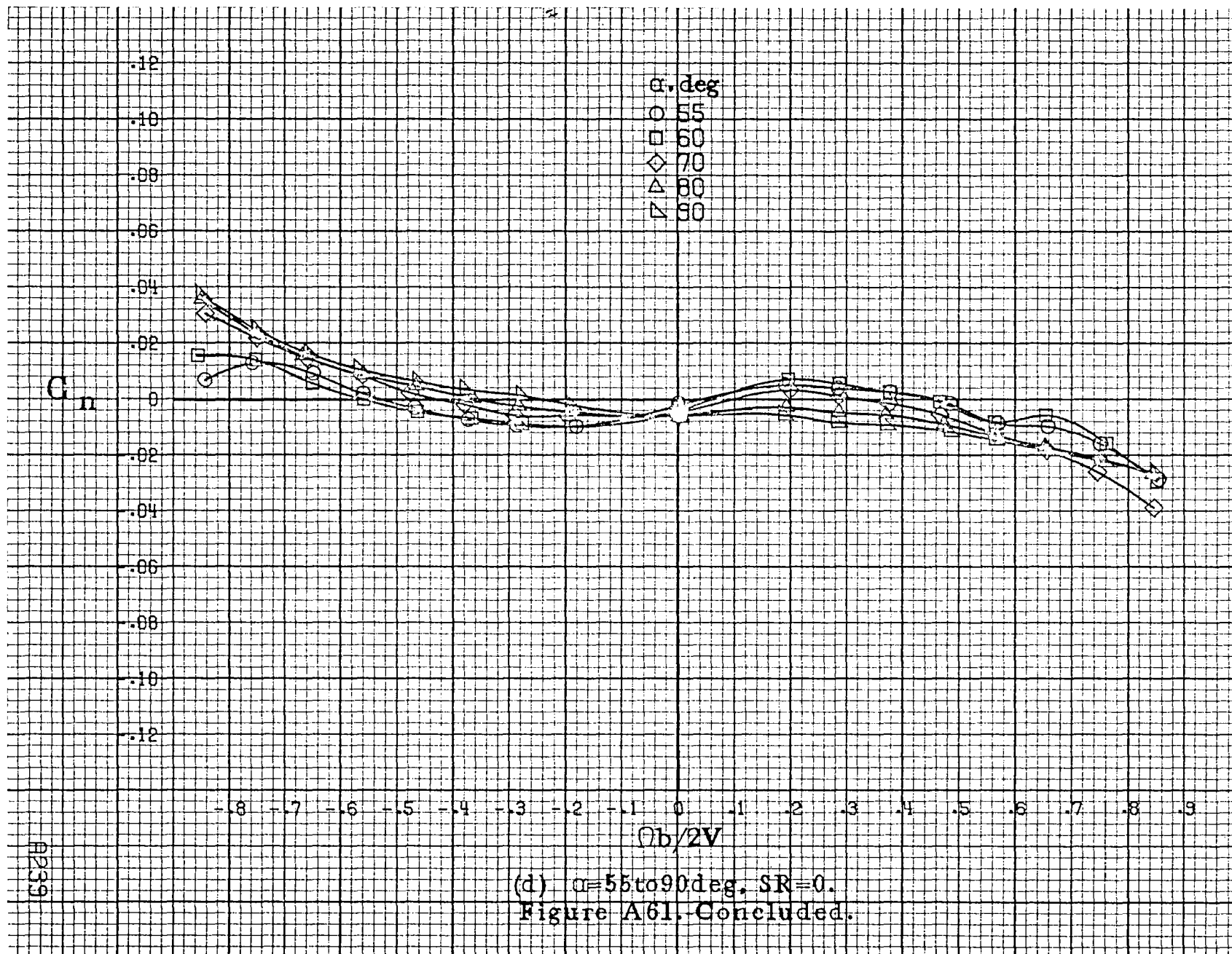
Figure A61. Effect of rotation rate and angle of attack on yawing-moment coefficient for configuration having sharp-edged fuselage bottom aft of engine cowlings.  $\delta_e=0^\circ$ ,  $\delta_a=0^\circ$ ,  $\delta_r=0^\circ$ ,  $\beta=0^\circ$ .

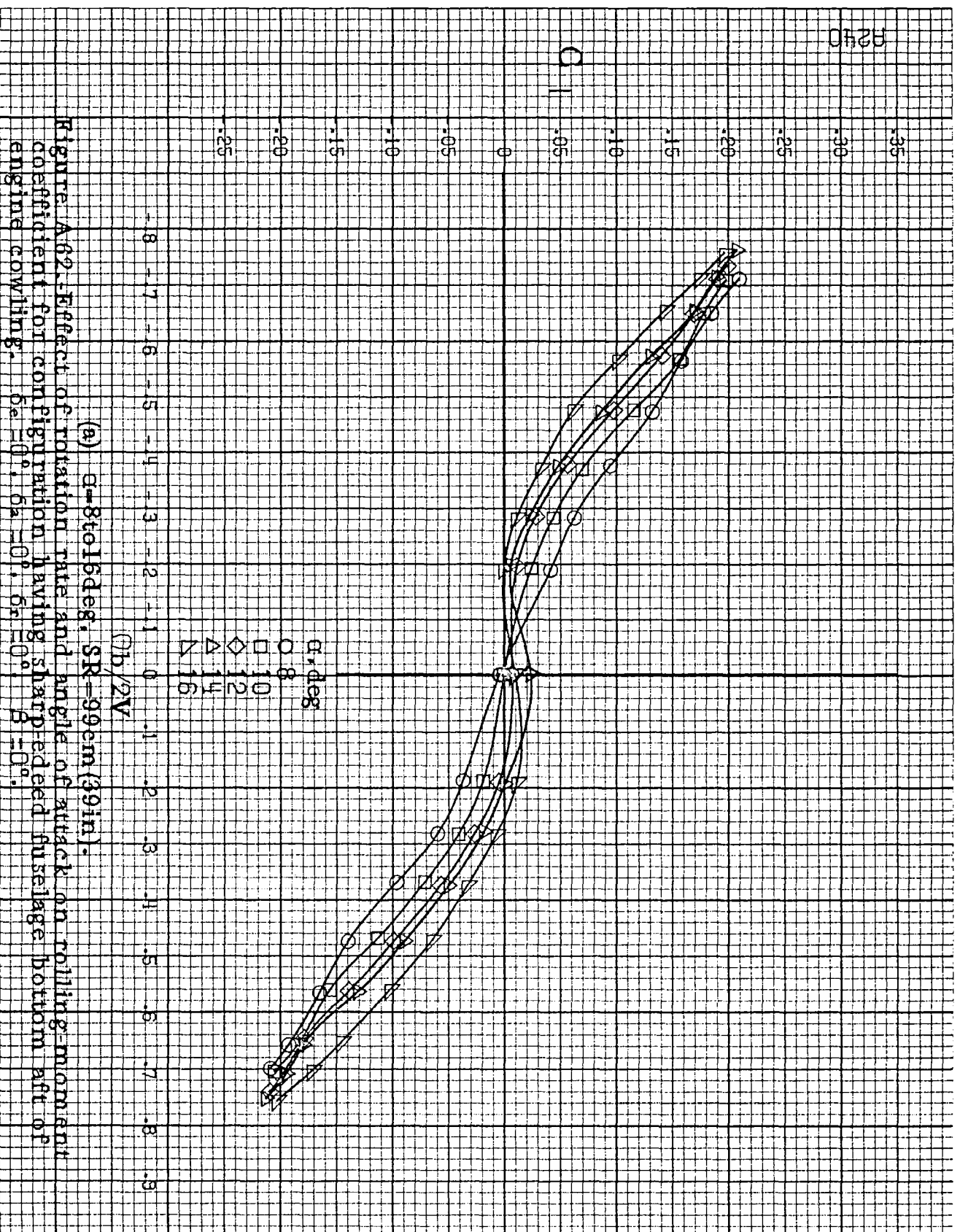


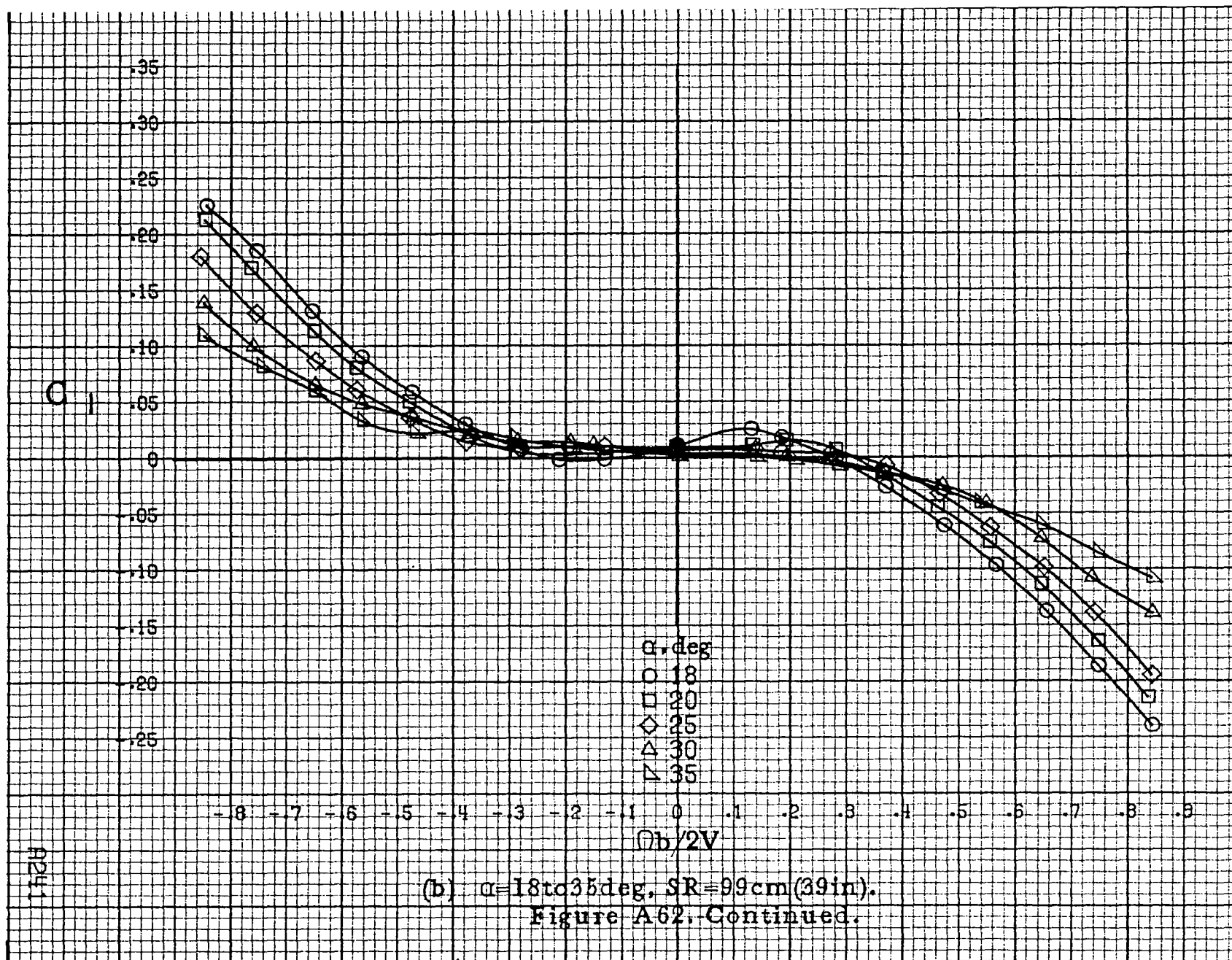
A238



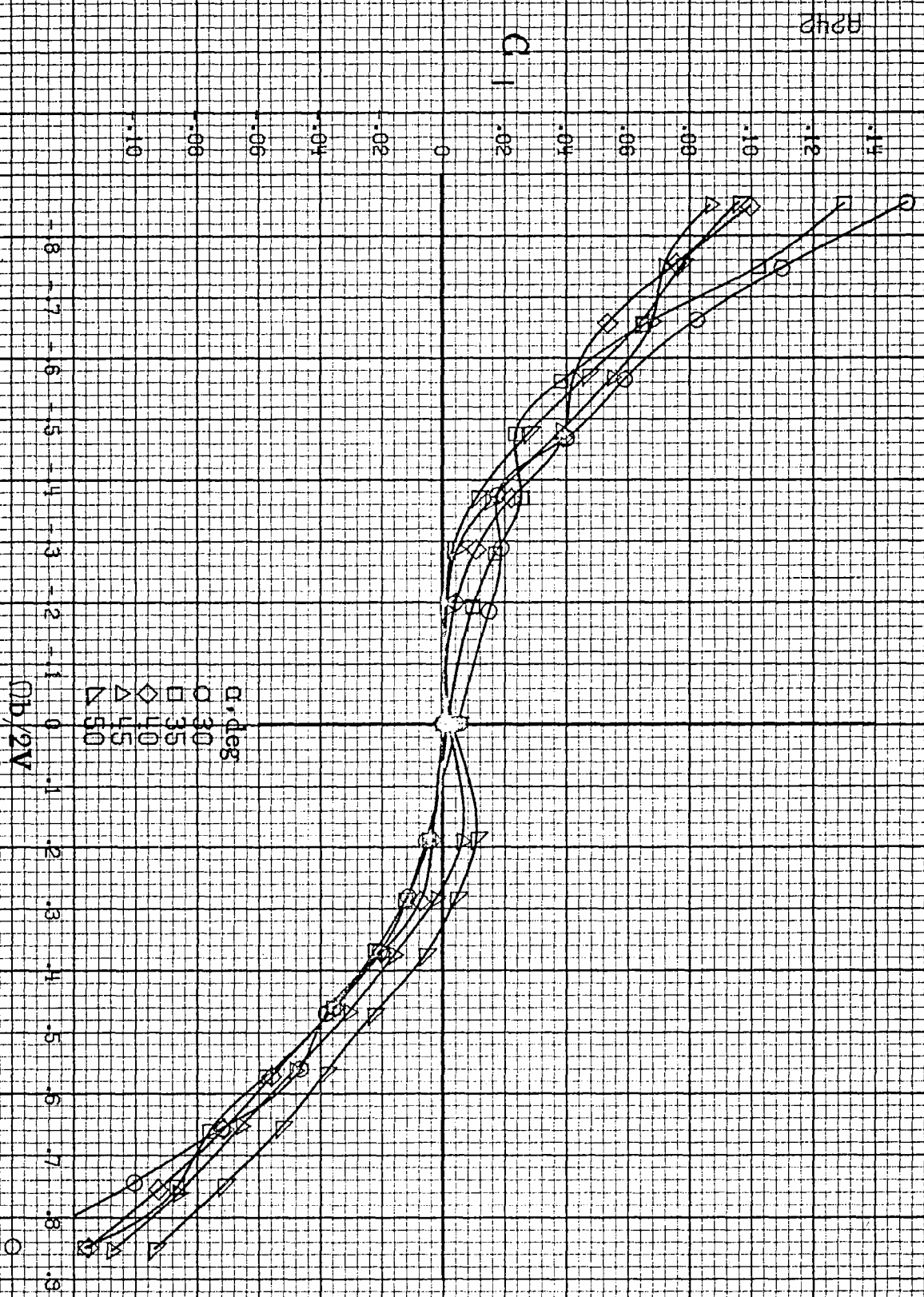
(c)  $\alpha=30$  to  $50^\circ$ ,  $SR=0$ .  
Figure A61. Continued.





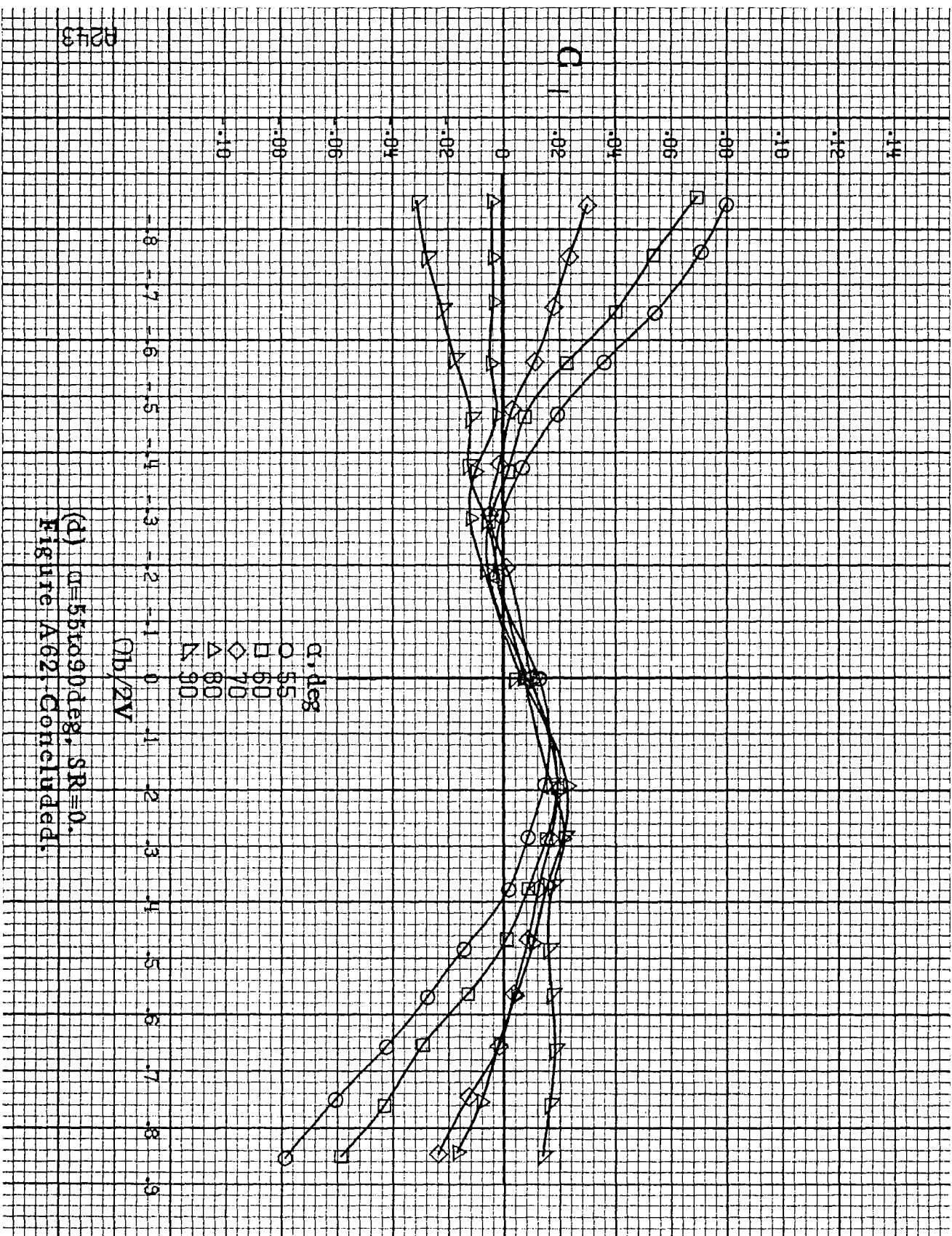




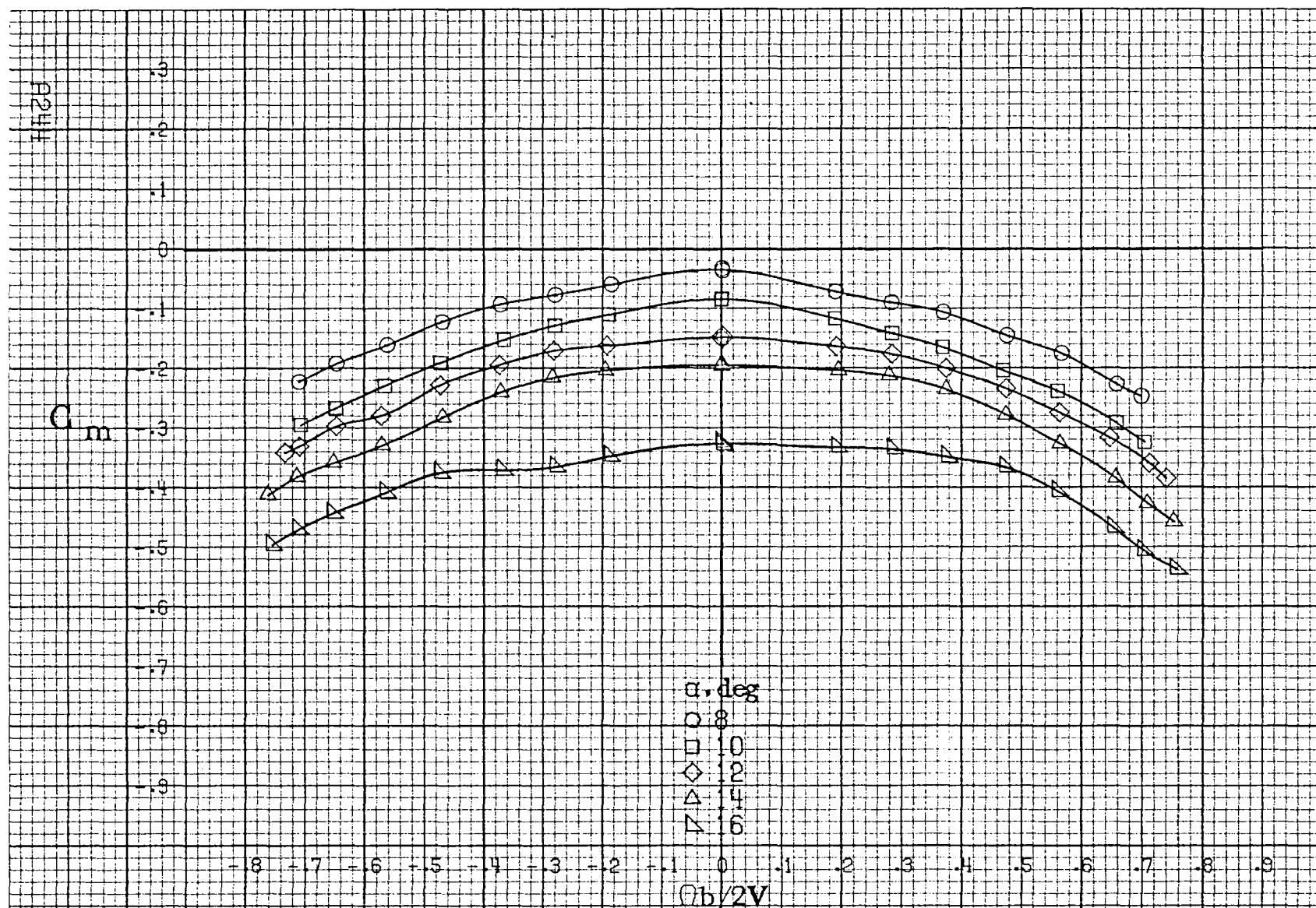


(c)  $\alpha=30$  to  $50^\circ$ ,  $SR=0$ .  
Figure A62, Continued.



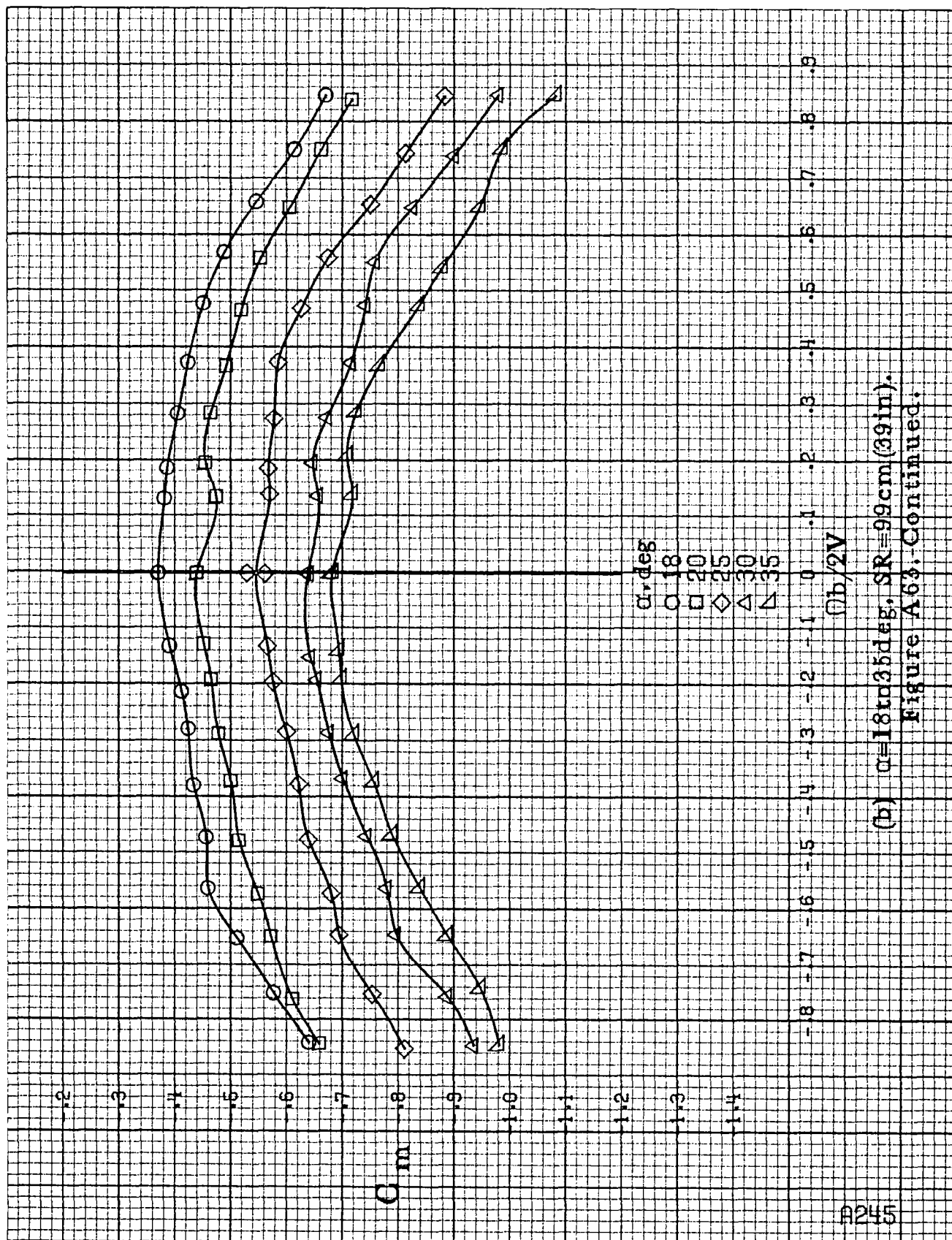


(d)  $\alpha=55$  to  $90^\circ$ ,  $SR=0$ .  
Figure A62, Concluded.

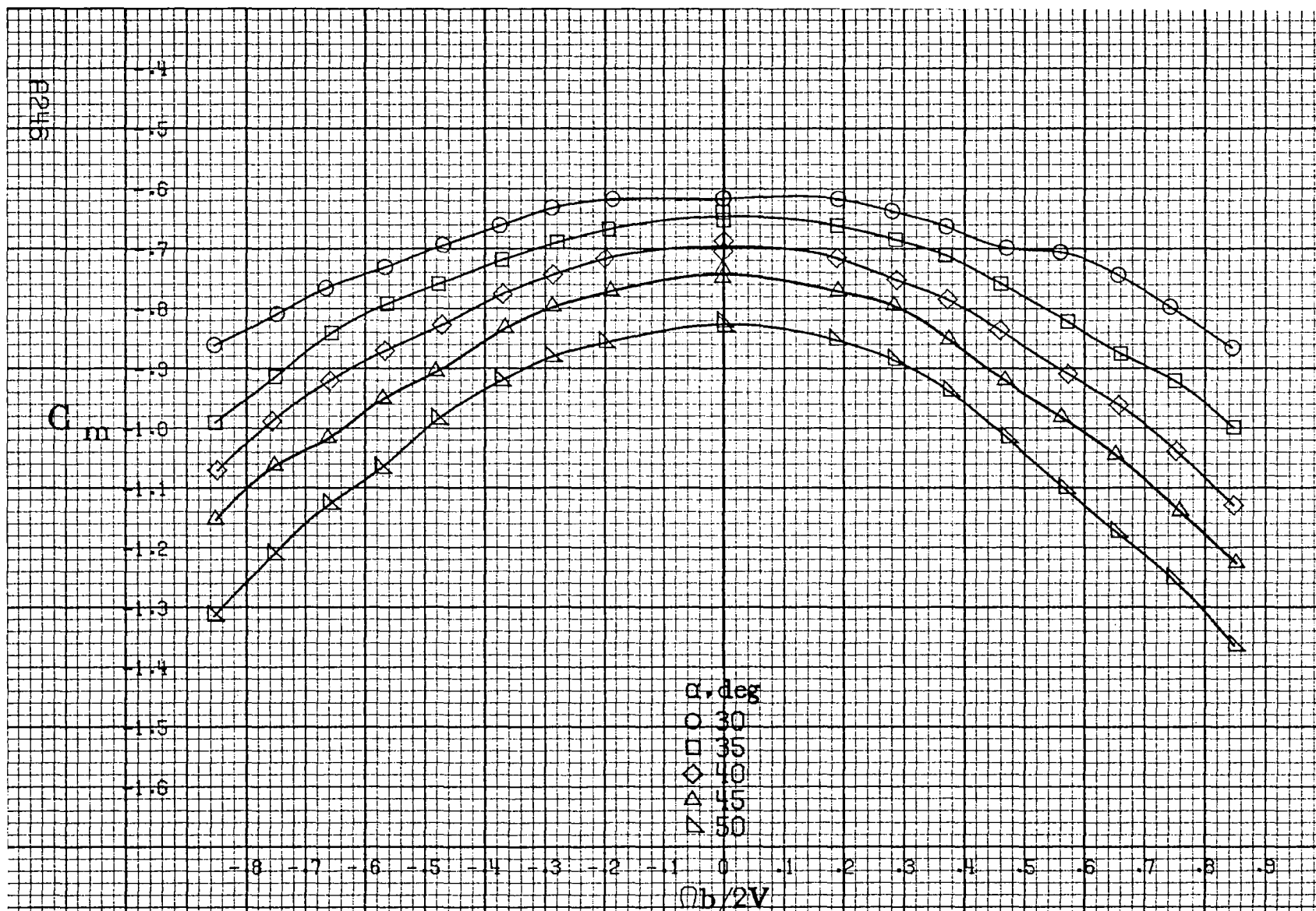


(a)  $\alpha = 8$  to  $16^\circ$ ,  $SR = 99\text{cm (39in)}$ .

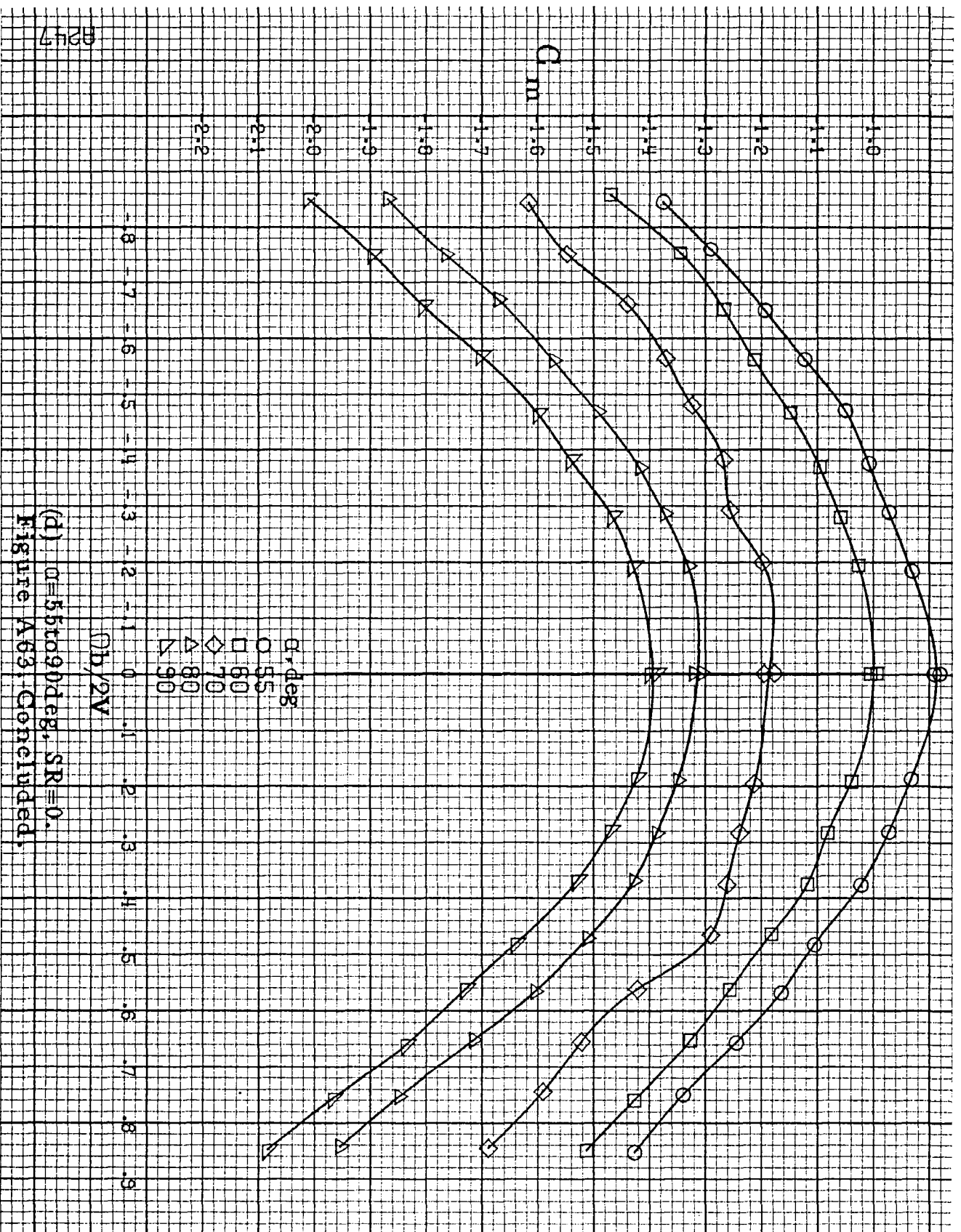
Figure A63. Effect of rotation rate and angle of attack on pitching moment coefficient for configuration having sharp-edged fuselage bottom aft of engine cowlings.  $\delta_a = 0^\circ$ ,  $\delta_e = 0^\circ$ ,  $\delta_r = 0^\circ$ ,  $\beta = 0^\circ$ .



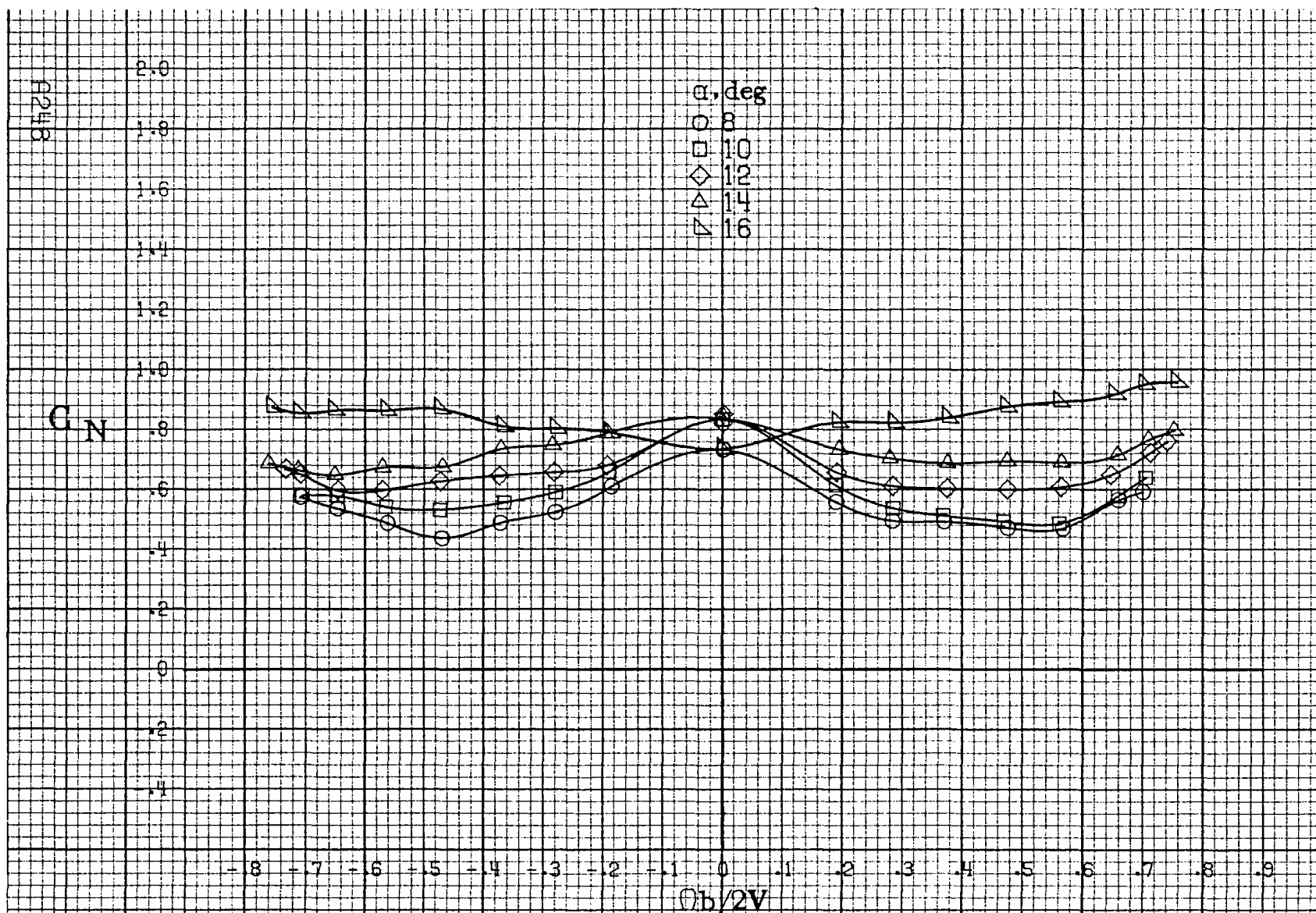
(b)  $\alpha=18$  to  $35^\circ$ ,  $SR=99\text{cm}(39\text{in})$ .  
Figure A63. Continued.



(c)  $\alpha = 30$  to  $50$  deg,  $SR = 0$ .  
Figure A63. Continued.



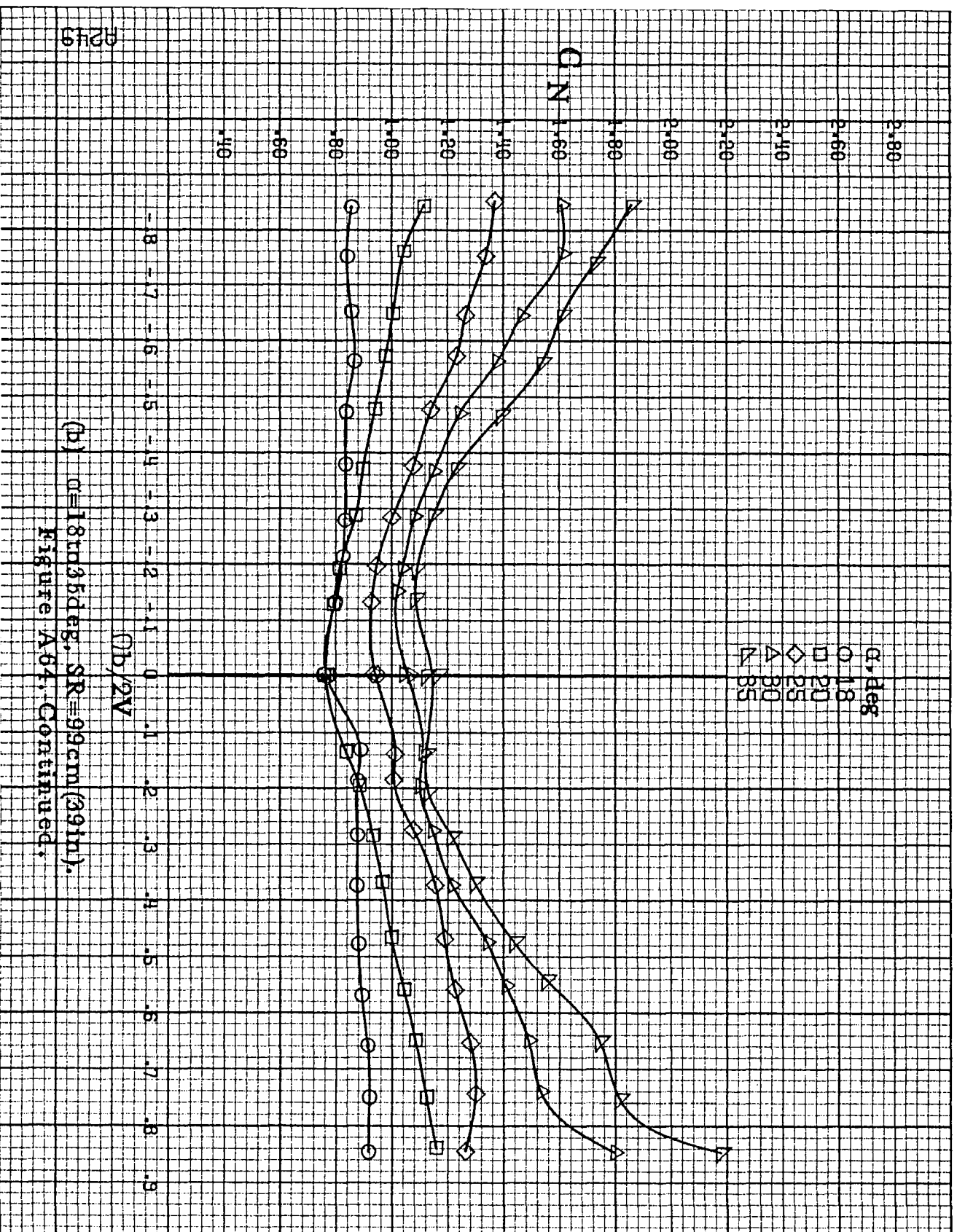
(d)  $\theta=55$  to  $90$  deg,  $SR=0$ .  
Figure A63, Concluded.



(a)  $\alpha=8$  to  $16^\circ$ ,  $SR=99\text{cm}$  (39 in).

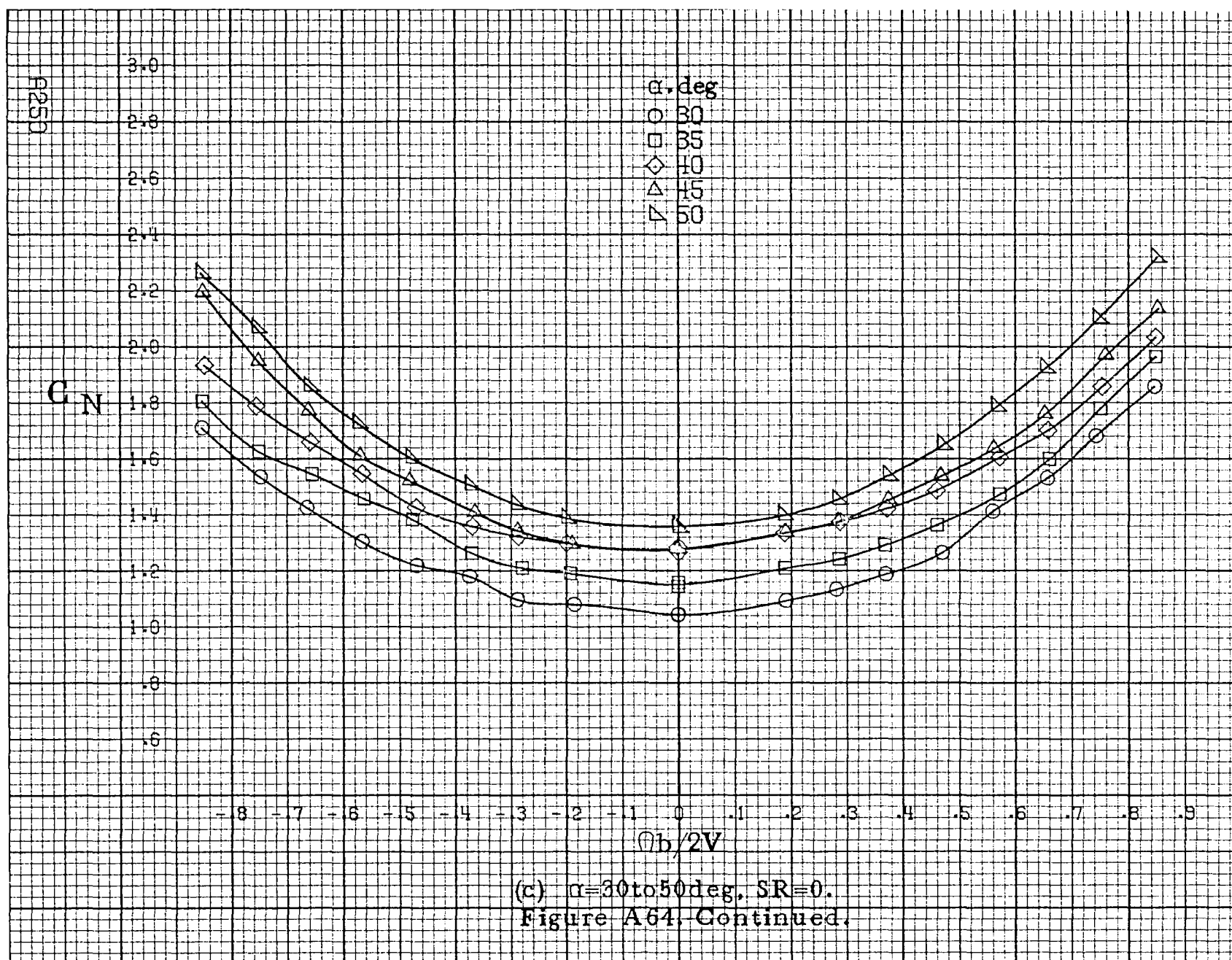
Figure A64. Effect of rotation rate and angle of attack on normal-force coefficient for configuration having sharp-edged fuselage bottom aft of engine cowlings.  $\delta_a=0^\circ$ ,  $\delta_z=0^\circ$ ,  $\delta_r=0^\circ$ ,  $\beta=0^\circ$ .

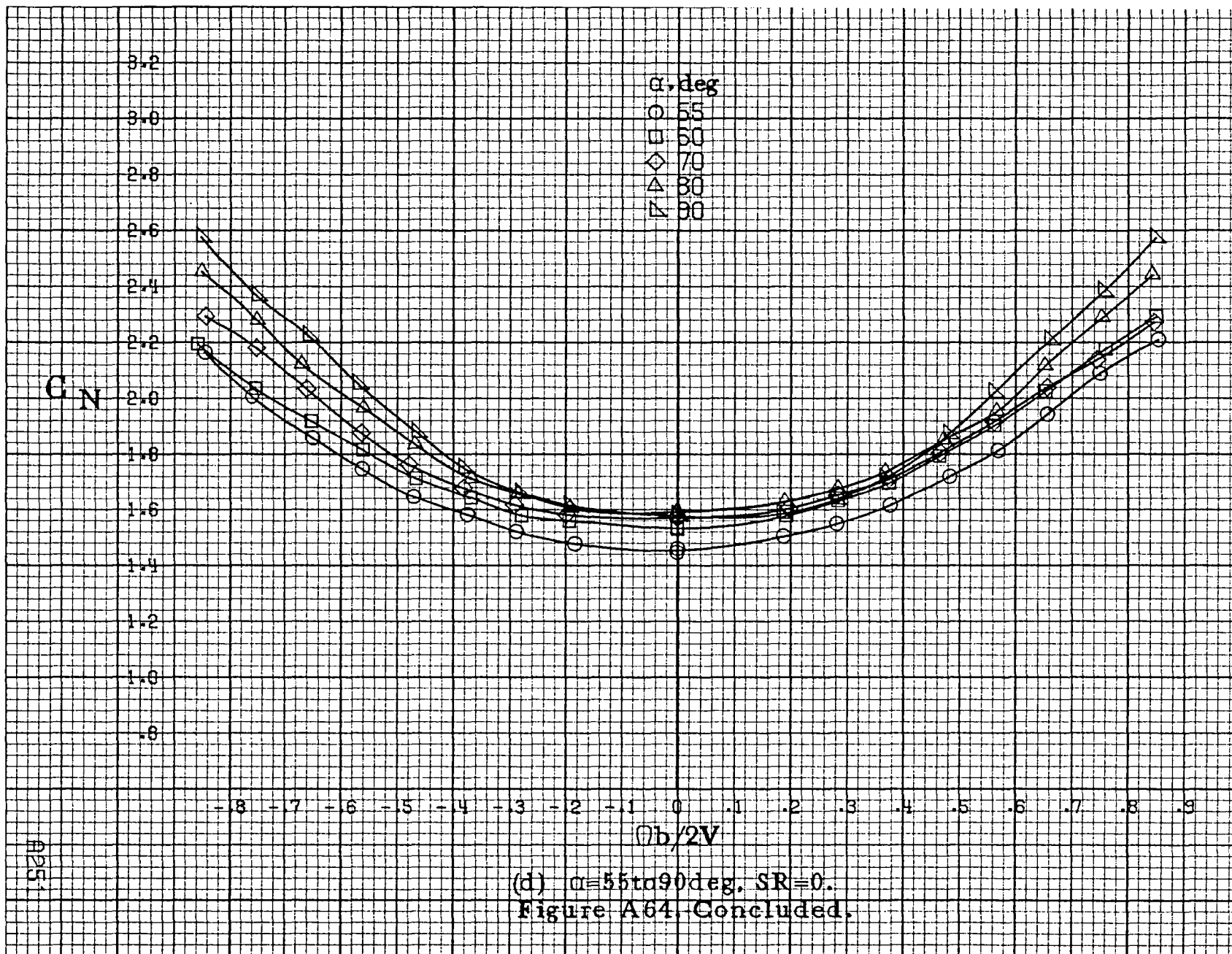


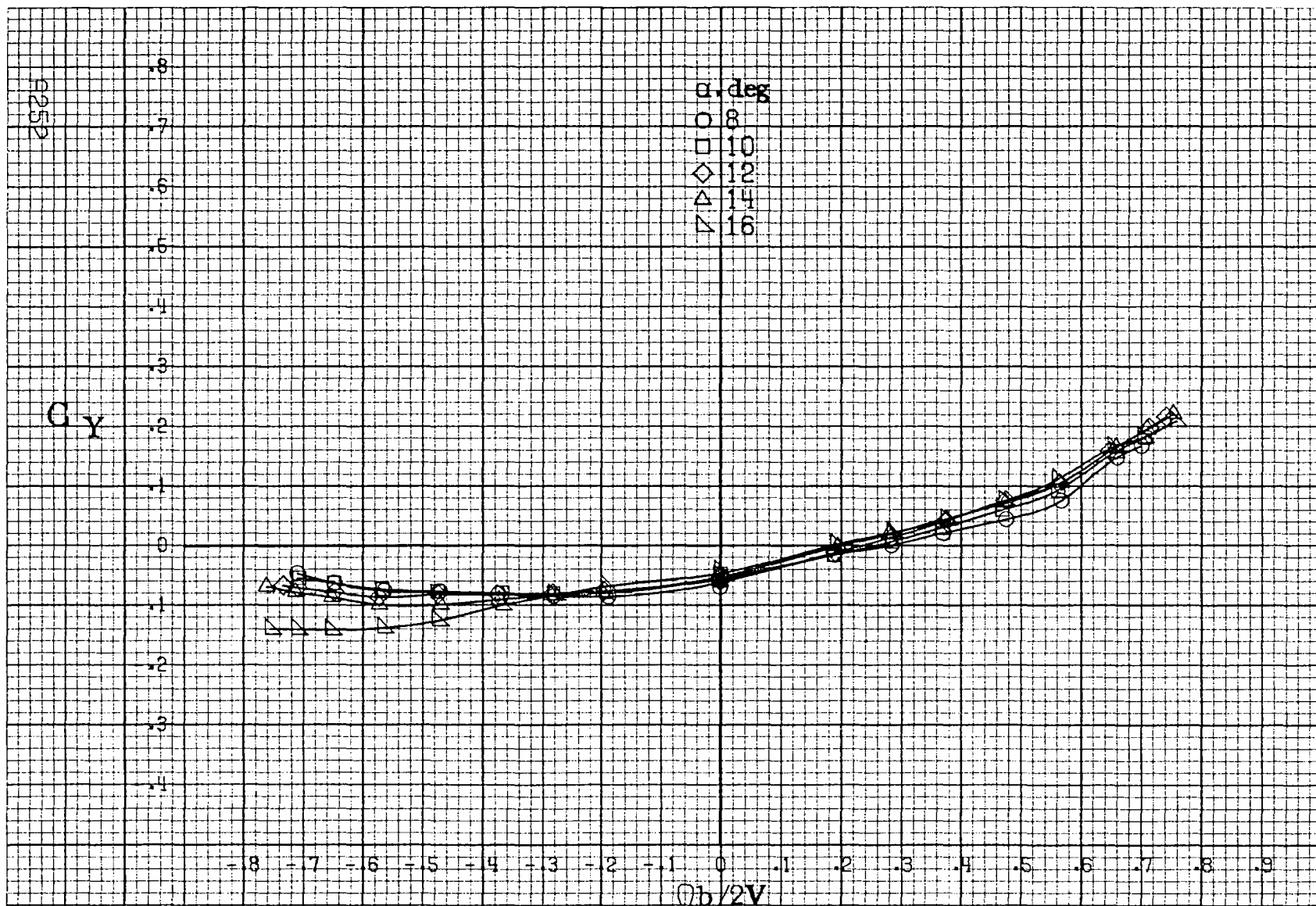


(b)  $\alpha=18$  to  $35$  deg,  $SR=99$  cm (39 in.).  
Figure A64. Continued.



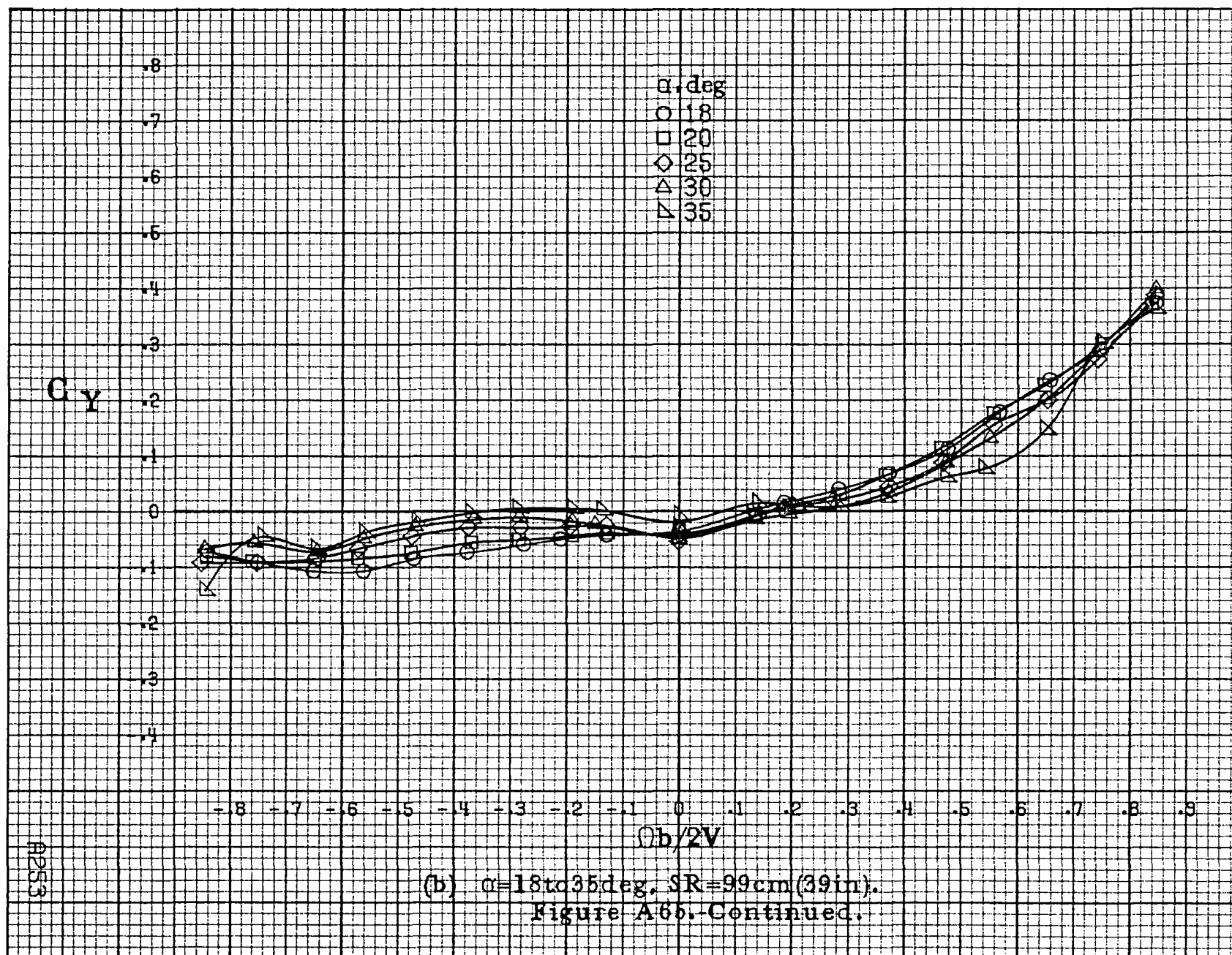


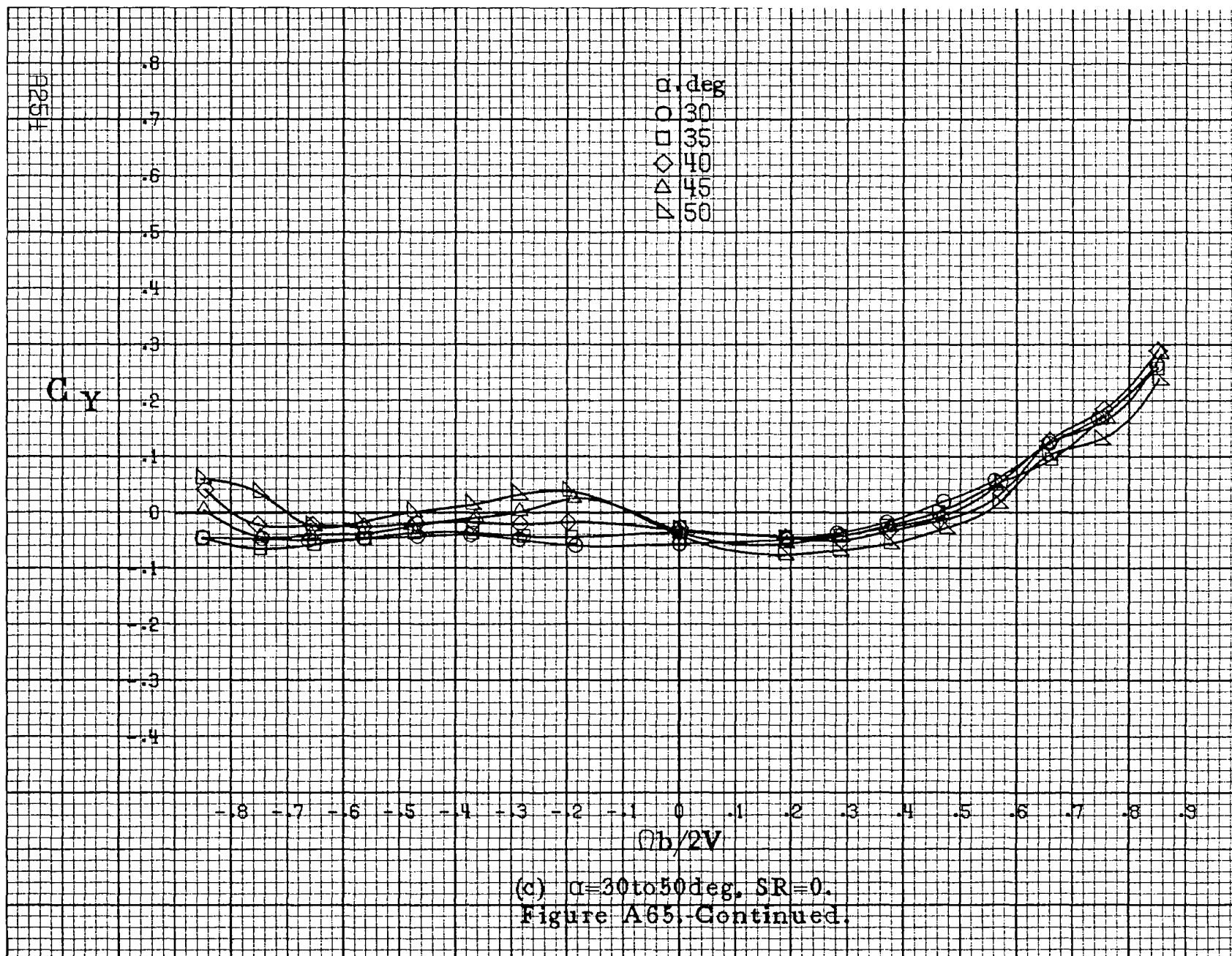


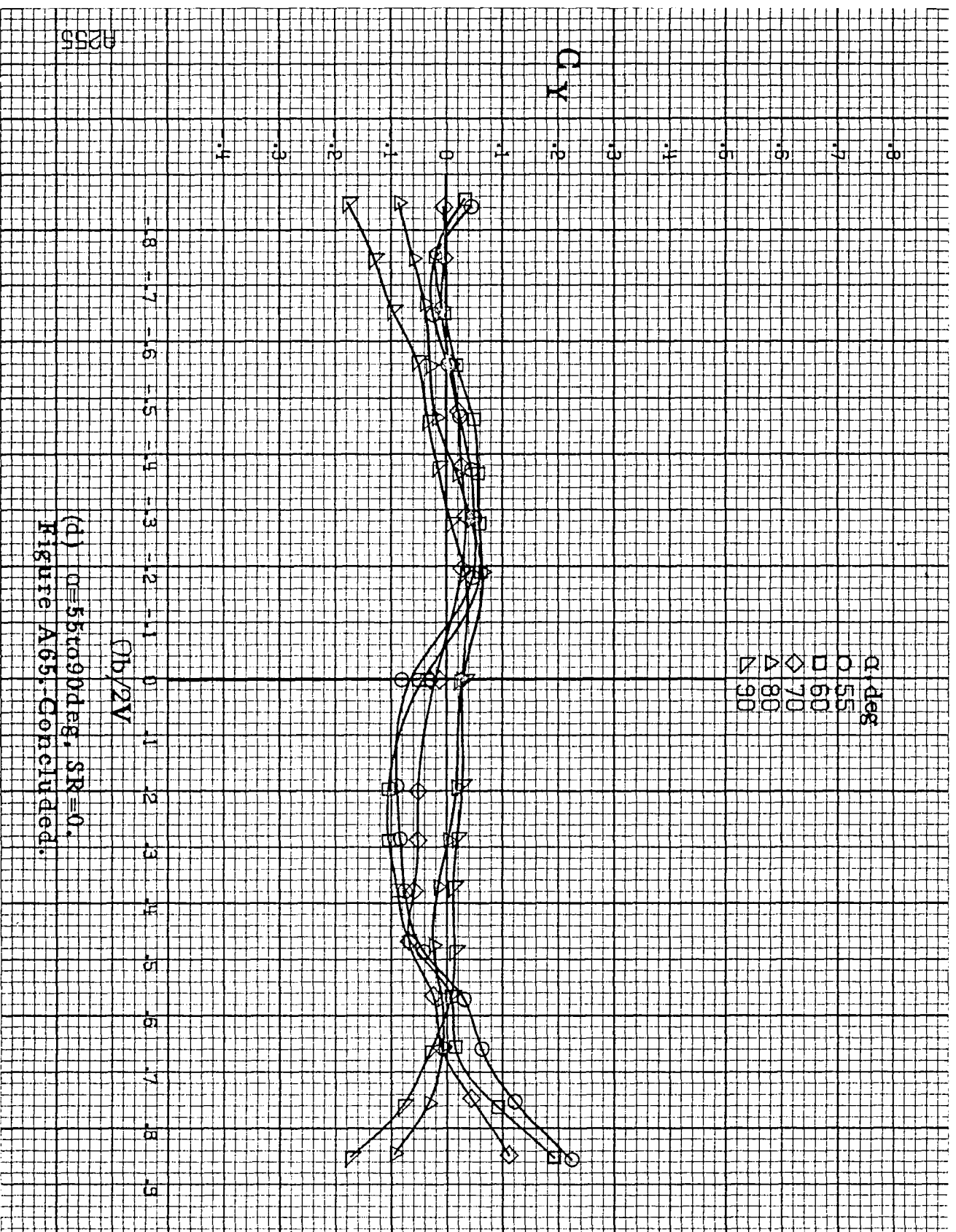


(a)  $\alpha=8\text{ to }16^\circ$ ,  $SR=99\text{ cm (39 in)}$ .

Figure A65. Effect of rotation rate and angle of attack on side-force coefficient for configuration having sharp-edged fuselage bottom aft of engine cowlings.  $\delta_e=0^\circ$ ,  $\delta_a=0^\circ$ ,  $\delta_r=0^\circ$ ,  $\beta=0^\circ$ .

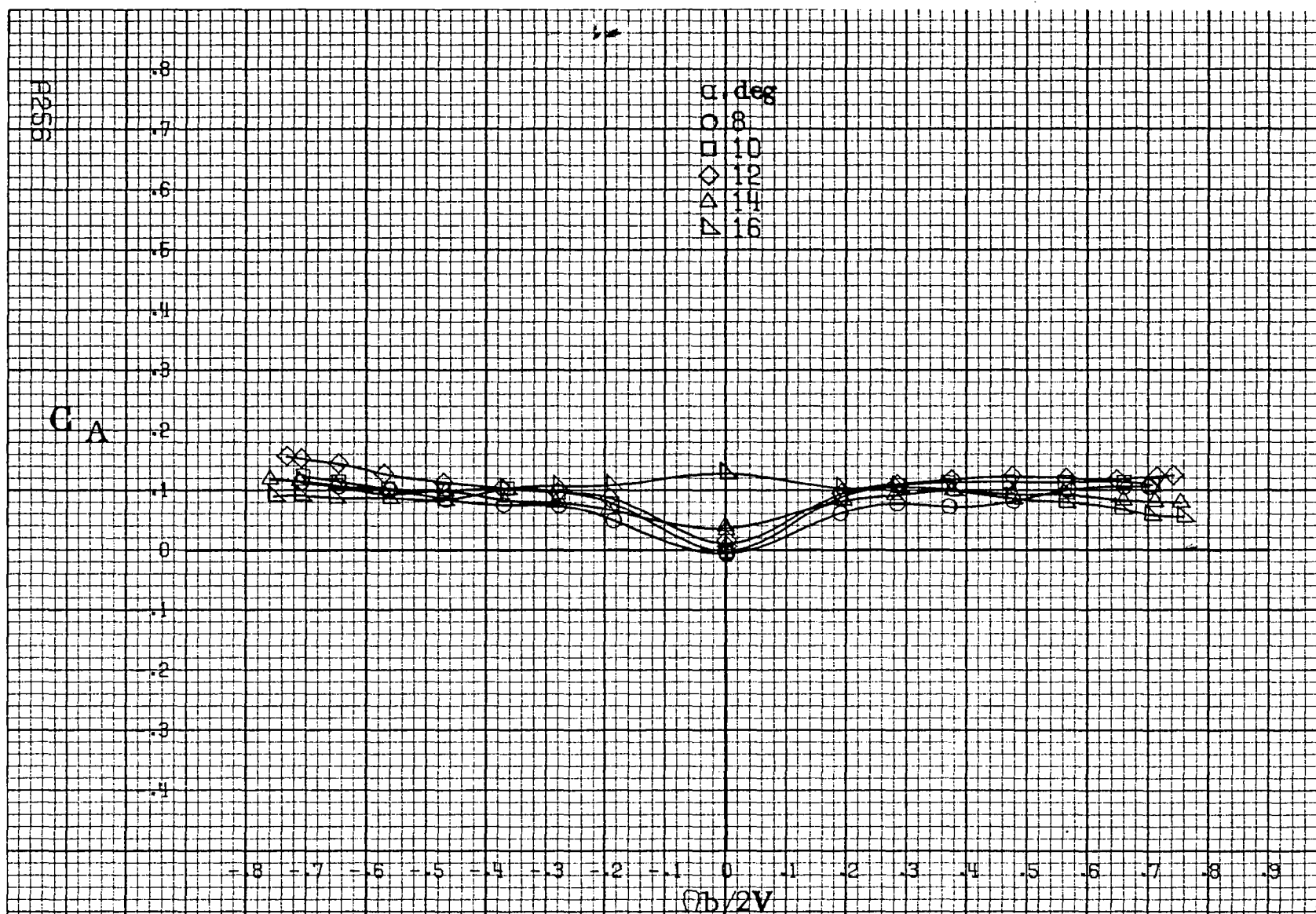






(d)  $0 = 55$  to  $90$  deg,  $SR = 0$ ,  
 Figure A65.-Concluded.

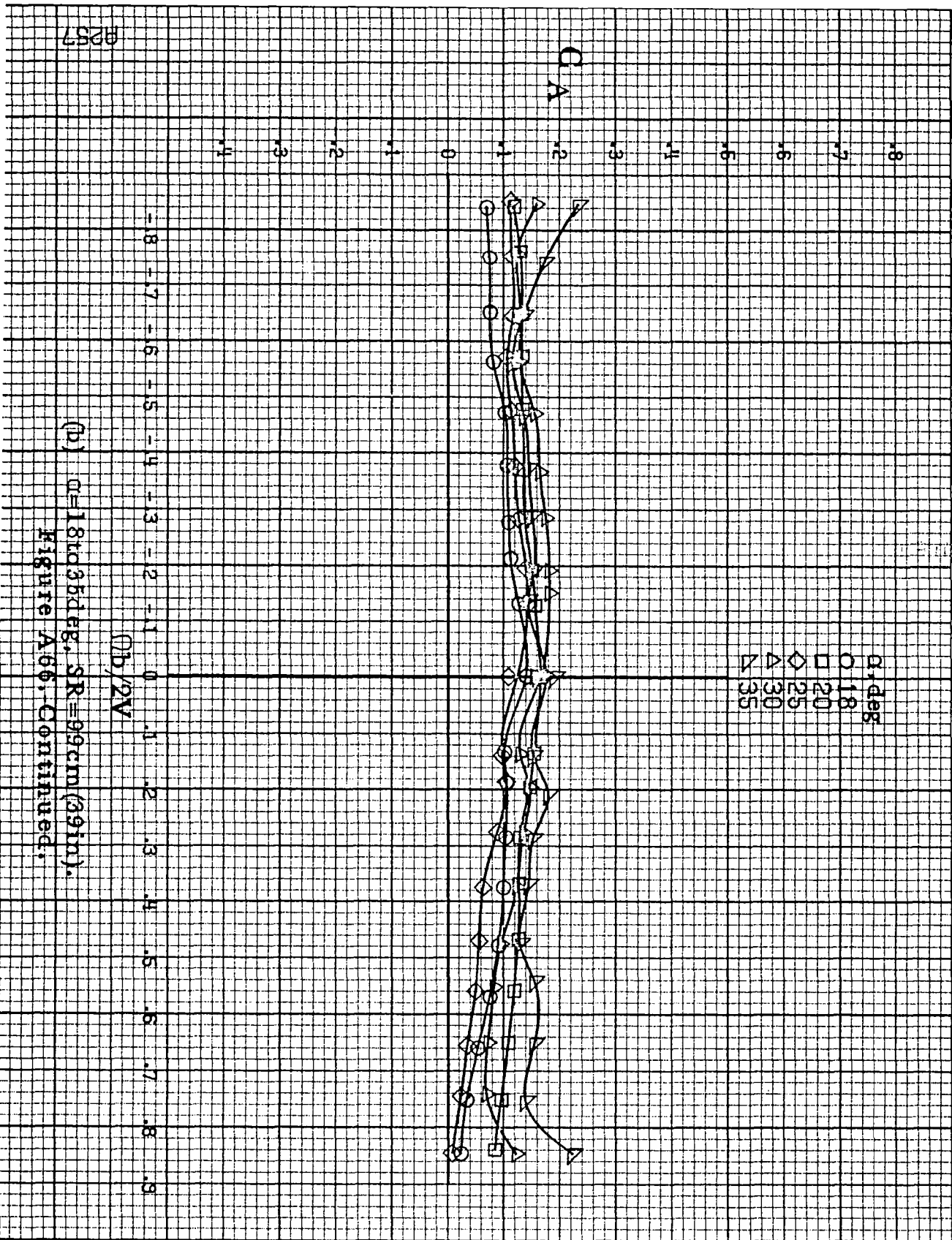




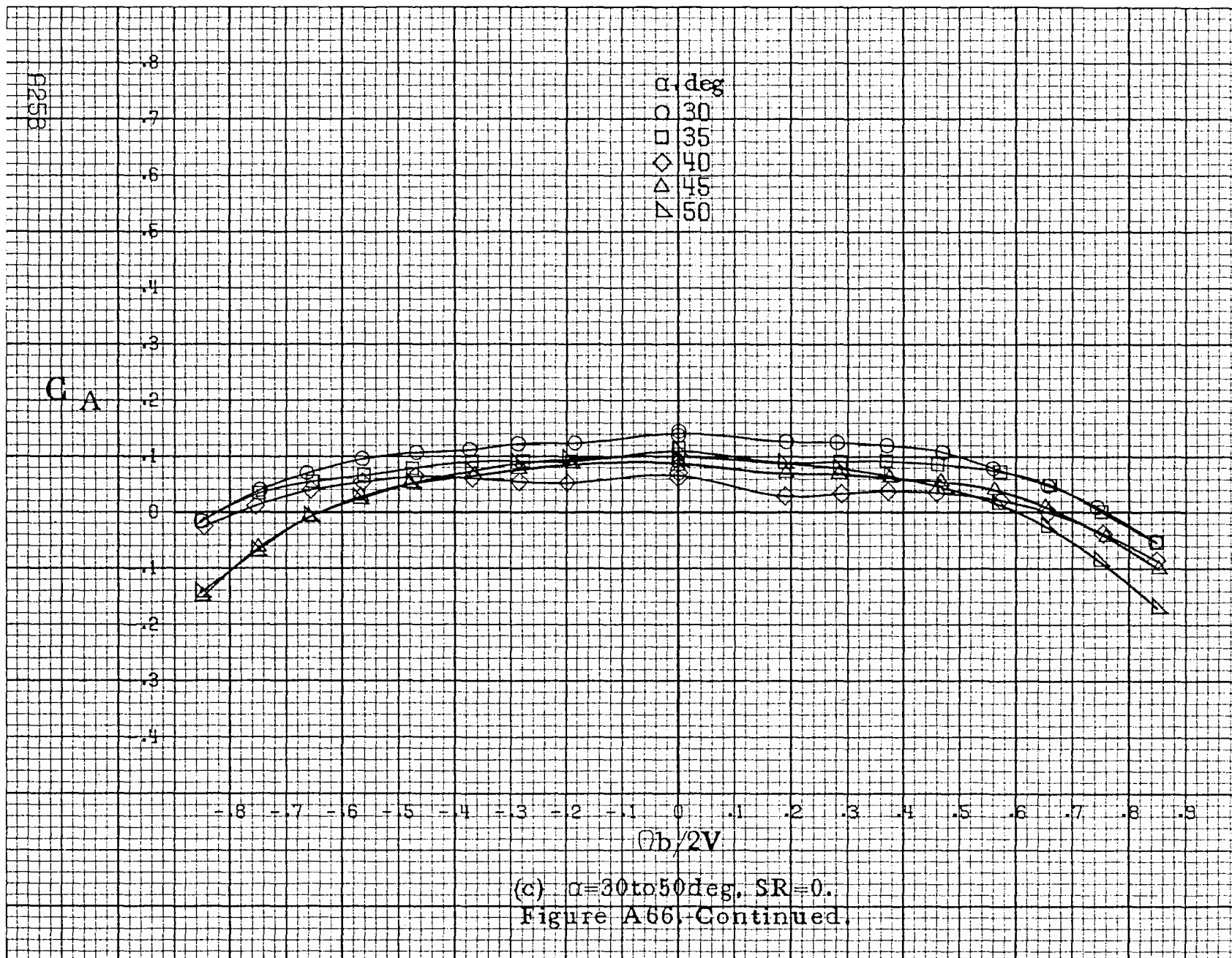
(a)  $\alpha=8$  to  $16^\circ$ ,  $SR=99$  cm (39 in).

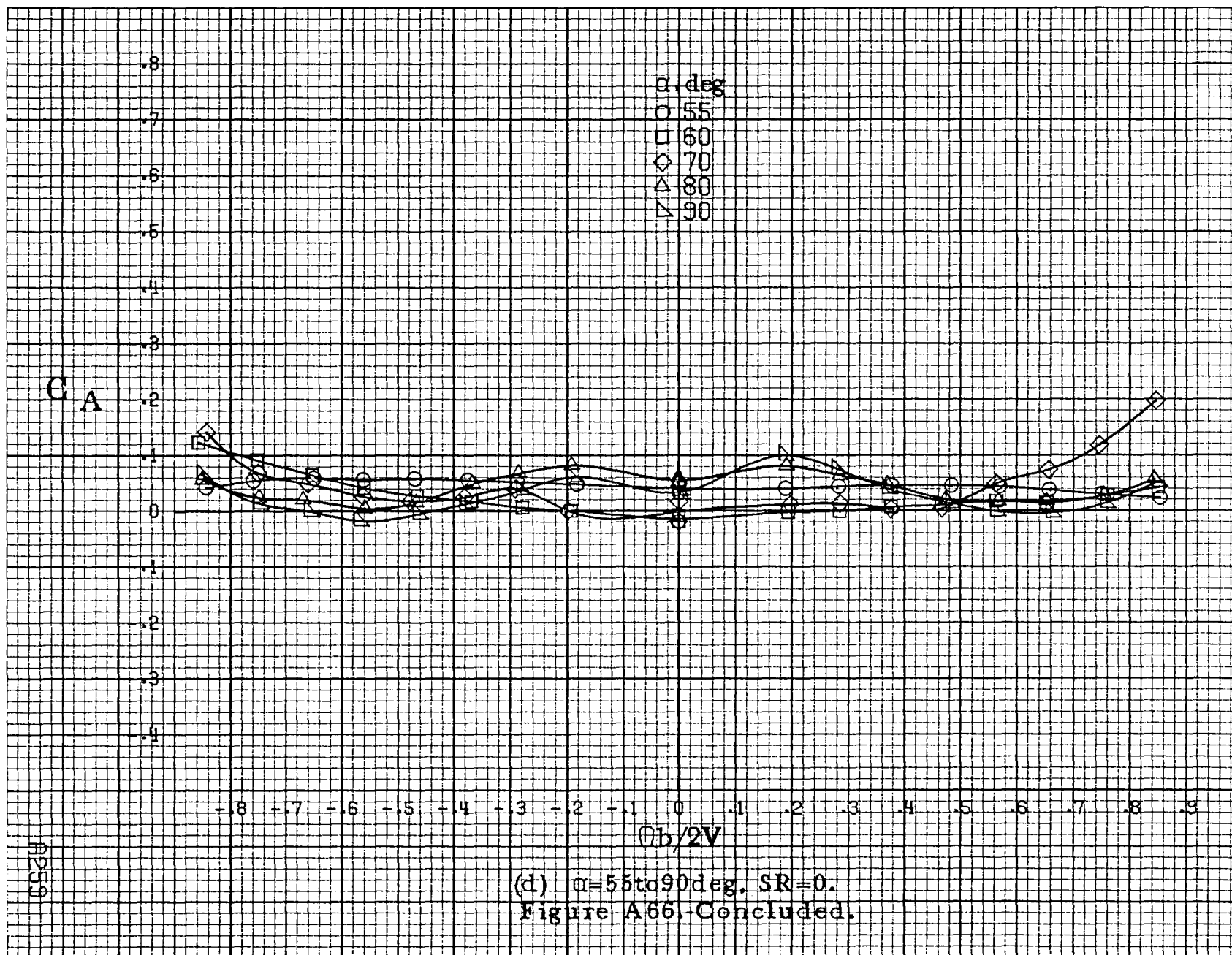
Figure A66.-Effect of rotation rate and angle of attack on axial-force coefficient for configuration having sharp-edged fuselage bottom aft of engine cowlings.  $\delta_a=0^\circ$ ,  $\delta_x=0^\circ$ ,  $\delta_r=0^\circ$ ,  $\beta=0^\circ$ .

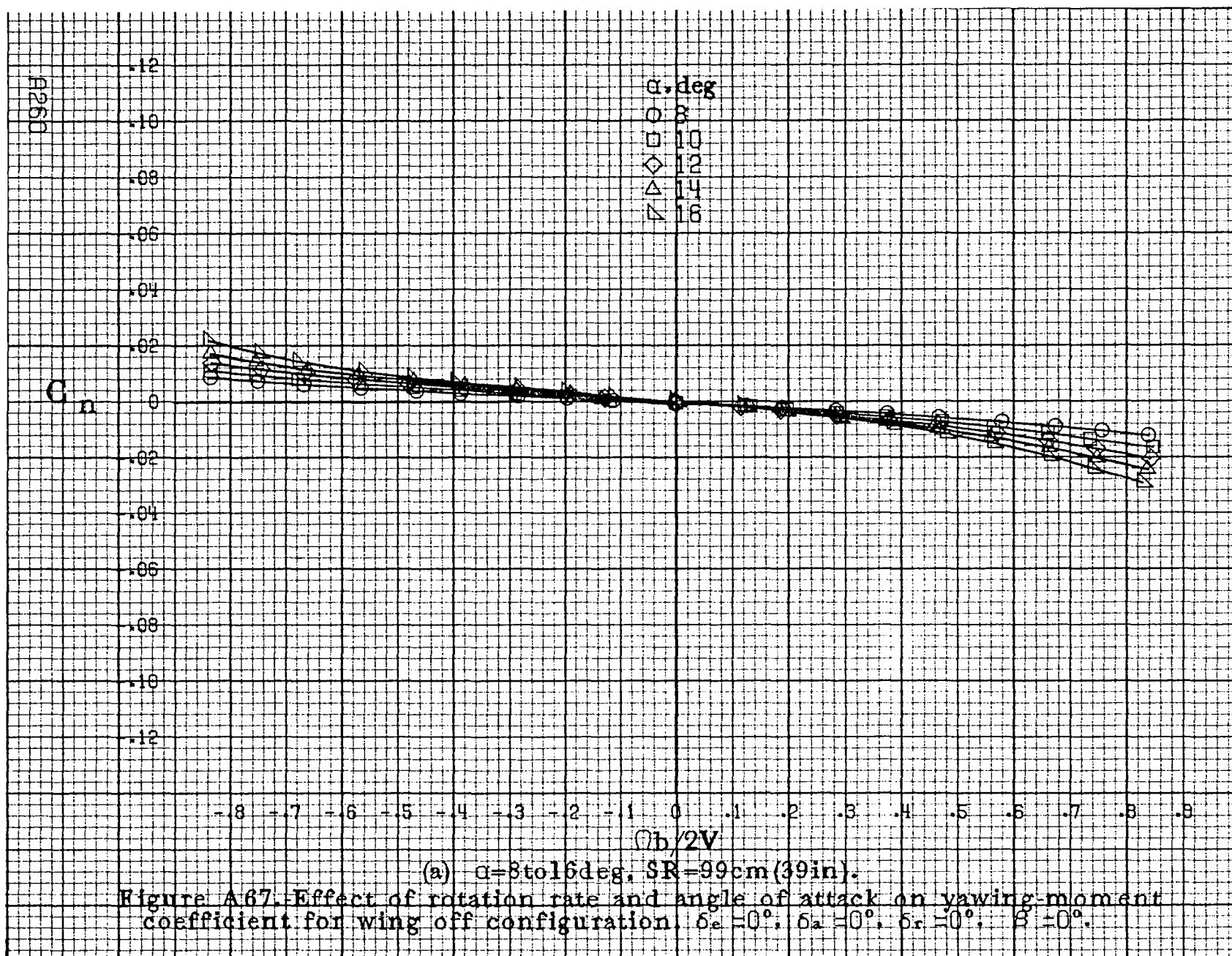


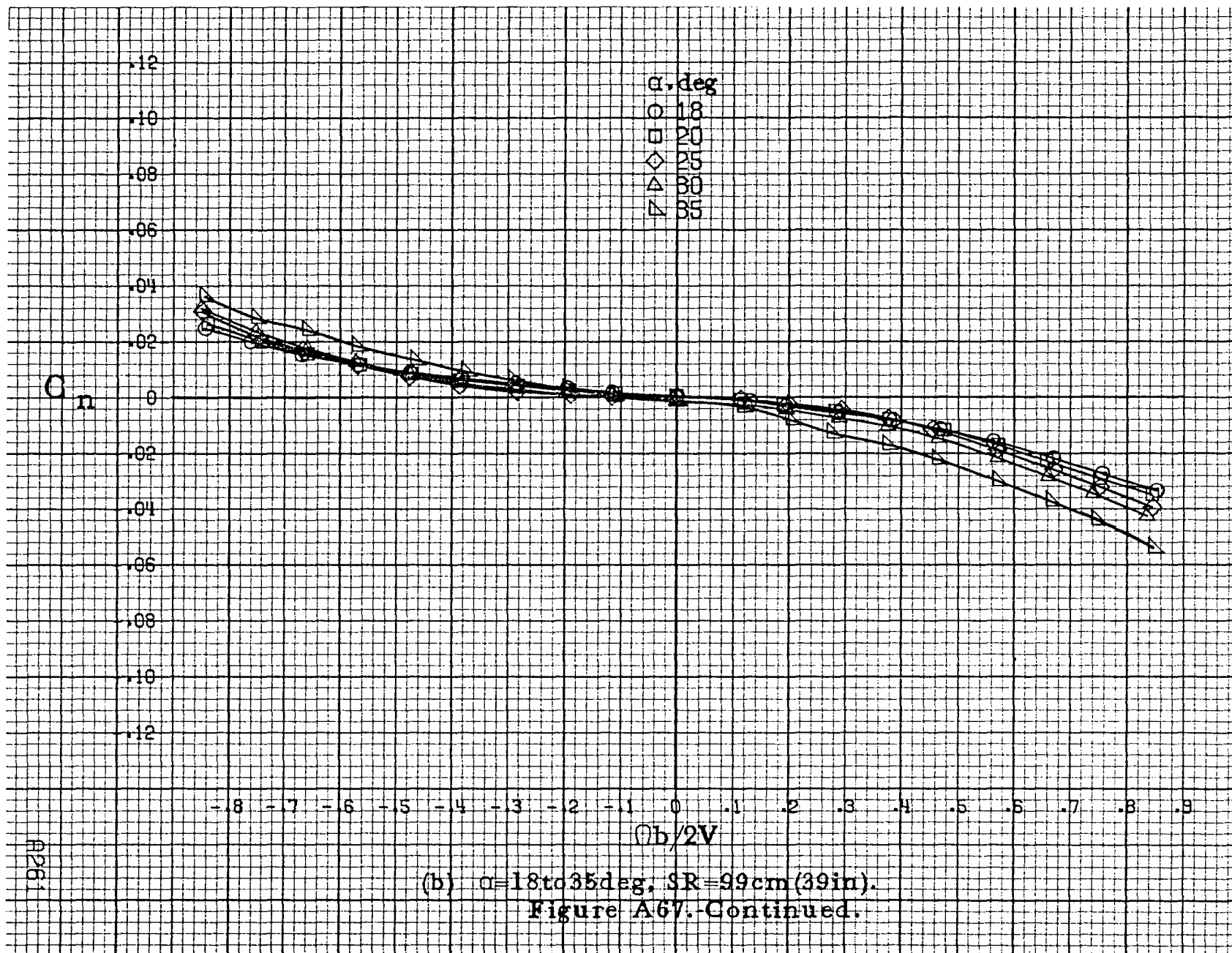


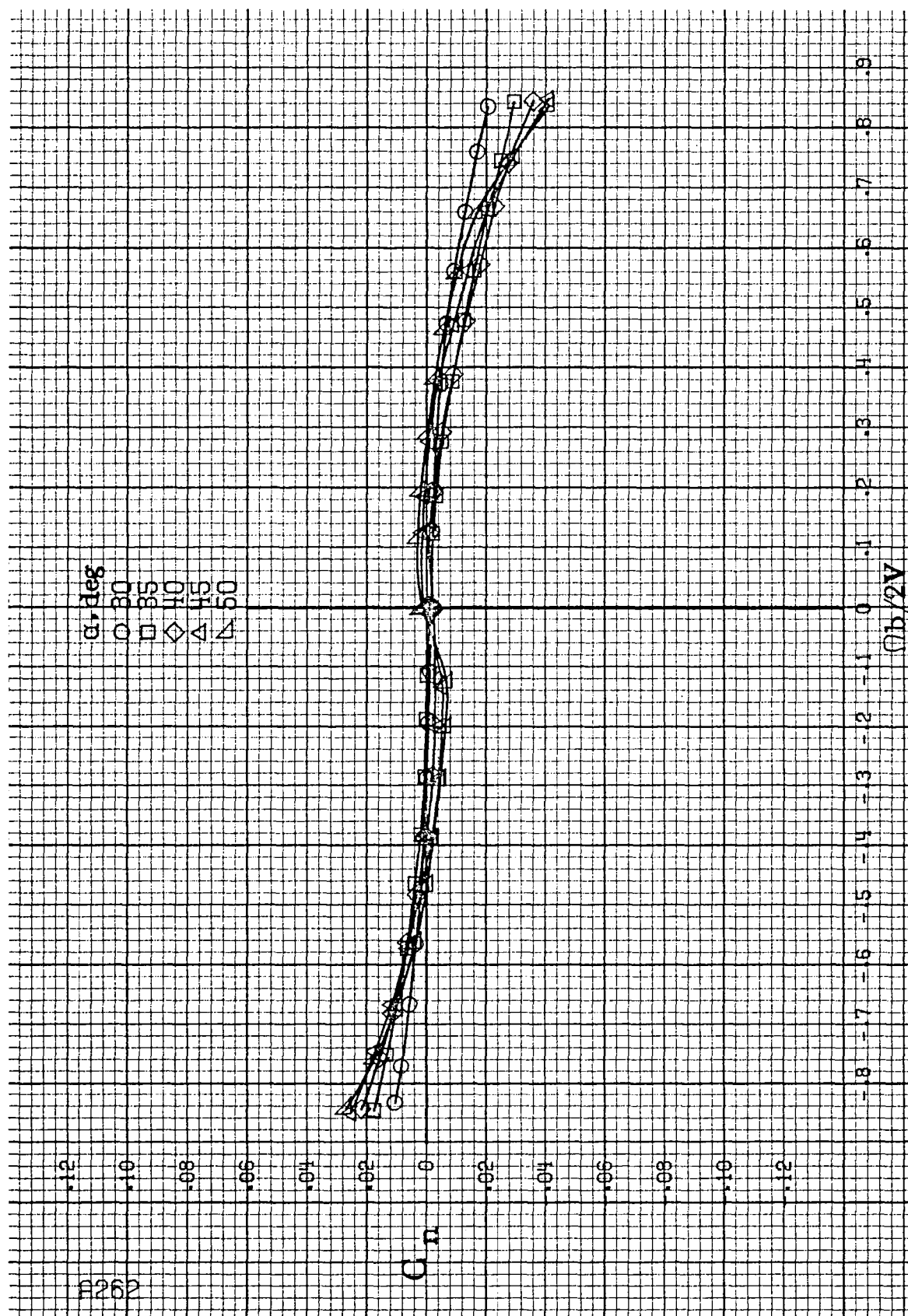
(b)  $\alpha=18$  to  $35$  deg,  $SR=99$  cm (39 in).  
Figure A86, Continued.





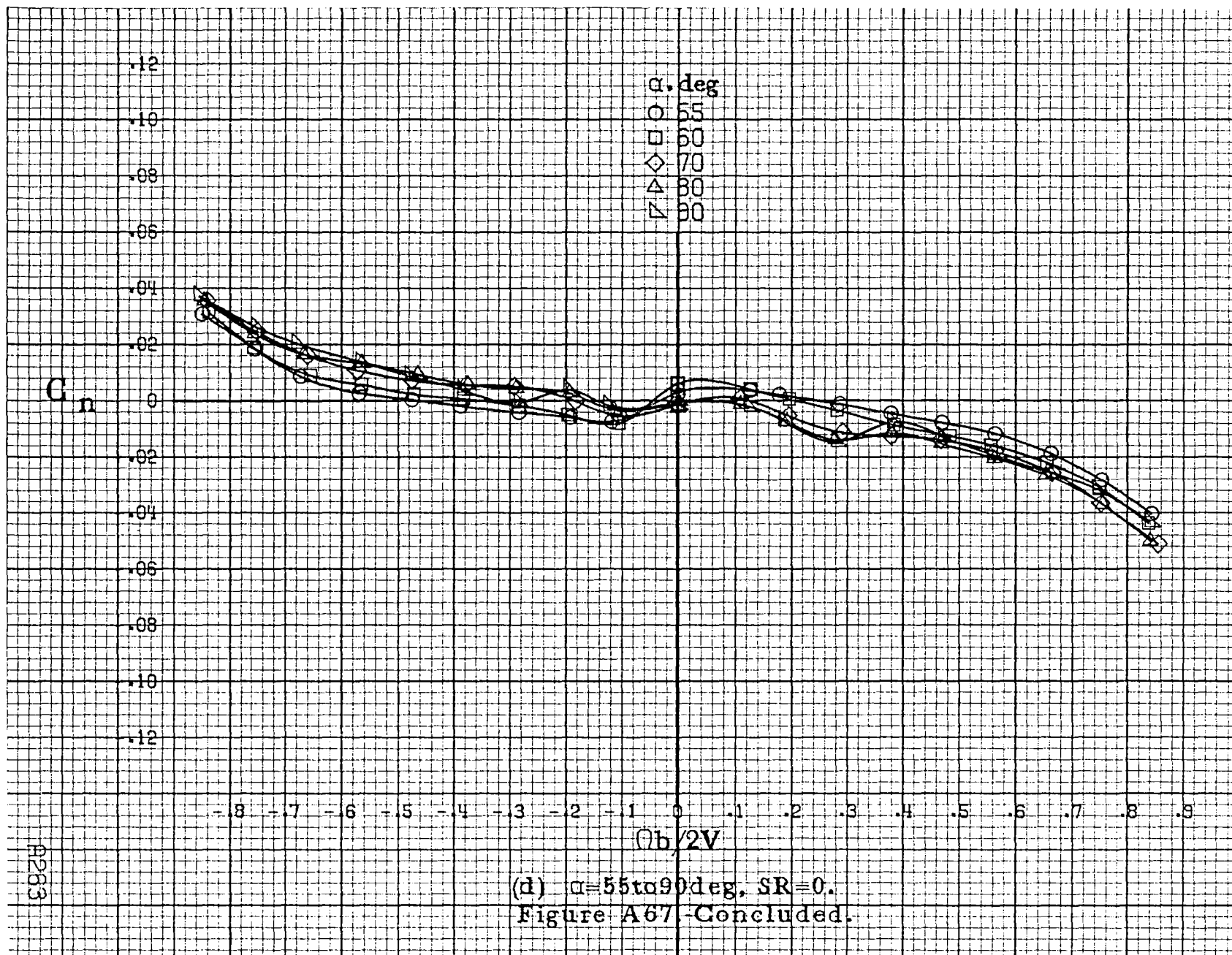






(c)  $\alpha=30$  to  $50$  deg,  $SR=0$ .  
Figure A67. Continued.







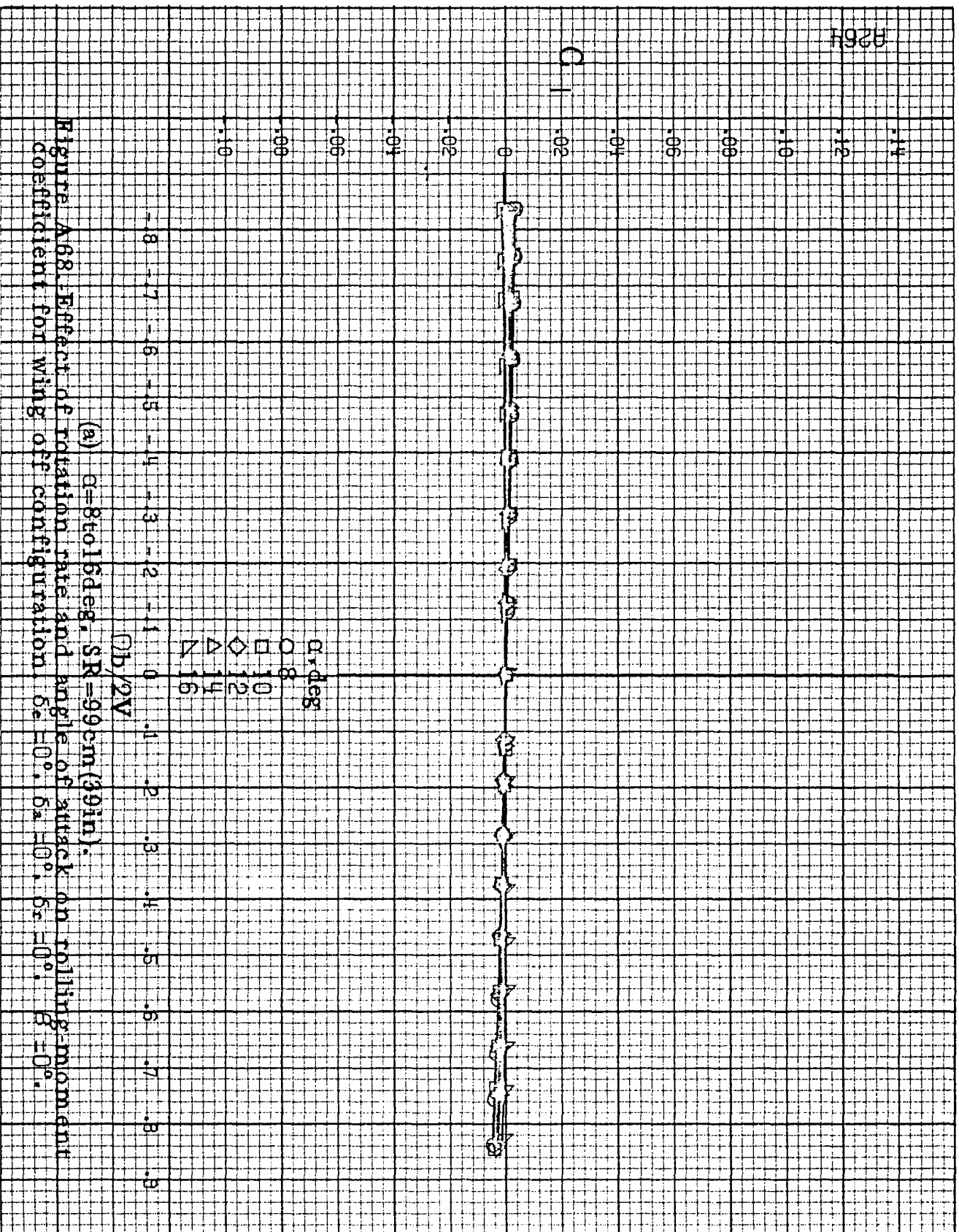
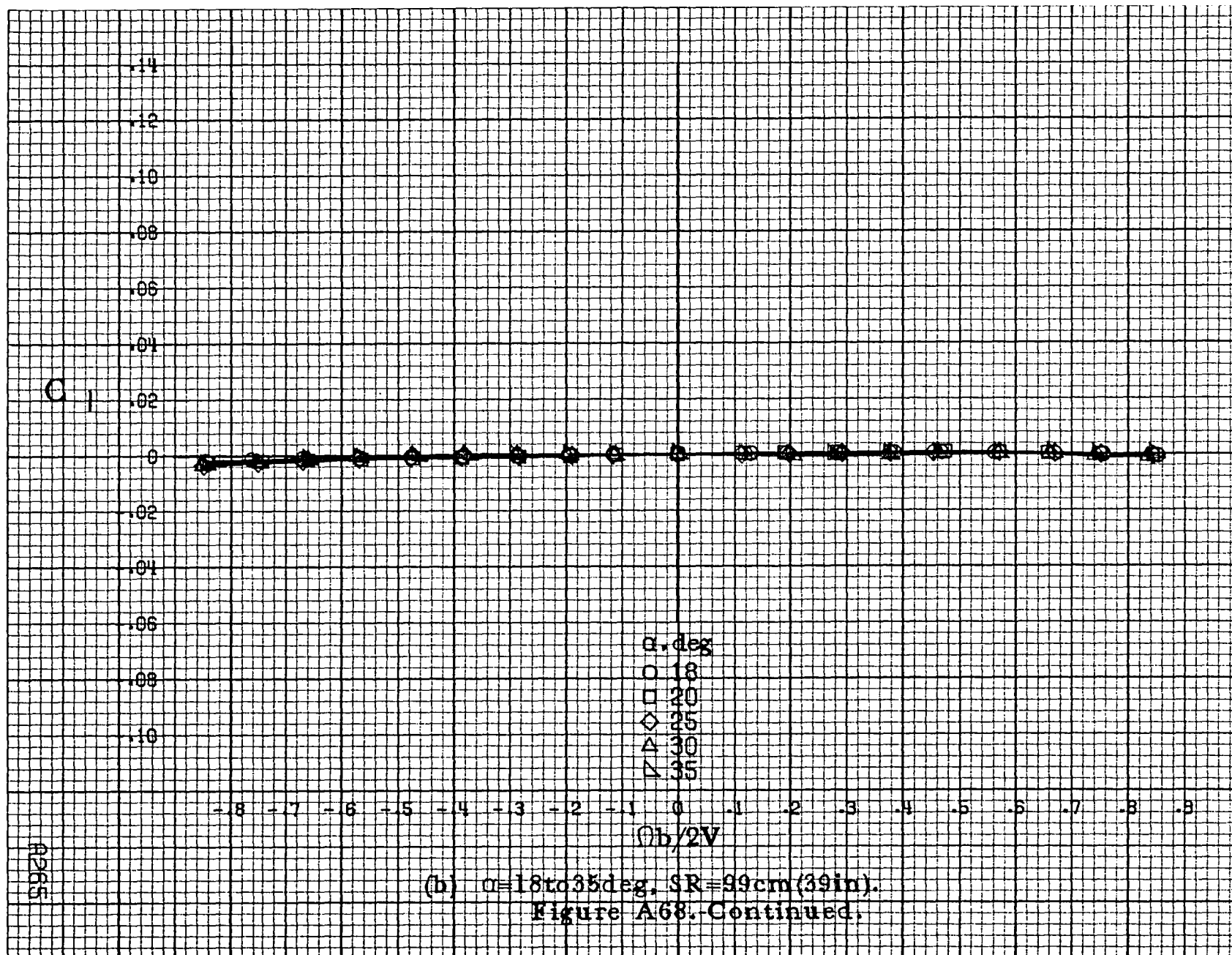


Figure A68. Effect of rotation rate and angle of attack on rolling moment coefficient for wing off configuration.  $\delta_e = 0^\circ$ ,  $\delta_a = 0^\circ$ ,  $\delta_c = 0^\circ$ ,  $\delta = 0^\circ$ .



A265

 $C_1$ 

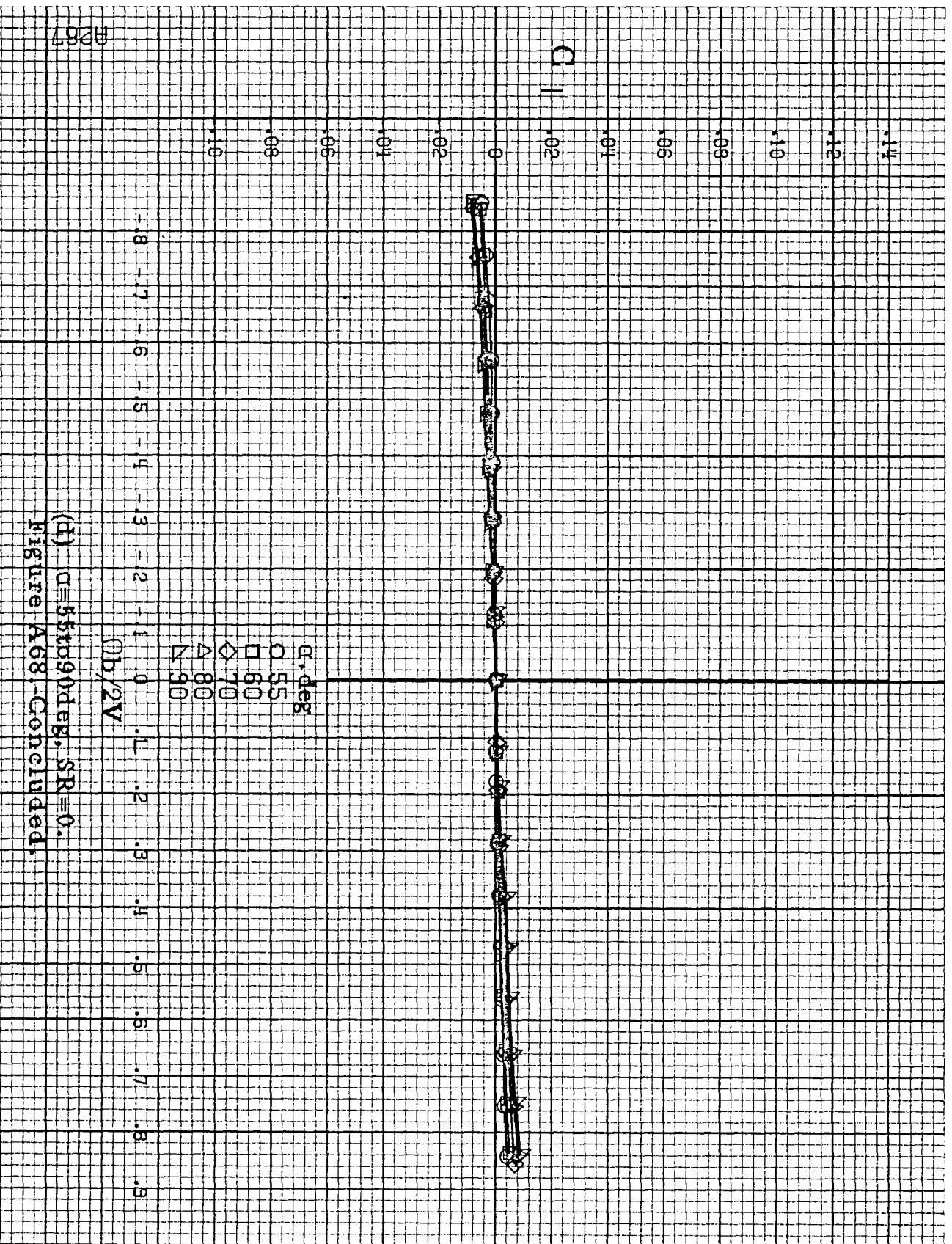
.14  
.12  
.10  
.08  
.06  
.04  
.02  
0  
-.02  
-.04  
-.06  
-.08  
-.10

$\alpha, \text{deg}$   
○ 30  
□ 35  
◇ 40  
△ 45  
▽ 50

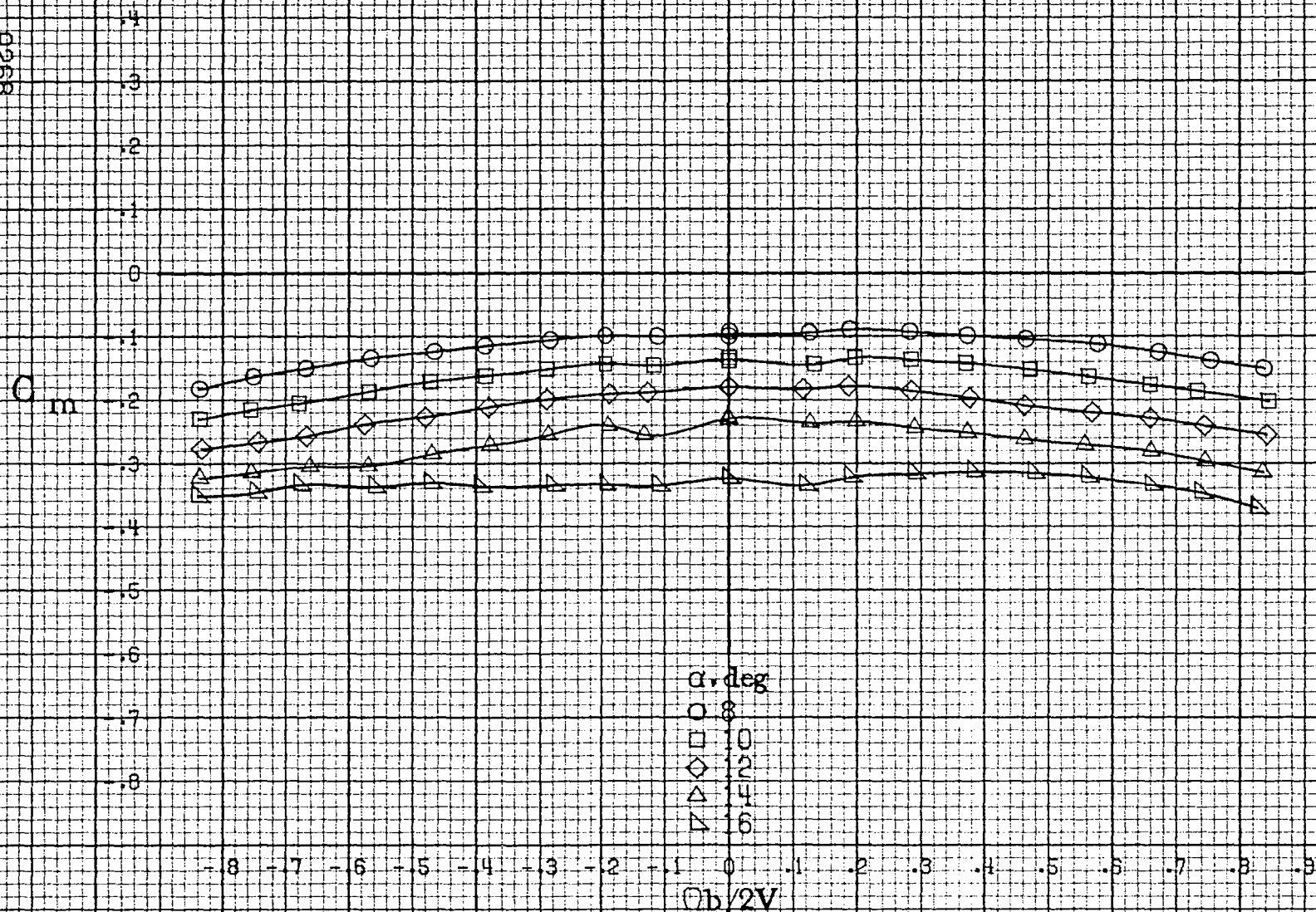
-.8 -.7 -.6 -.5 -.4 -.3 -.2 -.1 0 .1 .2 .3 .4 .5 .6 .7 .8 .9

 $b/2V$ 

(c)  $\alpha=30$  to  $50$  deg,  $SR=0$ .  
Figure A68.-Continued.

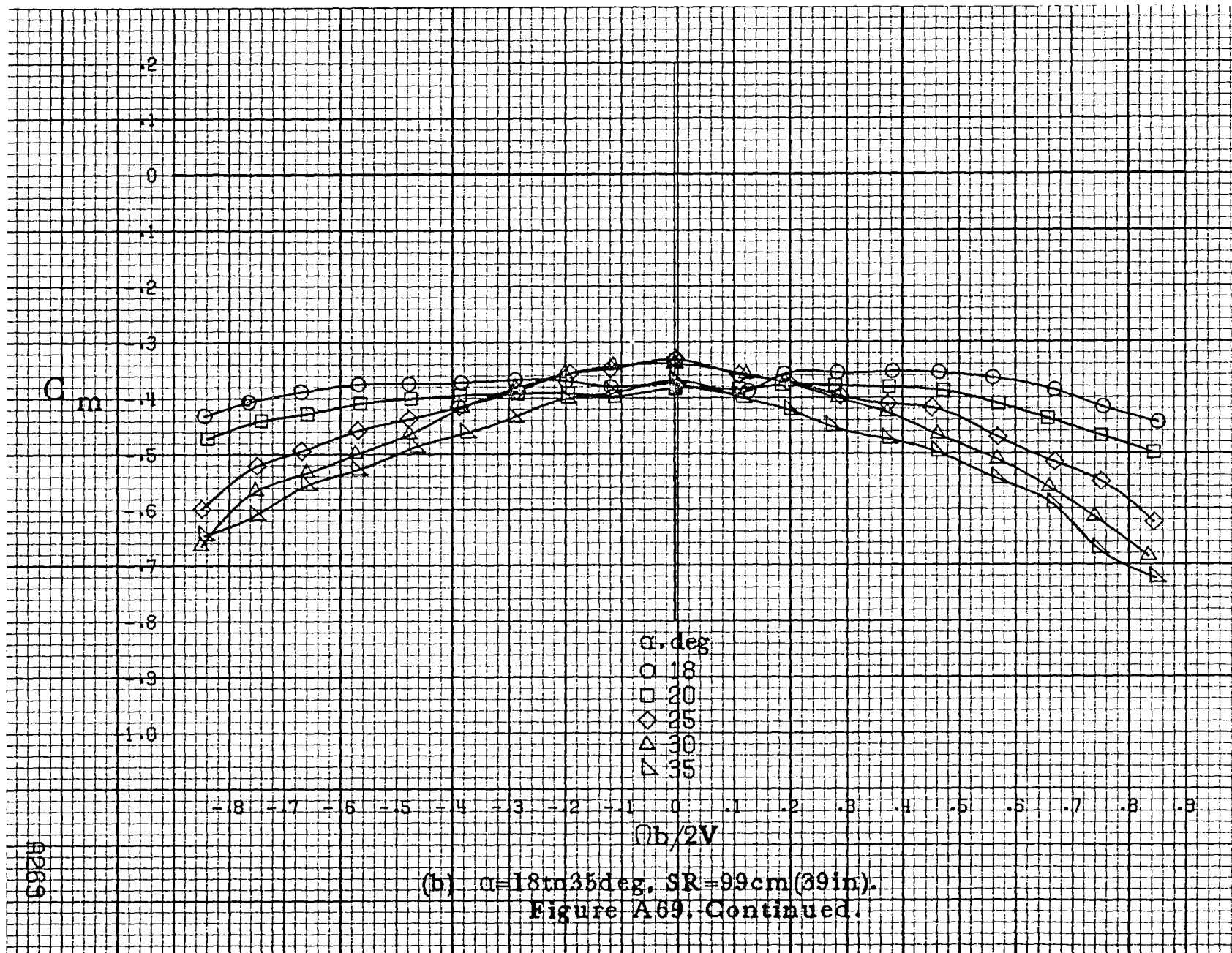


(d)  $\alpha=55$  to  $90$  deg,  $SR=0$ .  
Figure A68-Concluded.

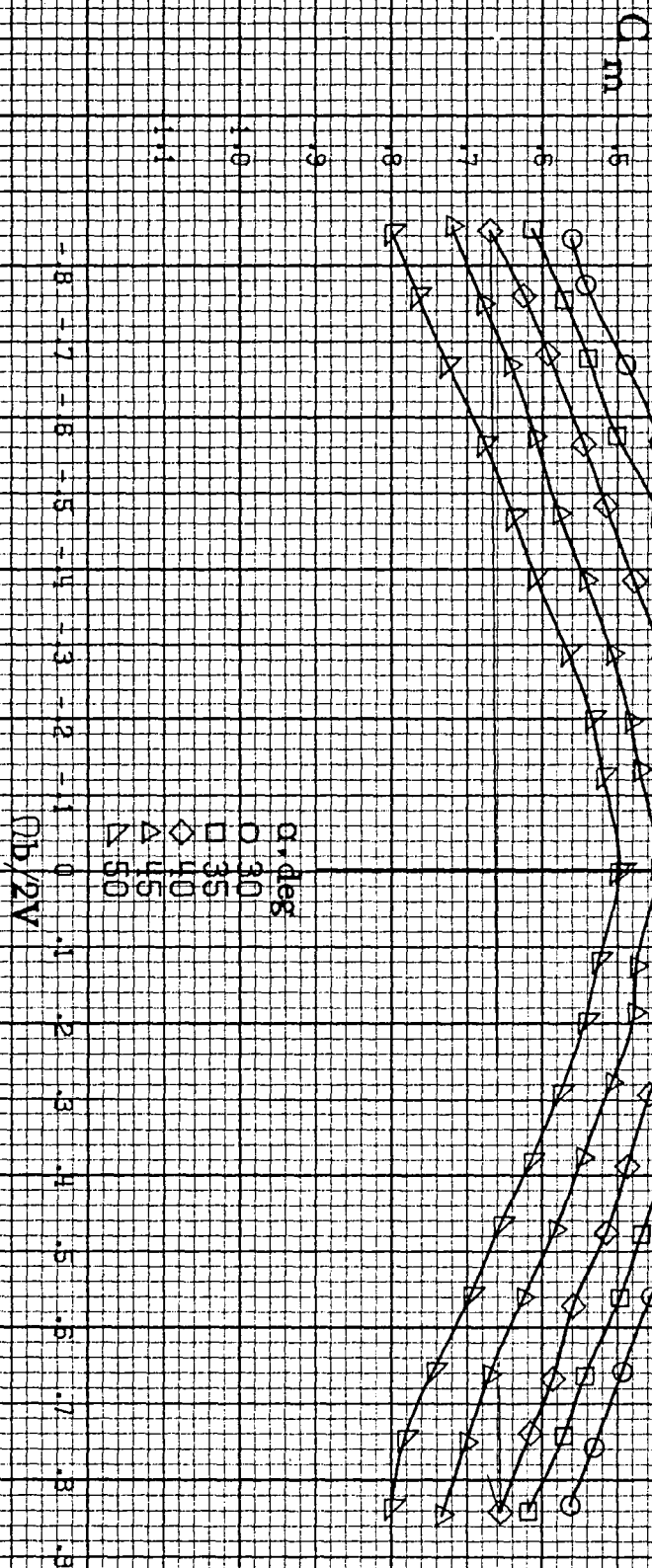


(a)  $\alpha = 8$  to  $16^\circ$ ,  $SR = 99\text{ cm (39 in.)}$ .

Figure A69. Effect of rotation rate and angle of attack on pitching moment coefficient for wing off configuration.  $\delta_e = 0^\circ$ ,  $\delta_a = 0^\circ$ ,  $\delta_r = 0^\circ$ ,  $\beta = 0^\circ$ .

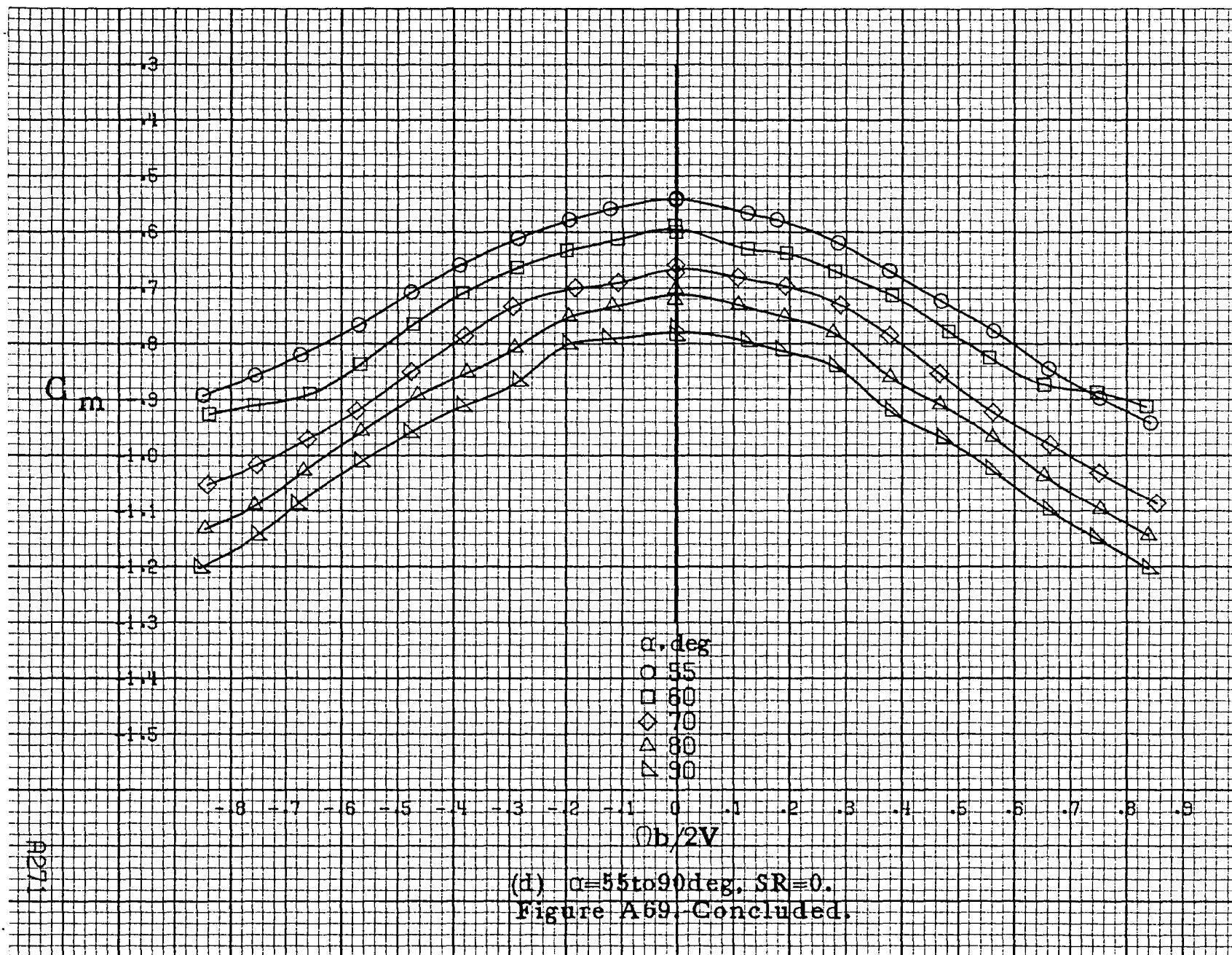






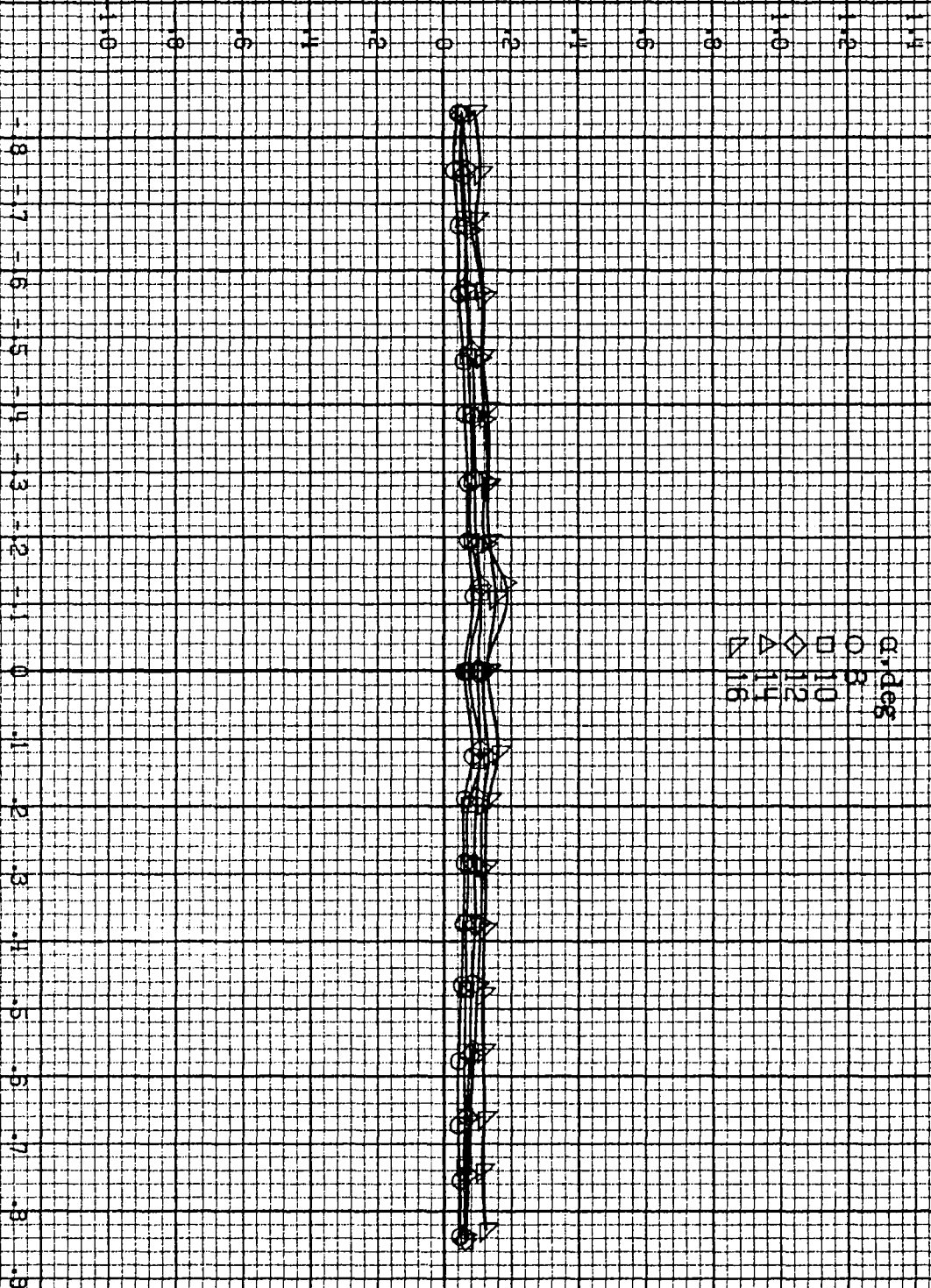
(c)  $\alpha=30$  to  $50$  deg,  $SR=0$ .  
Figure A69-Continued.





5272

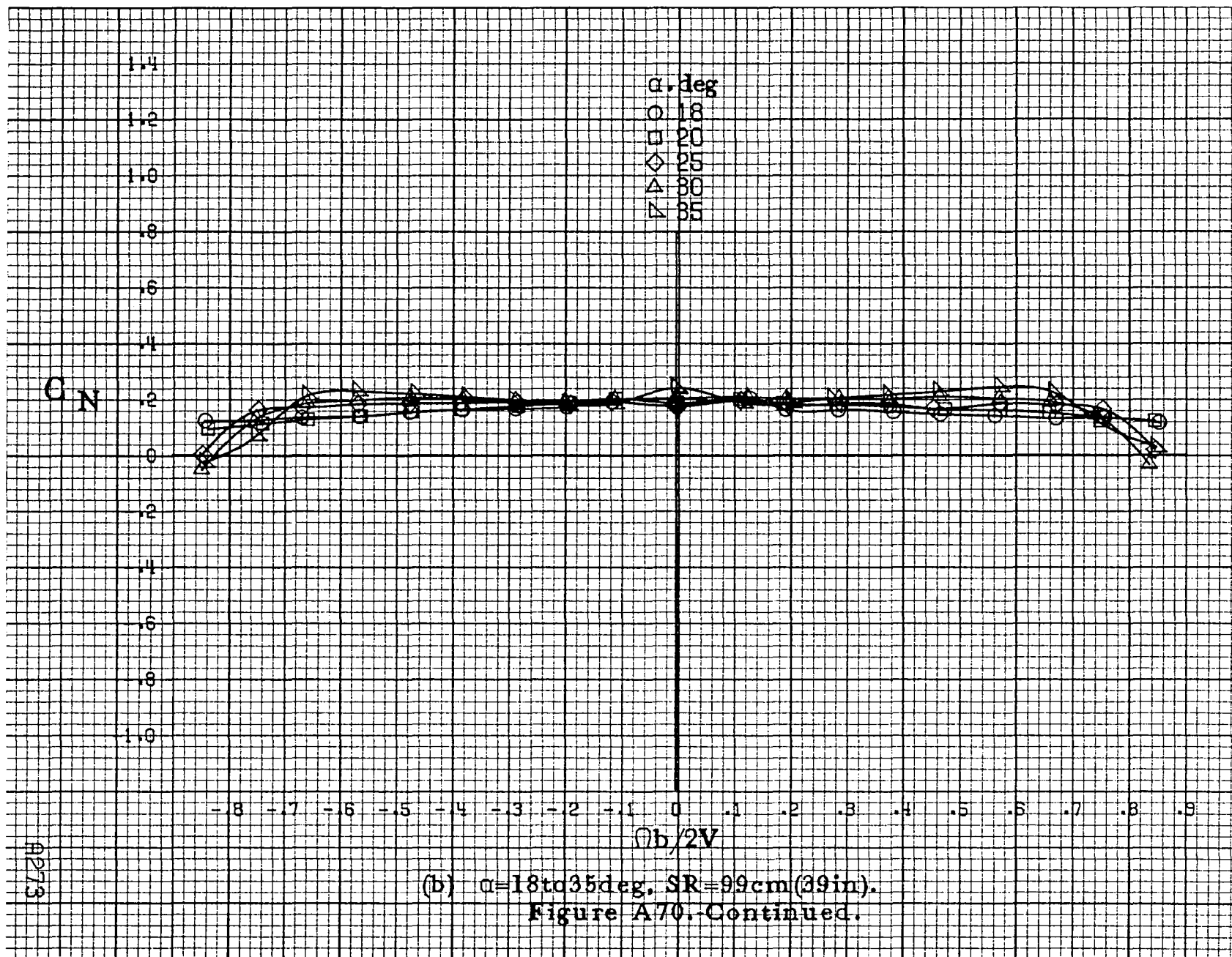
$C_N$

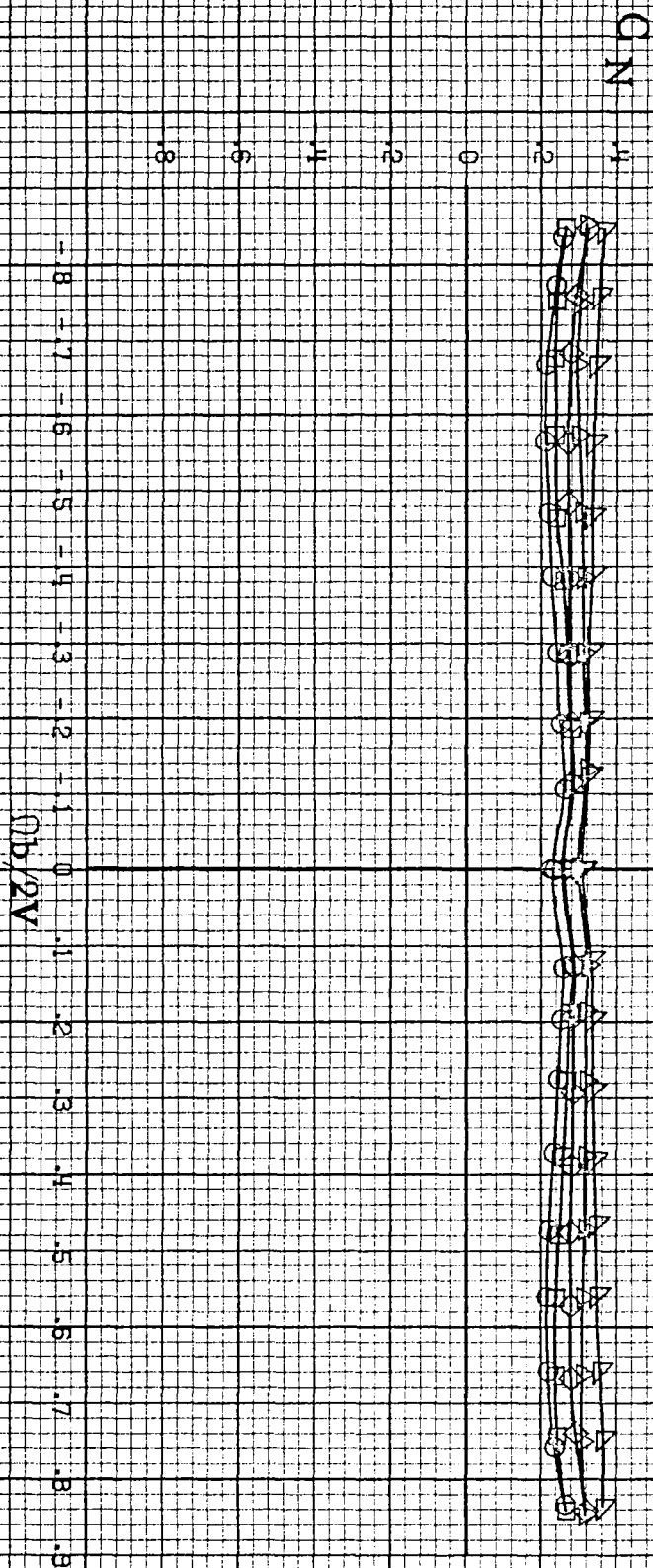


(a)  $G=8$  to  $16$  deg,  $SR=99$  cm (39 in).

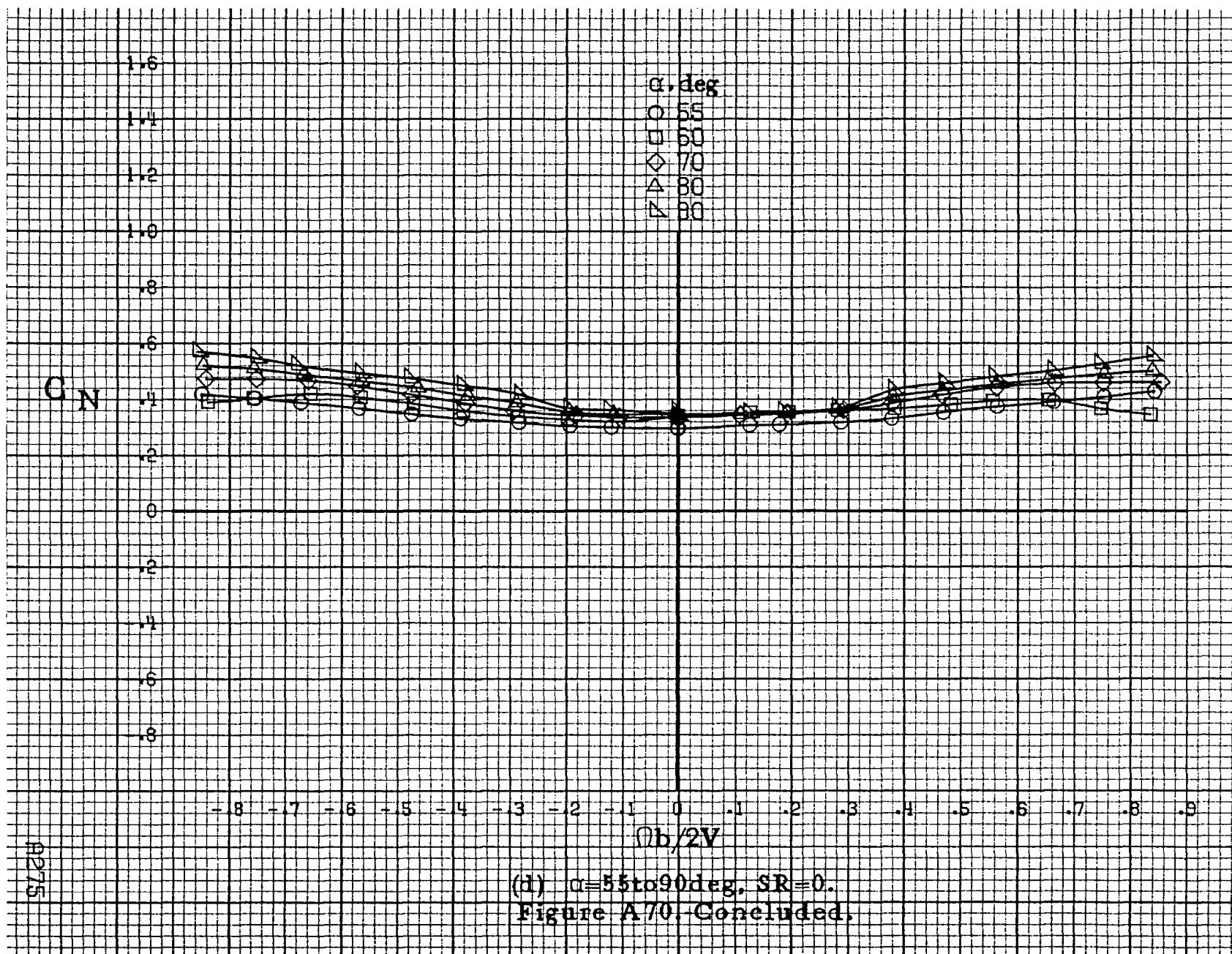
(b)  $V=2V$

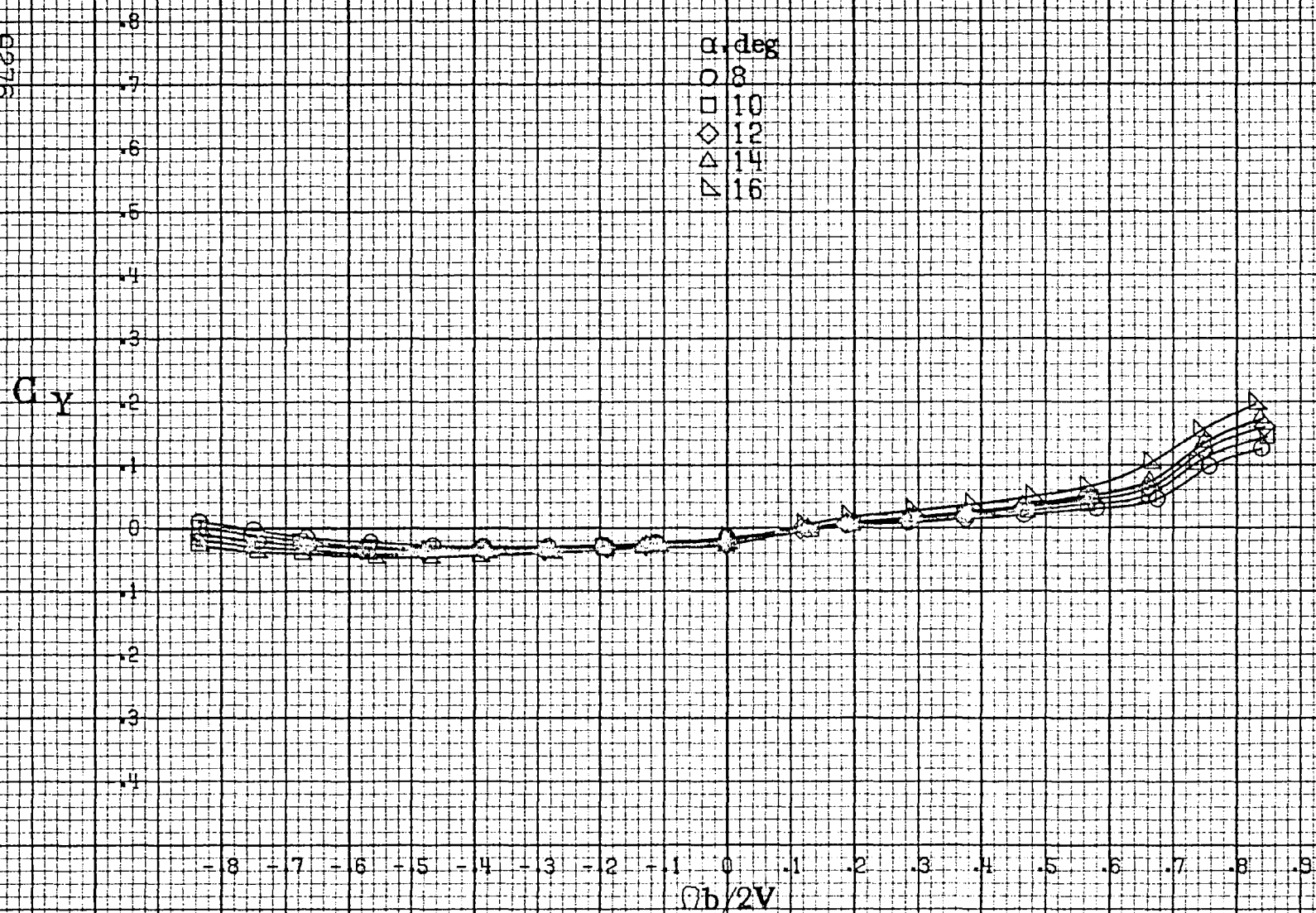
Figure A70. Effect of rotation rate and angle of attack on normal-force coefficient for wing off configuration.  $\delta_e = 0^\circ$ .  $\delta_a = 0^\circ$ .  $\delta_r = 0^\circ$ .  $\delta = 0^\circ$ .





(c)  $\alpha = 30$  to  $50^\circ$ ,  $SR = 0$ ,  
Figure A70, Continued.

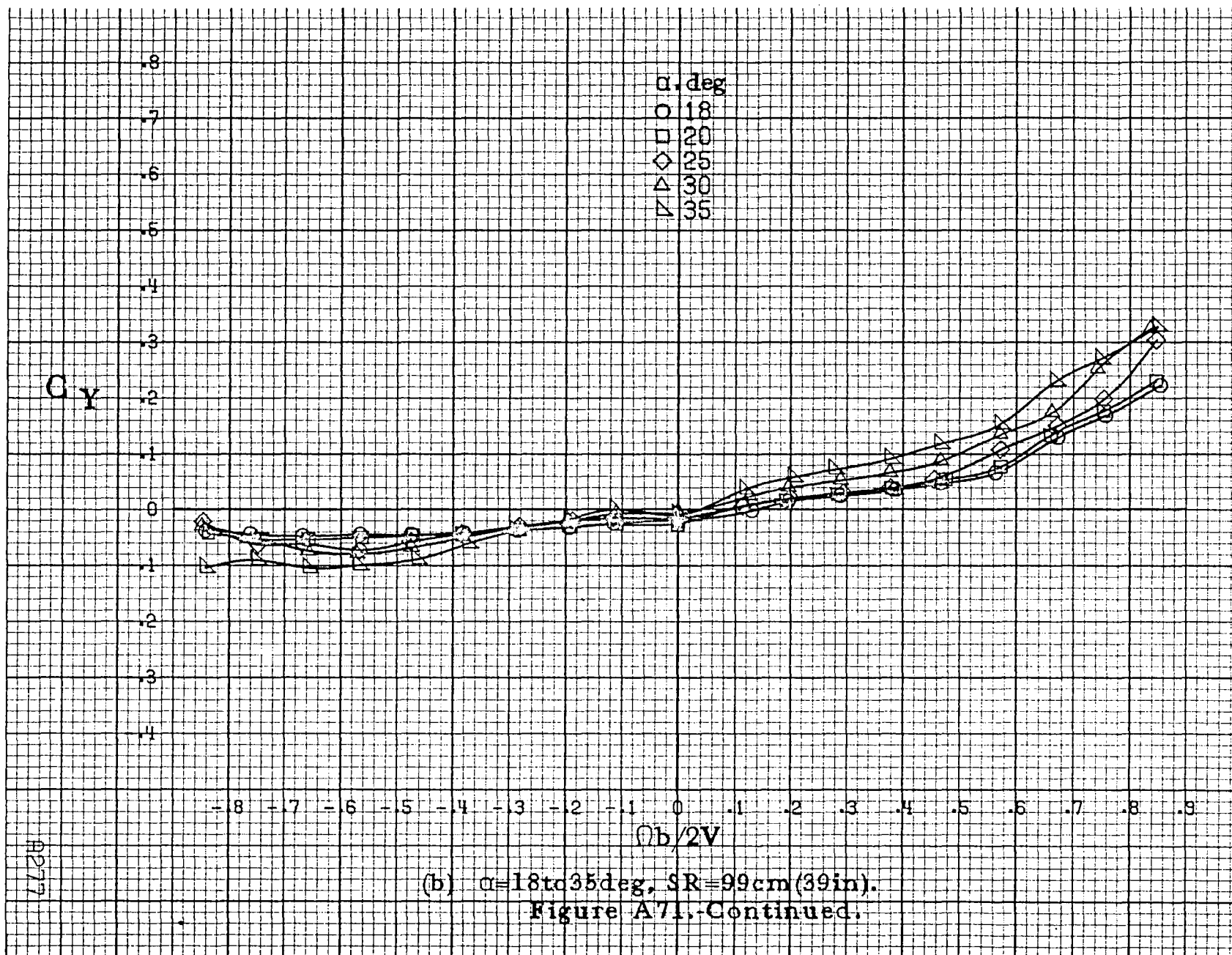




(a)  $\alpha = 8$  to  $16$  deg,  $SR = 99$  cm (39 in).

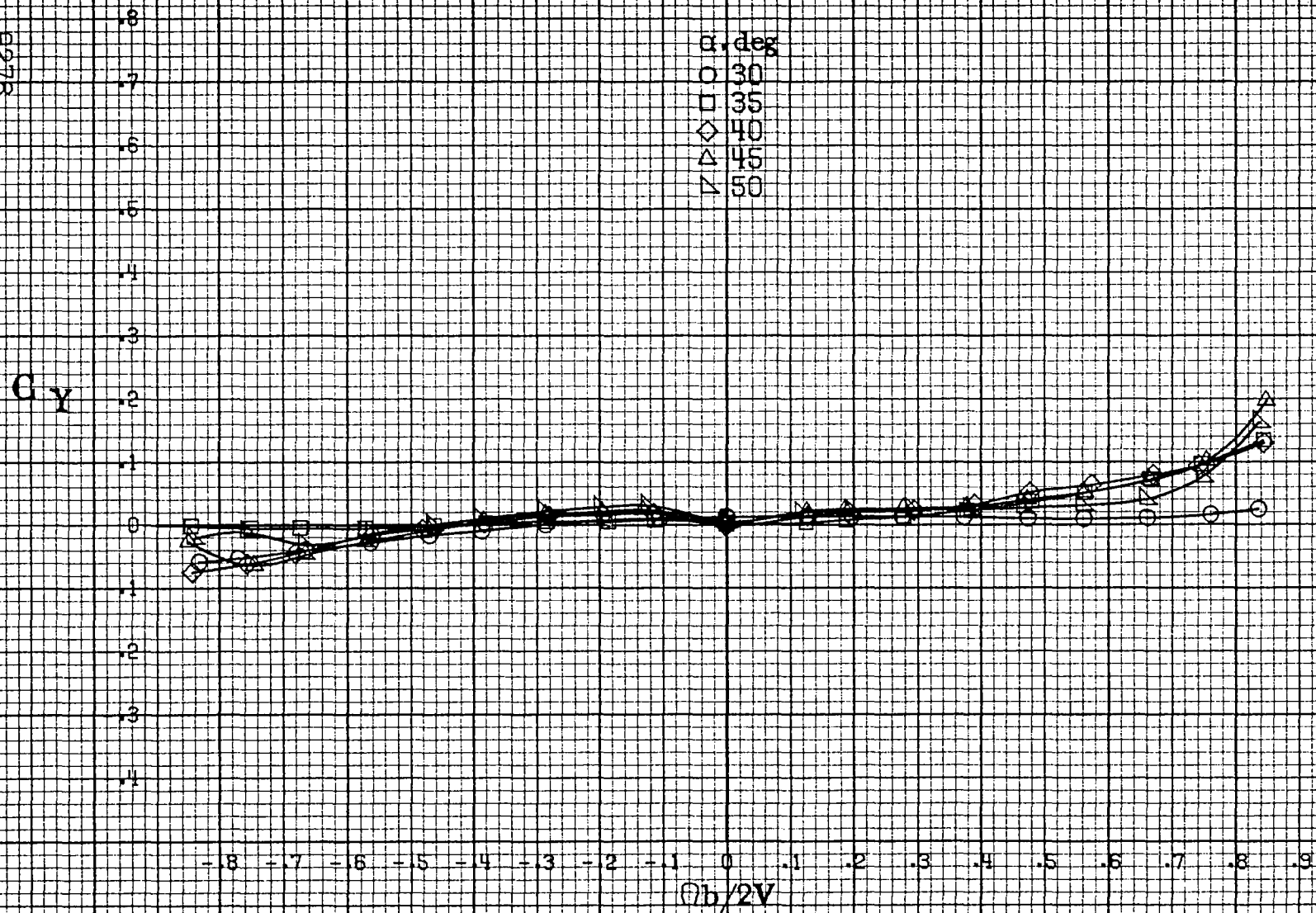
Figure A71. Effect of rotation rate and angle of attack on side-force coefficient for wing off configuration.  $\delta_a = 0^\circ$ ,  $\delta_s = 0^\circ$ ,  $\delta_r = 0^\circ$ ,  $\beta = 0^\circ$ .



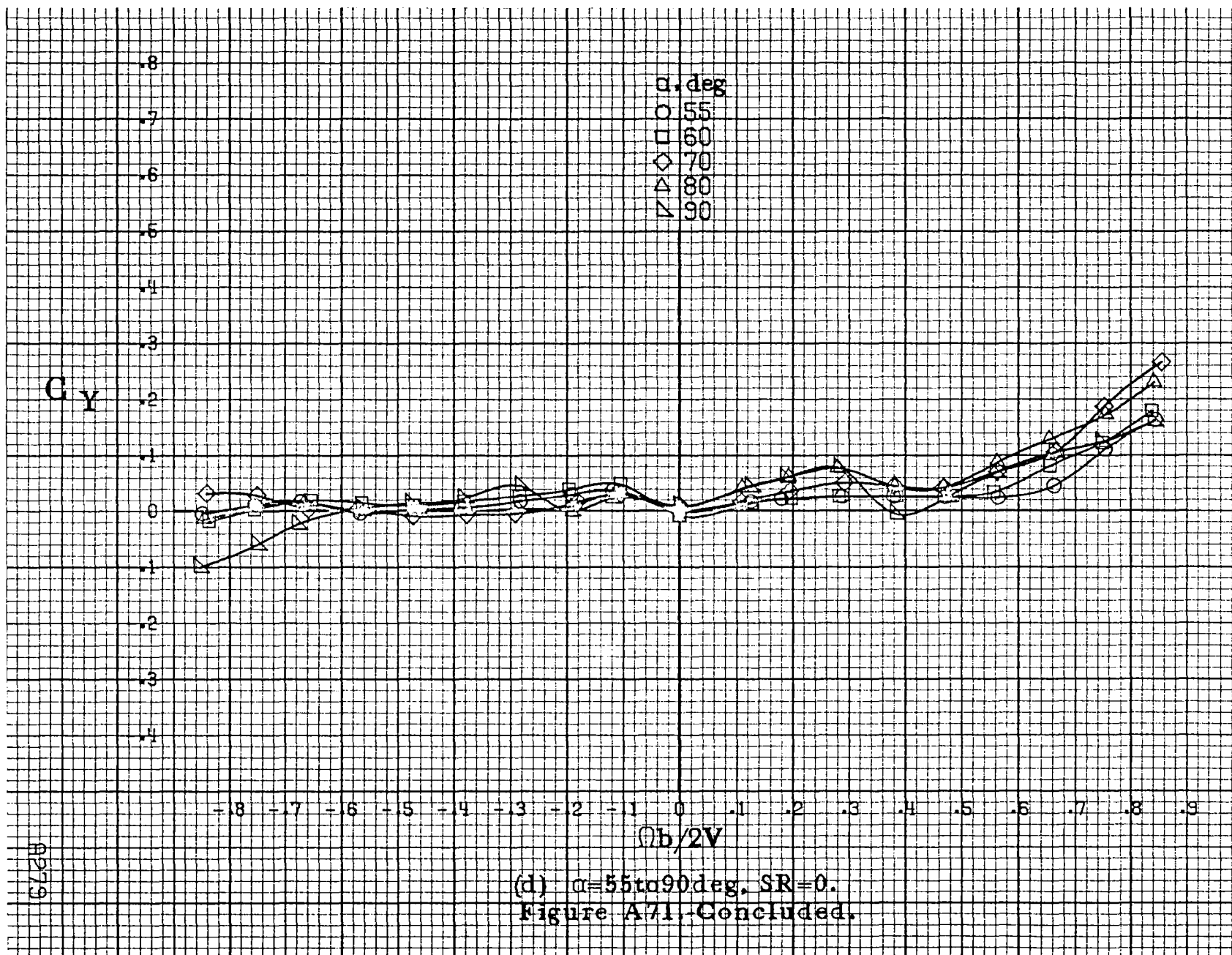


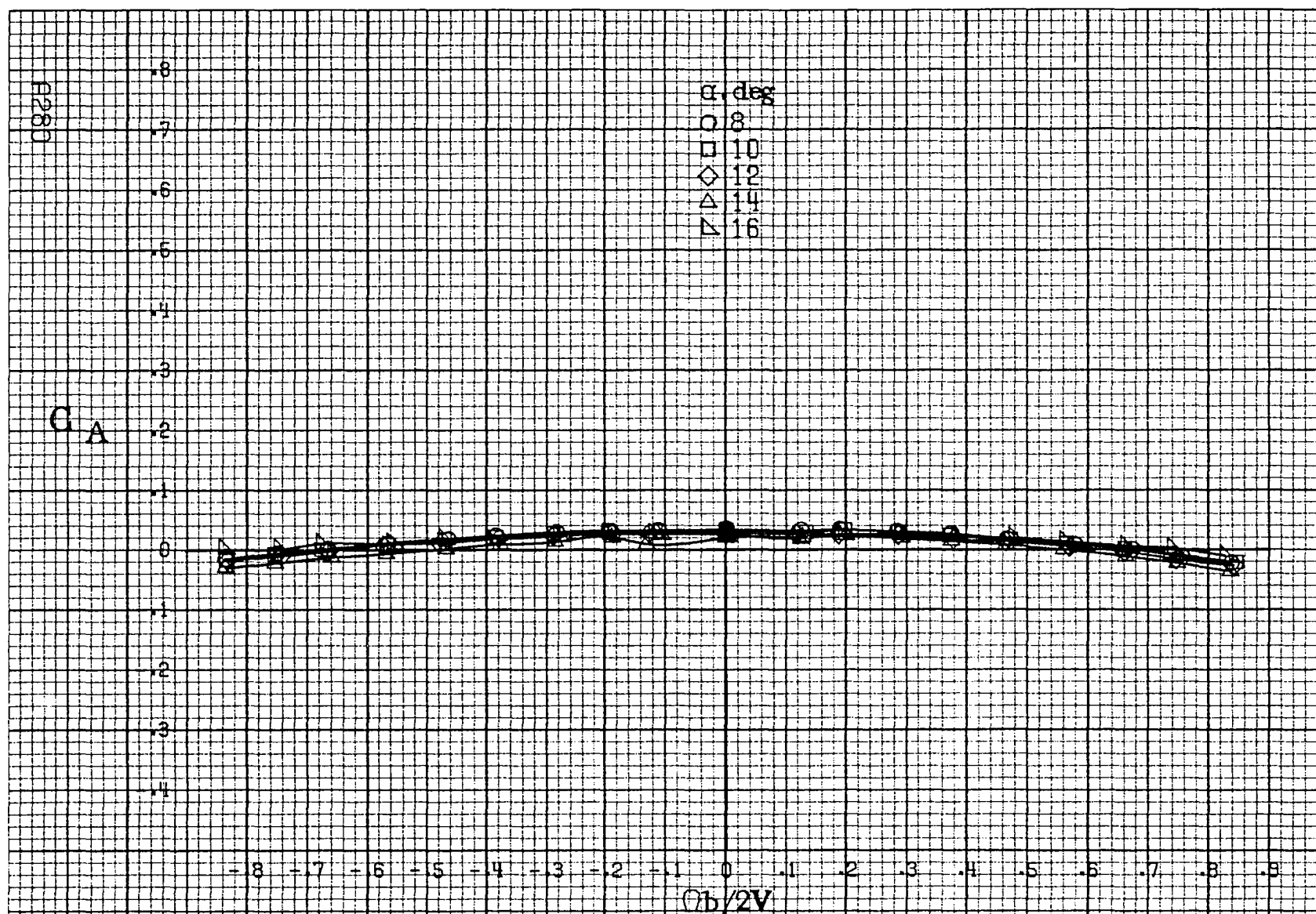


8278



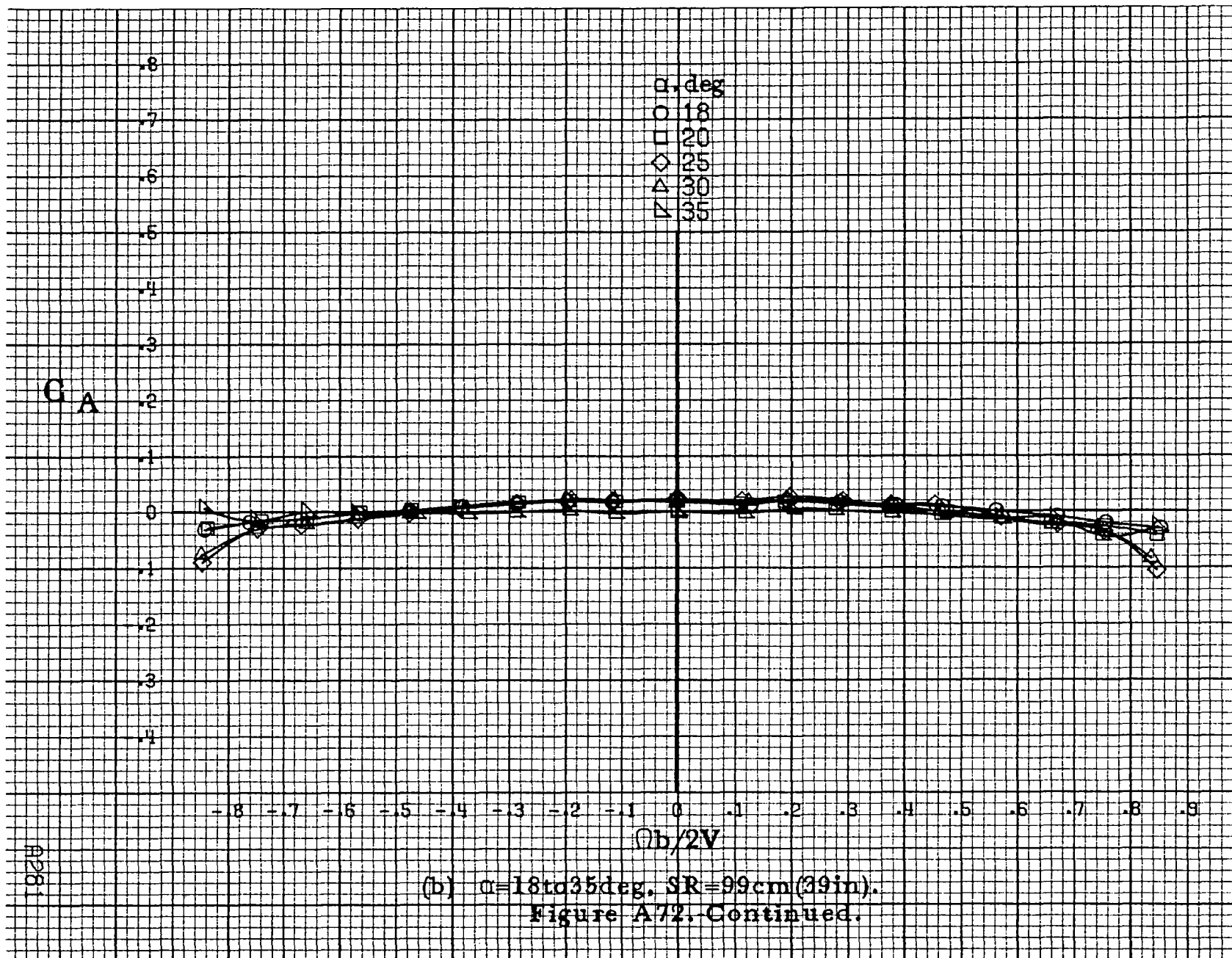
(c)  $\alpha=30$  to  $50$  deg,  $SR=0$ .  
Figure A71, Continued.



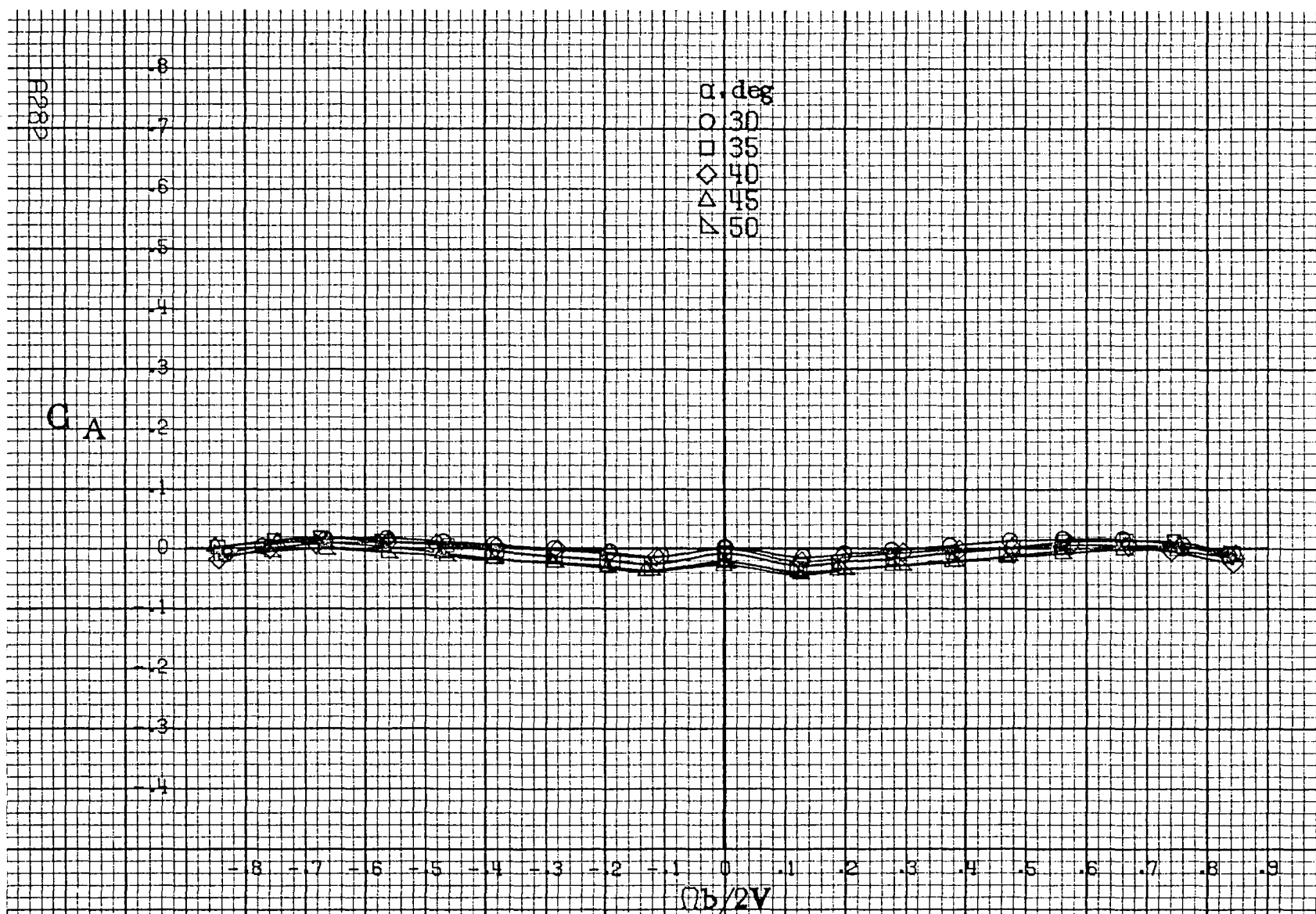


(a)  $\alpha=8$  to  $16^\circ$ ,  $SR=99\text{cm}(39\text{in})$ .

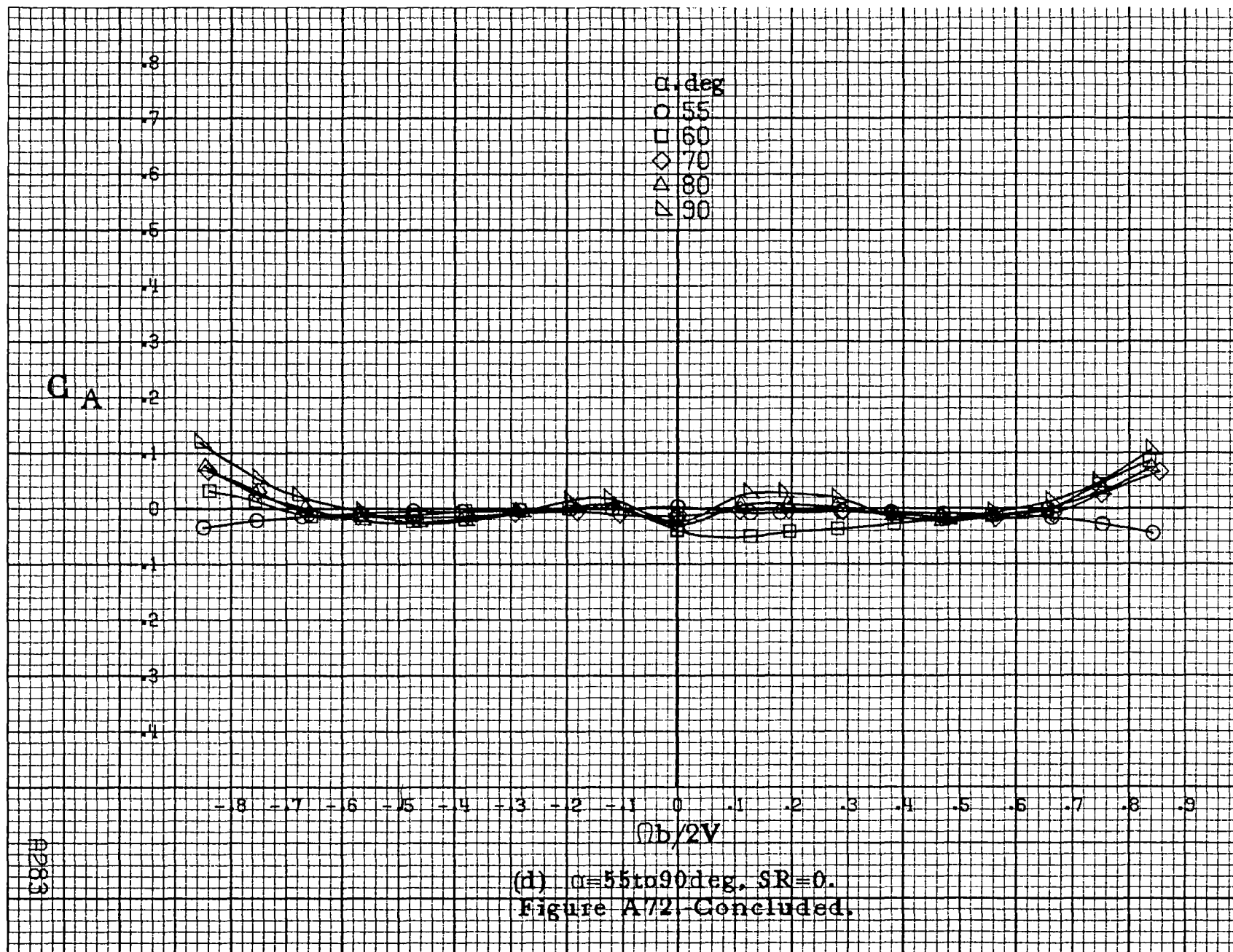
Figure A72. Effect of rotation rate and angle of attack on axial force coefficient for wing off configuration.  $\delta_e=0^\circ$ ,  $\delta_a=0^\circ$ ,  $\delta_r=0^\circ$ ,  $\beta=0^\circ$ .



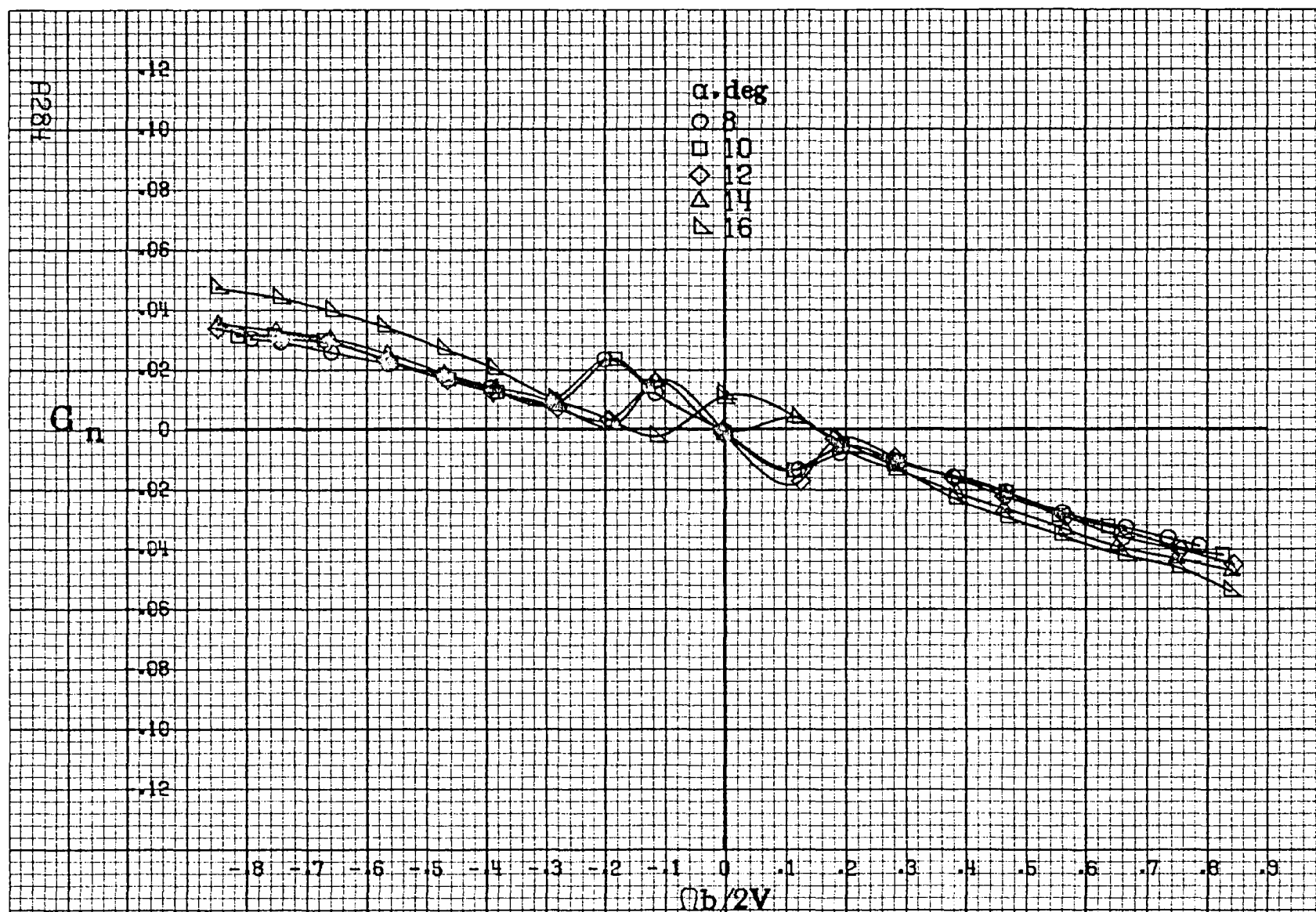
A281



(c)  $\alpha=30$  to  $50^\circ$ ,  $SR=0$ .  
Figure A72. Continued.



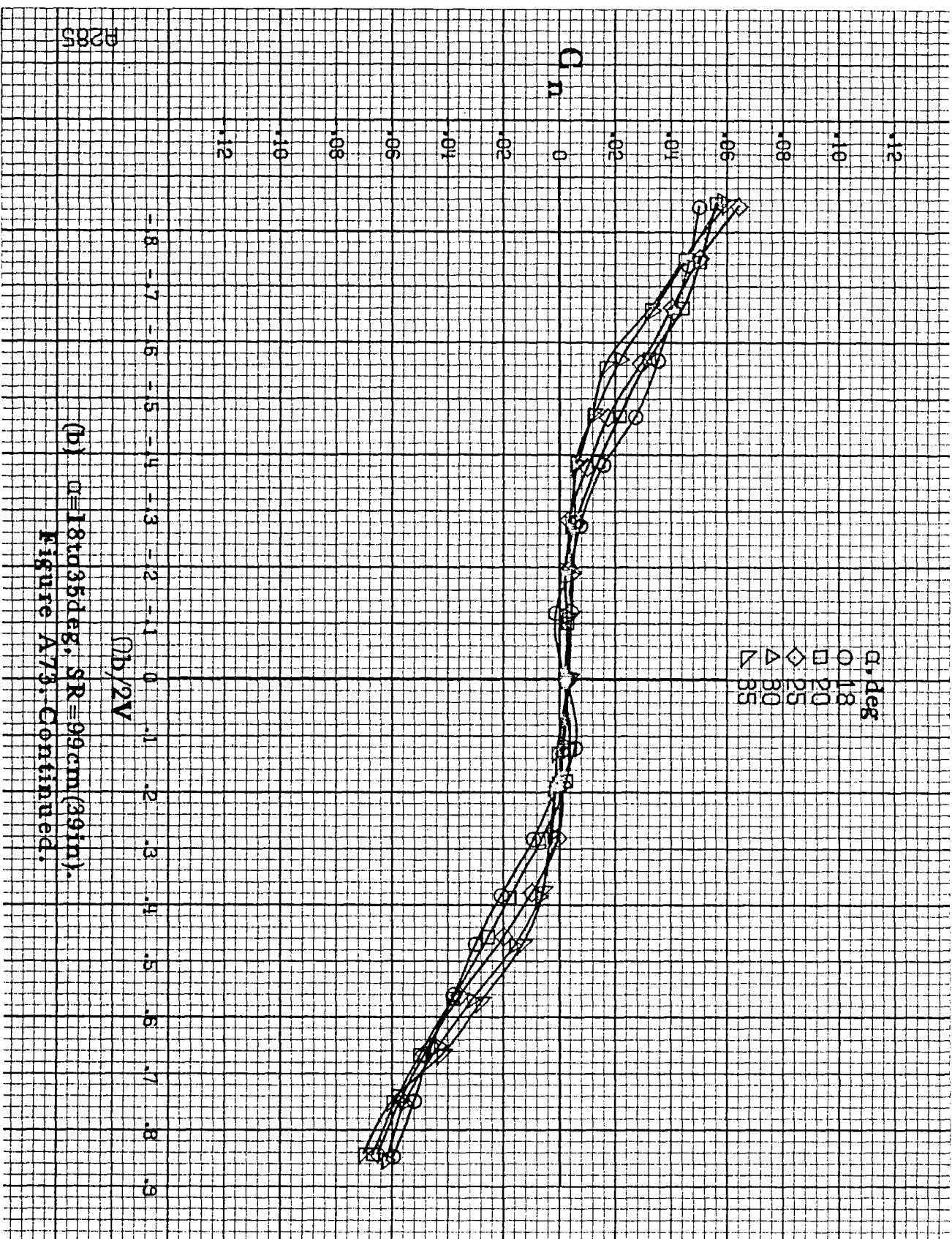




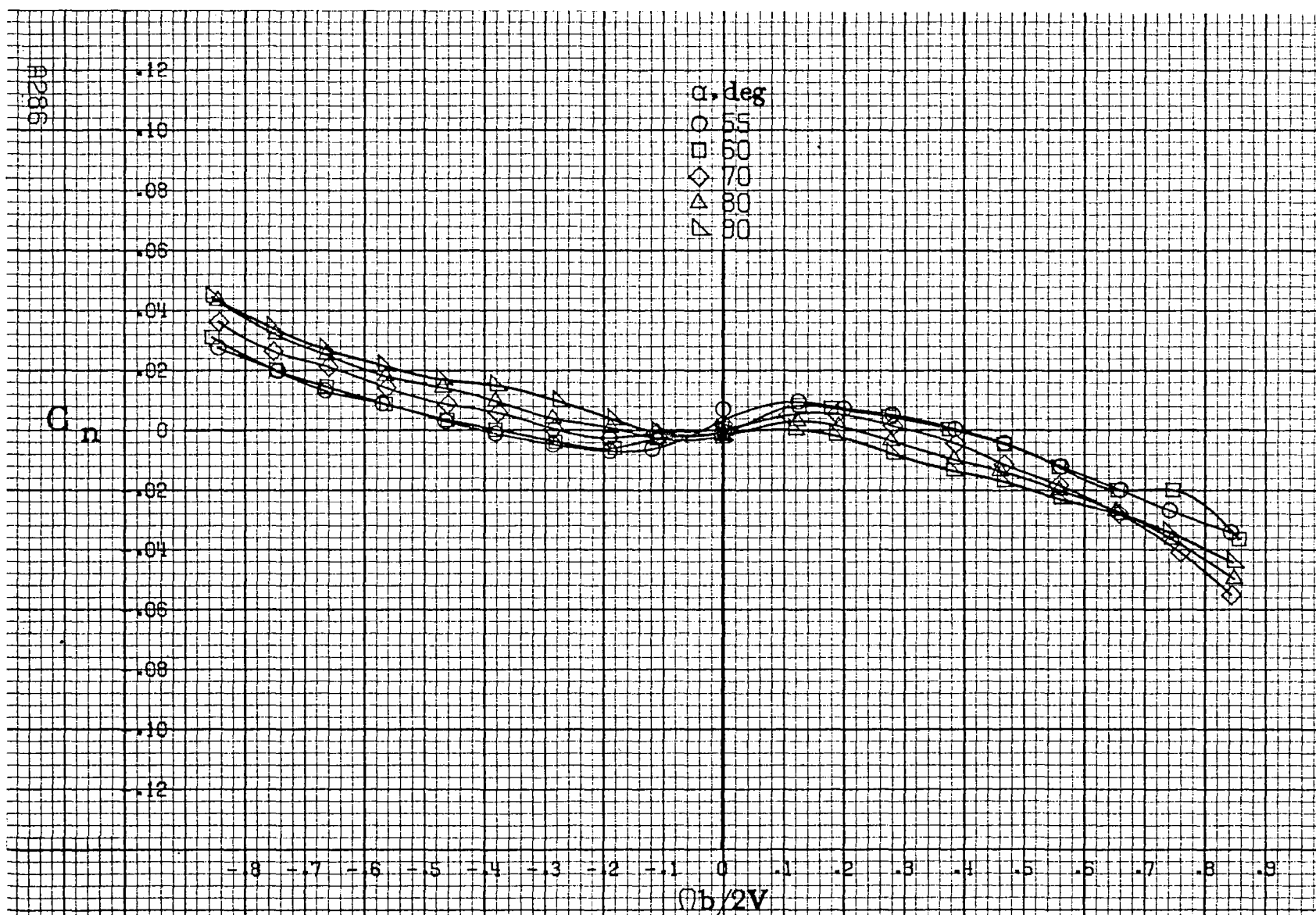
(a)  $\alpha=8$  to  $16^\circ$ ,  $SR=99\text{cm}(39\text{in})$ .

Figure A78. Effect of rotation rate and angle of attack on yawing-moment coefficient for configuration having full-span LE wing droop with moderate nose radius.  $\delta_1=0^\circ$ ,  $\delta_2=0^\circ$ ,  $\delta_3=0^\circ$ ,  $\beta=0^\circ$ .



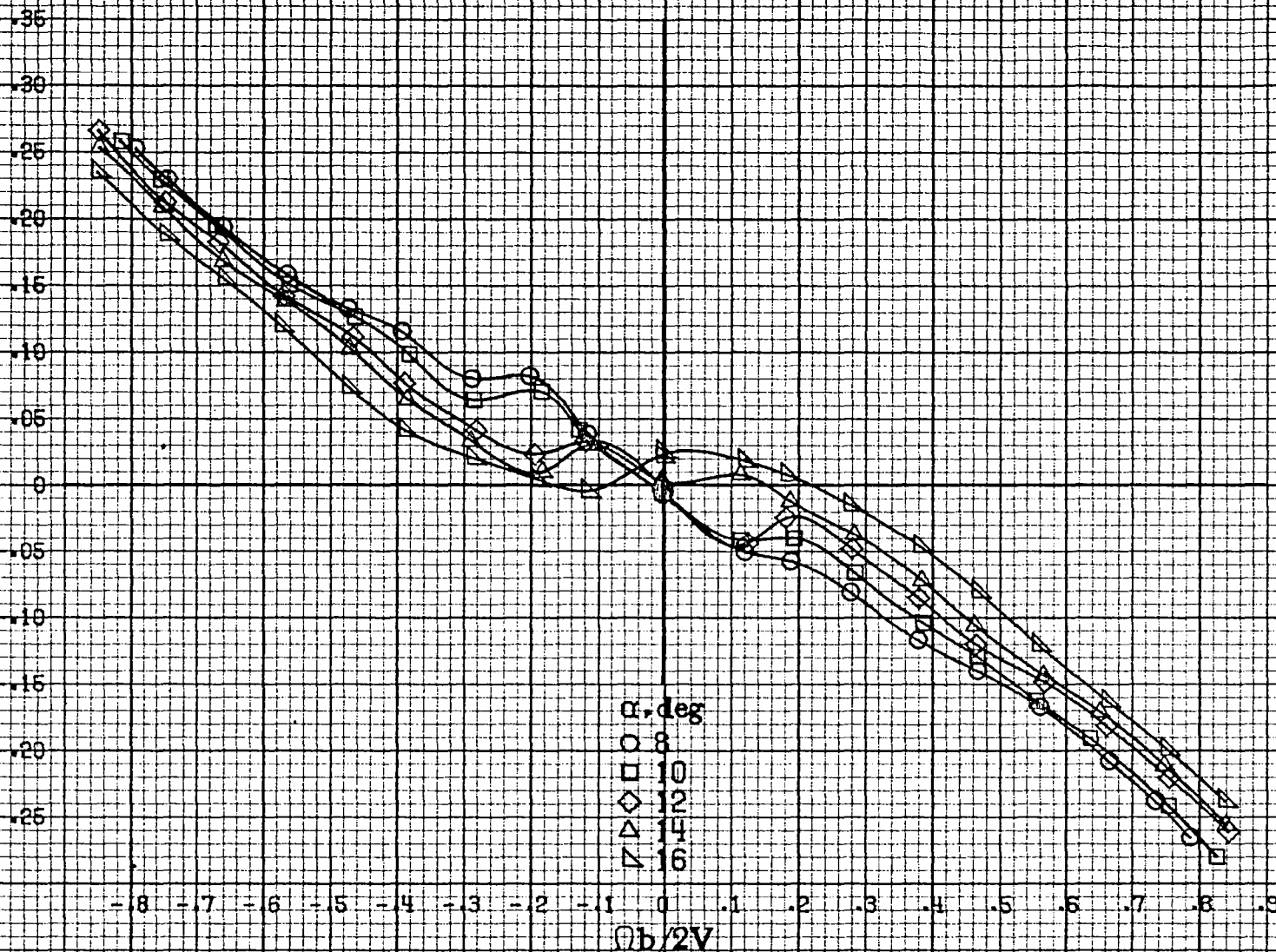


(b)  $\alpha = 18$  to  $35$  deg,  $SR = 99$  cm (39 in).  
Figure A73. Continued.



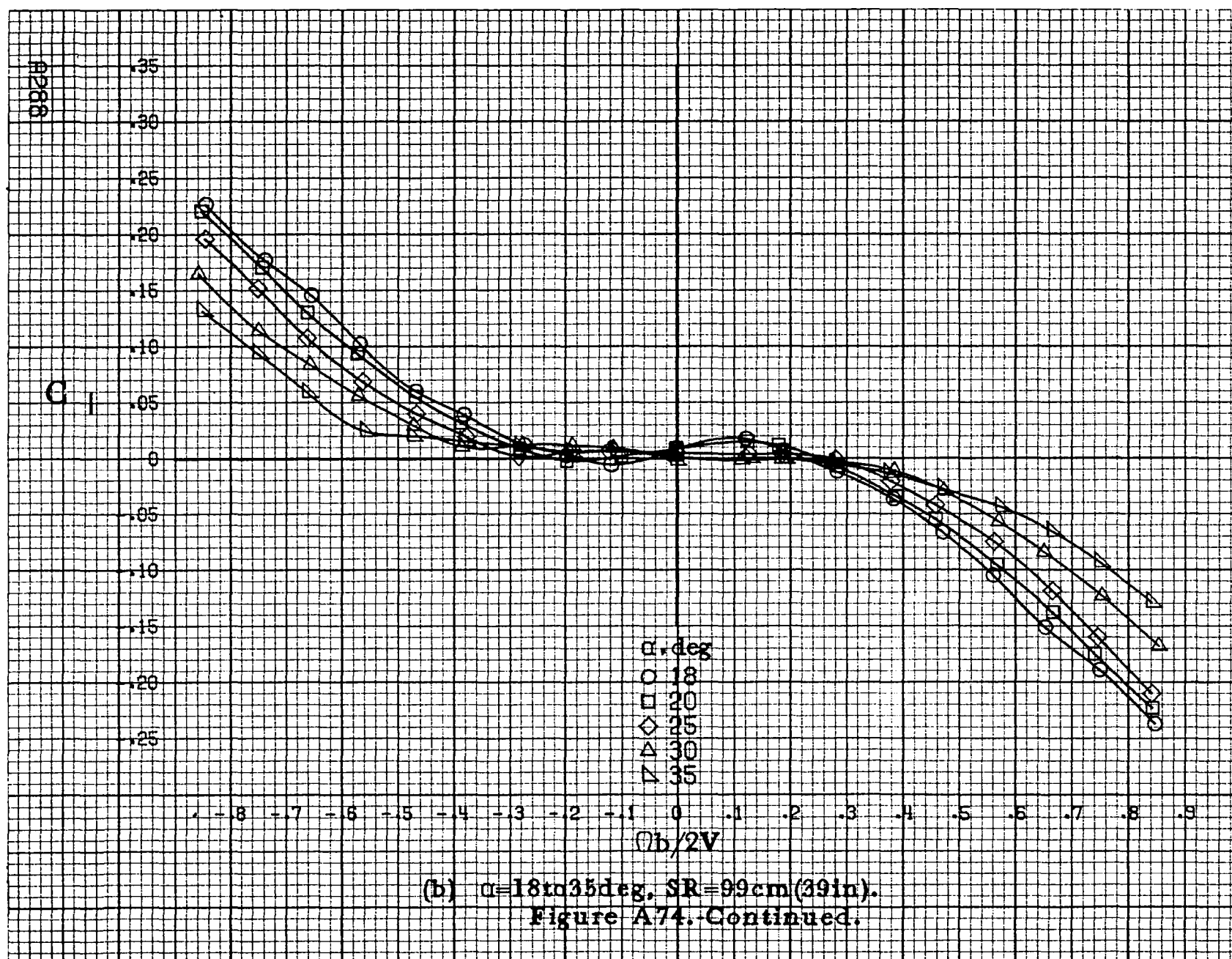
(c)  $\alpha=55$  to  $90^\circ$ ,  $SR=0$ .  
Figure A73. Concluded.

C<sub>l</sub>



(a)  $\alpha = 8$  to  $16$  deg,  $SR = 99$  cm (39 in).

Figure A74. Effect of rotation rate and angle of attack on rolling-moment coefficient for configuration having full-span LE wing droop with moderate nose radius.  $\delta_1 = 0^\circ$ ,  $\delta_2 = 0^\circ$ ,  $\delta_3 = 0^\circ$ ,  $\beta = 0^\circ$ .



$C_1$

.14  
.12  
.10  
.08  
.06  
.04  
.02  
0  
-.02  
-.04  
-.06  
-.08  
-.10

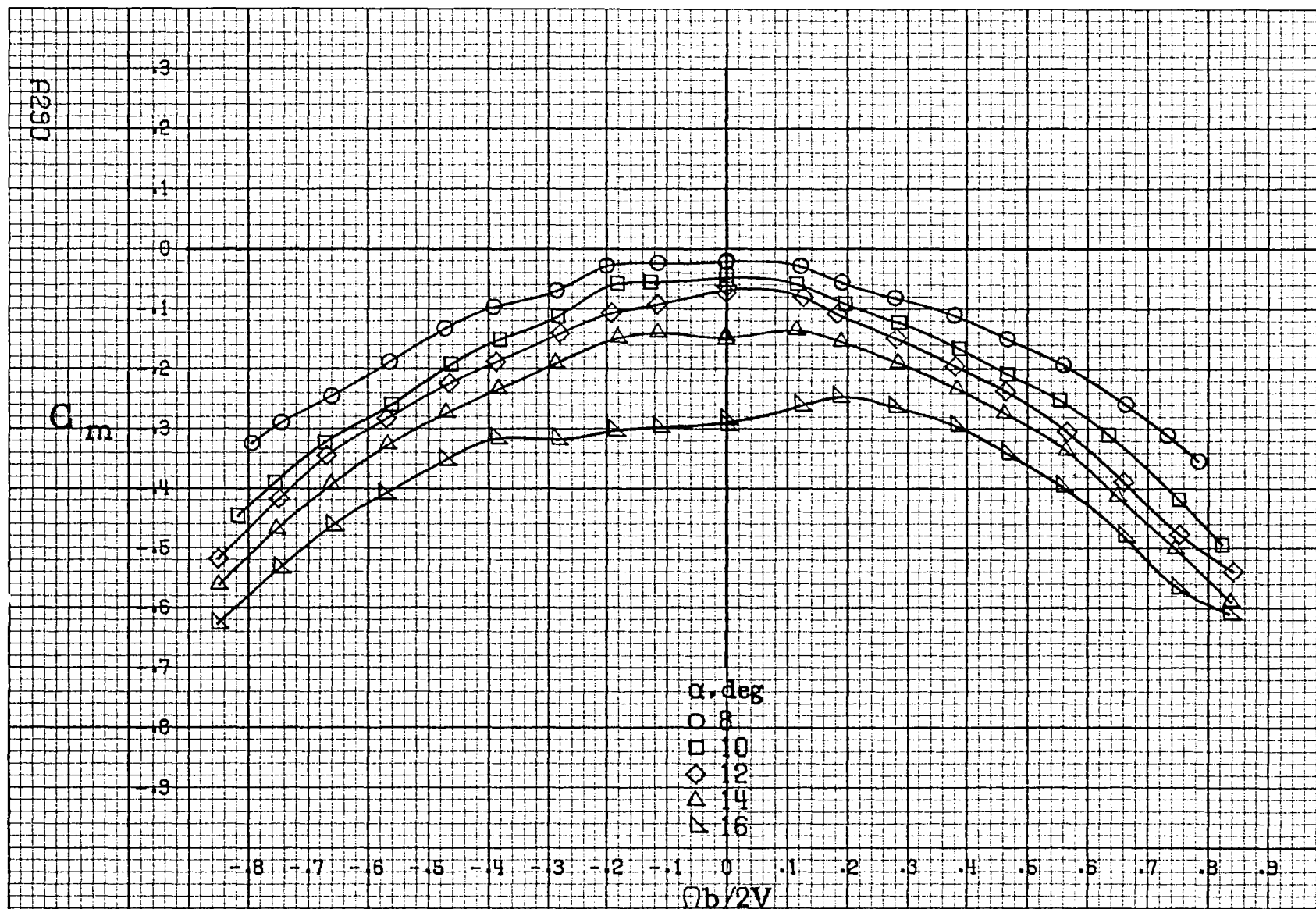
-.8 -.7 -.6 -.5 -.4 -.3 -.2 -.1 0 .1 .2 .3 .4 .5 .6 .7 .8 .9

$\alpha, \text{deg}$   
○ 55  
□ 60  
◇ 70  
△ 80  
▽ 90

$\Omega b/2V$

(c)  $\alpha=55$  to  $90$  deg,  $SR=0$ .  
Figure A74-Continued.

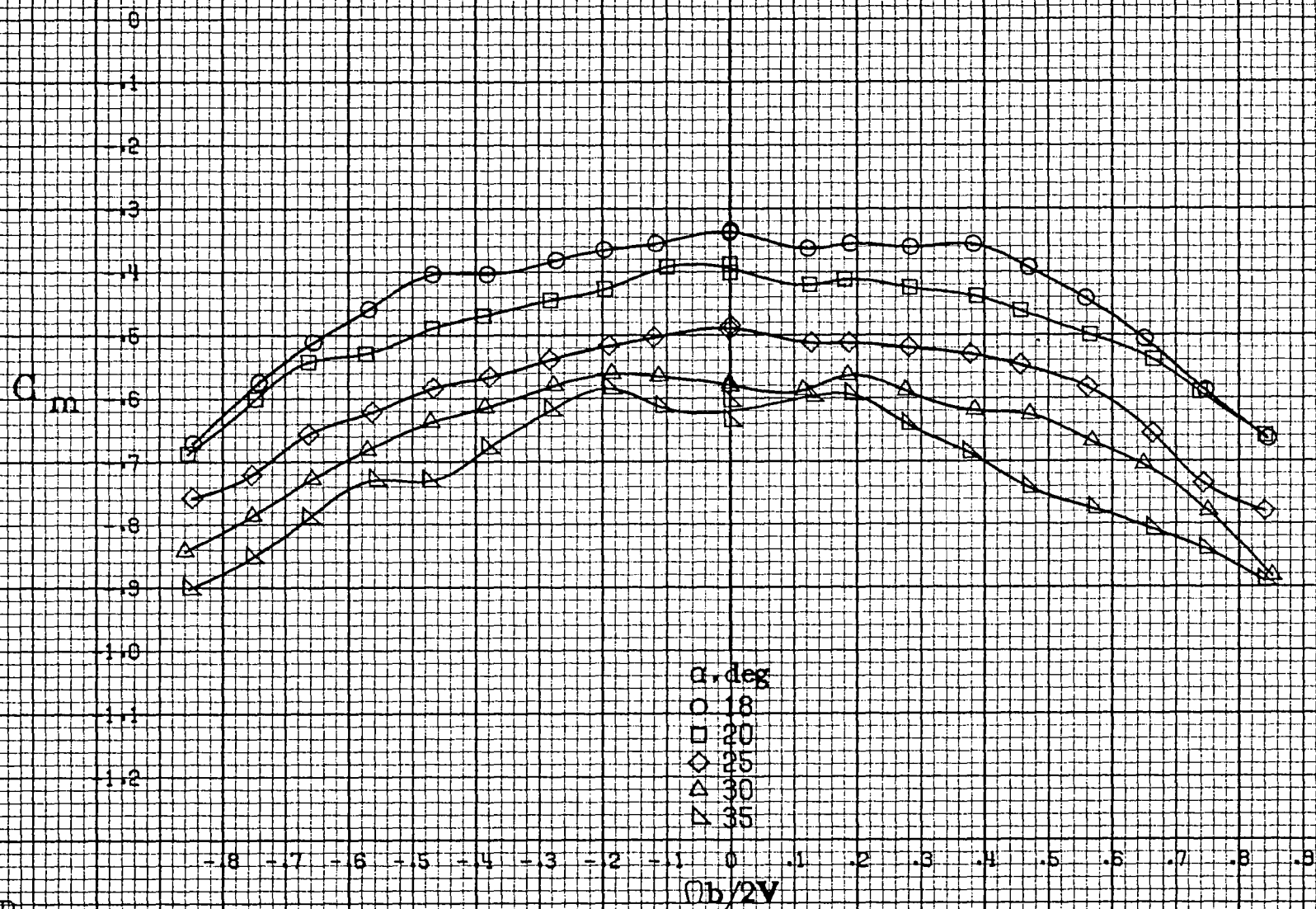
2289



(a)  $\alpha=8$  to  $16$  deg,  $SR=99$  cm (39 in).

Figure A75. Effect of rotation rate and angle of attack on pitching moment coefficient for configuration having full-span LE wing droop with moderate nose radius.  $\delta_a=0^\circ$ ,  $\delta_s=0^\circ$ ,  $\delta_r=0^\circ$ .  $\beta=0^\circ$ .





(b)  $\alpha=18$  to  $35^\circ$ ,  $SR=99\text{cm}(39\text{in})$ .  
Figure A75. Continued.



#292

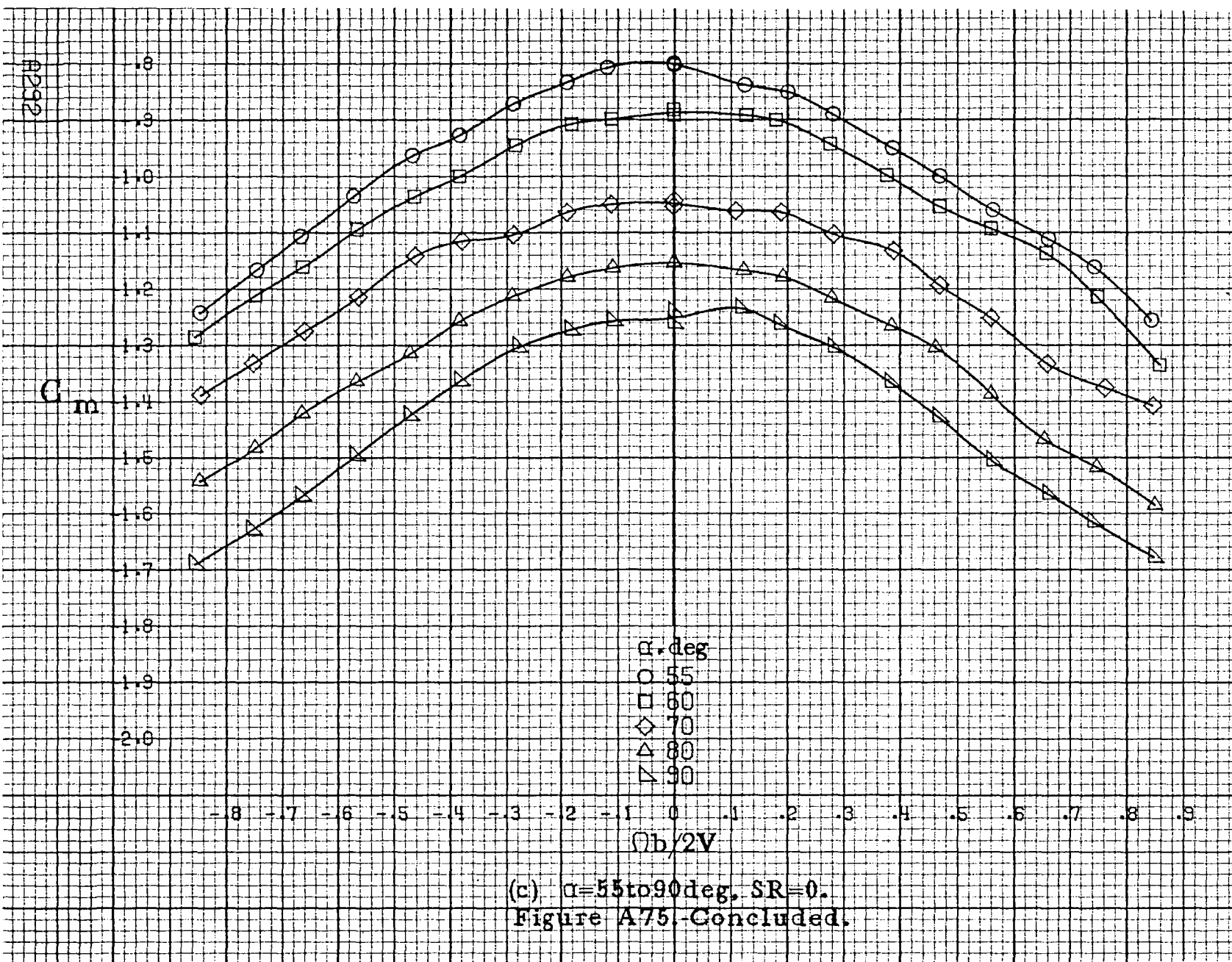
$C_m$

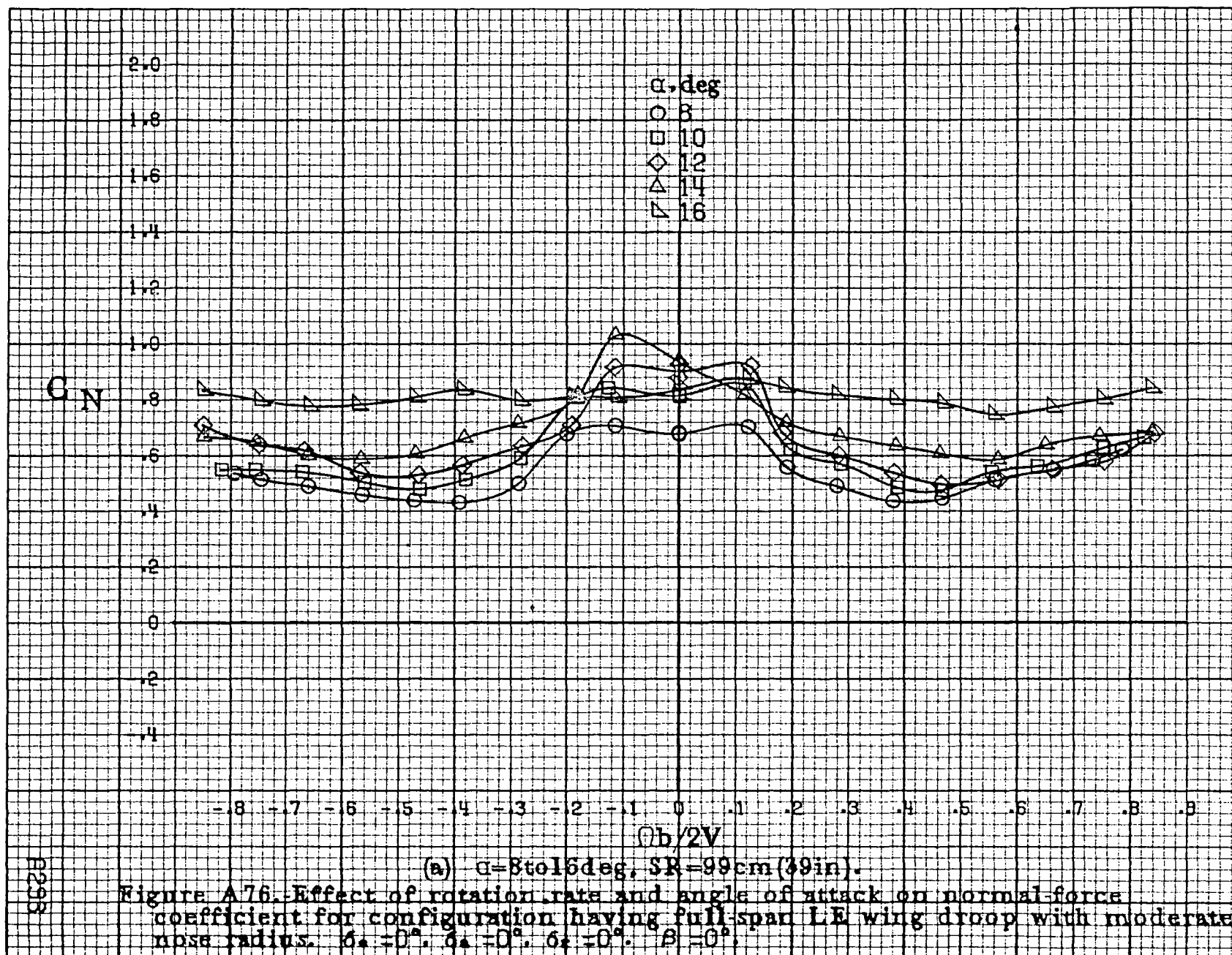
$\alpha, \text{deg}$

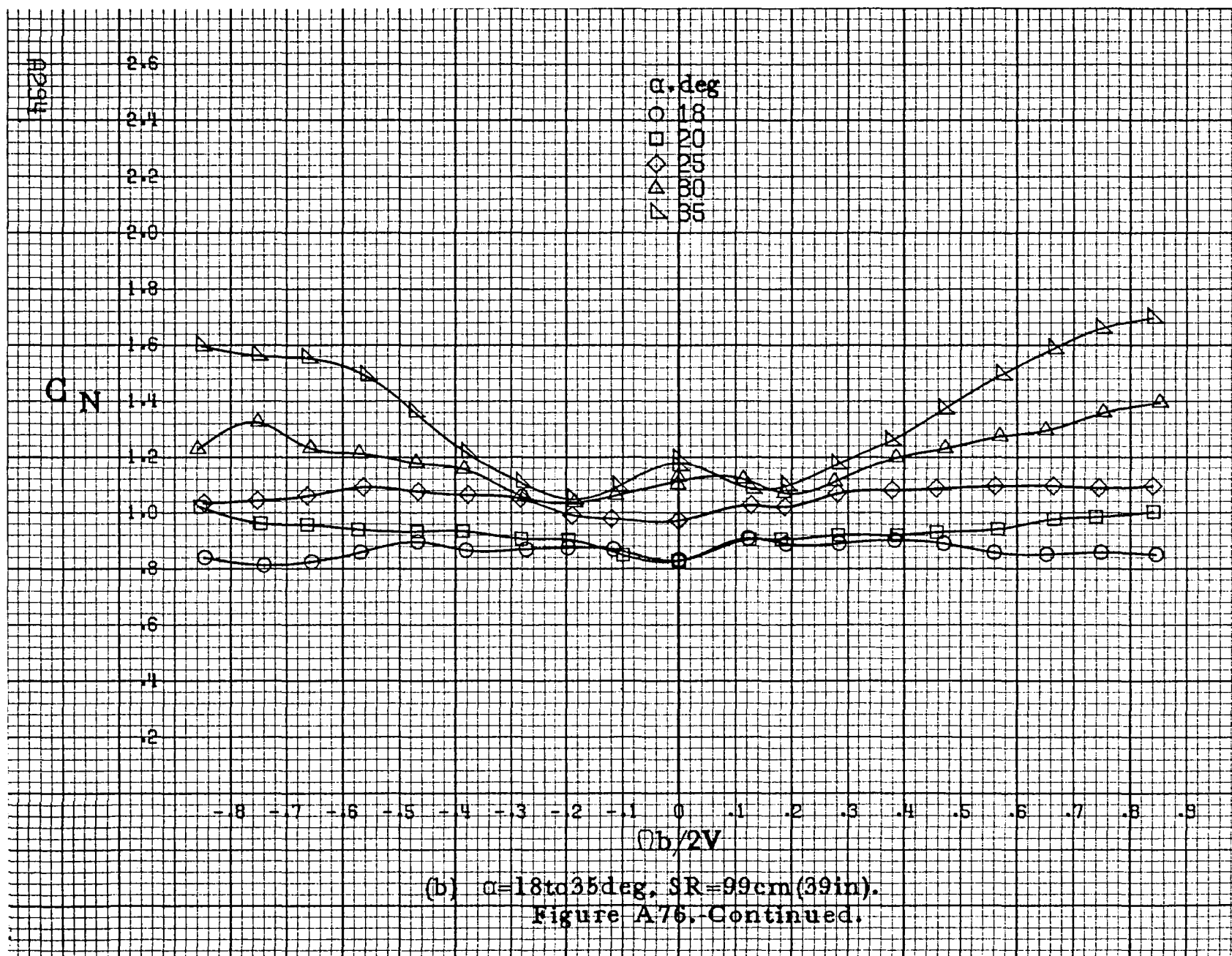
- 55
- 60
- ◇ 70
- △ 80
- ▽ 90

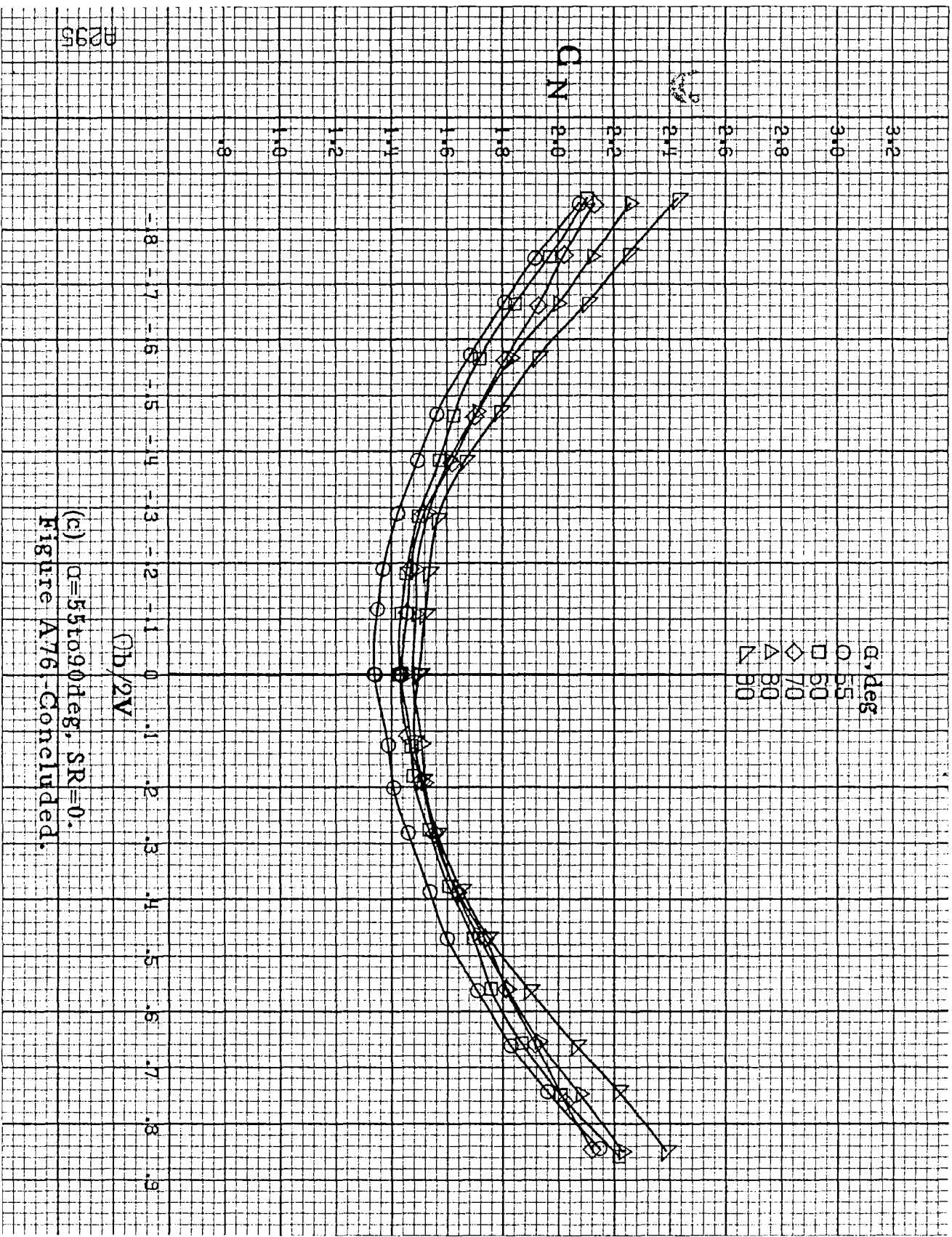
$\Omega b/2V$

(c)  $\alpha=55$  to  $90$  deg.  $SR=0$ .  
Figure A75.-Concluded.

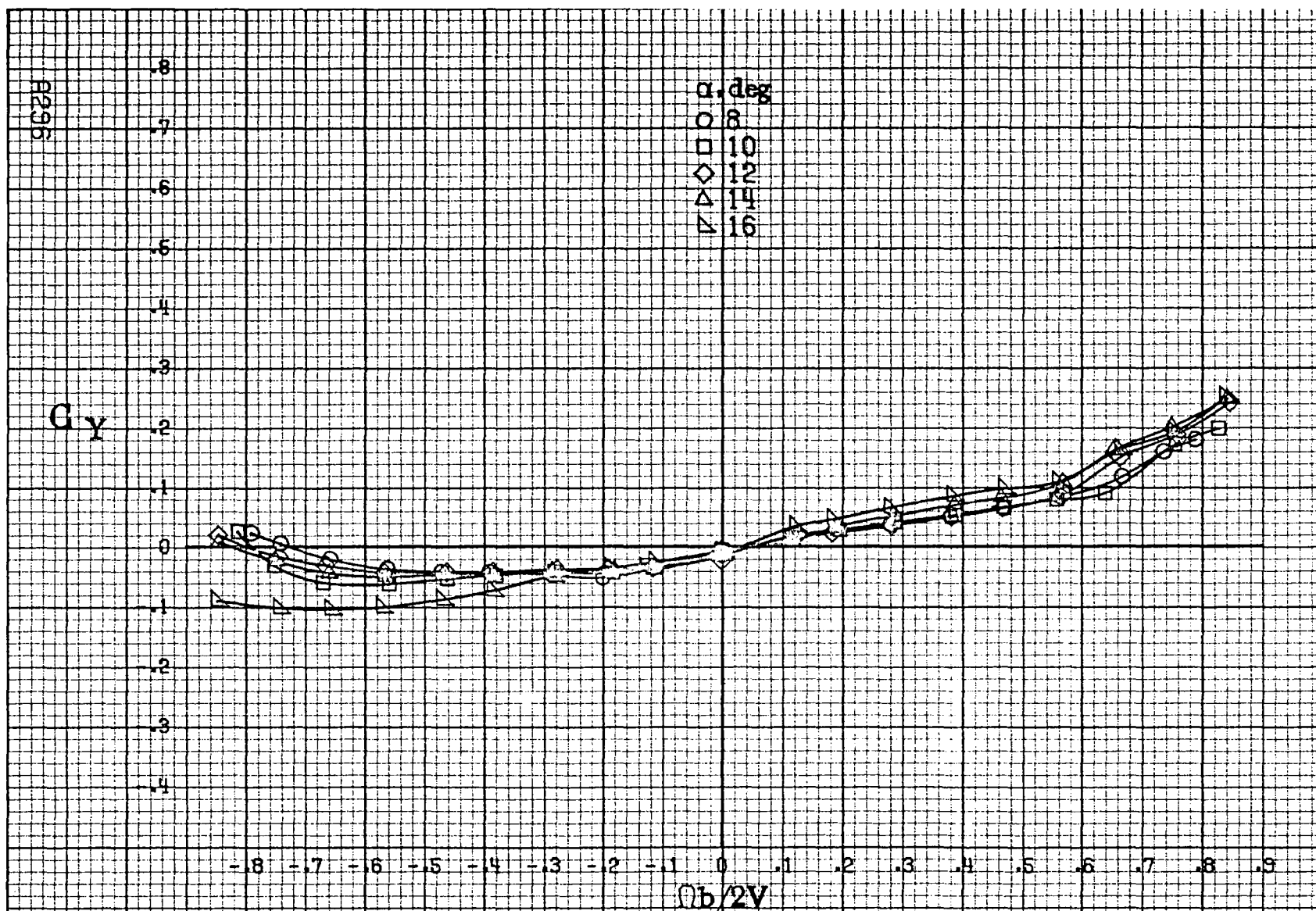






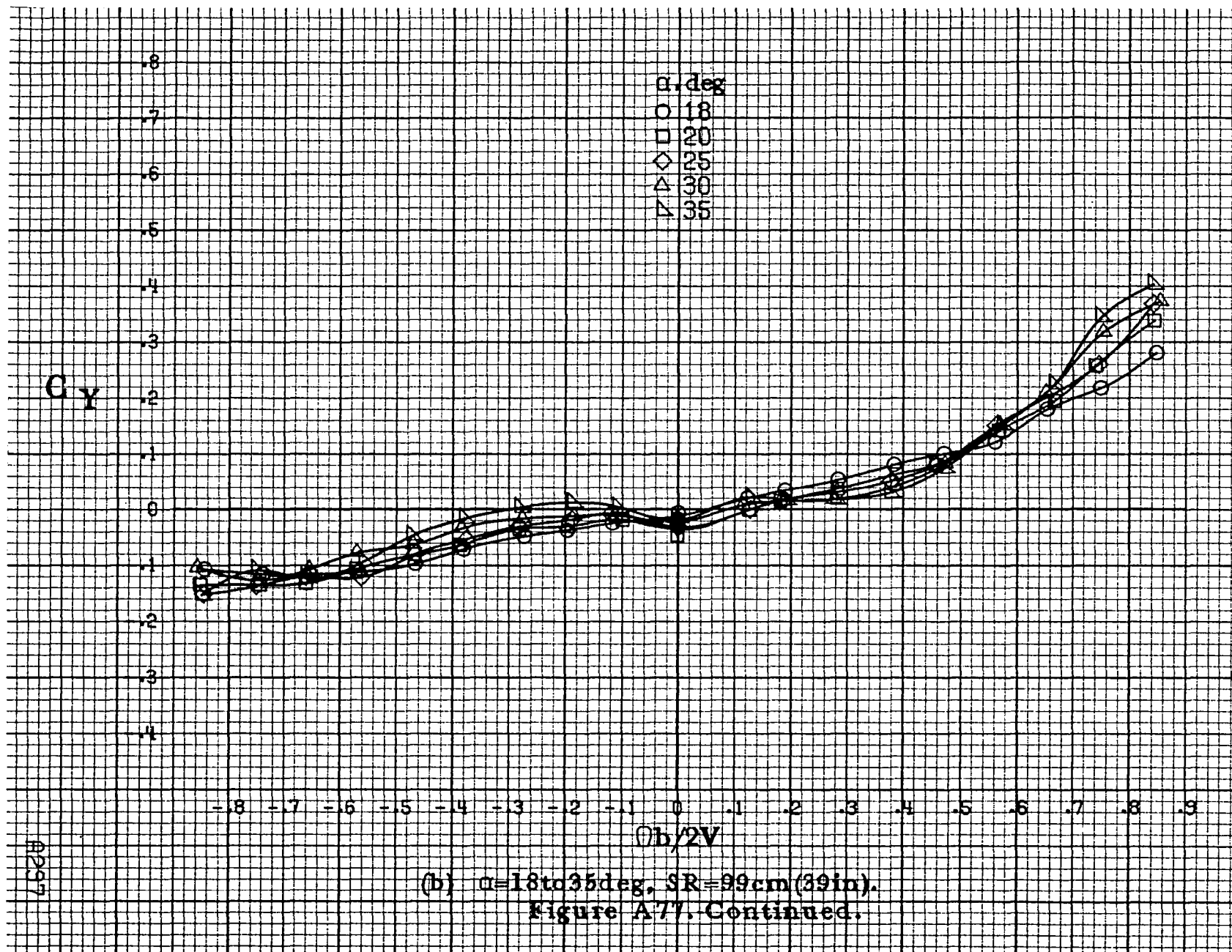


(c)  $\alpha=55$  to  $90^\circ$ ,  $SR=0$ .  
 Figure A.76.-Concluded.

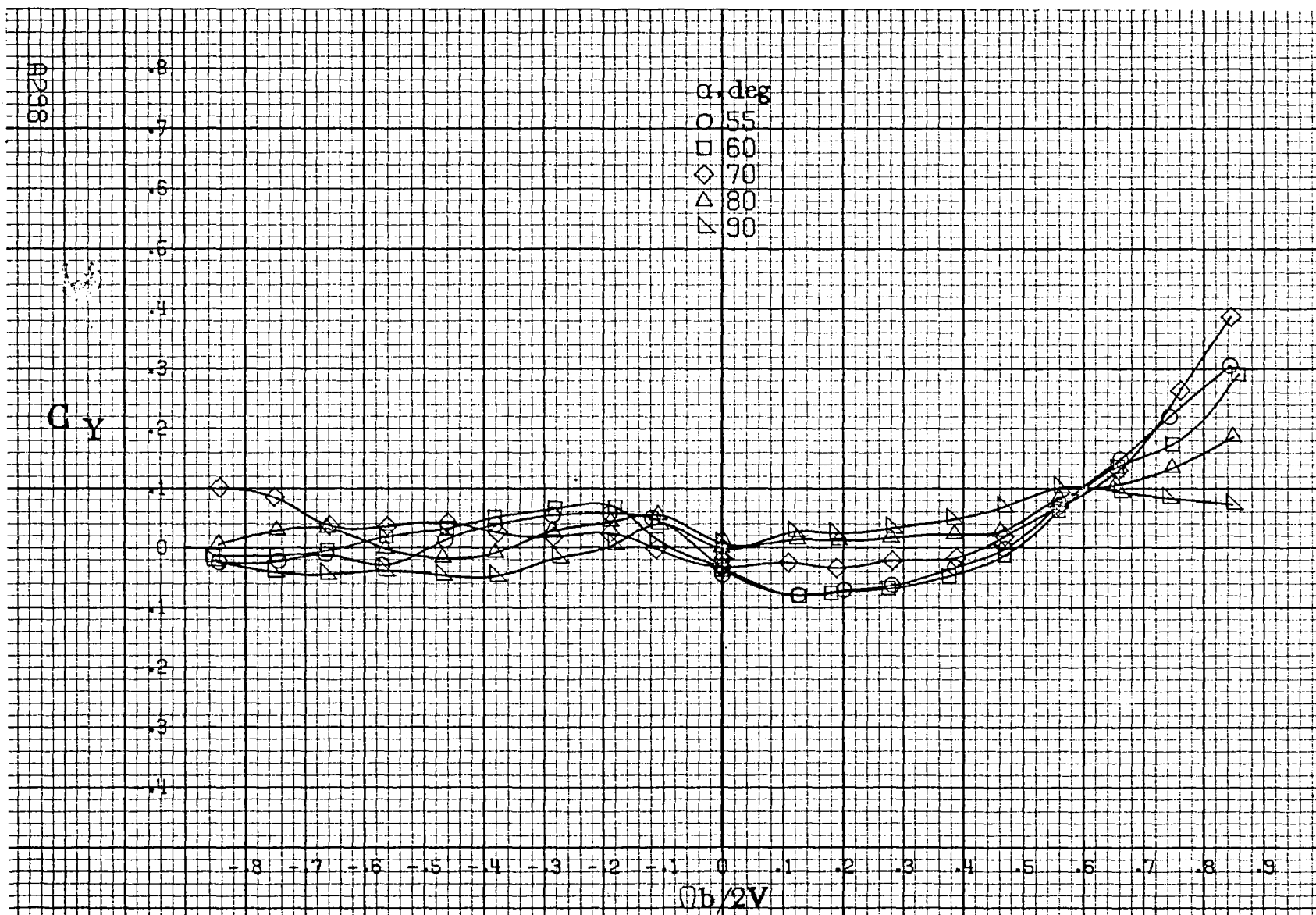


(a)  $\alpha=8\text{ to }16^\circ$ ,  $SR=99\text{ cm (39 in.)}$ .

Figure A77.-Effect of rotation rate and angle of attack on side-force coefficient for configuration having full-span LE wing droop with moderate nose radius.  $\delta_e=0^\circ$ ,  $\delta_s=0^\circ$ ,  $\delta_r=0^\circ$ .  $\beta=0^\circ$ .

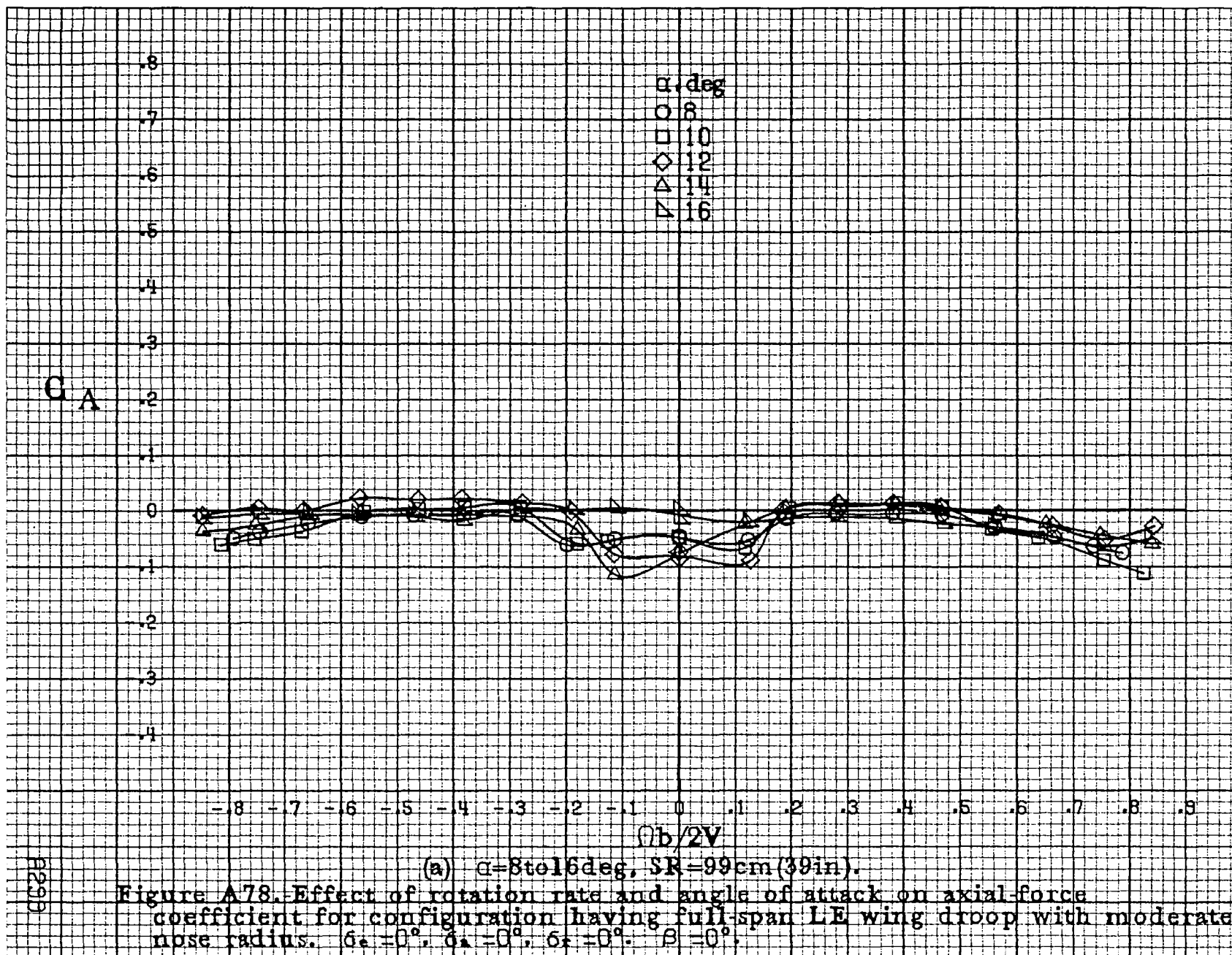


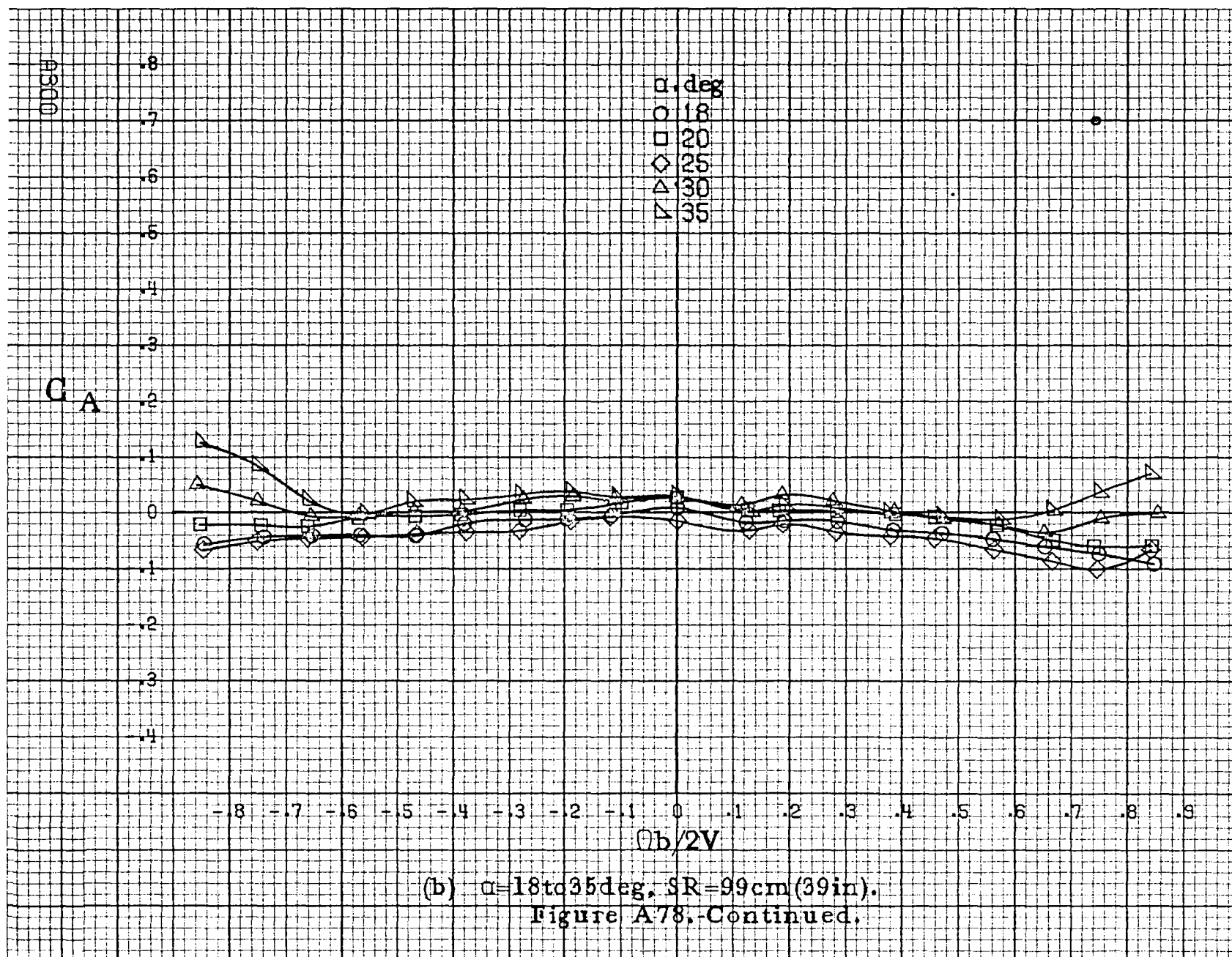


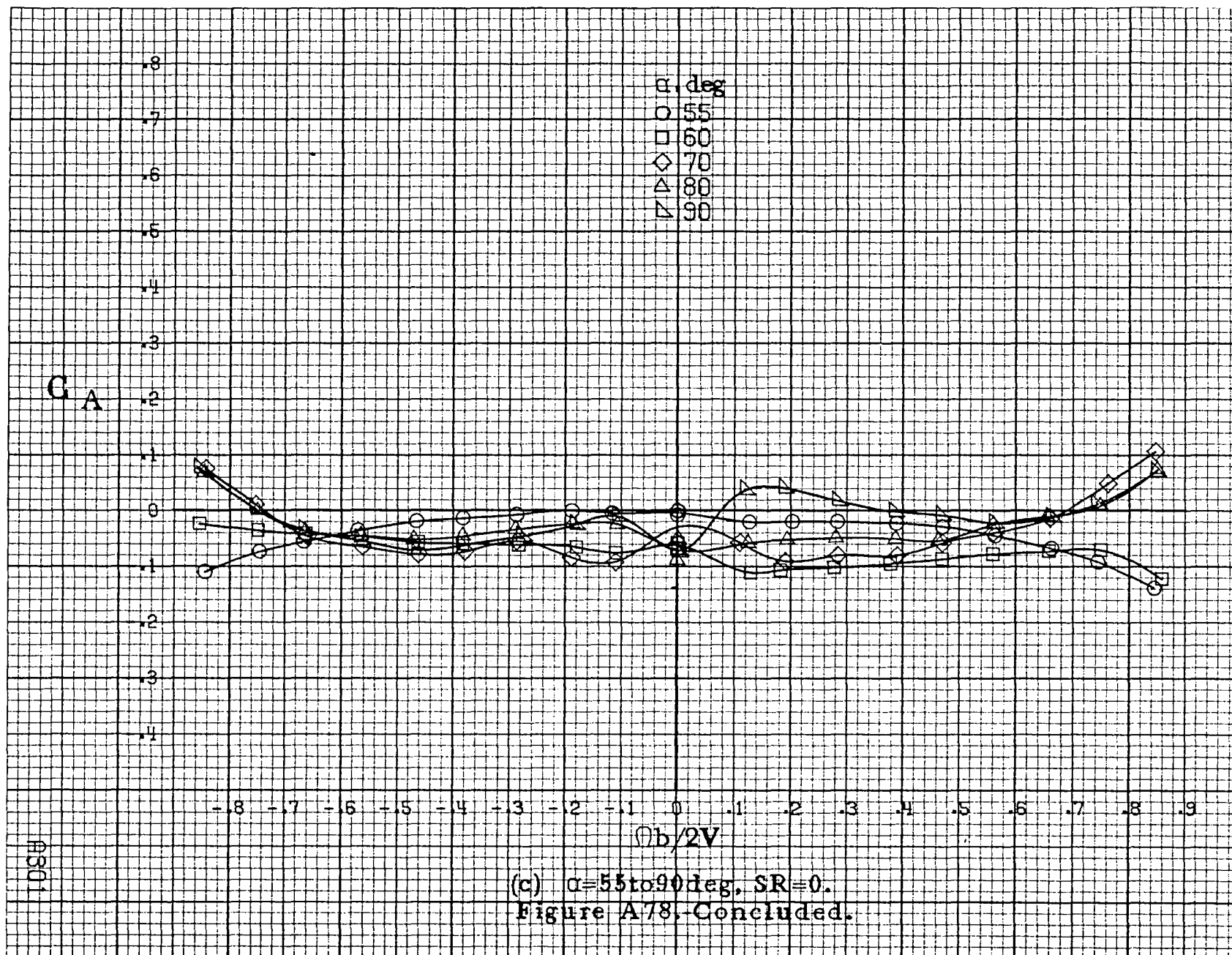


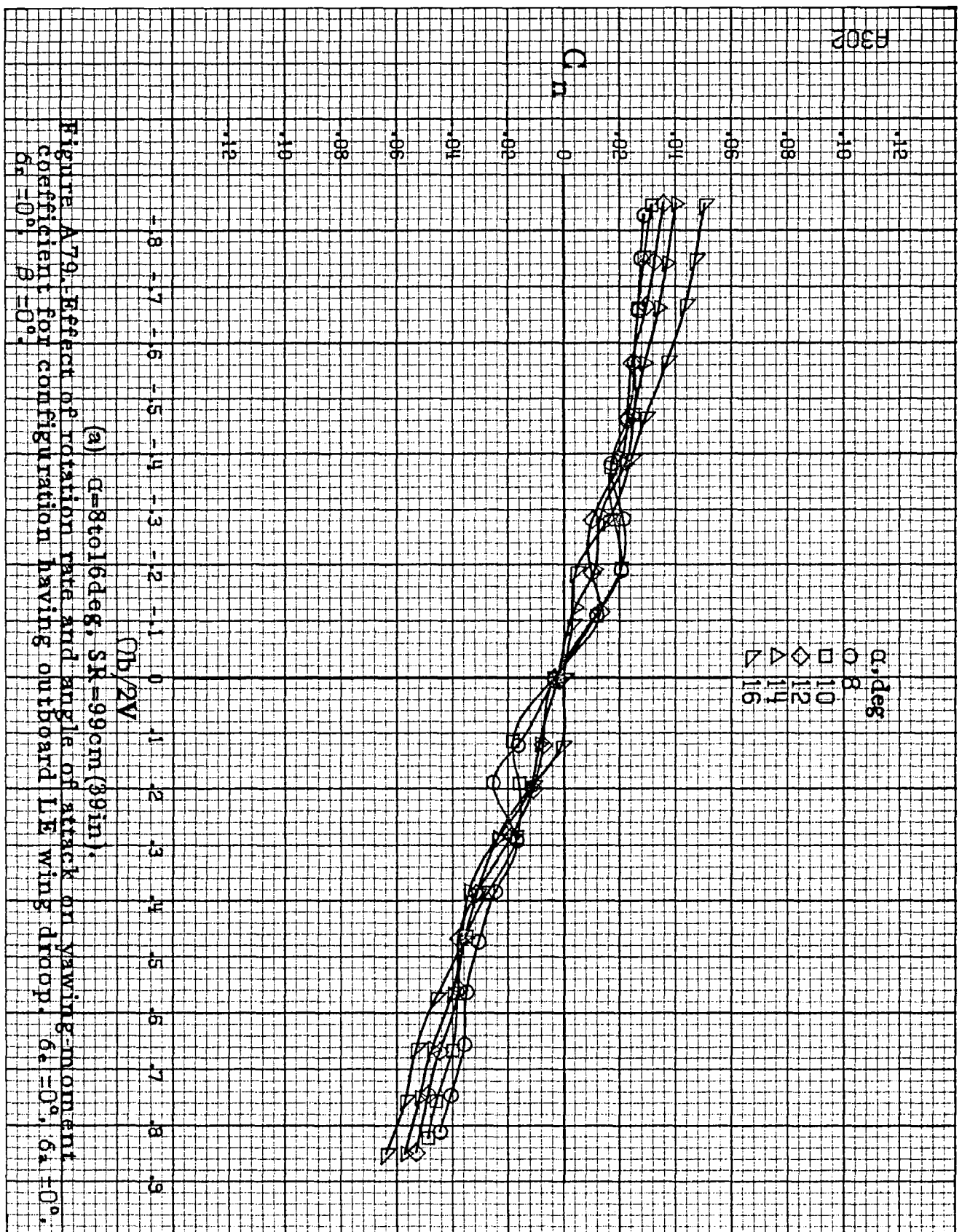
(c)  $\alpha = 55$  to  $90^\circ$ ,  $SR = 0$ .  
Figure A77. Concluded.

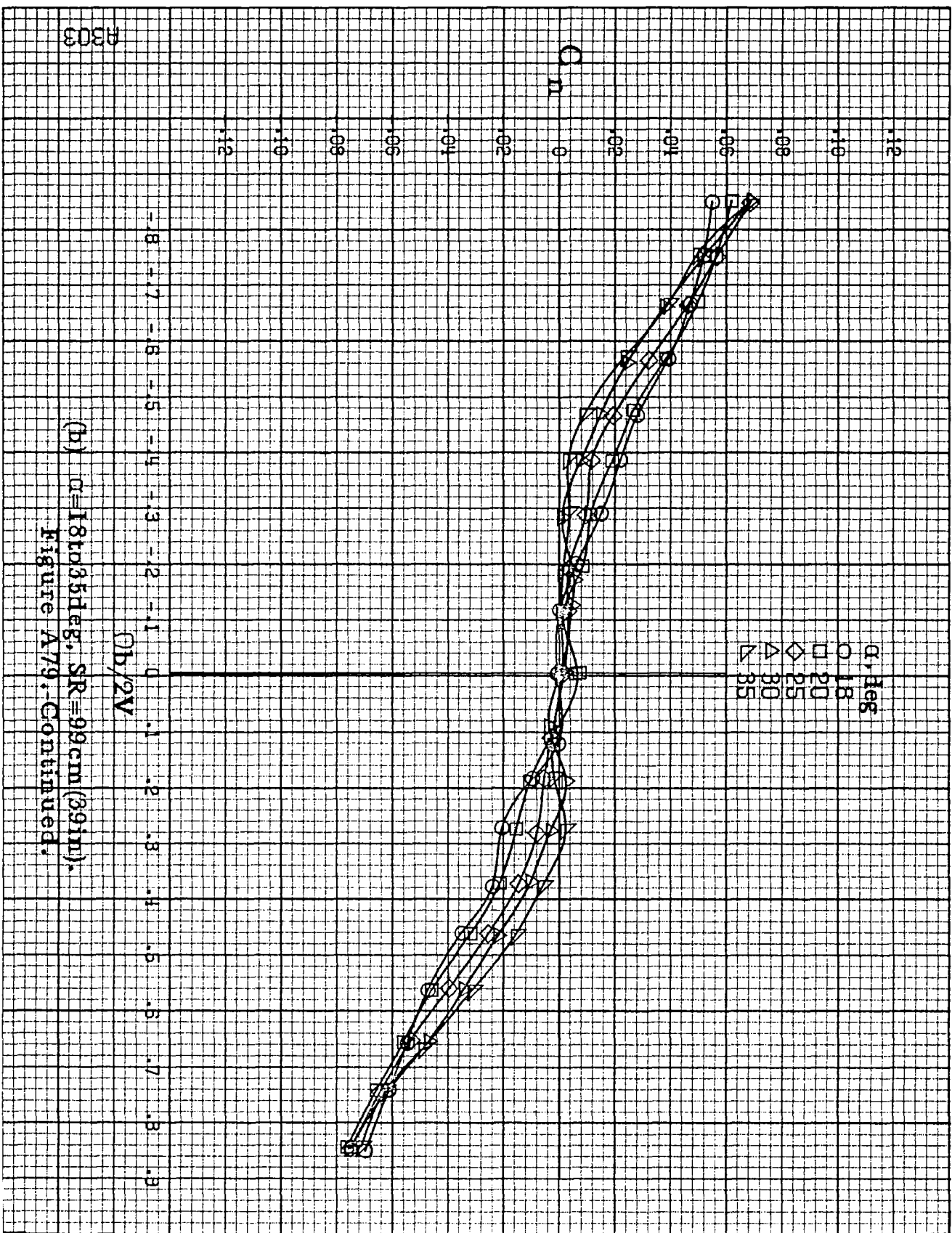


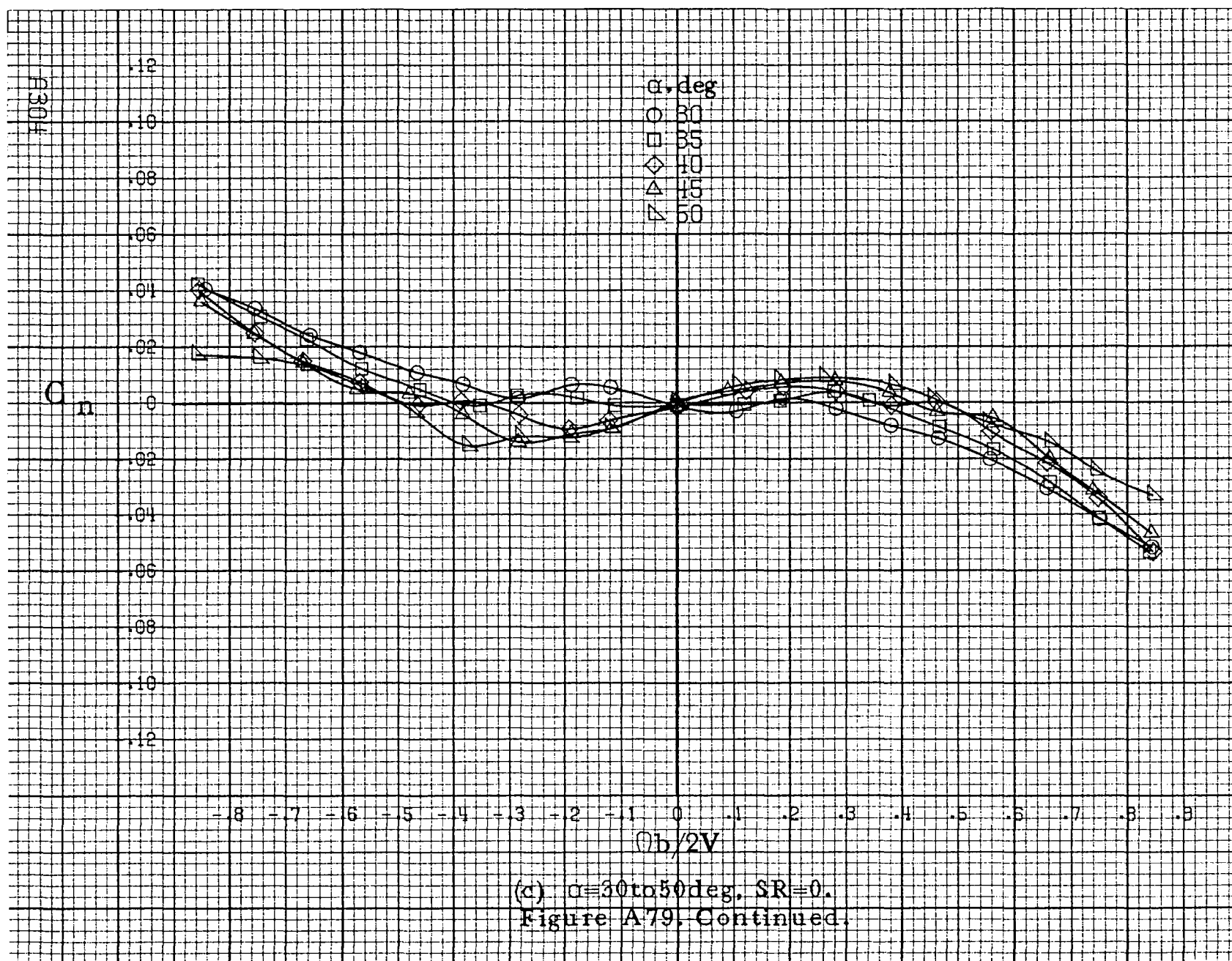




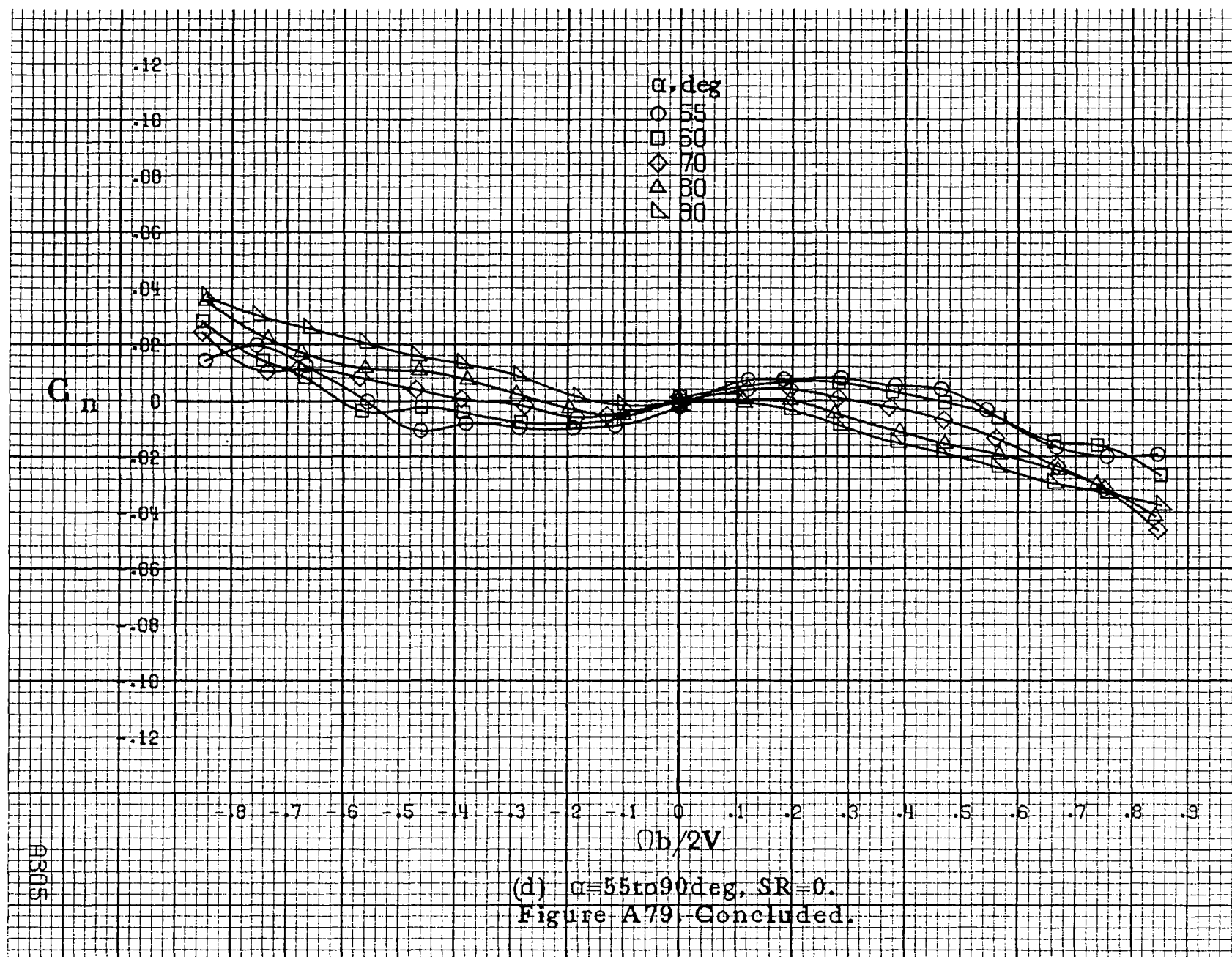




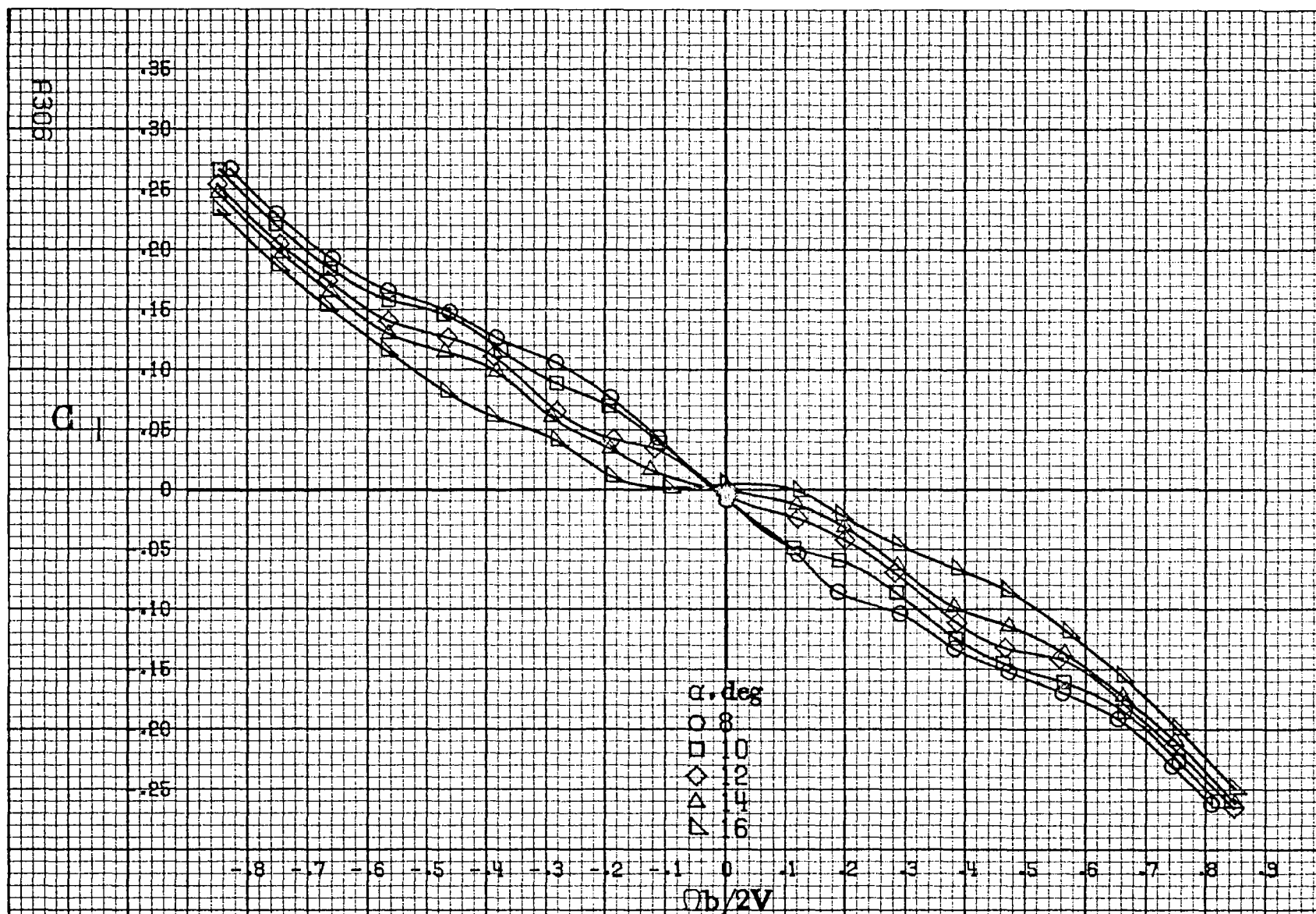












(a)  $\alpha=8$  to  $16^\circ$ ,  $SR=99\text{cm}(39\text{in})$ .

Figure A80. Effect of rotation rate and angle of attack on rolling-moment coefficient for configuration having outboard LE wing droop.  $\delta_a = 0^\circ$ ,  $\delta_s = 0^\circ$ ,  $\beta = 0^\circ$ .

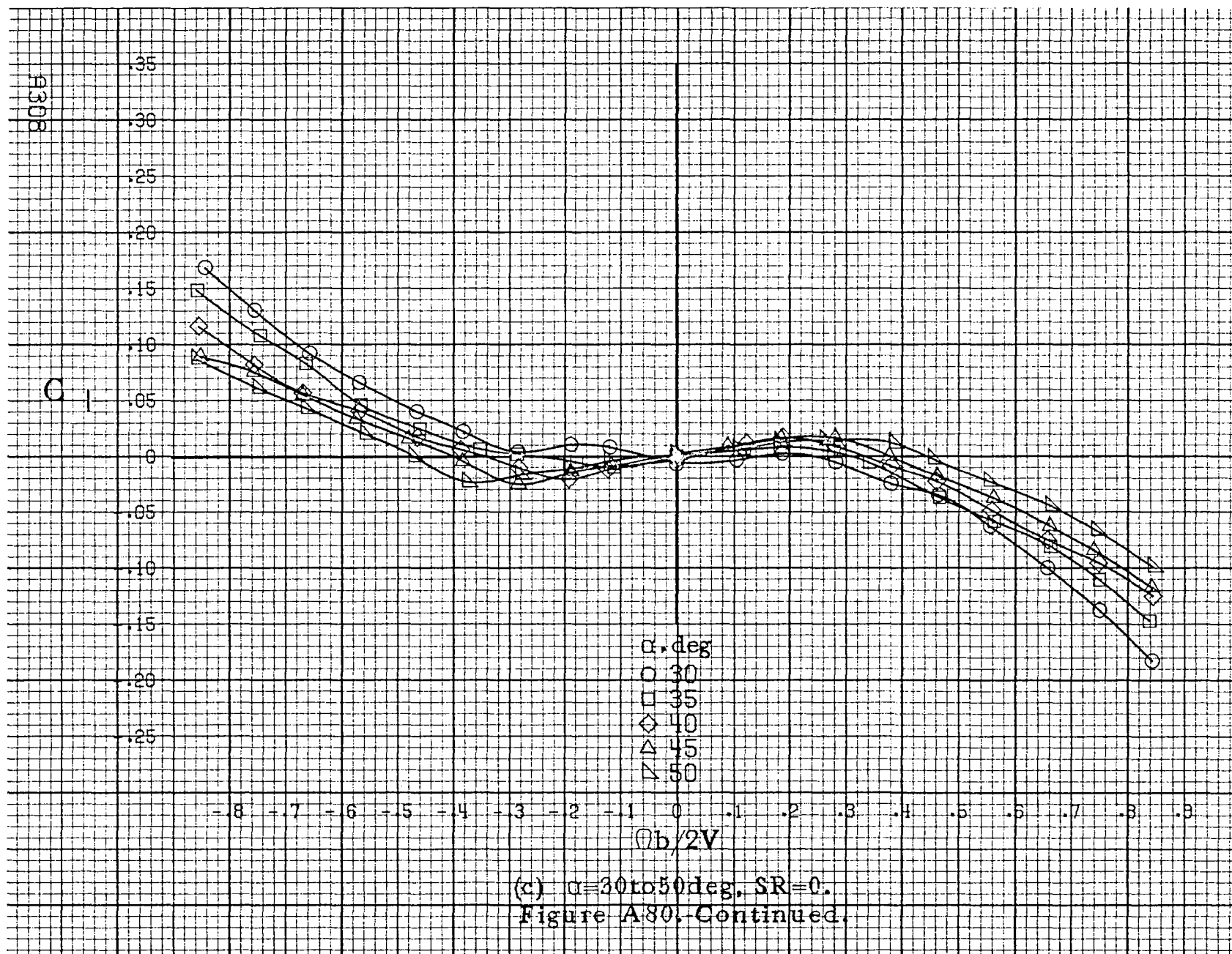
$C_I$

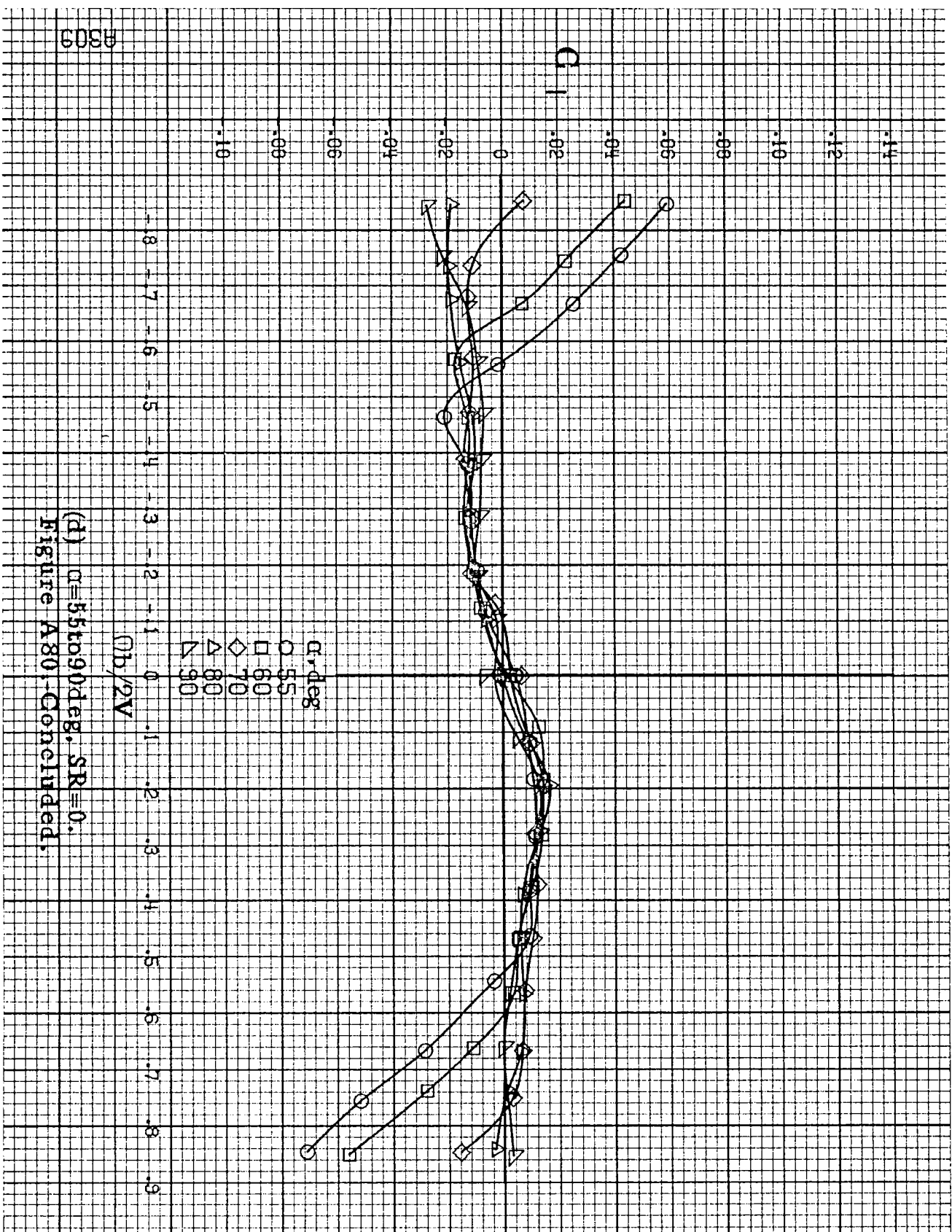
.35  
.30  
.25  
.20  
.15  
.10  
.05  
0  
-.05  
-.10  
-.15  
-.20  
-.25

$\alpha, \text{deg}$   
○ 18  
□ 20  
◇ 25  
△ 30  
▽ 35

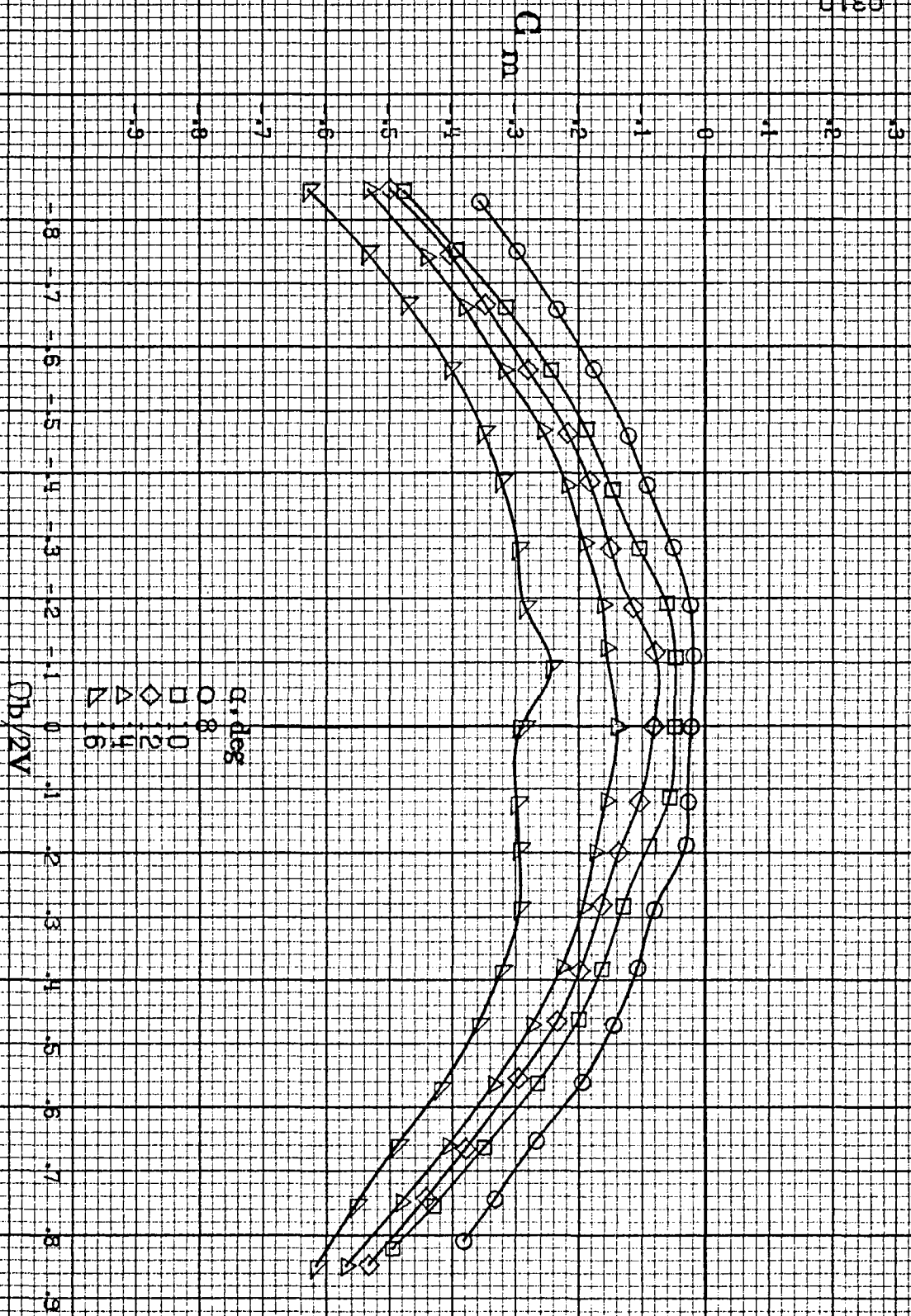
-.8 -.7 -.6 -.5 -.4 -.3 -.2 -.1 0 .1 .2 .3 .4 .5 .6 .7 .8 .9  
 $b/2V$

(b)  $\alpha=18\text{to}35\text{deg}$ ,  $SR=99\text{cm}(39\text{in})$ .  
Figure A80. Continued.





(d)  $\alpha=55$  to  $90$  deg.  $SR=0$ .  
Figure A80-Concluded.



(a)  $\alpha=8$  to  $16$  deg,  $SR=99$  cm (39 in).

Figure A8.1. Effect of rotation rate and angle of attack on pitching-moment coefficient for configuration having outboard LE wing droop.  $\delta_a=0^\circ$ ,  $\delta_x=0^\circ$ .

$C_m$

0  
 .1  
 .2  
 .3  
 .4  
 .5  
 .6  
 .7  
 .8  
 .9  
 1.0  
 1.1  
 1.2

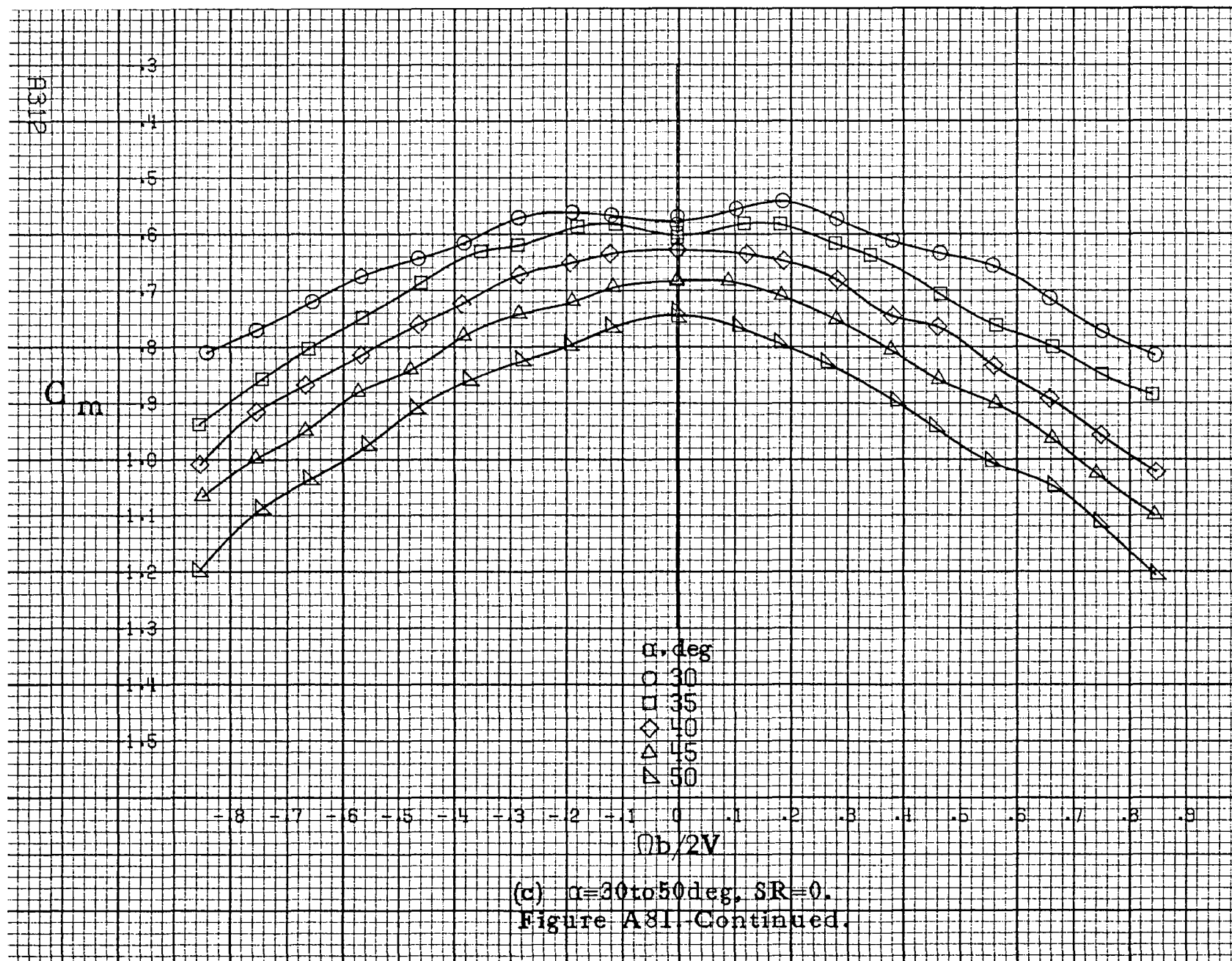
$\alpha, \text{deg}$   
 ○ 18  
 □ 20  
 ◇ 25  
 △ 30  
 ▴ 35

$b/2V$

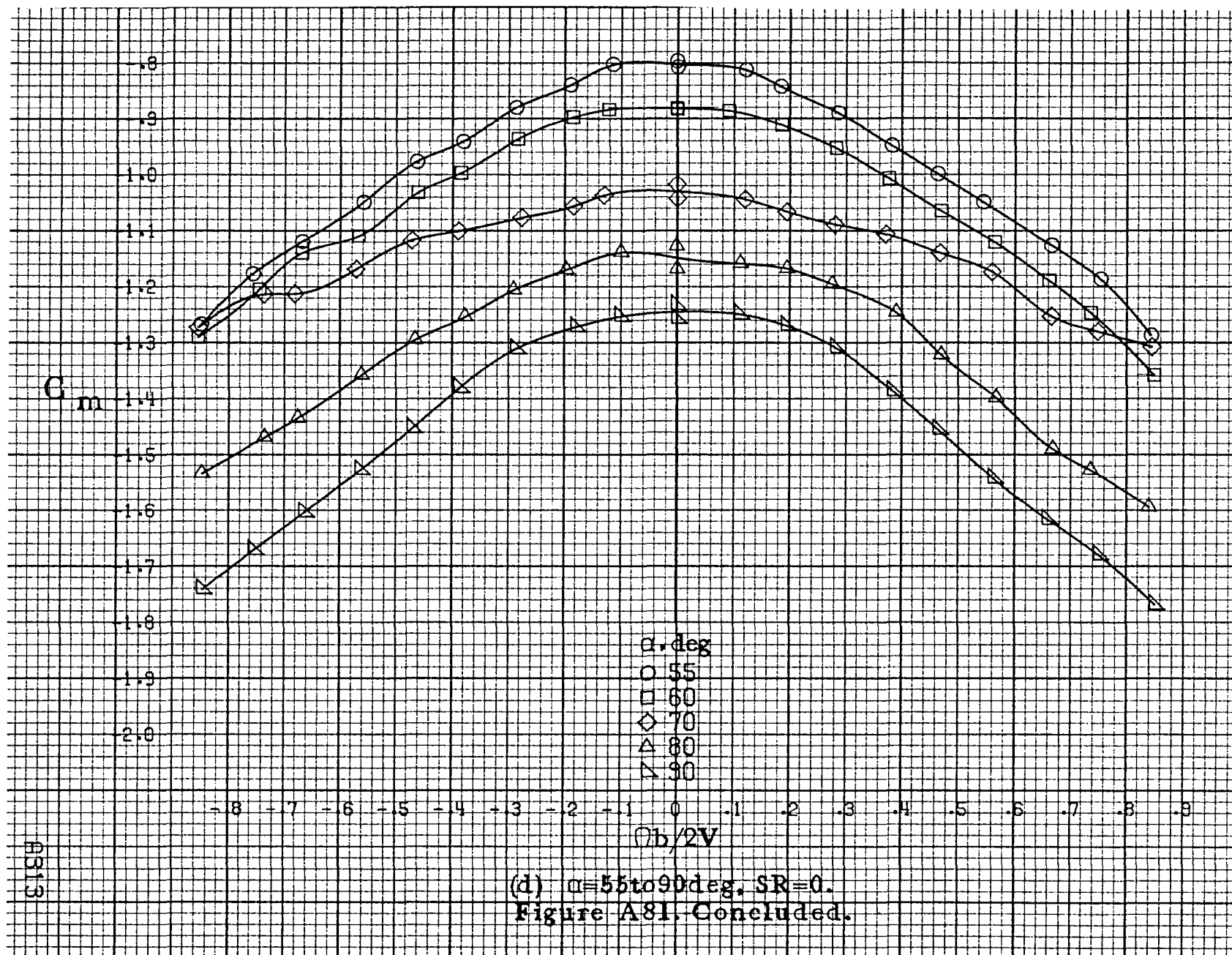
-0.8 -0.7 -0.6 -0.5 -0.4 -0.3 -0.2 -0.1 0 .1 .2 .3 .4 .5 .6 .7 .8 .9

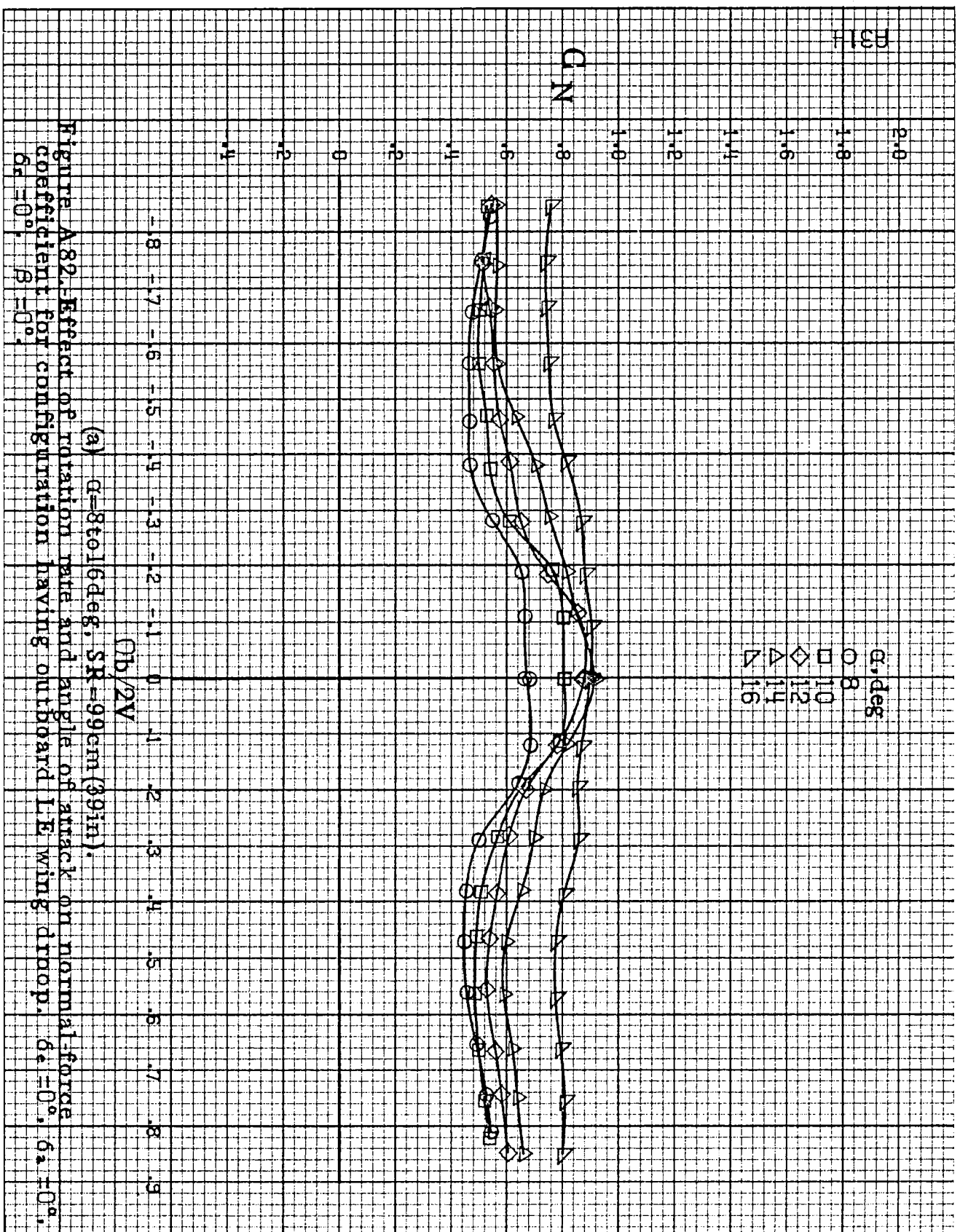
(b)  $\alpha=18$  to  $35$  deg,  $SR=99\text{cm}(39\text{in})$ .  
 Figure A81. Continued.

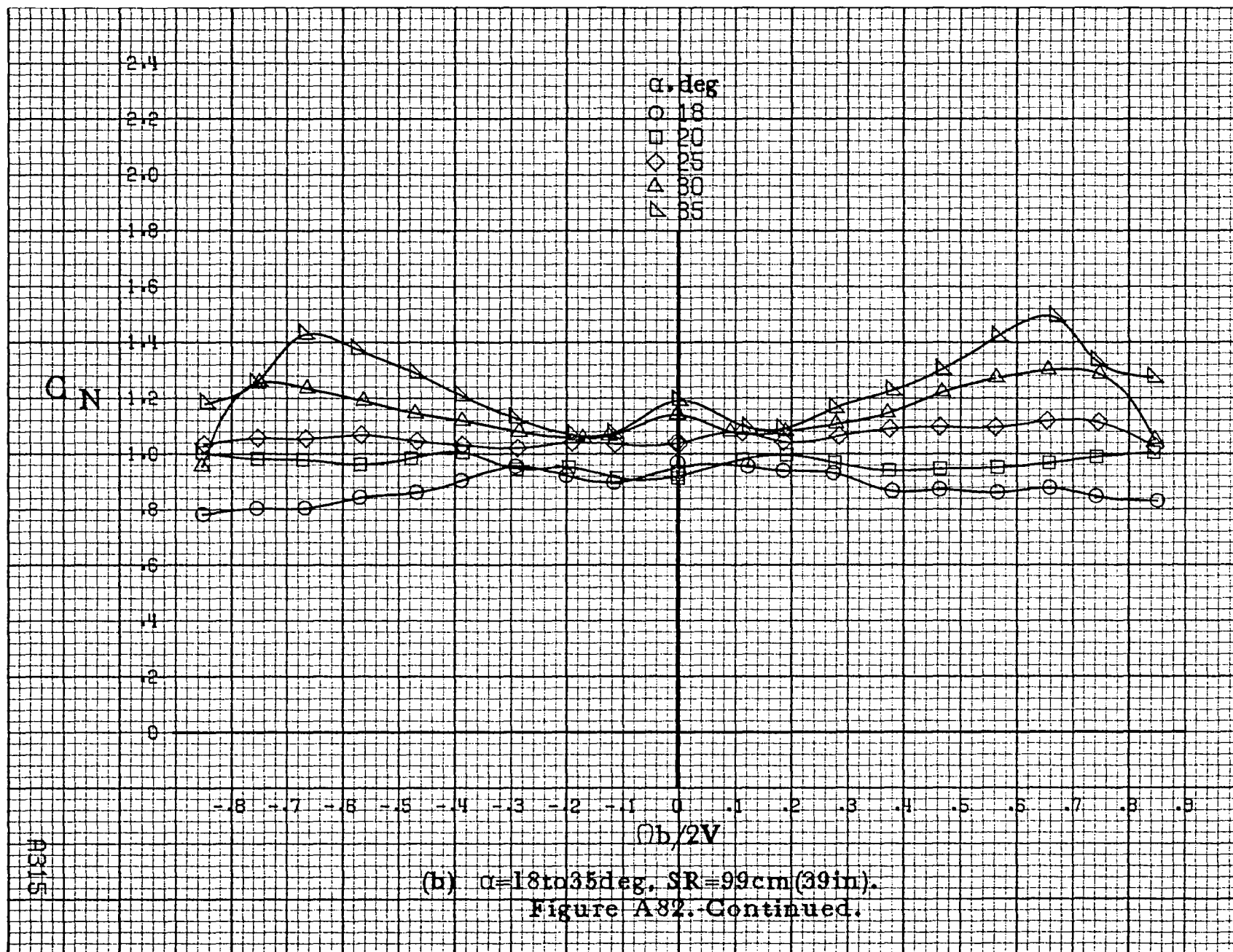


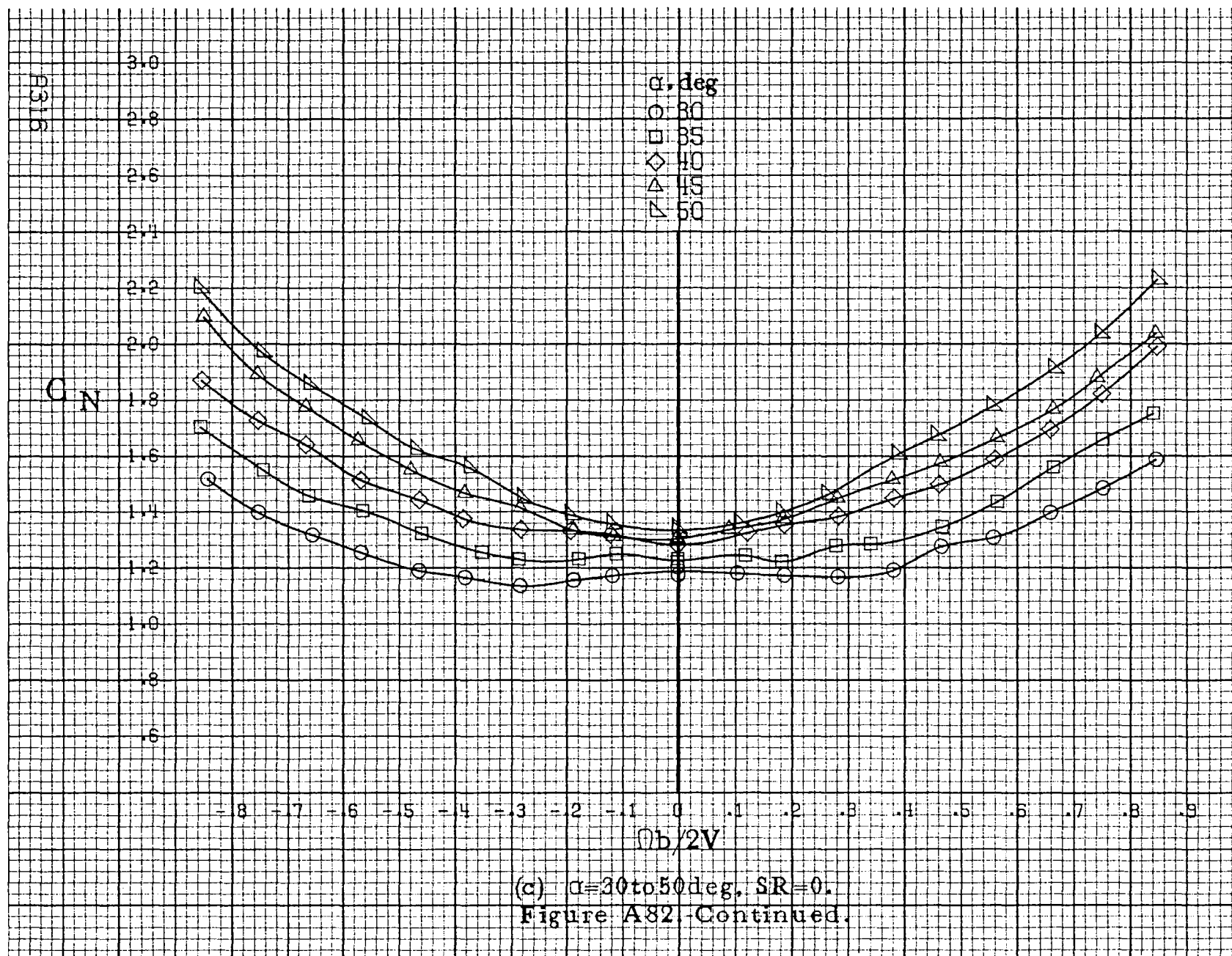


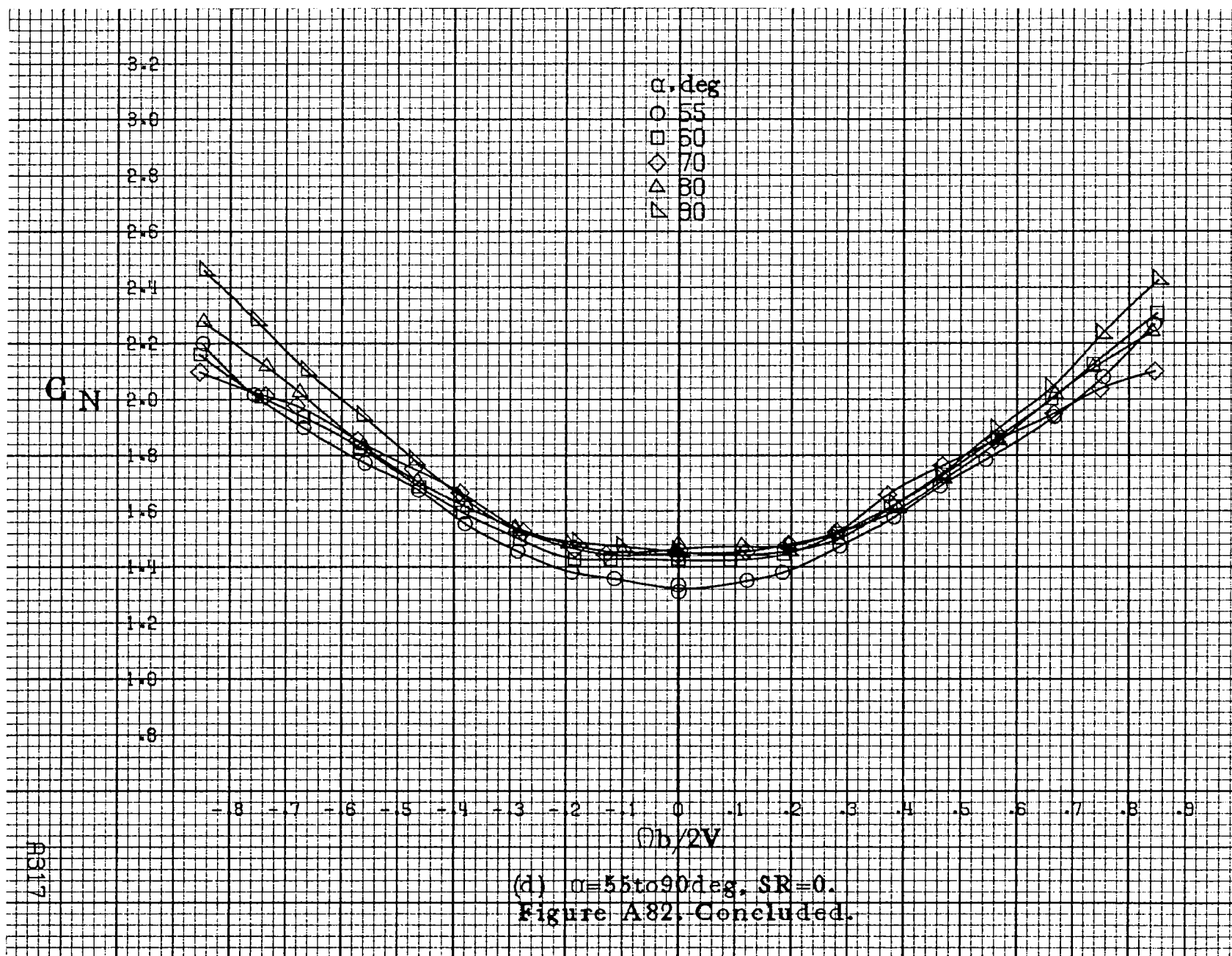












B318

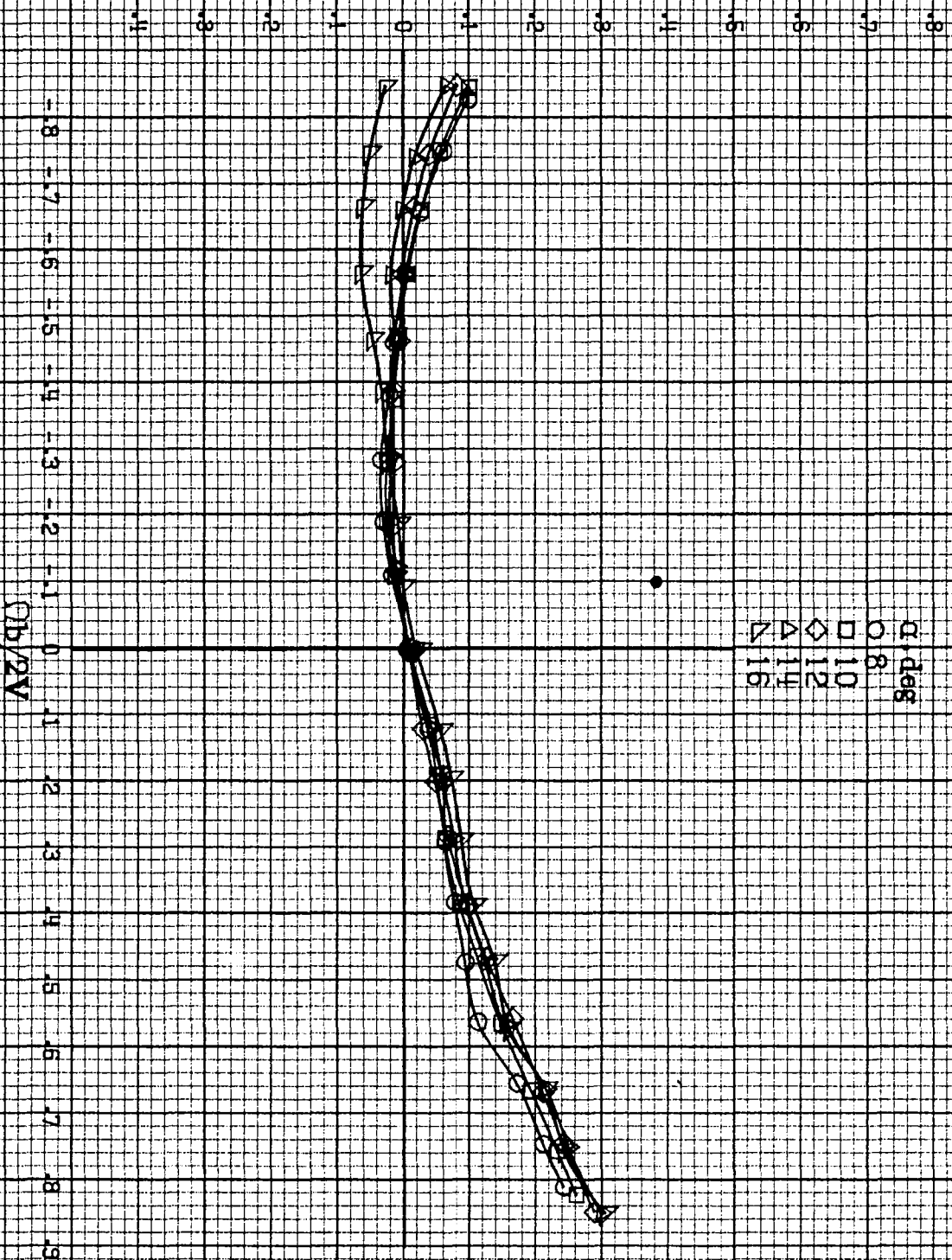
 $C_Y$ (a)  $\alpha = 8$  to  $16$  deg,  $S_R = 99$  cm (39 in). $Cb/2V$ 

Figure A83. Effect of rotation rate and angle of attack on side-force coefficient for configuration having outward LE wing droop.  $\phi_a = 0^\circ$ ,  $\phi_b = 0^\circ$ .



$C_y$

$\alpha, \text{deg}$   
 ○ 18  
 □ 20  
 ◇ 25  
 △ 30  
 ▴ 35

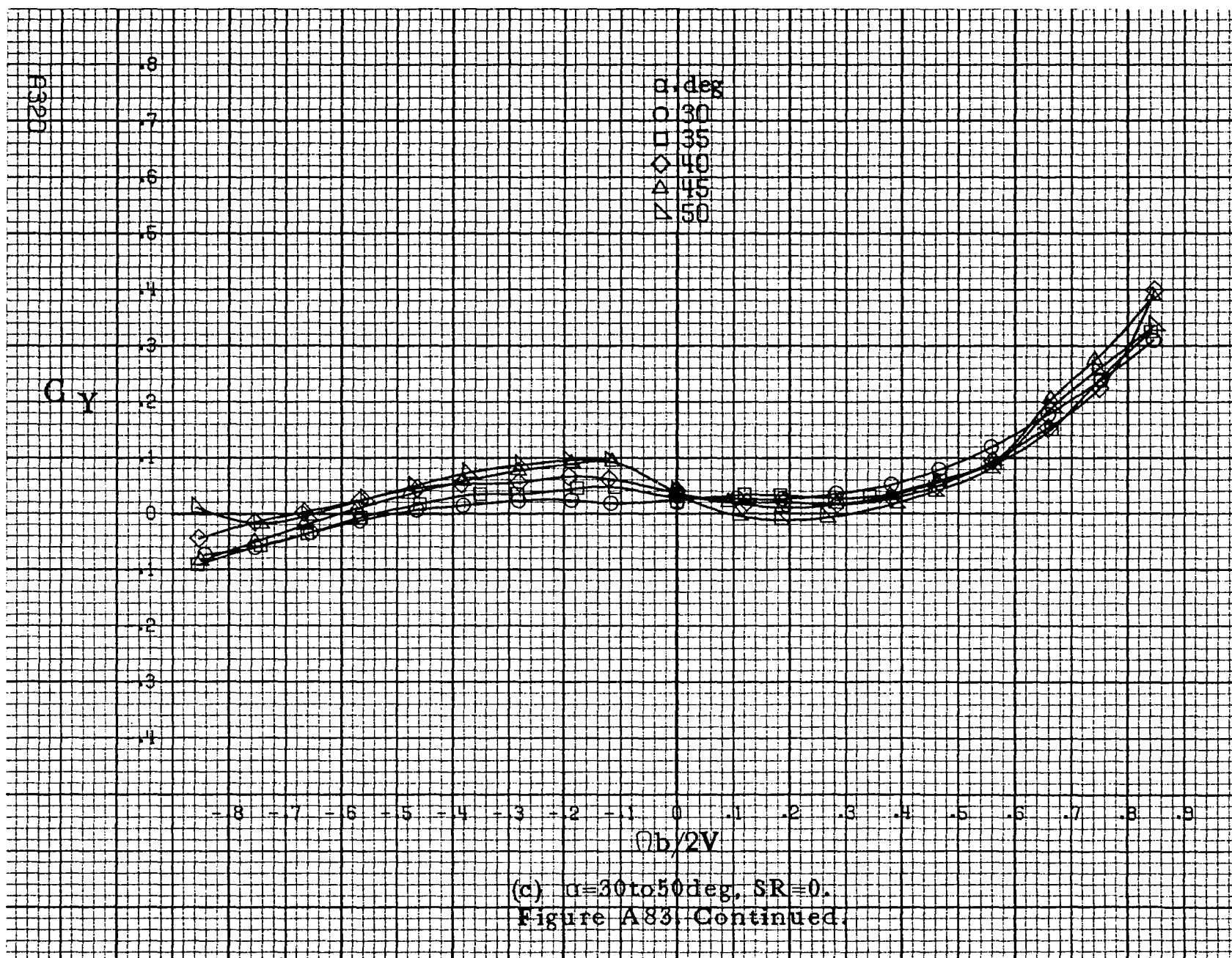
0  
 .1  
 .2  
 .3  
 .4  
 .5  
 .6  
 .7  
 .8

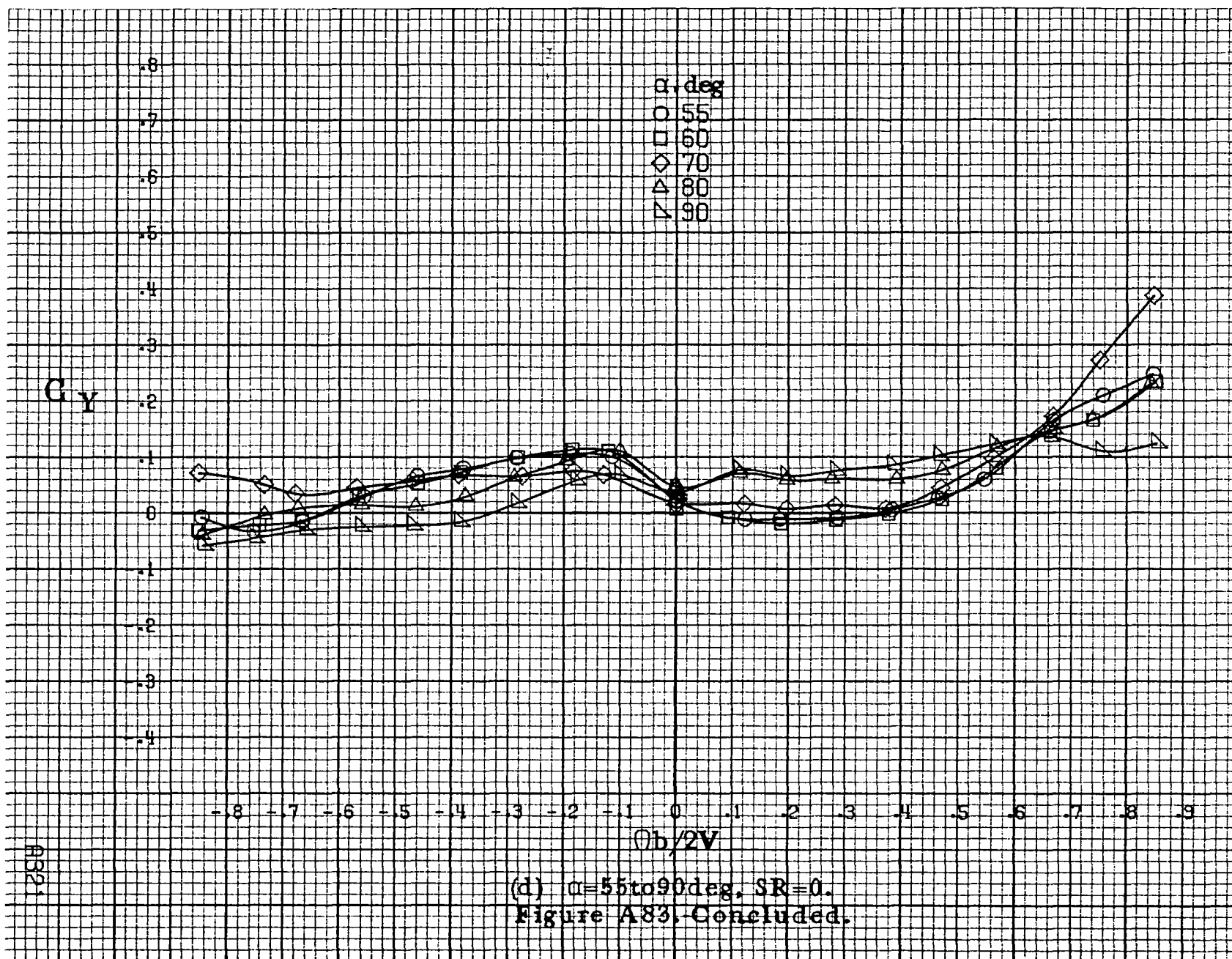
-0.8 -0.7 -0.6 -0.5 -0.4 -0.3 -0.2 -0.1 0 .1 .2 .3 .4 .5 .6 .7 .8

$b/2V$

(b)  $\alpha=18\text{ to }35\text{deg}$ ,  $SR=99\text{cm}(39\text{in})$ .  
 Figure A83. Continued.







F322

C A

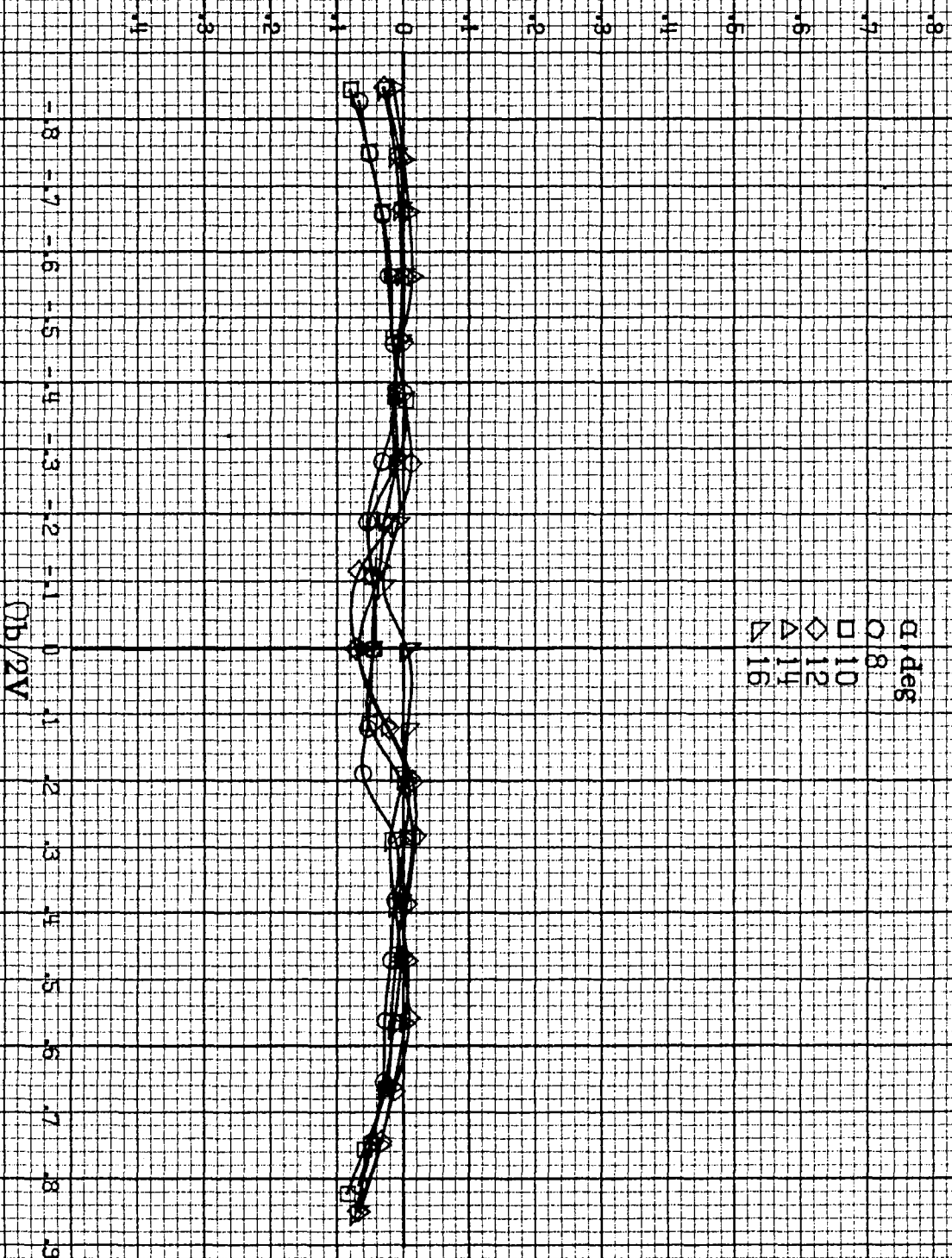
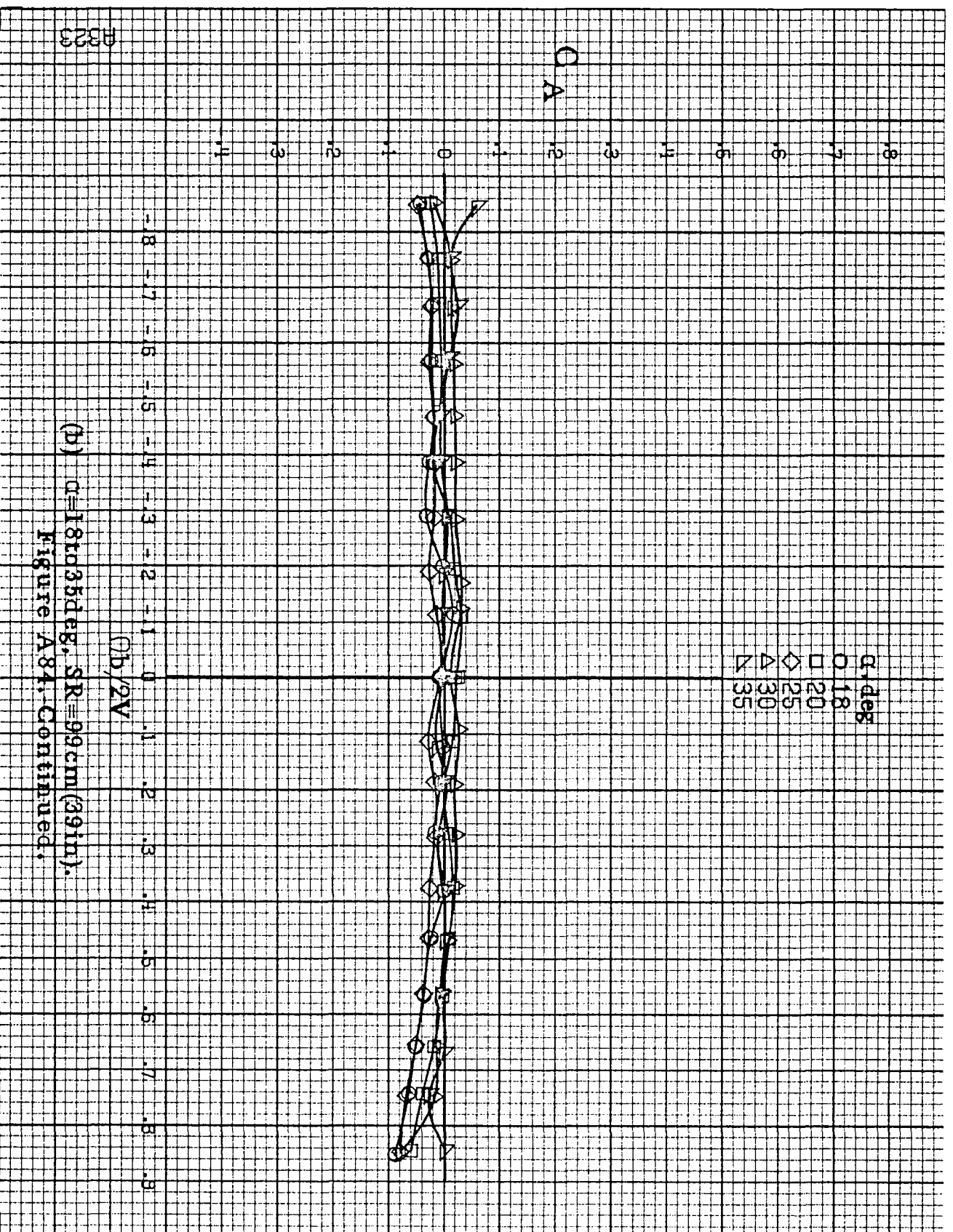
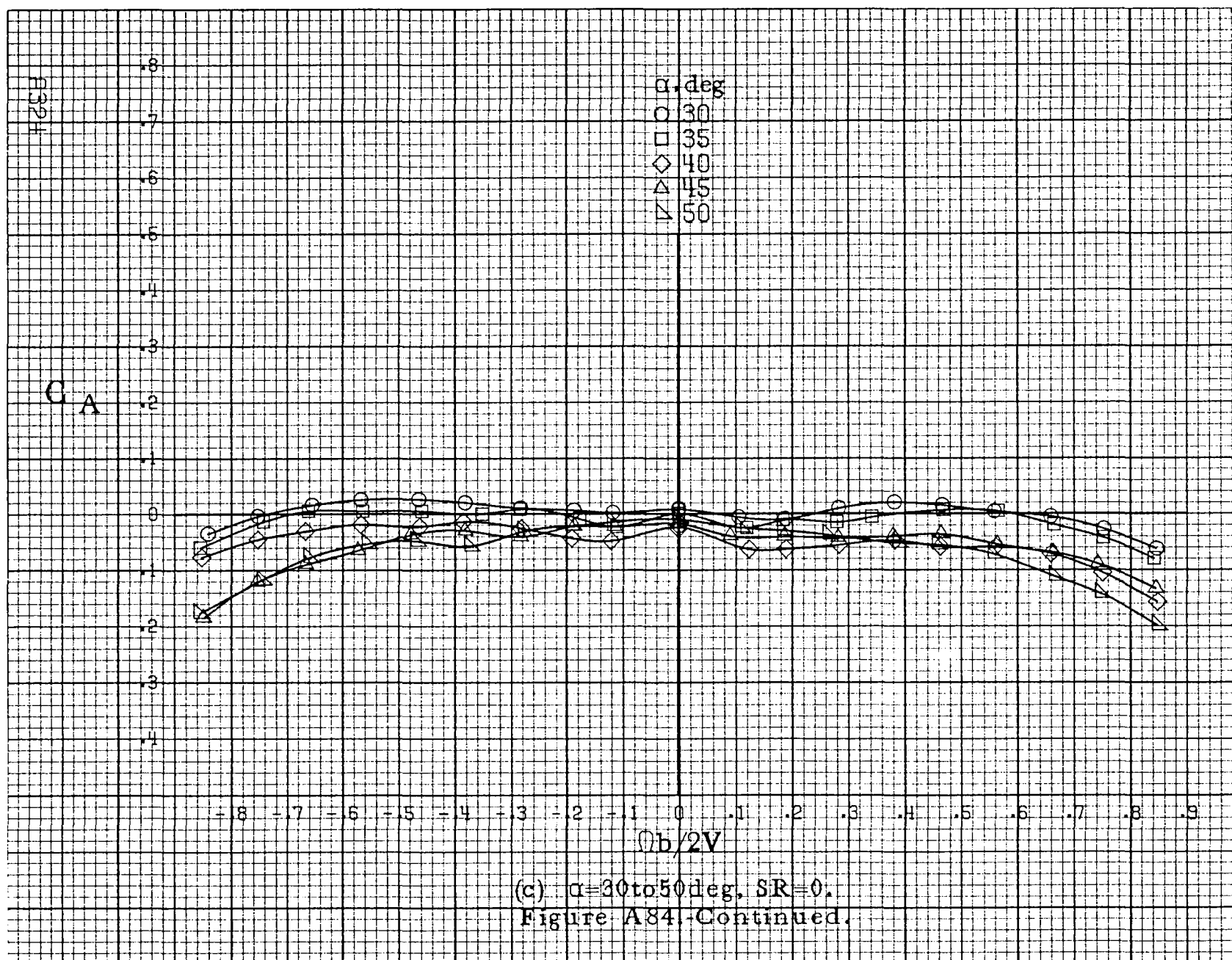
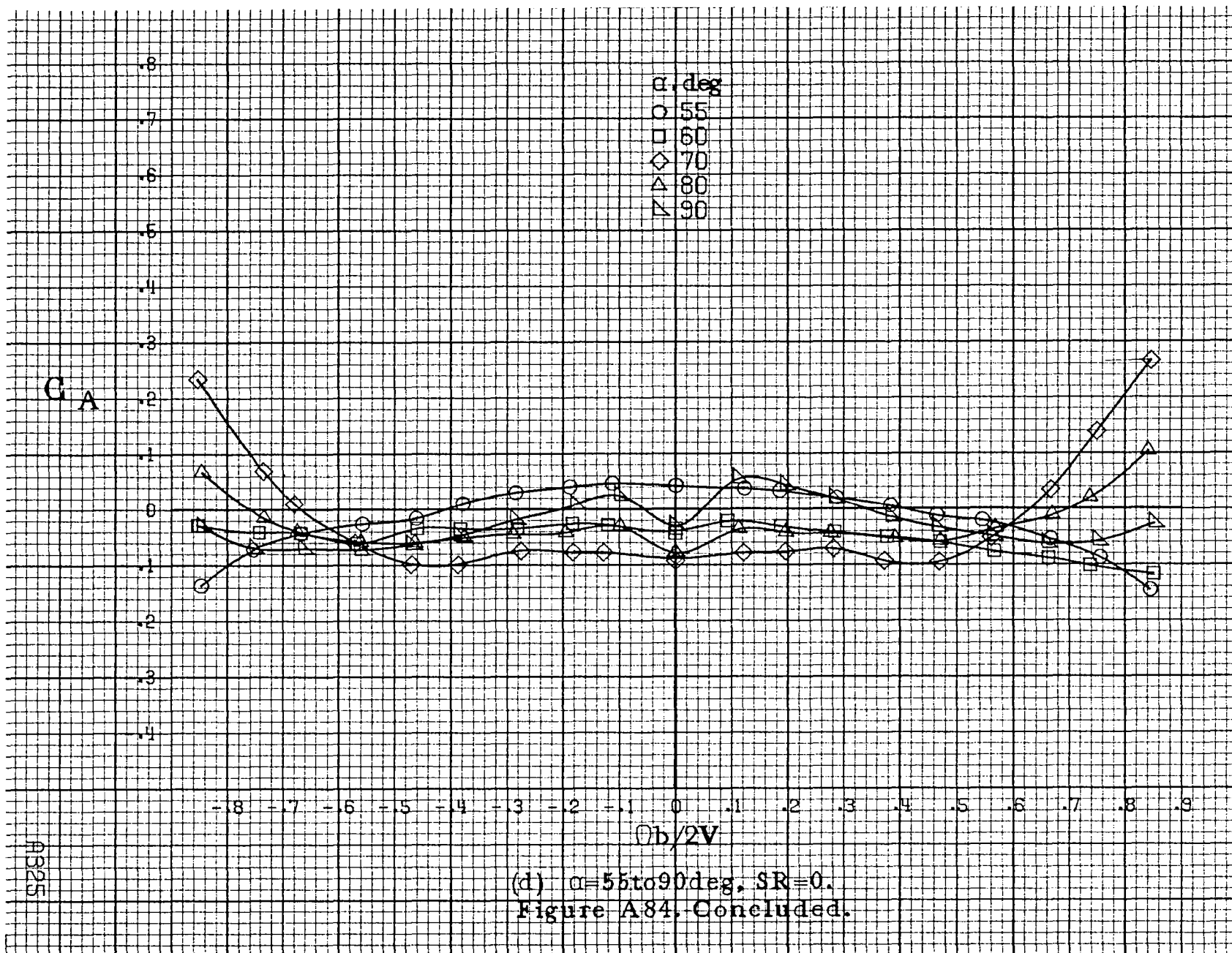
(a)  $G=8$  to  $16$  deg,  $SR=99$  cm (39 in).(b)  $2V$ 

Figure A84. Effect of rotation rate and angle of attack on axial force coefficient for configuration having outward LE wing droop.  $\delta_a = 0^\circ$ ,  $\delta_s = 0^\circ$ .

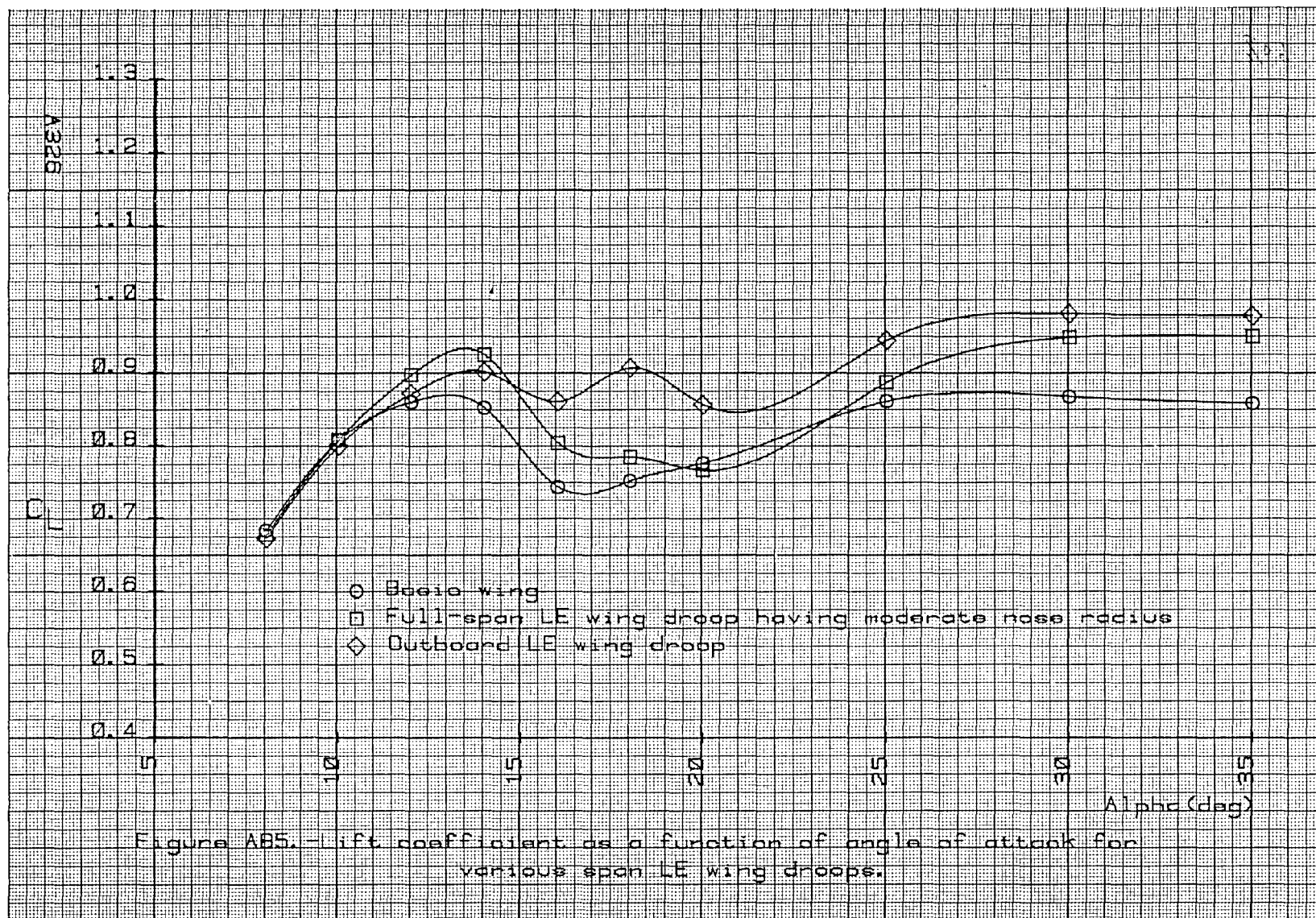


(b)  $\alpha = 18$  to  $35$  deg,  $SR = 99$  cm (39 in.).  
Figure A84. Continued.





















1. Report No. NASA CR-3098		2. Government Accession No.		3. Recipient's Catalog No.	
4. Title and Subtitle Rotary Balance Data for a Typical Single-Engine General Aviation Design for an Angle-of-Attack Range of 8° to 90°. II - Low-Wing Model B				5. Report Date September 1979	
				6. Performing Organization Code	
7. Author(s) William Bihrlé, Jr. Randy S. Hultberg				8. Performing Organization Report No.	
				10. Work Unit No. 505-10-13-07	
9. Performing Organization Name and Address Bihrlé Applied Research, Inc. 400 Jericho Turnpike Jericho, New York 11753				11. Contract or Grant No. NAS1-14849, Task 30	
				13. Type of Report and Period Covered Contractor Report	
12. Sponsoring Agency Name and Address National Aeronautics and Space Administration Washington, DC 20546				14. Sponsoring Agency Code	
15. Supplementary Notes Langley Technical Monitor: James S. Bowman, Jr.  Topical report					
16. Abstract  Aerodynamic characteristics obtained in a rotational flow environment utilizing a rotary balance located in the Langley spin tunnel are presented in plotted form for a 1/6.5-scale, single-engine, low-wing, general aviation airplane model. The configurations tested included the basic airplane, various wing leading-edge devices, tail designs, and rudder control settings as well as airplane components. Data are presented without analysis for an angle-of-attack range of 8° to 90° and clockwise and counter-clockwise rotations covering an $\frac{\Omega b}{2V}$ range from 0 to 0.85.					
17. Key Words (Suggested by Author(s))  General Aviation Spinning Rotary Balance High angle-of-attack wind tunnel data				18. Distribution Statement  Unclassified - Unlimited  Subject Category 02	
19. Security Classif. (of this report) Unclassified	20. Security Classif. (of this page) Unclassified	21. No. of Pages 343	22. Price* \$12.00		





National Aeronautics and  
Space Administration

Washington, D.C.  
20546

Official Business

Penalty for Private Use, \$300



Postage and Fees Paid  
National Aeronautics and  
Space Administration  
NASA-451



**NASA**

LIBRARY MATERIAL SLIP		
DO NOT REMOVE SLIP FROM MATERIAL		
Delete your name from this slip when returning material to the library.		
NAME	DATE	MS
P. Luchessa	11/01	267

If Undeliverable (Section 158  
Postal Manual) Do Not Return